



AFRL-RQ-WP-TR-2017-0163

AIRFRAME DIGITAL TWIN SPIRAL 1

**Task Order 0002: Scalable Accurate Flexible Efficient Robust -
Prognostic and Probabilistic Individual Aircraft Tracking (SAFER-
P²IAT) Full Scale Wing Experiment Plans, Requirements, and
Development**

Liping Wang, Isaac Asher, Kevin Ryan, Genghis Khan, and Randy Longtin

**GE Global Research
General Electric Company**

**Dale Ball, Robert Shannon, and Elias Dakwar
Lockheed Martin Corporation**

**Jochen Hoffmann
KBRWyle**

**APRIL 2017
Final Report**

**DISTRIBUTION STATEMENT A: Approved for public release.
Distribution is unlimited.**

**AIR FORCE RESEARCH LABORATORY
AEROSPACE SYSTEMS DIRECTORATE
WRIGHT-PATTERSON AIR FORCE BASE, OH 45433-7542
AIR FORCE MATERIEL COMMAND
UNITED STATES AIR FORCE**

NOTICE AND SIGNATURE PAGE

Using Government drawings, specifications, or other data included in this document for any purpose other than Government procurement does not in any way obligate the U.S. Government. The fact that the Government formulated or supplied the drawings, specifications, or other data does not license the holder or any other person or corporation; or convey any rights or permission to manufacture, use, or sell any patented invention that may relate to them.

This paper was cleared for public release by the USAF 88th Air Base Wing (88 ABW) Public Affairs Office (PAO) and is available to the general public, including foreign nationals.

Copies may be obtained from the Defense Technical Information Center (DTIC) (<http://www.dtic.mil>).

AFRL-RQ-WP-TR-2017-0163 has been reviewed and is approved for publication in accordance with assigned distribution statement.

This report is published in the interest of scientific and technical information exchange and its publication does not constitute the Government's approval or disapproval of its ideas or findings.

REPORT DOCUMENTATION PAGE					Form Approved OMB No. 0704-0188	
<p>The public reporting burden for this collection of information is estimated to average 1 hour per response, including the time for reviewing instructions, searching existing data sources, gathering and maintaining the data needed, and completing and reviewing the collection of information. Send comments regarding this burden estimate or any other aspect of this collection of information, including suggestions for reducing this burden, to Department of Defense, Washington Headquarters Services, Directorate for Information Operations and Reports (0704-0188), 1215 Jefferson Davis Highway, Suite 1204, Arlington, VA 22202-4302. Respondents should be aware that notwithstanding any other provision of law, no person shall be subject to any penalty for failing to comply with a collection of information if it does not display a currently valid OMB control number. PLEASE DO NOT RETURN YOUR FORM TO THE ABOVE ADDRESS.</p>						
1. REPORT DATE (DD-MM-YY) April 2017		2. REPORT TYPE Final		3. DATES COVERED (From - To) 24 November 2014 – 20 March 2017		
4. TITLE AND SUBTITLE AIRFRAME DIGITAL TWIN SPIRAL 1 Task Order 0002: Scalable Accurate Flexible Efficient Robust - Prognostic and Probabilistic Individual Aircraft Tracking (SAFER-P2IAT) Full Scale Wing Experiment Plans, Requirements, and Development				5a. CONTRACT NUMBER FA8650-14-D-2443-0002		
				5b. GRANT NUMBER		
				5c. PROGRAM ELEMENT NUMBER 62201F		
6. AUTHOR(S) Liping Wang, Isaac Asher, Kevin Ryan, Genghis Khan, and Randy Longtin (GE Global Research, General Electric Company) Dale Ball, Robert Shannon, and Elias Dakwar (Lockheed Martin Corporation) Jochen Hoffmann (KBRWyle)				5d. PROJECT NUMBER 2401		
				5e. TASK NUMBER		
				5f. WORK UNIT NUMBER Q1C2		
7. PERFORMING ORGANIZATION NAME(S) AND ADDRESS(ES) GE Global Research General Electric Company 1 Research Circle Niskayuna, NY 12309				8. PERFORMING ORGANIZATION REPORT NUMBER Lockheed Martin Corporation KBRWyle		
9. SPONSORING/MONITORING AGENCY NAME(S) AND ADDRESS(ES) Air Force Research Laboratory Aerospace Systems Directorate Wright-Patterson Air Force Base, OH 45433-7542 Air Force Materiel Command United States Air Force				10. SPONSORING/MONITORING AGENCY ACRONYM(S) AFRL/RQVS		
				11. SPONSORING/MONITORING AGENCY REPORT NUMBER(S) AFRL-RQ-WP-TR-2017-0163		
12. DISTRIBUTION/AVAILABILITY STATEMENT DISTRIBUTION STATEMENT A: Approved for public release. Distribution is unlimited.						
13. SUPPLEMENTARY NOTES PA Case Number: 88ABW-2018-5202; Clearance Date: 17 October 2018.						
14. ABSTRACT Improving the accuracy of structural diagnosis and prognosis to make better maintenance decisions is accomplished through more realistic structural analysis of fatigue crack growth, including sources of uncertainty into predictions, and fusing usage and inspection data to update and reduce uncertainty. A set of methods for uncertainty quantification and updating form the basis of the framework. Modularity supports transition to other platforms and reliability problems. Uncertainty in inputs and outputs is described by parametric or non-parametric probability distributions. Criteria for performing inspections can be established based on probabilities of events.						
15. SUBJECT TERMS Uncertainty quantification, Bayesian updating, inspection scheduling, probabilistic crack growth						
16. SECURITY CLASSIFICATION OF:			17. LIMITATION OF ABSTRACT: SAR	18. NUMBER OF PAGES 304	19a. NAME OF RESPONSIBLE PERSON (Monitor) Eric J. Tuegel 19b. TELEPHONE NUMBER (Include Area Code) N/A	
a. REPORT Unclassified	b. ABSTRACT Unclassified	c. THIS PAGE Unclassified				

TABLE OF CONTENTS

Section	Page
LIST OF FIGURES	ii
LIST OF TABLES	iv
ACKNOWLEDGEMENTS	v
1.0 EXECUTIVE SUMMARY	1
2.0 INTRODUCTION.....	2
3.0 CONTROL POINT SELECTION	4
4.0 WING LOAD APPLICATION	19
4.1 Test Load Cases	19
4.1.1 Actuator Loads.....	39
4.1.2 Reaction Loads.....	44
4.1.3 Tare Loads.....	46
4.2 Baseline Spectrum	46
5.0 FLIGHT RECORDER DATA & TEST SPECTRUM.....	48
6.0 INSTRUMENTATION AND DATA ACQUISITION	50
6.1 Internal Safety of Test and CP Instrumentation	51
6.2 Outer Mold Line (OML) Safety of Test Instrumentation	51
7.0 INSPECTION TECHNIQUES AND PROCEDURES	56
7.1 Inspection Plan and Procedures.....	56
7.2 Coupon Testing	57
8.0 FINALIZING P ² IAT: FE & SIF MODELS, BASELINE PREDICTIONS.....	63
8.1 Global and Local FE models	65
8.2 FE model levels of fidelity	74
8.3 Green's Function	82
8.4 SIF Models	85
8.5 Initial SFPOF Predictions	88
9.0 CONCLUSIONS.....	94
10.0 REFERENCES.....	95
Appendix A – Internal Safety of Test and CP Gauges	96
Appendix B – OML Safety of Test Gauges	118
Appendix C – Inspection Plan Details	160
Appendix D – Control Point SIF Models.....	176
Appendix E – Baseline Prediction Initial Conditions.....	223
Appendix F – Control Point Baseline Predictions.....	233
Appendix G – Master Event Sequence	263
Appendix H – Load Application TRD.....	264
LIST OF SYMBOLS, ABBREVIATIONS, AND ACRONYMS	295

LIST OF FIGURES

Figure	Page
Figure 1. IAT control point summary	7
Figure 2. GE01 control point details	9
Figure 3. GE02 control point details	10
Figure 4. GE03 control point details	11
Figure 5. GE04 control point details	12
Figure 6. GE05 control point details	13
Figure 7. GE06 control point details	14
Figure 8. GE07 control point details	15
Figure 9. GE08 control point details	16
Figure 10. GE09 control point details	17
Figure 11. GE10 control point details	18
Figure 12. Wing station 3 moment vs. torque diagram for maneuver load cases	20
Figure 13. Moment vs. wing station for limit load case 100101 (Cond. 1)	21
Figure 14. Shear vs. wing station for limit load case 100101 (Cond. 1)	22
Figure 15. Torque vs. wing station for limit load case 100101 (Cond. 1)	23
Figure 16. Moment vs. wing station for limit load case 100102 (Cond. 2)	24
Figure 17. Shear vs. wing station for limit load case 100102 (Cond. 2)	25
Figure 18. Torque vs. wing station for limit load case 100102 (Cond. 2)	26
Figure 19. Moment vs. wing station for limit load case 100201 (Cond. 3)	27
Figure 20. Shear vs. wing station for limit load case 100201 (Cond. 3)	28
Figure 21. Torque vs. wing station for limit load case 100201 (Cond. 3)	29
Figure 22. Moment vs. wing station for limit load case 100202 (Cond. 4)	30
Figure 23. Shear vs. wing station for limit load case 100202 (Cond. 4)	31
Figure 24. Torque vs. wing station for limit load case 100202 (Cond. 4)	32
Figure 25. Moment vs. wing station for limit load case 100301 (Cond. 5)	33
Figure 26. Shear vs. wing station for limit load case 100301 (Cond. 5)	34
Figure 27. Torque vs. wing station for limit load case 100301 (Cond. 5)	35
Figure 28. Wing displacement for limit load case 100101 (Cond. 1)	36
Figure 29. Wing displacement for limit load case 100102 (Cond. 2)	37
Figure 30. Wing displacement for limit load Case 100201 (Cond. 3)	37
Figure 31. Wing displacement for limit load case 100202 (Cond. 4)	38
Figure 32. Wing displacement for limit load case 100301 (Cond. 5)	38
Figure 33. ADT test article with load jacks in place	39
Figure 34. Load pad configuration and FS-BL coordinates (in.) for load actuators	40
Figure 35. Wing station 3 moment vs. torque diagram for the baseline MES	47
Figure 36. Process for creating the FRD to loads model	49
Figure 37. Left upper torque box skin strain gage locations and measurements	52
Figure 38. Detail of LAISU-2 strain gauge installation location	53
Figure 39. Detail location of LAISU strain gauge	54
Figure 40. Outboard lower skin OML strain gauge locations	55
Figure 41. Fatigue cracks introduced in GE09 simulating coupon panel	59
Figure 42. Microscopic images of cracks in GE09 simulating coupon panel	60
Figure 43. Eddy current inspection approach	62
Figure 44. Process for Creating Stress Intensity Factor Model	65

Figure 45. GE0 5/GE07 submodel details	67
Figure 46. GE04/GE08 fine-grid FE submodel	68
Figure 47. GE05/GE07 (left/right, respectively) morphing definitions.....	69
Figure 48. GE04/GE08 (left/right, respectively) morphing definitions.....	69
Figure 49. GE05/GE07 morphing DOE stress results	72
Figure 50. GE04/GE08 morphing DOE stress results	73
Figure 51. Crack plane orientation and far-field stress comparisons for GE04.....	74
Figure 52. Crack plane stress field for GE04 DOE run number 4.....	74
Figure 53. Table of levels of FE model fidelity.....	76
Figure 54. GE04 crack plane stress orientation with level 3 model fidelity.....	76
Figure 55. High bearing load stress field (GE4- level 3 results)	77
Figure 56. Tension load only stress field (benchmark example).....	78
Figure 57. Crack plane orientation and far-field stress comparison for GE04 level 3 and level 4 FE models	79
Figure 58. Crack plane stress comparison for GE04 level 3 and level 4 FE models.....	79
Figure 59. Comparison of bolt hole frictionless contact models	81
Figure 60. FE Model Definition for Green's Function.....	83
Figure 61. Surface crack configuration.....	85
Figure 62. Table of SIF models	86
Figure 63. Example SIF probabilistic model	87
Figure 64. Initial SFPOF prediction plot for GE02	89
Figure 65. Initial SFPOF prediction for GE04.....	90
Figure 66. Initial SFPOF prediction for GE07.....	91
Figure 67. Example SFPOF without smoothing (interpolation).....	92
Figure 68. SFPOF before and after smoothing logic	92
Figure 69. Initial crack growth predictions- SFPOF plot for GE07 for 1000 flights.....	93

LIST OF TABLES

Table	Page
Table 1. IAT Control Point Summary.....	5
Table 2. IAT Control Point Summary (continued)	6
Table 3. Control point geometry details	8
Table 4. Jack load for limit cases (in-lbs)	41
Table 5. Up-bend max actuator displacements each actuator zone	42
Table 6. Down-bend min actuator displacements each actuator zone	42
Table 7. Pad locations and loads for minimum and maximum actuator loads	43
Table 8. Wing to test frame attach locations and reaction loads for limit load cases (in-lbs)	45
Table 9. Tare loads (in-lbs)	46
Table 10. NDI Control point overview	57
Table 11. CP morphing DOE parameters	71

ACKNOWLEDGEMENTS

This report is based upon work supported by AFRL under Contract FA8650-14-D-2443-0002, under the direction of Dr. Pam Kobryn, Dr. Eric Tuegel and Mr. Scott Wacker.

The authors would like to thank the following for their contributions to the Airframe Digital Twin project that helped make it a success. From GE Global Research, the original team which formed the basis of our approach was Felipe Viana and Sergio Choze. All the finite element work at GE was performed by Changjie Sun, Sunilkumar Soni, and Randy Longtin.

At Lockheed Martin, Don Dubowski shared engineering insight and helped run many analyses. Elias Dakwar helped with control point selection and loads development.

At Wyle Aerospace, Jochen Hoffman was our knowledgeable NDI expert.

At Unison, Hua Jiang was always helpful and retrieved all blueprint drawings.

At Vanderbilt University, Professor Sankaran Mahadevan provided guidance on methods and early proofs-of-concept. Chenzhao Li interned with GE, worked on a GUI, and developed the sensitivity methods.

At the Air Force Research Laboratory, the entire digital twin team has been wonderful to work with. They have consistently provided guidance and insight and pushed us to do our best. We remember Ned Lindsley fondly and appreciate his insight into fighter aircraft systems and analyses. His practical and straight forward advice kept the project going forward. Daniel Sparkman provided mathematical insight and encouraged excellent discourse. We also thank Scott Wacker for taking over an important role with seriousness, commitment, and a strong vision.

It is difficult to overstate the impact of Pam Kobryn, Eric Tuegel, and Doug Henderson. Their vision of digital twin inspired the team and much of the engineering world. Their relentless and detailed work has brought the concept of digital twin to life.

1.0 EXECUTIVE SUMMARY

The overall goal of the Airframe Digital Twin program is to improve the accuracy of structural diagnosis and prognosis in order to make better maintenance decisions. This is accomplished by more realistic structural analysis models of fatigue crack growth, including a variety of sources of uncertainty into predictions, and fusing usage and inspection data to update and reduce uncertainty in predictions. The integrated models comprise the Prognostic and Probabilistic Individual Aircraft Tracking framework. A set of methods for uncertainty quantification and updating form the basis of the framework. Modularity allows the methods to be easily applied to other platforms and reliability problems. Uncertainty in input parameters and output variables can be described by parametric and non-parametric probability distributions. Criteria for performing inspections can be established based on probabilities of events or known schedules.

The primary objective of the Airframe Digital Twin Task Order 0002 is to develop the requirements and plans for the experiments to demonstrate the Scalable Accurate Flexible Efficient Robust (SAFER) - Prognostic, Probabilistic Individual Aircraft Tracking (P²IAT) process developed in Task Order 0001, and to prepare two fighter aircraft wings to be used in the demonstration experiment. The demonstration experiment will consist of scheduled cyclical loading of two wings to simulate flight conditions. At regular intervals, the wings will be inspected and the test data will be fed into the SAFER-P²IAT framework.

The requirements, plans, and development efforts for the full-scale experiment are provided. A baseline set of predictions from the SAFER-P²IAT framework is also provided to demonstrate the performance of the method.

2.0 INTRODUCTION

The first task in the Prognostic and Probabilistic Individual Aircraft Tracking - SAFER-P²IAT is the development of probabilistic aircraft usage and loads, followed by the probabilistic structural reliability analysis, statistical updating, and decision making analysis. A report number, AFRL-RQ-WP-TR-2016-0140 [1], has been submitted documenting the engineering analyses modeling efforts in building the SAFER-P²IAT framework.

The second task order (Task Order 2) in the Airframe Digital Twin program is the development of the requirements and plans for the full-scale ground test experiments that demonstrates the SAFER-P²IAT framework developed in the first task. The second task includes the following objectives:

- **Selection of locations to be tracked:** Select a list of locations to be tracked by the P²IAT framework during the experiment. These locations are referred to as Control Points (CPs). Each control point will be chosen as a result of a rigorous all-source analysis of critical locations on the wing. The geometry for each CP is to be fully investigated and inspected- complete with structural analyses and crack growth models.
- **Wing load application:** Develop actuator layout and loads for the outer wing that adequately represents the maneuvers in the probabilistic load spectrum developed in Task Order 1 of the program. Design the loading equipment and test fixtures, along with a defined jack-load actuator sequence in a baseline Master Event Sequence (MES) from which the demonstration experiment load spectrum will be created.
- **Conversion of test spectrum to flight recorder data:** Build a model capable of translating the flight recorder data (FRD) to the appropriate wing loading configuration. This translation will allow for simulated flight data generated during the experiment. Each ‘maneuver’ in the MES will be represented by a set of loads and corresponding actuator positions.
- **Instrumentation and data acquisition:** Determine the instrumentation necessary to monitor the condition of the wings during the entirety of the experiment. The goal is to quickly ascertain the condition of each wing without stopping the test. A primary focus is set on safety of test. Acquire and install all internal instrumentation (sensors, wiring, and data acquisition equipment) necessary for the test.
- **Inspection plan:** Develop a plan for inspecting the Control Points for fatigue crack growth during the experiment. Create an inspection plan that identifies the locations to be inspected, the frequency of inspections, and details on the inspection technique. Include all sensor information- including data, calibration procedures, location and orientation of the sensors.
- **Finalize P²IAT for all control points:** Finalize the P²IAT framework in its entirety for the Control Points selected in Task Order 2. Build probabilistic stress models (fine-grid or coarse-grid) for each control point. Use the stress models to build probabilistic stress intensity factor (SIF) models for direct implementation into the

P²IAT framework developed in Task 1. Use the finalized P²IAT framework to perform initial baseline crack growth forecasts for all the control points.

The successful completion of Task Order 2 culminates in the execution of the P²IAT framework on the control point locations to be tracked during the ground-test experiment. Running the P²IAT framework and calculating baseline crack growth predictions provides a first-look at how the software will perform during the experiment. The following Task Order 2 final report will discuss the goals and accomplishments of each of the objectives (or subtasks) outlined above.

3.0 CONTROL POINT SELECTION

The CPs to be monitored during the ADT wing test are to be selected per the following four criteria (in order of highest to lowest priority):

- Cracks found during full-scale durability tests (FSDT), i.e., locations with known cracking from the FSDT
- Inspectability – i.e. locations at which NDI is possible. The aircraft specific inspection technical order was used to aid in criterion.
- Finite Element Analysis (FEA) Survey – i.e. locations for which the medium grid air vehicle finite element model (AV FEM) indicates high stresses when subjected to a reference load case (+8.4g symmetric pullup maneuver)
- Short life indicated in legacy Damage Tolerance Assessment (DTA) reports– i.e. locations at which comparatively short fatigue crack growth life was predicted during previous DTAs.

Whether cracks are found or not during full-scale durability tests is the primary source for selection of the control points, followed by accessibility for NDI inspections. The FEA survey under multiple load cases using the AV FEM analysis is used to consider the high stress locations. Finally, the short life indicated in the DTA report is also considered as one of the important criteria in refinement of the control points. Another primary source of information for the selection and detailing of control points is the engineering drawings of the wing where the location, shape, nominal dimensions and manufacturing tolerances (for uncertainty propagation) can be obtained.

The control point selection process resulted in the selection of ten locations. Using the four criteria above, and after coordination with both AFRL and the Northrop-Grumman (NGC) team, ten CPs (labelled GE01 through GE10) were selected, as shown in Table 1 / Table 2 and Figure 1. As shown in Figure 1, five of the GE CPs are common with NGC CPs. Geometry details of the control points are provided in Table 3. Data and photographs for each of the ten CPs are shown in Figure 2 through Figure 11. CP locations in these figures are listed in terms of the fuselage station (FS), butt line (BL), and wing station (WS) values.

Table 1. IAT Control Point Summary

Control Point	Location	Cracking History	Flaw Details	Inspection Instrumentation	FEA Survey σ_{\max} Up Bend
GE01	Lower wing skin, fastener hole common to XW206 rib, first hole forward of main spar	Crack found at this location during FSDT	Corner crack at fastener hole in wing skin. (1 st layer corner crack at faying surface)	PAUT and SEC from the outside lower surface	10 ksi
GE02	Aft lower wing skin at aft closure spar, Thickness step approx. XW 157	No known cracks during FSDT. No known cracks in the fleet.	Surface crack in fillet radius at thickness step. Consider installation of pre-flaw at test start.	Inspection from outside using EC possible due to 0.045" thickness. Crack gage placed on starter notch.	40 ksi
GE03	Lower wing skin trailing edge. Fastener hole common with aft closure beam, 3rd hole outbd from XW155	Crack found at 16,000 hours during FSDT	Corner crack at fastener hole in wing skin	Same as GE01	16 ksi
GE04	Lower trailing edge wing skin, at rear spar	No known cracks during FSDT. No known cracks in the fleet.	Single corner crack at fastener hole (crack at faying surface). Interference fit fastener	PAUT and SEC from the outside lower surface	32 ksi
GE05	Lower wing skin forward edge thickness step at XW 158	Crack found at 18,100 hours during FSDT	Corner crack in radius	PAUT from the outside; Crack gage placed at edge of flange or OML surface	25 ksi
GE06	Lower forward wing skin, 1st fastener inboard from XW 188; fwd from 2nd stringer from leading edge	Crack found at 18,100 hours during FSDT	Corner crack in fastener hole (1st layer corner crack at faying surface)	Same as GE01	9 ksi

Table 2. IAT Control Point Summary (continued)

Control Point	Location	Cracking History	Flaw Details	Inspection Instrumentation	FEA Survey σ_{\max} Up Bend
GE07	Lower forward wing skin at front spar	No known cracks during FSDT. No known cracks in the fleet.	Single corner crack at fastener hole (crack at faying surface). Interference fit fastener.	PAUT and SEC from the outside lower surface.	20 ksi
GE08	Aft lower wing skin under the aft spar, fastener hole at XW 162	No known cracks during FSDT. No known cracks in the fleet.	Corner crack in fastener hole.	PAUT and SEC from the outside lower surface.	22 ksi
GE09	Main spar, fastener hole in lower flange at approx. XW168	No known cracks during FSDT. No known cracks in the fleet.	Corner crack at fastener hole in spar cap (1st layer corner crack at faying surface)	PAUT and SEC from the inside through access port in upper skin	25 ksi
GE10	Lower aft wing skin at main spar, 5th fastener from XW155 aft from main spar	Broken ligament found at 18,100 hours during FSDT	Corner crack at fastener hole in wing skin (1st layer corner crack at faying surface)	Same as GE1	20 ksi

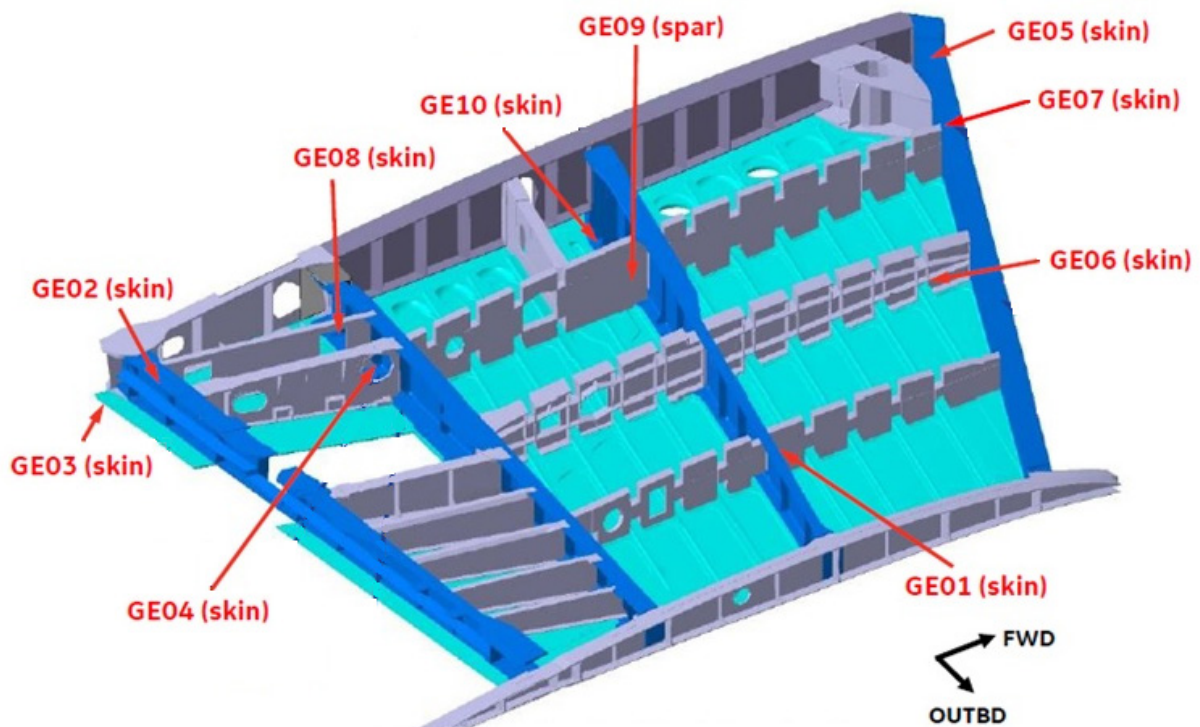


Figure 1. IAT control point summary

Table 3. Control point geometry details

Parameter	GE01	GE02	GE03	GE04	GE05
width (in):	2	4	2	2	4
diameter (in):	0.19	0	0.19	0.19	0
edge distance (in):	0.4	2	0.4	0.4	2
height (in):	10	10	10	10	10
thickness (in):	0.12	0.045	0.16	0.075	0.045
joint type:	single shear clamped	N/A	single shear clamped	single shear clamped	N/A
analysis location:	bottom (faying) surface	N/A	bottom (faying) surface	bottom (faying) surface	N/A
fastener fit:	neat-fit (default)	N/A	neat-fit (default)	neat-fit (default)	N/A
Parameter	GE06	GE07	GE08	GE09	GE10
width (in):	2	2	2	2	2
diameter (in):	0.19	0.19	0.19	0.19	0.19
edge distance (in):	0.4	0.4	0.4	0.4	0.4
height (in):	10	10	10	10	10
thickness (in):	0.12	0.154	0.109	0.235	0.14
joint type:	single shear clamped	single shear clamped	single shear clamped	single shear clamped	single shear clamped
analysis location:	bottom (faying) surface	bottom (faying) surface	bottom (faying) surface	bottom (faying) surface	bottom (faying) surface
fastener fit:	neat-fit (default)	neat-fit (default)	neat-fit (default)	neat-fit (default)	neat-fit (default)
*width and height measurements are engineering estimates of applicable region of influence limits					

GE01 – Wing Skin, Lower, Forward, Fastener Hole at XW206 Rib

Control Point	Location	Cracking History	Ref. Stress (mg-FEM)	Geometry / Flaw Details	Inspection Instrumentation
GE01	FS = 650.0 BL = 205.8 WL = 125.0	Crack found at this location during FSDT	$\sigma_{\max-\text{prin}} = 15 \text{ ksi}$ (LC: +8.4g symmetric pullup)	Single corner crack at fastener hole (crack at faying surface). Neat-fit fastener type.	PAUT and SEC from the outside lower surface

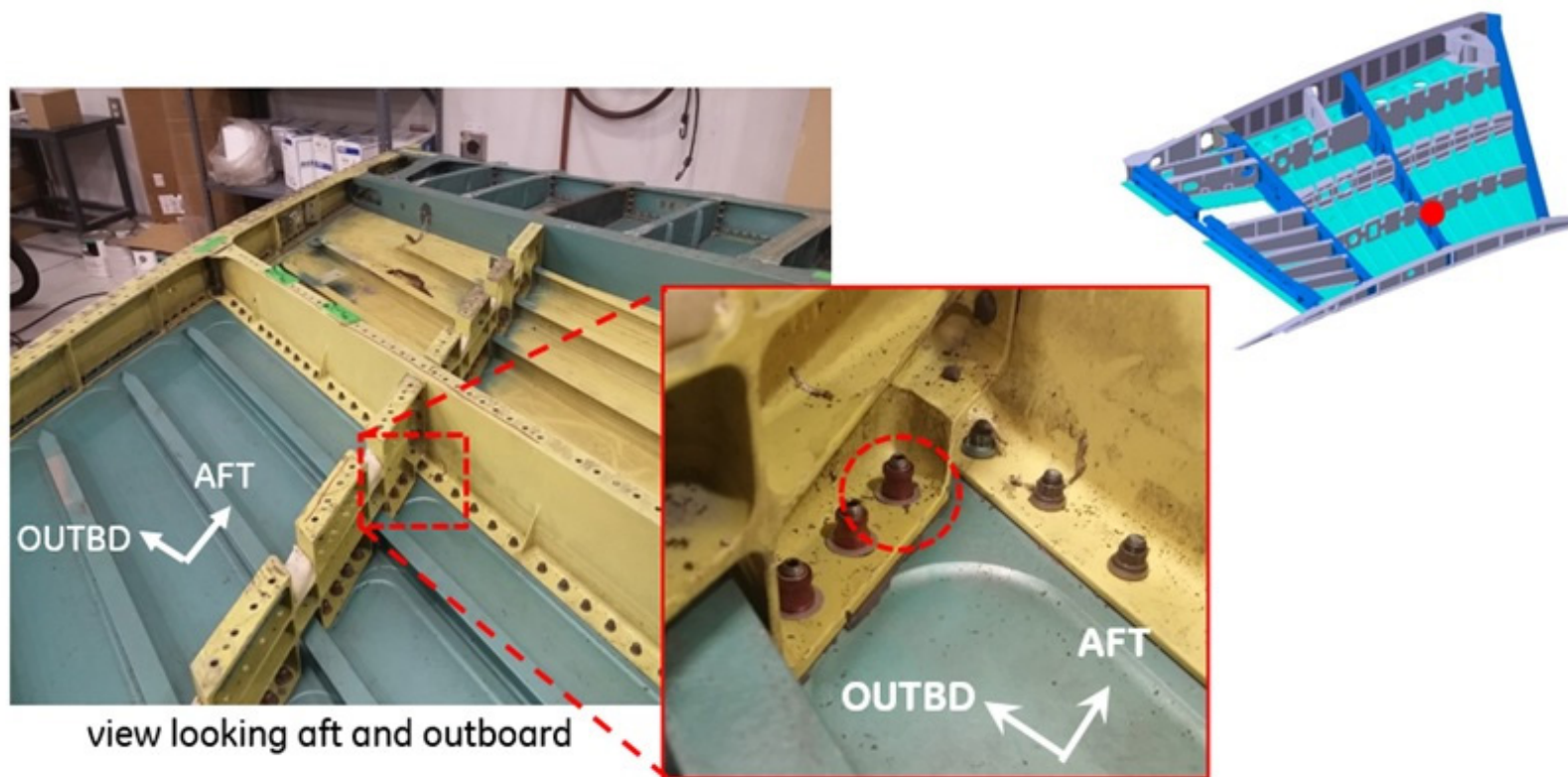


Figure 2. GE01 control point details

GE02 – Wing Skin, Lower Trailing Edge, at Aft Closure Spar at XW157

Control Point	Location	Cracking History	Ref. Stress (mg-FEM)	Geometry / Flaw Details	Inspection Instrumentation
GE02	FS = 671.7 BL = 159.0 WL = 125.7	No known cracks during FSDT No known cracks in the fleet.	$\sigma_{\text{max-prin}} = 40 \text{ ksi}$ (LC: +8.4g symmetric pullup)	Surface crack in fillet radius at thickness step. (crack at interior surface).	SEC Inspection from outside. Crack gages on expected crack path on inside.

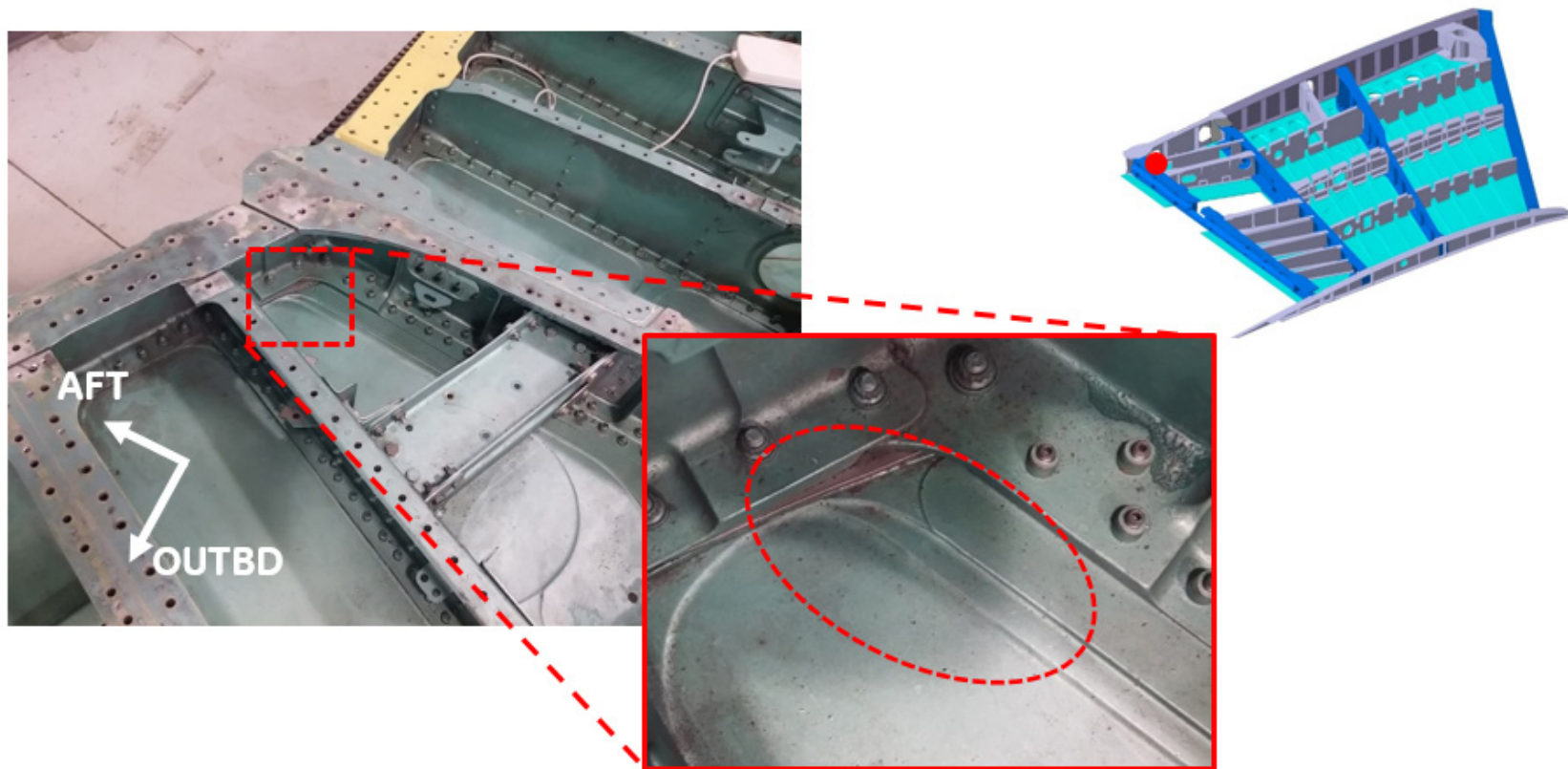


Figure 3. GE02 control point details

GE03 – Wing Skin, Lower Trailing Edge, Fastener Hole at XW158

Control Point	Location	Cracking History	Ref. Stress (mg-FEM)	Geometry / Flaw Details	Inspection Instrumentation
GE03	FS = 673.4 BL = 155.0 WL = 125.8	Crack found at 16,000 hours during FSDT	$\sigma_{max-prin} = 16$ ksi (LC: +8.4g symmetric pullup)	Single corner crack at fastener hole (crack at faying surface). Interference-fit fastener.	PAUT and SEC from the outside lower surface

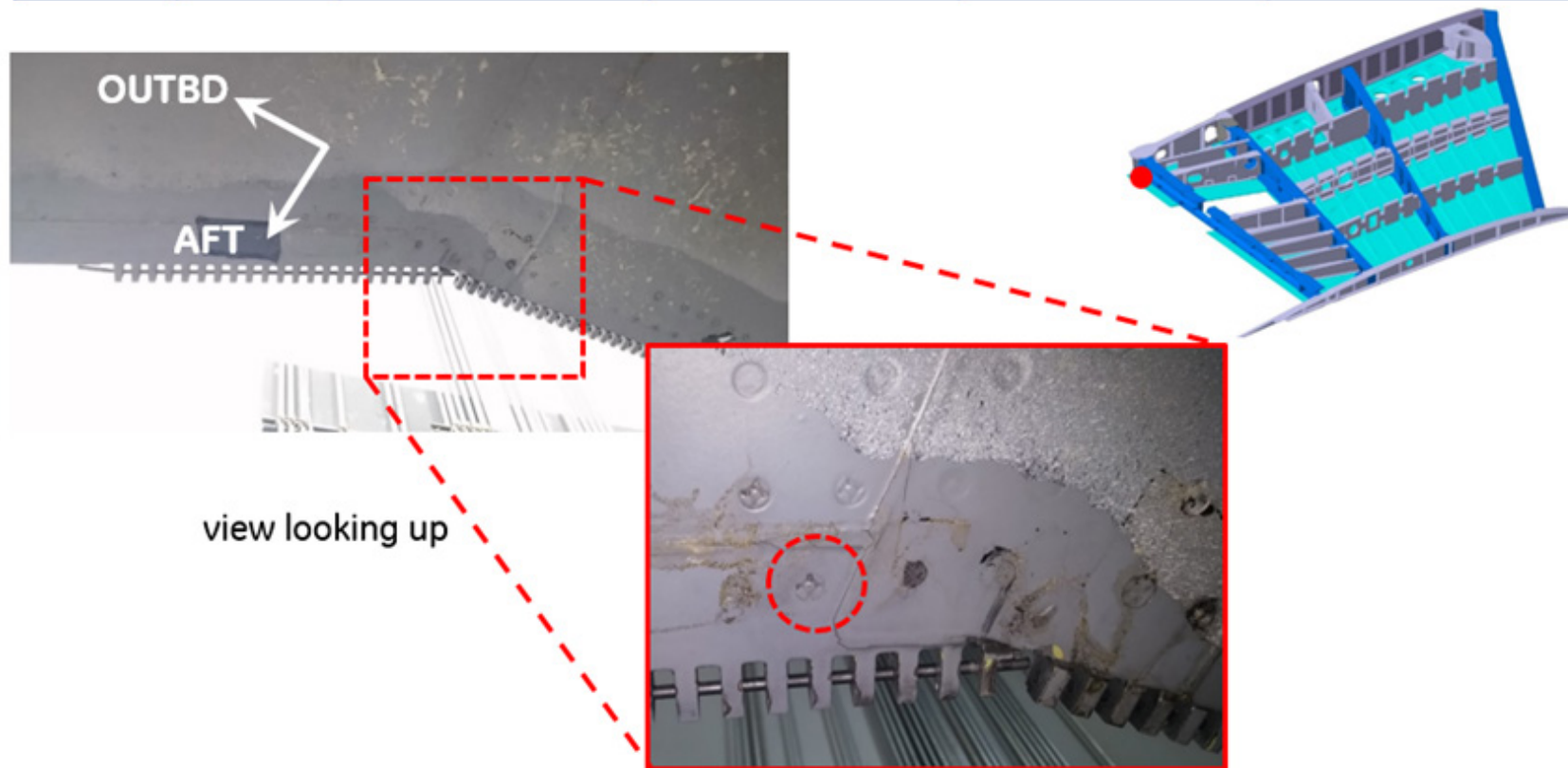


Figure 4. GE03 control point details

GE04 – Lower Trailing Edge Wing Skin, Fastener Hole at Rear Spar

Control Point	Location	Cracking History	Ref. Stress (mg-FEM)	Geometry / Flaw Details	Inspection Instrumentation
GE04	FS = 656.7 BL = 167.7 WL = 125.1	No known cracks during FSDT. No known cracks in the fleet.	$\sigma_{\text{max-prin}} = 32 \text{ ksi}$ (LC: +8.4g symmetric pullup)	Single corner crack at fastener hole (crack at faying surface). Interference-fit fastener.	PAUT and SEC from the outside lower surface

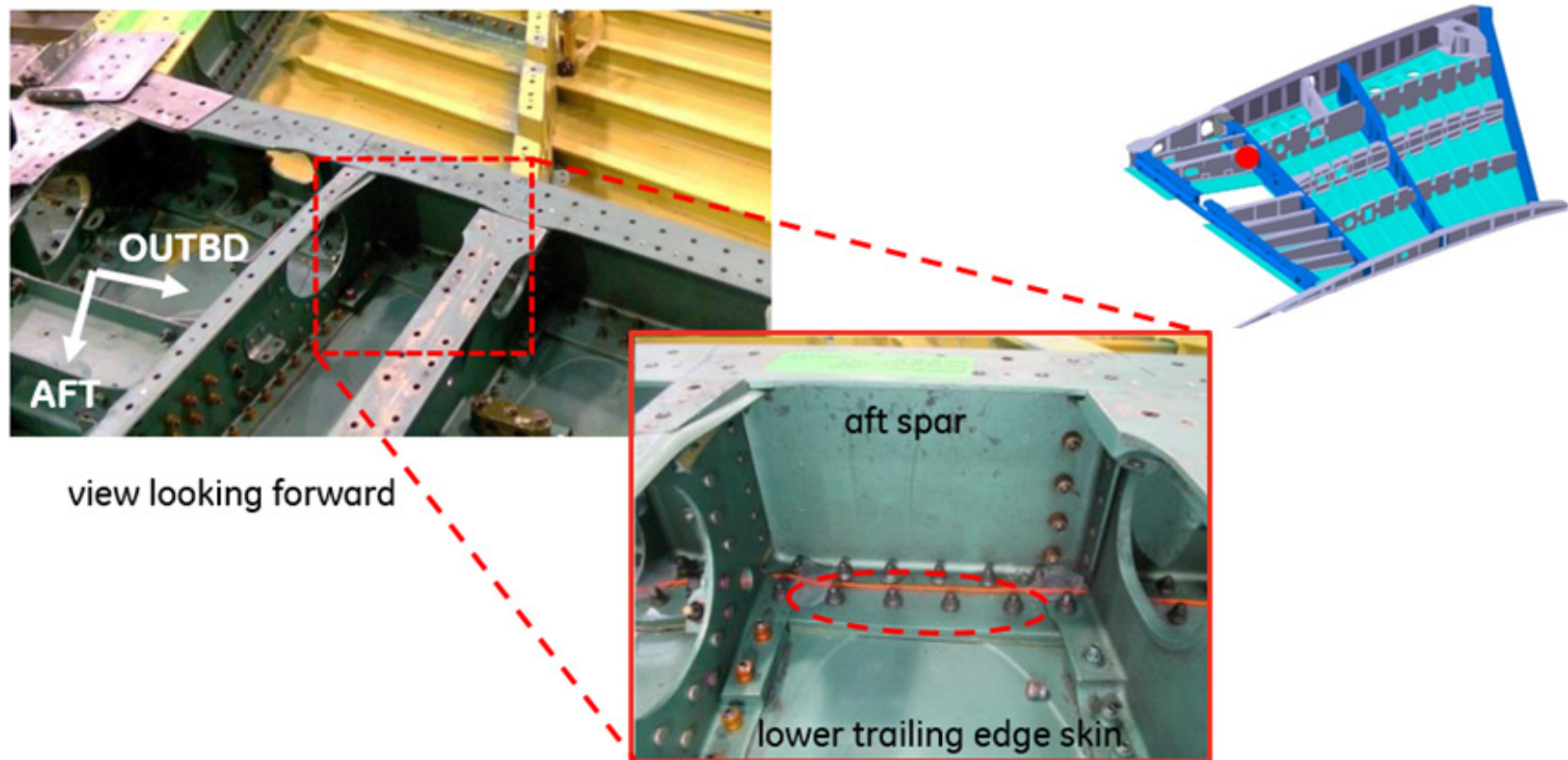


Figure 5. GE04 control point details

GE05 – Lower Wing Skin, Fwd Edge Thickness Step at XW156

Control Point	Location	Cracking History	Ref. Stress (mg-FEM)	Geometry / Flaw Details	Inspection Instrumentation
GE05	FS = 580.8 BL = 159.8 WL = 124.8	Crack found at 18,100 hours during FSDT	$\sigma_{max-prin} = 25 \text{ ksi}$ (LC: +8.4g symmetric pullup)	Corner crack in radius	PAUT and SEC from the outside; Crack gage placed at edge of flange or OML surface

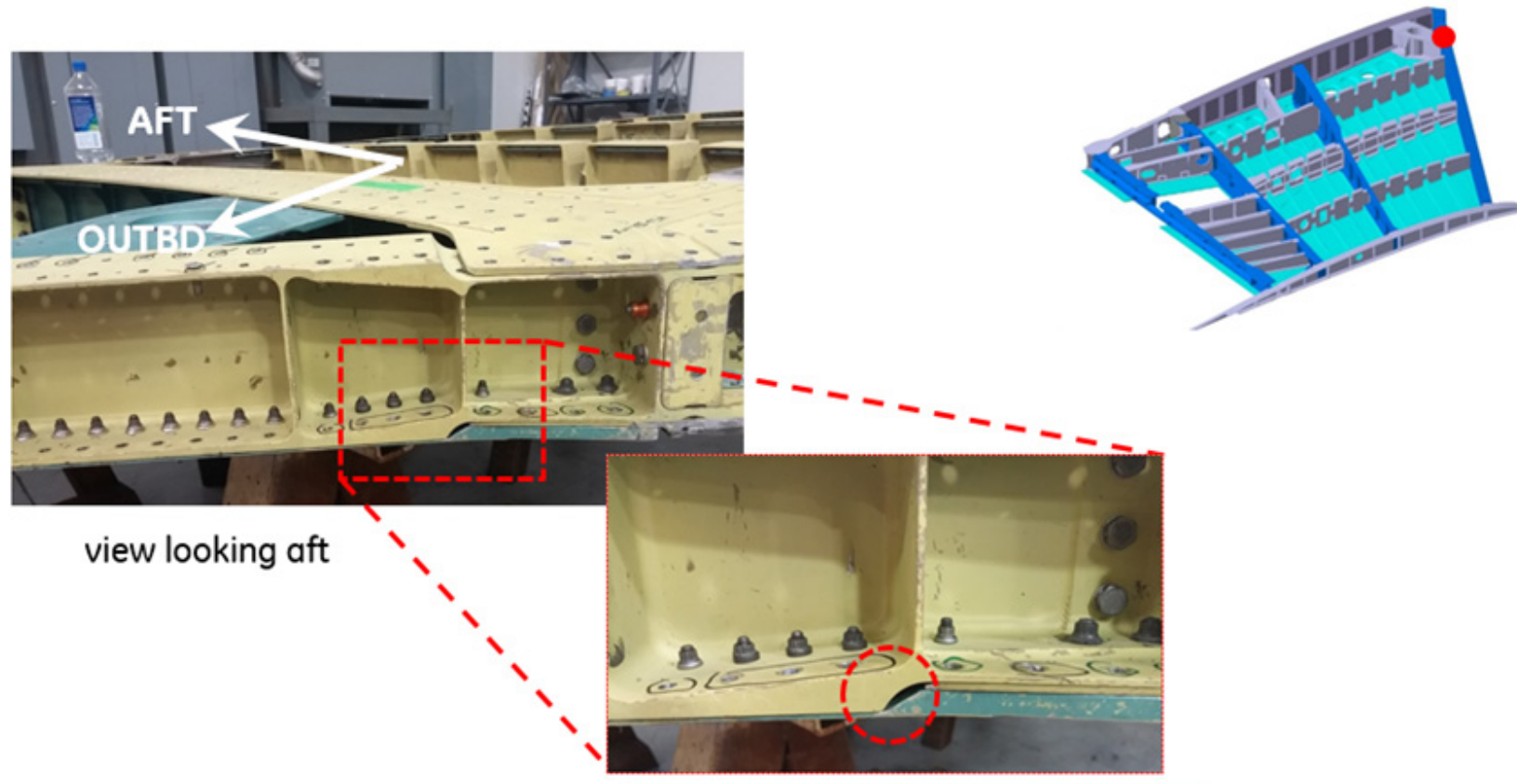
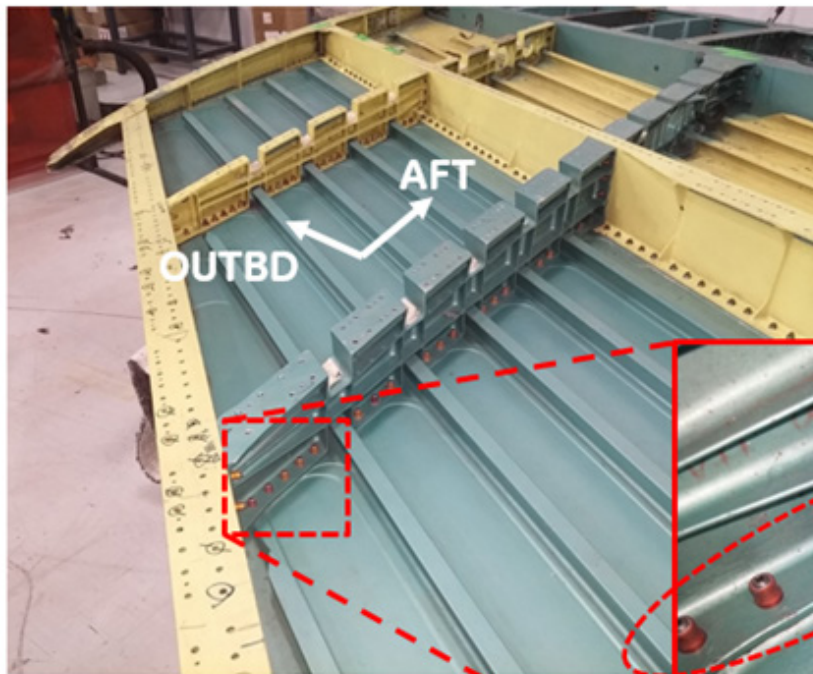


Figure 6. GE05 control point details

GE06 – Lower Wing Skin, Fastener Hole, XW188 Rib

Control Point	Location	Cracking History	Ref. Stress (mg-FEM)	Geometry / Flaw Details	Inspection Instrumentation
GE06	FS = 613.3 BL = 187.7 WL = 124.6	Crack found at 18,100 hours during FSDT	$\sigma_{max-prin} = 9 \text{ ksi}$ (LC: +8.4g symmetric pullup)	Single corner crack at fastener hole (crack at faying surface). Neat-fit fastener.	PAUT and SEC from the outside lower surface



view looking outb'd & aft

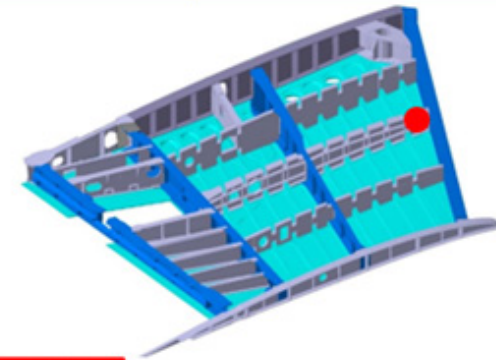


Figure 7. GE06 control point details

GE07 – Lower Forward Wing Skin, Fastener Hole at Front Spar

Control Point	Location	Cracking History	Ref. Stress (mg-FEM)	Geometry / Flaw Details	Inspection Instrumentation
GE07	FS = 591.8 BL = 169.7 WL = 124.67	No known cracks during FSDT. No known cracks in the fleet.	$\sigma_{\max-prin} = 20$ ksi (LC: +8.4g symmetric pullup)	Single corner crack at fastener hole (crack at faying surface). Interference fit fastener.	PAUT and SEC from the outside lower surface

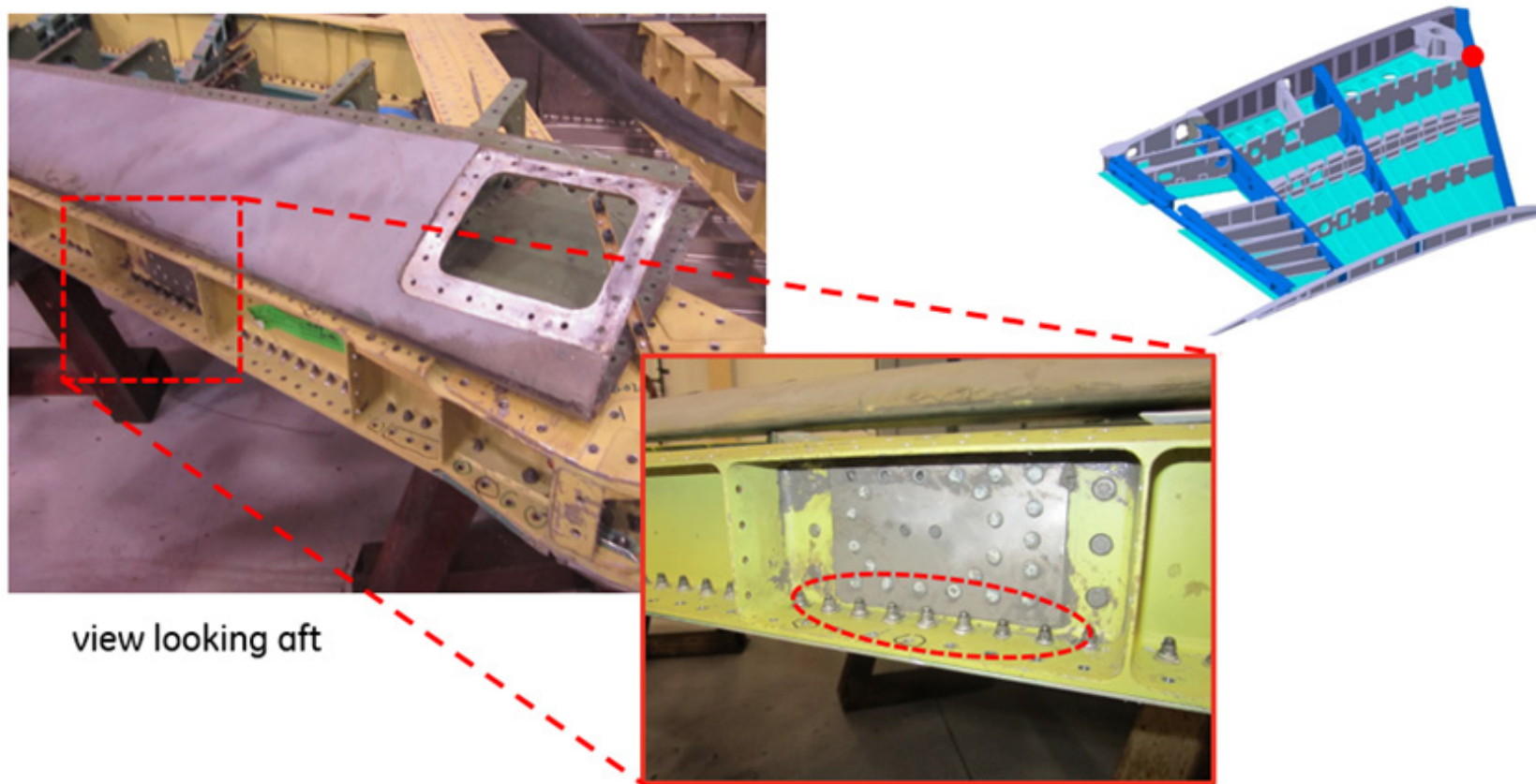


Figure 8. GE07 control point details

GE08 – Lwr Wing Skin, fastener hole at XW162 (under aft spar)

Control Point	Location	Cracking History	Ref. Stress (mg-FEM)	Geometry / Flaw Details	Inspection Instrumentation
GE08	FS = 651.9 BL = 161.5 WL = 125.0	No known cracks during FSDT. No known cracks in the fleet.	$\sigma_{max-prin} = 33 \text{ ksi}$ (LC: +8.4g symmetric pullup)	Single corner crack at fastener hole (crack at faying surface). Interference fit <u>astener</u> .	PAUT and SEC from the outside lower surface

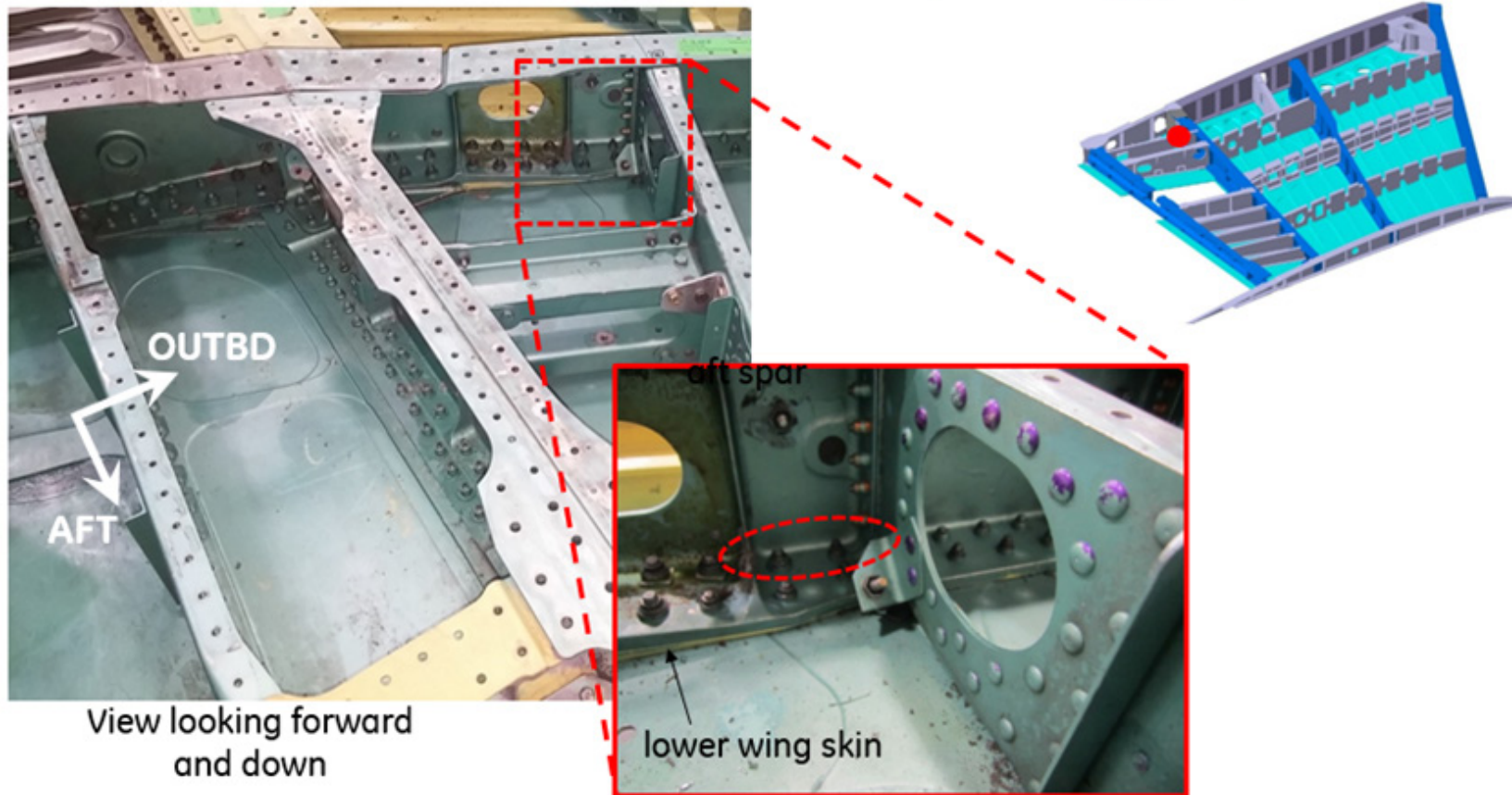


Figure 9. GE08 control point details

GE09 – Main Spar, Fastener Hole in Lower Flange at XW168

Control Point	Location	Cracking History	Ref. Stress (mg-FEM)	Geometry / Flaw Details	Inspection Instrumentation
GE09	FS = 627.5 BL = 168.4 WL = 124.7	No known cracks during FSDT. No known cracks in the fleet.	$\sigma_{\max-prin} = 25 \text{ ksi}$ (LC: +8.4g symmetric pullup)	Corner crack at fastener hole in spar cap (1 st layer corner crack at faying surface) Interference fit fastener.	PAUT and SEC from the inside through access port in upper skin

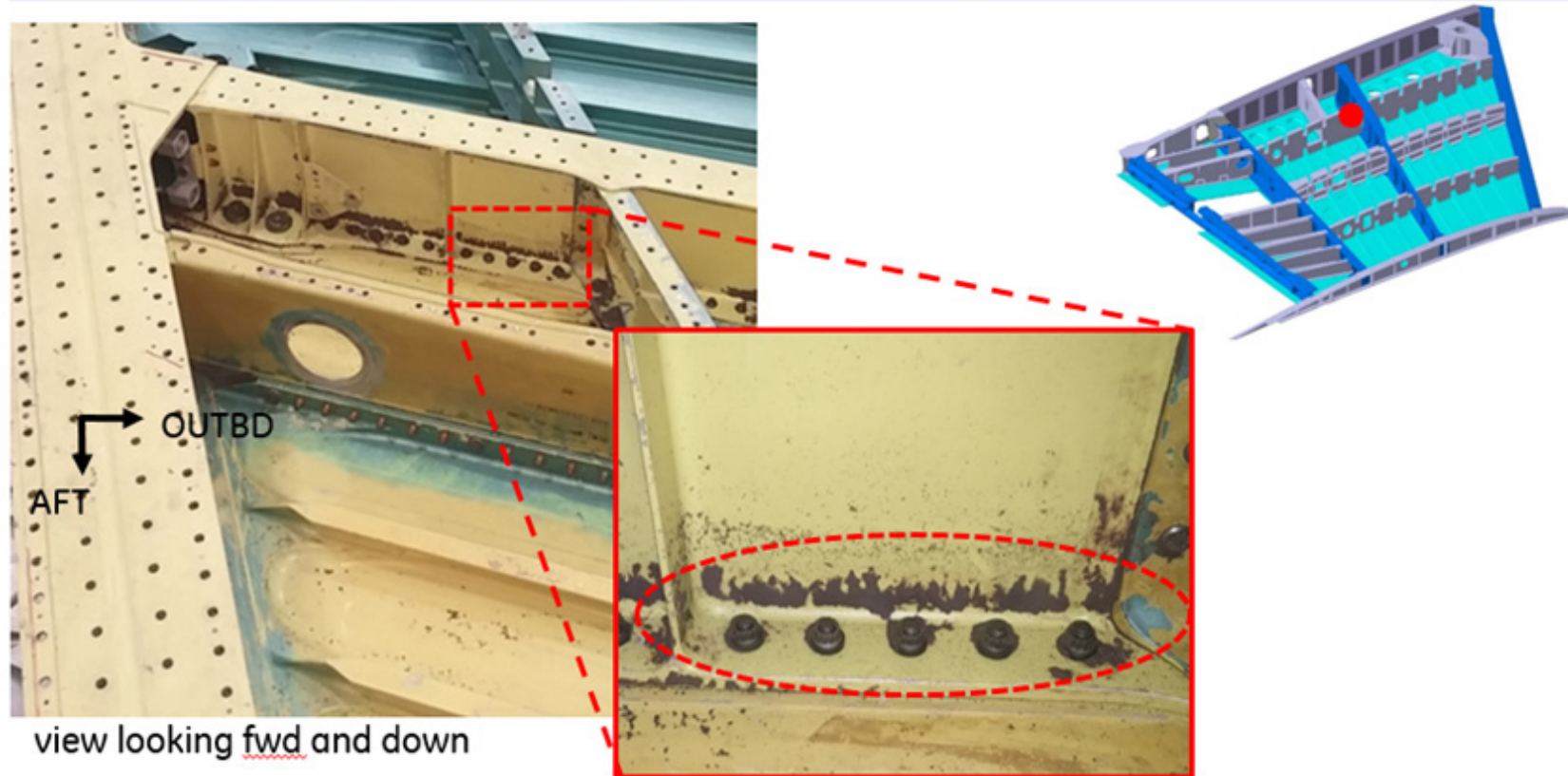


Figure 10. GE09 control point details

GE10 – Lwr Aft Wing Skin, Fastener Hole at XW164 (under main spar)

Control Point	Location	Cracking History	Ref. Stress (mg-FEM)	Geometry / Flaw Details	Inspection Instrumentation
GE10	FS = 625.5 BL = 165.5 WL = 124.7	Broken ligament found at 18,100 hours during FSDT	$\sigma_{\text{max-prin}} = 20 \text{ ksi}$ (LC: +8.4g symmetric pullup)	Corner crack at fastener hole in wing skin (1 st layer corner crack at faying surface)	PAUT and SEC from the outside lower surface

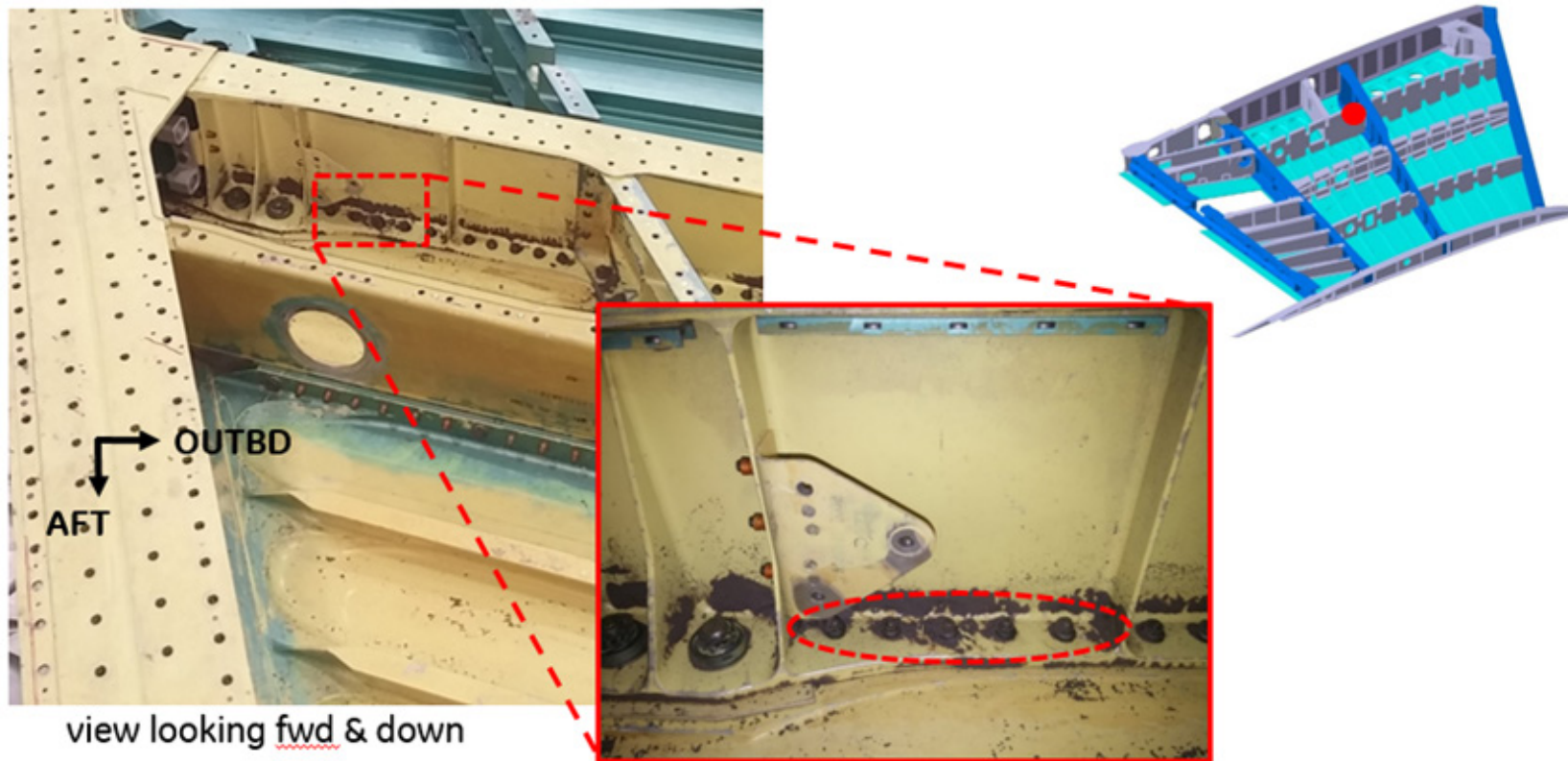


Figure 11. GE10 control point details

4.0 WING LOAD APPLICATION

One of the activities in Task Order 2 was to develop an actuator layout and applied loads to reproduce the bending, moment, and torque for the maneuvers in the baseline MES for application to the outer wing during the demonstration experiment. This baseline load spectrum needs to adequately represent the probabilistic load spectrum defined in Task Order 1, and ensure meaningful fatigue damage with no catastrophic failure during the entirety of the test. The wing load application task includes supporting AFRL in developing and designing test article loading and test article fixtures. Full test procedures and additional details on the Wing Load Application task is documented in the Test Requirements Document DI-MISC-80711A/T and available in Appendix H.

4.1 Test Load Cases

Each load case in the ADT baseline spectrum is defined as a linear combination of a pure moment and pure torque limit load case. The eight (five unique) limit load cases were defined based on the moment vs. torque content of the version 5 MES. The maximum and minimum moments and maximum and minimum torque values are shown in Figure 12. The wing station 3 location is defined as the location 24.3 inches outboard from the inboard-outboard transition location (XW155) along the main spar. (Note that Sta.3 torque values less than $-3.5E5$ in-lb and greater than $+3.5E5$ in-lb were deemed to be unsafe for the test article and were excluded). The span-wise distributions of moment, shear and torque for each of the five unique limit load cases are shown in Figure 13 through Figure 27.

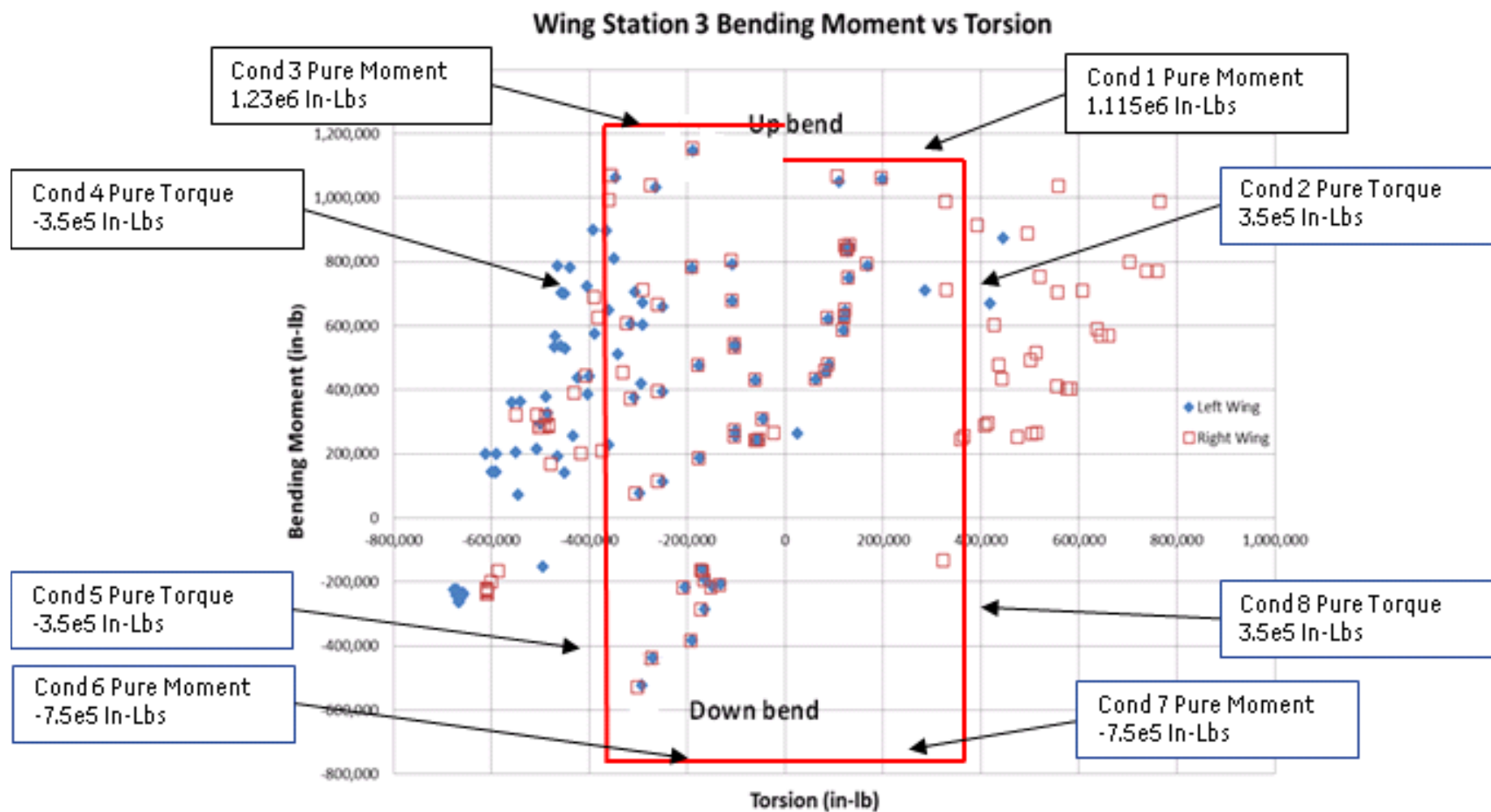


Figure 12. Wing station 3 moment vs. torque diagram for maneuver load cases

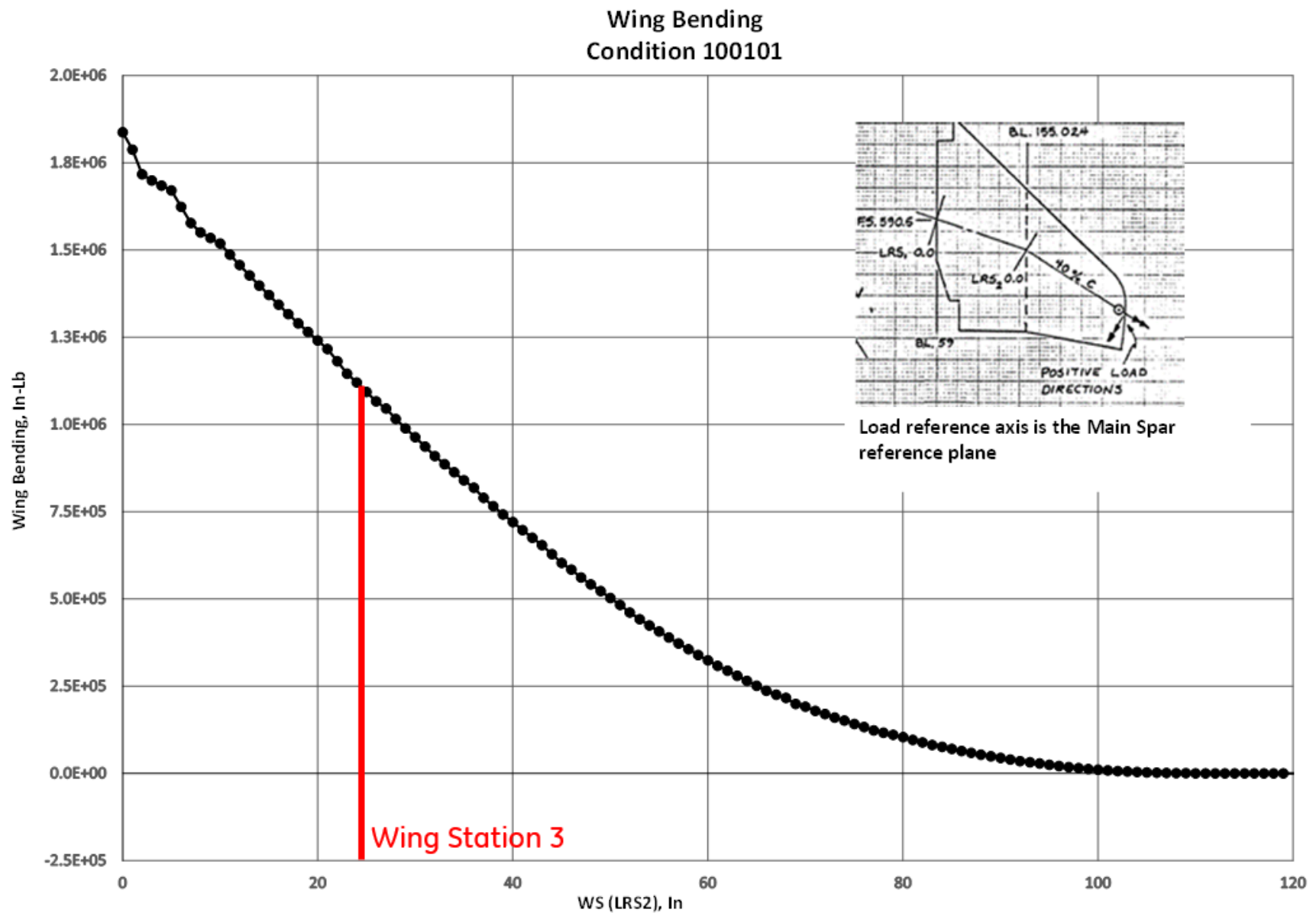


Figure 13. Moment vs. wing station for limit load case 100101 (Cond. 1)

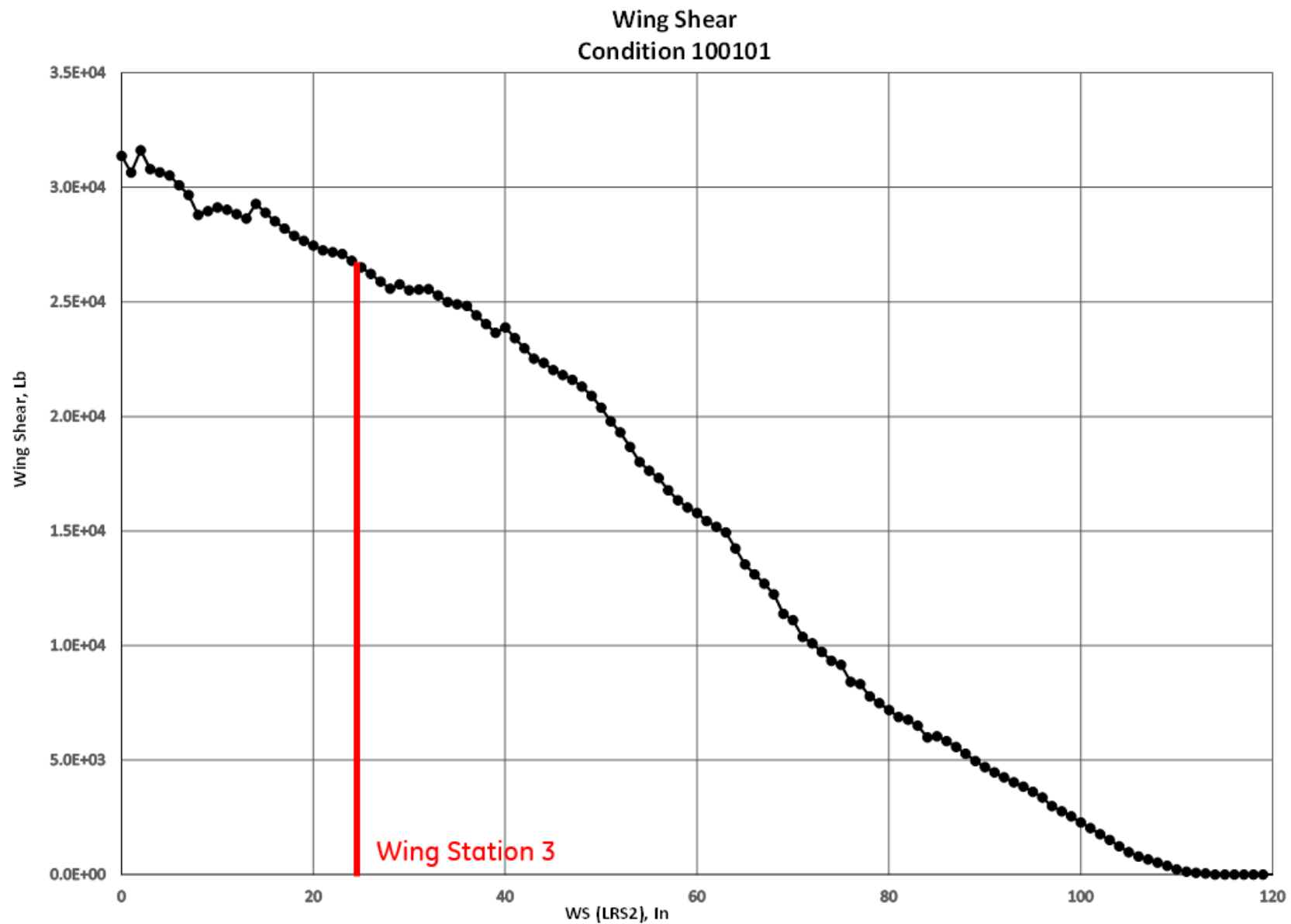


Figure 14. Shear vs. wing station for limit load case 100101 (Cond. 1)

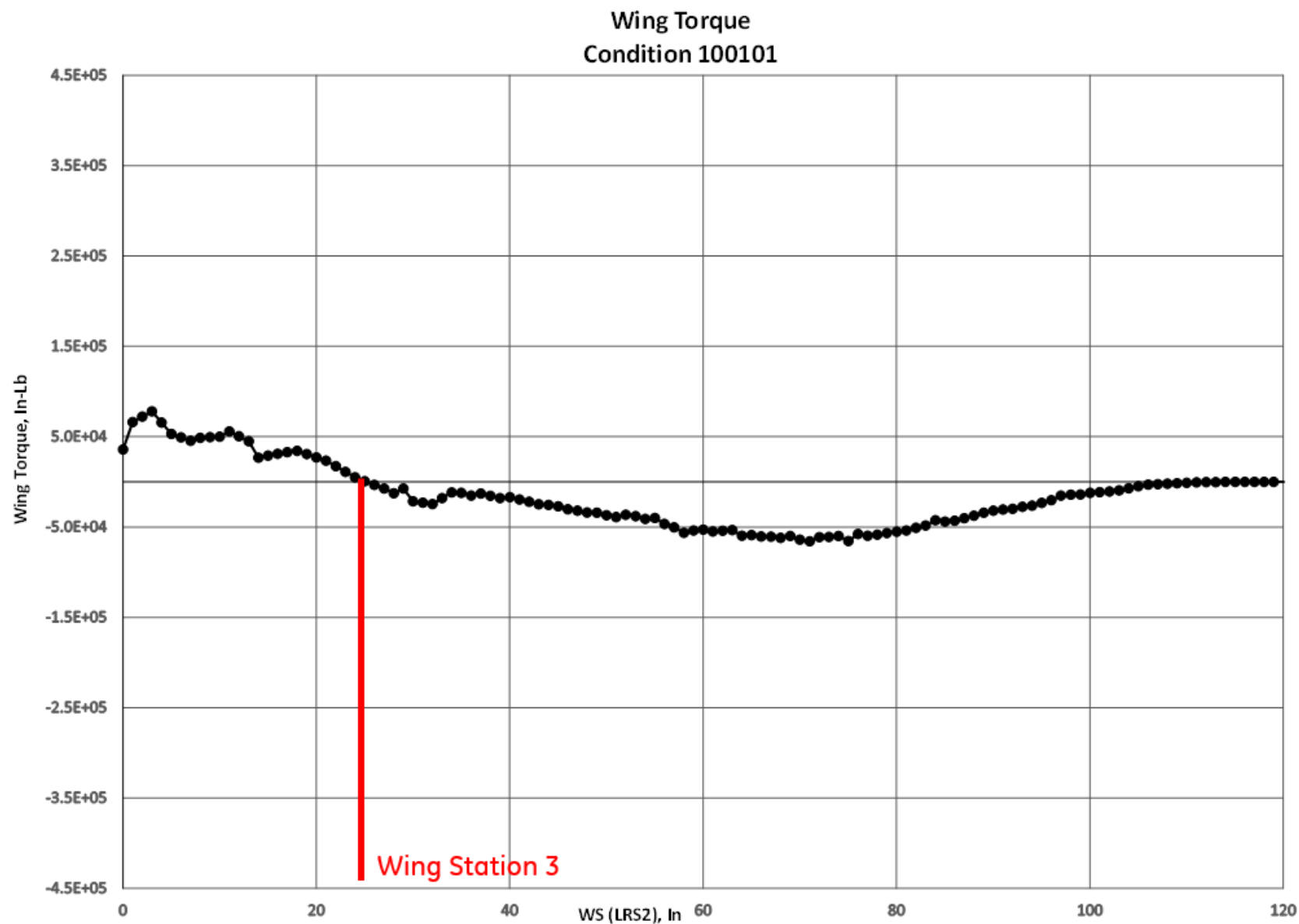


Figure 15. Torque vs. wing station for limit load case 100101 (Cond. 1)

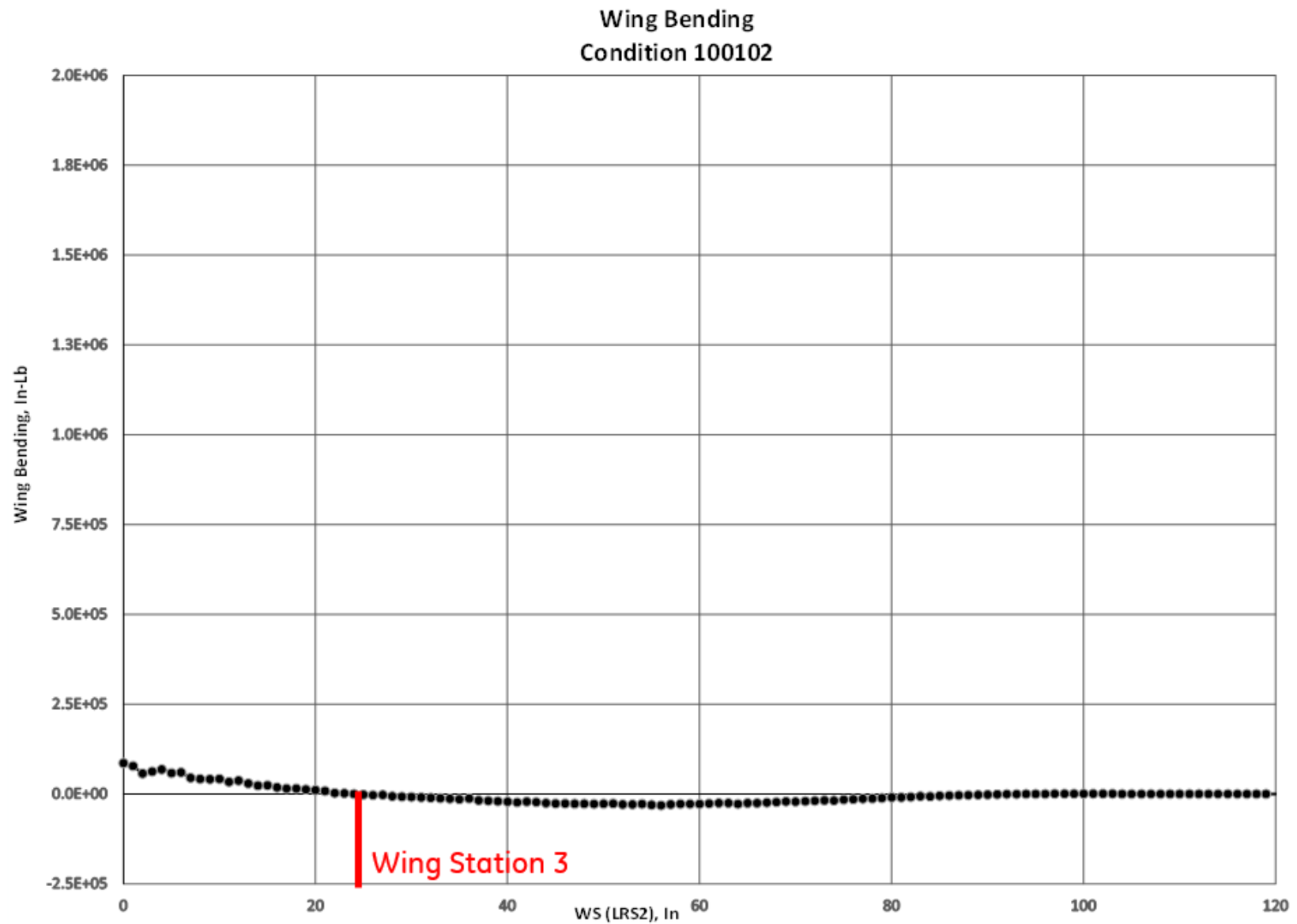


Figure 16. Moment vs. wing station for limit load case 100102 (Cond. 2)

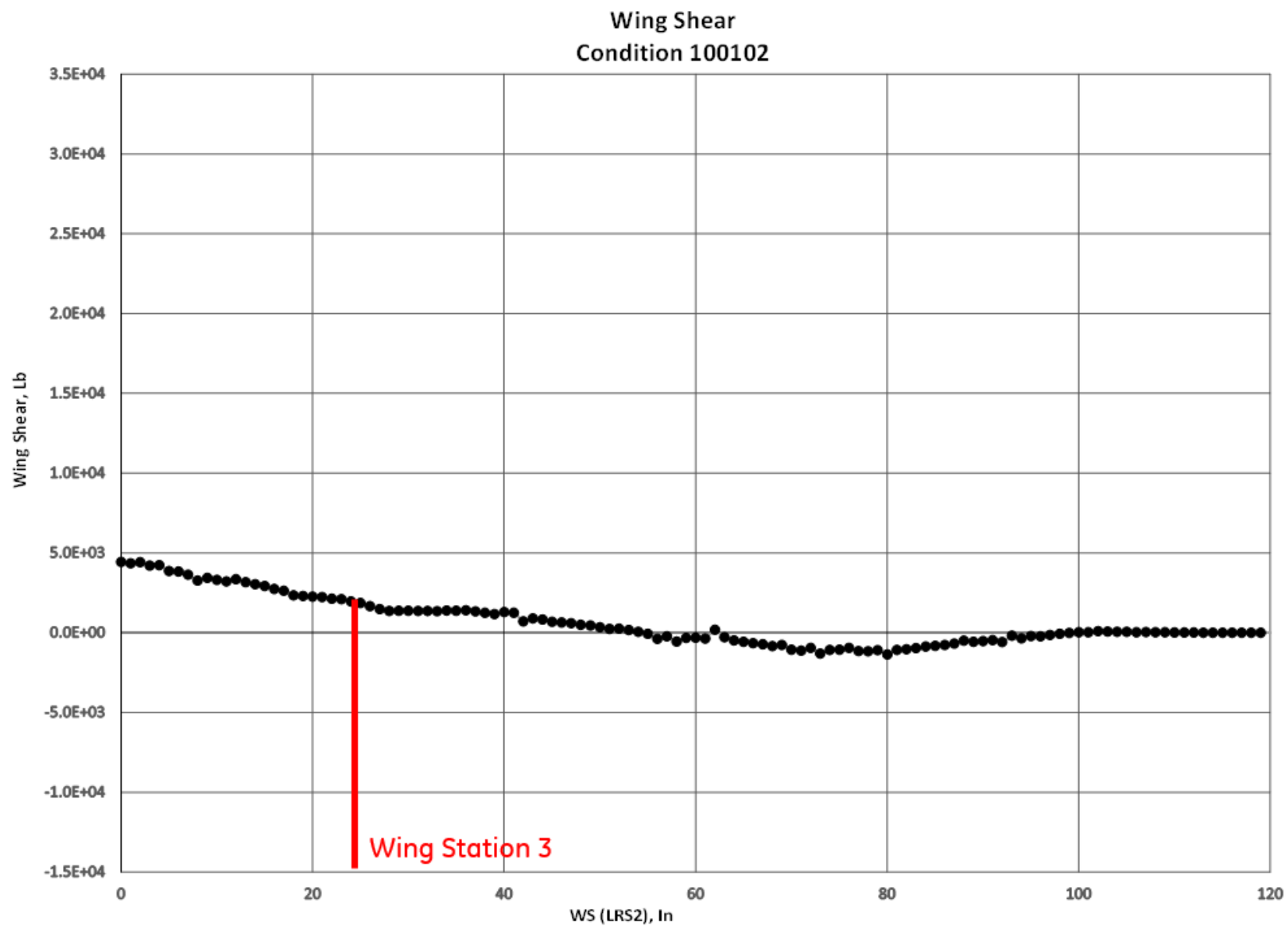


Figure 17. Shear vs. wing station for limit load case 100102 (Cond. 2)

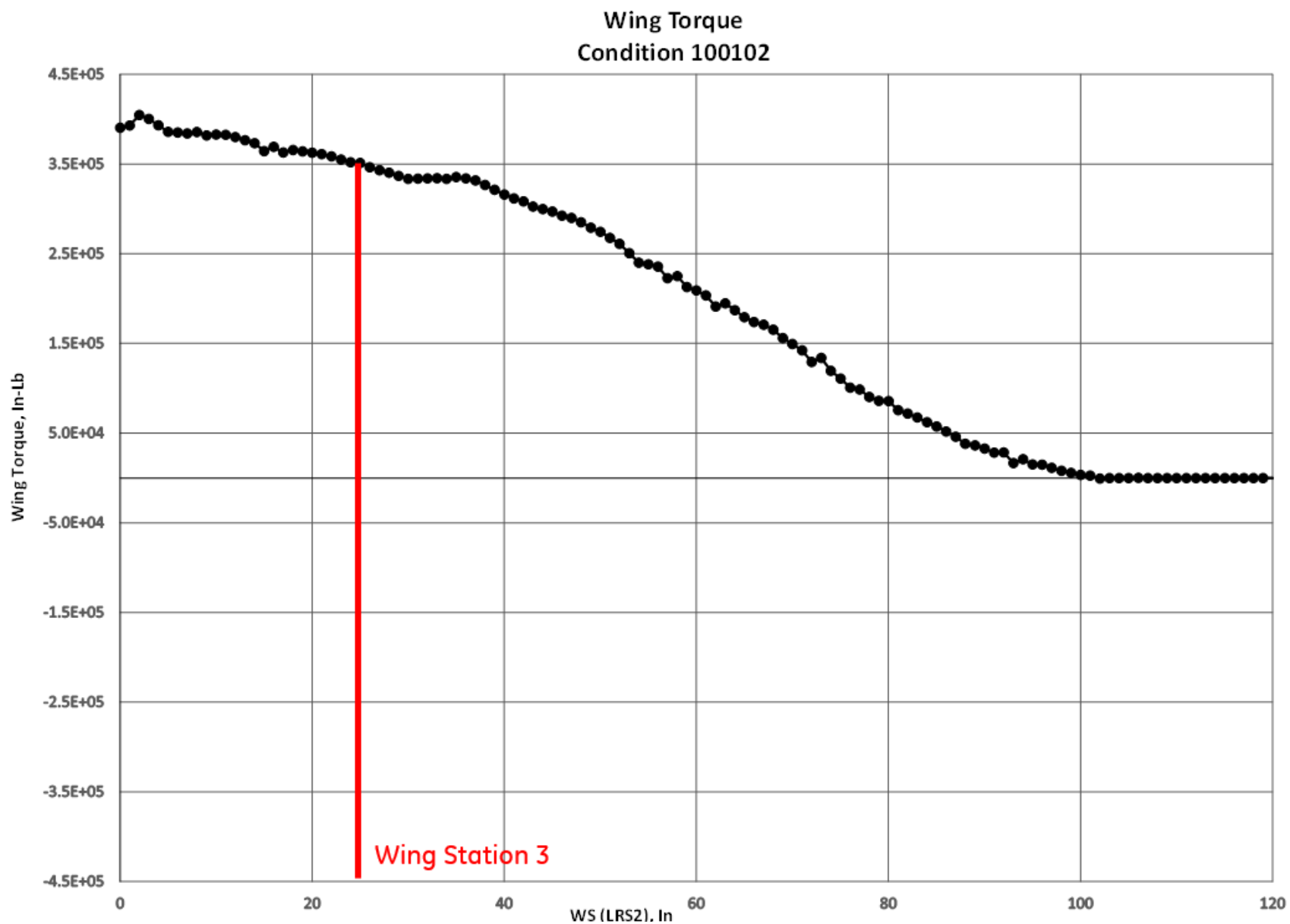


Figure 18. Torque vs. wing station for limit load case 100102 (Cond. 2)

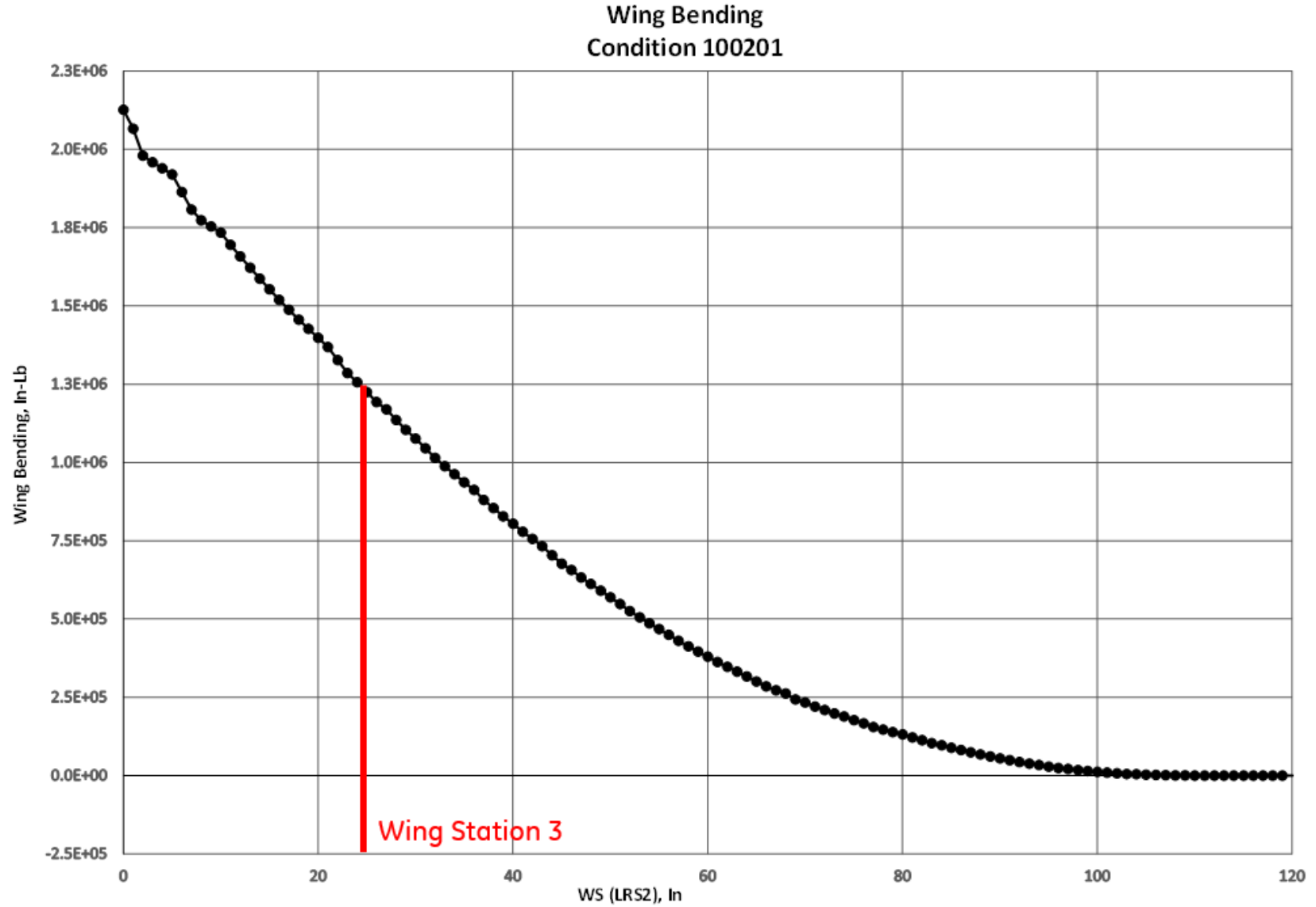


Figure 19. Moment vs. wing station for limit load case 100201 (Cond. 3)

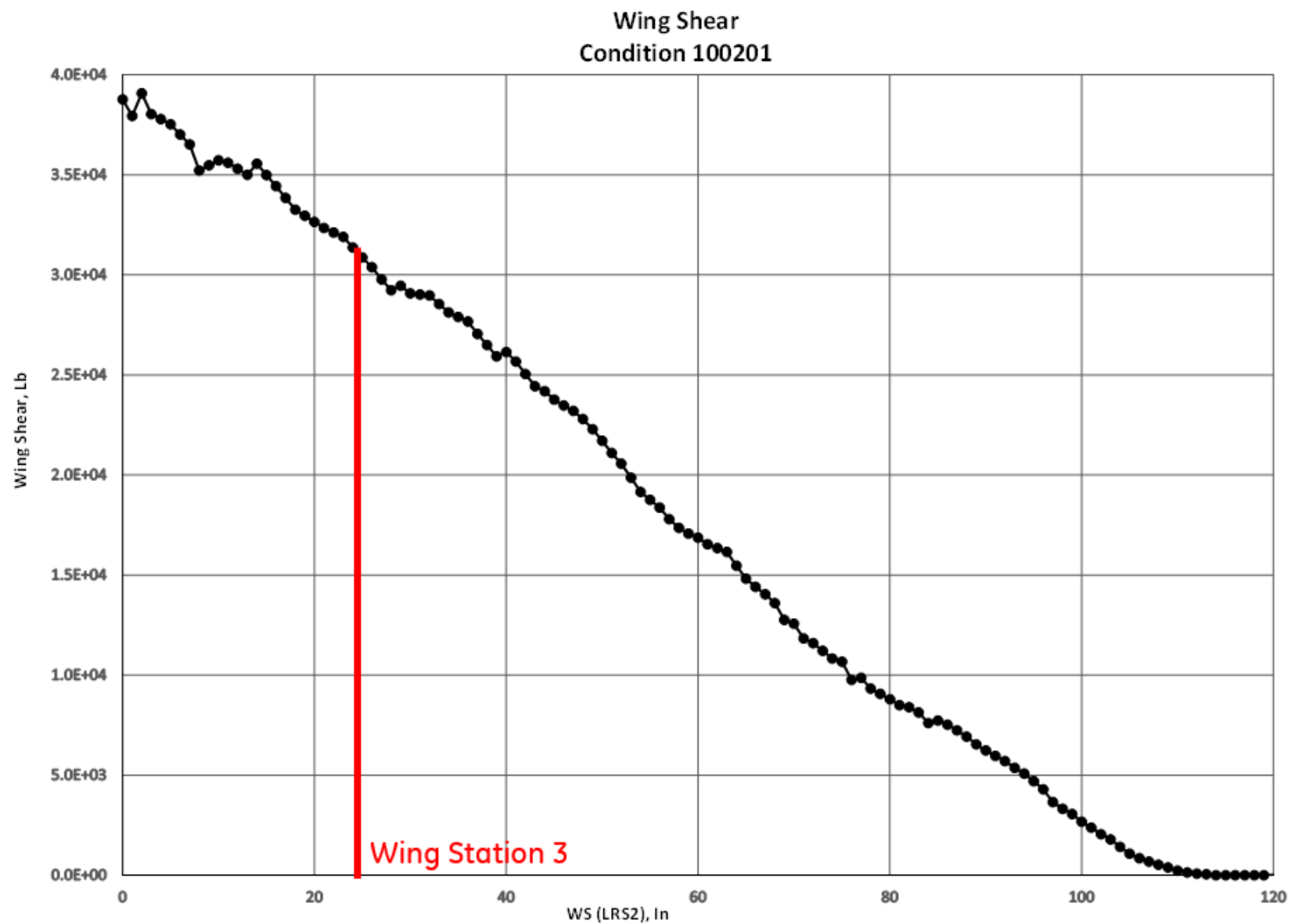


Figure 20. Shear vs. wing station for limit load case 100201 (Cond. 3)

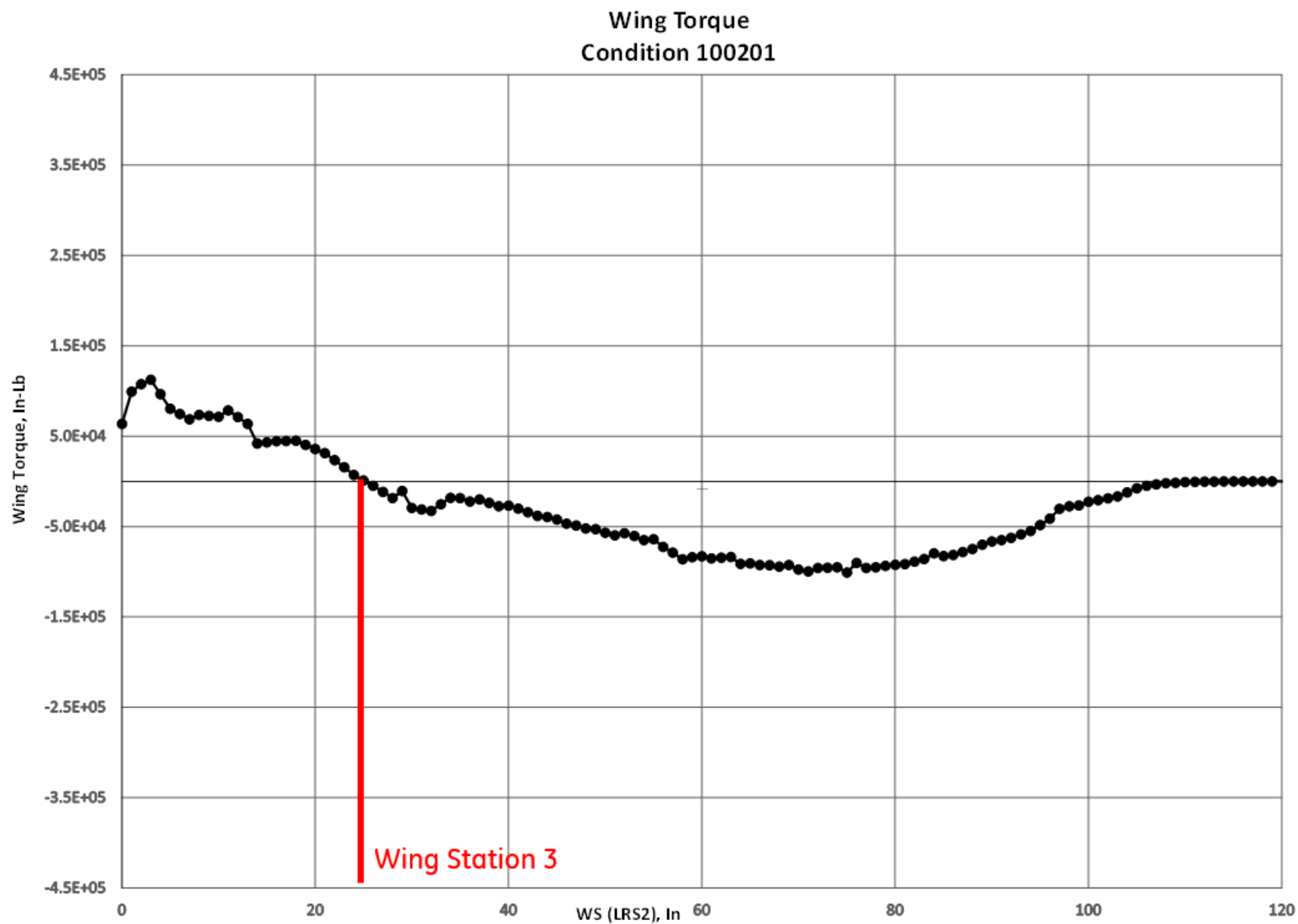


Figure 21. Torque vs. wing station for limit load case 100201 (Cond. 3)

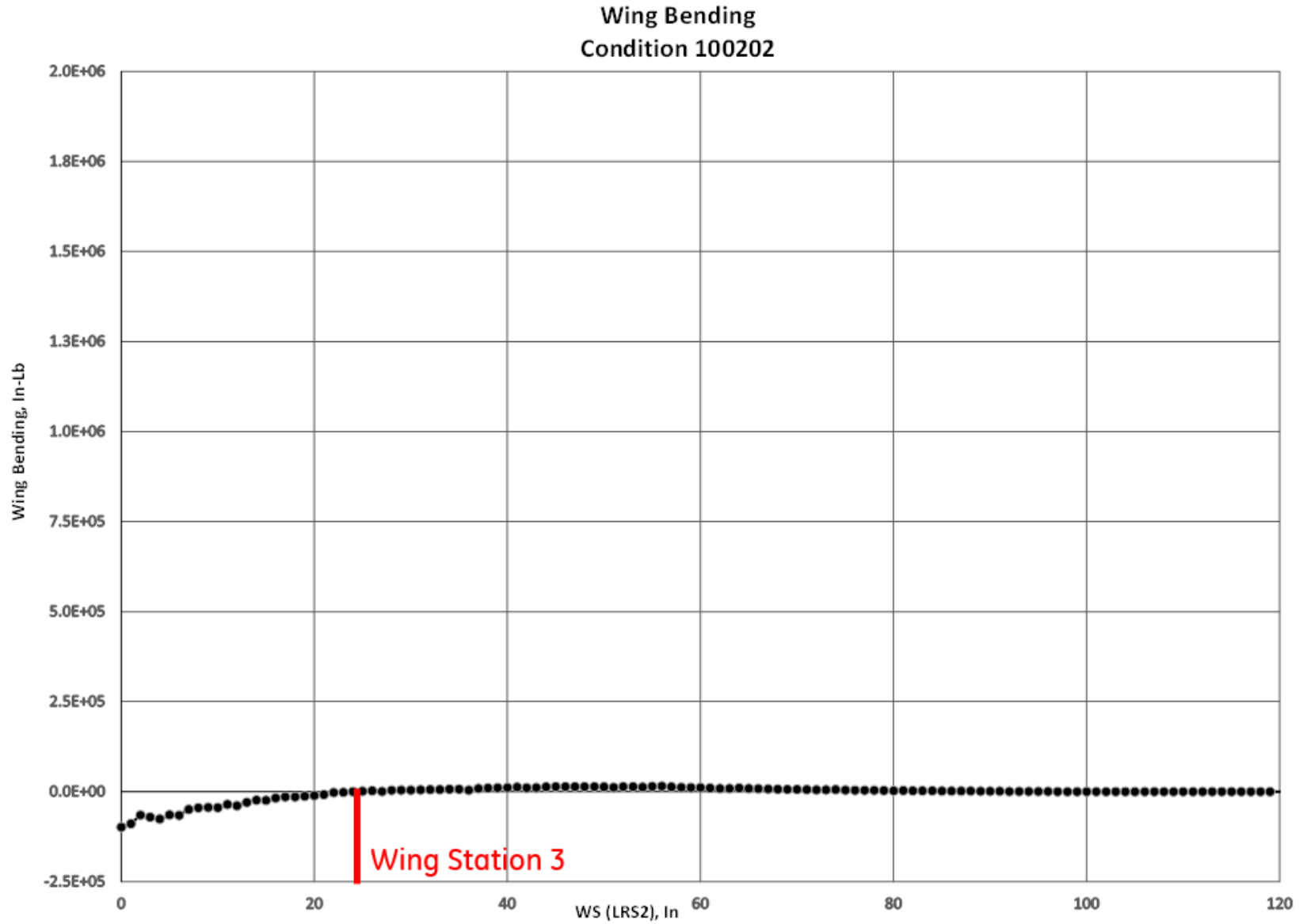


Figure 22. Moment vs. wing station for limit load case 100202 (Cond. 4)

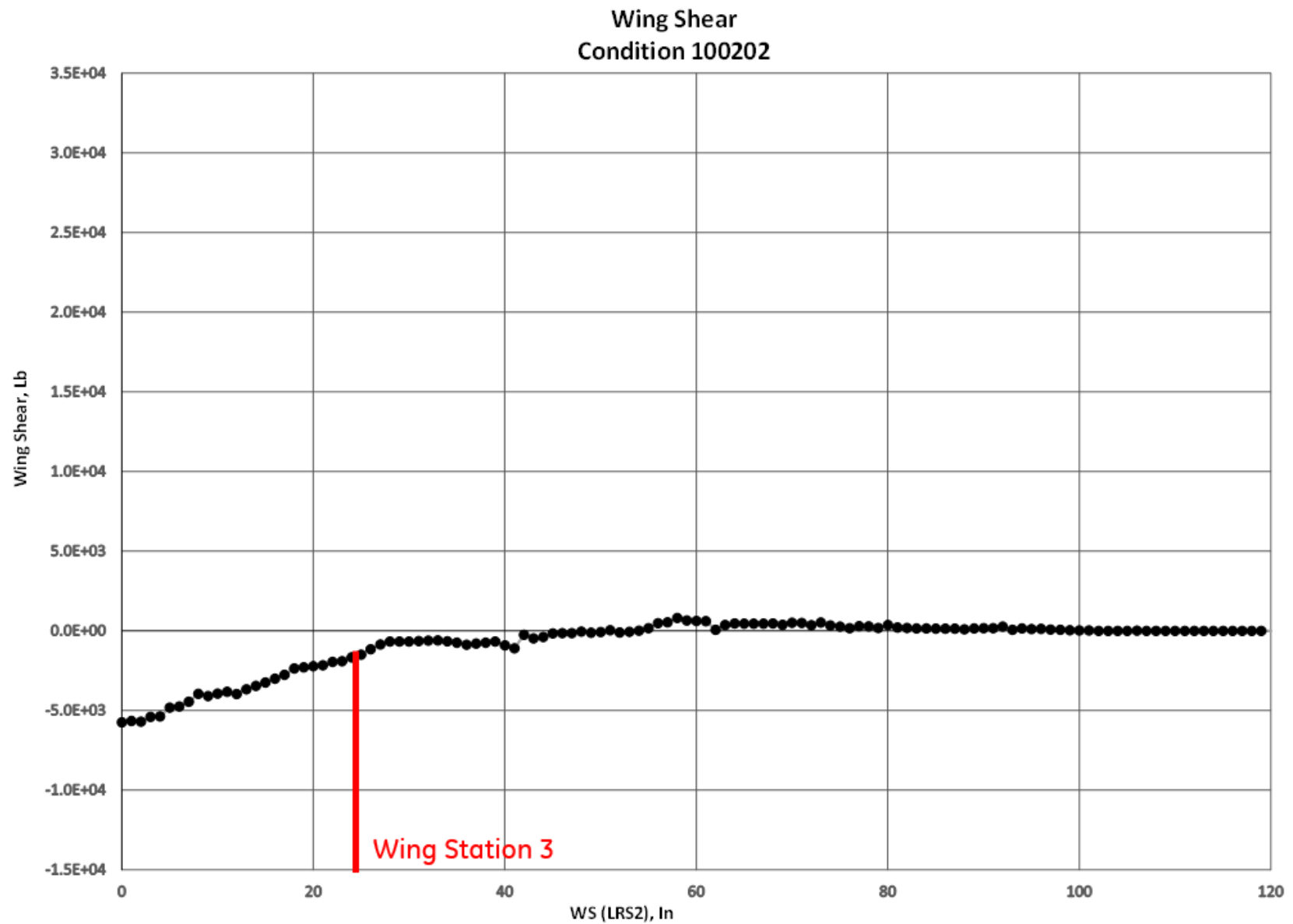


Figure 23. Shear vs. wing station for limit load case 100202 (Cond. 4)

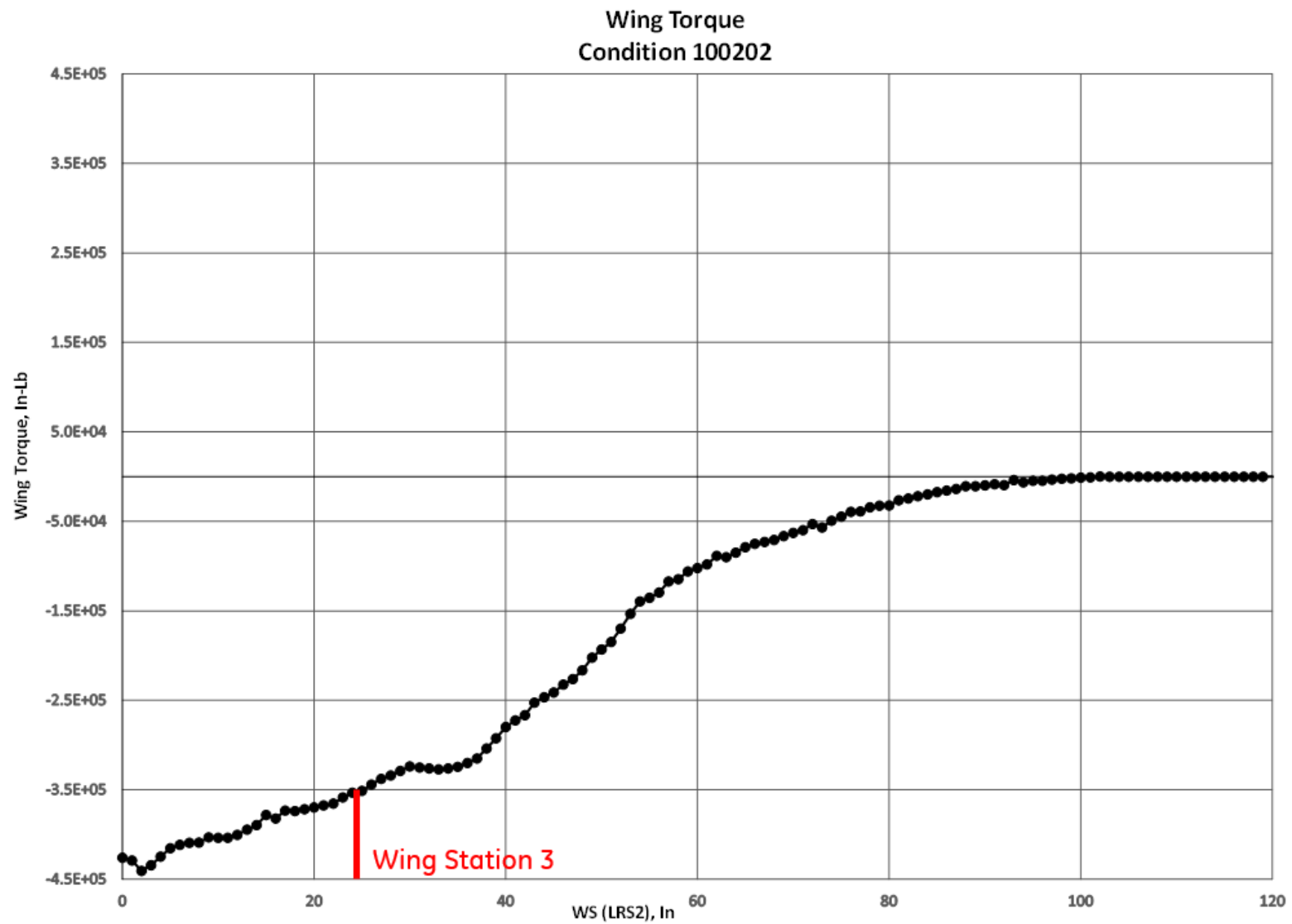


Figure 24. Torque vs. wing station for limit load case 100202 (Cond. 4)

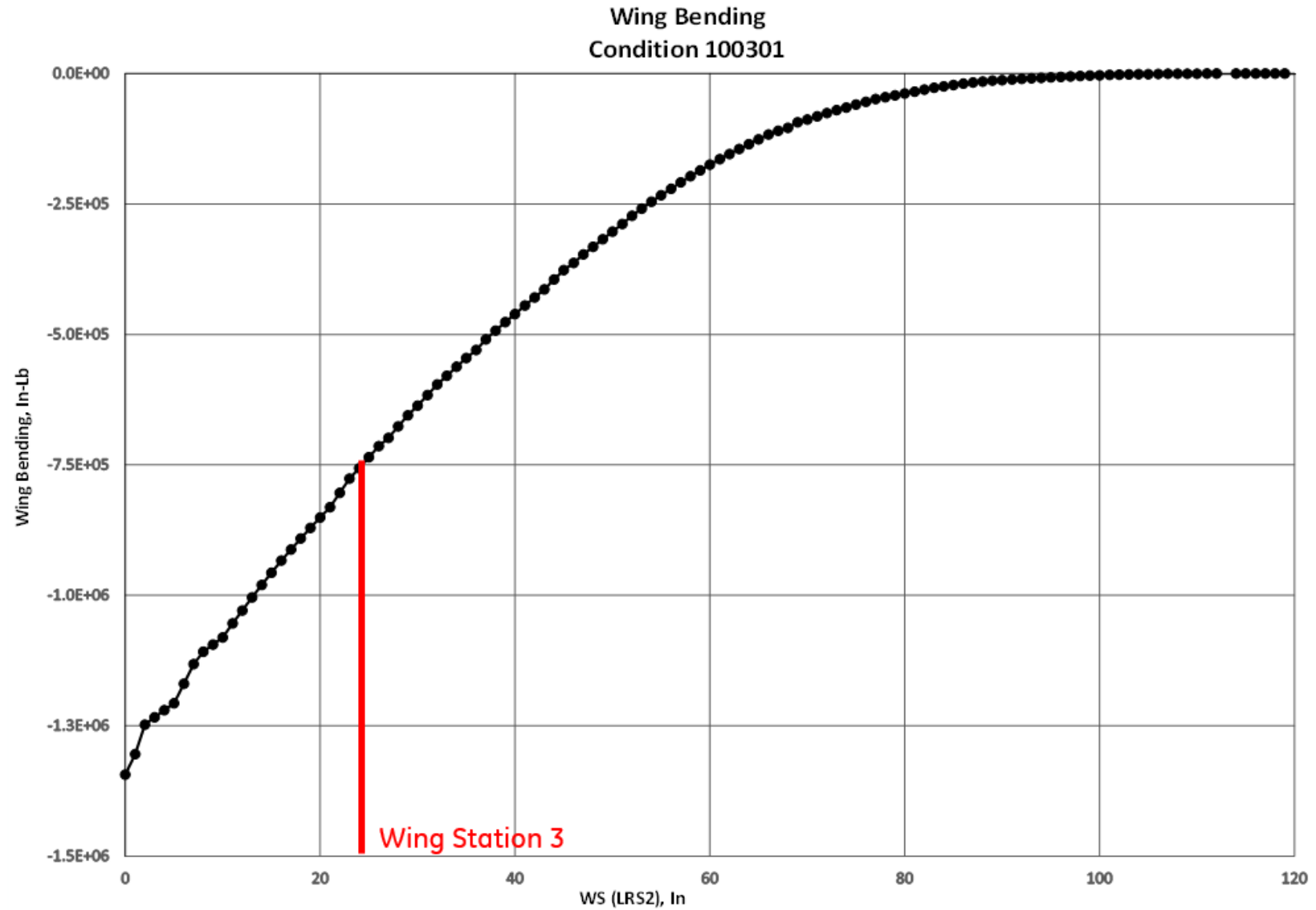


Figure 25. Moment vs. wing station for limit load case 100301 (Cond. 5)

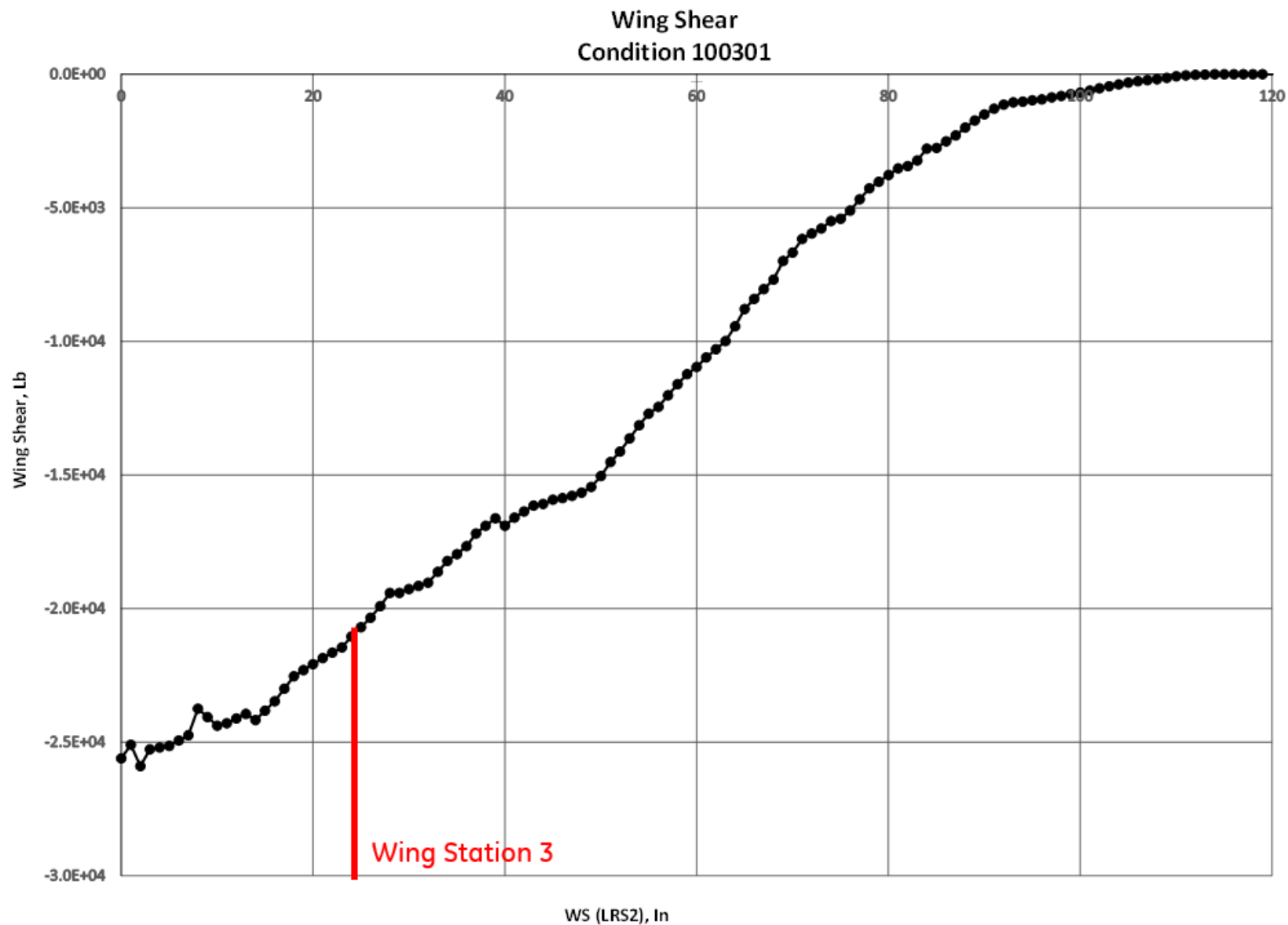


Figure 26. Shear vs. wing station for limit load case 100301 (Cond. 5)

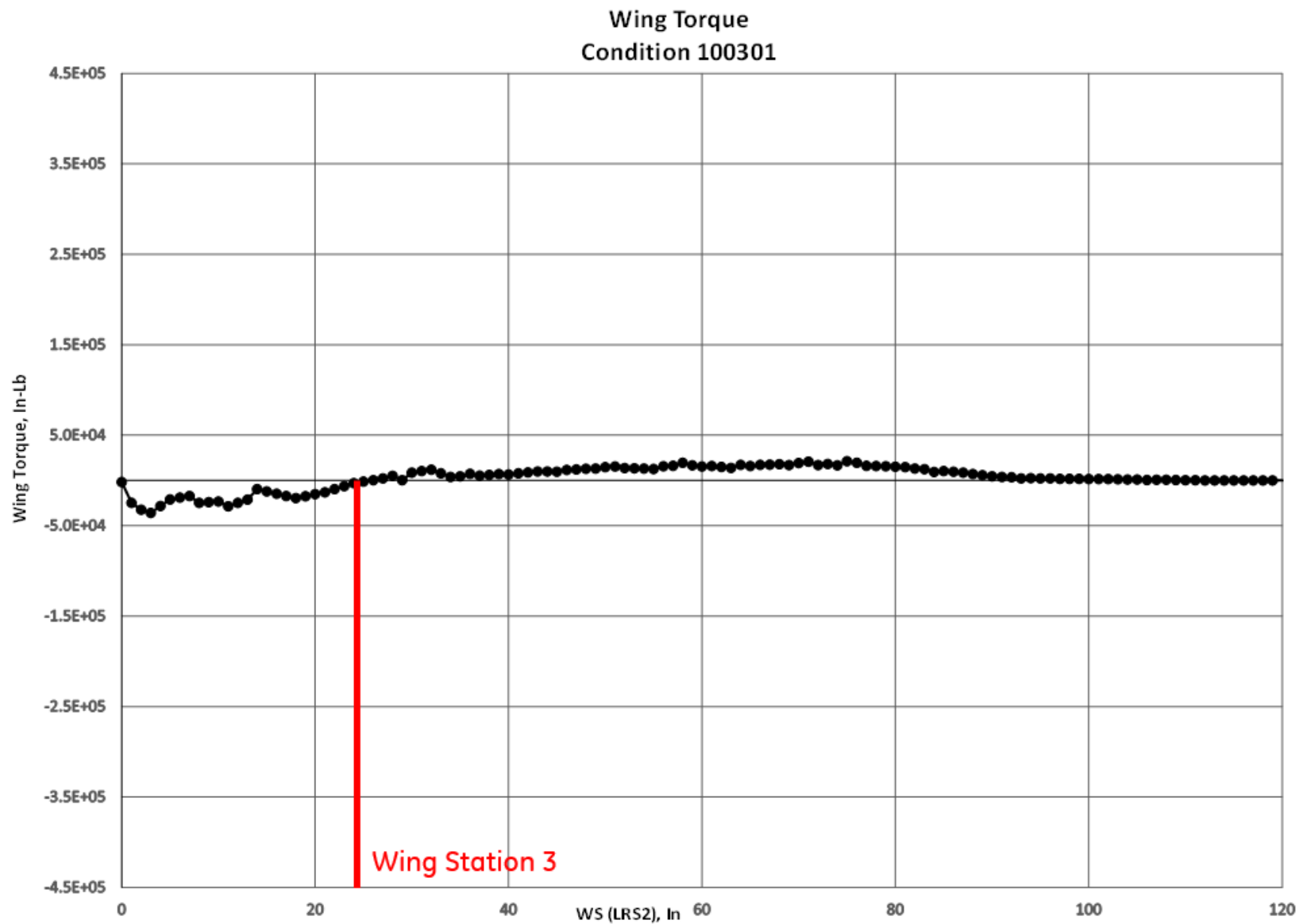


Figure 27. Torque vs. wing station for limit load case 100301 (Cond. 5)

The deflected wing shapes (fringe values in inches), along with maximum wing displacement at the wing tip, for each of the five unique limit load cases are shown in Figure 28 through Figure 32.

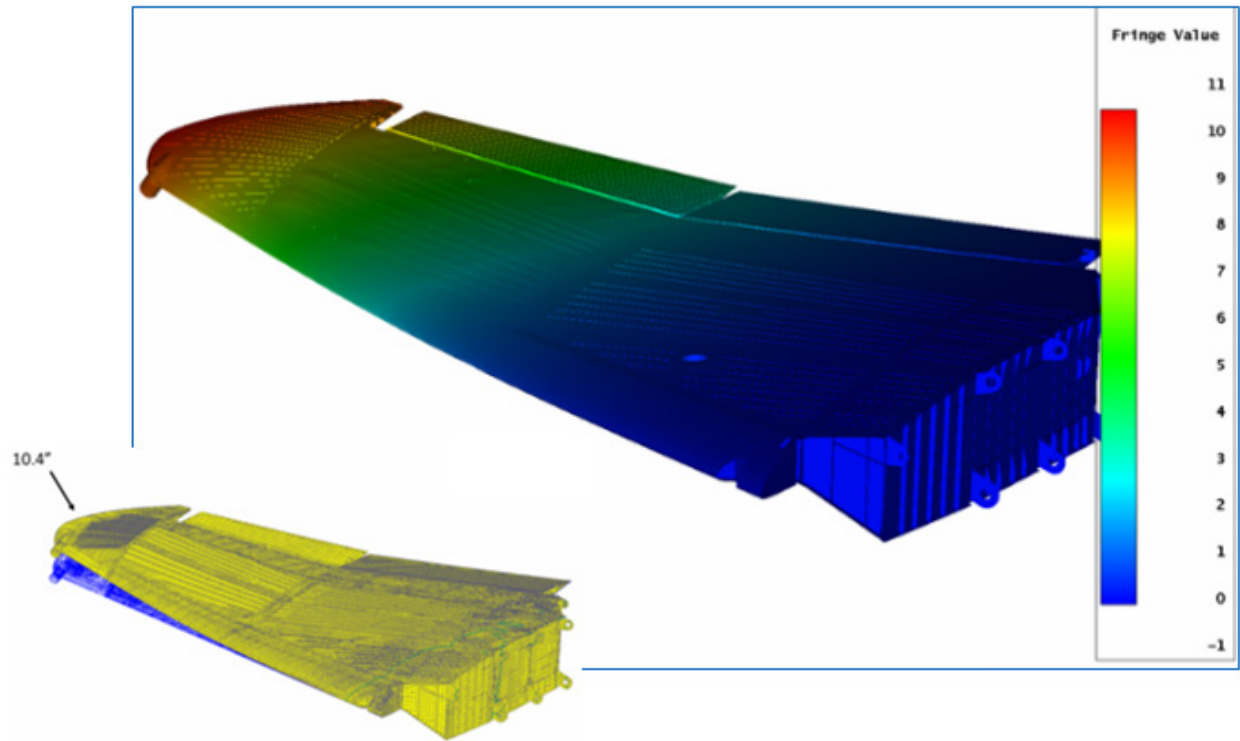


Figure 28. Wing displacement for limit load case 100101 (Cond. 1)

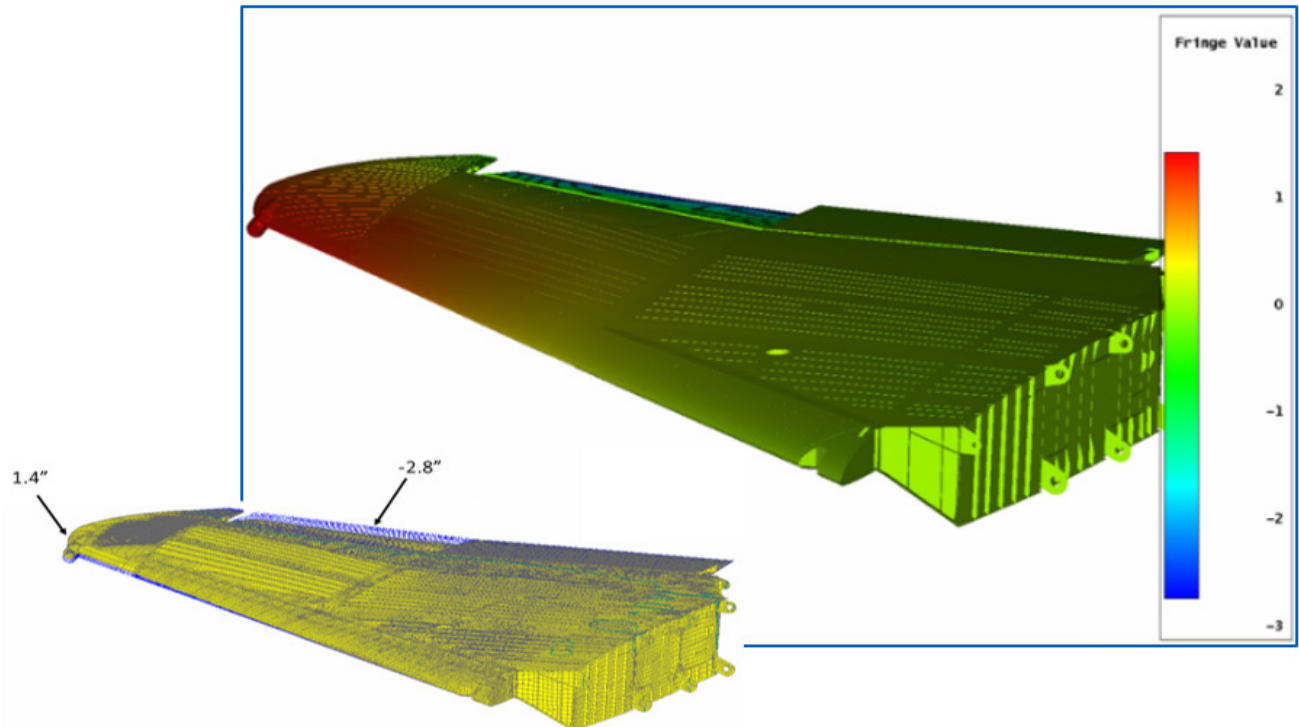


Figure 29. Wing displacement for limit load case 100102 (Cond. 2)

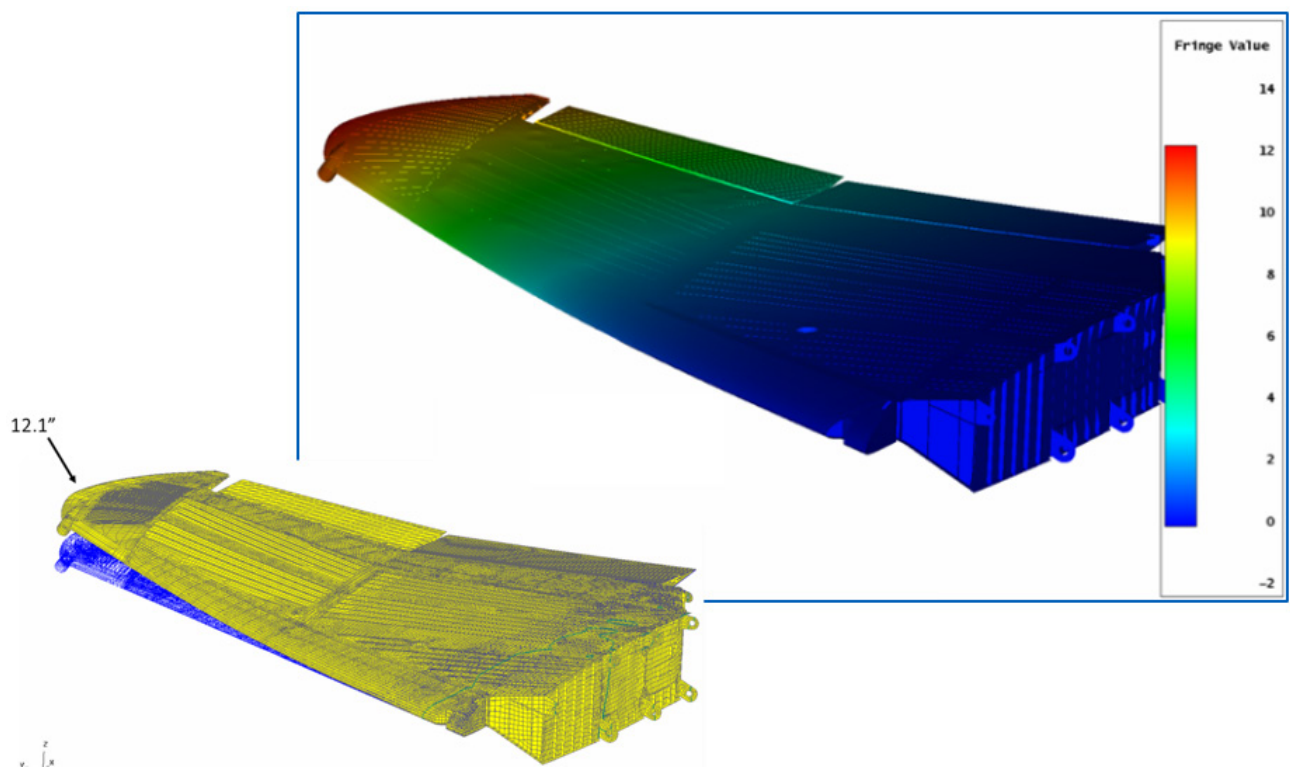


Figure 30. Wing displacement for limit load Case 100201 (Cond. 3)

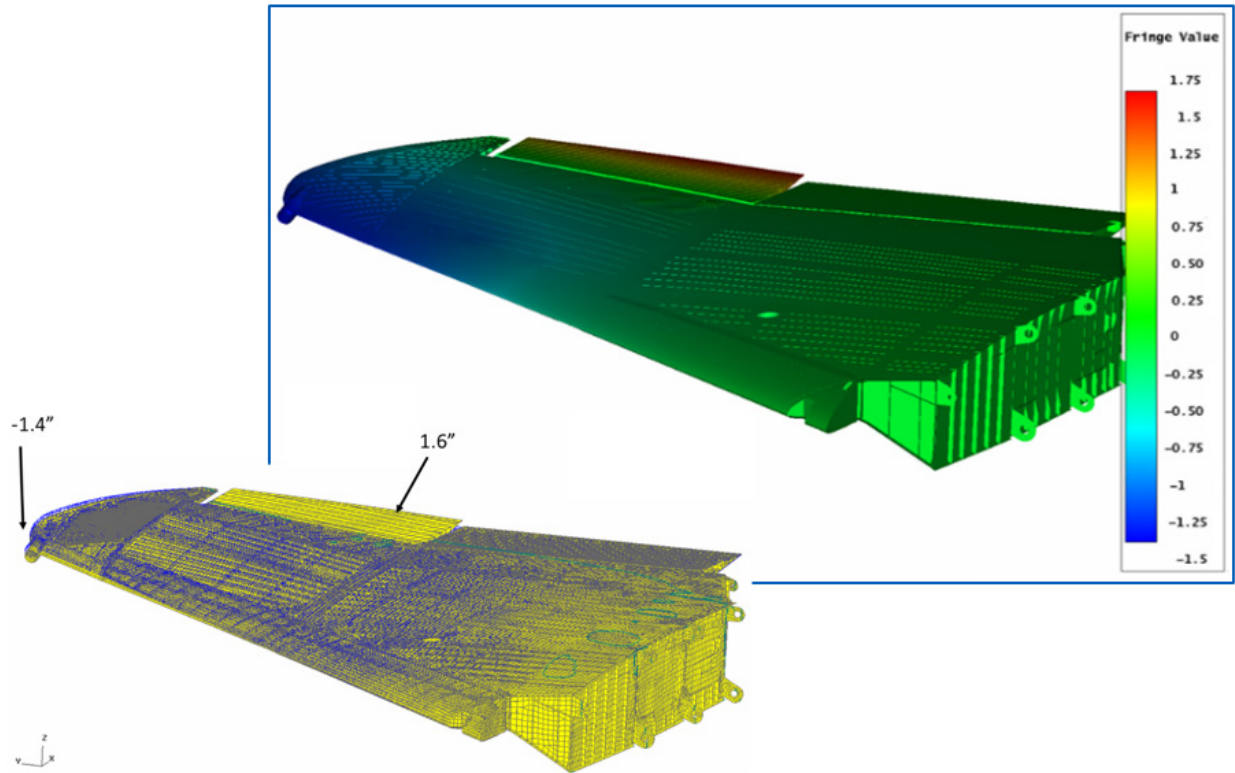


Figure 31. Wing displacement for limit load case 100202 (Cond. 4)

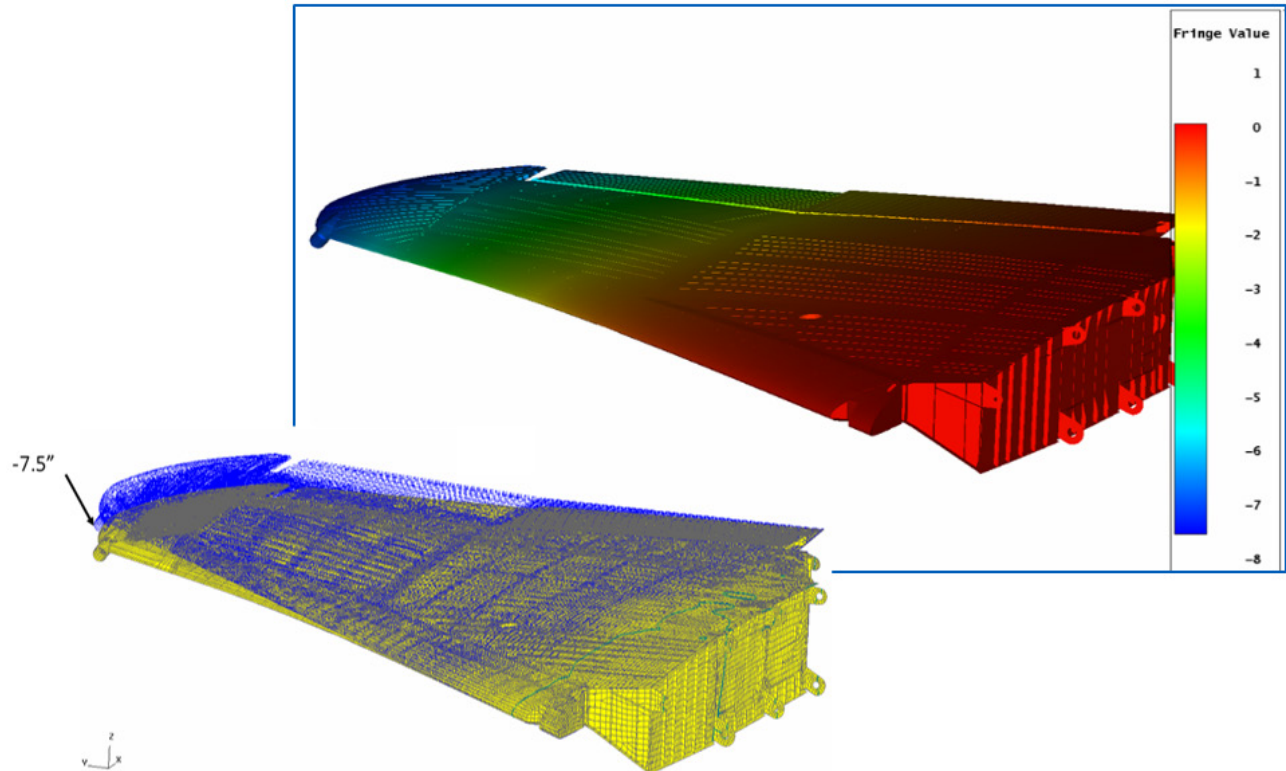


Figure 32. Wing displacement for limit load case 100301 (Cond. 5)

4.1.1 Actuator Loads

As shown in Figure 33, the loading apparatus will consist of thirteen discrete load actuators. Each actuator will be attached to a set of anywhere from three to six load pads, through a whiffle tree (not shown). The load pads will be bonded to the upper skin of the test article. AFRL/RQVS will be responsible for the design and installation of the load pads and the whiffle trees. (Note that jacks 11, 12 and 13 are exceptions in that they are connected directly to the aileron).

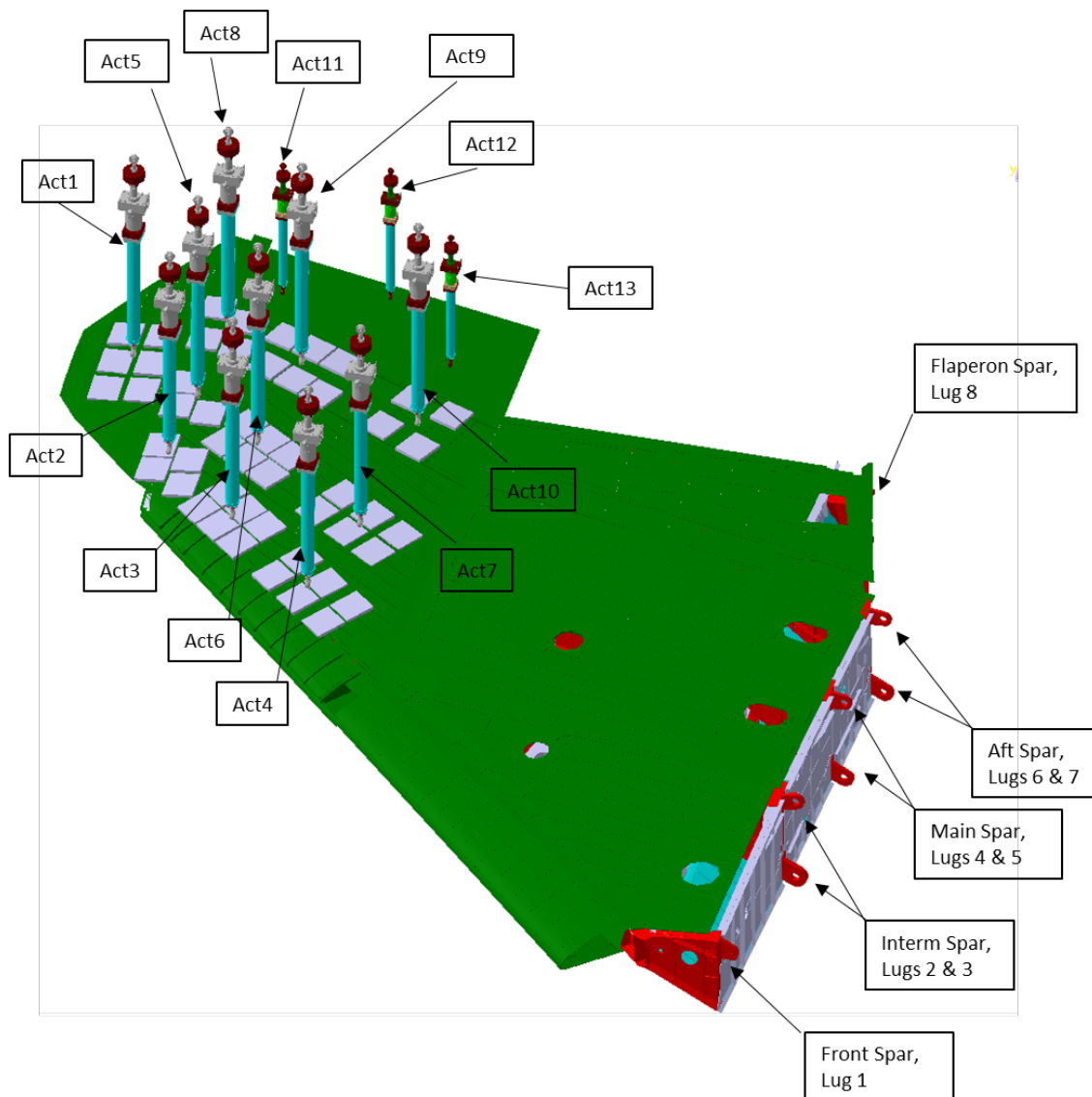


Figure 33. ADT test article with load jacks in place

A plan view of the general arrangement of the actuators and load pads, together with the actuator center of pressure locations (FS, BL, WL in inches), and load vectors are given in Figure 34.

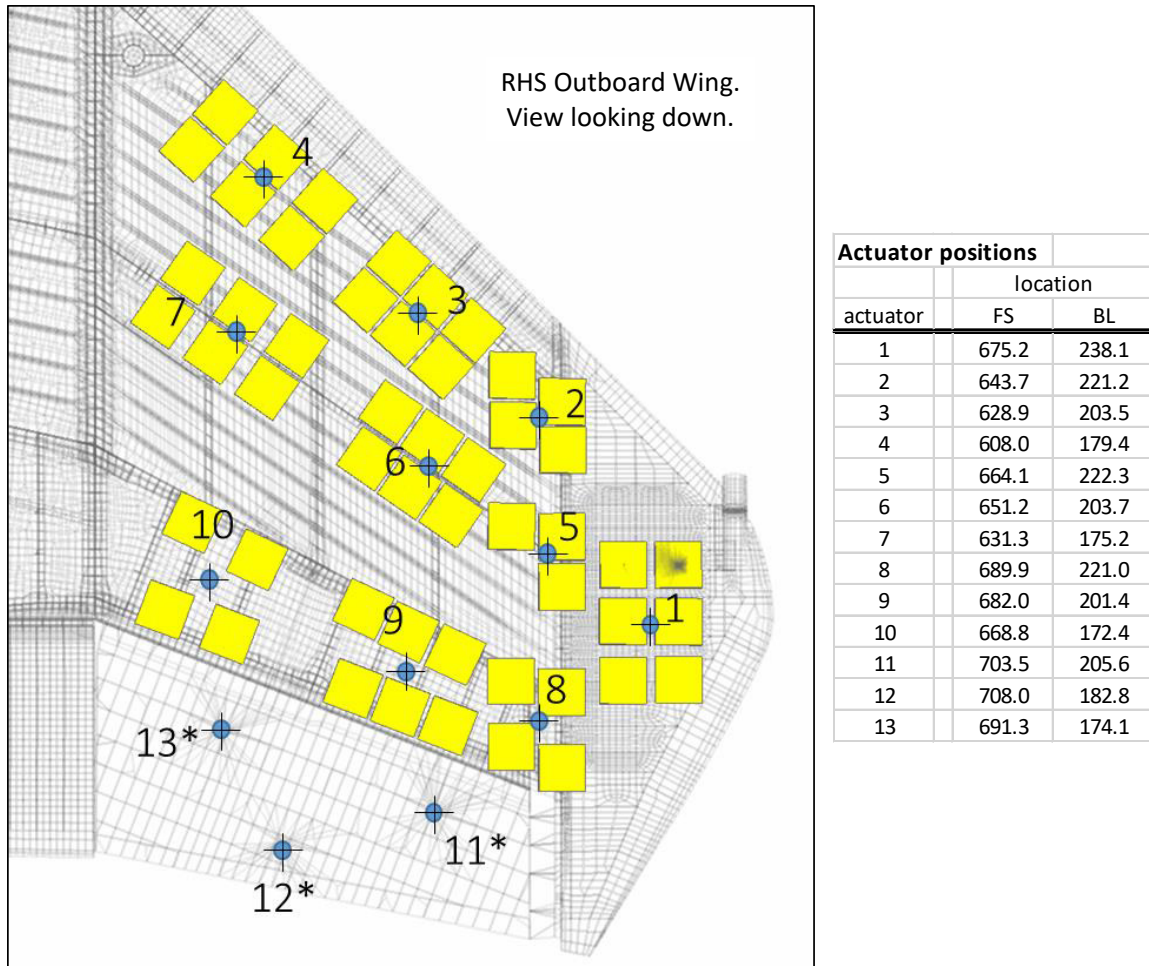


Figure 34. Load pad configuration and FS-BL coordinates (in.) for load actuators

The jack loads for each of the limit load cases are given in Table 4. The minimum and maximum load and displacement (+and -) per actuator zone are given in Tables 5 and 6. The individual pad locations (FS, BL, WL) and loads are given in Table 7.

Table 4. Jack load for limit cases (in-lbs)

actuator	location			limit load cases								spectrum cases	
ID	FS	BL	WL ^[1]	100101	100102	100201	100202	100301	100302	100401	100402	min	max
1	675.2	238.1	127.8	3113	169	3075	0	-1088	-2644	-1088	863	-2198	2410
2	643.7	221.2	127.2	3087	1813	3185	-245	-1617	-3283	-1617	2058	-2755	3461
3	628.9	203.5	128.1	4557	2793	6248	-4631	-1838	-4337	-1838	3087	-3610	5198
4	608.0	179.4	129.2	4263	3087	6248	-5145	-1838	-4190	-1838	3087	-3968	5222
5	664.1	222.3	128.6	2756	919	2499	-698	-3510	-147	-3510	882	-1116	2560
6	651.2	203.7	129.4	5807	1544	4998	-1066	-7056	-294	-7056	1838	-2244	5095
7	631.3	175.2	130.5	2205	0	4998	0	-6615	-294	-6615	1838	-2111	3674
8	689.9	221.0	128.4	1519	0	3430	0	0	4802	0	-1421	-9	3798
9	682.0	201.4	128.8	2279	-735	2205	368	-882	0	-882	-2352	-266	1753
10	668.8	172.4	129.6	1372	-1201	1666	3234	-588	0	-588	-2205	-707	3464
11	703.5	205.6	127.6	73	-1464	0	439	-146	1464	-146	-615	-1137	1144
12	708.0	182.8	127.2	62	-1241	0	745	-124	323	-124	-521	-964	594
13	691.3	174.1	128.3	67	-1330	0	1330	-200	346	-200	-559	-1033	1061

[1] Water lines are on OML of the AV FEM

Table 5. Up-bend max actuator displacements each actuator zone

Actuator ID	100101			100102			100201			100202			Spectrum Case Max Displacement		
	X	Y	Z	X	Y	Z	X	Y	Z	X	Y	Z	X	Y	Z
1	-0.06	0.02	8.86	0.02	-0.01	0.79	-0.07	0.02	10.35	-0.02	0.01	-0.88	-0.06	0.02	7.29
2	-0.03	0.09	6.54	-0.01	0.02	1.04	-0.03	0.11	7.65	0.00	-0.02	-1.05	-0.02	0.07	5.24
3	-0.04	0.05	4.72	-0.01	0.01	0.84	-0.04	0.06	5.60	0.01	-0.02	-0.95	-0.03	0.04	3.83
4	-0.03	0.00	2.66	-0.01	0.00	0.53	-0.03	0.00	3.21	0.01	-0.01	-0.63	-0.02	0.00	2.20
5	-0.07	-0.03	7.23	0.02	-0.01	0.73	-0.08	-0.04	8.46	-0.02	0.01	-0.81	-0.07	-0.02	5.92
6	-0.07	-0.05	5.38	0.02	-0.01	0.62	-0.07	-0.05	6.32	-0.01	0.01	-0.70	-0.06	-0.03	4.39
7	-0.05	-0.07	2.96	0.01	-0.01	0.39	-0.06	-0.08	3.55	0.00	0.01	-0.47	-0.04	-0.06	2.44
8	-0.06	0.00	7.87	0.02	-0.02	0.21	-0.07	0.00	9.28	-0.02	0.02	-0.41	-0.05	0.00	6.68
9	-0.05	-0.04	6.04	0.02	-0.02	0.08	-0.06	-0.05	7.10	-0.02	0.02	-0.25	-0.05	-0.03	5.13
10	-0.03	-0.06	3.57	0.01	-0.01	0.05	-0.04	-0.07	4.23	-0.01	0.01	-0.10	-0.03	-0.04	3.07
11	-0.02	0.08	6.99	0.06	-0.03	-1.07	-0.02	0.09	8.19	-0.03	0.01	0.42	-0.02	0.07	6.17
12	0.00	0.10	5.33	0.01	-0.01	-2.08	0.00	0.11	6.18	0.00	0.01	1.22	0.00	0.08	4.98
13	-0.02	0.01	4.22	0.08	-0.02	-0.84	-0.02	0.01	4.95	-0.05	0.02	0.50	-0.03	0.01	3.81

Table 6. Down-bend min actuator displacements each actuator zone

Actuator ID	100301			100302			100401			100402			Spectrum Case Min Displacement		
	X	Y	Z	X	Y	Z	X	Y	Z	X	Y	Z	X	Y	Z
1	0.03	-0.02	-6.42	-0.03	0.01	-1.19	0.03	-0.02	-6.42	0.02	-0.01	0.97	-0.01	0.00	-2.50
2	0.02	-0.06	-4.85	0.01	-0.04	-1.56	0.02	-0.06	-4.85	-0.01	0.03	1.23	0.01	-0.04	-2.33
3	0.02	-0.03	-3.56	0.01	-0.02	-1.24	0.02	-0.03	-3.56	-0.01	0.02	0.99	0.01	-0.02	-1.78
4	0.02	0.00	-2.05	0.01	0.00	-0.79	0.02	0.00	-2.05	-0.01	0.00	0.63	0.01	0.00	-1.07
5	0.04	0.02	-5.36	-0.03	0.02	-1.08	0.04	0.02	-5.36	0.03	-0.01	0.89	-0.01	0.02	-2.15
6	0.04	0.03	-4.07	-0.02	0.01	-0.94	0.04	0.03	-4.07	0.02	-0.01	0.76	0.00	0.02	-1.71
7	0.04	0.05	-2.30	-0.01	0.02	-0.63	0.04	0.05	-2.30	0.00	-0.01	0.50	0.01	0.02	-1.03
8	0.03	0.00	-5.69	-0.03	0.02	-0.30	0.03	0.00	-5.69	0.02	-0.02	0.32	0.00	0.01	-1.84
9	0.03	0.03	-4.44	-0.03	0.01	-0.31	0.03	0.03	-4.44	0.02	-0.02	0.19	0.00	0.01	-1.46
10	0.02	0.04	-2.70	-0.01	0.01	-0.31	0.02	0.04	-2.70	0.01	-0.01	0.14	0.00	0.02	-0.93
11	0.02	-0.06	-5.13	-0.03	0.01	0.61	0.02	-0.06	-5.13	0.02	-0.01	-0.45	0.00	-0.02	-1.31
12	0.00	-0.07	-4.03	0.00	0.00	1.01	0.00	-0.07	-4.03	0.00	0.00	-1.00	0.00	-0.02	-0.83
13	0.02	-0.01	-3.20	-0.04	0.00	0.27	0.02	-0.01	-3.20	0.04	-0.01	-0.37	-0.01	0.00	-0.86

Table 7. Pad locations and loads for minimum and maximum actuator loads

actuator ID	Load Pad	location			limit load cases								spectrum cases	
		FS	BL	WL ^[2]	100101	100102	100201	100202	100301	100302	100401	100402	min	max
1	1	666.4	242.2	126.7	519	28	513	0	-181	-441	-181	144	-366.3	401.7
	2	666.4	234.0	127.7	519	28	513	0	-181	-441	-181	144	-366.3	401.7
	3	674.9	242.3	127.4	519	28	513	0	-181	-441	-181	144	-366.3	401.7
	4	674.8	233.9	128.1	519	28	513	0	-181	-441	-181	144	-366.3	401.7
	5	683.6	242.3	127.7	519	28	513	0	-181	-441	-181	144	-366.3	401.7
	6	683.7	233.9	128.2	519	28	513	0	-181	-441	-181	144	-366.3	401.7
2	1	641.9	224.8	126.4	772	453	796	-61	-404	-821	-404	515	-688.8	865.3
	2	637.9	217.4	127.1	772	453	796	-61	-404	-821	-404	515	-688.8	865.3
	3	649.1	224.9	127.4	772	453	796	-61	-404	-821	-404	515	-688.8	865.3
	4	645.4	217.5	127.9	772	453	796	-61	-404	-821	-404	515	-688.8	865.3
3	1	631.2	211.5	127.2	760	466	1041	-772	-306	-723	-306	515	-601.7	866.3
	2	626.1	205.9	127.5	760	466	1041	-772	-306	-723	-306	515	-601.7	866.3
	3	621.1	200.4	127.7	760	466	1041	-772	-306	-723	-306	515	-601.7	866.3
	4	636.7	206.7	128.4	760	466	1041	-772	-306	-723	-306	515	-601.7	866.3
	5	631.7	201.1	128.7	760	466	1041	-772	-306	-723	-306	515	-601.7	866.3
	6	626.7	195.4	128.9	760	466	1041	-772	-306	-723	-306	515	-601.7	866.3
4	1	611.9	189.3	128.3	711	515	1041	-858	-306	-698	-306	515	-661.3	870.3
	2	605.3	182.1	128.6	711	515	1041	-858	-306	-698	-306	515	-661.3	870.3
	3	598.5	174.5	128.9	711	515	1041	-858	-306	-698	-306	515	-661.3	870.3
	4	617.4	184.4	129.4	711	515	1041	-858	-306	-698	-306	515	-661.3	870.3
	5	610.8	177.1	129.7	711	515	1041	-858	-306	-698	-306	515	-661.3	870.3
	6	604.0	169.4	129.9	711	515	1041	-858	-306	-698	-306	515	-661.3	870.3
5	1	662.1	224.8	128.4	919	306	833	-233	-1170	-49	-1170	294	-372	853
	2	660.6	217.3	128.8	919	306	833	-233	-1170	-49	-1170	294	-372	853
	3	669.6	224.8	128.7	919	306	833	-233	-1170	-49	-1170	294	-372	853
6	1	652.1	211.6	128.9	967.8	257.3	833.0	-177.6	-1176.0	-49.0	-1176.0	306.3	-374.0	849.2
	2	647.8	205.5	129.2	967.8	257.3	833.0	-177.6	-1176.0	-49.0	-1176.0	306.3	-374.0	849.2
	3	643.4	199.2	129.5	967.8	257.3	833.0	-177.6	-1176.0	-49.0	-1176.0	306.3	-374.0	849.2
	4	658.9	208.2	129.3	967.8	257.3	833.0	-177.6	-1176.0	-49.0	-1176.0	306.3	-374.0	849.2
	5	654.7	202.1	129.5	967.8	257.3	833.0	-177.6	-1176.0	-49.0	-1176.0	306.3	-374.0	849.2
	6	650.4	195.9	129.8	967.8	257.3	833.0	-177.6	-1176.0	-49.0	-1176.0	306.3	-374.0	849.2
7	1	633.5	185.2	130.1	367.5	0.0	833.0	0.0	-1102.5	-49.0	-1102.5	306.3	-351.8	612.3
	2	628.1	177.4	130.4	367.5	0.0	833.0	0.0	-1102.5	-49.0	-1102.5	306.3	-351.8	612.3
	3	622.6	169.6	130.6	367.5	0.0	833.0	0.0	-1102.5	-49.0	-1102.5	306.3	-351.8	612.3
	4	639.8	180.7	130.3	367.5	0.0	833.0	0.0	-1102.5	-49.0	-1102.5	306.3	-351.8	612.3
	5	634.5	173.0	130.6	367.5	0.0	833.0	0.0	-1102.5	-49.0	-1102.5	306.3	-351.8	612.3
	6	629.1	165.2	130.8	367.5	0.0	833.0	0.0	-1102.5	-49.0	-1102.5	306.3	-351.8	612.3
8	1	685.4	224.8	128.5	253.2	0.0	571.7	0.0	0.0	800.3	0.0	-236.8	-1.5	633.0
	2	683.8	217.2	128.6	253.2	0.0	571.7	0.0	0.0	800.3	0.0	-236.8	-1.5	633.0
	3	696.8	224.9	128.0	253.2	0.0	571.7	0.0	0.0	800.3	0.0	-236.8	-1.5	633.0
	4	693.7	217.3	128.2	253.2	0.0	571.7	0.0	0.0	800.3	0.0	-236.8	-1.5	633.0
9	1	679.8	208.9	128.9	570	-184	551	92	-221	0	-221	-588	-66.5	438.3
	2	676.4	201.9	129.1	570	-184	551	92	-221	0	-221	-588	-66.5	438.3
	3	673.0	195.1	129.2	570	-184	551	92	-221	0	-221	-588	-66.5	438.3
	4	690.4	207.8	128.4	570	-184	551	92	-221	0	-221	-588	-66.5	438.3
	5	687.7	200.7	128.5	570	-184	551	92	-221	0	-221	-588	-66.5	438.3
	6	684.8	193.6	128.7	570	-184	551	92	-221	0	-221	-588	-66.5	438.3
10	1	665.6	179.3	129.7	228.7	-200.1	277.7	539.0	-98.0	0.0	-98.0	-367.5	-117.8	577.3
	2	660.0	169.6	130.0	228.7	-200.1	277.7	539.0	-98.0	0.0	-98.0	-367.5	-117.8	577.3
	3	676.7	175.1	129.2	228.7	-200.1	277.7	539.0	-98.0	0.0	-98.0	-367.5	-117.8	577.3
	4	673.0	165.4	129.4	228.7	-200.1	277.7	539.0	-98.0	0.0	-98.0	-367.5	-117.8	577.3
11	[3]	703.5	205.6	127.6	73	-1464	0	439	-146	1464	-146	-615	-1137	1144
12		708.0	182.8	127.2	62	-1241	0	745	-124	323	-124	-521	-964	594
13		691.3	174.1	128.3	67	-1330	0	1330	-200	346	-200	-559	-1033	1061

[1] Actuator Loads are evenly distributed on the load Pads. [2] Water lines are on OML of the AV FEM. [3] Actuators 11, 12, and 13 have a single pad at the end of each actuator.

4.1.2 Reaction Loads

The ID and location (FS, BL, WL) for each of the eight wing to test frame attach lugs, as well as the reaction loads for each of the limit load cases are given in Table 8.

Table 8. Wing to test frame attach locations and reaction loads for limit load cases (in-lbs)

reaction	Spar	location			limit load cases								spectrum cases	
		FS	BL	WL	100101	100102	100201	100202	100301	100302	100401	100402	min	max
lug1-Fy	Front	509.5	58.5	131.4	-3012	1124	-3372	-1237	2235	-1093	2235	1084	-2924	366
lug1-Fz		509.5	58.5	131.4	10062	1065	12061	-1325	-7800	-1933	-7800	1425	-3366	8388
lug2-Fy	Interm	558.5	57.3	135.5	54590	15156	67258	-17905	-43319	-21593	-43319	17663	-25990	48391
lug2-Fz		558.5	57.3	135.5	5019	41	5883	-89	-3786	-354	-3786	176	-1279	4292
lug3-Fy		558.5	57.3	114.3	-56942	-17584	-70400	20660	45240	24517	45240	-20249	-51821	28464
lug3-Fz		558.5	57.3	114.3	-9335	-4547	-11877	5290	7614	5995	7614	-5085	-9757	6046
lug4-Fy	Main	595.9	56.3	133.9	87593	12997	105861	-15798	-68511	-21332	-68511	16395	-32491	72121
lug4-Fz		595.9	56.3	133.9	12093	1616	14502	-1956	-9334	-2671	-9334	2044	-4268	9955
lug5-Fy		595.9	56.3	112.9	-70995	-11897	-86159	14406	55805	19021	55805	-14797	-58141	27570
lug5-Fz		595.9	56.3	112.9	-21315	-3859	-25976	4664	16861	6089	16861	-4767	-17413	8560
lug6-Fy	Aft	626.9	55.7	132.5	81523	6622	98089	-8747	-63860	-14121	-63860	9769	-26412	68946
lug6-Fz		626.9	55.7	132.5	11248	1580	13502	-1913	-8681	-2576	-8681	1983	-4032	9235
lug7-Fy		626.9	55.7	112.0	-92757	-6419	-111278	8621	72408	14602	72409	-9866	-78686	29001
lug7-Fz		626.9	55.7	112.0	-37190	-2012	-44633	2855	29135	5313	29135	-3415	-31777	11291
lug8-Fz*	Flaperon	671.8	71.4	129.0	-1740	1761	-2014	-1855	1491	-1609	1491	1660	-2548	1083
* NOTE: reaction loads for flaperon spar lug pending fixture design. For a/c installation, lug carries z-direction load only.														

4.1.3 Tare Loads

The 15 reaction and 13 jack loads for support of the empty wing are given in Table 9.

Table 9. Tare loads (in-lbs)

Reaction	Spar	Load ^[1]	Actuator	Reaction
			ID	Load ^[1]
lug1-Fy	Front	-55	1	27
lug1-Fz		-5	2	14
lug2-Fy	Interm	-992	3	20
lug2-Fz		76	4	56
lug3-Fy		1088	5	15
lug3-Fz		357	6	22
lug4-Fy	Main	-1059	7	62
lug4-Fz		-44	8	19
lug5-Fy		936	9	9
lug5-Fz		370	10	78
lug6-Fy	Aft	-999	11	7
lug6-Fz		-41	12	14
lug7-Fy		1163	13	15
lug7-Fz		559		
lug8-Fz ^[2]	Flaperon	130		
[1]Reactions correspond to a T/A (including control surfaces) empty weight of 1755 Lbs.				
[2] Reaction loads for flaperon spar lug pending fixture design. For a/c installation, lug carries z-direction load only.				

4.2 Baseline Spectrum

The baseline spectrum (BS) was generated based on the probabilistic fatigue spectrum developed during Task Order 1 of the ADT program [1]. It includes estimated ground and flight dynamics model derived flight events arranged in physically meaningful flight segments, which in turn have been grouped into flights. The baseline spectrum was scaled to produce the estimated damage rates necessary to demonstrate an IAT system, and truncated in order to keep the test duration within a twelve month window. The resulting baseline spectrum has 1001 flights (including one marker band flight), representing 1000 flight hours. The spectrum is written in the form of an event sequence in which the events are listed in sequential order, with all pertinent flight and sequence numbers, time values, integrated load values (M and T at both the wing root and at station 3), jack loads and control point stresses provided on a single line.

The baseline ADT fatigue test spectrum was delivered in the form of a single comma separated value file and is available in Appendix G. A summary of the file and its contents is as follows:

- 1000 flight hours
- 1001 flights (including marker band flight)
- 91,770 end points
- Load set: ADT-TO2-R7- 2016
- Delivered in MSEXcel format
- Cumulative flight time (minutes)
- Maneuver
- g force level
- Altitude
- Flight ID
- Mission ID
- Wing station 3 loads
- 13 jack loads

Sufficient information is given in this file (specifically mission type IDs, flight IDs, and flight segment descriptions) to allow construction of test spectra as required by AFRL. It is understood that in order to simulate realistic IAT system operation with realistic aircraft usage variation, AFRL will re-sequence flights and will intermittently withhold FDR data during the execution of the test in order to simulate missing flight data.

A moment vs. torque diagram for moment and torque at wing station 3 is shown in Figure 35. This diagram is like Figure 12, but enforces the max bending and torsion limits (removed flights outside the defined bounds).

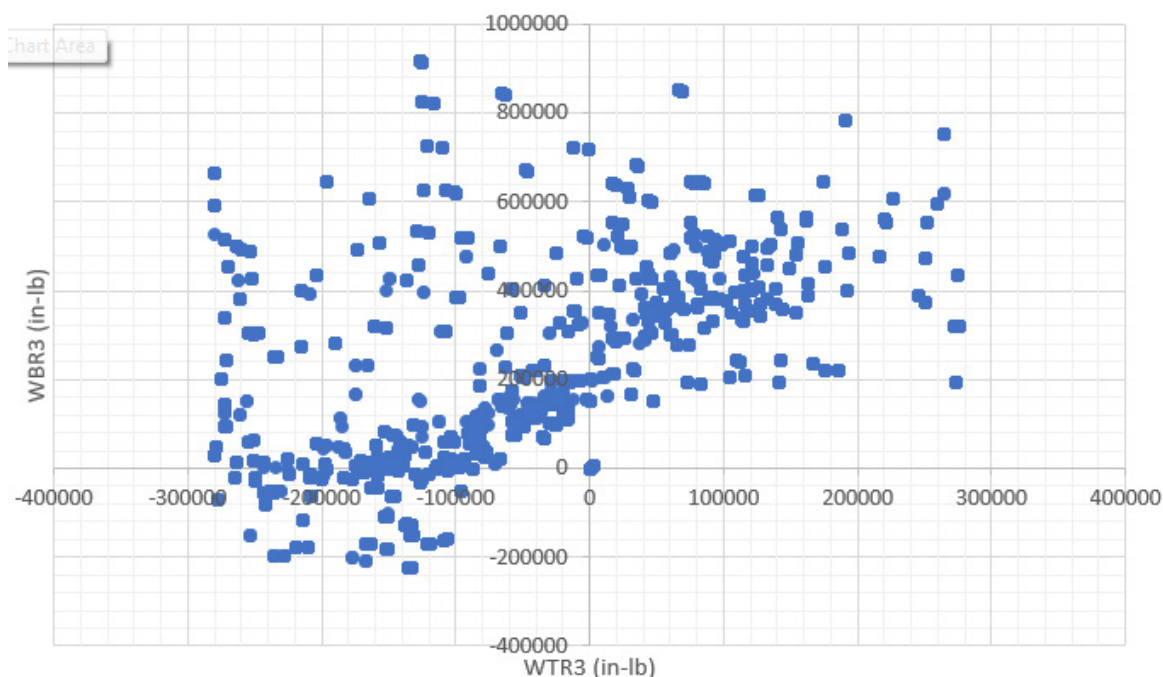


Figure 35. Wing station 3 moment vs. torque diagram for the baseline MES

5.0 FLIGHT RECORDER DATA & TEST SPECTRUM

On a time-hack by time-hack basis, FRD must be converted to external loads. The external loads are a parameterization of the distributed load on the asset. While this could come from a complex analysis (e.g. principal components), if the area of interest is relatively simple geometry then a few bending moments and torques may be sufficient to define most or all loading cases. In the case of the outer wing of an aircraft, it was found that the bending and torque on the main spar at one location (i.e. two scalar numbers) were sufficient to parameterize nearly all loading conditions. These values are referred to as WBR3 and WTR3 for Wing Bending and Wing Torque, respectively, on the right side at station 3. In general, though, any number of scalar values which describe the overall external loading can be used.

The model which converts FRD to loads is created using outputs from the six degree-of-freedom flight simulator. Figure 36 shows how the model is created. The flight simulator generates both FRD and external loads when control input (e.g. stick input for an aircraft) are supplied. The simulator was run for a variety of maneuvers which covered the operational envelope. The FRD and external loads were collected for all the runs (each simulator run results in a time history with hundreds of points, each of which can be used to train the model). Then, a Gaussian Process meta-model [2] was built to predict external loads from FRD data; this model was trained on some of the data from the simulator. The model was validated on the remaining data.

The model was built using the Bayesian Hybrid Model/Intelligent Design and Analysis of Computer Experiments (GE-BHM/IDACE) tool. The tool builds a Gaussian Process meta-model, training the model parameters using a Markov Chain Monte Carlo (MCMC) algorithm. The tool is an implementation of the Kennedy and O'Hagan framework [3] [4]. In IDACE mode, the tool attempts to build a model by taking a subset of the data. This is done iteratively:

1. Build a model with a subset of points (training set) and predict on the rest (test set) for validation
2. Identify points in the test set with large errors; stop if error is below threshold
3. Add points with largest errors to the training set and return to step 1.

The final model predicts both a mean and standard deviation of the external load parameters for given FRD. The BHM model (filename: *pout_fdr_to_loads_final.mat*) and prediction software (filename: *BHM_predict.exe*) was provided to AFRL, accompanied by an example input file (filename: *sample_input_file.csv*). To make predictions on the BHM model perform the following steps:

1. Open a windows command prompt
2. Change directories to the folder containing the BHM software, BHM model and input file
3. Execute the following command:
BHM_predict.exe fdr_to_loads_final <name of input file>
4. To run the sample input file, replace <name of input file> with *sample_input_file.csv*
5. To run the prediction on a new input file, do the following:
 - a. Create a .csv file
 - b. The first row of the input file must be a header with the 9 input parameter names

- mach,alt,nnzcg,nnxcg,nnycg,rollrate,pitchrate,rollaccel,pitchaccel*
- c. Each row under the header is a data point the user wishes to predict using the BHM model.
 - d. Save the csv file and run the command given in step 4.

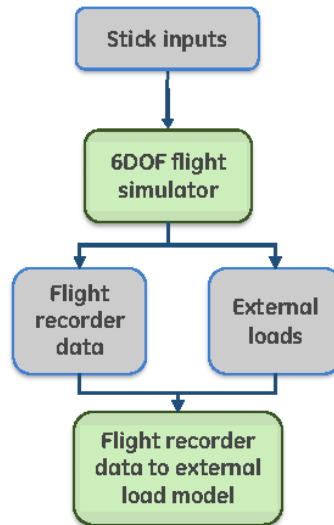


Figure 36. Process for creating the FRD to loads model

6.0 INSTRUMENTATION AND DATA ACQUISITION

The locations for installation of the internal and outer mold line (OML) instrumentation required for safety of test are defined in this section. The gage installation locations, measurements, and process for location of the gages were prepared with the assistance of the Mercer Engineering Research Center. Reference images are in Appendix A and Appendix B for reference.

The technical approach to develop the instrumentation plan is summarized below:

- (a) Define instrumentation necessary and available to monitor overall health of the test article. Instrumentation shall be monitored for changes in test article compliance and will be designated as SOT instrumentation.
- (b) Define instrumentation necessary to monitor strain and crack response at each CP. Strain measurements and crack growth rate shall be used to validate the predictive crack growth models.
 - Determine accessibility of each CP
- (c) Define type of sensors required and measurement sensitivity based on predicted strain values and expected crack propagation paths identified in Task Order 2.
- (d) Define necessary coupon tests
 - Correlation of results
 - Drives health monitoring criteria
 - Affects crack propagation measurement plan
 - Represents dry run for sensor mounting plan
 - CP accessibility
 - Mounting requirements
- (e) Prepare preliminary sensor installation plan and documentation based on information available
 - External strain/crack gage specifications/data documentation for locations, orientation, and sensor type (axial or rosette)
 - Internal strain gage specifications/data documentation
 - Locations (drawings)
 - Sensor type and applicable data
 - Sensor electrical wiring configuration
 - Predicted strain data values for designated test conditions
 - Deflection/Displacement information
 - Sensor locations
 - Maximum displacement (+ and -) at each sensor location
- (f) Document the sensor data format, data storage, acquisition rate, etc.

Sections 6.1 through 6.3 discuss the details of the instrumentation plan and execution that resulted following the approach outlined above.

6.1 Internal Safety of Test and CP Instrumentation

All definitions of the SOT instrumentation for the internal structure of the wings were completed for Task Order 2. A detailed coordination was executed with the NGC team as to avoid any conflicts with installation of both the GE and NGC internal wing instrumentation. Figures documenting the SOT instrumentation installation locations and definitions of the gage type, location, and required orientation of each sensor are in Appendix A. The internal instrumentation consists of 27 strain gauges.

Information in Appendix A covers all internal gage locations for both wings, upper and lower skins, and a single crack gage location at GE02 on the lower wing skins at the leading edge attachment point. The crack gage was installed across the cord wise thickness change in the outboard lower wing skin as close to the leading edge flange as possible. The area of interest lies below the wing skin attachment flange in the minimum thickness transition but geometry limitations prevent installation of the crack gage in the faying surface between the wing skin and the leading edge flange. This location represents a best effort for detection of a significant crack in an un-inspectable area of the wing structure.

6.2 Outer Mold Line (OML) Safety of Test Instrumentation

OML SOT instrumentation was designed and installed as a part of Task 2. In total, 19 axial strain gauges were installed on the OML surface of the lower skins. Six of those axial gauges were installed located over integral stiffeners and the remaining thirteen in panel acreage locations with constant skin thickness. A single crack gauge was also included at the location of GE05. Detailed information is provided in Appendix B.1 and B.2 covering the overall OML gage locations for both wings, upper and lower skins, and a single crack gage location near GE05 on the lower wing skins at the leading edge attachment point.

Determination of the location of the integral wing skin stiffeners relative to the existing fastener patterns was critical for proper location and orientation for many of the OML strain gages. To that end GE contracted with the MERC to obtain measurements locating the integral wing skin stiffeners relative to existing fastener holes and structural features evident on the exterior of the wing skins. In most cases measurements were taken from outboard aft fastener locations at wing rib pass troughs for the wing skin integral stiffeners unless noted otherwise. See Figure 37.

Left Upper Torque Box Skin

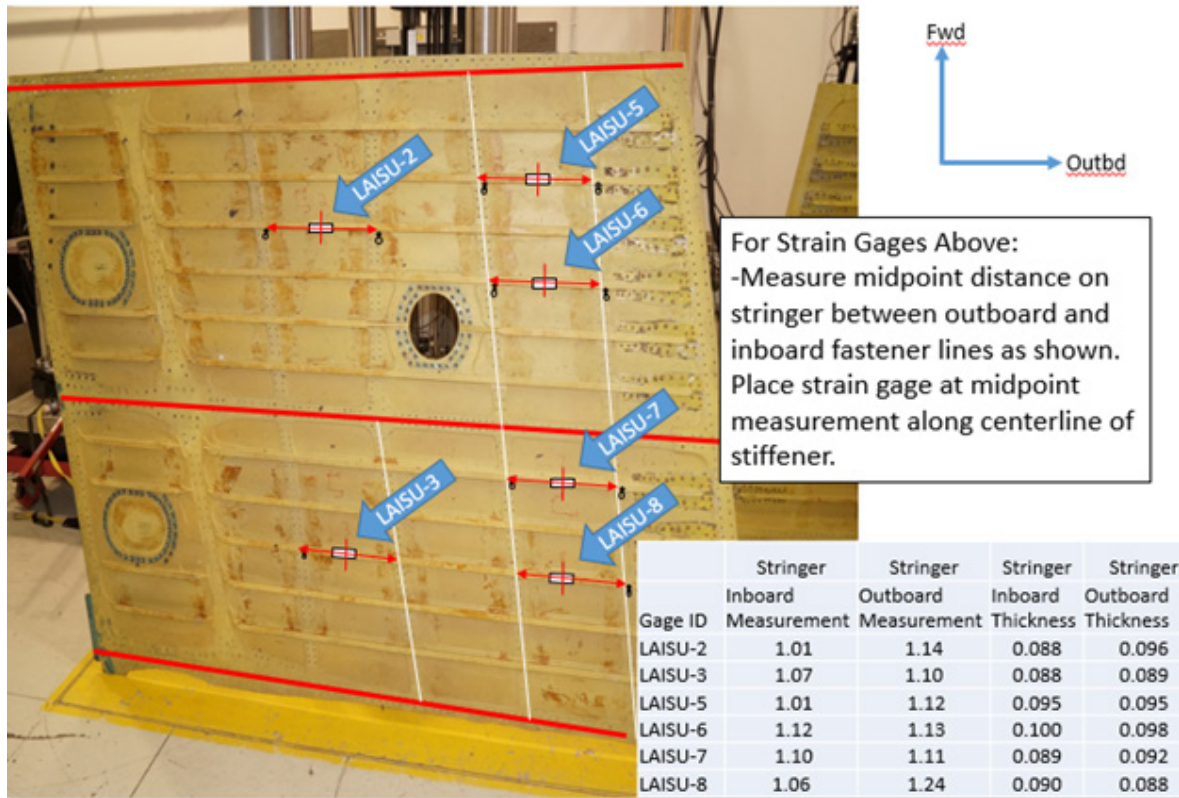


Figure 37. Left upper torque box skin strain gage locations and measurements

In this case for location of LAISU-2, the strain gage installer first locates the outboard aft fasteners for the correct integral stiffener and appropriate rib locations based on the documentation of the wing skin (See Figure 38).

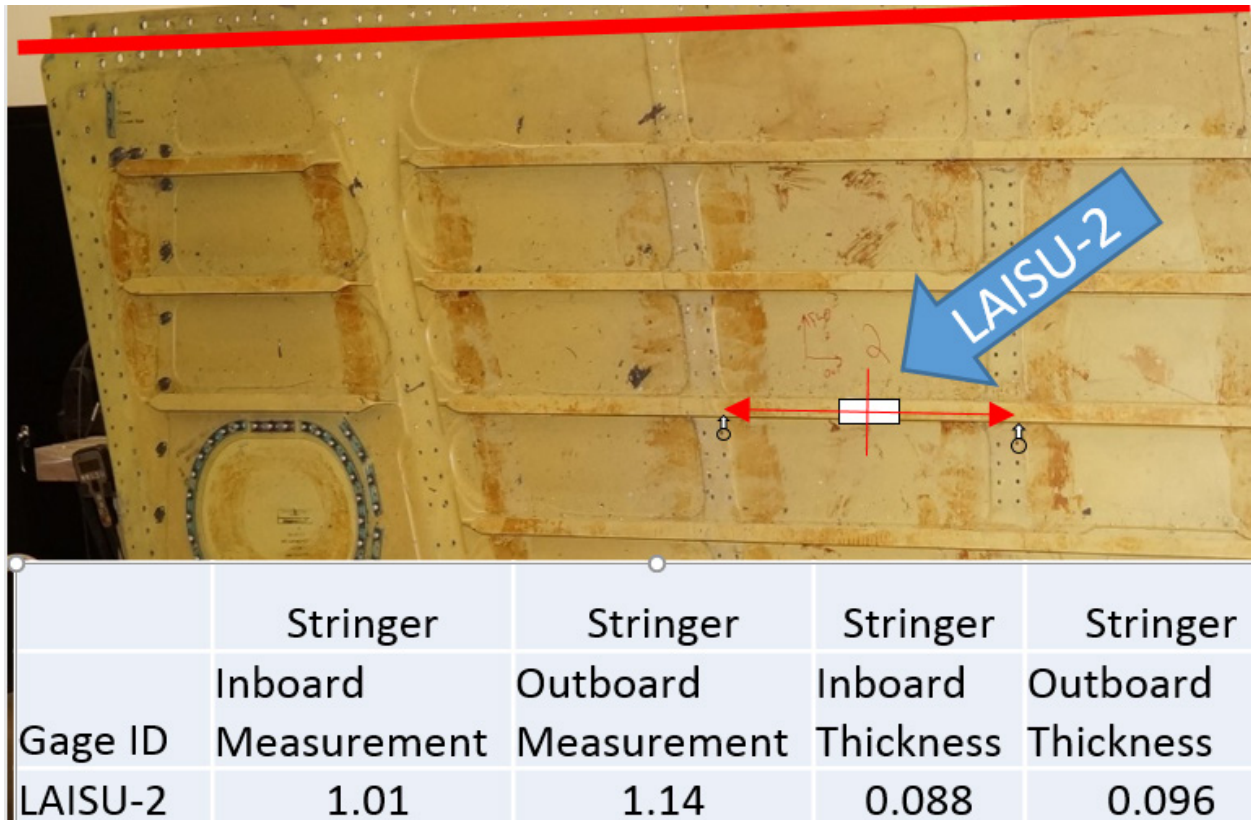


Figure 38. Detail of LAISU-2 strain gauge installation location

Note: photo taken of inside skin surface, gauge location would be on outside skin surface.

Once the stiffener and wing rib fasteners patterns have been located on the OML surface of the wing, the outboard aft fasteners are located. The measurements detail the distance from the center of the fasteners to the edge of the stiffener web and the thickness of the stiffener web at the corresponding locations. The distance from the center of the fastener holes to the centerline of the stiffener consist of the sum of the distance to the web plus half the thickness of the stiffener. Placement of the gage in the center span over the stiffener is accomplished using the fastener hole distances as shown in Figure 39. The axial gage must be aligned to the axis of the integral stiffener center line. In each case, all strain gage locations over integral wing skin stiffeners were measured relative to fastener holes and detailed geometry was specified for installation of the gages.

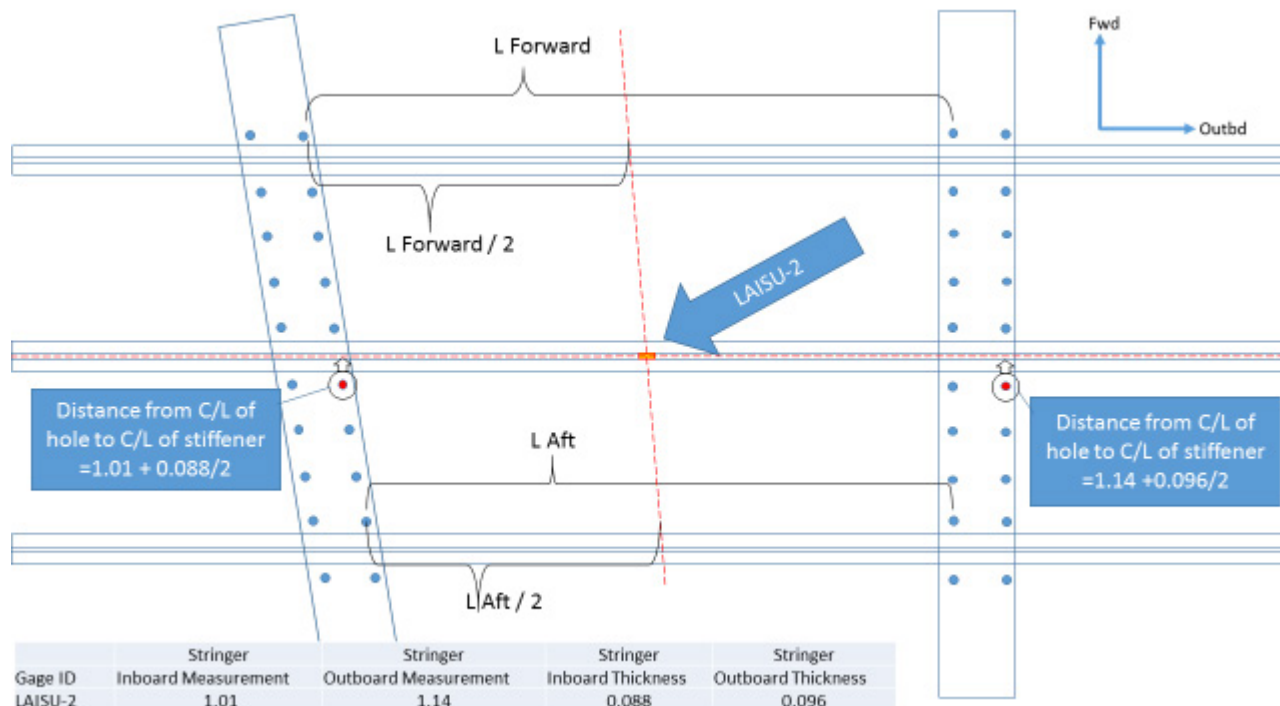


Figure 39. Detail location of LAISU strain gauge

In the case of strain gages located in the constant skin thickness areas of the wing skin between integral stiffeners, the geometry was more loosely defined. Orientation of the gages is dependent upon orientation of fastener lines and placement of the gage is less critical due to the constant skin thickness and resulting uniform strain. An example of locating the strain gages installed between stiffeners is illustrated in Figure 40.

The stringer locations are first determined based on the fastener patterns in the wing skins. Fastener spacing is greater when the integral wing skin stiffeners pass through openings in the ribs. The locations for the integral stiffeners are approximated as half way between the widely spaced fasteners. The locations of the stiffeners are laid out on the wing skin OML surface using tape. The fastener lines in the wing skins due to the wing ribs are also marked on the OML surface of the wing skins. Once this is completed the center of the bays between the stiffeners can be determined. The strain gage is placed in the center of the bay unless noted with its long axis oriented parallel to the integral stiffeners. In cases where the stiffeners do not run parallel, the half width points between the stringers at the bounding wing ribs are approximated. Connect these two points with a line. This line defines the orientation of the axis of the strain gage. The axial strain gage is installed on this line midway between the two ribs. In particular, RAOSL-3 required this method of approximating its correct location.

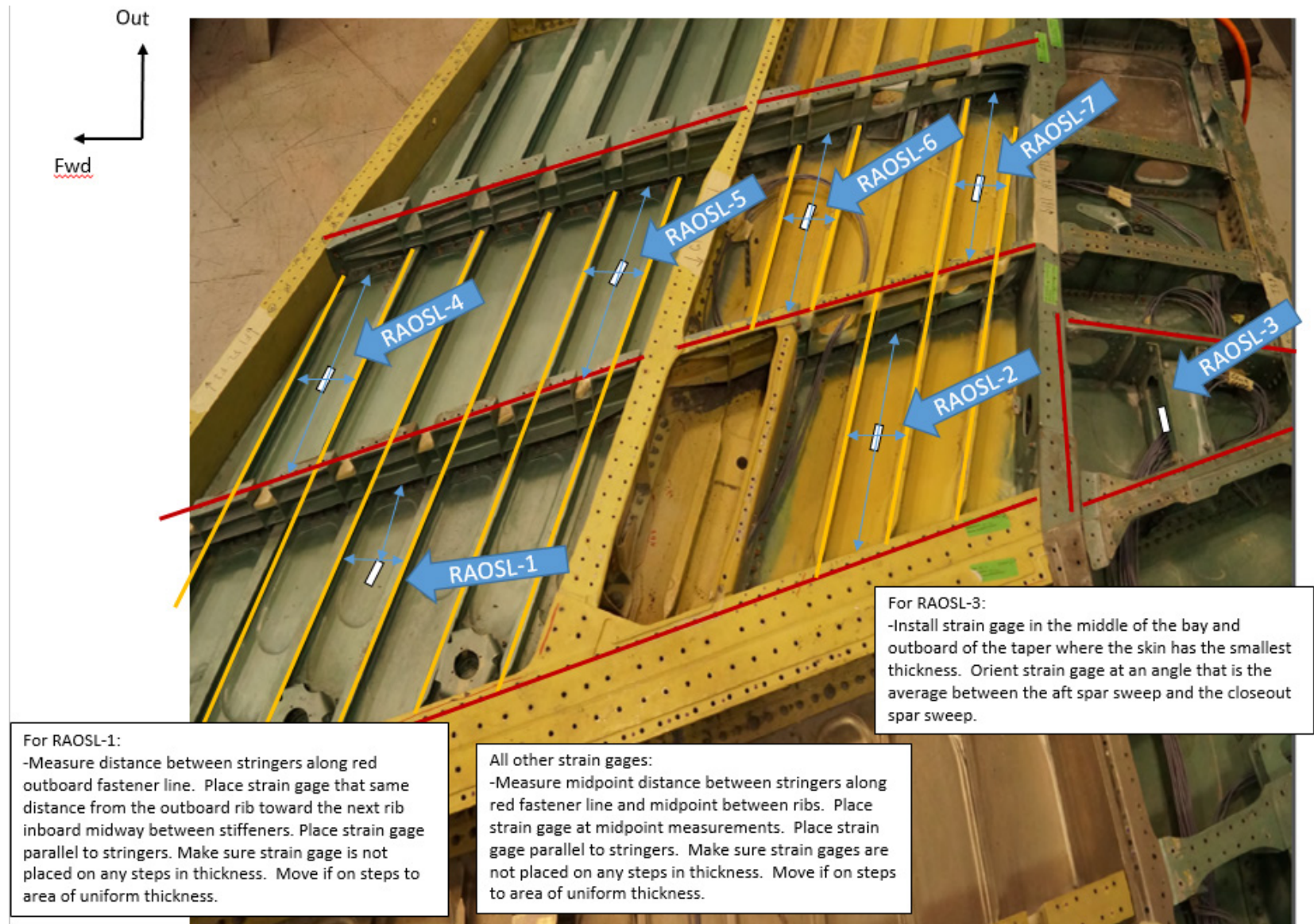


Figure 40. Outboard lower skin OML strain gauge locations

7.0 INSPECTION TECHNIQUES AND PROCEDURES

The main objective of the inspection plan development task was to identify a nondestructive inspection (NDI) approach for each control point, enabling not just detection, but quantification of crack damage growth during the fatigue testing at sizes below and up to the respective repair limits. The inspection data are to entail crack size information, including accompanying measurement uncertainties, to update and validate the probabilistic model predictions within the P²IAT initiative. More specifically, the objective of this task was to identify the frequency and locations of inspection to update and validate the probabilistic model predictions. The inspection schedule was also planned probabilistically, i.e. the schedule will be adjusted based on the predictions from the probabilistic models.

The inspection plan was generated in iterations based on the availability of information. Initially, the efforts concentrated on assessing the feasibility of current inspection approaches for this aircraft type. Studying this document enables determining the inspection requirements and criteria as well as identifying the current procedures and their respective feasibility to provide adequate input data for P²IAT.

The development of this inspection plan required a clear understanding of all pertinent structural components, anticipated crack damage and the resulting challenges to incorporate a suitable inspection approach. Challenges included the need to inspect complex, multi-layered structures, cracks located deep in the structure, cracks emanating at faying surfaces under fastener heads, as well as general control point accessibility, regarding sensor placement or sensor access limitations. These issues were addressed for each control point and, if necessary, mitigation processes were identified.

The inspection plan discusses the NDI approach selection process for each control point. The inspection concentrates on traditional nondestructive techniques due to lower costs, better availability and proven reliability. Either eddy current or ultrasonic based NDI methods are recommended for most currently considered CPs. In general, eddy current testing (ET) enables flaw size assessment for surface and near-surface cracks, assuming well known flaw shapes. However, the penetration depth of ET, i.e. inspection ability with sufficient sensitivity at certain flaw depth is limited. Ultrasonic testing (UT), on the other hand, allows inspection for deeper flaws, but flaw sizing can be problematic, limited by transducer size as well as immanent movement or coupling inaccuracies. It was critical to select the optimal approach for each CP application.

The inspection plan provides a detailed inspection procedure, including inspection site preparation processes, instrument set-up, sensor selection, calibration processes, and data assessment, processing, analysis and reporting procedures.

7.1 Inspection Plan and Procedures

As part of the Digital Twin Spiral 1 initiative, an inspection plan was developed for NDI of ten CP locations, tracked for fatigue crack growth during the fatigue experiments performed on two outer wings. These CPs were selected partly to ensure inspectability during the fatigue test, i.e. enable inspection without any disassembly or interference with the fatigue test.

Both, phased array ultrasonic testing (PAUT) and surface eddy current (SEC) will be employed to perform this inspection task. Additionally, crack gages are placed to assess and detect cracks occurring at CPs otherwise inaccessible to NDI. SEC is a well-established approach to detect surface-breaking or near surface cracks, however, the technique has significant penetration depth limitations. PAUT is an advanced NDI approach, not yet incorporated for aerospace applications, providing the means to detect smaller cracks prior to the cracks reaching the top surface and/or the critical crack length c_{crit} .

This inspection procedure is developed to detect cracking at selected CP locations in F-15 outer wing structures using a phased array ultrasonic testing (PAUT) approach. The inspections will occur at yet to be defined intervals during full scale fatigue testing of two F-15 wings.

Table 1 provides an overview over all GE CPs and the inspection approach to be performed for each CP. A total of six CPs can be inspected using the PAUT method, all of which are accessible from the outside, without disassembly, at the lower wing. More information regarding the inspection personnel requirements, equipment requirements, and inspection procedure details are in Appendix C.

Table 10. NDI Control point overview

CP Number	Outer Wing CP Location	CP Flaw Details	NDI Approach
GE01	Wing Skin, Lower, Forward, Fastener Hole at XW206 Rib	Single corner crack at fastener hole (crack at faying surface).	PAUT, SEC
GE02	Wing Skin, Lower Trailing Edge, at Aft Closure Spar at	Interior surface crack in fillet radius at thickness step.	SEC, crack gages
GE03	Wing Skin, Lower Trailing Edge, Fastener Hole at XW158	Single corner crack at fastener hole (crack at faying surface).	PAUT, SEC
GE04	Lower Trailing Edge Wing Skin, Fastener Hole at Rear Spar	Single corner crack at fastener hole (crack at faying surface).	SEC
GE05	Lower Wing Skin, Forward Edge Thickness Step at XW156	Corner crack in radius	SEC, crack gages
GE06	Lower Wing Skin, Fastener Hole, XW188 Rib	Single corner crack at fastener hole (crack at faying surface).	PAUT, SEC
GE07	Lower Forward Wing Skin, Fastener Hole at Front Spar	Single corner crack at fastener hole (crack at faying surface).	PAUT, SEC
GE08	Lower Wing Skin, fastener hole at XW162 (under aft spar)	Single corner crack at fastener hole (crack at faying surface).	PAUT, SEC
GE09	GE09 removed from CP list due to inability to reach CP after test rig was assembled		
GE10	Lower Aft Wing Skin, Fastener Hole at XW164 (under main spar)	Single corner crack at fastener hole (crack at faying surface).	PAUT, SEC

7.2 Coupon Testing

Coupon tests were conducted to simulate both actual outer wing CP structure and anticipated crack flaws as closely as possible. Large flaw size ranges and actual cracks were used in the

coupons to adequately simulate actual aircraft structures. The coupons all addressed corner cracks emanating from fastener holes at the first interface in the first (wing skin) layer.

The coupons provided means to develop PAUT of CPs with cracks anticipated to occur at fastener holes at first layer faying surfaces. The coupons are, furthermore, useful as calibration specimens.

Wyle developed coupons for seven (7) CPs (GE01, GE03, GE06, GE07, GE08, GE09, and GE10). The following main considerations for generating the new coupon design were made:

- The coupon flaw size range was not limited to the critical crack length range. In other words, we want to investigate NDI capability beyond what flaw sizes should be detected to those that can be detected. The larger range also allowed obtaining clear signal responses for flaws sizes in the range of the transducer aperture, enabling a clear reference signal to establish signal response transfer functions.
- The coupons were not used for eddy current NDI, only for ultrasonic approaches. Ultrasonic properties of various Al alloys are very similar, well within measurement uncertainties. Thus, Al 7075-T6 was used for all coupons as this alloy was the most readily available option.
- Coupon geometries were selected covering several CPs with the same fastener hole specifications as well as same or similar thicknesses. For instance, wing panel thicknesses of 0.120 and 0.160 inch will not change the ultrasonic response significantly, therefore, a coupon set was created that covered the simulation of CPs in that thickness range.

As a result three groups of panels were generated:

- Top layer with five holes with an EDM-notch of different size: 0.025, 0.050, 0.075, 0.100, and 0.250 inch, respectively.
- Top layer with one hole with crack of lengths: 0.025, 0.100, or 0.250 inch.
- 2nd layer with matching hole count/size.

All top layer panels matched the aircraft structure thickness and specific geometric features, for instance, for CP GE09, which is located in the main spar lower flange, a width of only about 0.5 inch from the fastener hole to the panel edge has to be observed.

Mil-spec fasteners, including Taperloks, Hiloks and Jobolts, were ordered through AFRL/RQVV. Wyle installed these fasteners, for which special reamers and install drivers were required. Both notch and crack introduction were performed by AFRL/RQVV.

Crack generation was completed for the coupons (e.g., Figure 41). Undersized holes (1/8 inch instead of the final 3/16 inch diameter) were machined and a crack starter notch was introduced using a diamond wire saw. This starter notch was less than 0.025 inch deep. The reaming to the final hole size occurred after a crack of the desired size was created in the specimen. After completion of the fatigue test, the fatigue machine grip region (approx. 2.5 inch on each side) was cut off.



Figure 41. Fatigue cracks introduced in GE09 simulating coupon panel

As an example, Figure 42 shows initial microscopic images the two (2) cracks for panels to simulate GE09 (main spar lower flange). These cracks were either 0.054 inch or 0.155 inch long after the final hole diameter was realized. Crack introduction for other CPs was completed with same crack lengths. NDI prior to coupon assembly was also initiated.

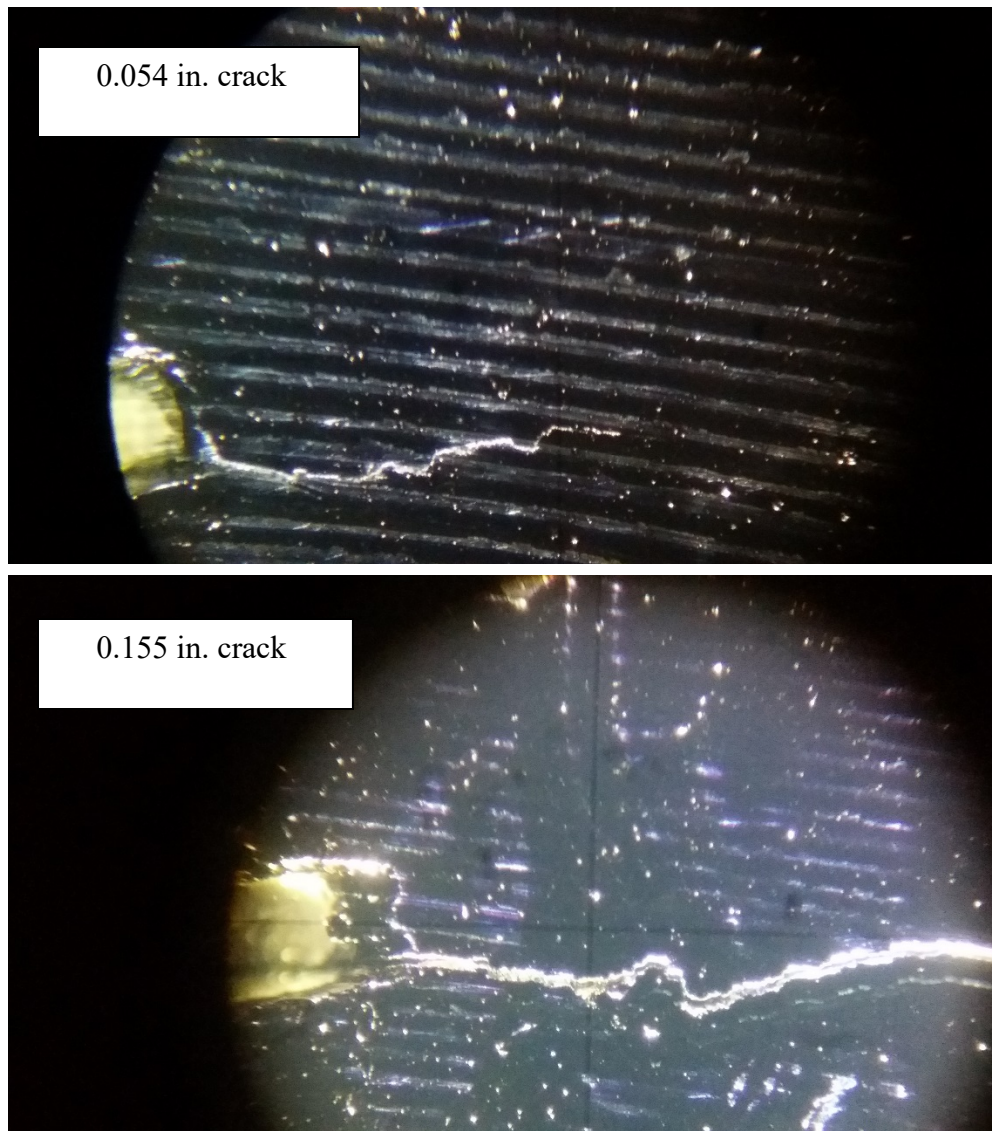


Figure 42. Microscopic images of cracks in GE09 simulating coupon panel

Wyle received all panels with electric discharge machined (EDM) notches in place. All coupons were assembled and NDI assessment could be initiated. The presence of the EDM-notch coupons enabled further improvement of the Phased Array Ultrasonic Testing (PAUT) approach. These studies enabled clear estimation of the PAUT inspection capabilities, as well as a comparison between crack and EDM-notch data.

The following main findings were made (the statements are valid for both EDM-notch and crack flaws):

- All large cracks (0.100 and 0.150 inch) – at or close to through thickness – have strong/stable indications and can easily be detected. The straight –forward, reliable detection of large cracks allows one to establish several set-up parameters, including

sensor positioning, gain settings etc. It supports identifying the crack reflection position within the data display features, especially the section scan images.

- Most mid-sized cracks (0.050 and 0.75 inch) have indications with sufficient Signal-to-Noise ratio (SNR) and distinct signal location in the PAUT S-scans in response to sensor movement. Here, the detection relies on identifying the reference fastener hole reflector and on sensor movement. The crack reflection can be identified by moving the sensor from the reference reflector. During repeated measurements on the aircraft wing, one can compare subsequent data to discriminate a newly occurring reflection at the correct location. Mid-sized flaws at holes with JoBolt fasteners can be detected with poor SNR.
- All small cracks (0.025 inch) were either not detected or only detected with insufficient SNR.
- Detection capability improved generally with increasing thickness. At smaller thicknesses larger incident angles become necessary, limiting the inspection range, thus, making it more difficult to place the sensor such that it can receive the crack reflection. Wyle used 25° angle wedge for 0.140 inch thick panel and thicker, 45° angle wedge for thinner coupon panels for optimal results.
- Detection capability appeared to be influenced by fastener type. As stated, Jo-Bolt fastener appeared to reduce the detectability of an adjacent crack (potential crack closure) and a Taperlok improved it, due to potential crack opening stresses. The Hilok reflection was in-between these extremes.
- Crack and EDM-Notches of the same size and coupon type yield similar reflection amplitudes. However, variations in crack topography influence reflection patterns. Concave or convex crack surface or crack propagation directions – with respect to the approaching ultrasonic wave - change the reflection characteristics. While reflection amplitudes are similar, the EDM-notch have an intermediate signal sharpness, with the concave crack have the tightest reflection amplitude.

NDI inspection techniques were practiced on the coupons and the procedures were documented. These dry-runs and notes will aid in a smooth NDI effort during the ground-test. For the eddy current inspection technique, the following was noted:

- A SEC Pencil Probe (50 kHz to 500 kHz, right angle shaft) will be used
- SEC to be used for all CPs,
 - Including GE02 and GE05: inside skin radii inspected from outside due to very thin skin thickness.
 - GE05 is partly covered by leading edge. There is limited access to this control point.
- Surface-breaking cracks are easily detected.
- Subsurface cracks can be detected.
- Subsurface cracks at a fastener is difficult, due to presence of fastener head.
- Additional use of EC Ring Probes for CPs at fastener locations enables inspection down to approximately 0.050 inch.

An illustration showing this SEC probe and reading is shown in Figure 43.

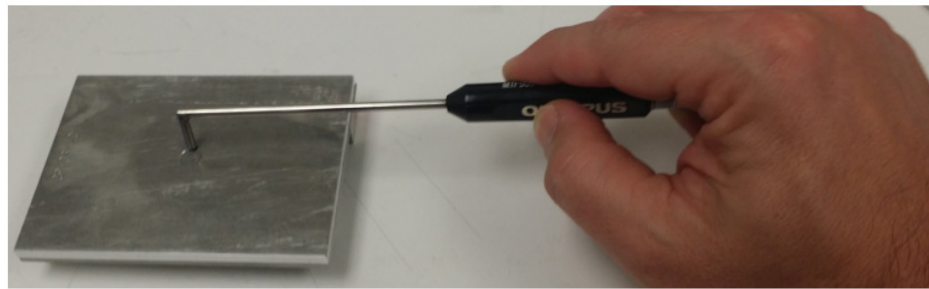
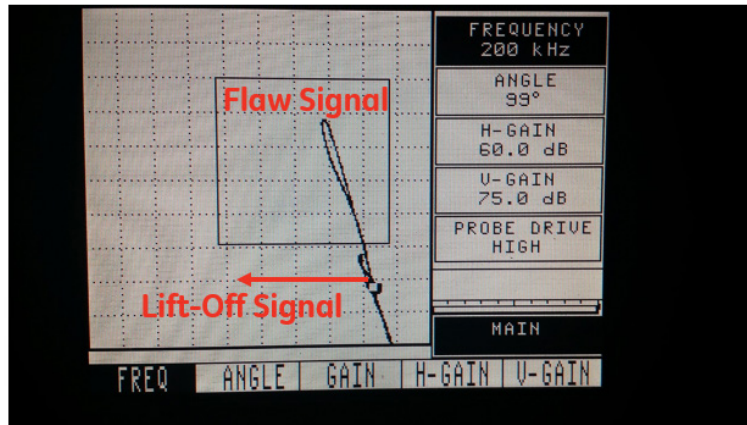


Figure 43. Eddy current inspection approach

8.0 FINALIZING P²IAT: FE & SIF MODELS, BASELINE PREDICTIONS

A stress intensity factor model, built for each control point of interest on an asset, is a computational model that takes external load, geometry, and crack state parameters as input and produces stress intensity factors as output. The stress intensity factor is a measure of the driving force which opens the crack at the control point, and in general it can be computed using the Green's function approach (Note, the current work only considers mode I stress intensity factor, crack opening mode, although other modes could be included as well):

$$K_I = \iint_{crack\ face} \sigma_{\perp}(x, y) \cdot G(x, y) dx dy \quad (3)$$

where $\sigma_{\perp}(x, y)$ refers to the stress component perpendicular to the crack plane (i.e. the crack opening stress) and $G(x, y)$ is the Green's function. Stress is generally calculated from a finite-element model, while the Green's function is usually assumed to take a particular form for a given crack type. A typical deterministic analysis would calculate a single value of K_I for a nominal geometry and a given crack state and loading condition. For P²IAT, though, it is necessary to be able to calculate K_I on demand given all of the parameters that are not known a-priori. The parameters of the K_I model must include the external load parameters (e.g. bending moment and torque) and the crack state. Any additional parameters can be included to allow P²IAT to propagate their uncertainty.

For demonstrating P²IAT, the K_I models for the CPs were built using several assumptions:

- To demonstrate the ability to incorporate both a coarse global FE model and a fine local FE model for GE04, GE05, GE06, GE07 and GE08.
- Use coarse-grid FE stresses to build a probabilistic K_I for GE01, GE02, GE03, GE09 and GE10.
- To demonstrate the ability to account for geometrical uncertainty by morphing the local FE model geometry
- To use a moderate resolution stress intensity factor model which considered the entire stress field on the crack plane from the local FE model
- To reduce analysis requirements by not accounting for multiple crack planes, curving crack trajectories, or how the presence of a crack modifies the load paths in the structure. Such analyses could be included by extending the flow chart (e.g. an arrow from "crack state" to "local FEM" to signify that the local FE could be modified to include the crack itself)

Once the crack opening stress model and the Green's function model had been developed, they were combined to produce the stress intensity factor model. This was done by defining a set of training points (i.e. a DOE or design of experiments) where each of the inputs were varied (some inputs, such as bolt hole diameter, were inputs to both models). For the CPs with a fine-grid FE model, the stress field and Green's function were calculated over the crack face for each set of inputs. A simple 2D integration scheme was used to calculate K_I . For the CPs with a coarse-grid-based stress model, the conventional approach taken by Lockheed Martin was used to calculate K_I at each set of inputs. In the end, for all CPs, the result is a table of inputs and a K_I

value for each. Finally, a probabilistic model was built to capture the overall input-output relationship:

$$K_I = K_I(\text{load}, \text{geometry}, \text{crack state}) \quad (4)$$

Another important factor is the distinction between corner and through cracks for bolt holes and part-through and through cracks for a surface. Generally, for a bolt hole a crack will start out as a corner crack and transition to a through crack. For a surface, a crack will start as a part-through crack and transition to a through crack. In P²IAT, separate corner crack, part-through crack, and through crack K_I models are built. The corner crack model is a function of both the crack length (along the surface) and depth (into the thickness), usually denoted c and a , respectively. Both part-through and corner cracks each have two separate Green's functions—one which represents growth in the surface direction and one in the depth direction. Thus, a part-through or corner crack K_I has two outputs: $K_{I,depth}$ and $K_{I,surf}$. The crack is assumed quarter-elliptical and P²IAT tracks c and a while the crack is a corner crack. Once the crack transitions to a through crack, a different Green's function is used and only the surface crack length is retained.

The following paragraphs describe in more detail the analyses in Figure 44 and how the stress intensity factor models were built for demonstrating P²IAT.

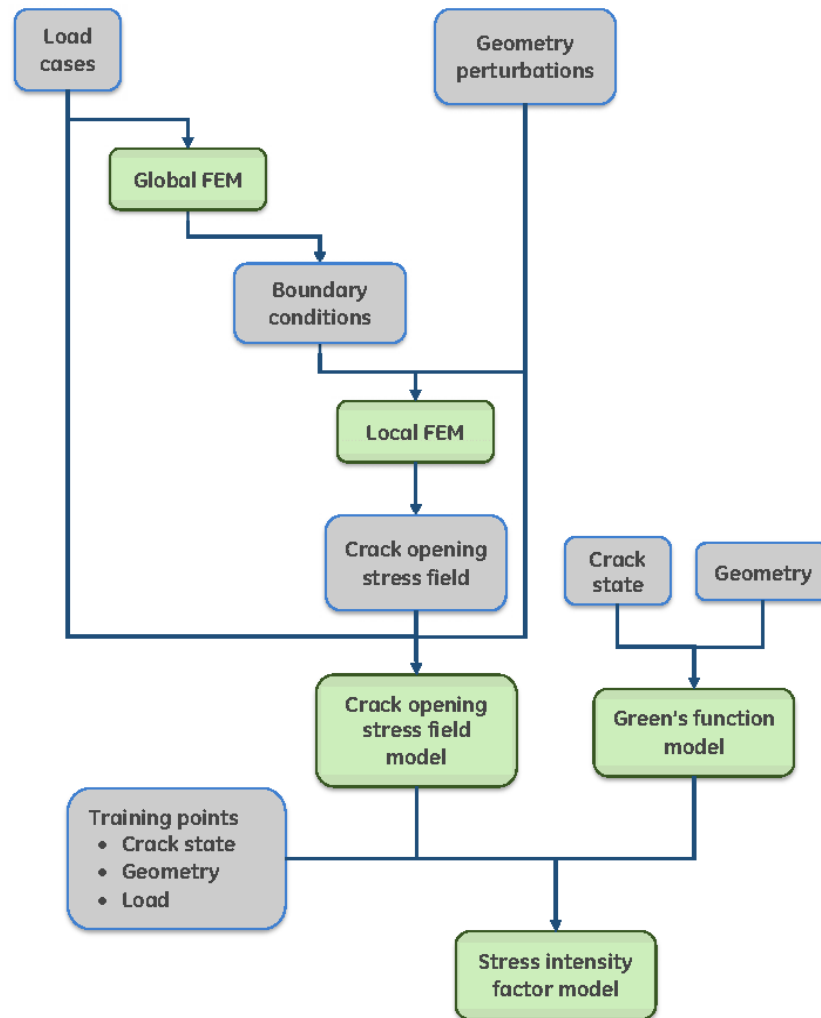


Figure 44. Process for Creating Stress Intensity Factor Model

8.1 Global and Local FE models

A local finite element model was used to evaluate local stress fields where cracks are expected to form. In Task Order 1 of the ADT program, a local model for the demonstration control point (GE06) was built. In Task Order 2, two submodels were built that include four more control points (GE04, GE05, GE07, and GE08). Once all models were built, the stress field were evaluated for a variety of load cases. An additional source of uncertainty which is necessary to include is the geometry. That is, the hole locations, diameters, radii of curvature, etc., are not known precisely. By morphing the geometric mesh of the FEM around each CP, this uncertainty can be quantified. The overall strategy was to solve the finite element model for various load cases and geometries (i.e. “samples”). Then, a BHM model was built to relate the local stress field to the input variables. If the model accuracy was low, new samples to improve accuracy were identified using IDACE. These new FE runs were performed and the model re-built. The process was repeated until sufficient accuracy was achieved.

The overall analysis approach was as follows:

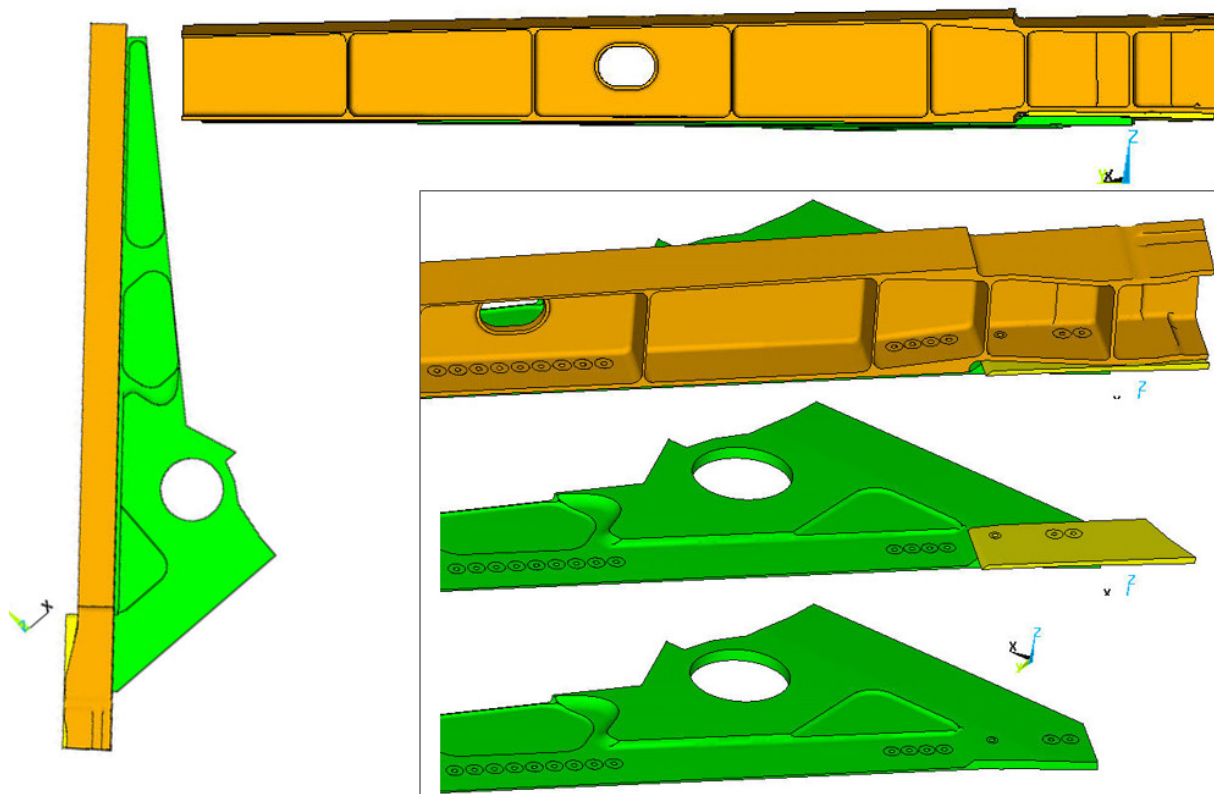
1. For a given load case, run the AV FEM to generate boundary conditions for the local FE model
2. For given geometry parameters, morph the local FE mesh
3. Apply the boundary conditions to the morphed mesh and solve
4. Identify the location of maximum stress at the area of interest (e.g. extending from the inner wall of a bolt hole into the bulk material) and extract the stress on the assumed crack plane.

Once these steps had been performed for a series of load conditions and geometry parameters, a BHM model was built that predicts the stress field on the crack plane as a function of the load and geometry. This model was then used to evaluate the stress intensity factor.

After the BHM model was built, input points that result in large uncertainty were identified and additional load/geometry cases run. The BHM model was updated when these runs were finished, and the process continued until a prescribed error tolerance was reached.

Load cases were selected by hand to be well-distributed across the input space of external loads (bending and torsion at the outboard wing station). It was also verified that the load cases were well distributed across the root bending, torsion, and shear space. The cases were chosen from the library of maneuvers run through the flight simulator.

The GE05 and GE07 submodel included three components—the front spar, skin, and splice strap (shown in Figure 45). The GE04 and GE08 FE submodel also consisted of three components- the rear spar, the aft skin, and the trailing edge skin. GE04 and GE08 are highlighted in Figure 46. In addition to these GE control points, NGC CP05 was included in the submodel due to its proximity to the GE CPs of interest. This makes the stress results for NG05 available for any future analysis in follow-on Air Force Digital Twin task orders.



spar (orange), skin (green), and splice strap (yellow).

Figure 45. GE0 5/GE07 submodel details

Submodel Locations of Interest

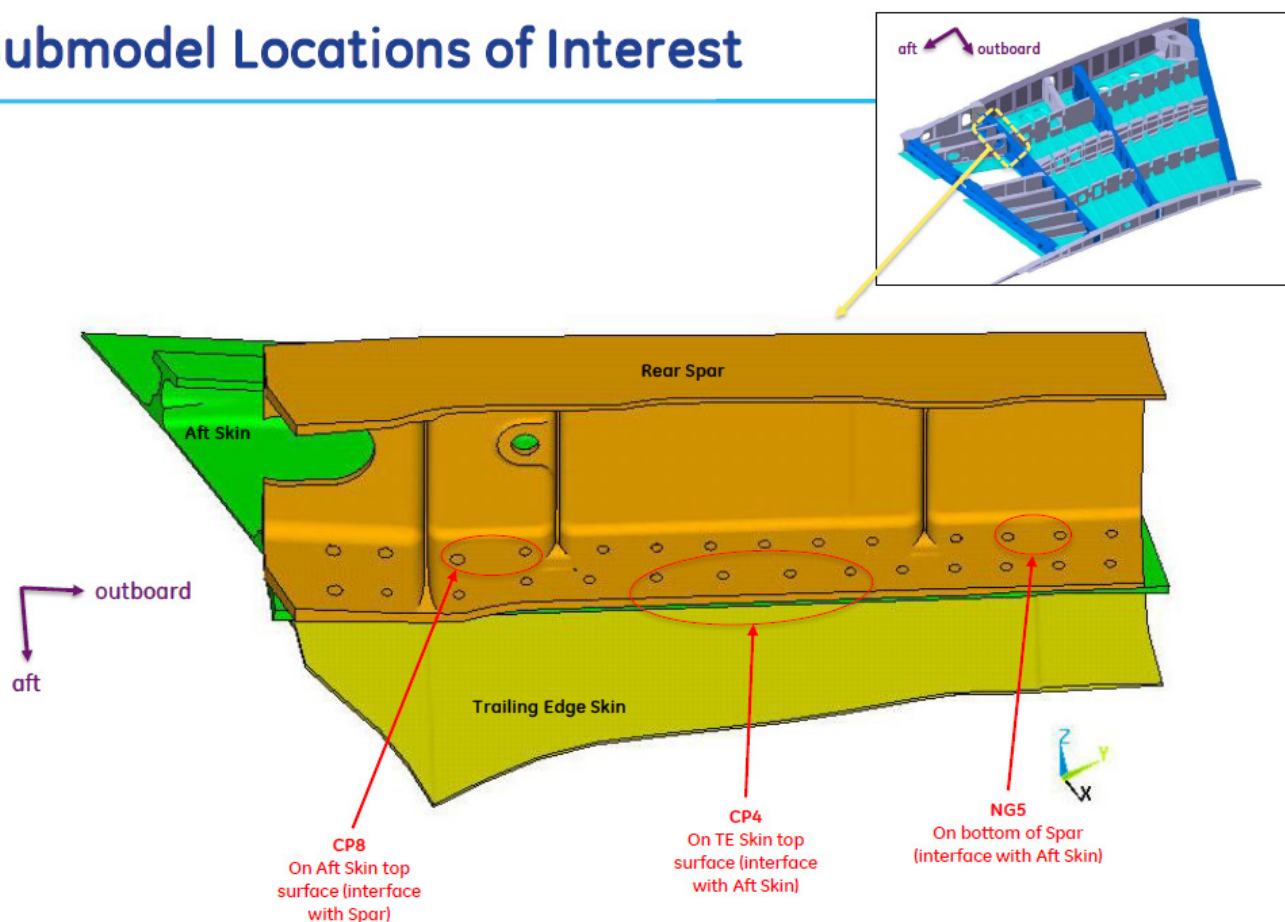
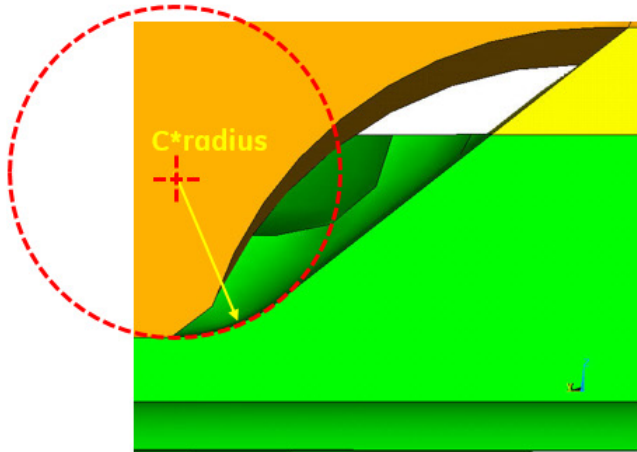


Figure 46. GE04/GE08 fine-grid FE submodel

Once boundary conditions for the local FE were extracted for each of the load cases, a DOE was generated for all of the input variables (load and geometry). The geometry variables had to be selected in a special way to minimize mesh distortion caused by the mesh-morphing procedure.

The same process for building the K_I stress intensity factor models outlined for GE06 was followed for GE04, GE05, GE07, and GE08. A DOE of load cases and geometry perturbations was generated to begin. To do so, geometry morphing parameters were defined. After discussions with AFRL and Lockheed, the morphing variables and bounds shown in Figure 47 and Figure 48 were defined.

DOE variable	Baseline	Lower	Upper
Radius	0.2"	0.16"	0.25"



DOE variable	Baseline	Lower	Upper
Diameter	0.19"	0.18"	0.25"
Dx	0.0"	-0.1"	0.1"
Dy	0.0"	-0.1"	0.1"

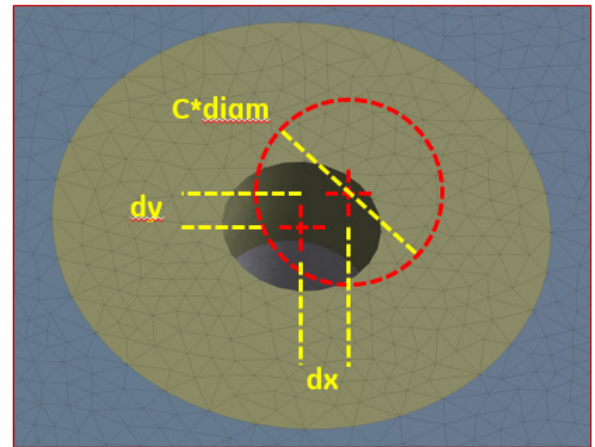
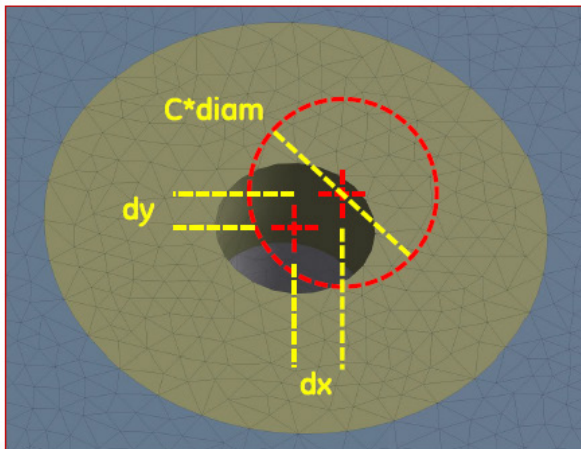


Figure 47. GE05/GE07 (left/right, respectively) morphing definitions

DOE variable	Baseline	Lower	Upper
Diameter	0.19"	0.18"	0.25"
Dx	0.0"	-0.1"	0.1"
Dy	0.0"	-0.1"	0.1"



DOE variable	Baseline	Lower	Upper
Diameter	0.19"	0.18"	0.25"
Dx	0.0"	-0.03"	0.1"
Dy	0.0"	-0.03"	0.1"

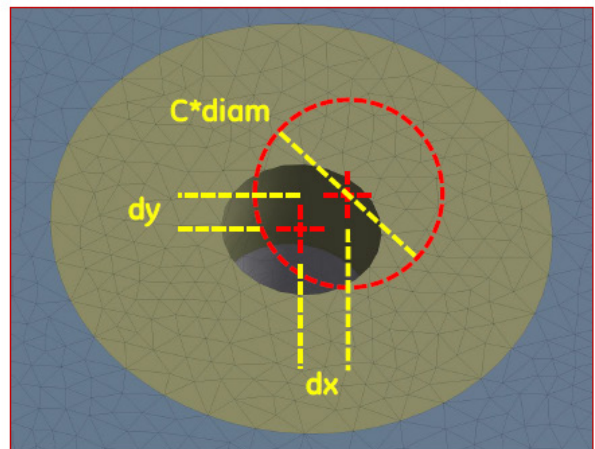


Figure 48. GE04/GE08 (left/right, respectively) morphing definitions

A Latin Hypercube sampling DOE was generated using the geometry and load variables, and the corresponding upper and lower bounds. Twelve DOE runs were generated in total. Each FE simulation, defined by its unique geometry and load case was run. The corresponding parameters for all CP FE runs are shown in Table 11. A graphical representation of the stress values is shown in Figure 49 and Figure 50. The size of each circle corresponds to the magnitude of the stress, and the x- and y-axes are the load case torsion and bending values, respectively. As an initial sanity-check, the stress increases with larger load, which is what we would expect to see. The next step was to build a K_I predictive model and analyze the trends in the predictions.

Table 11. CP morphing DOE parameters

	LOADS				GEOMETRY												
	CP7 / NG1 / NG3 / CP5 / CP4 / CP8 / NG5				CP7 / NG1 / NG3			CP5	CP4			CP8			NG5		
DOE Run #	Load #1 & Scale Factor		Load #2 & Scale Factor		dx	dy	dia. scale	radius	dx	dy	dia. scale	dx	dy	dia. scale	dx	dy	dia. scale
1	100301	0.02	100302	0.0857143	-0.03549	0.05354	1.08428	0.19424	-0.03549	0.05354	1.08428	0.03000	0.05354	1.08428	-0.03549	0.05354	1.08428
2	100101	0.34783	100102	1	0.08461	0.06863	1.18975	0.18436	0.08461	0.06863	1.18975	0.06000	0.06863	1.17448	0.02000	0.06863	1.18975
3	100201	0.56098	100202	0.3428571	0.01606	0.00096	1.26278	0.18010	0.01606	0.00095	1.26278	0.01606	0.00095	1.24751	0.01606	0.00095	1.26278
4	100101	0.86957	100102	1	-7.75E-07	-0.08000	1.31098	0.19874	0	-0.09384	1.29571	0	-0.00500	1.18473	0	-0.02000	1.29571
5	100301	0.06667	100302	0.8571429	-0.06322	-0.05239	1.02472	0.17250	-0.06322	-0.05239	1.02472	0	0.05000	1.02472	-0.06322	-0.05239	1.02472
6	100101	0.04348	100102	0.4285714	0.07934	0.08946	1.06243	0.21844	0.07934	0.08946	1.06243	0.03000	0.08946	1.06243	0.02000	0.08946	1.06243
7	100101	0.43478	100102	0.2857143	-0.02673	-0.08195	1.21843	0.23413	-0.02673	-0.08195	1.21843	-0.02673	0.05000	1.20316	-0.02673	-0.05000	1.21843
8	100201	0.2439	100202	1	0.02009	0.02826	0.99991	0.16410	0.02009	0.02826	0.99991	0.02009	0.02826	0.99991	0.02009	0.02826	0.99991
9	100201	1	100202	0.9428571	0.04396	-0.04577	1.12079	0.23538	0.04396	-0.04577	1.12079	0.03000	-0.02000	1.12079	0.02000	-0.02000	1.12079
10	100101	0.86957	100102	0.2857143	0.05183	0.04102	1.25128	0.22638	0.05183	0.04102	1.25128	0.02000	0.04102	1.23601	0.02000	0.04102	1.25128
11	100201	0	100202	0.5714286	-0.09000	-0.00076	0.95988	0.24690	-0.09927	-0.00084	0.95988	-0.00100	-0.00084	0.95988	-0.09927	-0.00084	0.95988
12	100201	0.21951	100202	0.1428571	-0.08119	-0.02180	1.13763	0.21205	-0.08119	-0.02180	1.13763	0.03000	-0.01000	1.13763	-0.08119	-0.02180	1.13763

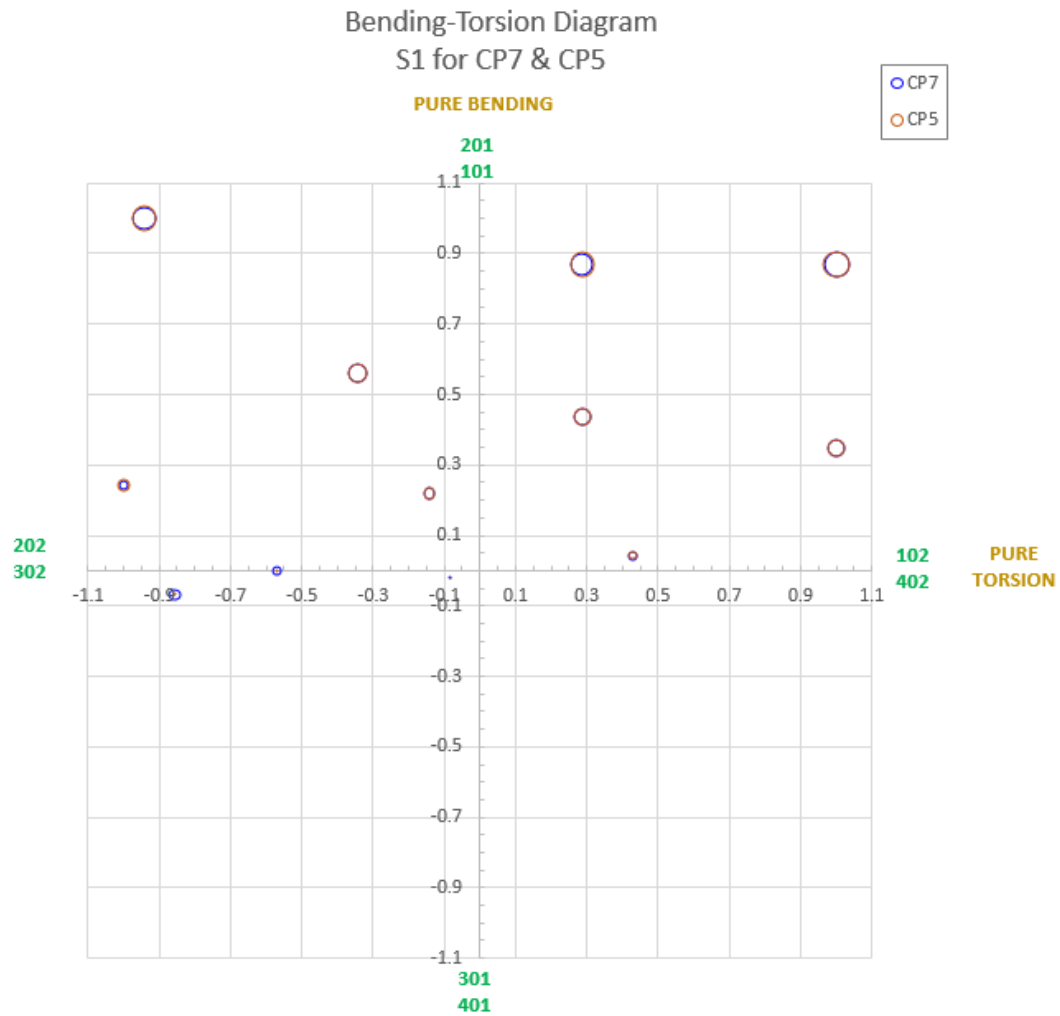


Figure 49. GE05/GE07 morphing DOE stress results

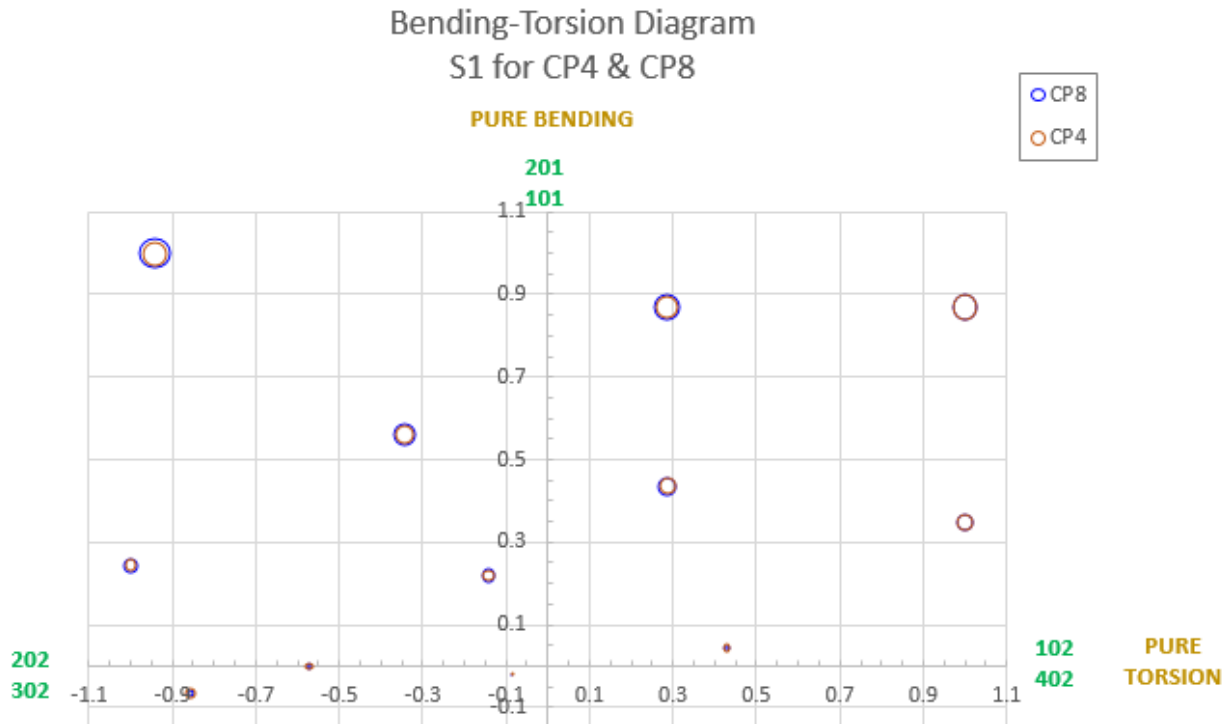


Figure 50. GE04/GE08 morphing DOE stress results

Once the finite element models were run, post-processing was done to extract the stress on the anticipated crack plane. The assumption of a single planar crack must be made carefully. While a crack may begin at the location of maximum tangential stress, the crack path is not necessarily straight. Still, for computational simplicity, we wanted to extract a single crack plane from the local FE model. In addition, the location and orientation of the maximum stress changes as the load and geometry parameters change. That is, the location and orientation of the crack plane changes with load parameters, geometry parameters, and of course time. A decision was made to compare all of the local FE results and create a BHM model to predict the generic crack plane stress.

In this work, we assumed that while a single crack will eventually form, at any time the relevant stress plane includes the maximum principle stress at that loading condition. That is, we took the conservative approach of taking the plane of the maximum principle stress, even though this may not be where the eventual crack forms. In addition, we assumed a planar crack and used the stress normal to this plane which may be inaccurate and potentially non-conservative. Compared to the other sources of uncertainty in the overall P²IAT approach (e.g. using one-dimensional crack growth curves), though, the inaccuracies are assumed to be small.

Figure 51 shows an example of an assumed crack plane (GE04 DOE run number 4). The conservative approach was taken, assuming the crack plane origin for any run is located at the point of highest stress. Once this local coordinate system is defined, FE post-processing scripts can then extract the planar stresses in that coordinate system. An example of this is shown in Figure 52. For each CP with a fine-grid model, a stress field was postprocessed for each of the

DOE runs. Then, a BHM model was built using these planes as training data. This model then predicted the crack plane stresses for any input (load and geometry).

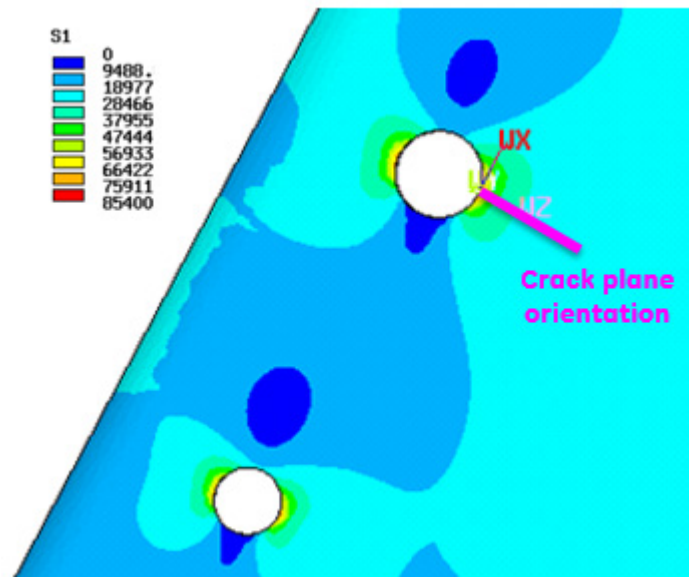


Figure 51. Crack plane orientation and far-field stress comparisons for GE04

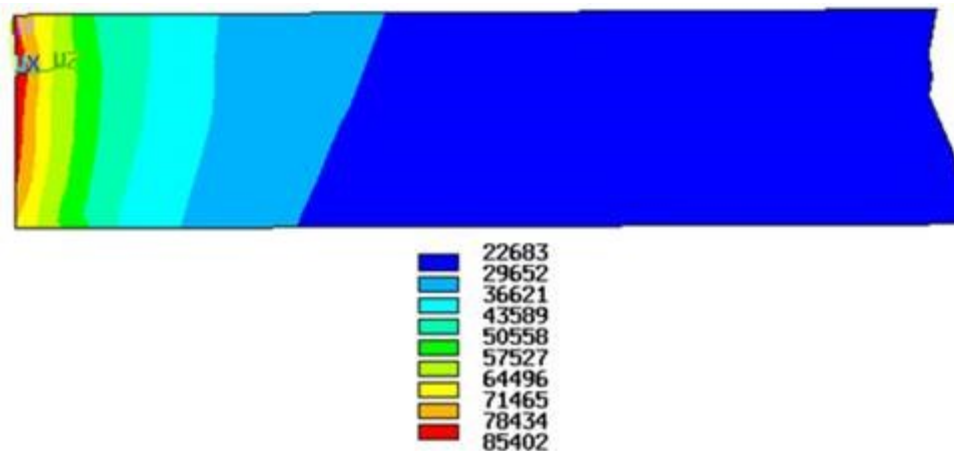


Figure 52. Crack plane stress field for GE04 DOE run number 4

8.2 FE model levels of fidelity

Throughout the FE modeling effort, an emphasis was put on understanding all the possible levels of fidelity that are available in modeling the stress at the wing control points. With each increased level of fidelity, the FE stress results will more accurately represent the structural physics that is occurring. Yet, with each increase in level of fidelity, added FE model assumptions need to be implemented—this often adds more work in building the model, and more time to converge to a solution. The balance between time/effort in building a fine-grid FE model for each CP and accuracy in the stress predictions had to be considered.

Figure 53 provides a high-level representation of the levels of FE modeling fidelity outlined by the GE team. Each row in the diagram represents a different level of fidelity. The columns represent the applicable FE model assumptions. Level 1 is the AV FEM. The mesh associated with the AV FEM is relatively coarse with respect to the fine-grid models developed as a part of this task order. No bolts were modeled and all the load transfer is happening through simulated bolt loads in a single constraint equation. A level 2 model was used in the GE06 FE modelling effort. The fidelity was greater than the level 1 model through a finer-mesh grid; the bolts were simulated with bolt holes and load was transferred as a flow-through mesh.

Task Order 2 efforts started by focusing on building and refining a level 3 FE model. Bolted joints were modeled as a cylinder of metal inside of a bolt hole in the CP, where the nodes around the annulus of the hole were merged out. This means all the load was transferred through the bolts and into the skin/spar as if the bolt was “welded” to the other components. This was done to keep the model in the linear-elastic mathematical regime and runtimes down. After a thorough analysis of these results, it was discovered that the resulting stress fields and crack plane orientations were not physically accurate enough for this project. It was necessary to move up to a level 4 FE model. The main change being the way the bolt interfaces with the skin/spar, through adding frictionless contact.

It is also important to note that there are several other assumptions and effects that can be utilized to make the model even more accurate. Through discussions with the team’s structural modeling and airframe experts, it was found that these effects can be considered negligible for now. A level 5 fidelity model could be realized through adding a friction-based contact model at the bolted joint. A level 6 model incorporates this as well as other “higher-order” effects. Higher order effects include, but are not limited to, things like plasticity, bolt-preloading, spar/skin contact, and interference fit fastener residual effects.

LEVEL	Mesh		Load transfer/contact				Govern. Eq.		+
	Mesh: "Coarse"	Mesh: "Fine"	Contact: Flow-through	Bolts: Merged nodes	Bolts: frictionless contact	Bolts: friction contact	Linear-elastic	Nonlinear-elastic	Higher-order*
1	✓		✓				✓		
2		✓	✓				✓		
3		✓		✓			✓		
Current 4		✓			✓			✓	
5		✓				✓		✓	
6		✓							✓

Figure 53. Table of levels of FE model fidelity

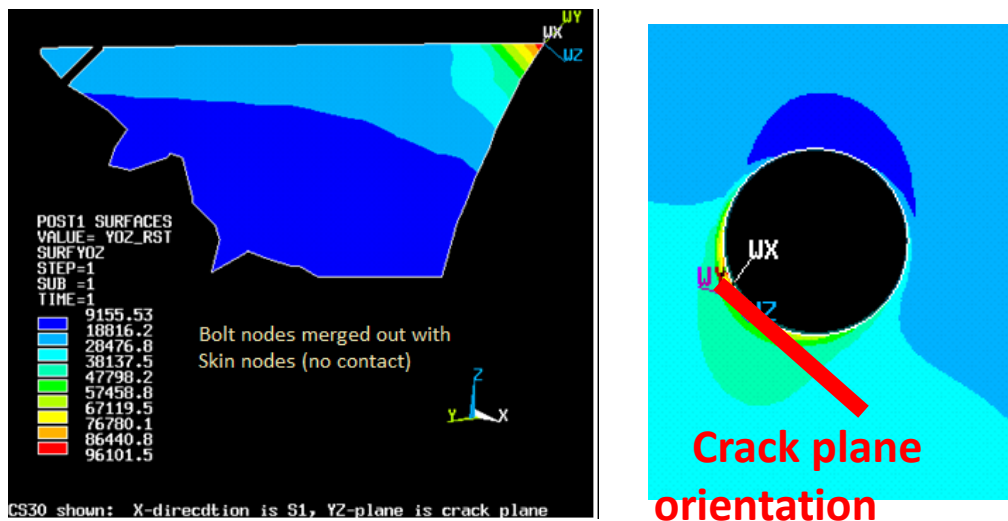


Figure 54. GE04 crack plane stress orientation with level 3 model fidelity

Level 3 FE model simulations for GE04, GE05, GE07, and GE08 were run and analyzed. In the process of analyzing these results, it was found that the stress values in the crack plane very quickly drop from the peak stress to the far field stress as you move in the depth and surface directions. An example of this is shown in the left image in Figure 54. This is the crack plane stresses for CP GE04, DOE run number 4. The peak stress of 96 ksi drops to about 25 ksi in as

little as 0.05 inches. Also, the crack plane orientation for this load case is unusual (shown in the right image in Figure 54). The crack plane is tangent to the bolt hole; not a typical orientation for bolted joints on an aircraft wing structure under typical flight loading conditions.

In general, there are three load types that contribute to the stresses at a bolted joint (GE04/7/8):

- Bypass (tension) loads,
- Bending loads,
- Bearing loads from movement of the bolt away from the bolt hole axis.

In the level 3 FE model, the bolt mesh nodes are merged with the skin/spar. Therefore, any movement of the bolt generates an unrealistically high bearing load, resulting in a high compressive stress field in the direction of the bolt movement, and a tensile stress on the opposite side (shown in Figure 55). The stresses due to the other two load contributions are completely masked. One would expect to see a higher contribution of bypass loads and see a stress field as in Figure 56. You would expect to see a compromise between the fields seen in Figure 55 and Figure 56 in real structure. The high bearing load contribution is also skewing the location and direction of the crack plane for GE04.

High bearing load contribution



Figure 55. High bearing load stress field (GE4- level 3 results)

**Tension loads only;
no bolt bearing load (example)**

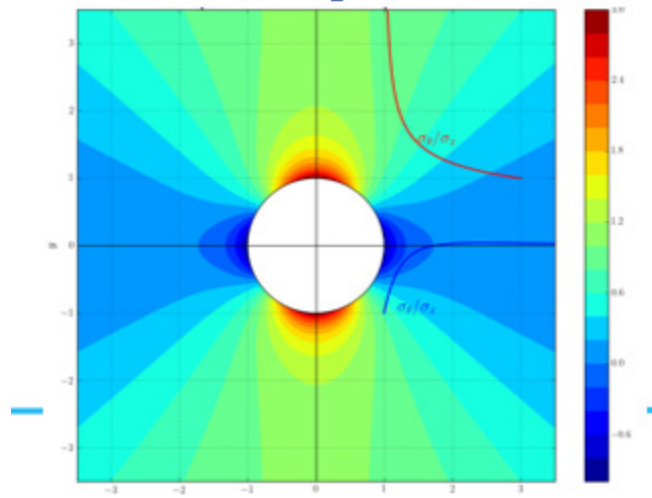


Figure 56. Tension load only stress field (benchmark example)

The FE models for the bolted joints (GE04, GE07, GE08) needed to be upgraded to a level 4 FE model fidelity. The bolt contact dynamics should be modeled more accurately to give a correct crack plane direction and stress field. After this contact model was added, major differences were seen. Figure 57 shows the changes in the stresses when adding bolt contact elements. The stress fields look more like the expected compromise of bearing- and bypass-based stresses, and the crack plane orientation is oriented radially to the bolt hole. Figure 58 shows the crack plane stresses associated with the crack planes depicted in Figure 57. The stress gradient is less severe when the bolt contact is modeled than when no bolt contact elements are used.

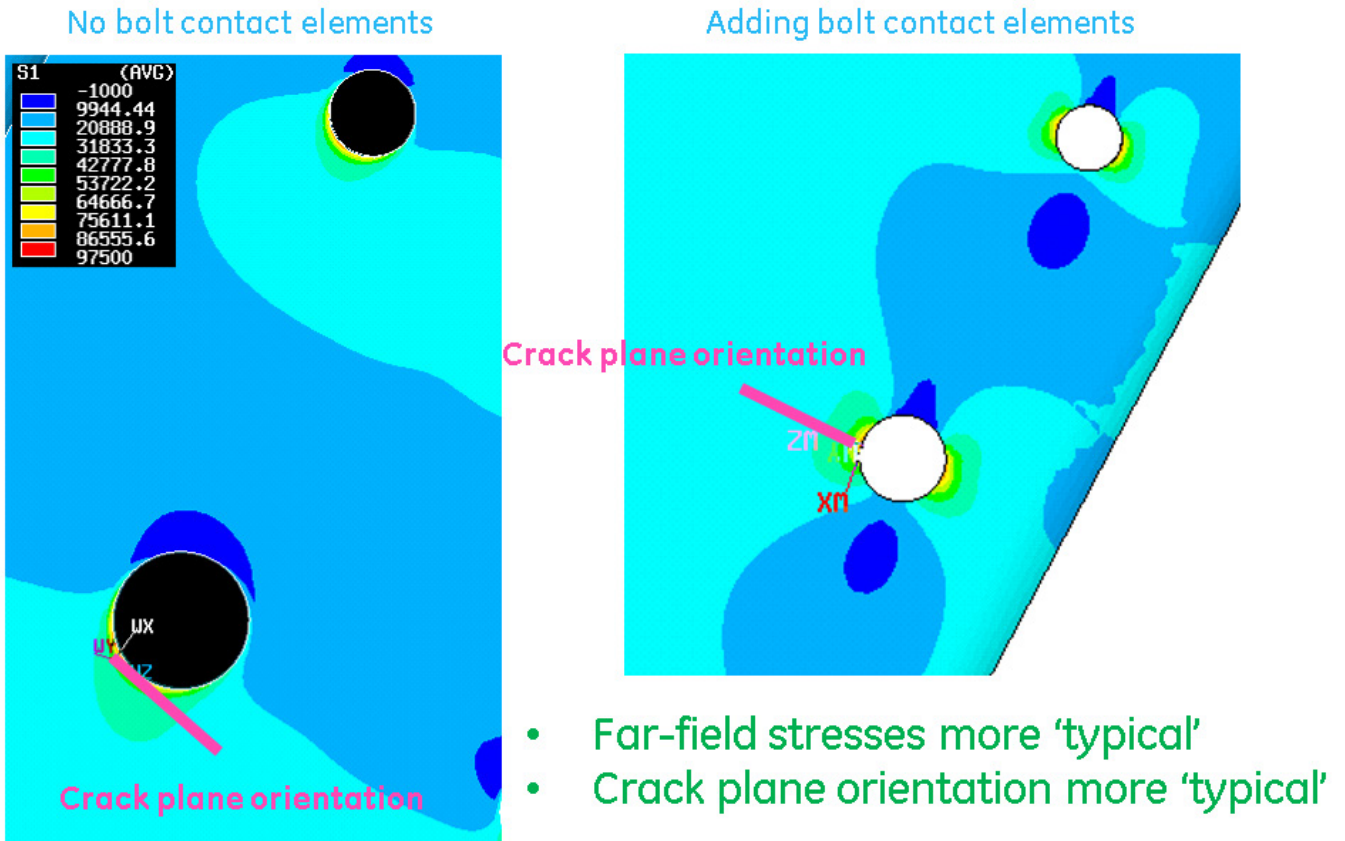


Figure 57. Crack plane orientation and far-field stress comparison for GE04 level 3 and level 4 FE models

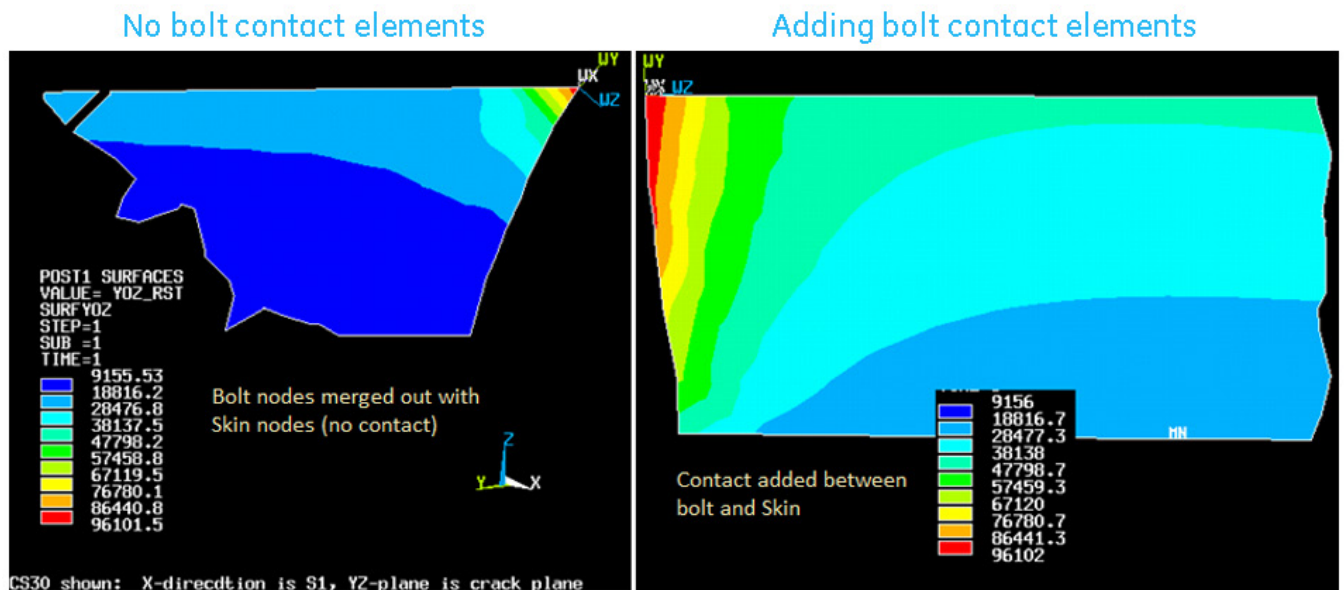


Figure 58. Crack plane stress comparison for GE04 level 3 and level 4 FE models

It was decided that level 4 FE models are necessary to obtain the accuracy needed to predict the crack propagation for bolted joints. Modeling frictionless contact between the bolts and the adjacent components can be achieved in several ways. Figure 59 shows the three possible scenarios that include frictionless contact, accompanied by the resulting stress fields.

The left most column in Figure 59 shows the baseline (level 3) FE model for GE04, where the bolt contact is modeled with merged nodes. The second column is an attempt to model bolt contact, while remaining in the linear-elastic regime. This is accomplished with replacing the bolt material with RBE3 constraint equation nodes. The third column shows the stress results of a model where contact is modeled using a cylinder of metal with contact nodes around the bolt hole where GE04 is located only. The last column in Figure 59 models contact with contact nodes but at all six bolt holes in the figure. This comparison was done to see if there are any interaction effects between adjacent bolt holes when modeling contact.

There are slight differences in the stress fields and peak stresses in the three level 4 models. Most importantly, there seems to be a big effect on the location of the peak stress in the bolt hole depth direction. When using RBE3s, the peak stress is located in the middle of the bolt hole. When modeling contact in one hole, the peak stress moves up closer to the faying surface. When contact is modeled in all six holes, the peak stress is located at the faying surface. The location of the peak stress in the depth direction has a direct impact on the SIF calculations. The interaction effects between adjacent bolt holes is enough to influence the location of the peak stress. Therefore, all models will use the approach of modeling contact in the CP bolt hole, along with all adjacent bolt holes.

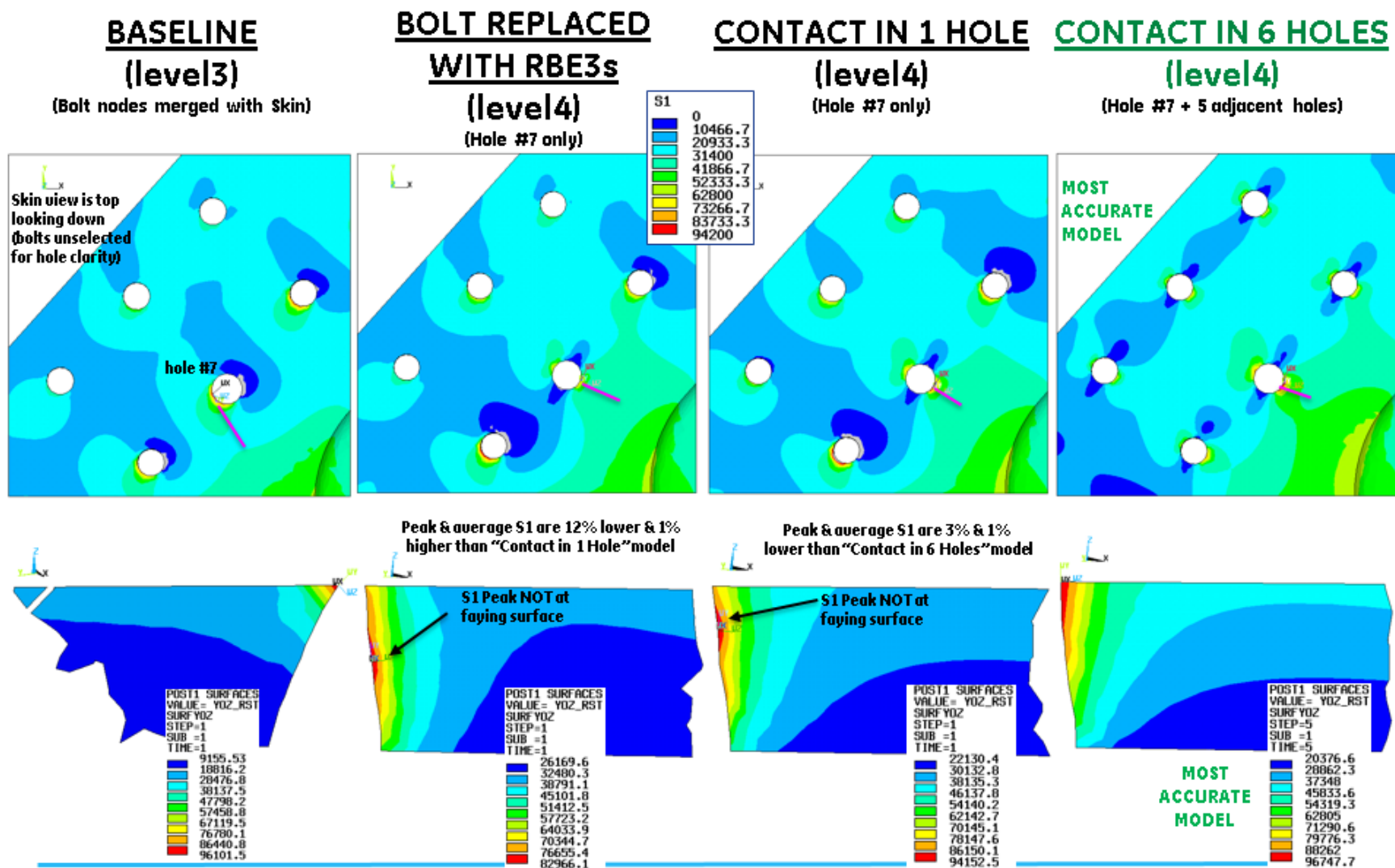


Figure 59. Comparison of bolt hole frictionless contact models

The two sub models (GE04/8 and GE05/7) were updated to a level 4 fidelity, and bolt hole contact was added as described in the last column in Figure 59. The models were run for the full DOE of loading and geometry morphing conditions. The next task was to follow the post-processing steps necessary to build K_I stress intensity models.

8.3 Green's Function

The Green's function has a relatively simple form for through the thickness cracks. For quarter-elliptical corner cracks at bolt holes, however, analytic forms are not available. Lockheed Martin has run a number of very fine grid finite element simulations with cracks that can be interrogated to get pointwise values of $G(x, y)$. Many FE runs were done in which the load point, evaluation point, and geometry were varied. The load point was parameterized by the radial and azimuthal location, (r, θ) . Two evaluation points were chosen, one near the surface and one into the depth of the material (parameterized by θ_e). This reflects the quarter-elliptical crack shape which is defined by a length along the surface (c) and along the thickness (a). The geometry was parameterized by the crack aspect ratio a/c and c/R , where R is the radius of the hole. The geometry is described in Figure 60.

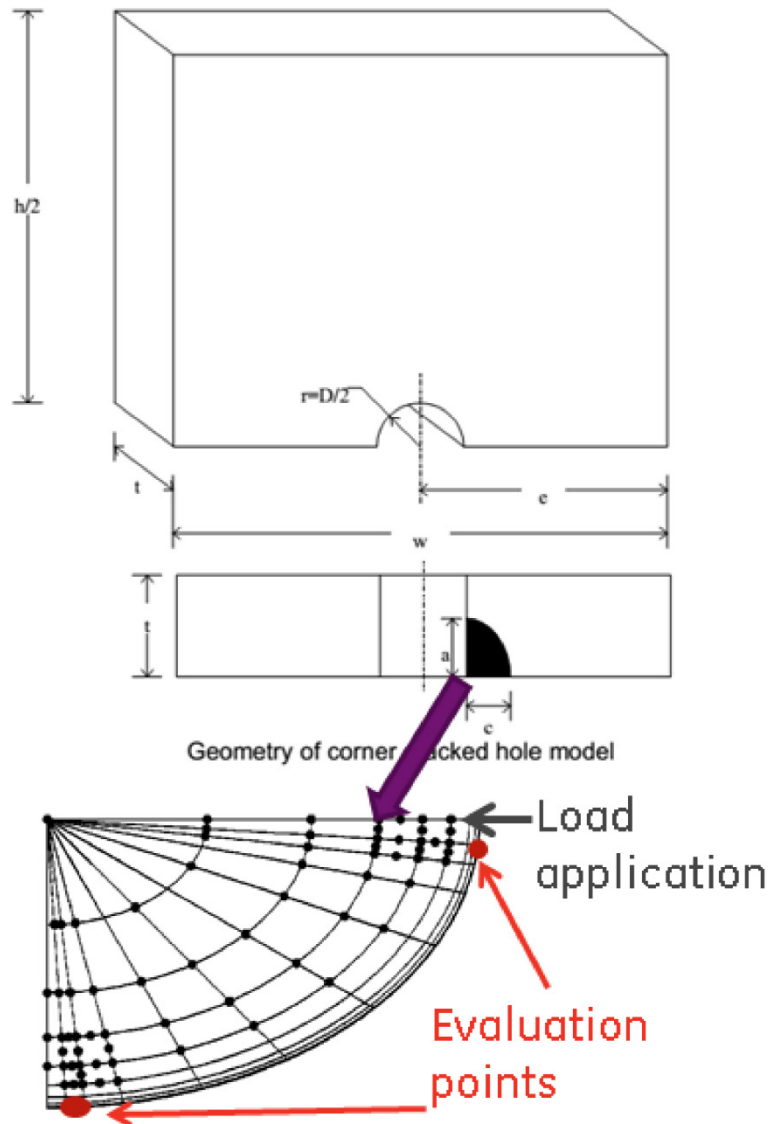


Figure 60. FE Model Definition for Green's Function

To get a predictive model of the Green's function at any point, the database of fine grid FE models run by Lockheed Martin was used to train an Artificial Neural Network (ANN). The resulting neural network is a predictive model that interpolates between the data points from the database. It can predict the Green's function value at any point on the crack face given geometry parameters (e.g. a/c and c/R).

In addition to the corner crack stress intensity factor work described above, it was also necessary to build K_I models for through-cracks. The transition from corner to through crack will occur when the crack length reaches the thickness of the material. In P²IAT, this transition will occur separately for each sample. Thus, at a particular time point, some samples may be using corner crack models while some may be using through crack models, since each sample has a different crack state.

The difference between a corner and through crack comes purely from the Green's function – the stress remains the same. A through-crack, one dimensional Green's function was derived from the Tada K-solution [5]:

$$G(a, b, y) = \left[\frac{2}{\sqrt{\pi a}(1-x)^{\frac{3}{2}}} \right] \left[\frac{g_4(x)y^3 + g_3(x)y^2 + g_2(x)y + g_1(x)}{\sqrt{1-y^2}} \right] \quad (5)$$

Here, y is the distance from the hole boundary to the point at which the Green's function is evaluated. The crack dimension is just the length along the surface, a (note that $0 \leq y \leq a$). The distance from the hole boundary to the edge of the plate is b and x is defined as $x = a/b$. The functions g_1 through g_4 are defined as follows:

$$g_1 = 0.46 + 3.06x + 0.84(1-x)^5 + 0.66x^2(1-x)^2 \quad (6)$$

$$g_2 = -3.52x^2 \quad (7)$$

$$g_3 = 6.17 - 28.22x + 34.54x^2 - 14.39x^3 - (1-x)^{\frac{3}{2}} - 5.88(1-x)^5 - 2.64x^2(1-x)^2 \quad (8)$$

$$g_4 = -6.63 + 25.16x - 31.04x^2 + 14.41x^3 + 2(1-x)^{\frac{3}{2}} + 5.04(1-x)^5 + 1.98x^2(1-x)^2 \quad (9)$$

Because the stress varies with the depth, the stress and Green's function are integrated over the crack length (surface) at various depth locations. These are averaged across the thickness to get an overall stress intensity factor of $K_{I,thru}$. Once a DOE of $K_{I,thru}$ values are calculated for the various parameters (loads, geometry, etc.), an overall probabilistic model for $K_{I,thru}$ as a function of load, geometry, and crack state parameters is built.

The final K_I models use the stress at the bottom corner of the assumed crack plane in the skin for the demonstration location. Using the stress at the bottom corner gives physically realistic values and is consistent with the Finite Element model predictions that the bottom surface of the skin has the highest stress.

Two of the control points (GE05 and GE02) are in the surface of the wing skin away from bolt holes. For these CPs, SIF calculations for surface cracks are needed.

The surface cracks are assumed to be semi-elliptical in nature as depicted in Figure 61 below. The crack is defined to have a depth of 'a', length of '2c', and exists in a plate of thickness 't'. The edge of the crack front in the surface direction is located at a distance of 'b - c' away from the edge of the plate.

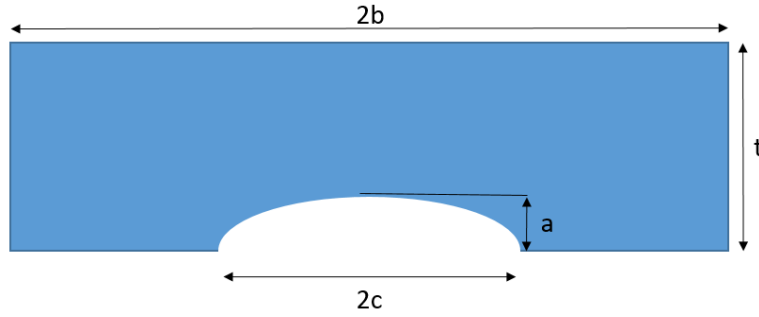
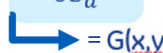


Figure 61. Surface crack configuration

Very few exact solutions for three-dimensional cracked bodies are available in the literature; this was also the case for corner- and through- crack SIF solutions. Therefore, an approximate solution based off curve fits of FE results will be used. The K-solutions from Newman & Raju's handbook of computational methods in the mechanics of fracture will be used as the groundwork for the computations. Values for the Green's function for a surface crack is calculated using the following two equations:

$$\frac{1}{dS_a} \int K(\phi)^2 dS_a = \frac{4E'}{\pi c} \int_x \int_y \sigma_r(x, y) \cdot \frac{\partial U}{\partial a} dx dy$$

$$K_a = \frac{E'}{K_{ra}} \int_x \int_y \sigma_{applied}(x, y) \cdot \frac{\partial U(x, y)}{\partial S_a} dx dy$$



 = G(x,y)

The top equation is used in conjunction with a database of FE results. Newman and Raju's method uses the known reference stresses and corresponding SIF values (σ_r and K in the top equation, respectively) to inversely solve for U . The result is an empirical curve-fit of U as a function of crack length, crack depth, bending and torsion of the plate. The curve-fit model of U can be used to find $G(x, y)$ in the bottom equation, and subsequently solve for K_a , given any applied stress ($\sigma_{applied}$).

8.4 SIF Models

Sections 8.1 through 8.3 described the process of modeling the stresses at each CP (either fine-grid or coarse-grid FE models), calculating the Green's functions, and finally the K_I values. As a result of the work done in these sections, each CP has a DOE set of K_I values (about 300 points). Each point in the DOE is a varying input value of load and geometric morphing condition. With these sets of data, a probabilistic SIF model was created using the K_I data set as training data. Figure 62 below shows the list of each CP and the corresponding SIF model(s) that was built for each. The first row of the table shows the CPs that have a coarse-grid FE-based probabilistic SIF model. The second row of the table shows which CPs have a fine-grid FE-based probabilistic SIF model. These models will provide an opportunity for comparisons between the two types of SIF models.

		Legend									
		TO2 add-on									
		Additional									
		CP1	CP2	CP3	CP4	CP5	CP6	CP7	CP8	CP9	CP10
Coarse-grid FE K_I models		✓	✓	✓	✓		✓	✓	✓	✓	✓
Fine-grid FE K_I models					✓	✓	✓	✓	✓		

Figure 62. Table of SIF models

An example of the probabilistic SIF models is shown in Figure 63 below. All ten CPs and the associated K_I model plots are given in Appendix D. The figure below shows the predicted K_I value at each of the training data points versus the actual K_I value. The SIF model was built as a second order polynomial regression of the following form:

$$\log(K_{I,predicted}) = f(\log(a), \log(c), bending, torsion)$$

The uncertainty of K_I predictions (shown as blue lines in the figure) were calculated by fitting a linear regression of the residuals:

$$\log(r^2) = f(K_{I,predicted})$$

The quadratic equations for each GE control points are available in Appendix D.

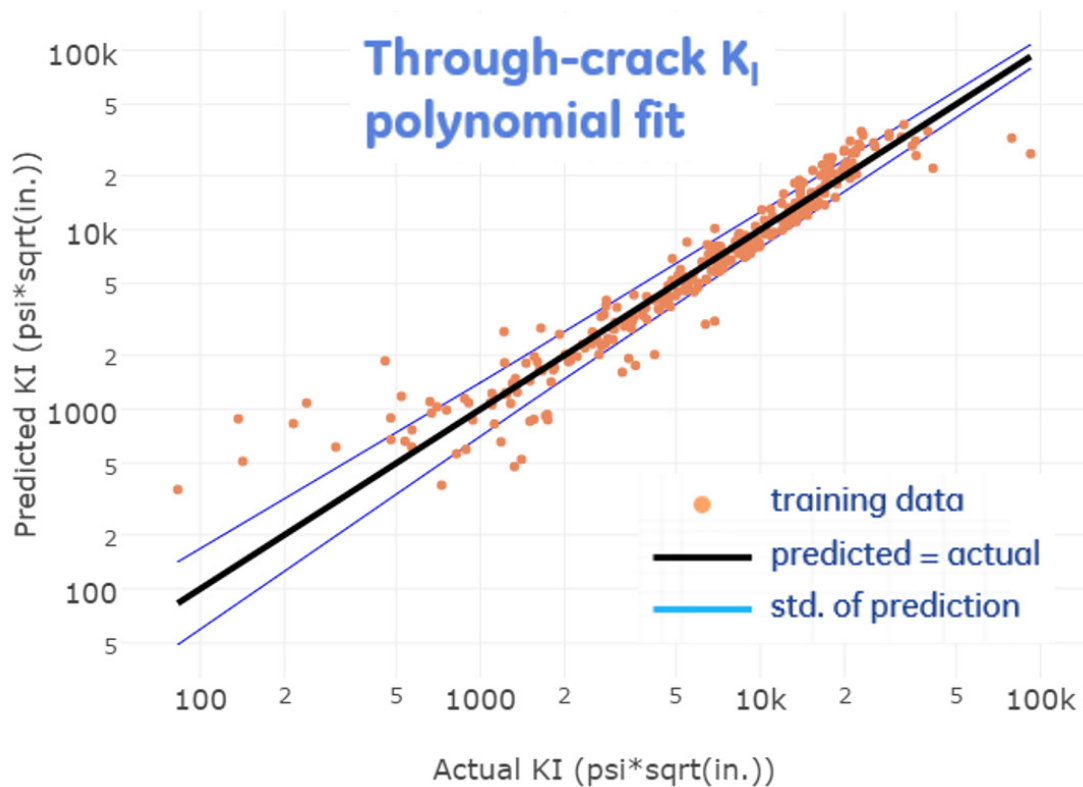
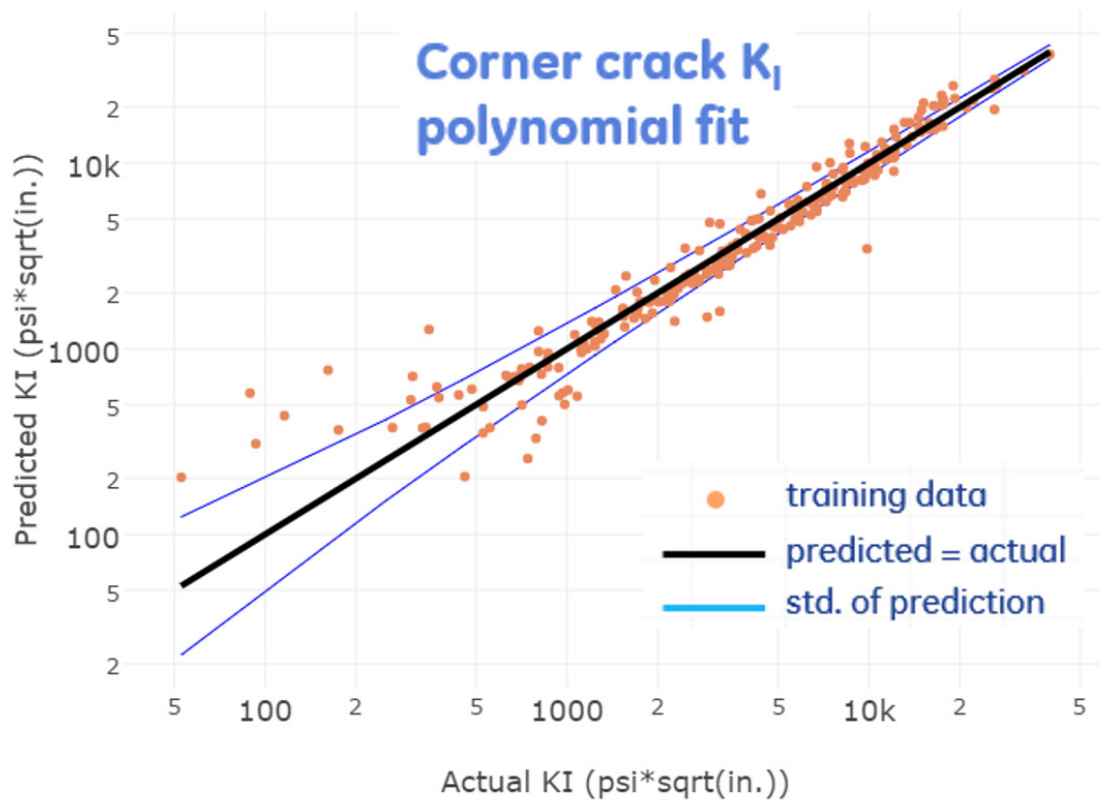


Figure 63. Example SIF probabilistic model

8.5 Initial SFPOF Predictions

With all K_I complete, the P²IAT method was used to make crack growth forecasts for all the control points. To run P²IAT, several preprocessing and data gathering tasks were first required:

1. Collect geometry and material property information for each CP, along with any uncertainty associated with these quantities.
2. Analyze each CP to estimate what initial flaw size distribution to use. This was estimated based on the CP's geometry, estimated structural life details before the test, and previous repairs done to the location. This is best estimated by analyzing da/dN data, S-N data, and DTA reports available for each CP.

Once these steps were complete, the P²IAT tracking was performed for the GE CPs on the right wing using the baseline load spectrum. P²IAT tracking information included both CP life forecasting and inspection scheduling. Inspection scheduling was performed using a variety of options—a risk criterion, information gain, or fixed interval criterion, a repair on/off setting, and defined inspection interval constraints.

Initial crack growth forecasts for the ten control points were made. The following list of assumptions and P²IAT settings were used to run the initial predictions:

1. Used coarse-grid K_I model for CP GE01, 02, 03, 09 10. Used fine-grid K_I model for CP GE04, 05, 06, 07, 08.
2. K_I model predictions uncertainty were propagated through P²IAT.
3. Probability of Detection (POD) models was nominal; POD curves based on inspection data are still being finalized.
4. Forecasts were made out to 2000 flight hours. The full-scale experiment is planned to go out to as many as 16,000 flight hours.
5. If a crack was detected, it was assumed to be repaired to a size-distribution with a mean value of 0.00025 inches (0.25 mils).
6. Inspections were set to occur every 200 flight hours if and only if the single flight probability of failure (SFPOF) at that mark is greater than 10^{-7} .
7. 1000 particles were used in the P²IAT framework.
8. Once a particle failure was detected, SFPOF calculations were corrected to account for fractions of a particle failing over time (i.e. failure interpolation is used). This technique enabled smooth SFPOF curves with only 1000 particles.

This section will show and describe a few of the initial crack propagation predictions. SFPOF and crack growth plots for all CPs are provided in Appendix F.

Figure 64 shows the SFPOF plot for GE02. This control point was modeled using the coarse-grid FE-based SIF models. The SFPOF quickly rises over the first few flight hours into the yellow shaded region (a SFPOF between 10^{-7} and 10^{-5}). The trend slowly rises over the next 175 flight hours or so until the first inspection at 200 flight hours. At the first inspection, each of the 1000 particles that still survive (have not failed before inspection) pass through a possible probability of detection based on their current crack size. If the crack is detected, it is repaired. If the crack happens to not be detected (either by chance or because it is small), it will survive in

its current state. All the repairs to the particles at 200FH drops the SFPOF to a value just above 10^{-20} . This cycle repeats for the next 200 flights. After the second inspection (400 flights), the SFPOF does not grow to any significant amount for the rest of the 1600 flights. This is because all the 1000 particles in the initial crack size distribution that were large enough to grow significantly in the 2000 flights have grown and failed or grown, been detected, and repaired, in the first 400 flights.

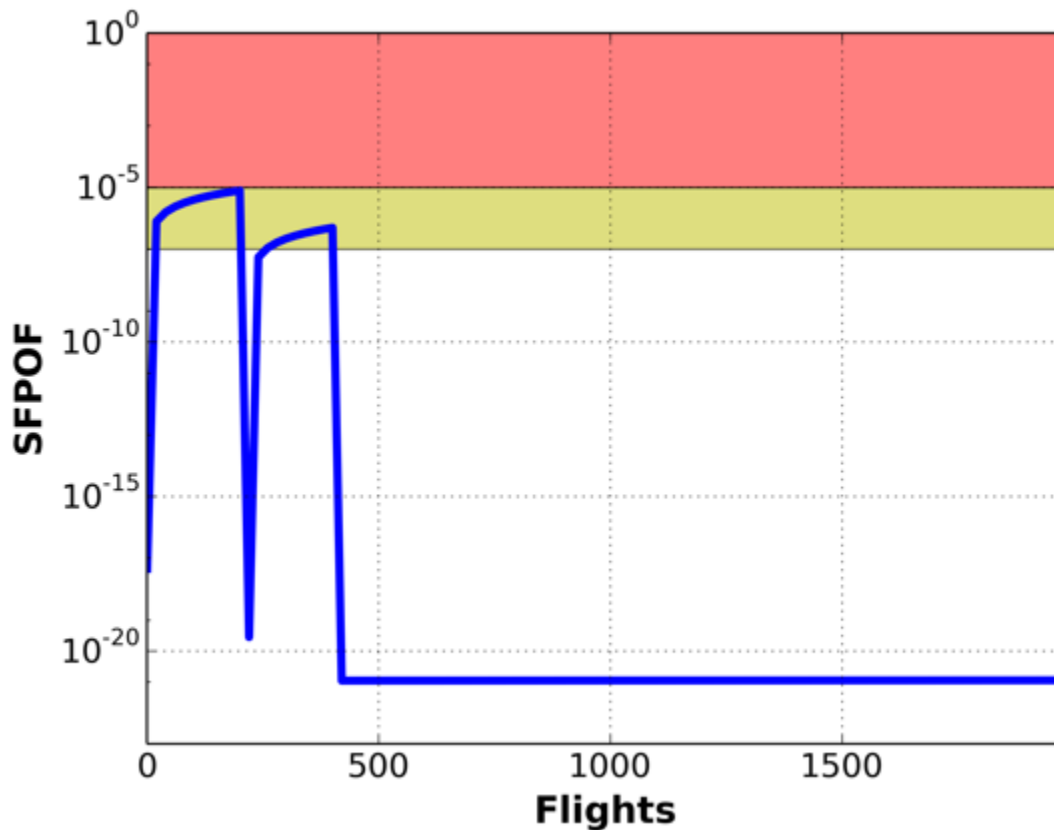


Figure 64. Initial SFPOF prediction plot for GE02

Figure 65 shows an initial lifing forecast for GE04. This SFPOF vs. flight hours plot shows a different pattern from that of GE02. For this control point, at the initial conditions and setting set for this example shows that GE04 will not grow in SFPOF for all of the first 2000 flight hours.

The value of SFPOF stays below 10^{-20} for the entirety of the forecast.

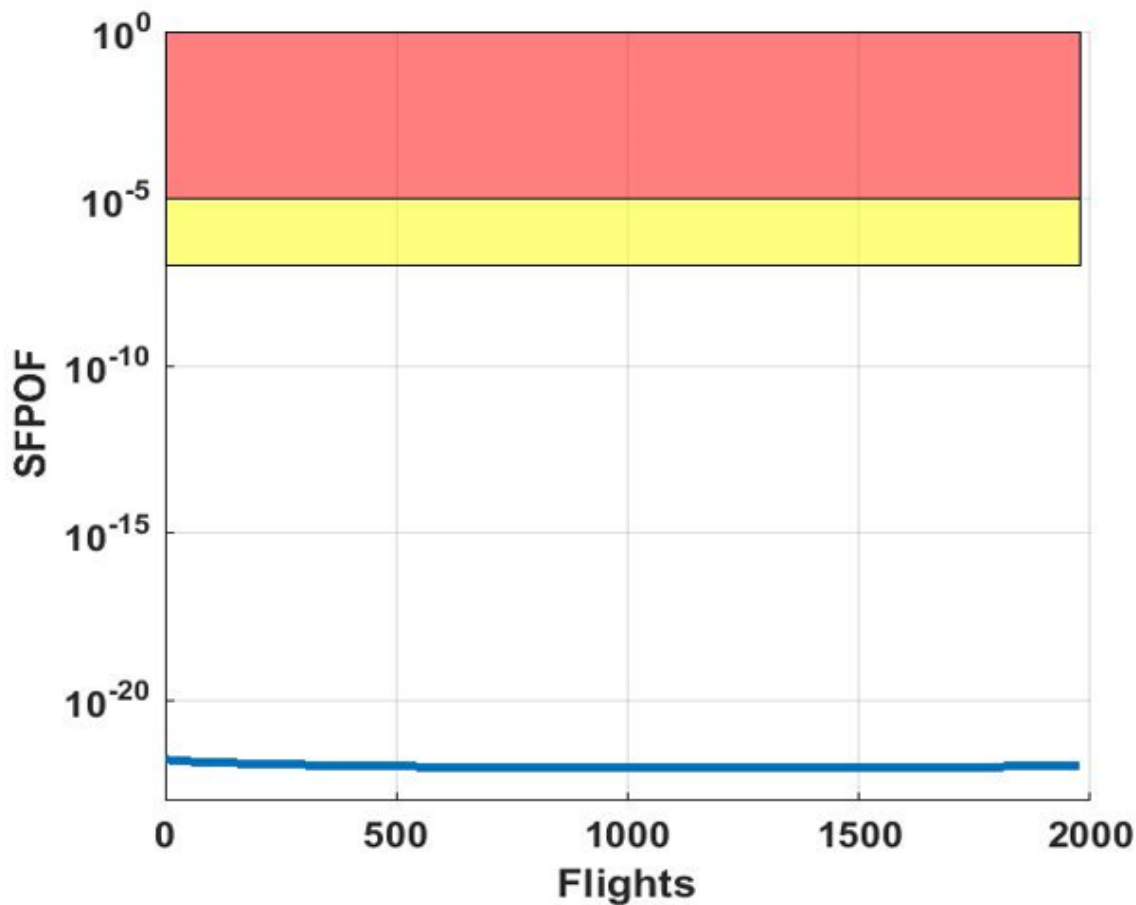


Figure 65. Initial SFPOF prediction for GE04

Figure 66 is an initial forecasted life prediction for GE07. The SFPOF value slowly grows from about 10^{-23} to 10^{-19} over the 2000 flights. If you only forecast for 2000 flights, none of the 1000 particles become critical enough to have failed within this envelope. However, if the forecast predicted further past the 2000 mark, a particle may fail. This would cause a spike or ‘jump’ in SFPOF. An example of what this ‘jump’ in SFPOF looks like is shown in Figure 67. These spikes are mathematically correct values, but are an artifact of calculating SFPOF values on the order of 10^{-7} with only 1000 particles. Each particle has a drastic effect on the SFPOF. The goal of forecasting is to predict when the SFPOF first crosses a 10^{-7} threshold. To most accurately accomplish this task, it is necessary to ‘smooth out’ the effect seen in Figure 67. This smoothing is done by first finding the flight hour for which a particle failure occurs. Then the SFPOF curve is recalculated using interpolated values of failure. In other words, it finds the ‘fractions’ of a particle failing at any given time. This effectively smooths out the SFPOF. An example of this before and after effect is given in Figure 68.

Figure 69 shows what the SFPOF plots look like if GE07 is forecasted out to 10,000 flight hours. Here you can see the interpolated particle failure SFPOF correction in effect. Not long after the 2000 flight hour mark a discrete (integer) number of particles out of the 1000 fail.

Then, the SFPOF plot is recalculated such that it can interpolate the fraction of particles that fail at times before 2000 flight hours. This effectively smooths out and gives better estimate of SFPOF than that seen in Figure 66. The information of a particle failing just after 2000 flight hours better informs the predictions prior to 2000 flight hours. Therefore, a rule-of-thumb can be recommended— forecast until at least the next scheduled or initiated (i.e. 10^{-7} SFPOF) inspection.

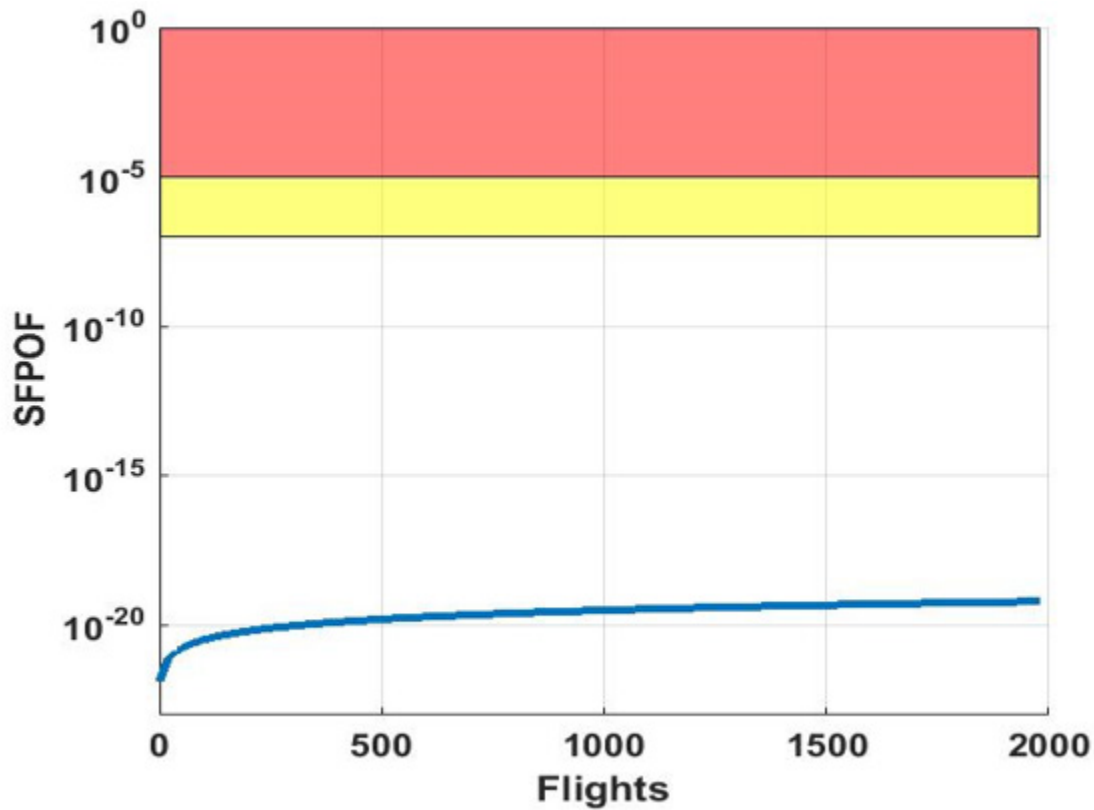


Figure 66. Initial SFPOF prediction for GE07

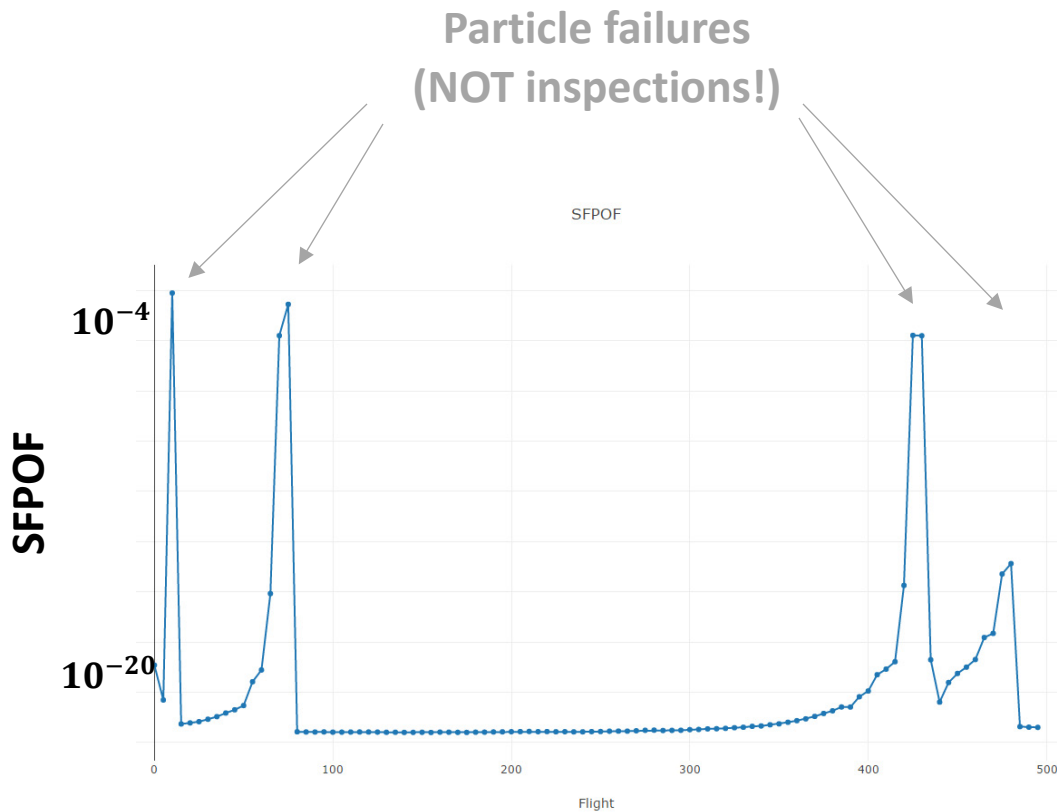


Figure 67. Example SFPOF without smoothing (interpolation)

Jumps in SFPOF are indications of individual particle failures and removals from the sample set.



Figure 68. SFPOF before and after smoothing logic

Left- before smoothing, integer number of particles fail. Right- after smoothing, interpolated such that fractions of particles can fail.

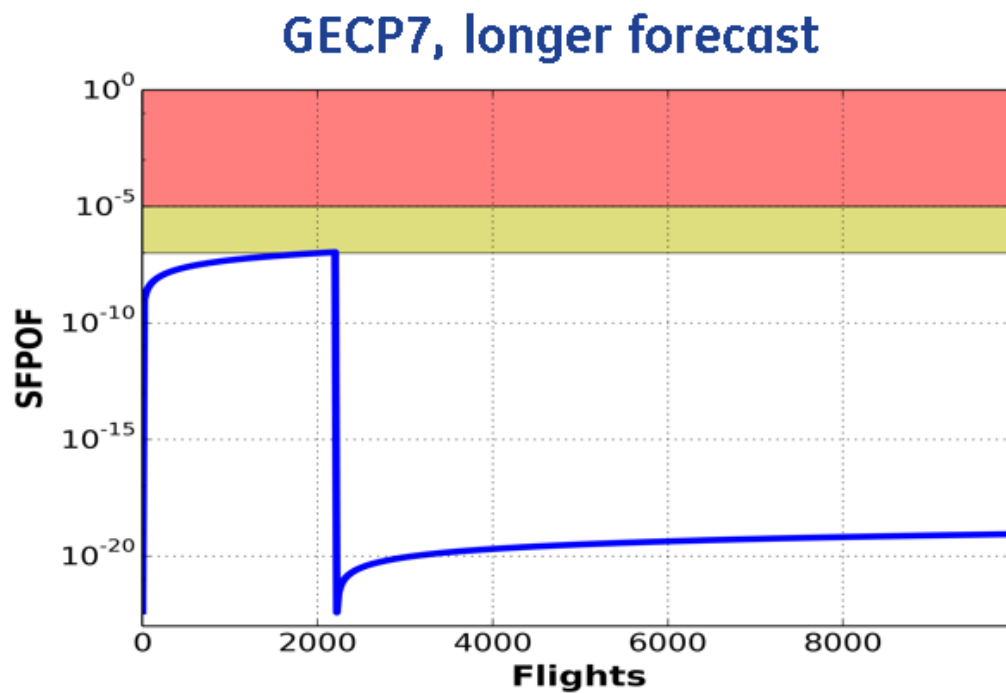


Figure 69. Initial crack growth predictions- SFPOF plot for GE07 for 1000 flights

9.0 CONCLUSIONS

The requirements and plans necessary to demonstrate the Scalable, Accurate, Flexible, Efficient, and Robust Probabilistic and Prognostic Individual Aircraft Tracking (SAFER-P²IAT) have been developed. Two fighter aircraft outer wings have been prepared and instrumented to be used in a full-scale ground-test experiment, where the SAFER-P²IAT framework will be utilized to track and forecast fatigue crack growth at several selected locations.

Complete and detailed plans and procedures were established for the following components necessary for a full-scale experiment:

- Selection of locations to be tracked
- Designing and applying experimental loads on the wings
- Instrumenting the wings and experimental data acquisition
- Performing structural health inspections during test

The successful completion of these tasks now enables the use of P²IAT to track at least ten control point locations on two fully instrumented wings. The experimental loading Master Event Sequence (MES) was designed with the ability to cyclically load the wings for more than 16,000 flight hours—simulating flying missions typical of fighter aircraft. Loading jack configurations were designed to replicate the loads called out in the MES. Safety of test instrumentation was designed and installed, ensuring a safe and constructive experimental test. All necessary inspection techniques, equipment, and procedures have been outlined, ensuring a useful input data feedback into the P²IAT framework. All of these accomplishments have made it possible to fully demonstrate the P²IAT methodology in an experimental setting.

10.0 REFERENCES

- [1] L. Wang, I. Asher, G. Khan, D. Ball and J. Hoffman, "Airframe Digital Twin Spiral 1: SAFER-P2IAT," U.S. Air Force Research Laboratory, Wright-Patterson AFB, 2016.
- [2] C. K. I. W. C. E. Rasmussen, Gaussian Processes for Machine Learning, MIT Press, 2006.
- [3] M. C. Kennedy and A. O'Hagan, "Bayesian calibration of computer models.," *Journal of the Royal Statistical Society: Series B (Statistical Methodology)*, vol. 63, no. 3, pp. 425-464, 2001.
- [4] J. Oakley and A. O'Hagan, "Bayesian inference for the uncertainty distribution of computer model outputs," *Biometrika*, vol. 89, no. 4, pp. 769-784, 2002.
- [5] H. Tada, P. C. Paris and G. R. Irwin, The stress analysis of cracks., Hellertown, PA: Del Research Corp, 1973.
- [6] D. Skinn, J. P. Gallagher, A. P. Berens, P. Huber and J. Smith, "USAF Damage Tolerant Design Handbook," U.S. Air Force Research Laboratory, Wright-Patterson Air Force Base, OH, 1994.
- [7] C. F. Babilon, R. H. Wygonik and G. E. Nordmark, "Mechanical Properties, Fracture Toughness, Fatigue, Environmental Fatigue Crack Growth Rates and Corrosion Characteristics of High-Toughness Aluminum Alloy Forgings, Sheet and Plate," Aluminum Company of America, 1973.
- [8] N. Friedman, K. Murphy and S. Russell, "Learning the structure of dynamic probabilistic networks," *Proceedings of the Fourteenth conference on Uncertainty in artificial intelligence*, pp. 139-147, 1998.
- [9] G. Bartram and S. Mahadevan, "Integration of heterogeneous information in SHM models," *Struct. Control Heal. Monit.*, vol. 21, no. 3, pp. 403-422, 2014.
- [10] A. Doucet, N. De Freitas, K. Murphy and S. Russell, "Rao-Blackwellised particle filtering for dynamic Bayesian networks.," in *Proceedings of the Sixteenth conference on Uncertainty in artificial intelligence*, 2000.
- [11] A. Doucet, S. Godsill and C. Andrieu, "On sequential Monte Carlo sampling methods for Bayesian filtering.," *Statistics and computing*, vol. 10, no. 3, pp. 197-208, 2000.
- [12] B. W. Silverman, "Density Estimation for Statistics and Data Analysis," *Monographs on Statistics and Applied Probability.*, vol. 26, 1986.

- [13] United States Air Force, "Technical Manual: Nondestructive Inspection, USAF Series, F-15A 73-085 and up, F-15B 73-108 and up, F-15 C/D/E Aircraft (Change 24 - 1 March 2014)," USAF.
- [14] Boeing, "F-15 Damage Tolerance Assessment Report," 2004.

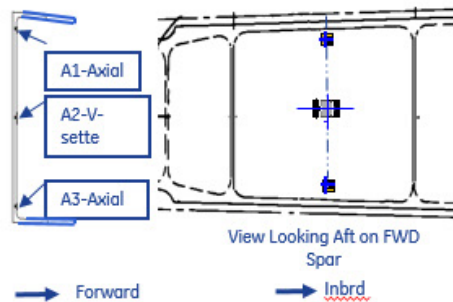
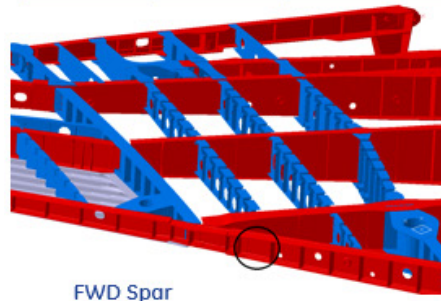
Safety of Test Instrumentation Summary Inboard Wing

Gage ID	Gage Location	Gage Type	STC Compensation	Resistance	Strain Level	Cycles to Failure
A1	Inboard Wing Forward Spar Forward Face	WK13-125BT-350 Axial	-13 for aluminum substrate	350 Ohms	+/- 2200 +/- 2000	>10 ⁶ >10 ⁷
A2		WK13-125TH-350 V-sette				
A3		WK13-125BT-350 Axial				
B1	Inboard Wing Intermediate Spar Aft Face	WK13-125BT-350 Axial	-13 for aluminum substrate	350 Ohms	+/- 2200 +/- 2000	>10 ⁶ >10 ⁷
B2		WK13-125TH-350 V-sette				
B3		WK13-125BT-350 Axial				
C1	Inboard Wing Main Spar Aft Face	WK13-125BT-350 Axial	-13 for aluminum substrate	350 Ohms	+/- 2200 +/- 2000	>10 ⁶ >10 ⁷
C2		WK13-125TH-350 V-sette				
C3		WK13-125BT-350 Axial				
D1	Inboard Wing Aft Spar Aft Face	WK13-125BT-350 Axial	-13 for aluminum substrate	350 Ohms	+/- 2200 +/- 2000	>10 ⁶ >10 ⁷
D2		WK13-125TH-350 V-sette				
D3		WK13-125BT-350 Axial				
E1	Inboard Wing Trailing Edge Spar Forward Face	WK13-125BT-350 Axial	-13 for aluminum substrate	350 Ohms	+/- 2200 +/- 2000	>10 ⁶ >10 ⁷
E2		WK13-125TH-350 V-sette				
E3		WK13-125BT-350 Axial				

Figure A-3. Safety of Test gauge information table

A1,A2,A3 – Inboard Wing, Forward Spar, Forward Face

Gage ID	Gage Location	Gage Type	STC Compensation	Resistance	Strain Level	Cycles to Failure
A1	Inboard Wing	WK13-125BT-350 Axial	-13 for aluminum substrate	350 Ohms	+/- 2200 +/- 2000	>10 ⁶ >10 ⁷
A2	Forward Spar	WK13-125TH-350 V-sette				
A3	Forward Face	WK13-125BT-350 Axial				



FWD Face of FWD Spar

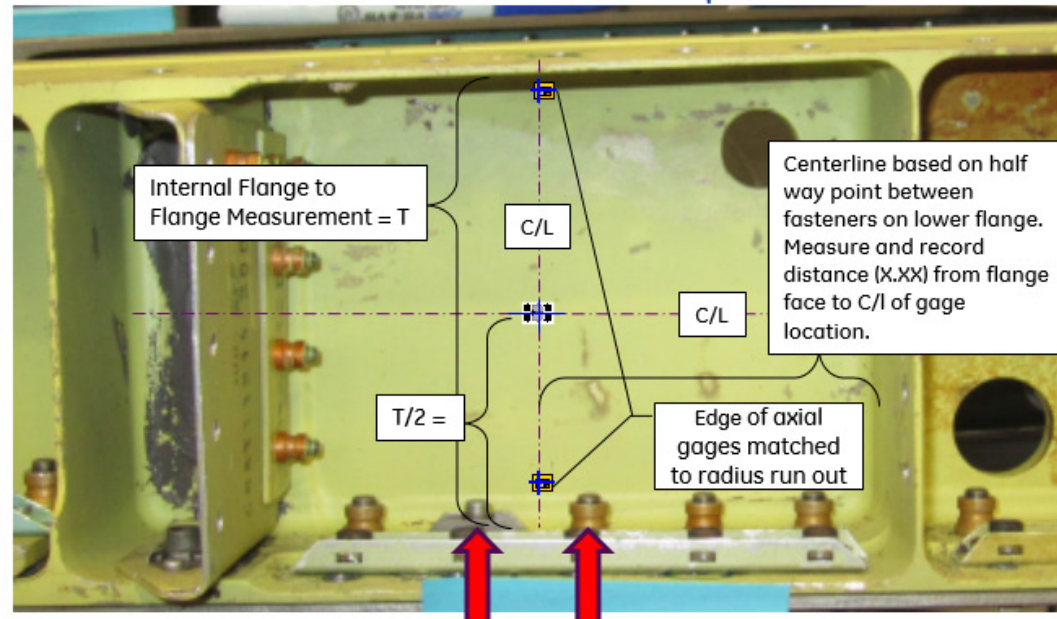
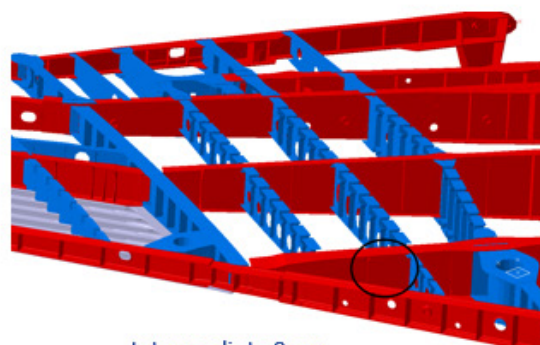


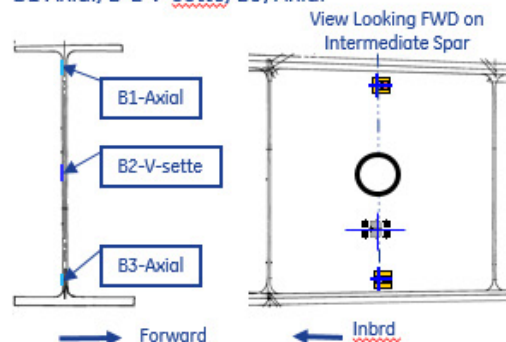
Figure A-4. Safety of Test gauge placement information

B1, B2, B3 – Inboard Wing, Intermediate Spar, Aft Face

Gage ID	Gage Location	Gage Type	STC Compensation	Resistance	Strain Level	Cycles to Failure
B1	Inboard Wing Intermediate Spar Aft Face	WK05125BT-350 Axial	-05 for Titanium substrate	350 Ohms	+/- 2200 +/- 2000	>10 ⁶ >10 ⁷
B2		WK05-125TH-350 V-sette				
B3		WK05-125BT-350 Axial				



Intermediate Spar
B1 Axial, B-2 V-sette, B3, Axial



Intermediate Spar

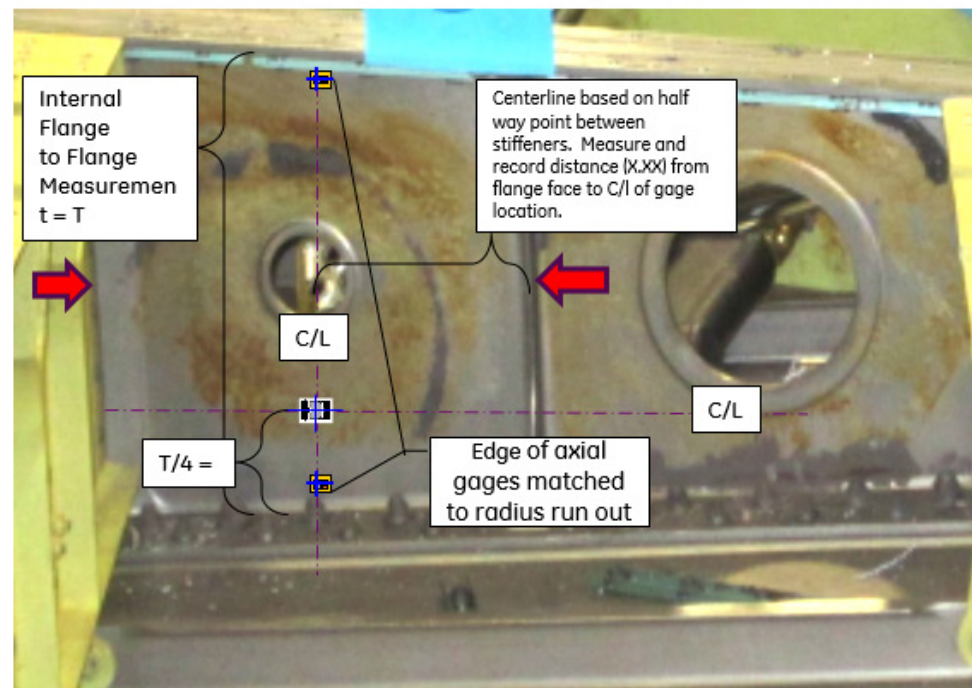


Figure A-5. Safety of Test gauge placement information

C1, C2, C3 – Inboard Wing, Main Spar, Aft Face

Gage ID	Gage Location	Gage Type	STC Compensation	Resistance	Strain Level	Cycles to Failure
C1	Inboard Wing Main Spar Aft Face	WK05-125BT-350 Axial	-05 for Titanium substrate	350 Ohms	+/- 2200 +/- 2000	$>10^6$ $>10^7$
C2		WK05-125TH-350 V-sette				
C3		WK05-125BT-350 Axial				

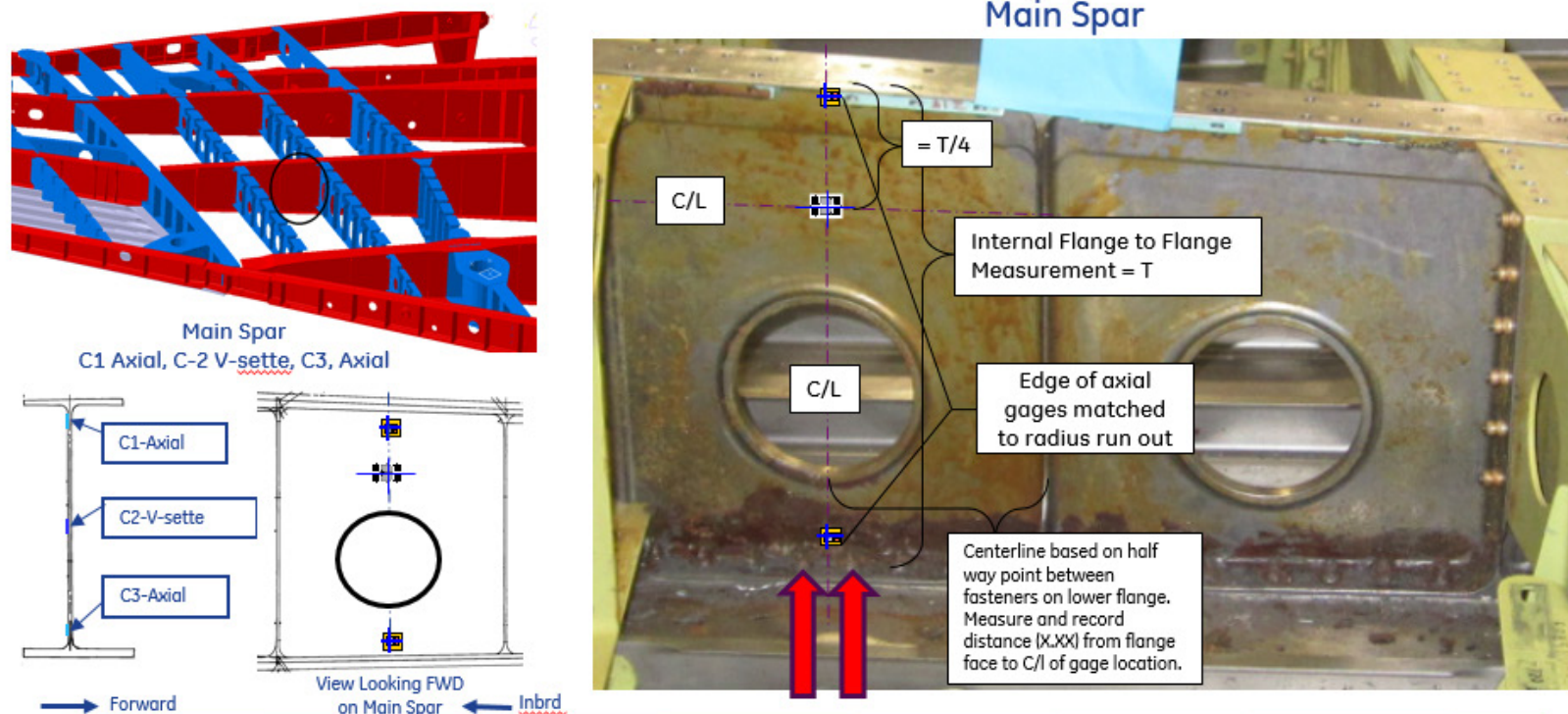


Figure A-6. Safety of Test gauge placement information

D1, D2, D3 – Inboard Wing, Aft Spar, Aft Face

Gage ID	Gage Location	Gage Type	STC Compensation	Resistance	Strain Level	Cycles to Failure
D1	Inboard Wing Aft Spar	WK05-125BT-350 Axial	-05 for Titanium substrate	350 Ohms	+/- 2200 +/- 2000	>10 ⁶ >10 ⁷
D2	Aft Spar	WK05-125TH-350 V-sette				
D3	Aft Face	WK05-125BT-350 Axial				

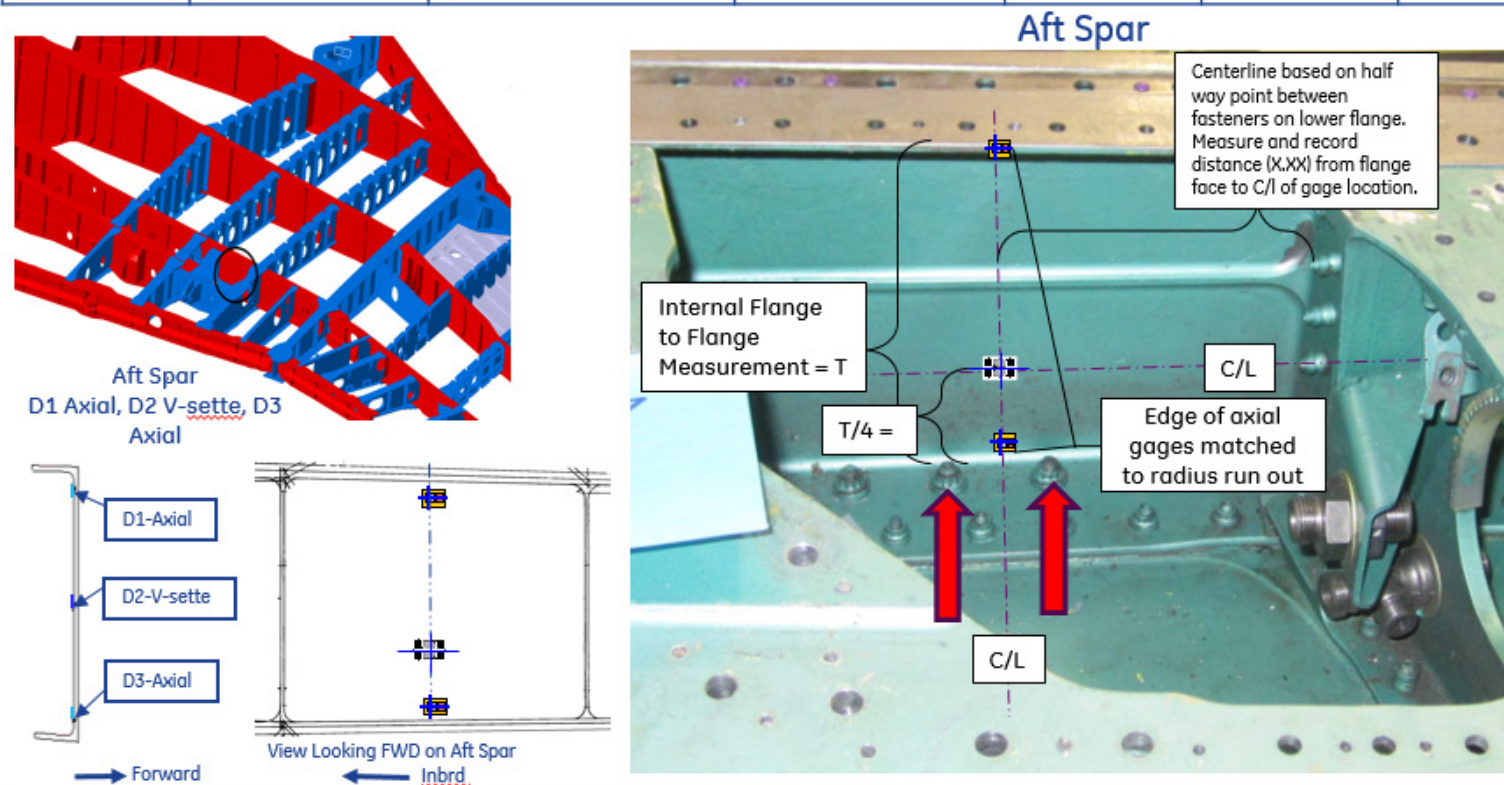


Figure A-7. Safety of Test gauge placement information

E1, E2, E3 – Inboard Wing, Trailing Edge Spar, Aft Face

Gage ID	Gage Location	Gage Type	STC Compensation	Resistance	Strain Level	Cycles to Failure
E1	Inboard Wing Trailing Edge Spar Forward Face	WK13-125BT-350 Axial	-13 for aluminum substrate	350 Ohms	+/- 2200 +/- 2000	>10 ⁶ >10 ⁷
E2		WK13-125TH-350 V-sette				
E3		WK13-125BT-350 Axial				

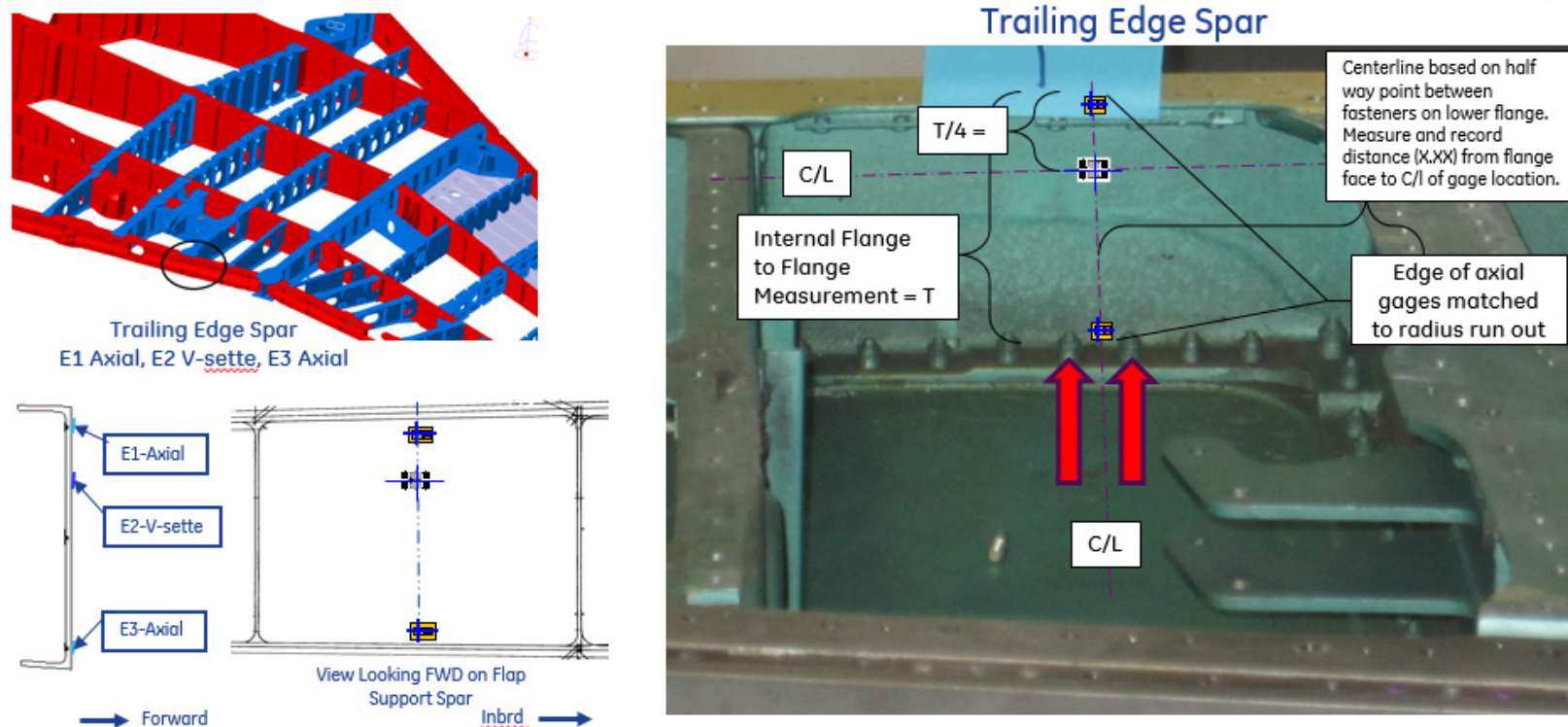
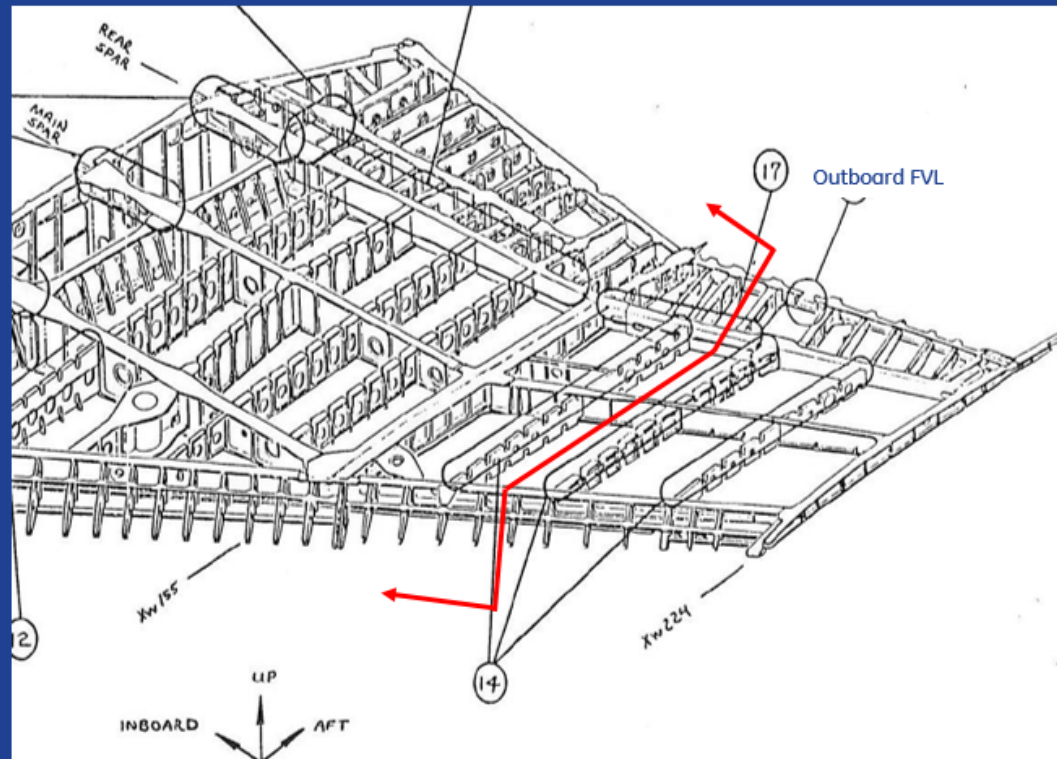


Figure A-8. Safety of Test gauge placement information

Outboard Wing FE Model Validation / Safety of Test Required Gages



FEM Validation Locations (FVLs) / Safety of Test

Figure A-9. Outboard instrumentation diagram

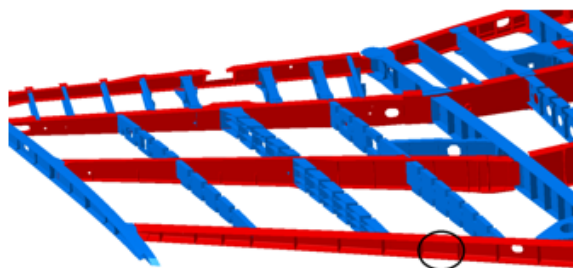
Safety of Test Instrumentation Summary Outboard Wing

Gage ID	Gage Location	Gage Type	STC #	Resistance	Strain Level	Cycles to Failure
F1	Outboard Wing Forward Spar Forward Face	WK13-125BT-350 Axial	-13 for aluminum substrate	350 Ohms	+/- 2200 +/- 2000	>10 ⁶ >10 ⁷
F2		WK13-125TH-350 V-sette				
F3		WK13-125BT-350 Axial				
G1	Outboard Wing Main Spar Aft Face	WK13-125BT-350 Axial	-13 for aluminum substrate	350 Ohms	+/- 2200 +/- 2000	>10 ⁶ >10 ⁷
G2		WK13-125TH-350 V-sette				
G3		WK13-125BT-350 Axial				
H1	Outboard Wing Aft Spar Aft Face	WK13-125BT-350 Axial	-13 for aluminum substrate	350 Ohms	+/- 2200 +/- 2000	>10 ⁶ >10 ⁷
H2		WK13-125TH-350 V-sette				
H3		WK13-125BT-350 Axial				
I1	Outboard Wing Trailing Edge Spar Aft Face	WK13-125BT-350 Axial	-13 for aluminum substrate	350 Ohms	+/- 2200 +/- 2000	>10 ⁶ >10 ⁷
I2		WK13-125TH-350 V-sette				
I3		WK13-125BT-350 Axial				

Figure A-10. Safety of Test gauge information table

F1, F2, F3 - Outboard Wing, Forward Spar, Forward Face

Gage ID	Gage Location	Gage Type	STC #	Resistance	Strain Level	Cycles to Failure
F1	Outboard Wing Forward Spar	WK13-125BT-350 Axial	-13 for aluminum substrate	350 Ohms	+/- 2200 +/- 2000	>10 ⁶ >10 ⁷
F2	Forward Spar Forward Face	WK13-125TH-350 V-sette				
F3		WK13-125BT-350 Axial				



FWD Spar
F1 Axial, F2 V-sette, F3 Axial

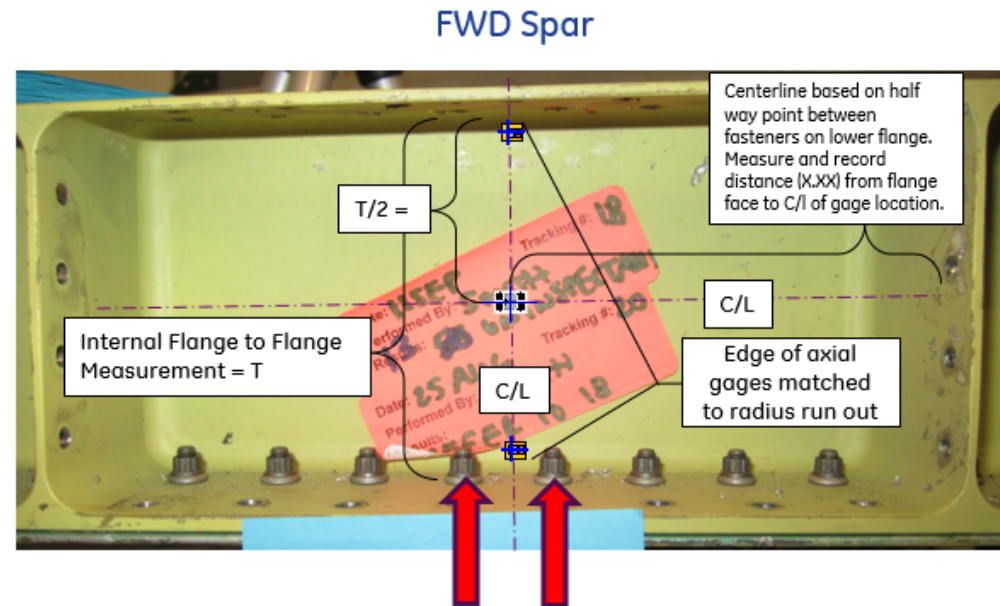
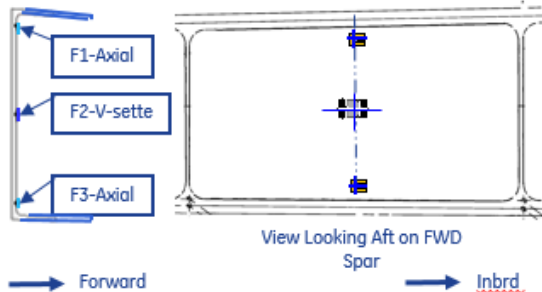
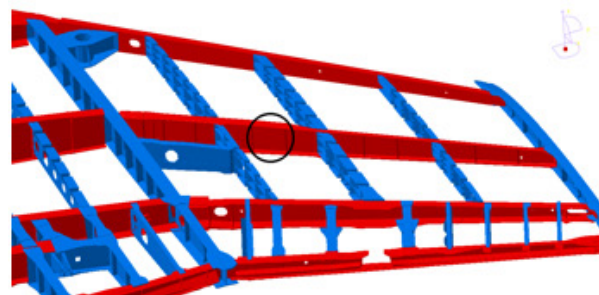


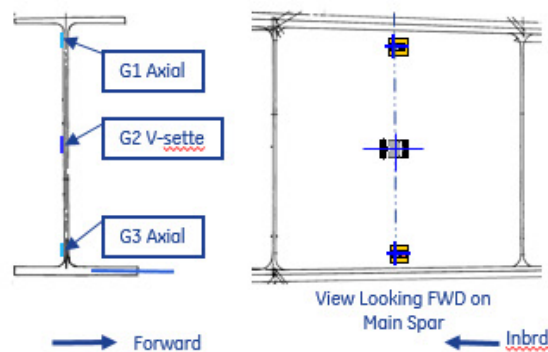
Figure A-11. Safety of Test gauge placement information

G1, G2, G3 – Outboard Wing, Main Spar, Aft Face

Gage ID	Gage Location	Gage Type	STC #	Resistance	Strain Level	Cycles to Failure
G1	Outboard Wing Main Spar Aft Face	WK13-125BT-350 Axial	-13 for aluminum substrate	350 Ohms	+/- 2200 +/- 2000	>10 ⁶ >10 ⁷
G2		WK13-125TH-350 V-sette				
G3		WK13-125BT-350 Axial				



Main Spar
G1 Axial, G2 V-sette, G3 Axial



Main Spar

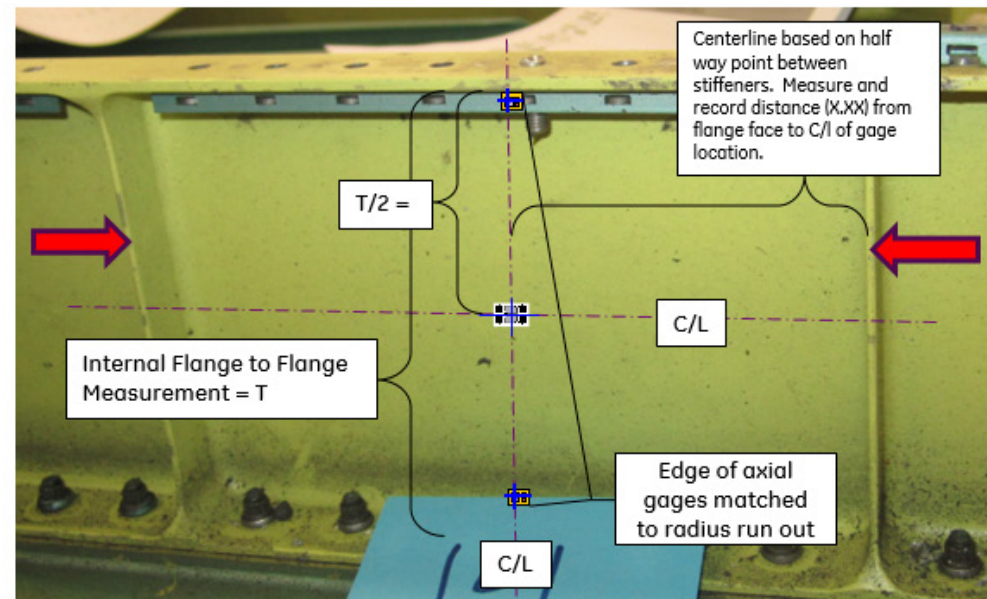
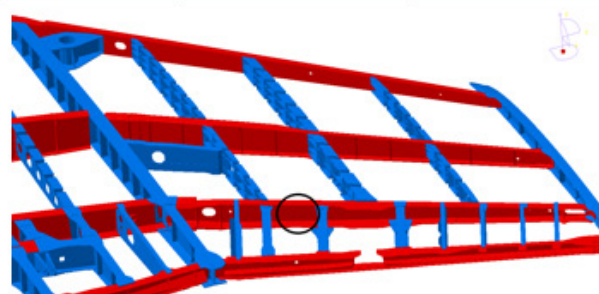


Figure A-12. Safety of Test gauge placement information

H1, H2, H3 – Outboard Wing, Aft Spar, Aft Face

Gage ID	Gage Location	Gage Type	STC #	Resistance	Strain Level	Cycles to Failure
H1	Outboard Wing Aft Spar	WK13-125BT-350 Axial	-13 for aluminum substrate	350 Ohms	+/- 2200 +/- 2000	>10 ⁶ >10 ⁷
H2	Aft Face	WK13-125TH-350 V-sette				
H3		WK13-125BT-350 Axial				



Aft Spar
H1 Axial, H2 V-sette, H3 Axial

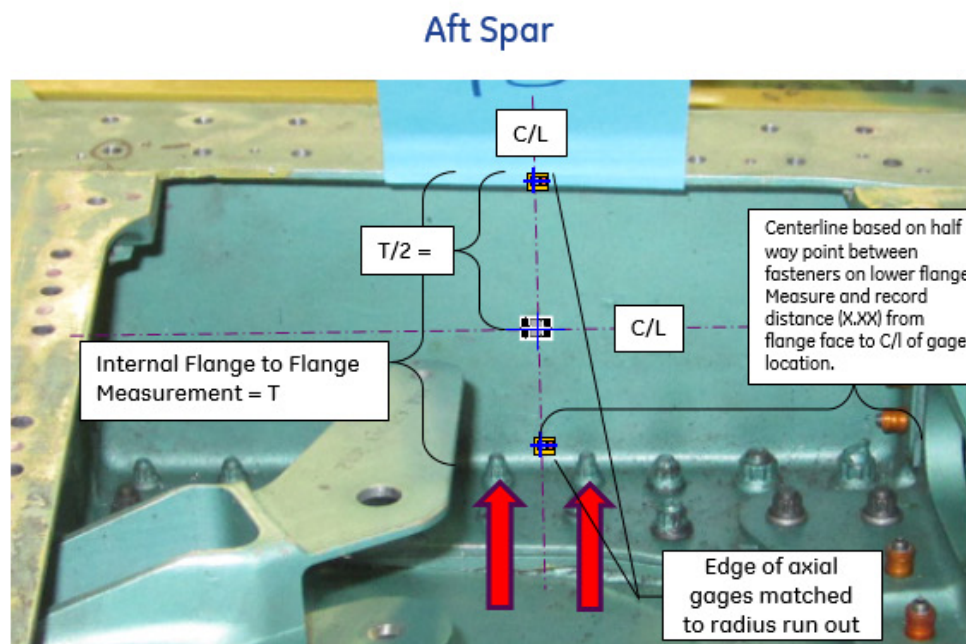
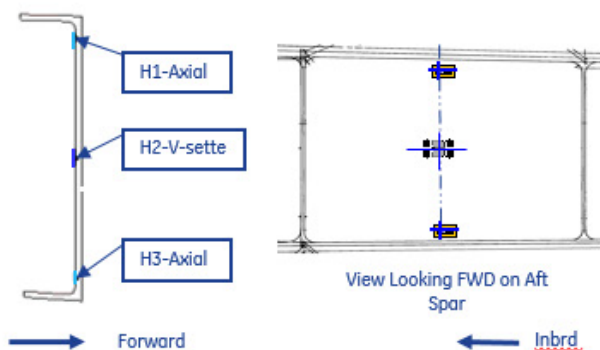
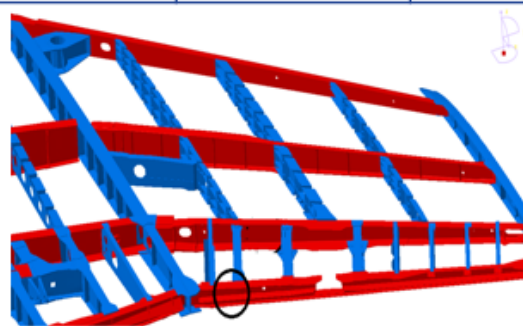


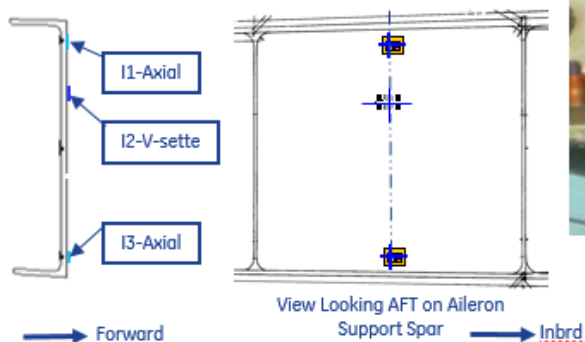
Figure A-13. Safety of Test gauge placement information

I1, I2, I3 – Outboard Wing, Trailing Edge Spar, Forward Face

Gage ID	Gage Location	Gage Type	STC #	Resistance	Strain Level	Cycles to Failure
I1	Outboard Wing Trailing Edge Spar Front Face	WK13-125BT-350 Axial	-13 for aluminum substrate	350 Ohms	+/- 2200 +/- 2000	>10 ⁶ >10 ⁷
I2		WK13-125TH-350 V-sette				
I3		WK13-125BT-350 Axial				



Aileron Support Spar
I1 Axial, I2 V-sette, I3 Axial



Aileron Support Spar

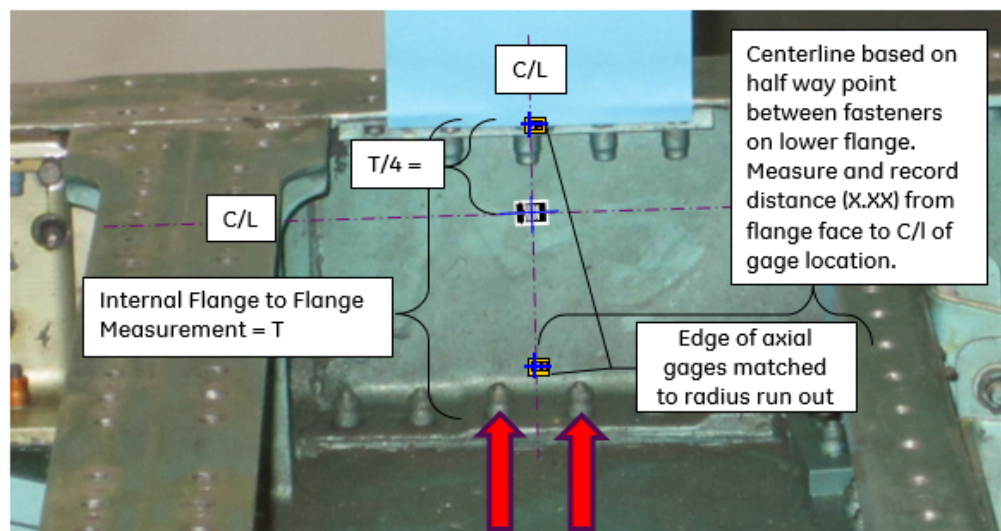


Figure A-14. Safety of Test gauge placement information

Control Point Instrumentation

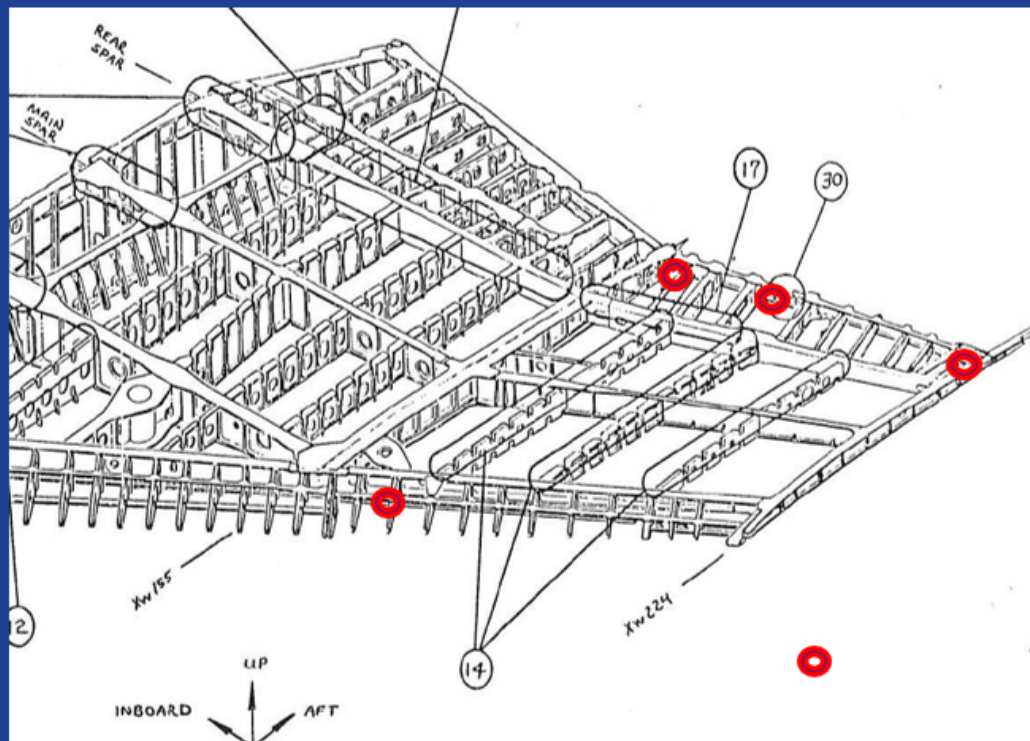


Figure A-15. Control point instrumentation diagram

GE05 – Lower Wing Skin, Fwd Edge Thickness Step at XW156

Control Point	Location	Cracking History	Flaw Details	SoT Instrumentation	IAT System Instrumentation
GE05	Lower wing skin forward edge thickness step at XW 158	Crack found at 18,100 hours during FTA-6	Corner crack in radius	none	PAUT from the outside; Crack gage placed at edge of flange or OML surface TBD

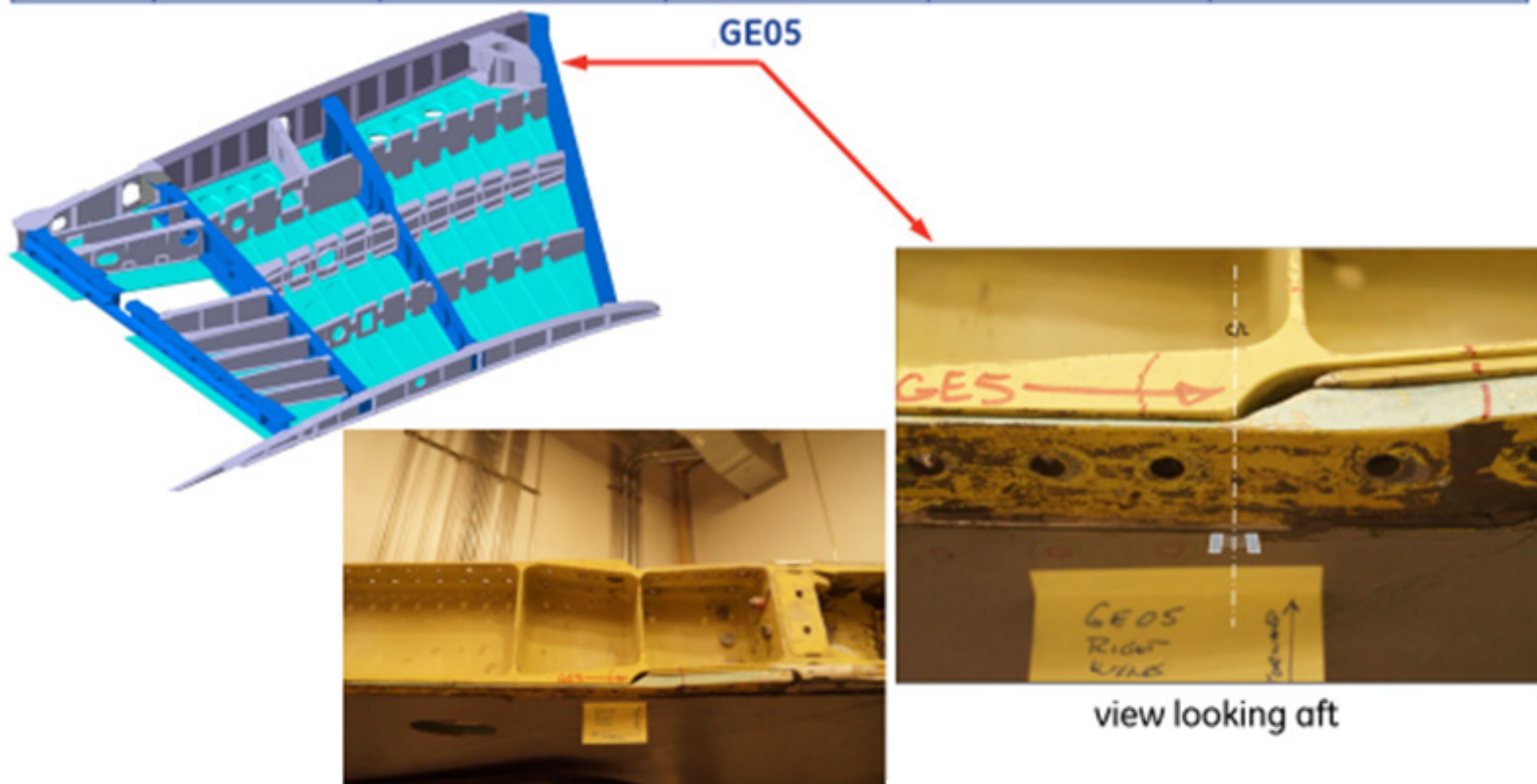


Figure A-16. GE05 control point instrumentation detail

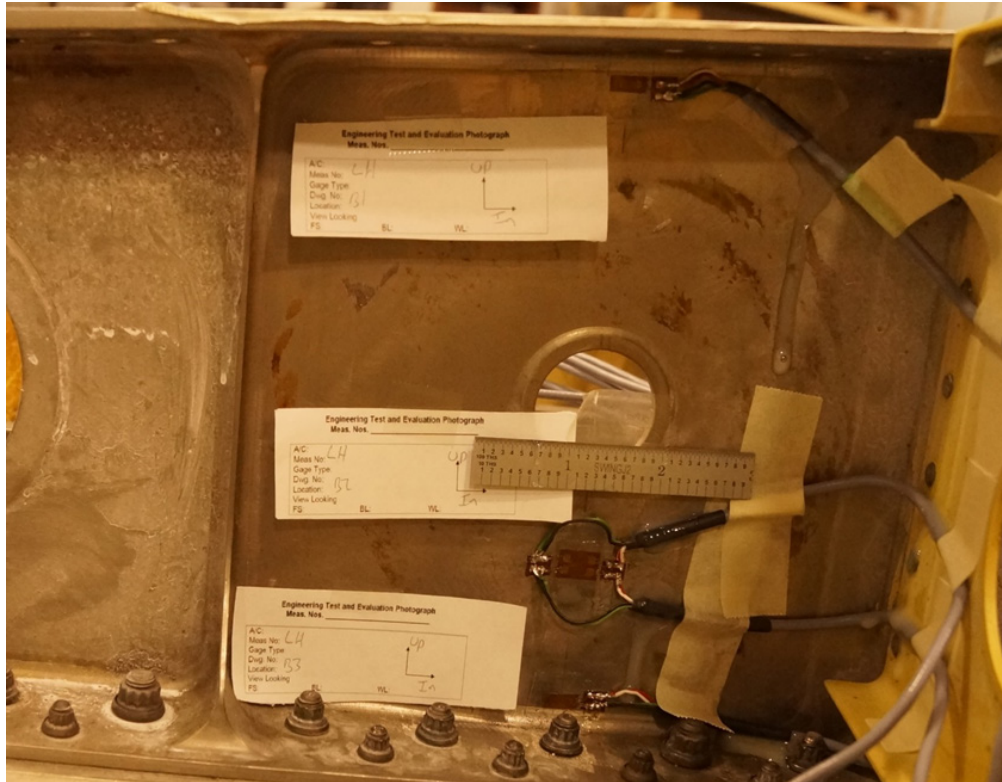


Figure A-17. LB1, LB2A, LB2B, and LB3 gauge installation

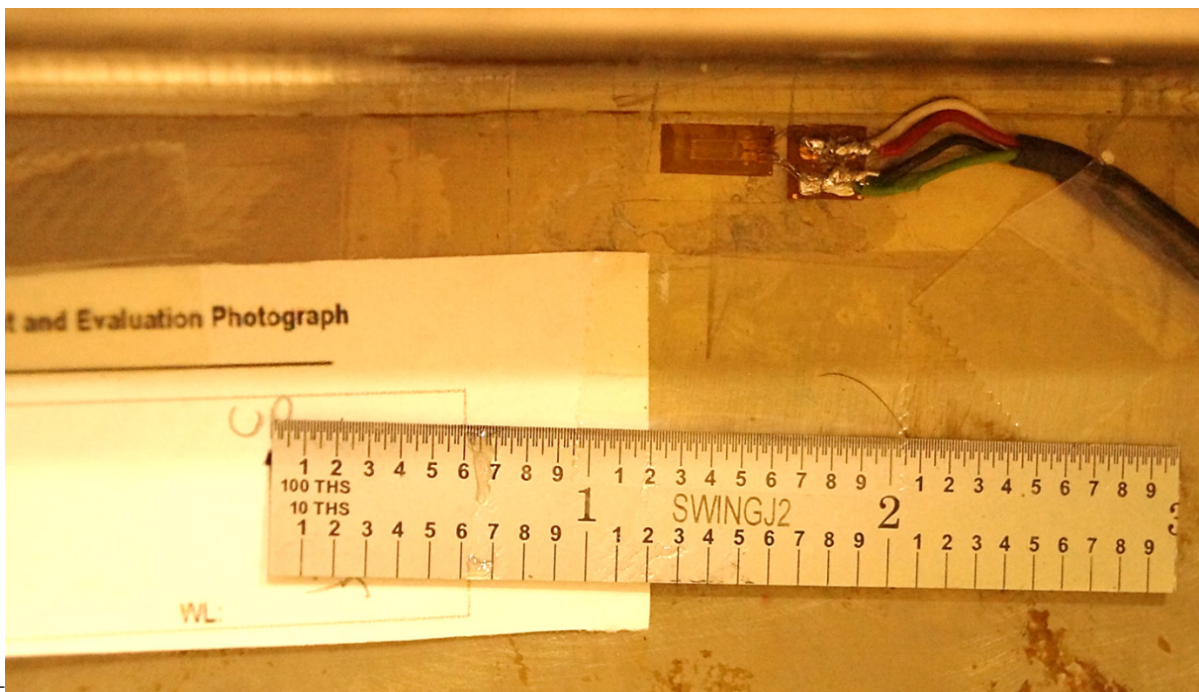


Figure A-18. LB1 close-up

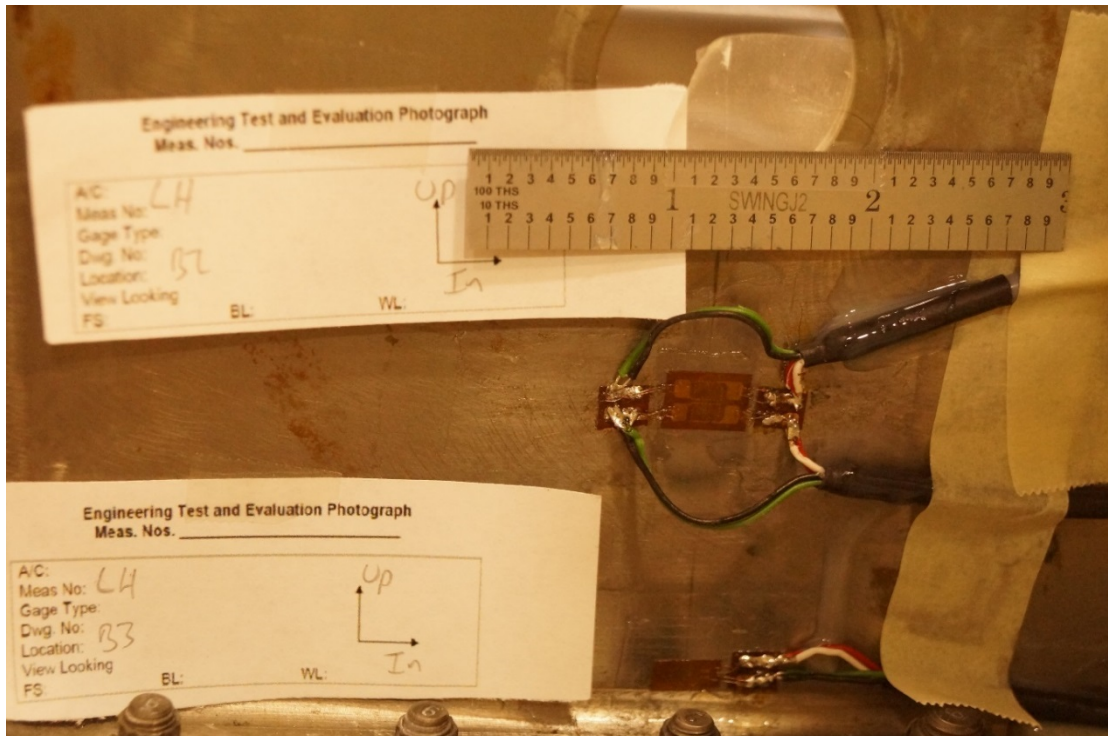


Figure A-19. LB2A, LB2B, and LB3 close-up



Figure A-20. LC1, LC2A, LC2B, and LC3 gauge installation

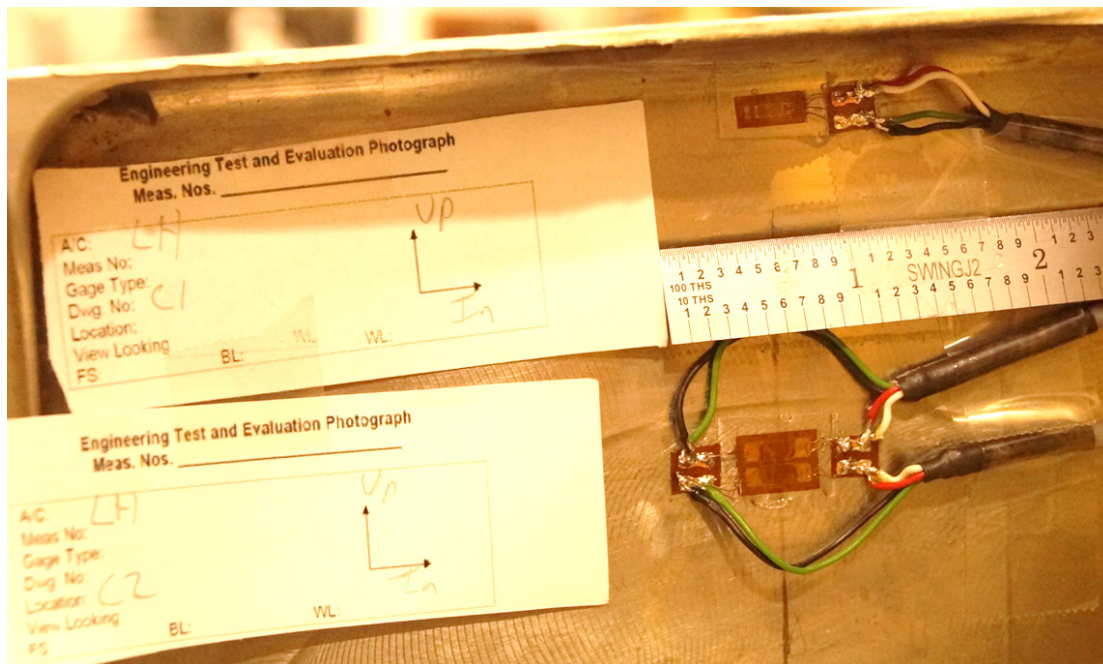


Figure A-21. LC1, LC2A, and LC2B close-up



Figure A-22. LC3 close-up

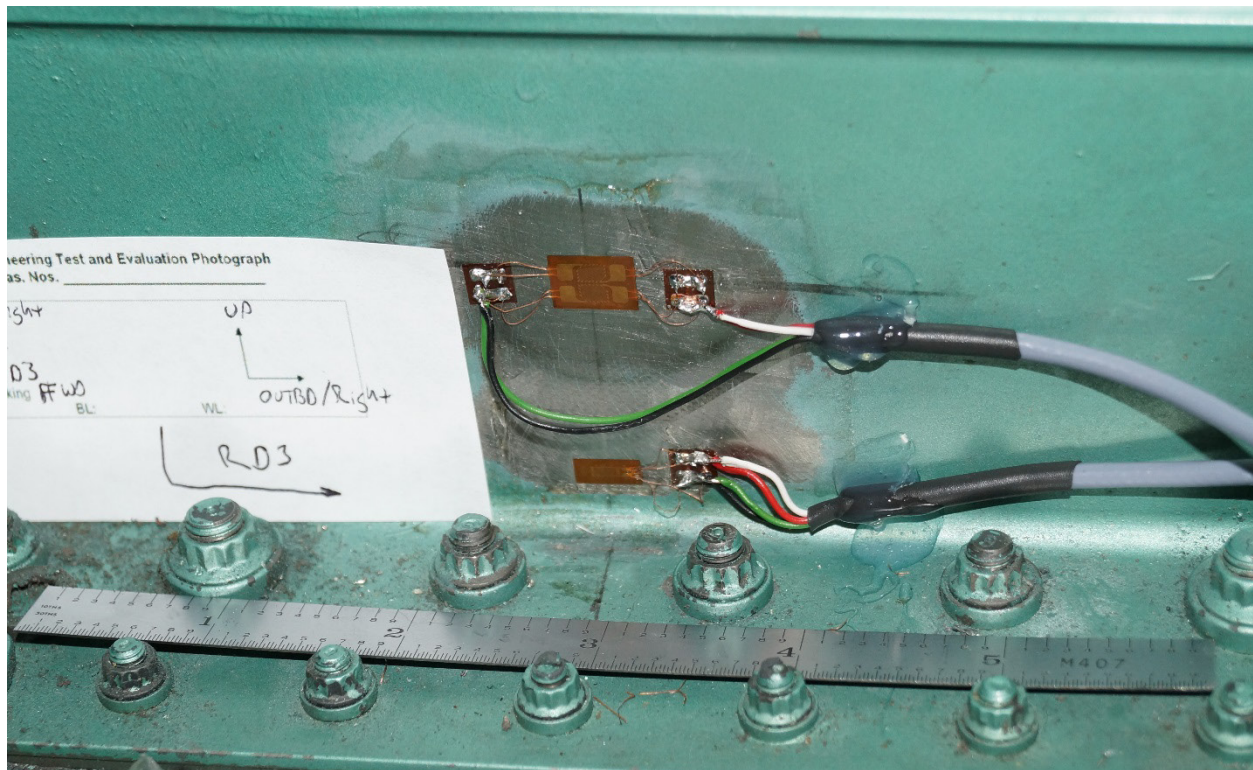


Figure A-23. RD2A, RD2B, and RD3 installation

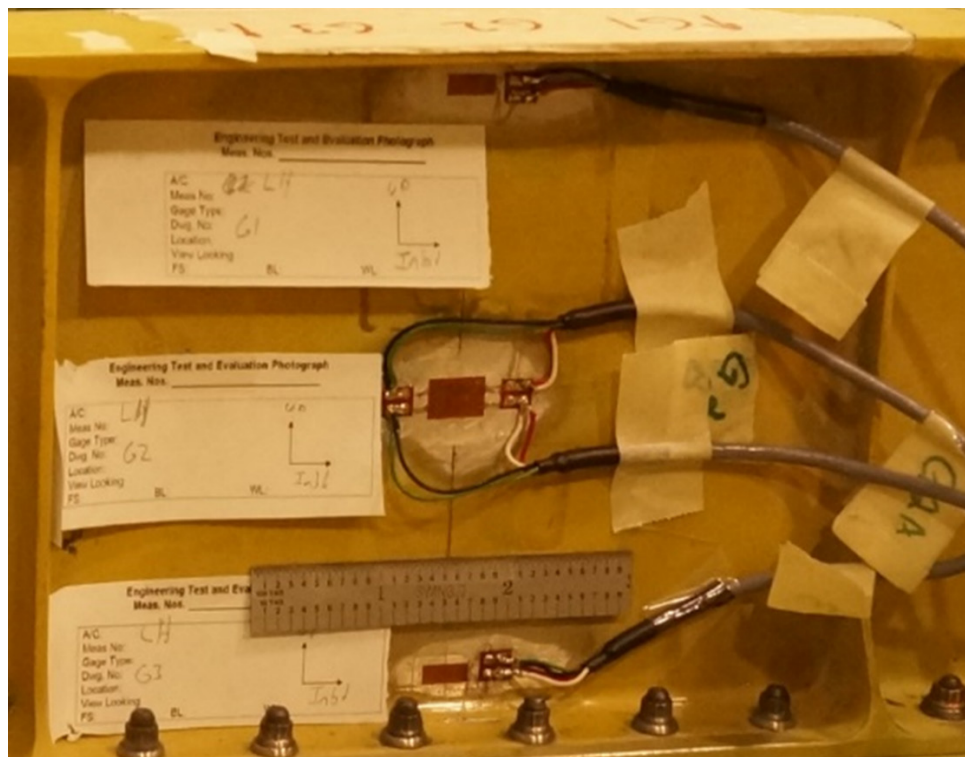


Figure A-24. LG1, LG2A, LG2B, LG3 installation

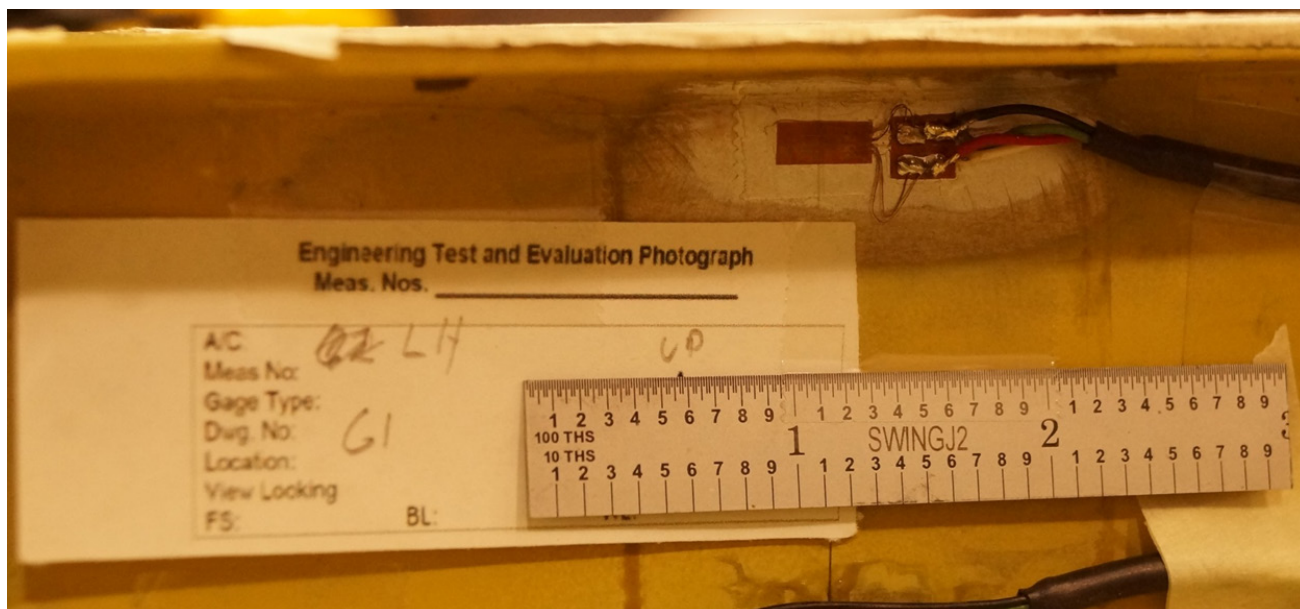


Figure A-25. LG1 close-up

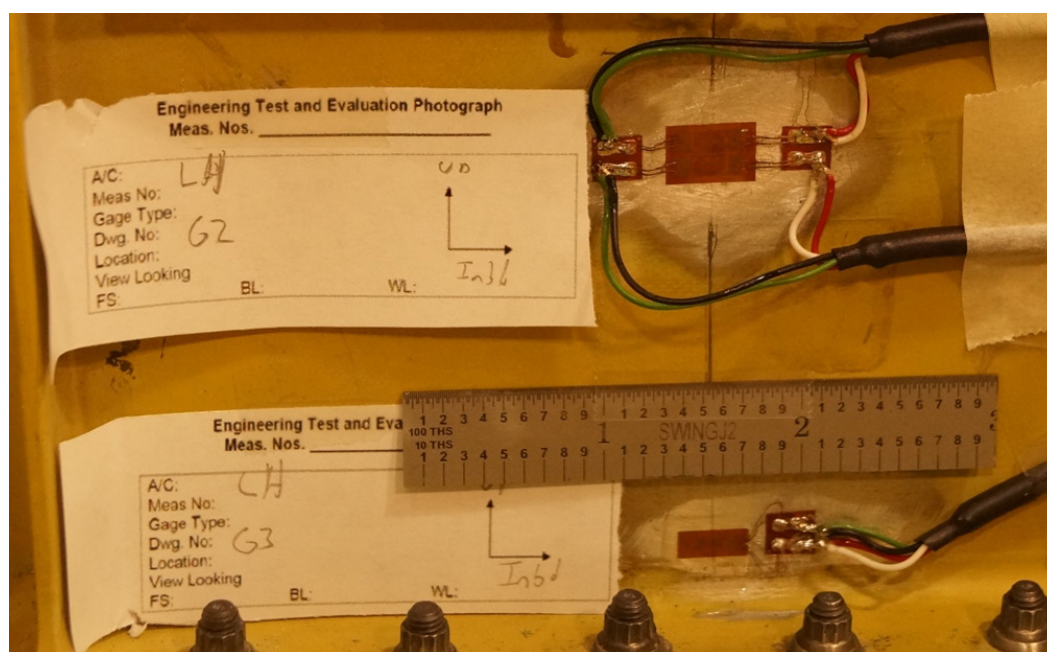


Figure A-26. LG2A, LG2B, and LG3 close-up

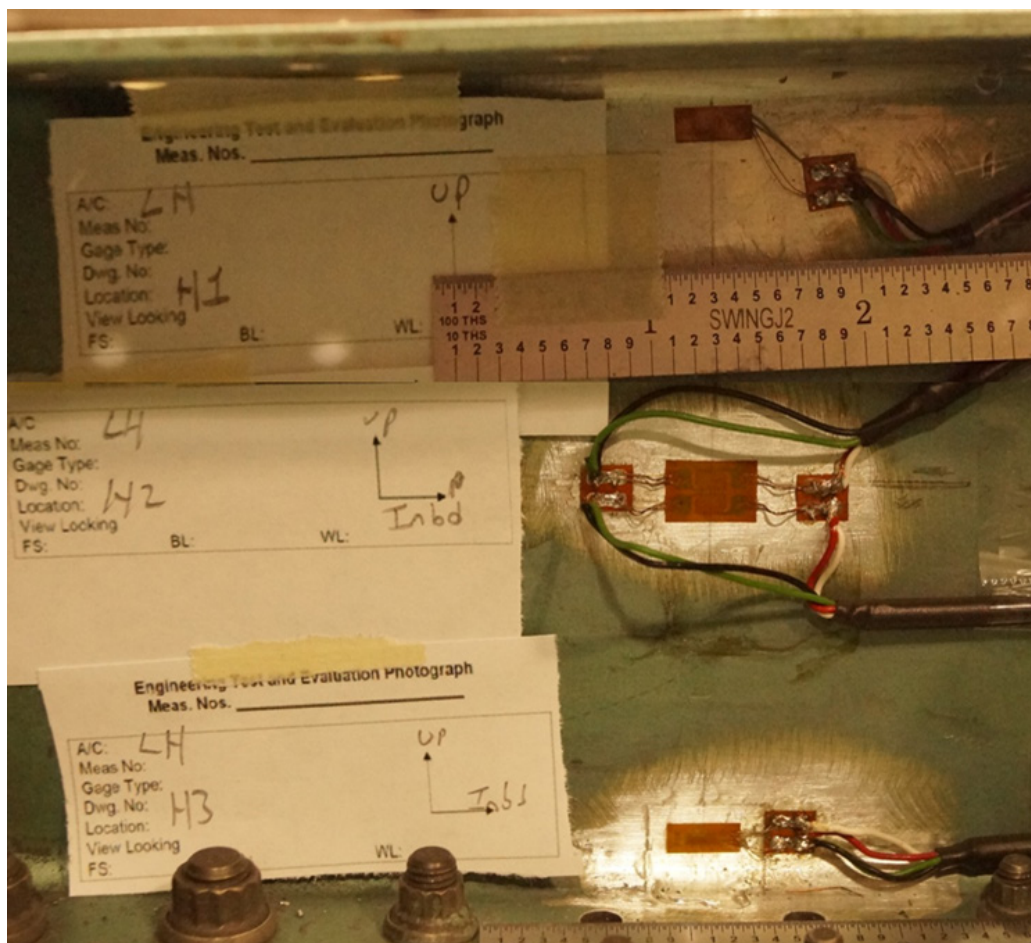


Figure A-27. LH1, LH2A, LH2B, and LH3 installation

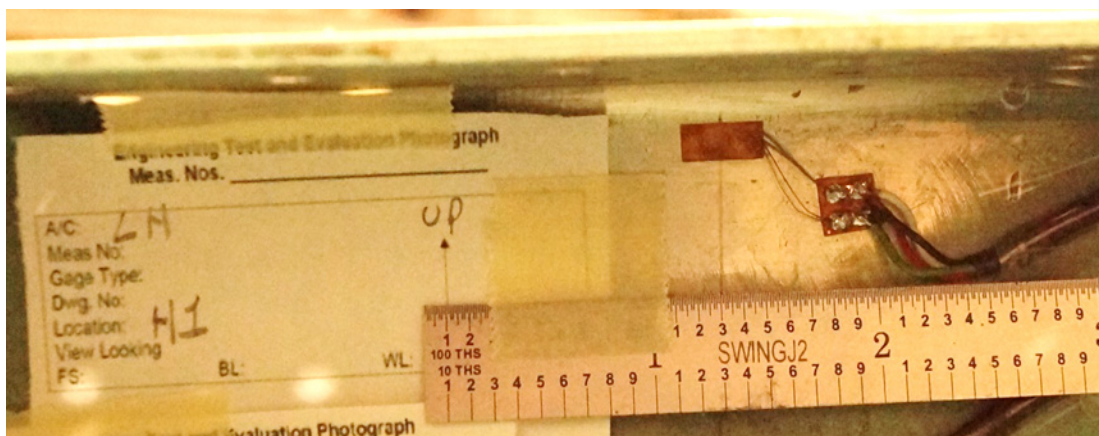


Figure A-28. LH1 close-up

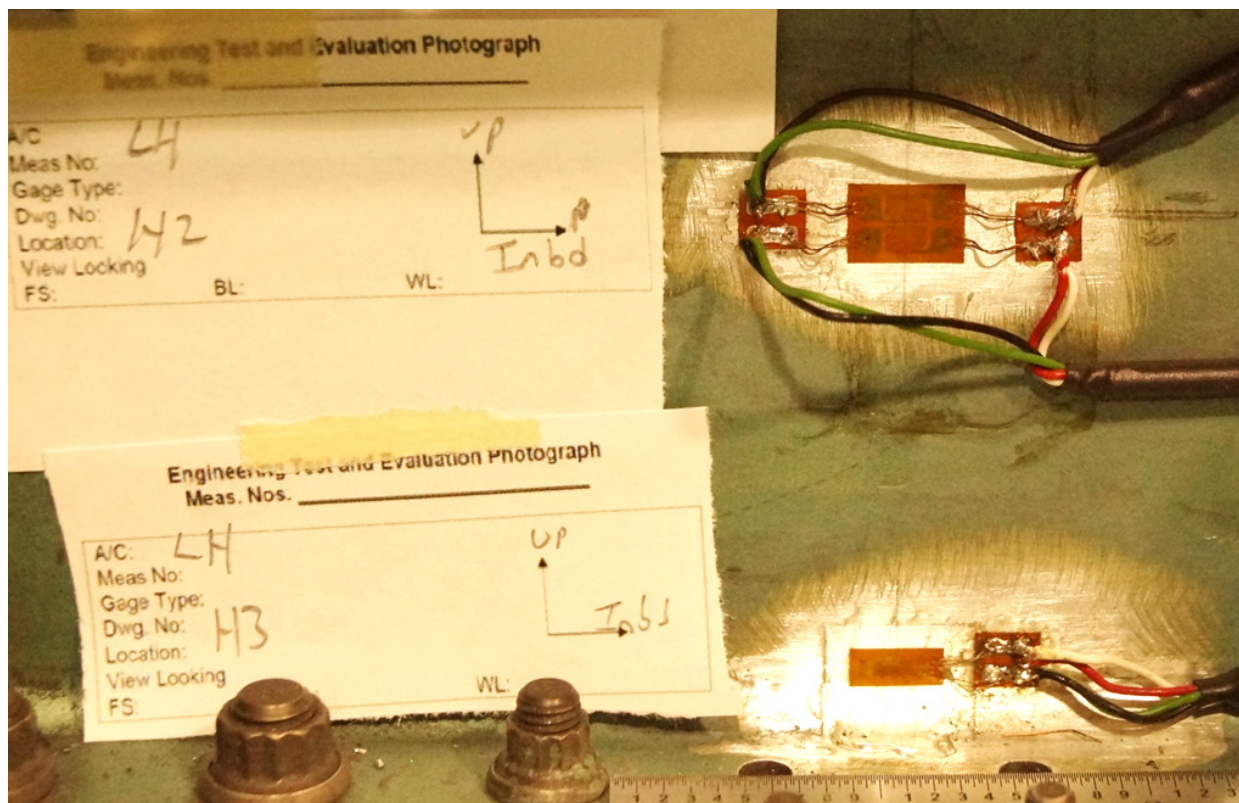


Figure A-29. LH2A, LH2B, LH3 close-up

Appendix B – OML Safety of Test Gauges



Digital Twin – SAFER-P²IAT
TASK ORDER 2
RHS Wing
FE Model Validation / Safety of Test / Control Point
Required Instrumentation



May 25, 2016

 GE Global Research
 GE Aviation Systems
 Lockheed Martin
 Wyle Aerospace

Figure B-1. OML gage introduction slide

Safety of Test Instrumentation Summary Inboard Wing

Gage ID	Gage Location	Gage Type	STC Compensation	Resistance	Strain Level	Cycles to Failure
J01	Inboard Wing, Skin, Lower	WK05-125BT-350	-05 for titanium substrate	350 Ohms	+/- 2200	>10 ⁶
K01	Inboard Wing, Skin, Lower	WK05-125BT-350	-05 for titanium substrate	350 Ohms	+/- 2200	>10 ⁶
L01	Inboard Wing, Skin, Lower	WK05-125BT-350	-05 for titanium substrate	350 Ohms	+/- 2200	>10 ⁶
M01	Inboard Wing, Skin, Lower	WK05-125BT-350	-05 for titanium substrate	350 Ohms	+/- 2200	>10 ⁶
N01	Inboard Wing, Skin, Lower	WK05-125BT-350	-05 for titanium substrate	350 Ohms	+/- 2200	>10 ⁶
P01	Inboard Wing, Skin, Lower	WK05-125BT-350	-05 for titanium substrate	350 Ohms	+/- 2200	>10 ⁶
Q01	Inboard Wing, Skin, Lower	WK05-125BT-350	-05 for titanium substrate	350 Ohms	+/- 2200	>10 ⁶
R01	Inboard Wing, Skin, Lower	WK05-125BT-350	-05 for titanium substrate	350 Ohms	+/- 2200	>10 ⁶
AD01	Inboard Wing, Skin, Upper	WK13-125BT-350	-13 for aluminum substrate	350 Ohms	+/- 2200	>10 ⁶
AE01	Inboard Wing, Skin, Upper	WK13-125BT-350	-13 for aluminum substrate	350 Ohms	+/- 2200	>10 ⁶
AF01	Inboard Wing, Skin, Upper	WK13-125BT-350	-13 for aluminum substrate	350 Ohms	+/- 2200	>10 ⁶
AG01	Inboard Wing, Skin, Upper	WK13-125BT-350	-13 for aluminum substrate	350 Ohms	+/- 2200	>10 ⁶
AH01	Inboard Wing, Skin, Upper	WK13-125BT-350	-13 for aluminum substrate	350 Ohms	+/- 2200	>10 ⁶
AI01	Inboard Wing, Skin, Upper	WK13-125BT-350	-13 for aluminum substrate	350 Ohms	+/- 2200	>10 ⁶
AJ01	Inboard Wing, Skin, Upper	WK13-125BT-350	-13 for aluminum substrate	350 Ohms	+/- 2200	>10 ⁶
AK01	Inboard Wing, Skin, Upper	WK13-125BT-350	-13 for aluminum substrate	350 Ohms	+/- 2200	>10 ⁶

Figure B-2. Summary of safety-of-test instrumentation

J01-R01 – Inboard Wing, Skin, Lower

Gage ID	Gage Location	Gage Type	STC Compensation	Resistance	Strain Level	Cycles to Failure
J01	Inboard Wing, Skin, Lower	WK05-125BT-350	-05 for titanium substrate	350 Ohms	+/- 2200	>10 ⁶
K01	Inboard Wing, Skin, Lower	WK05-125BT-350	-05 for titanium substrate	350 Ohms	+/- 2200	>10 ⁶
L01	Inboard Wing, Skin, Lower	WK05-125BT-350	-05 for titanium substrate	350 Ohms	+/- 2200	>10 ⁶
M01	Inboard Wing, Skin, Lower	WK05-125BT-350	-05 for titanium substrate	350 Ohms	+/- 2200	>10 ⁶
N01	Inboard Wing, Skin, Lower	WK05-125BT-350	-05 for titanium substrate	350 Ohms	+/- 2200	>10 ⁶
P01	Inboard Wing, Skin, Lower	WK05-125BT-350	-05 for titanium substrate	350 Ohms	+/- 2200	>10 ⁶
Q01	Inboard Wing, Skin, Lower	WK05-125BT-350	-05 for titanium substrate	350 Ohms	+/- 2200	>10 ⁶
R01	Inboard Wing, Skin, Lower	WK05-125BT-350	-05 for titanium substrate	350 Ohms	+/- 2200	>10 ⁶

OML of Lower Skins

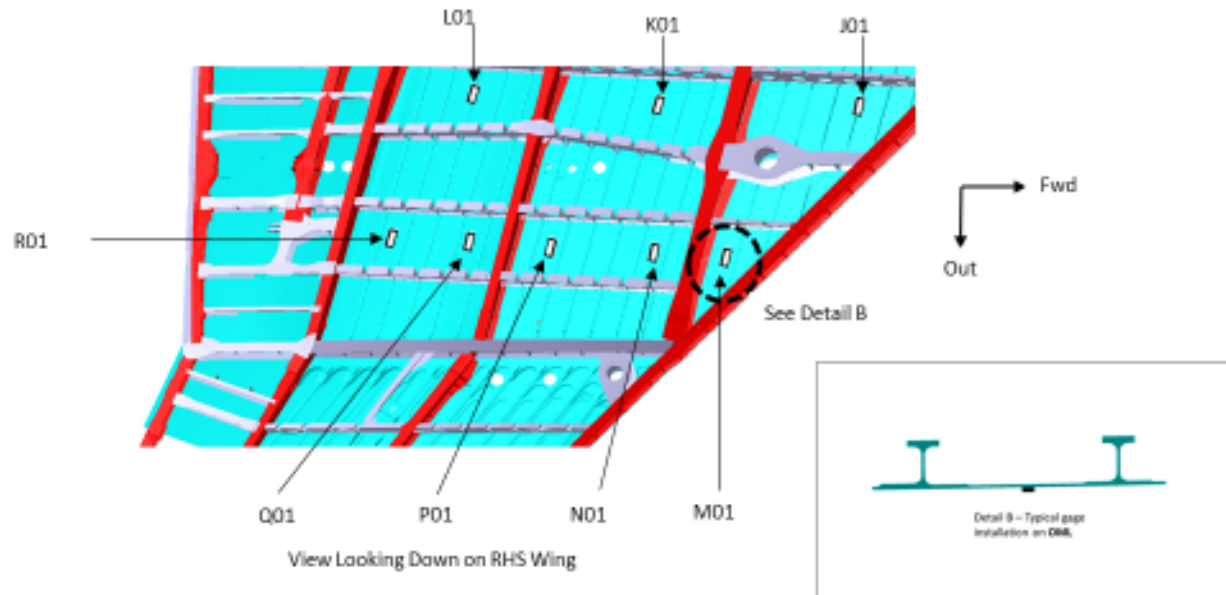


Figure B-3. OML reference diagram

AD01-AK01 – Inboard Wing, Skin, Upper

Gage ID	Gage Location	Gage Type	STC Compensation	Resistance	Strain Level	Cycles to Failure
AD01	Inboard Wing, Skin, Upper	WK13-125BT-350	-13 for aluminum substrate	350 Ohms	+/- 2200	>10 ⁶
AE01	Inboard Wing, Skin, Upper	WK13-125BT-350	-13 for aluminum substrate	350 Ohms	+/- 2200	>10 ⁶
AF01	Inboard Wing, Skin, Upper	WK13-125BT-350	-13 for aluminum substrate	350 Ohms	+/- 2200	>10 ⁶
AG01	Inboard Wing, Skin, Upper	WK13-125BT-350	-13 for aluminum substrate	350 Ohms	+/- 2200	>10 ⁶
AH01	Inboard Wing, Skin, Upper	WK13-125BT-350	-13 for aluminum substrate	350 Ohms	+/- 2200	>10 ⁶
AI01	Inboard Wing, Skin, Upper	WK13-125BT-350	-13 for aluminum substrate	350 Ohms	+/- 2200	>10 ⁶
AJ01	Inboard Wing, Skin, Upper	WK13-125BT-350	-13 for aluminum substrate	350 Ohms	+/- 2200	>10 ⁶
AK01	Inboard Wing, Skin, Upper	WK13-125BT-350	-13 for aluminum substrate	350 Ohms	+/- 2200	>10 ⁶

OML of Upper Skins

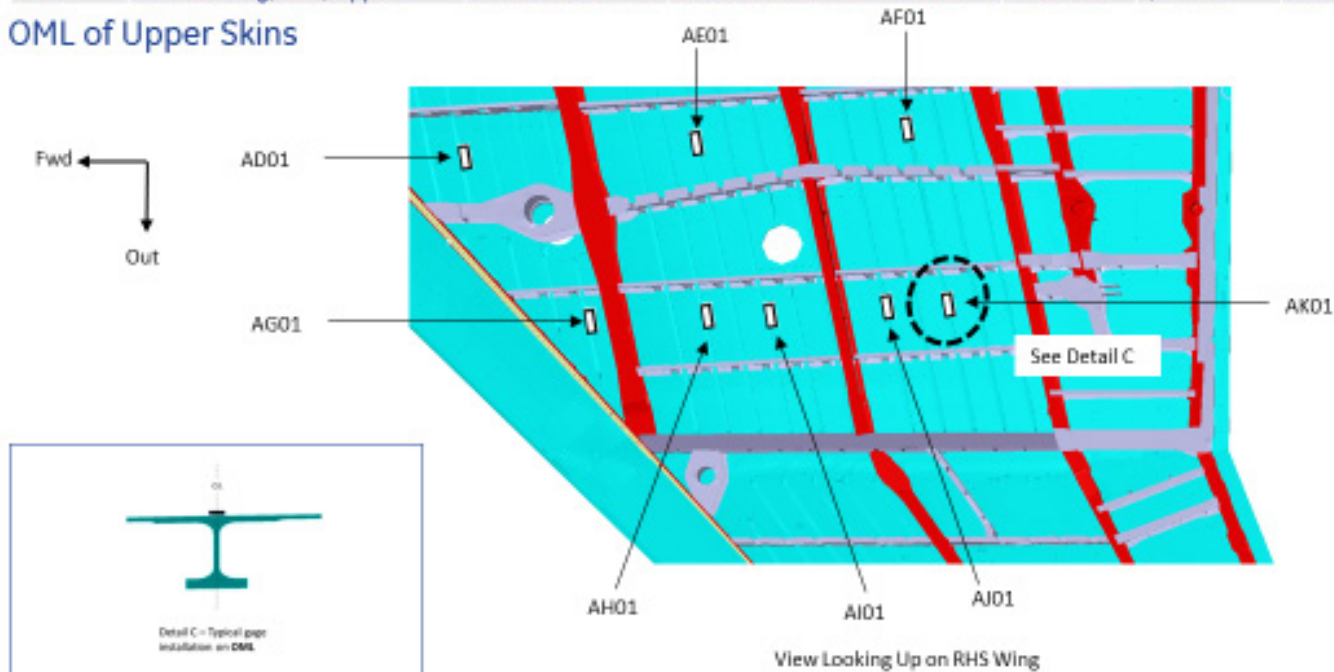


Figure B-4. OML reference diagram

Safety of Test Instrumentation Summary Outboard Wing

Gage ID	Gage Location	Gage Type	STC Compensation	Resistance	Strain Level	Cycles to Failure
S01	Outboard Wing, Skin, Lower	WK13-1258T-350	-13 for aluminum substrate	350 Ohms	+/- 2200	>10 ⁶
T01	Outboard Wing, Skin, Lower	WK13-1258T-350	-13 for aluminum substrate	350 Ohms	+/- 2200	>10 ⁶
U01	Outboard Wing, Skin, Lower	WK13-1258T-350	-13 for aluminum substrate	350 Ohms	+/- 2200	>10 ⁶
V01	Outboard Wing, Skin, Lower	WK13-1258T-350	-13 for aluminum substrate	350 Ohms	+/- 2200	>10 ⁶
W01	Outboard Wing, Skin, Lower	WK13-1258T-350	-13 for aluminum substrate	350 Ohms	+/- 2200	>10 ⁶
X01	Outboard Wing, Skin, Lower	WK13-1258T-350	-13 for aluminum substrate	350 Ohms	+/- 2200	>10 ⁶
Y01	Outboard Wing, Skin, Lower	WK13-1258T-350	-13 for aluminum substrate	350 Ohms	+/- 2200	>10 ⁶
Z01	Outboard Wing, Skin, Lower	WK13-1258T-350	-13 for aluminum substrate	350 Ohms	+/- 2200	>10 ⁶
AA01	Outboard Wing, Skin, Lower	WK13-1258T-350	-13 for aluminum substrate	350 Ohms	+/- 2200	>10 ⁶
AB01	Outboard Wing, Skin, Lower	WK13-1258T-350	-13 for aluminum substrate	350 Ohms	+/- 2200	>10 ⁶
AC01	Outboard Wing, Skin, Lower	WK13-1258T-350	-13 for aluminum substrate	350 Ohms	+/- 2200	>10 ⁶
AL01	Outboard Wing, Skin, Upper	WK13-1258T-350	-13 for aluminum substrate	350 Ohms	+/- 2200	>10 ⁶
AM01	Outboard Wing, Skin, Upper	WK13-1258T-350	-13 for aluminum substrate	350 Ohms	+/- 2200	>10 ⁶
AN01	Outboard Wing, Skin, Upper	WK13-1258T-350	-13 for aluminum substrate	350 Ohms	+/- 2200	>10 ⁶
AP01	Outboard Wing, Skin, Upper	WK13-1258T-350	-13 for aluminum substrate	350 Ohms	+/- 2200	>10 ⁶

Figure B-5. Summary of safety-of-test gages

S01-AC01 - Outboard Wing, Skin, Lower

Gage ID	Gage Location	Gage Type	STC Compensation	Resistance	Strain Level	Cycles to Failure
S01	Outboard Wing, Skin, Lower	WK13-125BT-350	-13 for aluminum substrate	350 Ohms	+/- 2200	>10 ⁶
T01	Outboard Wing, Skin, Lower	WK13-125BT-350	-13 for aluminum substrate	350 Ohms	+/- 2200	>10 ⁶
U01	Outboard Wing, Skin, Lower	WK13-125BT-350	-13 for aluminum substrate	350 Ohms	+/- 2200	>10 ⁶
V01	Outboard Wing, Skin, Lower	WK13-125BT-350	-13 for aluminum substrate	350 Ohms	+/- 2200	>10 ⁶
W01	Outboard Wing, Skin, Lower	WK13-125BT-350	-13 for aluminum substrate	350 Ohms	+/- 2200	>10 ⁶
X01	Outboard Wing, Skin, Lower	WK13-125BT-350	-13 for aluminum substrate	350 Ohms	+/- 2200	>10 ⁶
Y01	Outboard Wing, Skin, Lower	WK13-125BT-350	-13 for aluminum substrate	350 Ohms	+/- 2200	>10 ⁶
Z01	Outboard Wing, Skin, Lower	WK13-125BT-350	-13 for aluminum substrate	350 Ohms	+/- 2200	>10 ⁶
AA01	Outboard Wing, Skin, Lower	WK13-125BT-350	-13 for aluminum substrate	350 Ohms	+/- 2200	>10 ⁶
AB01	Outboard Wing, Skin, Lower	WK13-125BT-350	-13 for aluminum substrate	350 Ohms	+/- 2200	>10 ⁶
AC01	Outboard Wing, Skin, Lower	WK13-125BT-350	-13 for aluminum substrate	350 Ohms	+/- 2200	>10 ⁶

OML of Lower Skins

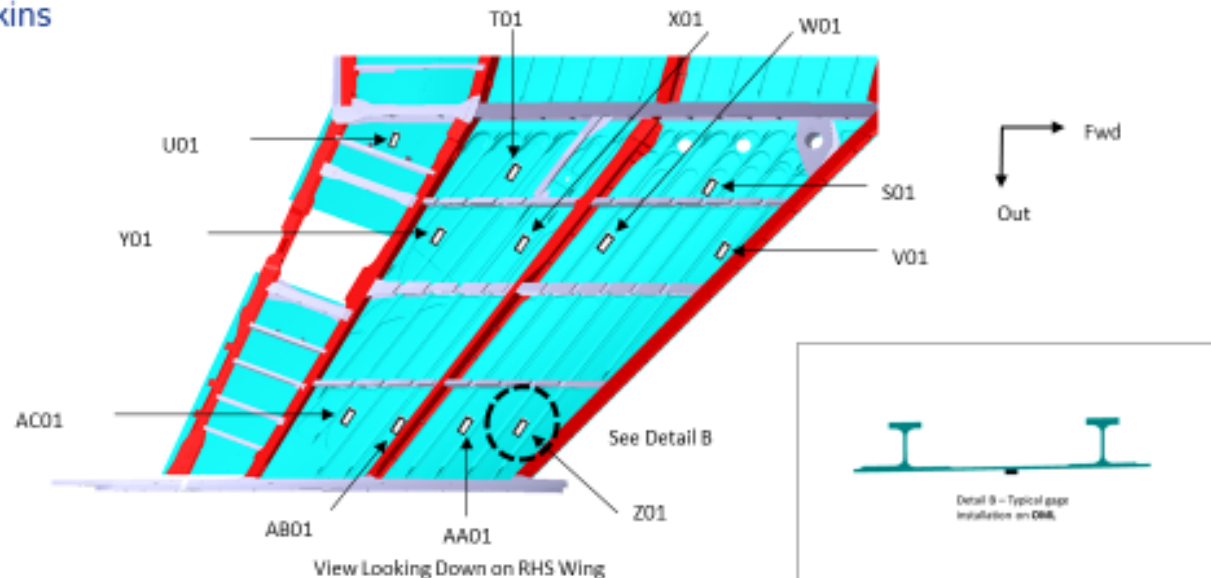


Figure B-6. OML reference diagram

AL01-AP01 – Outboard Wing, Skin, Upper

Gage ID	Gage Location	Gage Type	STC Compensation	Resistance	Strain Level	Cycles to Failure
AL01	Outboard Wing, Skin, Upper	WK13-125BT-350	-13 for aluminum substrate	350 Ohms	+/- 2200	>10 ⁶
AM01	Outboard Wing, Skin, Upper	WK13-125BT-350	-13 for aluminum substrate	350 Ohms	+/- 2200	>10 ⁶
AN01	Outboard Wing, Skin, Upper	WK13-125BT-350	-13 for aluminum substrate	350 Ohms	+/- 2200	>10 ⁶
AP01	Outboard Wing, Skin, Upper	WK13-125BT-350	-13 for aluminum substrate	350 Ohms	+/- 2200	>10 ⁶

OML of Upper Skins

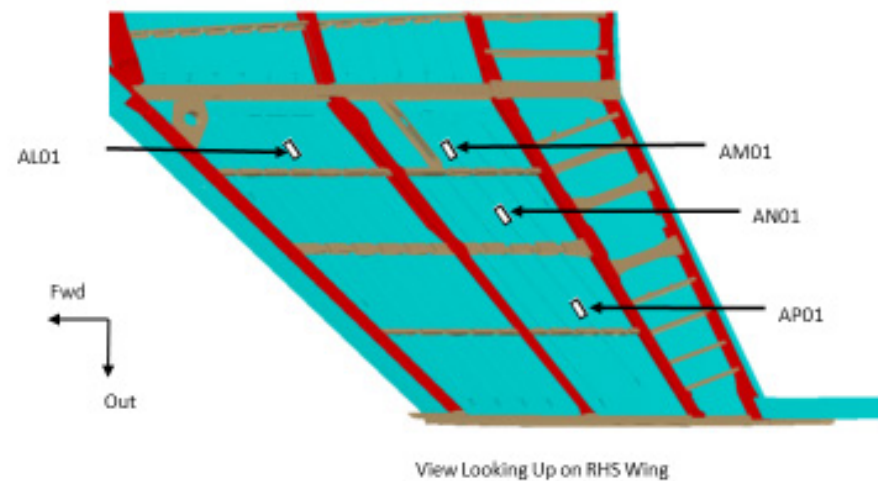


Figure B-7. OML reference diagram

B.1 Upper Wing Skin Reference Photos

Left Upper Forward Wing Skin

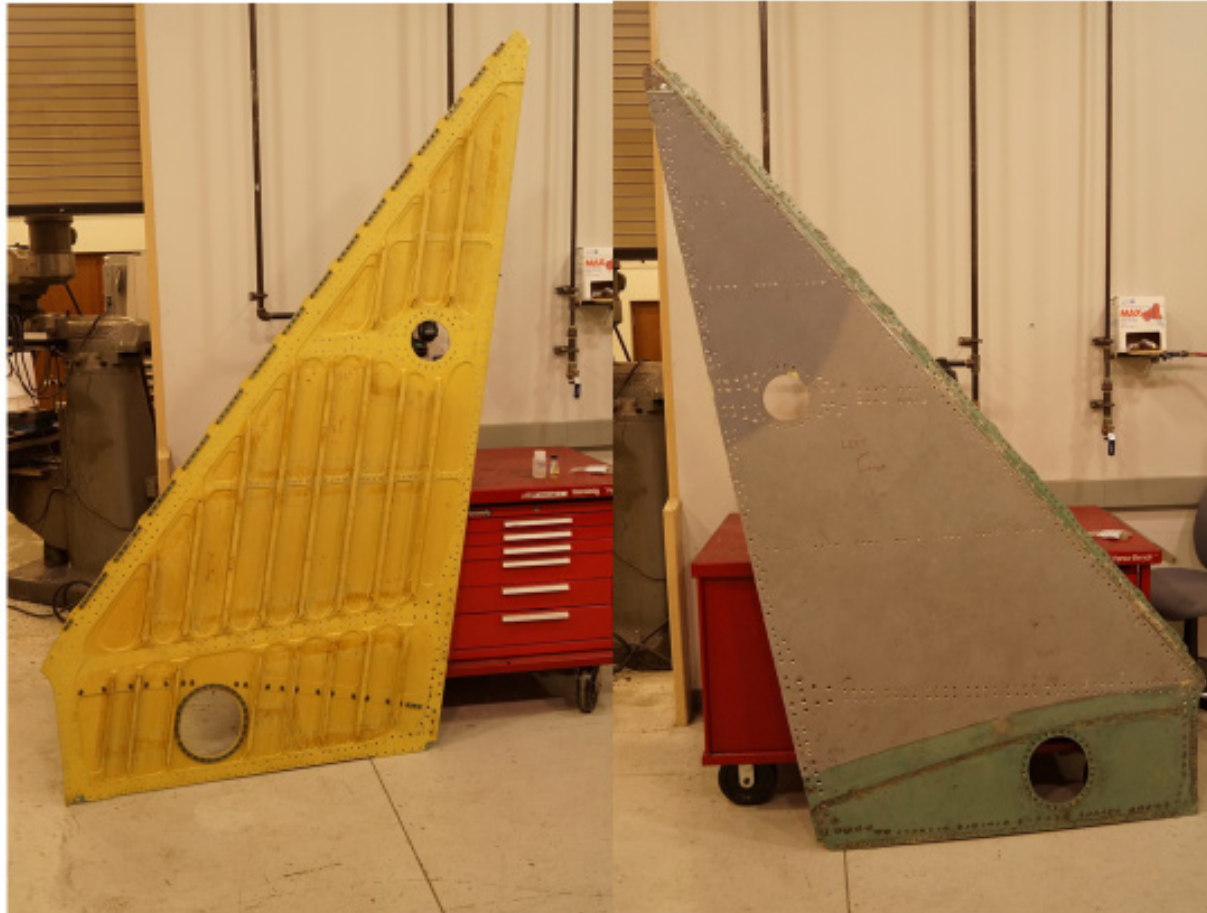


Figure B-8. Left upper forward wing skin

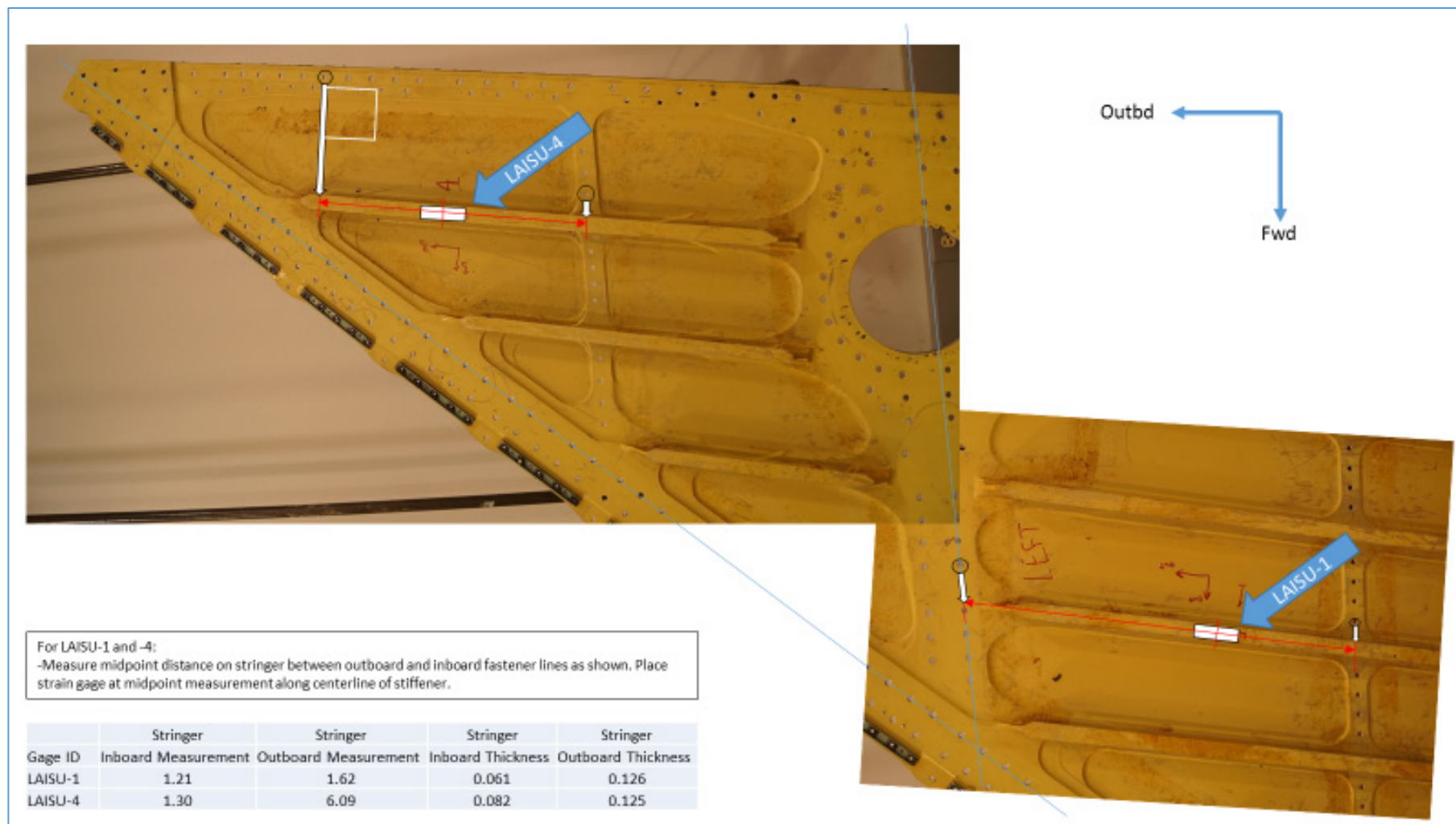


Figure B-9. Position of LAISU-1 and LAISU-4

Left Upper Torque Box Skin

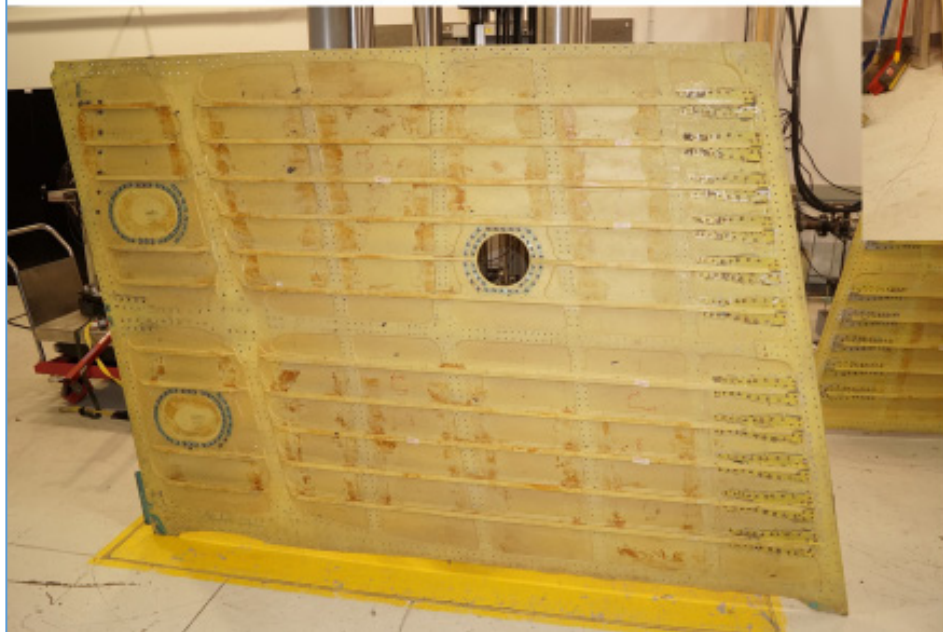


Figure B-10. Left upper torque box skin

Left Upper Torque Box Skin

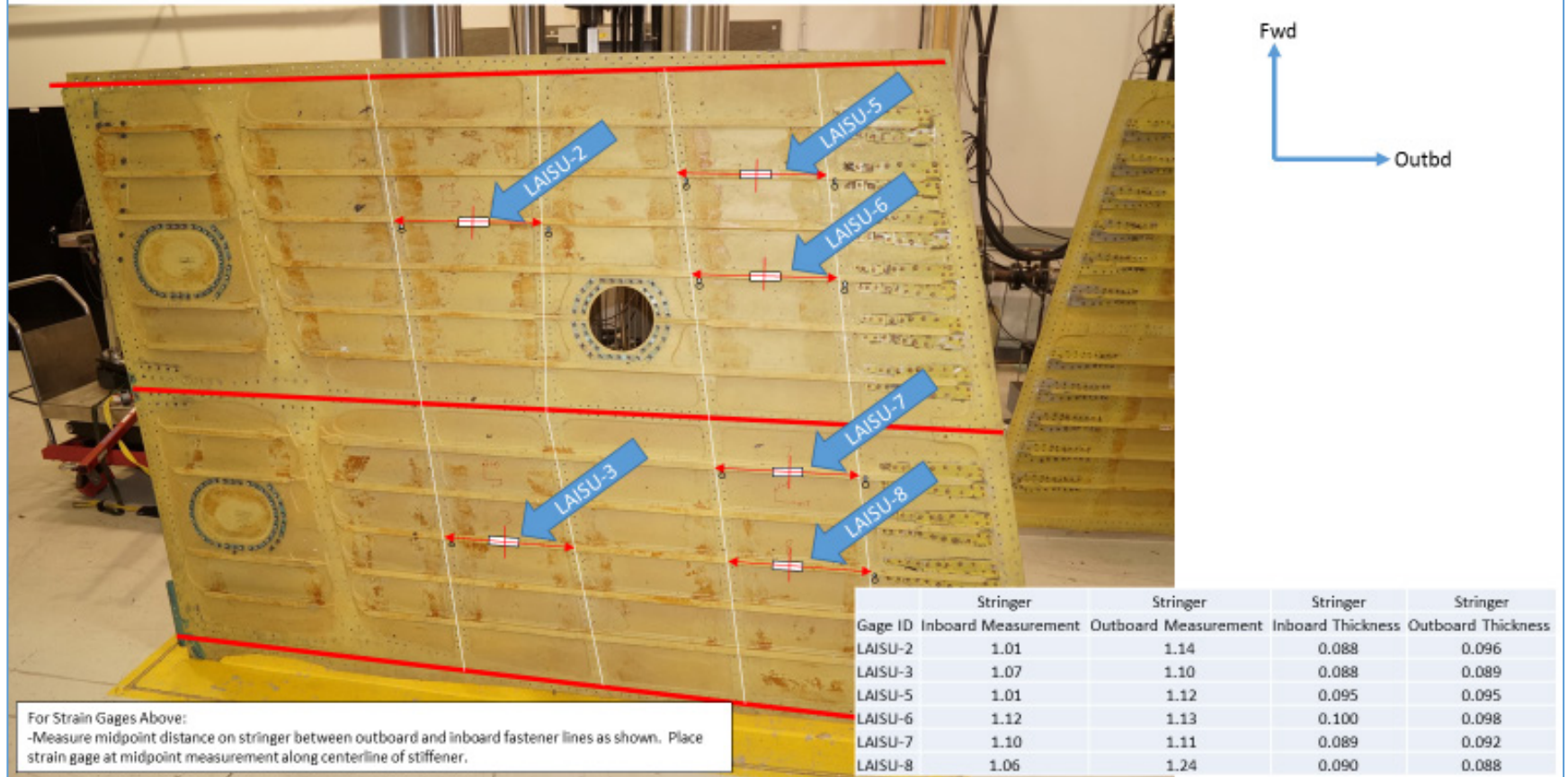


Figure B-11. Position of LAISU gages



Figure B-12. Close-up of LAISU skin



Figure B-12. Close-up of LAISU skin (continued)

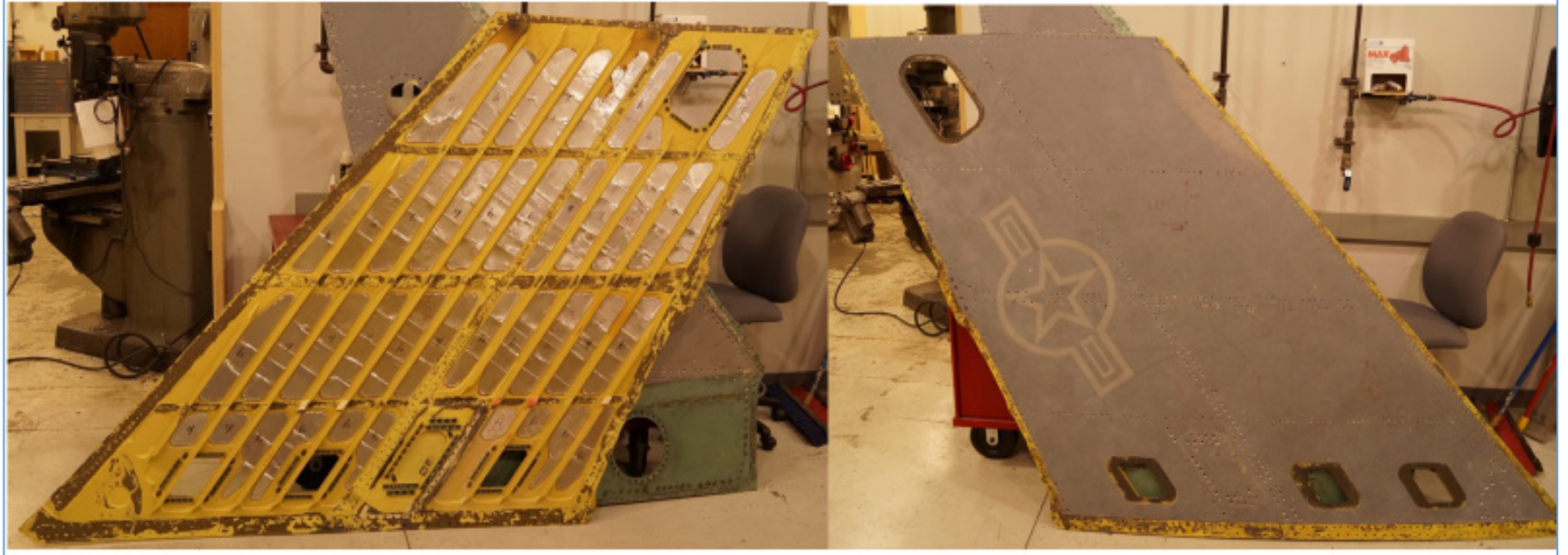


Figure B-13. Left upper outboard wing skin

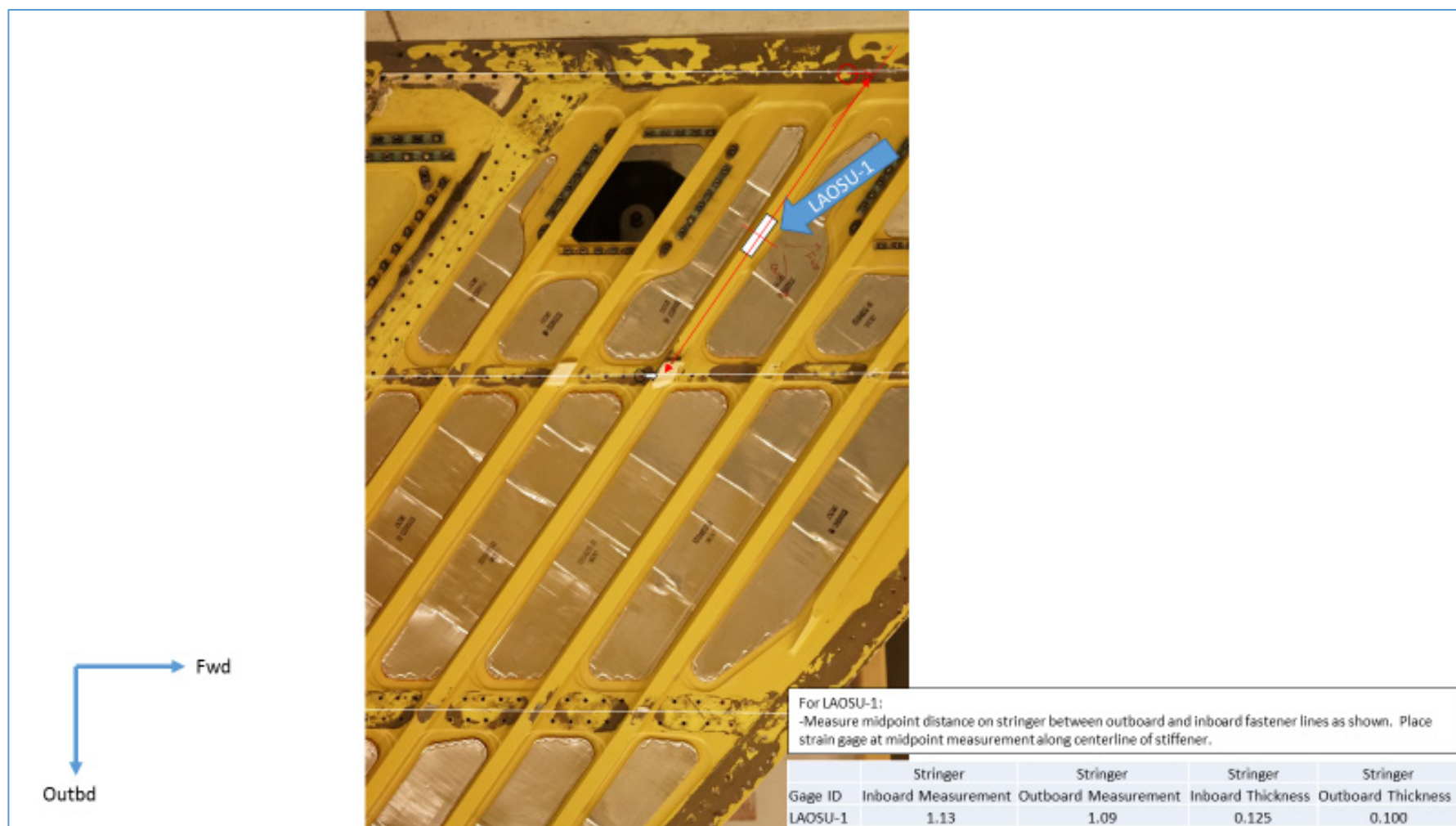


Figure B-14. Location of LAOSU-1



Figure B-15. Position of LAOSU gages

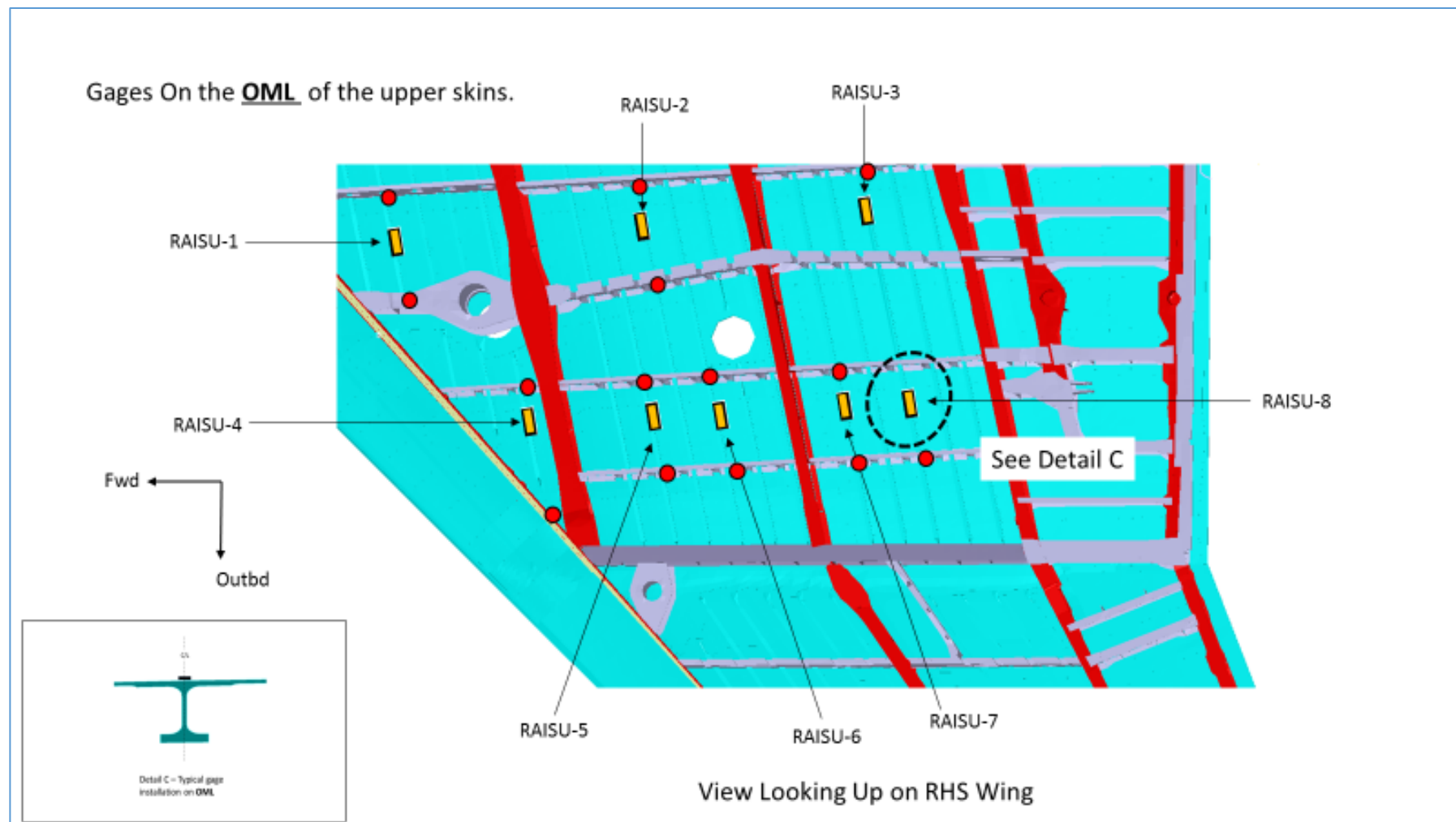


Figure B-16. Diagram of RAISU gages

Right Upper Forward Wing Skin



Figure B-17. Right upper forward wing skin

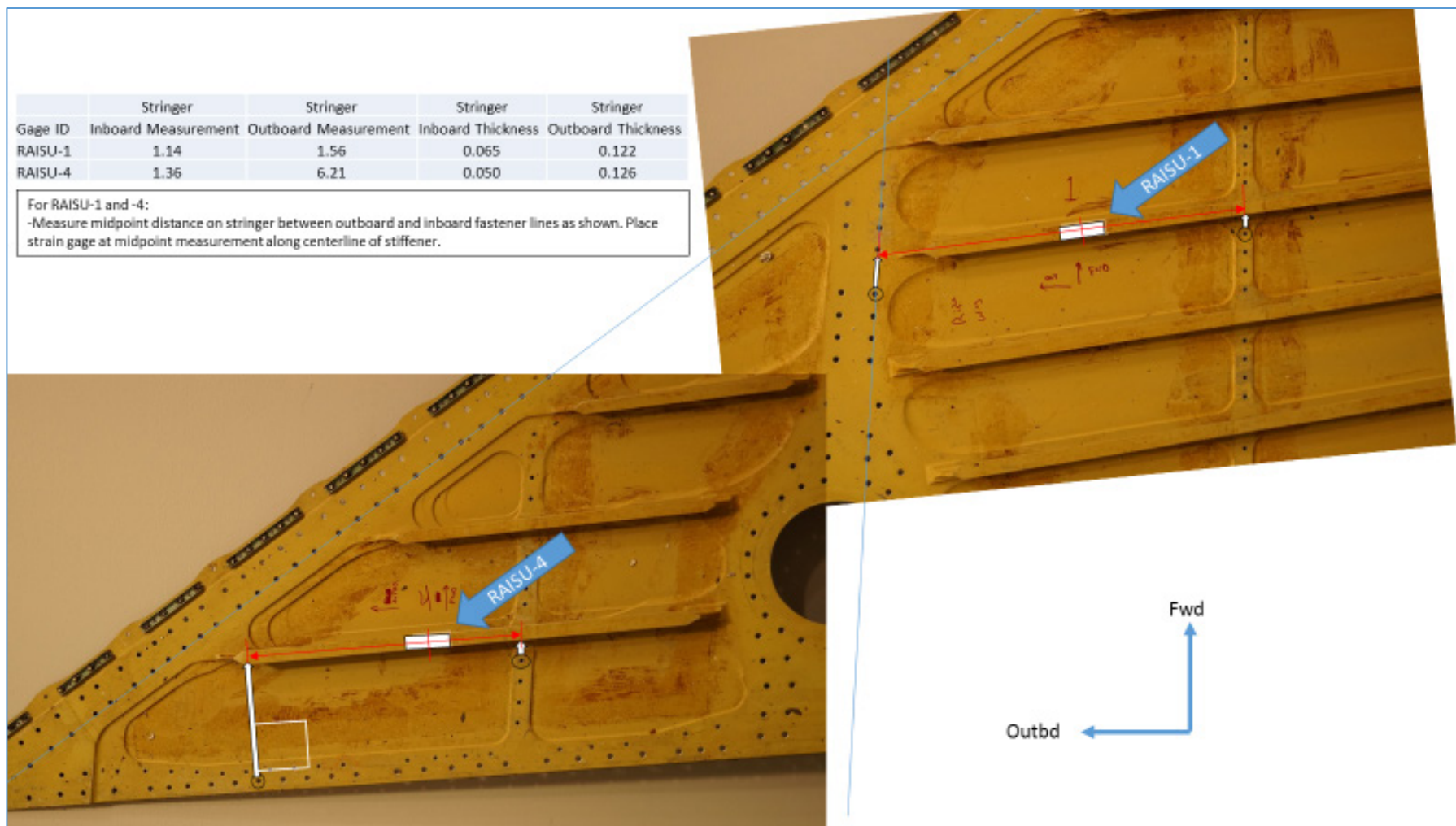


Figure B-18. Position of RAISU-1 and RAISU-4

Right Upper Torque Box Skin

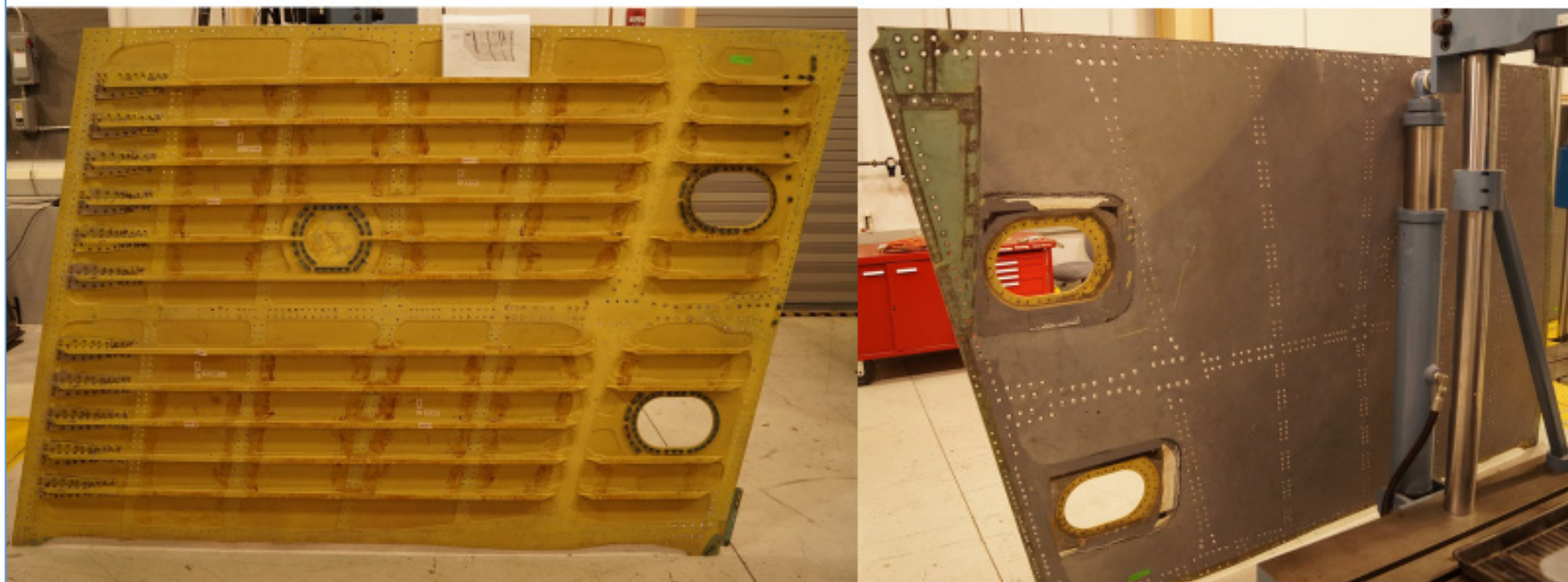


Figure B-19. Right upper torque box skin

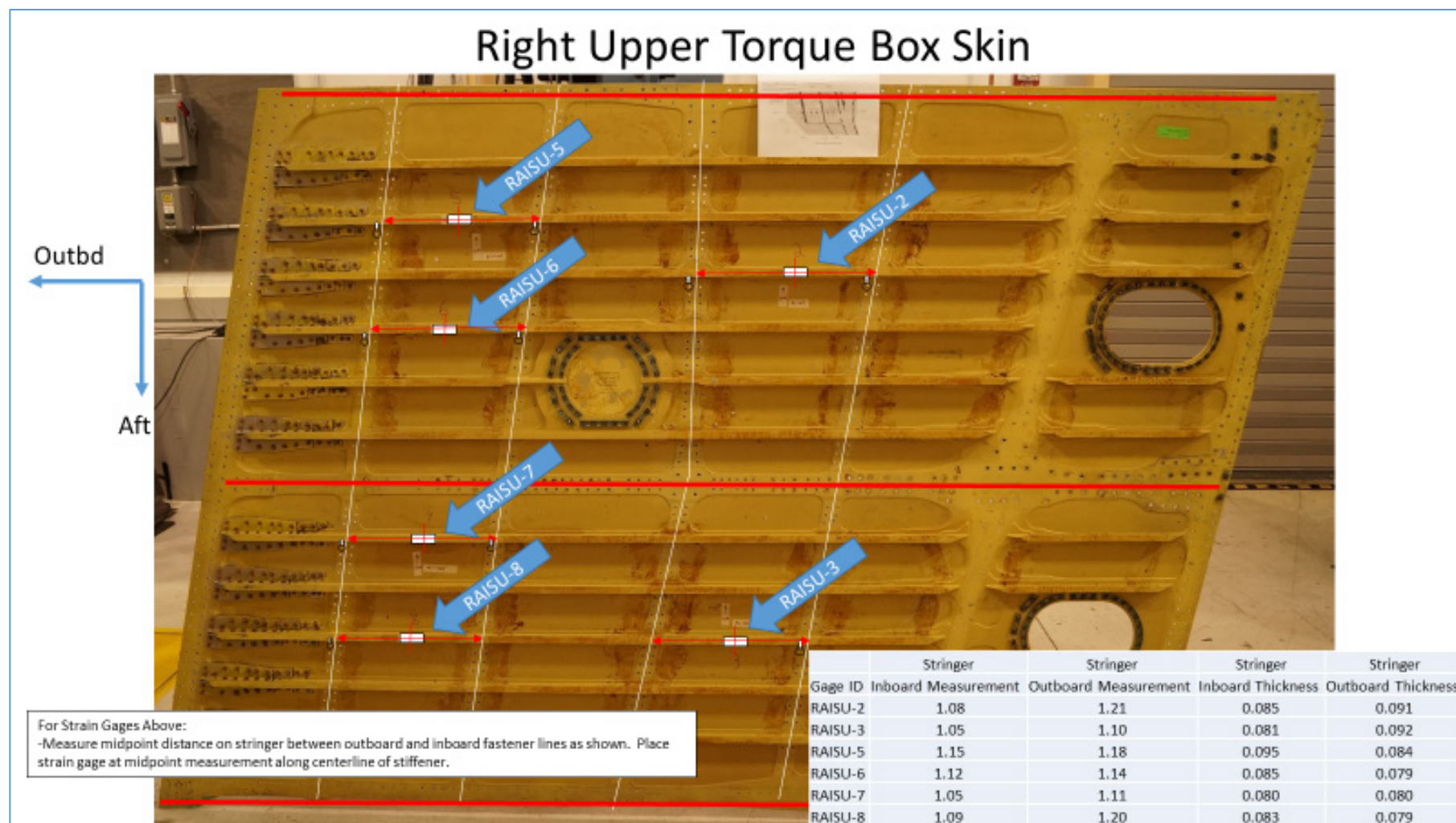


Figure B-20. Positions of RAISU gages



Figure B-21. Close-up of skins for RAISU gages

Gages On the OML of the upper skins.

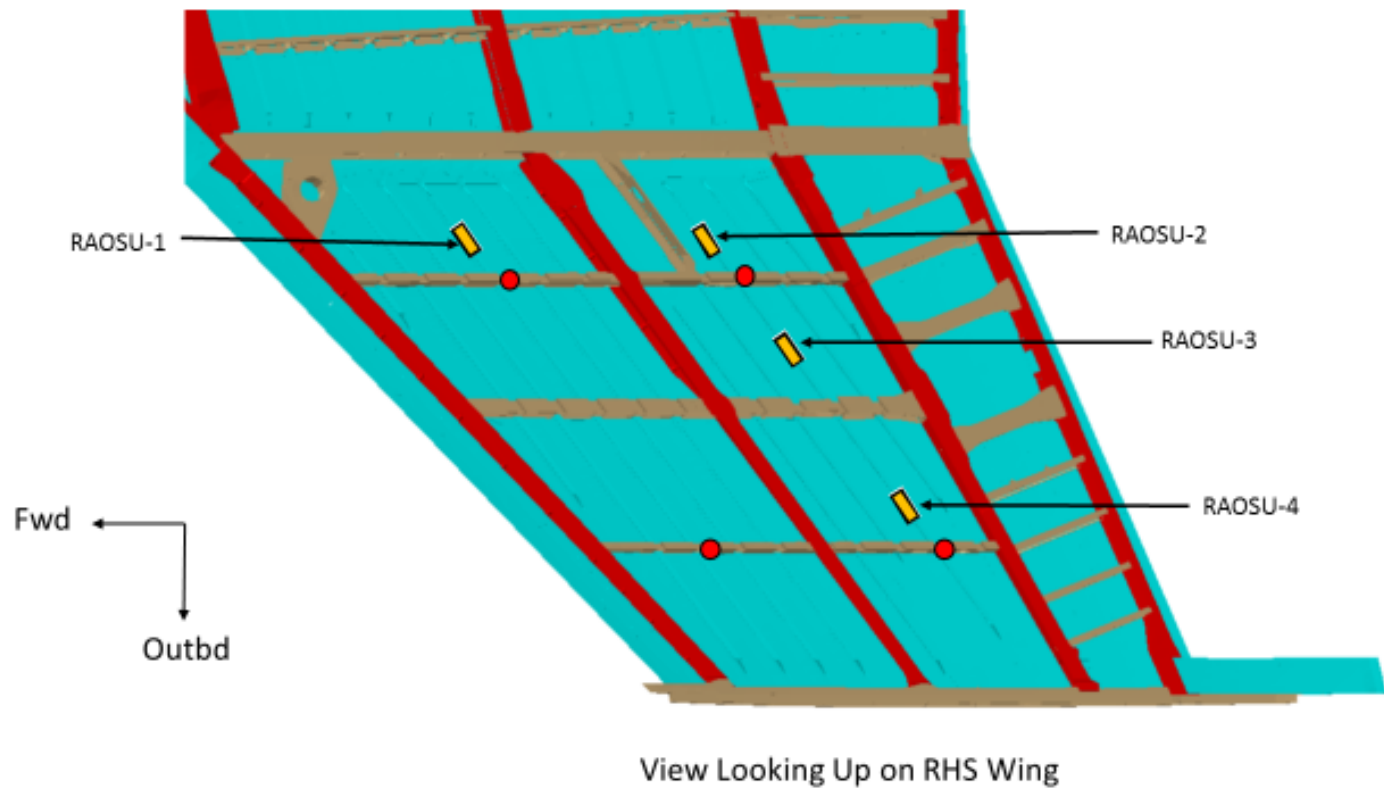


Figure B-22. Diagram of RAOSU gages



Figure B-23. Right upper outboard wing skin

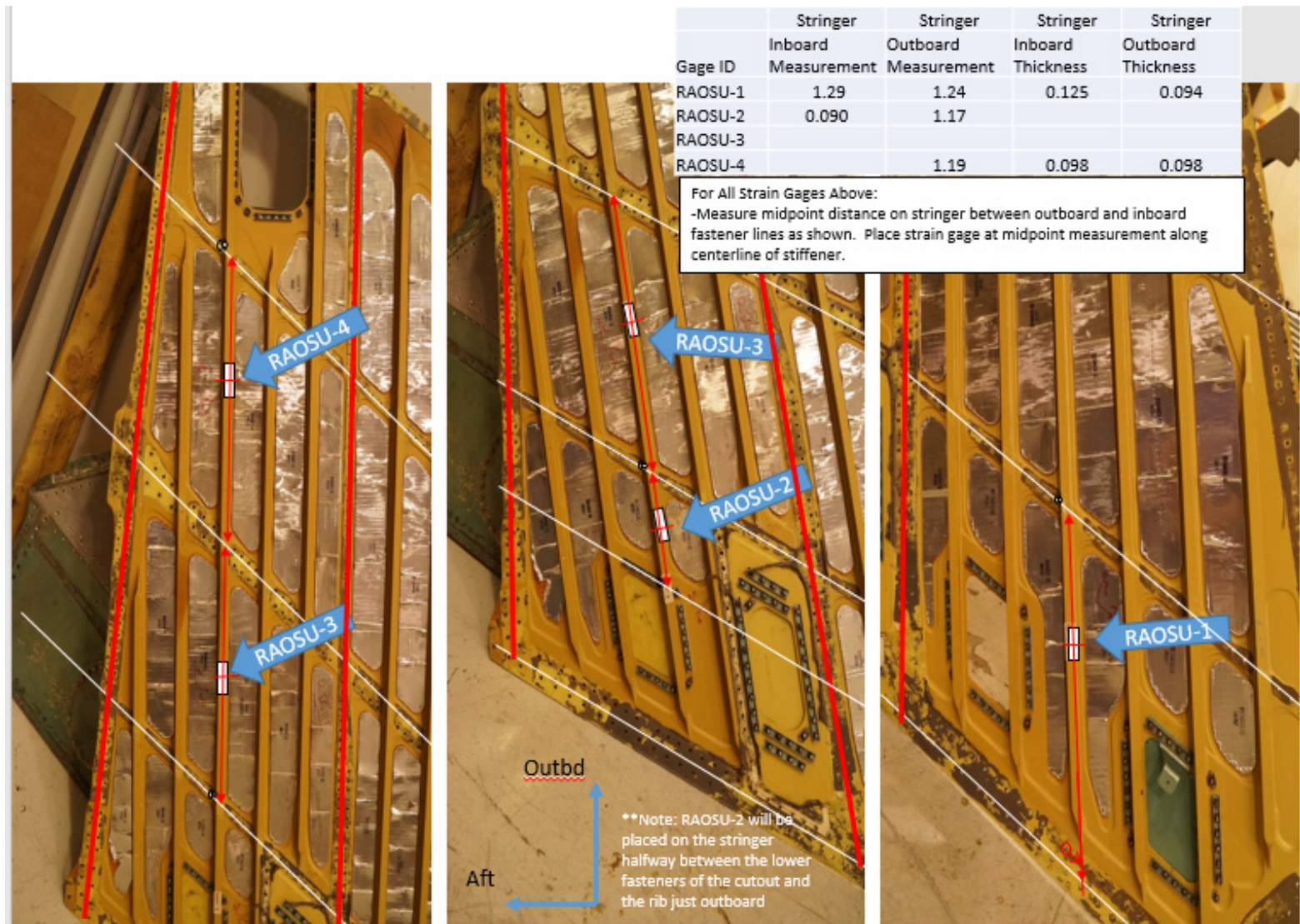


Figure B-24. Position of RAOSU gages

B.2 Lower Wing Skin Reference Photos

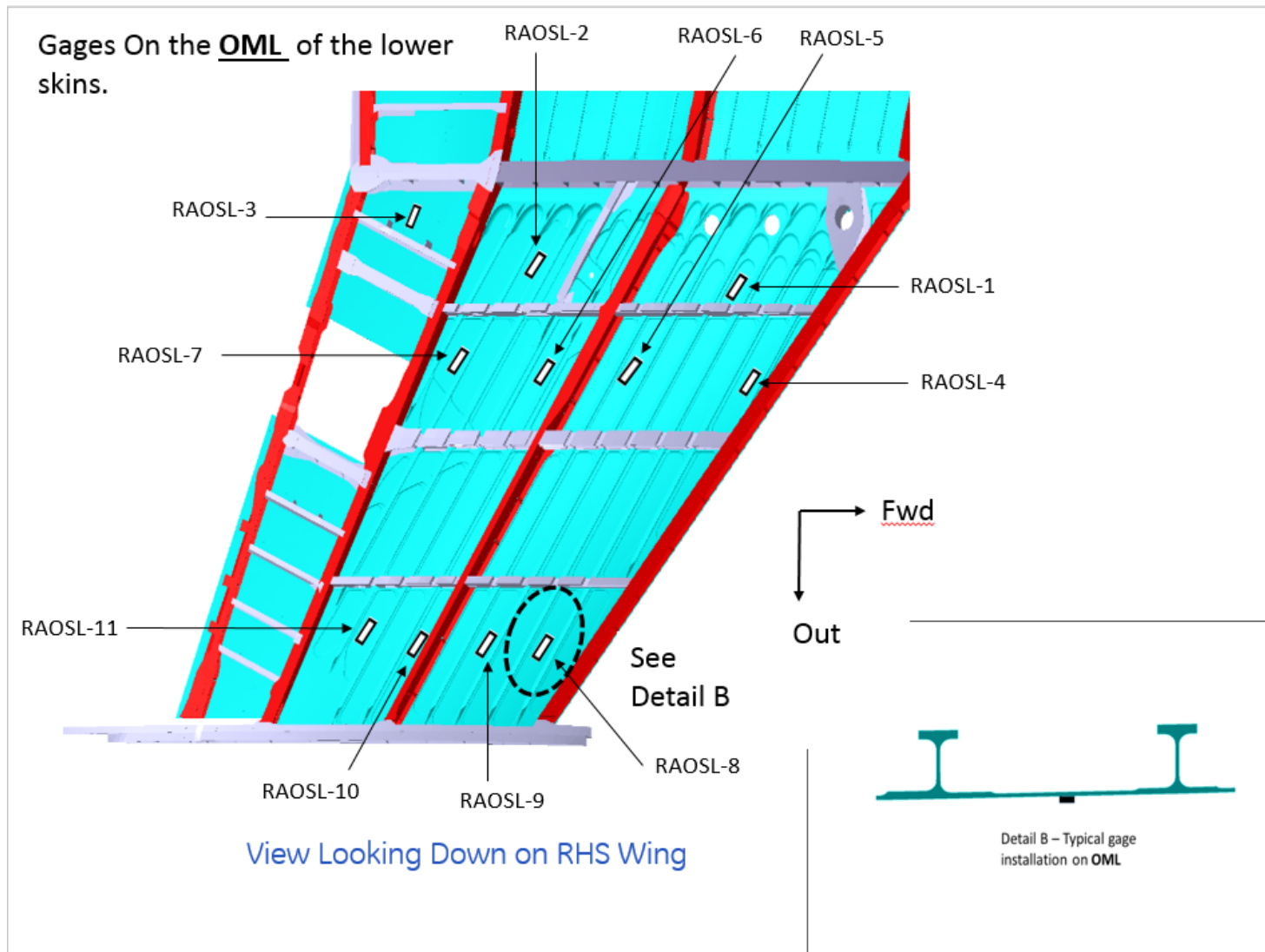


Figure B-25. Diagram of RAOSL gages

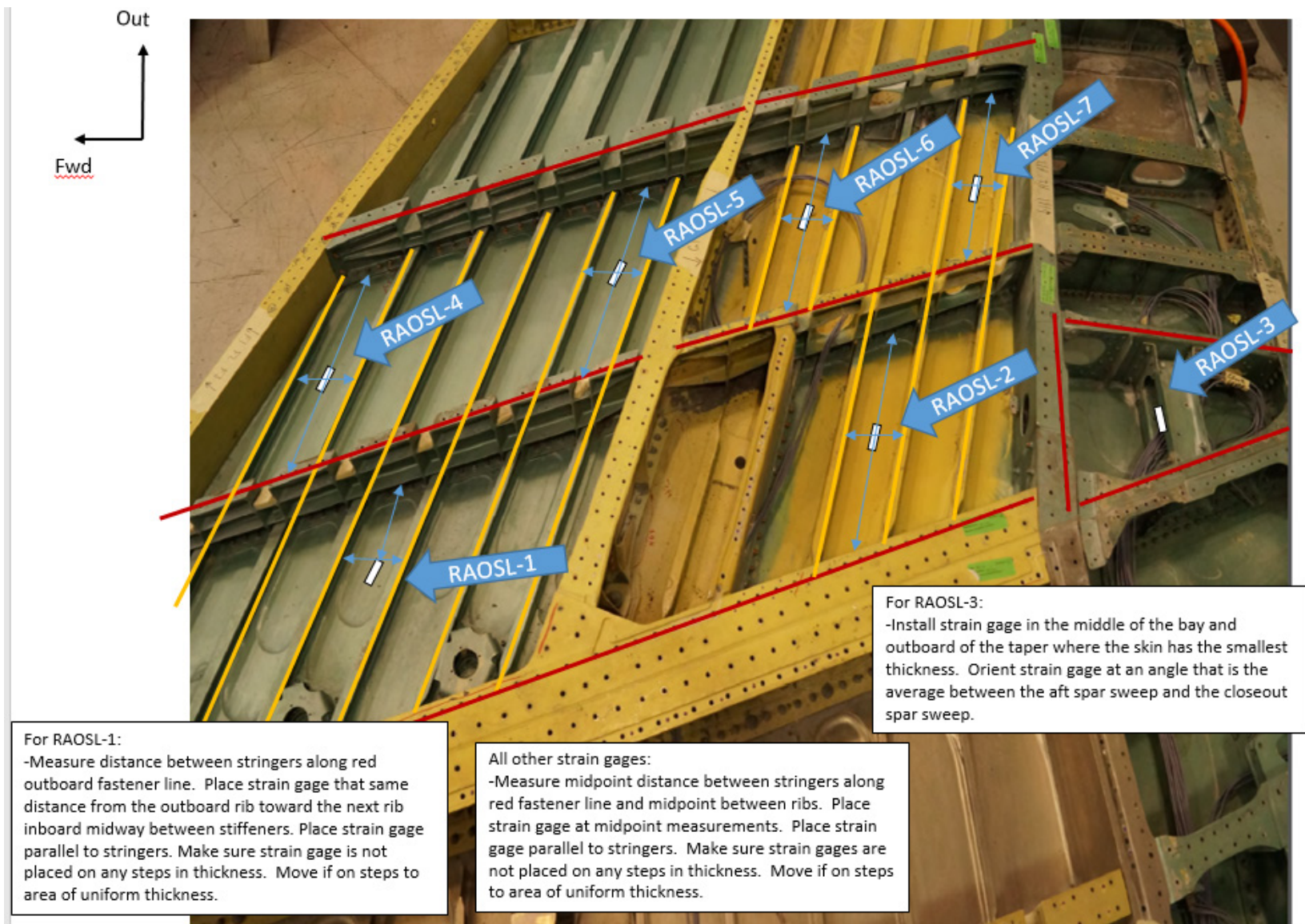


Figure B-26. Position of RAOSL-1 to RAOSL-7

For RAOSL-8 thru -11:
-Measure midpoint distance between stringers along red fastener line and midpoint between ribs. Place strain gage at midpoint measurements. Place strain gage parallel to stringers. Make sure strain gages are not placed on any steps in thickness. Move if on steps to area of uniform thickness.

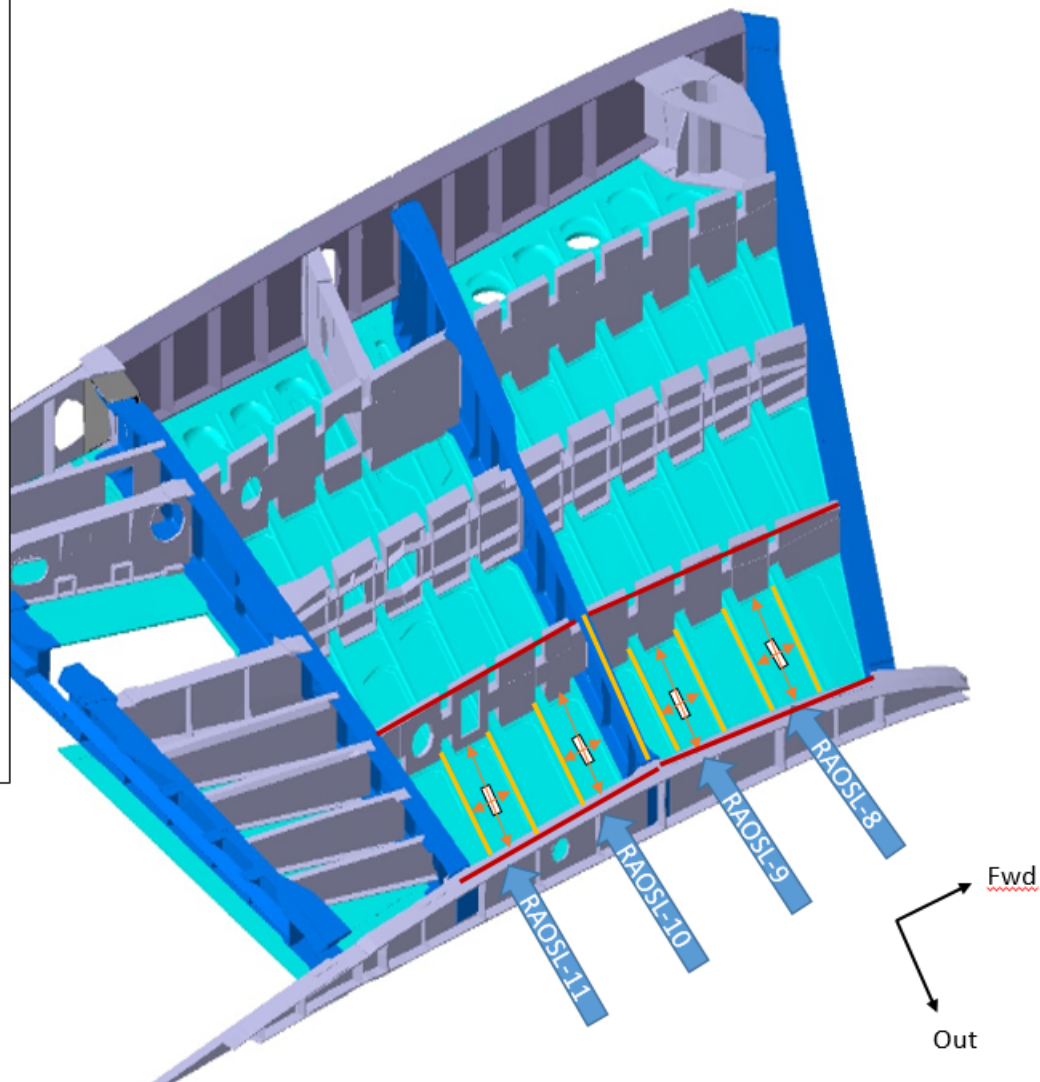


Figure B-27. Position of RAOSL-8 to RAOSL-11

Gages On the OML of the lower skins.

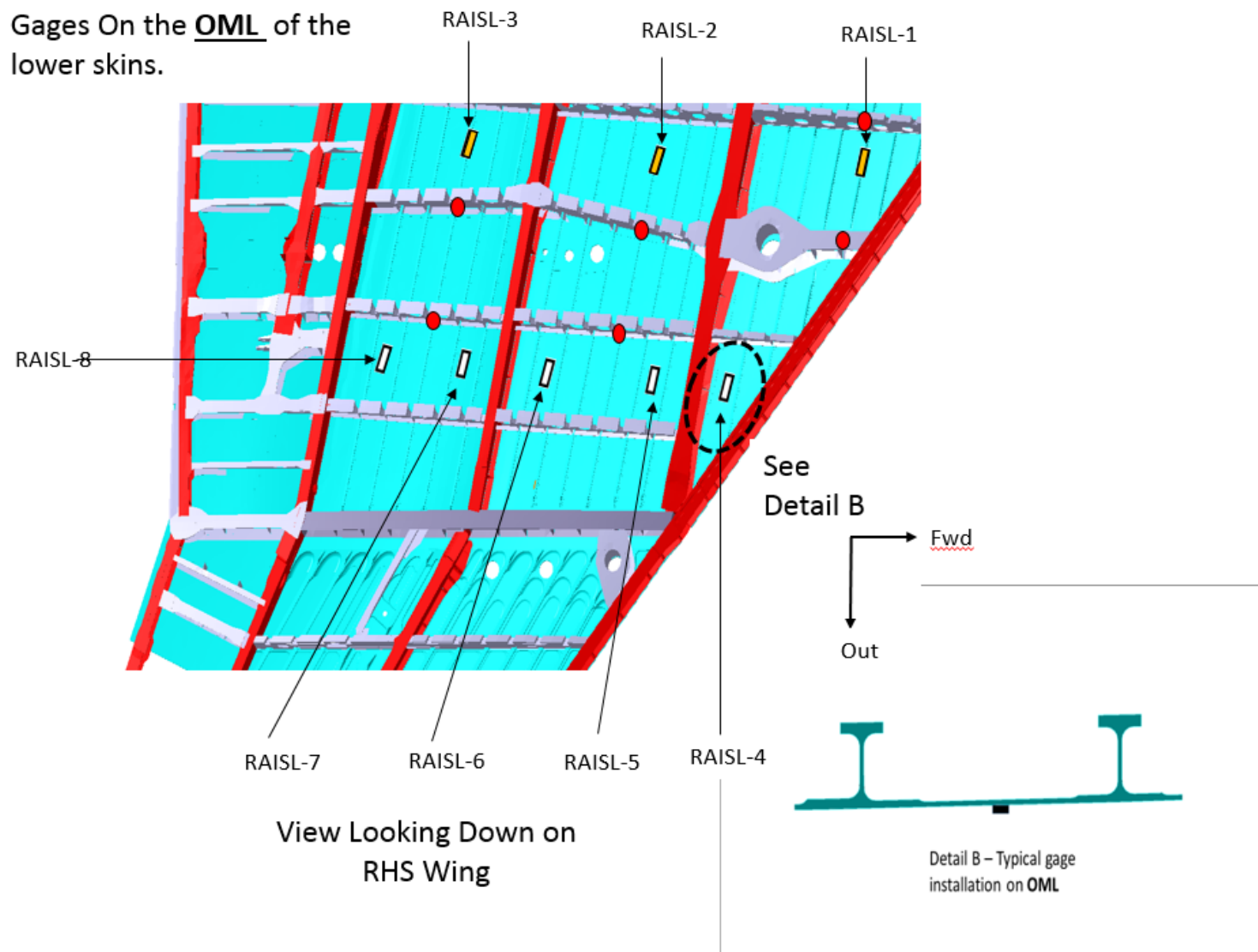
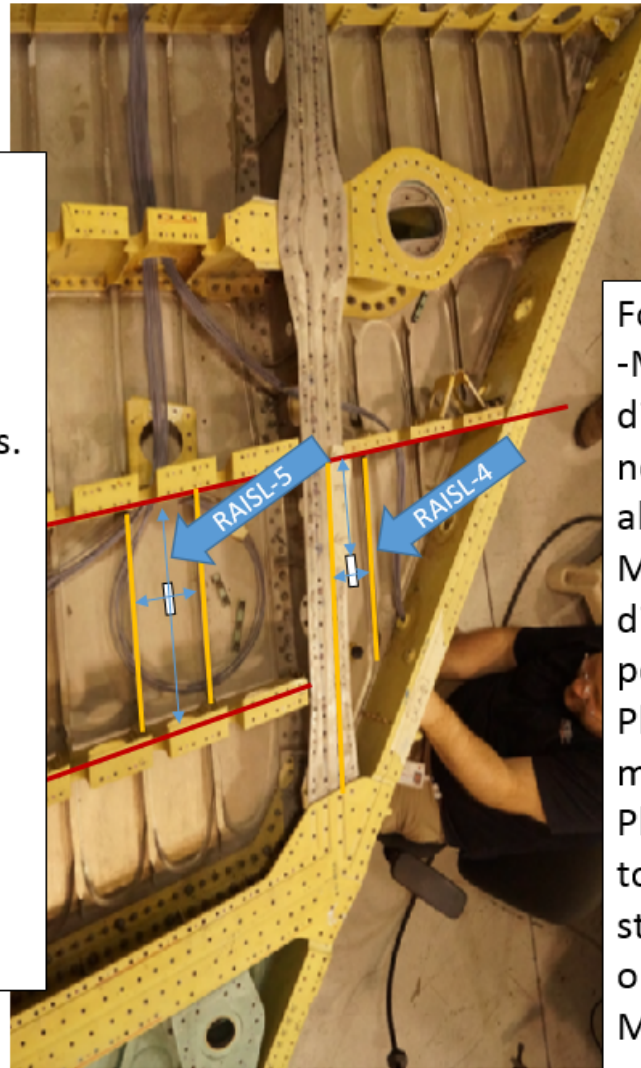


Figure B-28. Diagram of RAISL gages

For RAISL-5:

-Measure midpoint distance between stringers along red fastener line and midpoint between ribs. Place strain gage at midpoint measurements. Place strain gage parallel to stringers. Make sure strain gage is not placed on any steps in thickness. Move if on steps to area of uniform thickness.



For RAISL-4:

-Measure midpoint distance between spar and next forward stringer along red fastener. Measure midpoint distance between taper point and next inboard rib. Place strain gage at midpoint measurements. Place strain gage parallel to stringers. Make sure strain gage is not placed on any steps in thickness. Move if on steps to area of uniform thickness.

View Looking Down on RHS Wing

Figure B-29. Position of RAISL- 4 and RAISL-5

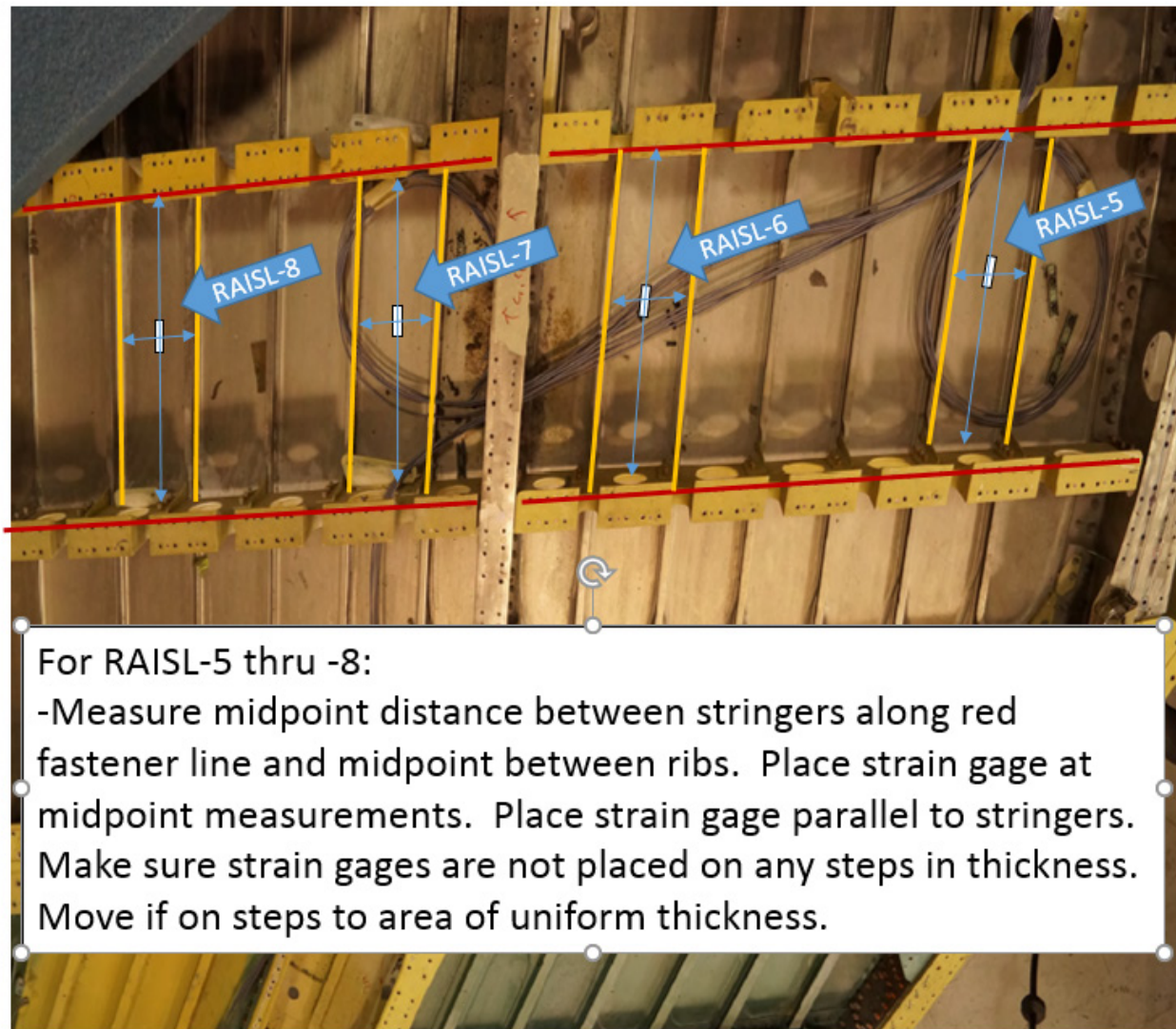


Figure B-30. Position of RAISL-5 to RAISL-8

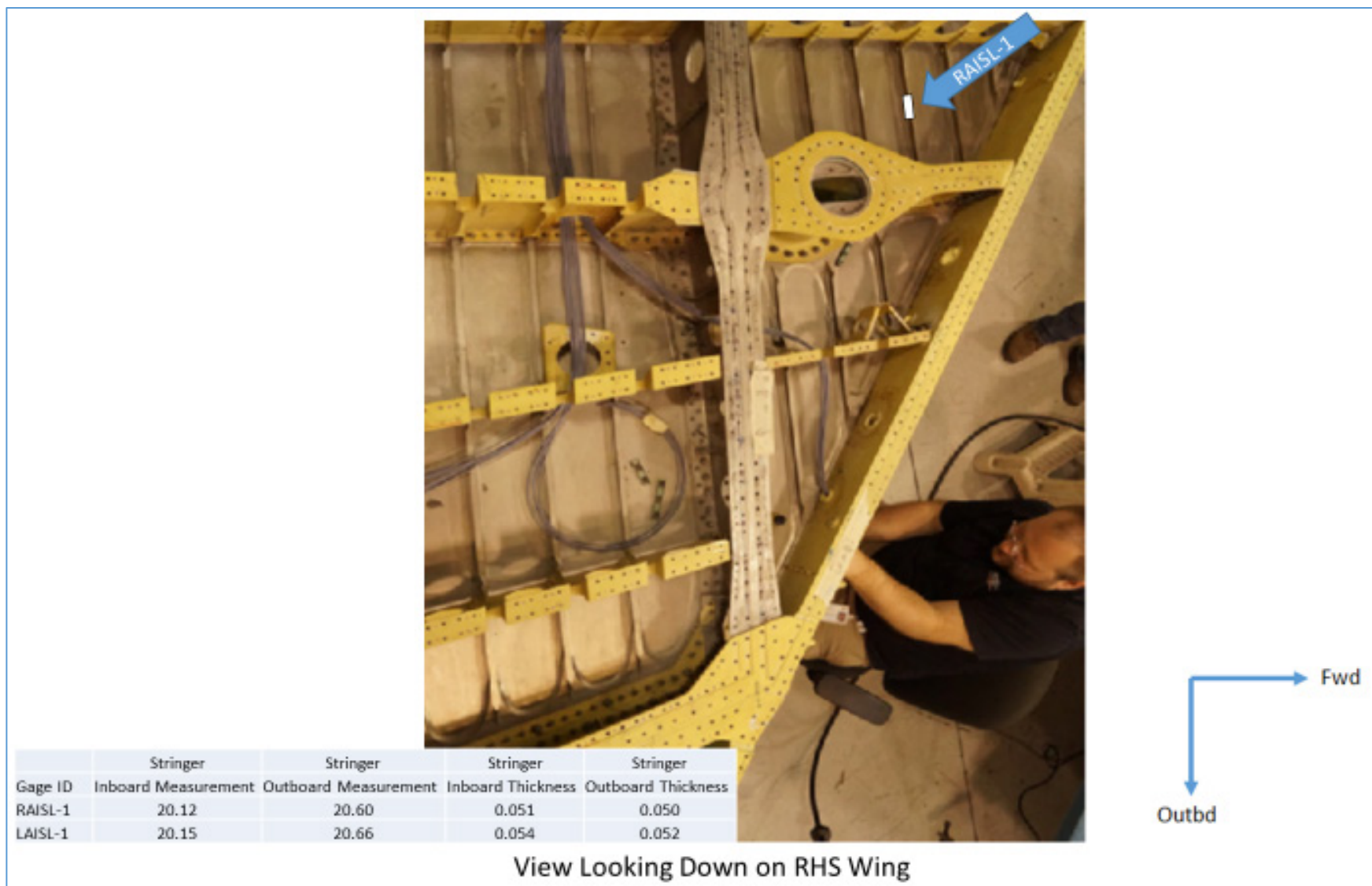


Figure B-31. Position of RAISL-1

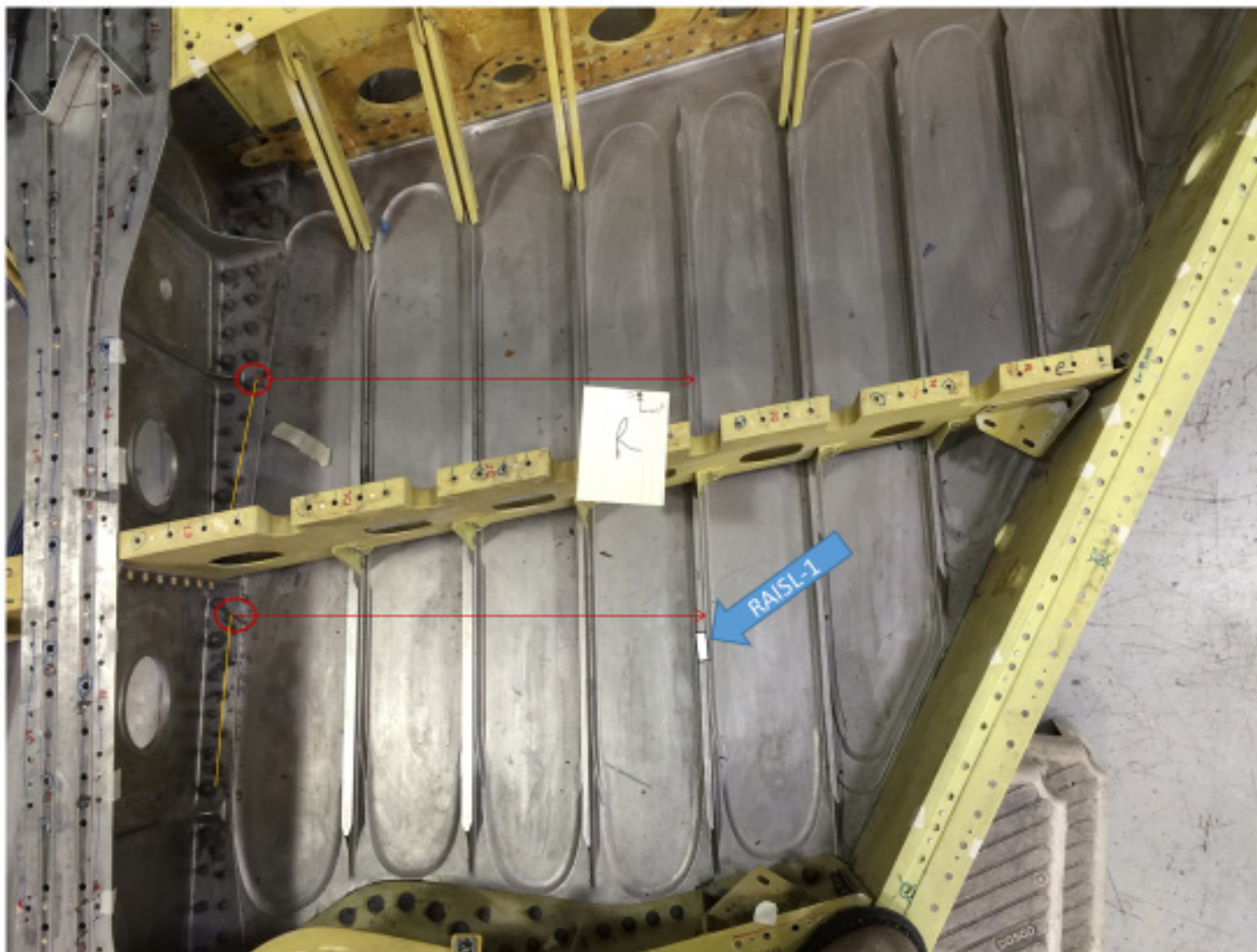


Figure B-32. Position of RAISL-1



Figure B-33. Position of LAISL-1

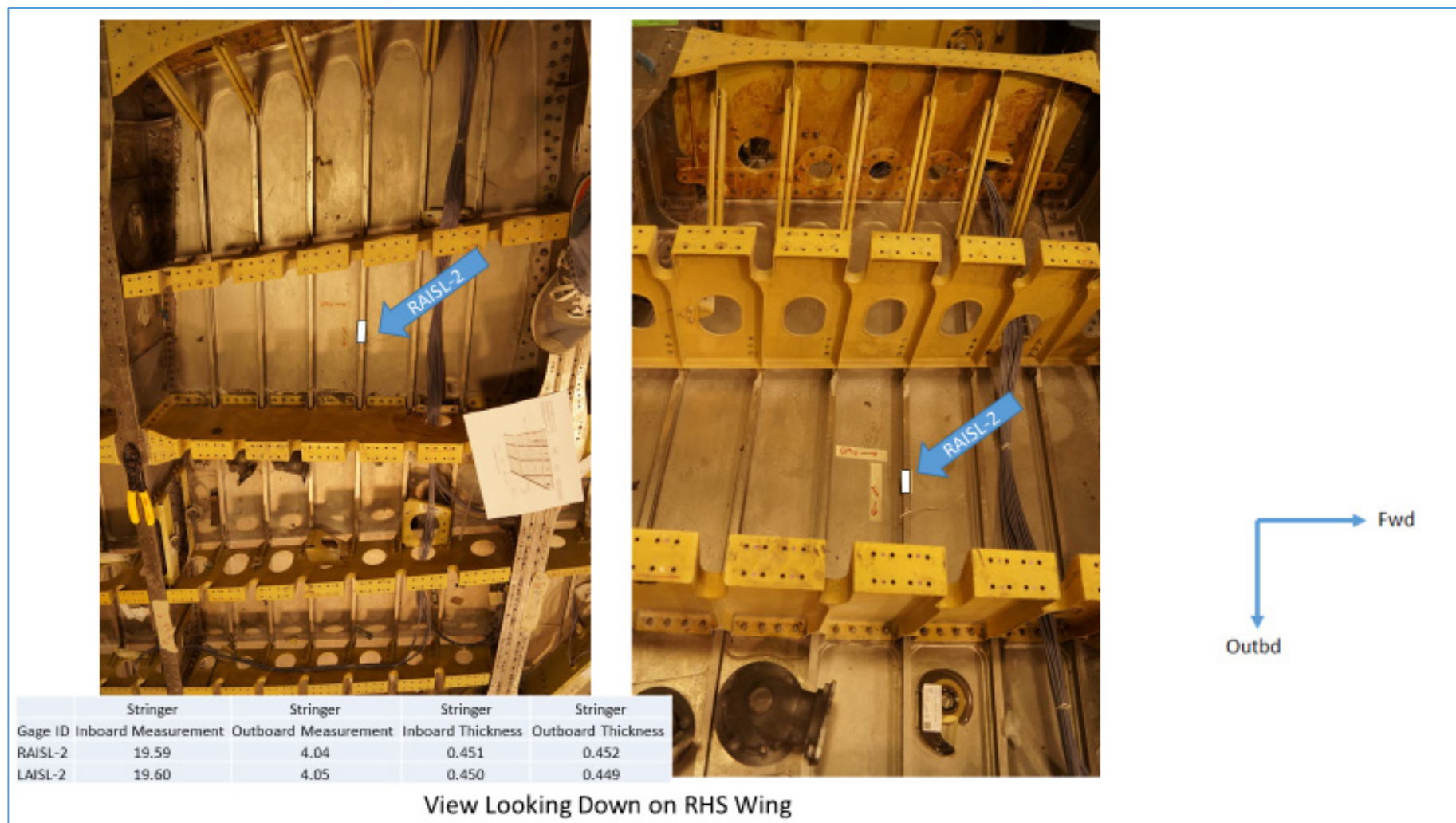


Figure B-34. Position of RAISL-2

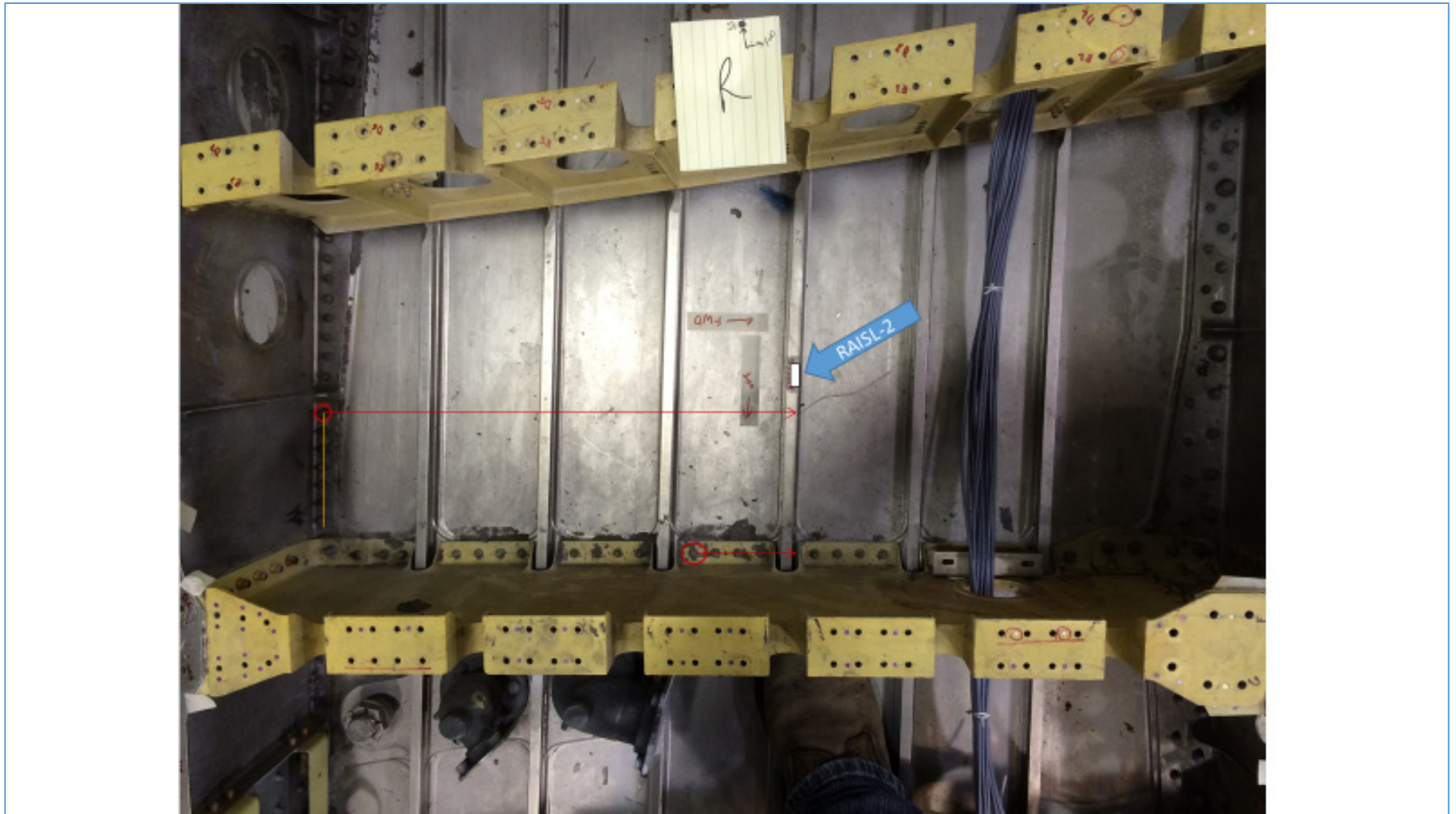


Figure B-35. Position of RAISL-2

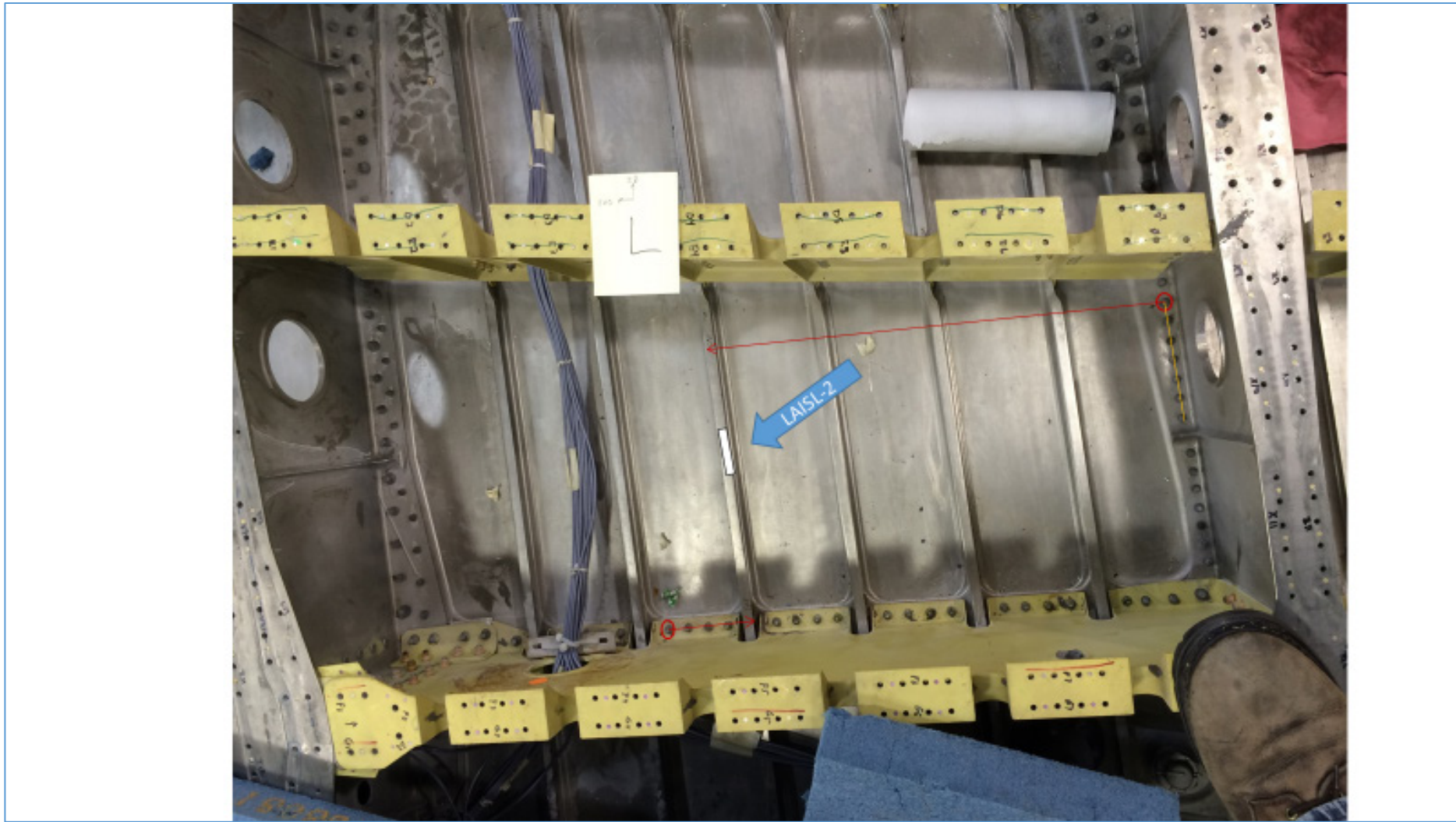
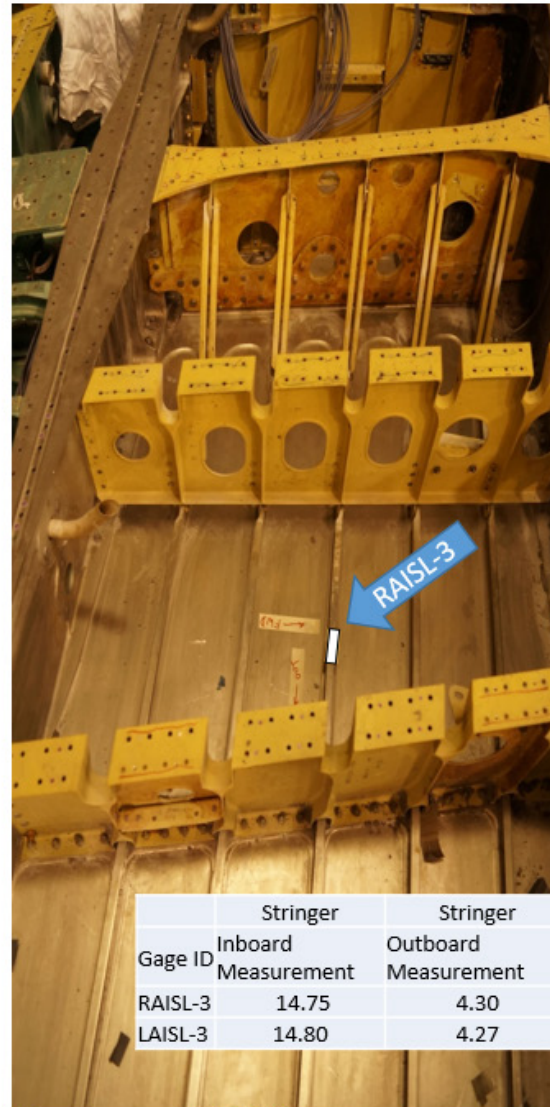


Figure B-36. Position of LAISL-2



	Stringer	Stringer	Stringer	Stringer
Gage ID	Inboard Measurement	Outboard Measurement	Inboard Thickness	Outboard Thickness
RAISL-3	14.75	4.30	0.450	0.451
LAISL-3	14.80	4.27	0.452	0.449

View Looking Down on RHS Wing

Figure B-37. Position of RAISL-3

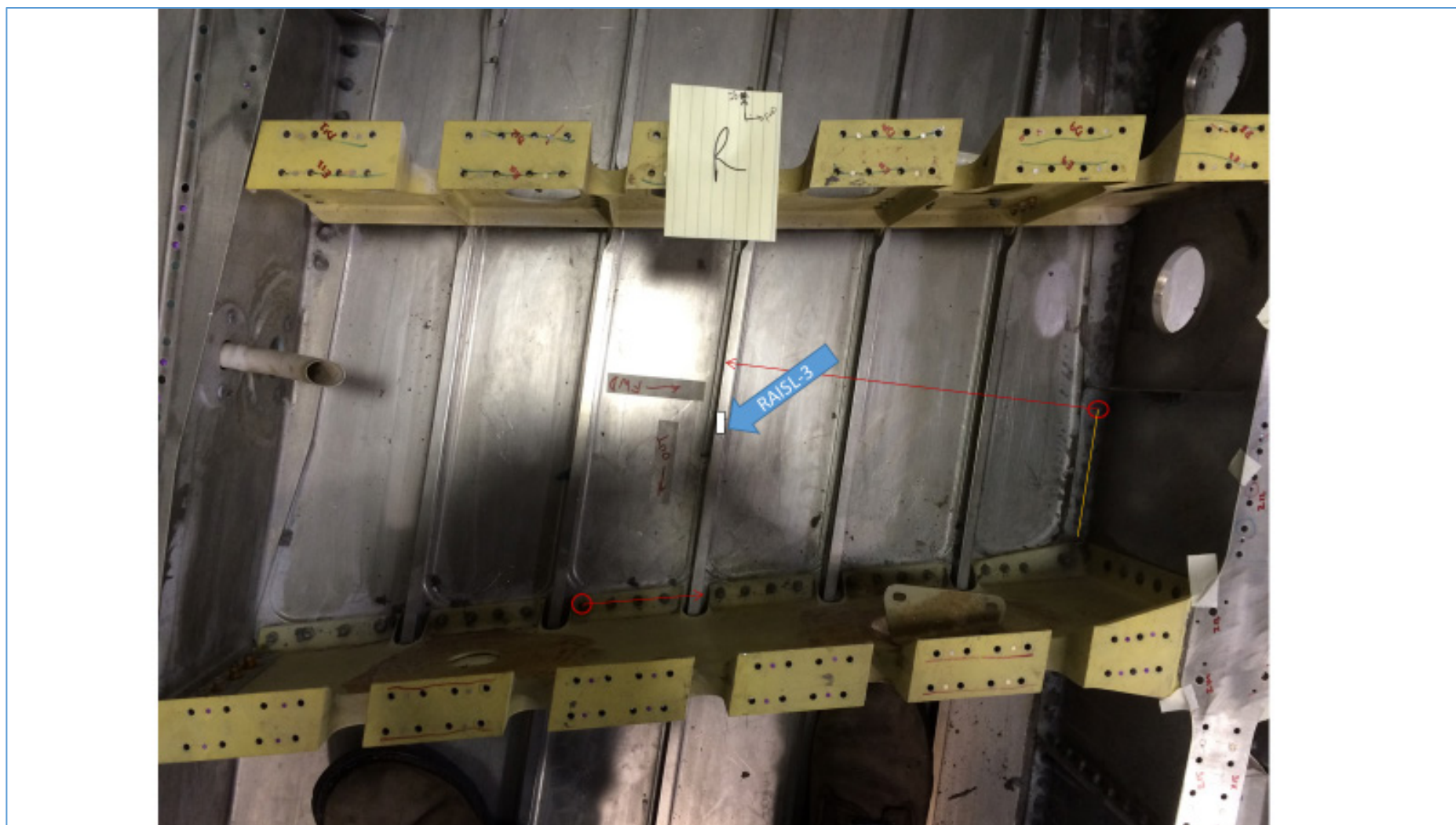


Figure B-38. Position of RAISL-3



Figure B-39. Position of LAISL-3

Notes:

- All measurements were from center of fastener
- Measurements were to the farthest side of the stiffener
- Yellow lines show which fasteners were used for establishing perpendicularity (Yellow lines are all perpendicular to red lines)
- Stiffener thicknesses given are hat width or web thickness as appropriate to find c/l of stiffener

Figure B-40. Notes on gage position locations



Far Field View Of GE05 Crack Gage Location On Right Hand Wing Lower Skin OML

Close-up View of GE05 Crack Gage Location On Right Hand Wing Lower Skin OML

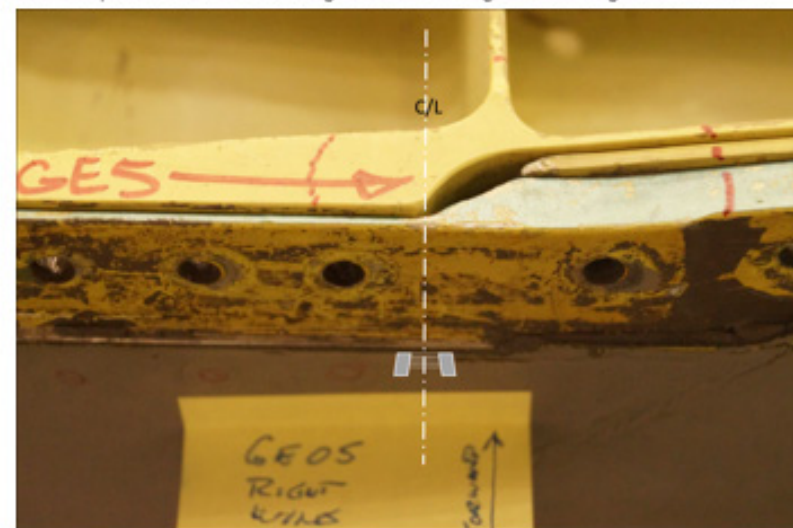


Figure B-41. Close up view of GE05 crack gage location

Appendix C – Inspection Plan Details

DESCRIPTION:

As part of the Digital Twin Spiral 1 initiative, an inspection plan was developed for nondestructive inspection (NDI) of ten (10) control point (CP) locations, tracked for fatigue crack growth during the fatigue experiments performed on two (2) outer wings. These CPs were selected partly to ensure inspectability, i.e. enable inspection without any disassembly or interference during the fatigue test.

Both, phased array ultrasonic testing (PAUT) and surface eddy current testing (SEC) will be employed to perform this inspection task. Additionally, crack gages are placed to assess and detect cracks occurring at CPs otherwise inaccessible or difficult to access for NDI. SEC is a well-established approach to detect surface-breaking or near surface cracks, however, the technique has significant penetration depth limitations. PAUT is an advanced NDI approach, not yet incorporated for aerospace applications, providing the means to detect smaller cracks prior to the cracks reaching the top surface and/or the critical crack length c_{crit} .

PURPOSE:

This inspection plan entails the procedure to detect cracking at selected CP locations in the outer wing structures using a phased array ultrasonic testing (PAUT) approach, as well as Surface Eddy current Testing (SEC) following the recommended procedures for these locations.

The CP selection process was performed by our contractor team led by General Electric Global Research (GE-GRG). Control Points are designated with GE+number. Table 1 provides an overview over all CPs and the inspection approach to be performed for each CP. A total of six (6) CPs can be inspected using the PAUT method, all accessible from the outside, without disassembly, at the lower wing. SEC will be used for all CPs. Crack gages will be used for two (2) CPs.

Table C-1: Control Point Overview

CP Number	Outer Wing CP Location	CP Flaw Details	NDI
GE01 (Figure 1)	Wing Skin, Lower, Forward, Fastener Hole at XW206 Rib	Single corner crack at fastener hole (crack at faying surface).	PAUT, SEC
GE02 (Figure 2)	Wing Skin, Lower Trailing Edge, at Aft Closure Spar at	Interior surface crack in fillet radius at thickness step.	SEC, crack gages
GE03 (Figure 3)	Wing Skin, Lower Trailing Edge, Fastener Hole at XW158	Single corner crack at fastener hole (crack at faying surface).	PAUT, SEC
GE04 (Figure 4)	Lower Trailing Edge Wing Skin, Fastener Hole at Rear Spar	Single corner crack at fastener hole (crack at faying surface).	SEC
GE05 (Figure 5)	Lower Wing Skin, Forward Edge Thickness Step at XW156	Corner crack in radius	SEC, crack gages
GE06 (Figure 6)	Lower Wing Skin, Fastener Hole, XW188 Rib	Single corner crack at fastener hole (crack at faying surface).	PAUT, SEC
GE07 (Figure 7)	Lower Forward Wing Skin, Fastener Hole at Front Spar	Single corner crack at fastener hole (crack at faying surface).	PAUT, SEC
GE08 (Figure 8)	Lower Wing Skin, fastener hole at XW162 (under aft spar)	Single corner crack at fastener hole (crack at faying surface).	PAUT, SEC
GE09	GE09 removed from CP list		
GE10 (Figure 9)	Lower Aft Wing Skin, Fastener Hole at XW164 (under main spar)	Single corner crack at fastener hole (crack at faying surface).	PAUT, SEC

INSPECTION CRITICALITY:

The PAUT and SEC inspections are not considered routine maintenance. They are specifically developed and employed for inspecting the CPs during the full scale fatigue test without disassembly.

PERSONNEL REQUIREMENTS:

Personnel conducting NDI examinations or performing data analysis must be qualified as follows:

1. At a minimum, Level II certified in ultrasonic testing (UT) and eddy current testing (ET) in accordance with NAS 410.
2. Trained in the procedure specifics, and equipment utilized, by an AFRL NDI Program Manager approved instructor.

EQUIPMENT AND MATERIALS:**PAUT:**

1. Phased Array System: OEMPA 128/128 from AOS (Advanced OEM Solutions) (Figure 10), including laptop with TPACquisition software (TPAC: The Phased Array Company).
2. Olympus PAUT probe: P/N 10L32A10 – 10 MHz, 32 elements, 0.67 by 1.16 inch footprint, 0.0122 inch pitch (Figure 11).
3. Wedges to enable shear wave inspection, 25° and 45°, respectively (Figure 12).
4. Couplant for ultrasonic testing.

5. Precision screw driver.

SEC:

6. Nortec 2000D+ eddy current instrument
7. Surface Probe, 50 kHz to 500 kHz, Right Angle Shaft, 0.50 inch Drop, 6 inch length (P/N MTF905-60) including cable

GENERAL:

8. Crack reference standard set simulating CP structures (Figure 13).
9. Machinist scale.
10. Approved aircraft marker.

FACILITY REQUIREMENTS:

The facility will require, as a minimum, the following:

1. 110 VAC service.
2. Lighting - Sufficient illumination of work area.
3. A moveable table to place the PAUT system; enabling reaching the inspection side with the probe.

PREPARATION OF AIRCRAFT:

1. Access to the CPs need to be established throughout the duration of the fatigue test.
2. During PAUT inspection the probe wedge will be partly positioned over the fastener heads and/or wing structure edges at the various CP locations. To ensure optimal ultrasonic coupling between the probe and the target aircraft structure, the fastener heads and sealant out of plane at the structure edges need to be milled down, flush with the surrounding wing skin material, if necessary.

PAUT INSPECTION SYSTEM SET-UP:

1. The OEMPA 128/128 PAUT system, as shown in Figure 10, consists of
 - a laptop with the TPACquisition software installed. The computer needs to fulfill the following minimum requirements: Windows 7 64-Bit, 16GB RAM, intel core i7, NVIDIA Graphics Card Nvidia® Quadro® K1100M w/2GB GDDR5, and
 - the OEMPA 128/128 (both 128 pulse and receive channels)
2. Both instruments need to be connected to a 110 VAC service power source. The OEMPA 128/128 and the laptop are connected with both a LAN connector and an USB 3.0 connector.

3. The probe connects to the OEMPA 128/128 as well. It is compatible to the regular LPA 32 probe adapter from Olympus, however, the probe adapter needs to have the optional anchor base included.
4. The inspection requires the use of wedges. Two wedges are available, 25° and 45°, respectively. Depending on the CP to be inspected, connect the correct wedge to the probe. Table 2 lists, which wedge is to be used for each CP. The wedges are connected to the probe via two screws, which are part of the probe. Probe and wedge need to be connected as shown in Figures 11 and 13. (An 180° opposite connection is possible, but not acceptable.)
5. To start the system, power up both the laptop and the OEMPA 128/128 and select the TPACquisition shortcut, visible on the desktop screen.



6. The software first asks, whether a Hardware (HW) calibration shall be performed. Temporarily remove probe and press 'Yes' (Figure 14). Reconnect probe.
7. After successful calibration, the next screen will then either be the 'Settings' screen (Figure 15) or the last 'Data Acquisition' screen, as shown exemplarily in Figure 16. If the latter is the case, press the 'Settings' button as indicated in Figure 16.
8. In the 'Settings' screen, load the settings file with the required settings for inspection of each CP, respectively, as indicated in Figure 15.
9. Table 2 lists the prepared 'Settings' files for calibration and inspection for each CP.

Table C-2: 'Settings' files to be used for each CP / wedge to be used for each CP

CP Number	Settings file name	Wedge
GE01	GECP01.txt	45°
GE03	GECP03.txt	25°
GE06	GECP06.txt	25°
GE07	GECP07.txt	25°
GE08	GECP08.txt	45°
GE10	GECP10.txt	25°

10. After loading the prepared settings, go to 'Data Acquisition' screen by pressing the 'Back' button on the 'Settings' screen, as indicated in Figure 15.
11. In the 'Data Acquisition' screen, change settings for the gain to 22dB and the range to 5.0 inches, as shown in Figure 16, using the up/down arrows as indicated.
12. The 'Data Acquisition' screen shows both a Sector-scan over the pre-set angle range and A-scan for one selectable angle. The A-scan can be selected using the respective up/down arrows (Figure 16).
13. The system is now ready to perform either reference measurements or on-aircraft inspection for the selected CP.

PAUT REFERENCE MEASUREMENTS:

1. Select the crack reference standards matching the CP to be inspected. Two (2) crack reference standards are available for each CP:
 - The standards are two (2) layer coupons.
 - The top layer matches material and thickness of the CP structure.
 - The fastener connecting the two layers matches the exact specifications of the fastener used at the respective CP aircraft structure.
 - One coupon for each CP includes a long crack (approx. 0.150 inch), the other a short crack (approx. 0.050 inch). The long crack can be visually seen. The short crack, emanating from the faying surface, cannot be visually seen.
 - The coupons have a designation on one side on the top layer, as shown in Figure 13. The designation entails the CP number and whether this coupon entails the long crack (-LC) or short crack (-SC).
2. Table 3 lists all available coupons.

Table C-3: List of Reference Standards / Coupons

CP Number	Designation on Coupon	
	Long Crack	Short Crack
GE01	CP-01-LC	CP-01-SC
GE03	CP-03-LC	CP-03-SC
GE06	CP-06-LC	CP-06-SC
GE07	CP-07-LC	CP-07-SC
GE08	CP-08-LC	CP-08-SC
GE10	CP-10-LC	CP-10-SC

3. Select coupon with designation LC for the CP to be inspected.
4. Apply couplant and position transducer 0.200 inch from fastener and aim at fastener 90° to crack orientation. Aim means pointing the front of the wedge in the desired direction.
5. Move transducer towards fastener hole until reflection maximizes as shown in Figure 17.
6. Move probe exactly perpendicular to initial movement along the crack orientation without changing the distance between transducer and target. The crack signal should look similar to Figure 18. Note that the fastener hole signal is not occurring at this position.
7. Move the probe in the exact opposite direction (side of hole opposite crack) and verify that no crack signal occurs.

8. Perform the same signal verification by selecting the coupon with designation SC for the CP to be inspected. The signal should look similar to Figure 19. Note that the fastener hole signal and the crack signal occur simultaneously at this position.
9. Reference measurements shall be performed as follows:
 - Immediately prior to a series of examinations;
 - At the completion of a series of examinations;
 - After any interruption in system continuity (e.g., power interruptions, search unit change-outs, activation of new examination setups, change in examination personnel, etc.);
 - After any instance of suspected system irregularity.

SEC SYSTEM SET-UP

1. SEC will be used for all CPs. This includes the fastener at GE04 with a thickness of 0.070 inch, as well as GE02 and GE05, for which lower wing skin inside radii will be inspected from the outside due to very thin skin thickness (0.040 and 0.070 inch, respectively). CP05, however, is partly covered by the leading edge, thus, the SEC inspection has limited access. Both GE02 and GE05 are also monitored via crack gages placed directly at inside skin radii at the anticipated crack locations.
2. General eddy current equipment set-up, standardization, and signal evaluation shall be performed per applicable USAF technical orders.
3. SEC inspection procedures are detailed in the applicable USAF technical order.
4. Connect the SEC probe with the Nortec 2000D+. Instrument set-up will enable discriminating between lift-off and flaw (crack) signals. Furthermore, flaw signal threshold settings are enabled (Figure 20).

INSPECTION

1. For both the PAUT and SEC inspections an on-aircraft verification / validation process could not yet be performed. Additional inspection procedure refinement will be required prior to finalizing the procedures.
2. Inspection frequency is anticipated to be one (1) inspection per week for the duration of the experiment.

RECORD KEEPING

1. Inspection results obtained during PAUT, SEC and crack gage CP monitoring will be recorded, processed and reported in accordance with the reporting requirements as identified by AFRL.
2. Archive all images/data that were collected to the appropriate storage media and label.

3. Recording nomenclature is yet to be determined, but shall include inspection location, inspection time and date, yes/no indication on flaw occurrence as well as flaw orientation, if applicable.
4. All inspection reports and disks shall be archived.

SYSTEMS SECURING

1. Following ultrasonic examination, couplant shall be removed from the exterior and interior of the aircraft using cloths dampened with water. The inspector should insure that the inspection surface is dry before leaving the work site.
2. Ensure that all equipment is powered down, properly stored, and removed from the inspection location. The inspection area shall be returned to its original, safe condition.

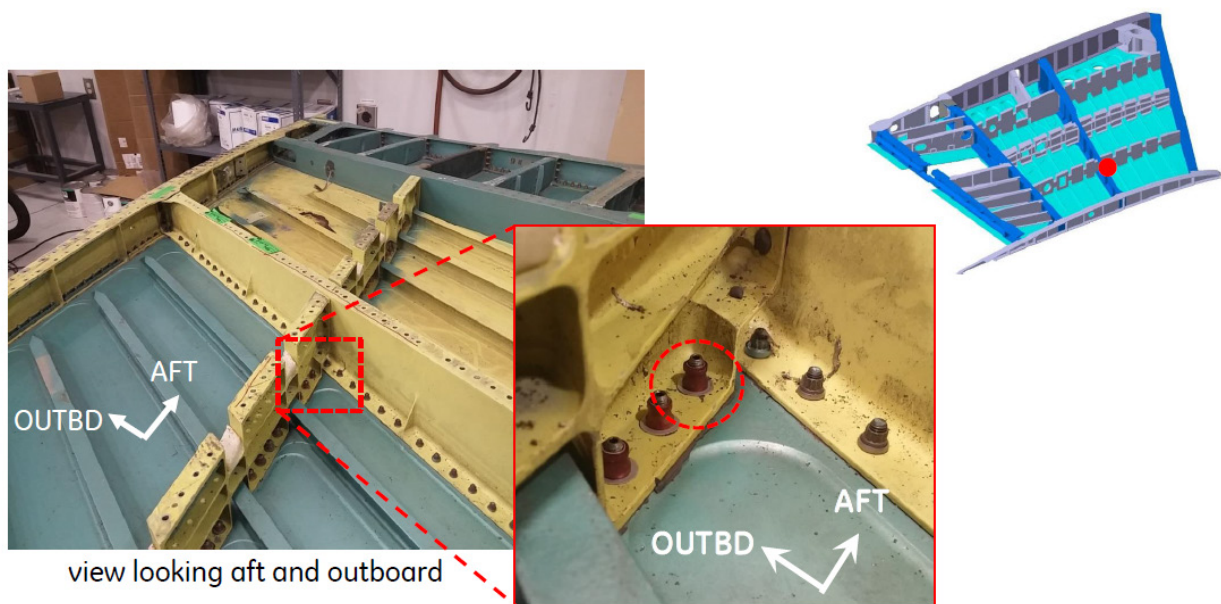


Figure C-1. Control Point GE01

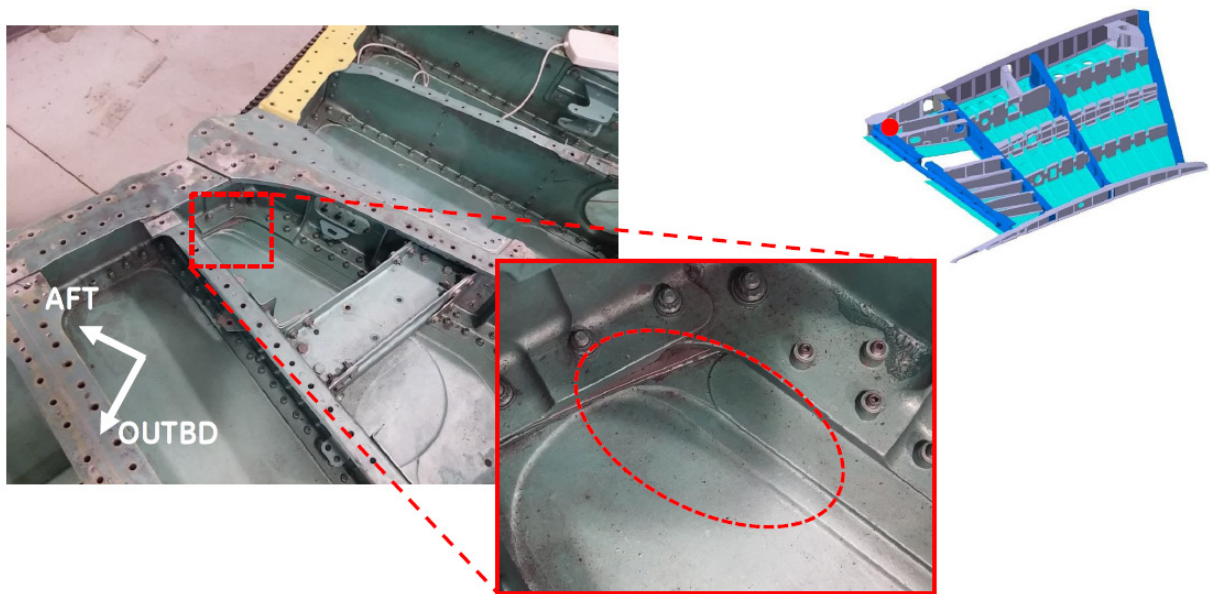


Figure C-2. Control Point GE02

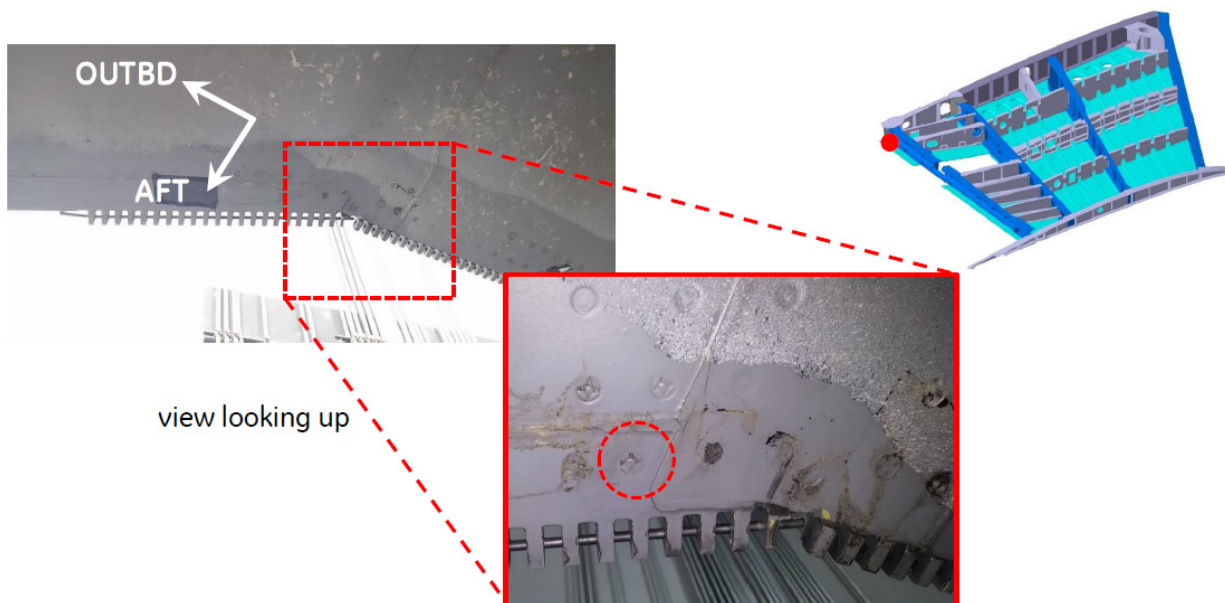


Figure C-3. Control Point GE03

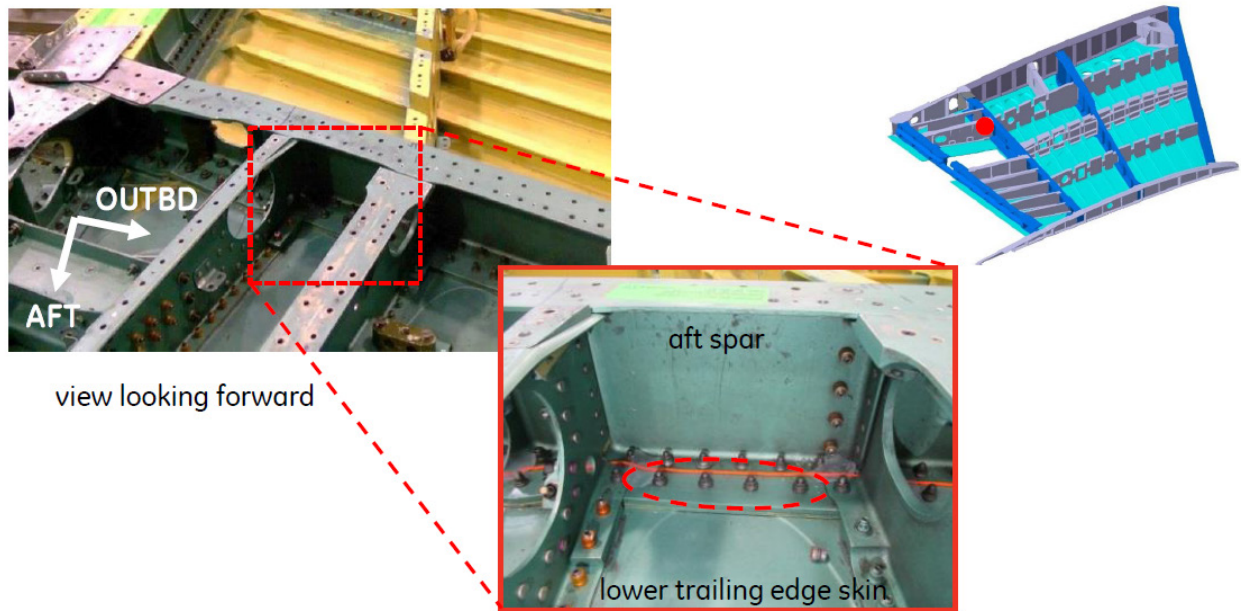


Figure C-4. Control Point GE04

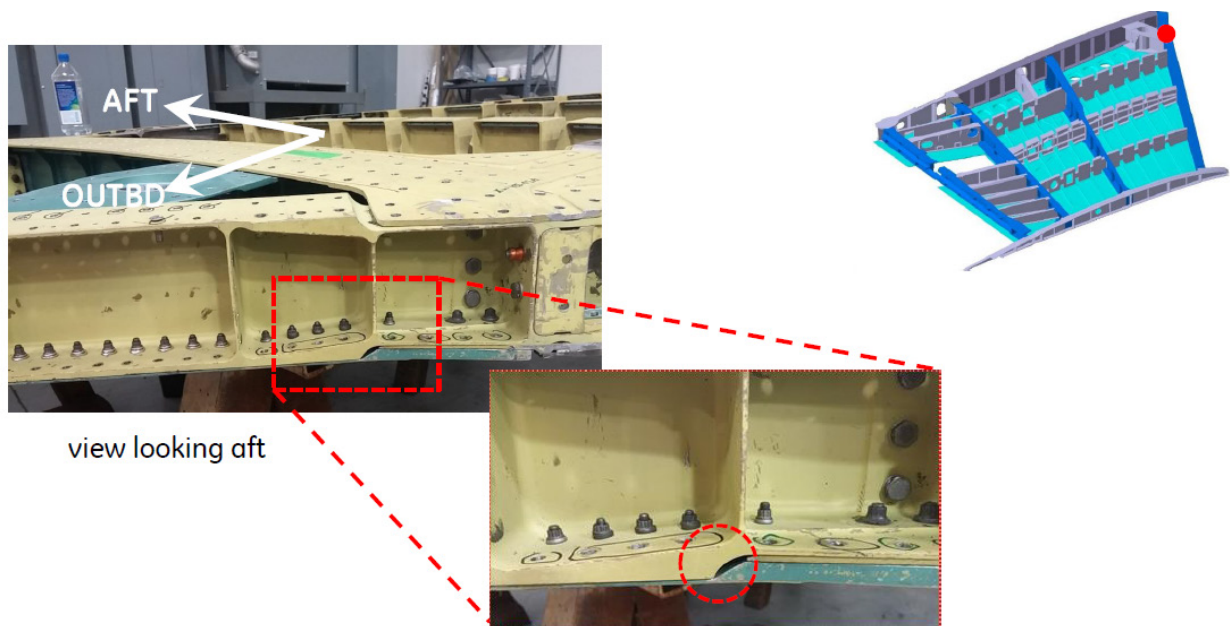


Figure C-5. Control Point GE05

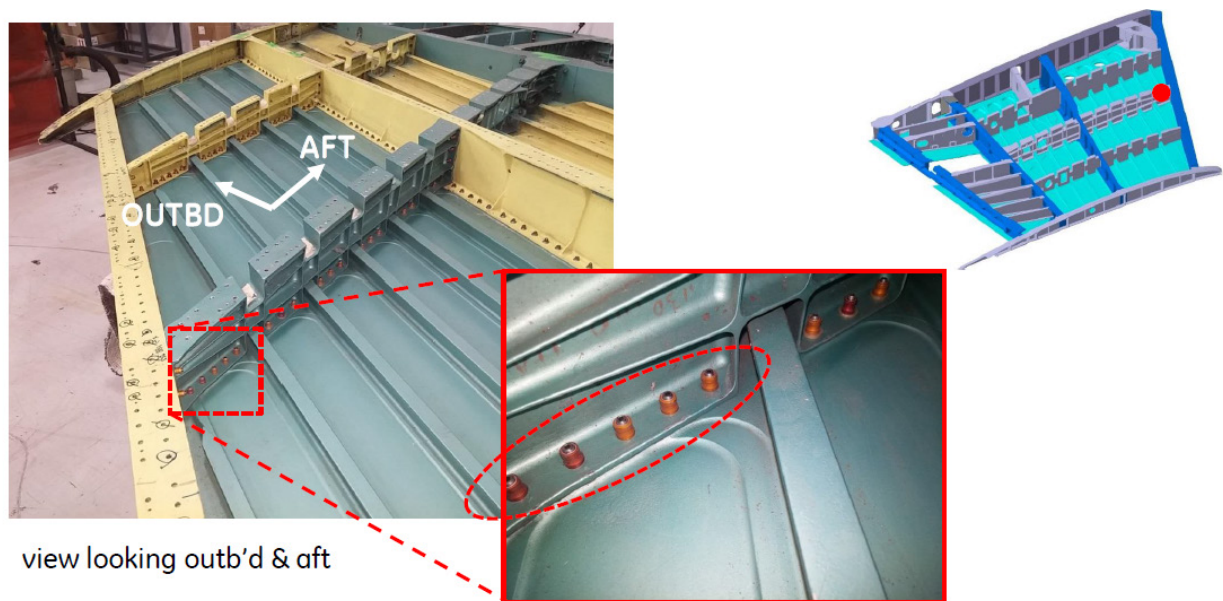


Figure C-6. Control Point GE06

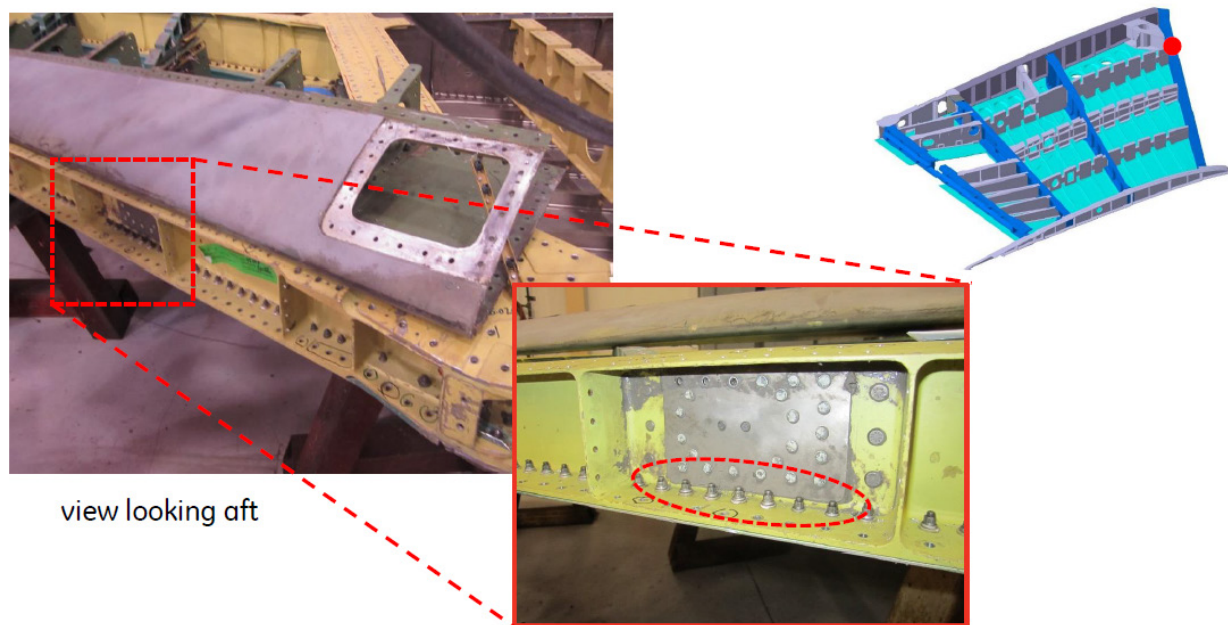


Figure C-7. Control Point GE07

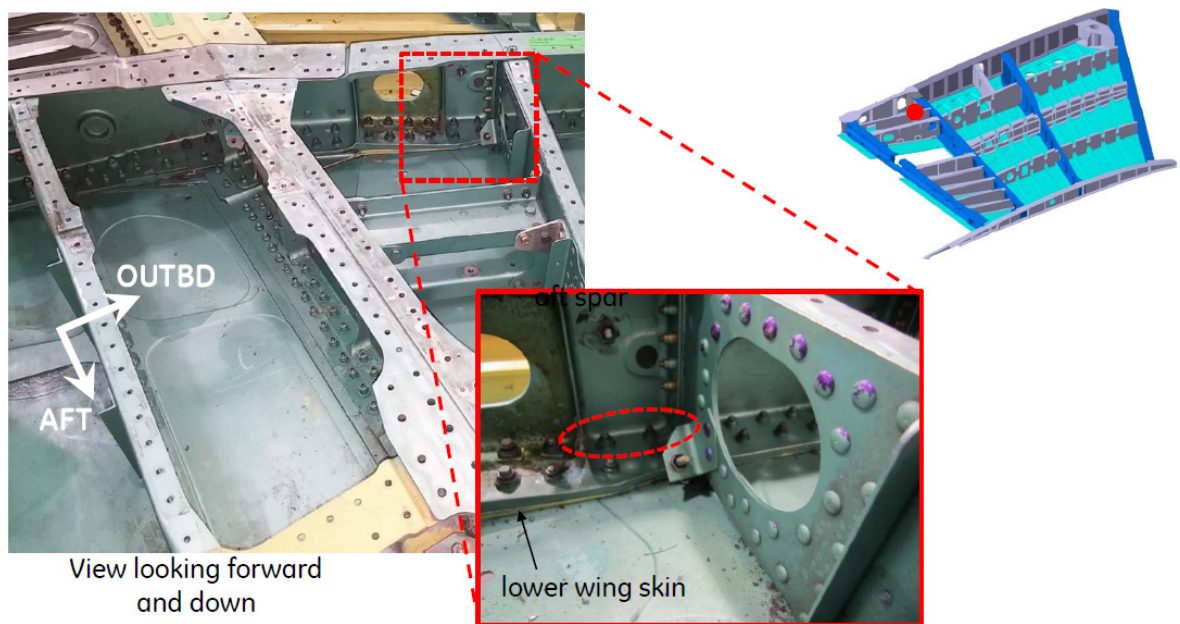


Figure C-8. Control Point GE08

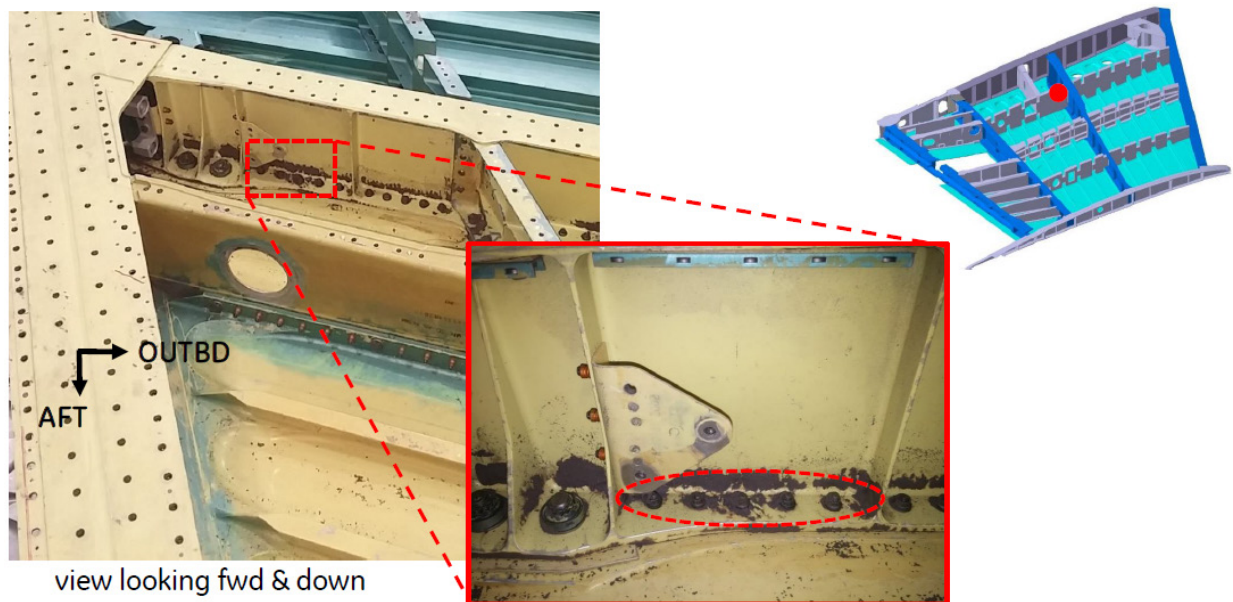


Figure C-9. Control Point GE10

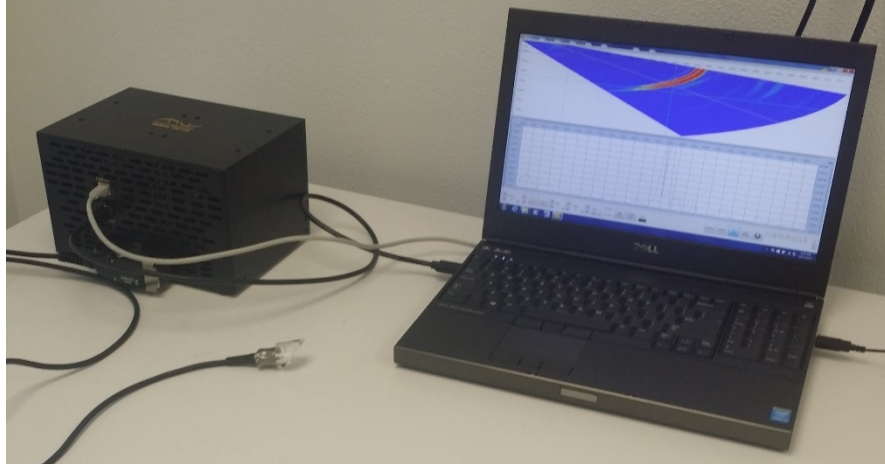


Figure C-10. OEMPA 128/128 including laptop with TPACquisition software



Figure C-11. Olympus PAUT probe: 10L32A10 – shown with wedge



Figure C-12. 25° wedge (left) and 45° wedge (right)

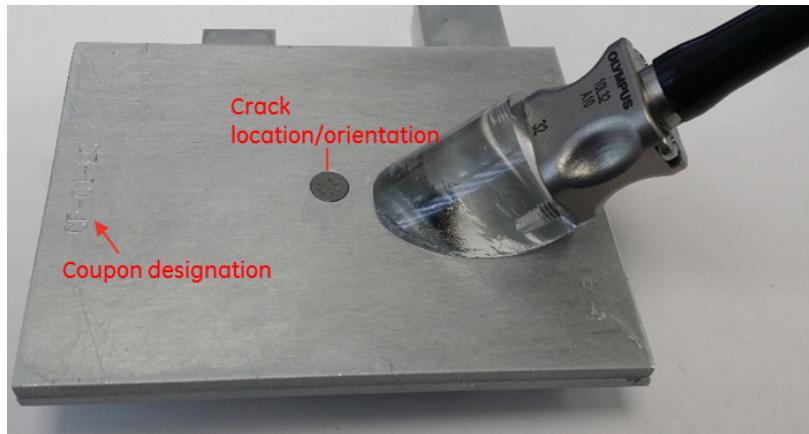


Figure C-13. Crack Reference Standard Set Example, shown with PAUT probe

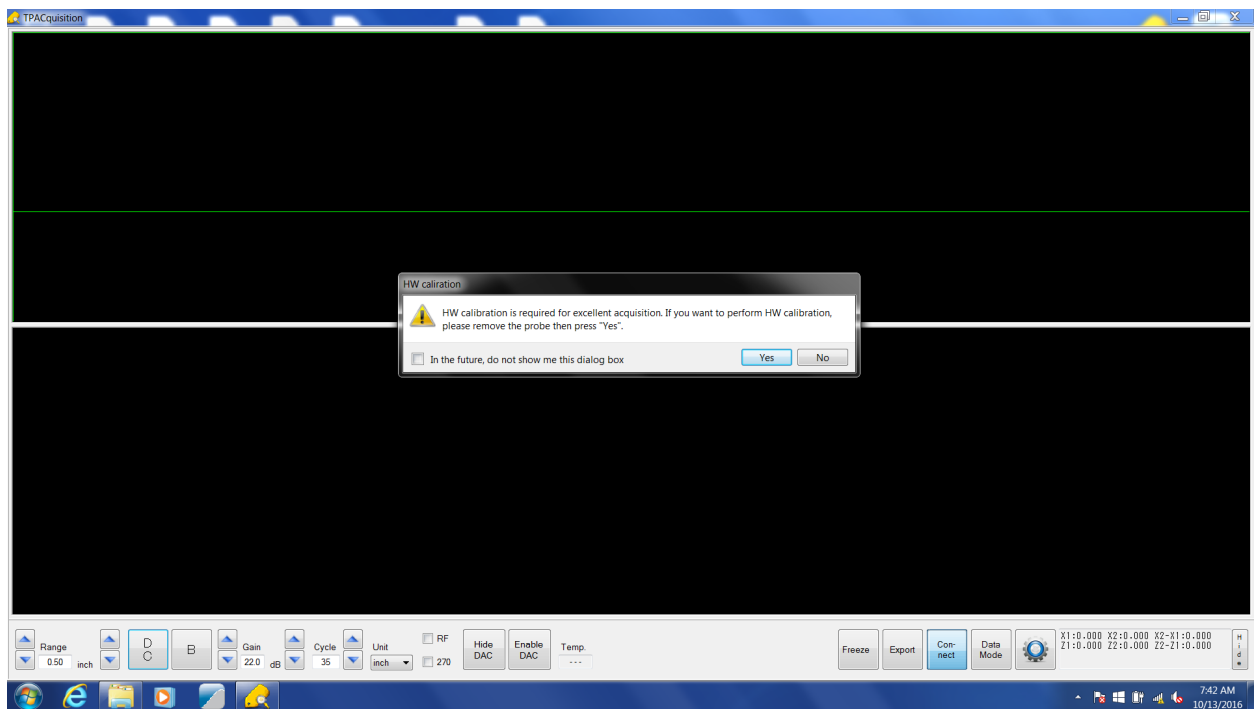


Figure C-14. Initial TPACquisition Screen

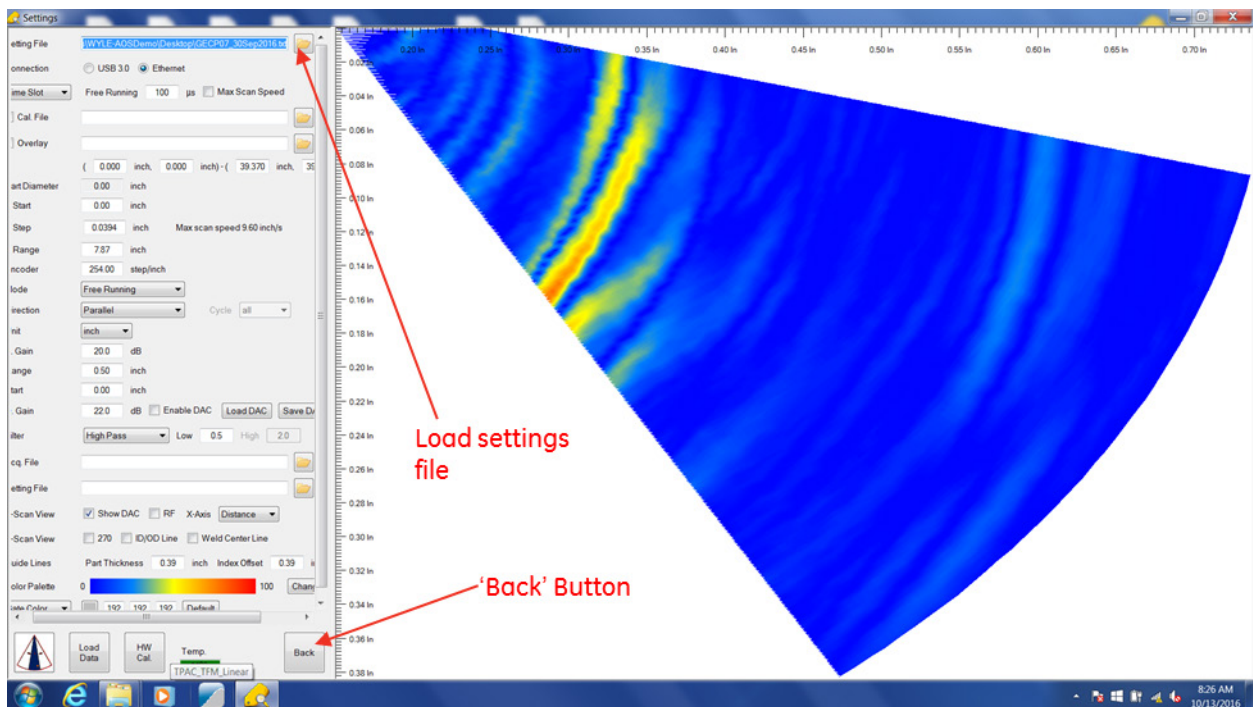


Figure C-15. 'Settings' Screen

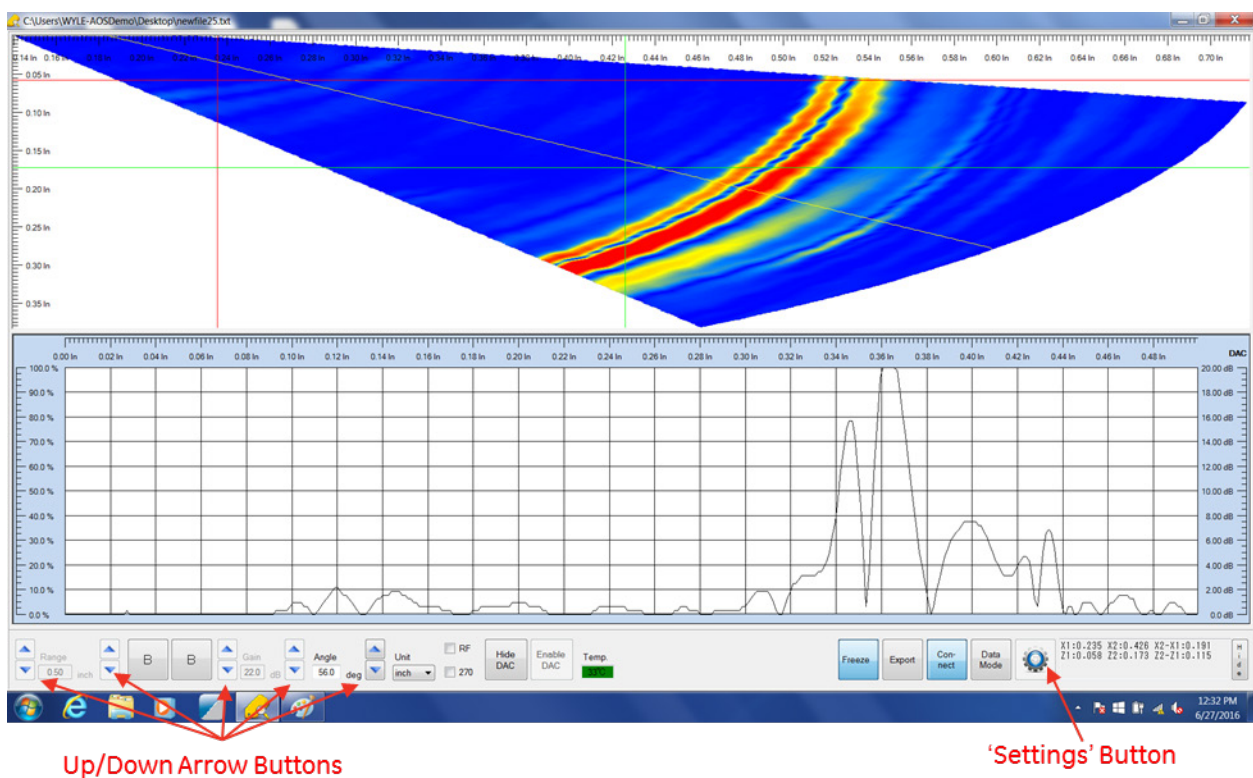


Figure C-16. 'Data Acquisition' Screen - Example

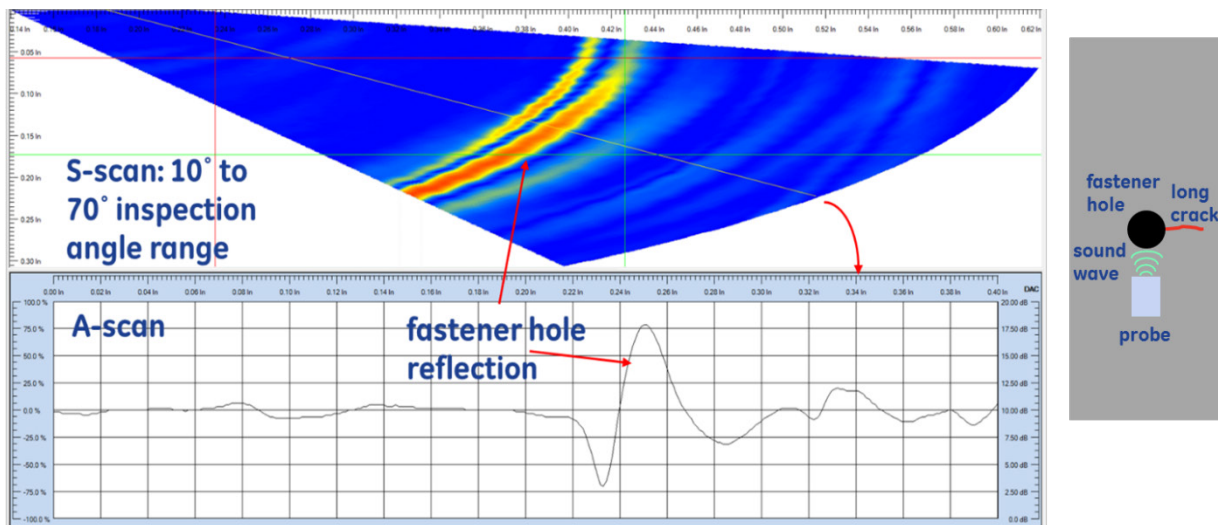


Figure C-17. Exemplary Reference Fastener Hole Reflection

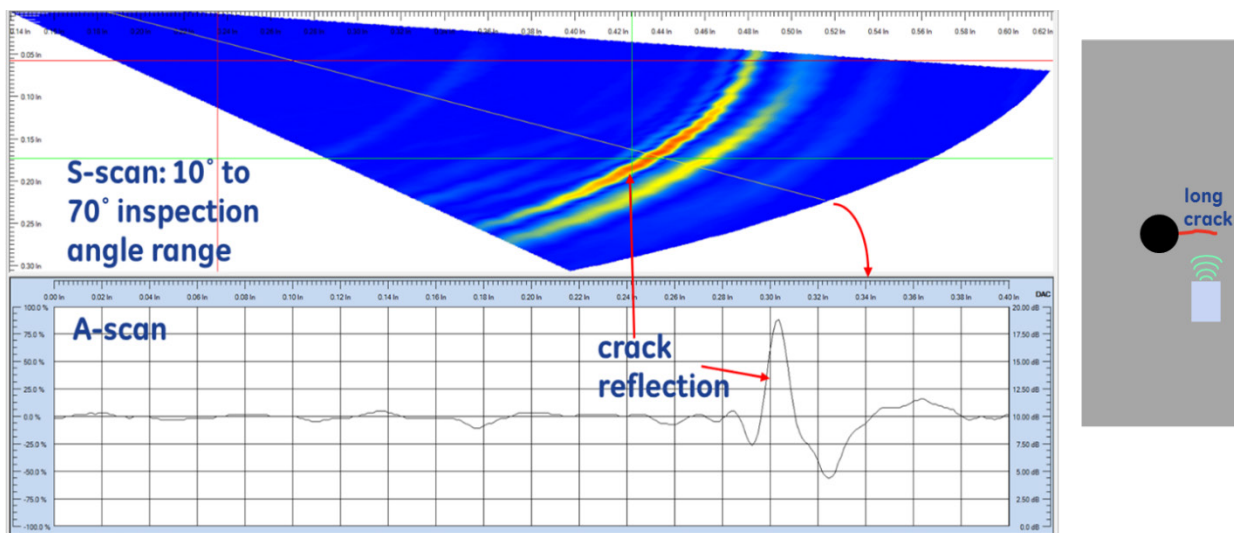


Figure C-18. Exemplary Reference Long Crack Reflection

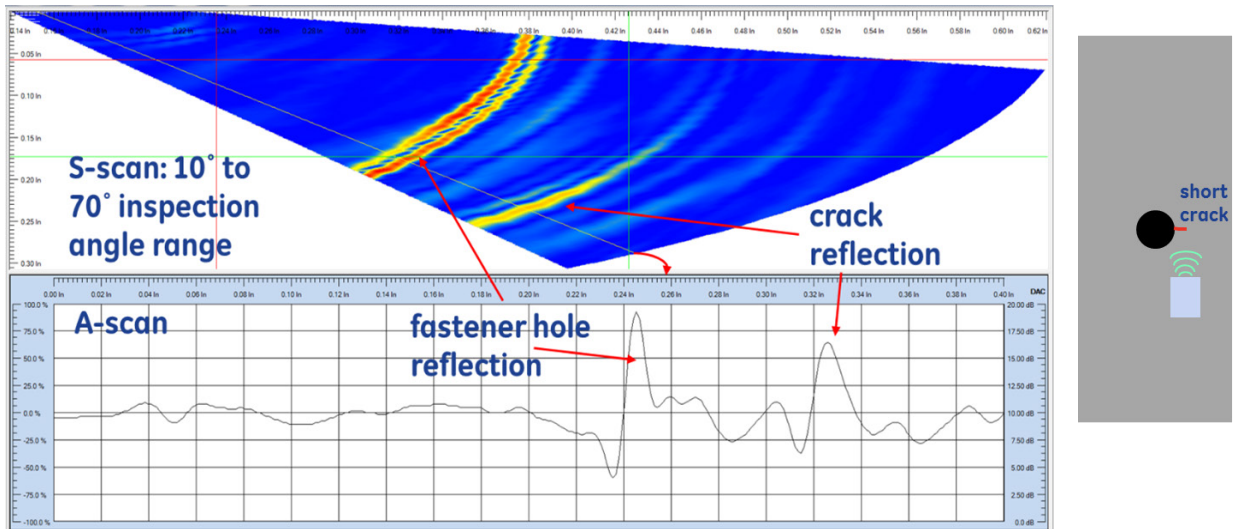


Figure C-19. Exemplary Reference Short Crack Reflection

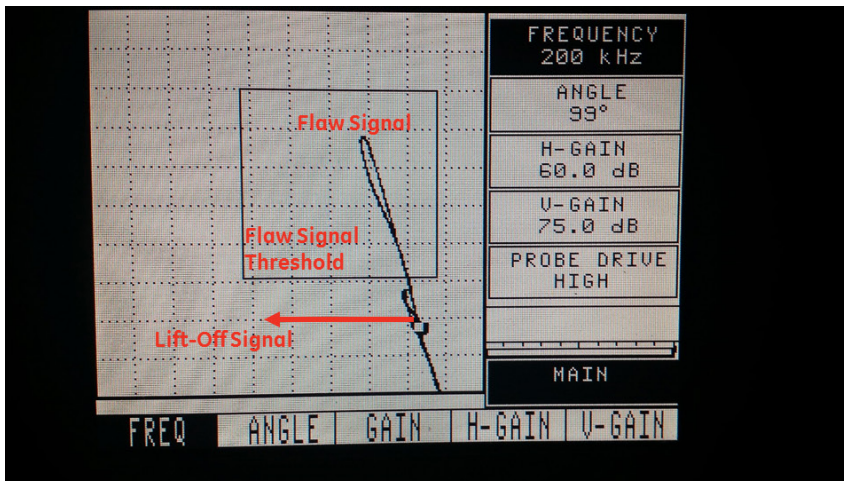


Figure C-20. Nortec 2000D+ ET instrument – exemplary crack inspection close to fastener head

Appendix D – Control Point SIF Models

GE01 SIF Model

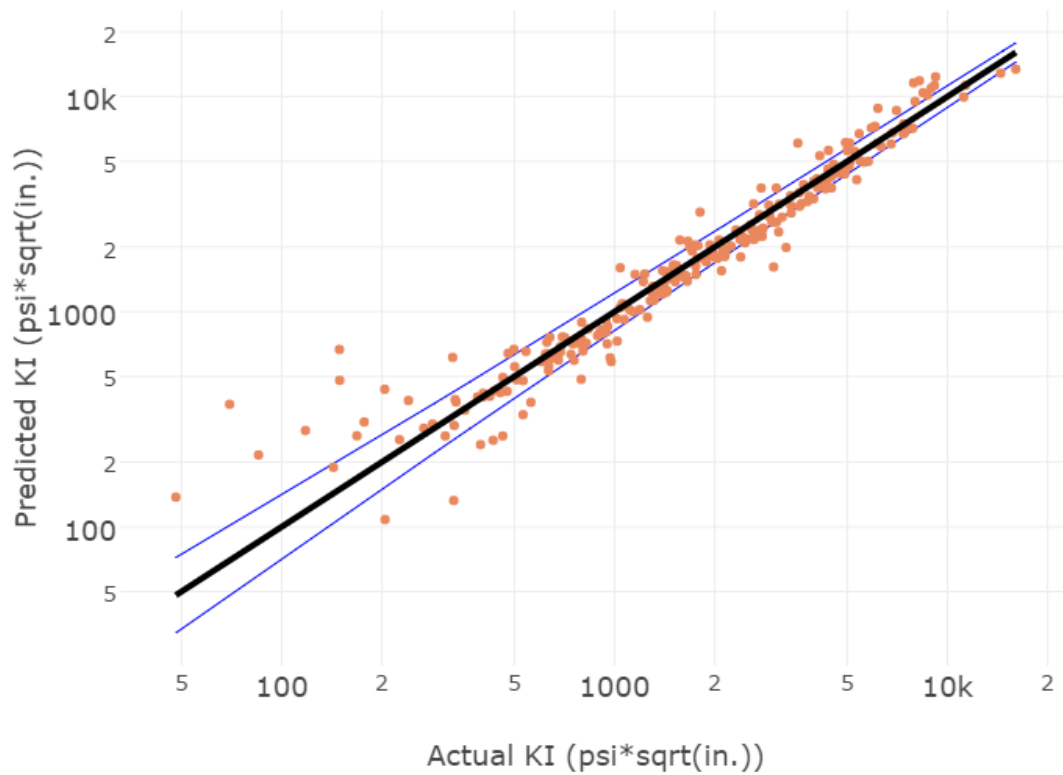


Figure D-1. GE01 SIF model predicted K_I vs. actual K_I : coarse-grid, corner crack, depth direction

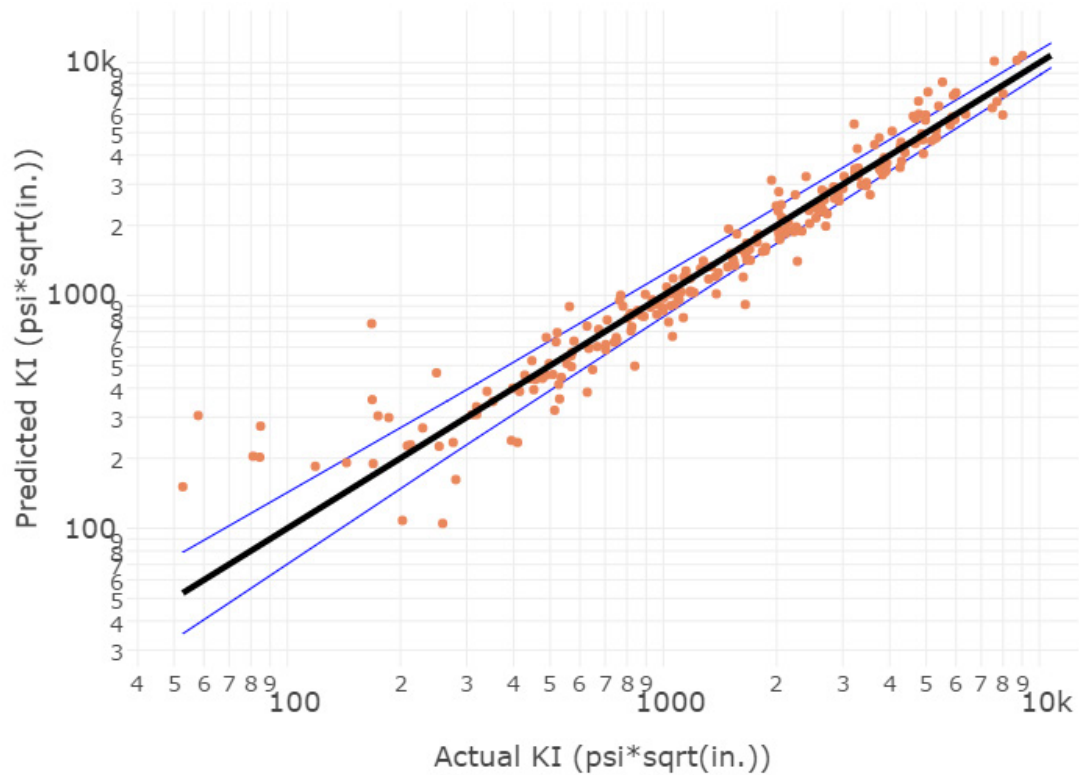


Figure D-2. GE01 SIF model predicted K_I vs. actual K_I : coarse-grid, corner crack, surface direction

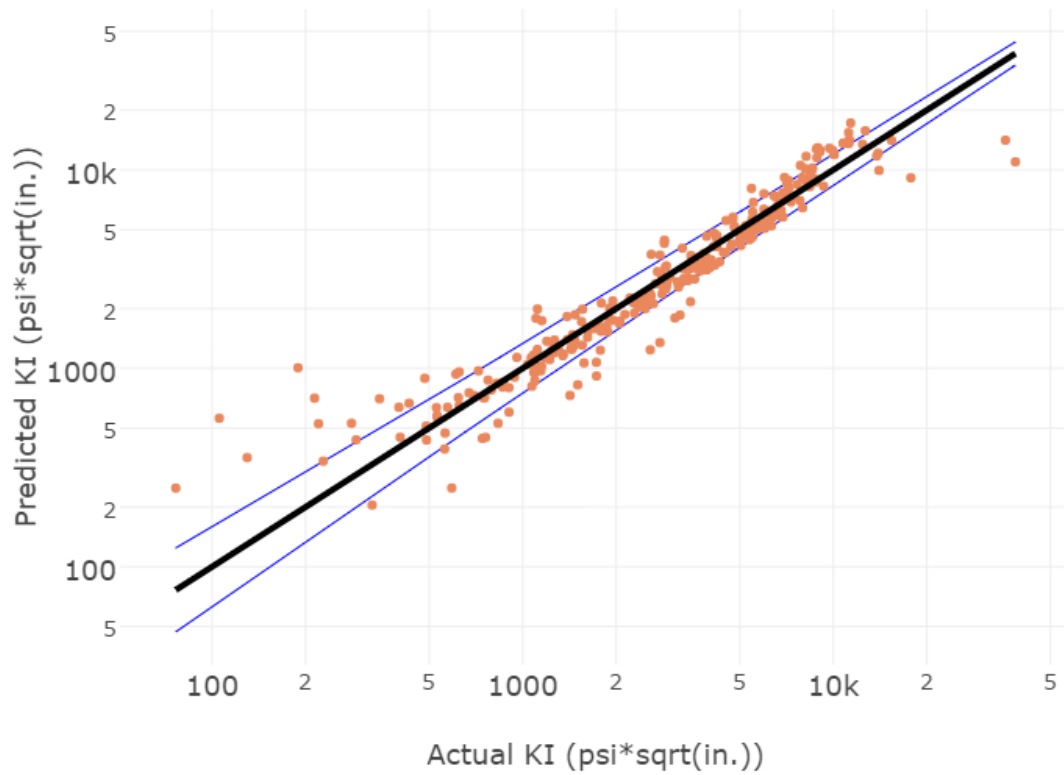


Figure D-3. GE01 SIF model predicted K_I vs. actual K_I : coarse-grid, through crack

GE02 SIF Model

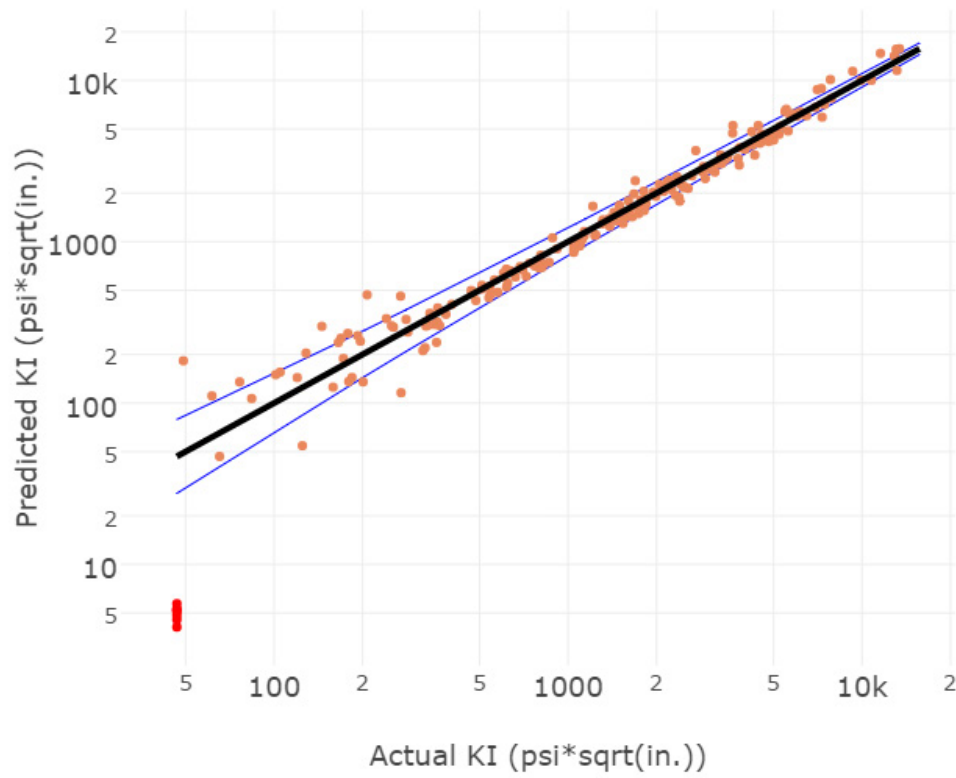


Figure D-4. GE02 SIF model predicted K_I vs. actual K_I : coarse-grid, corner crack, depth direction

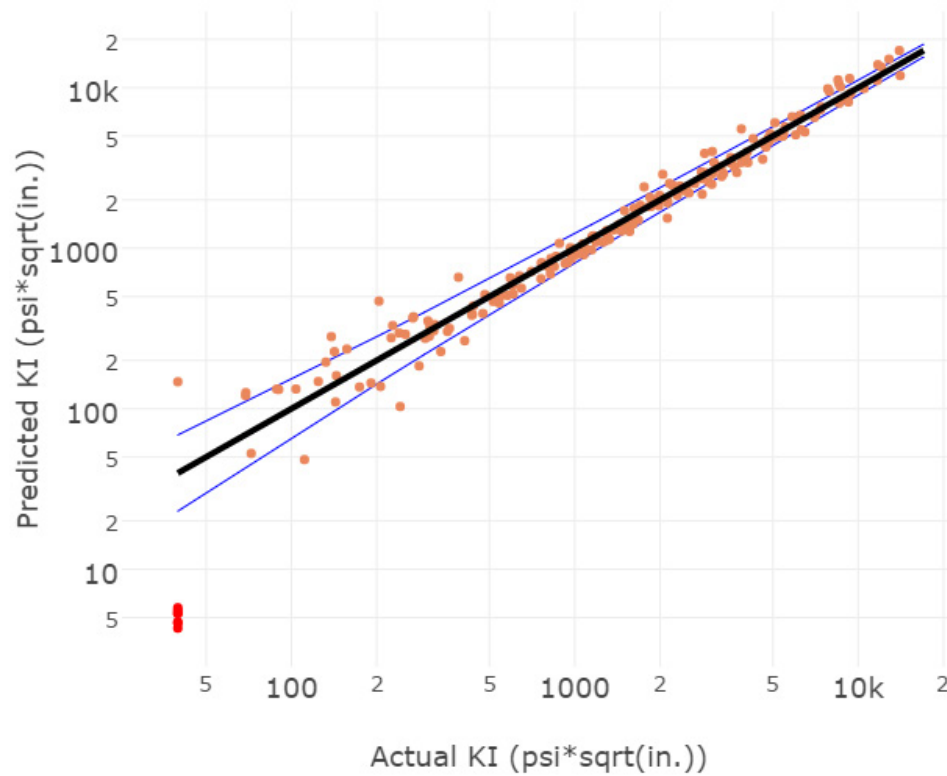


Figure D-5. GE02 SIF model predicted K_I vs. actual K_I : coarse-grid, corner crack, surface direction

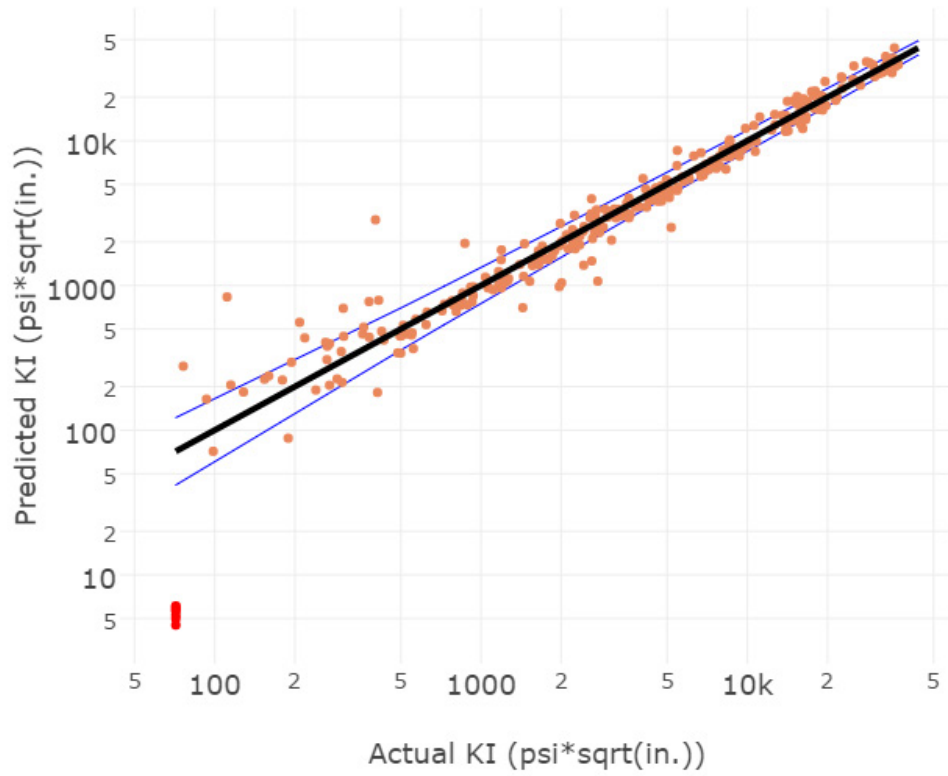


Figure D-6. GE02 SIF model predicted K_I vs. actual K_I : coarse-grid, through crack

GE03 SIF Model

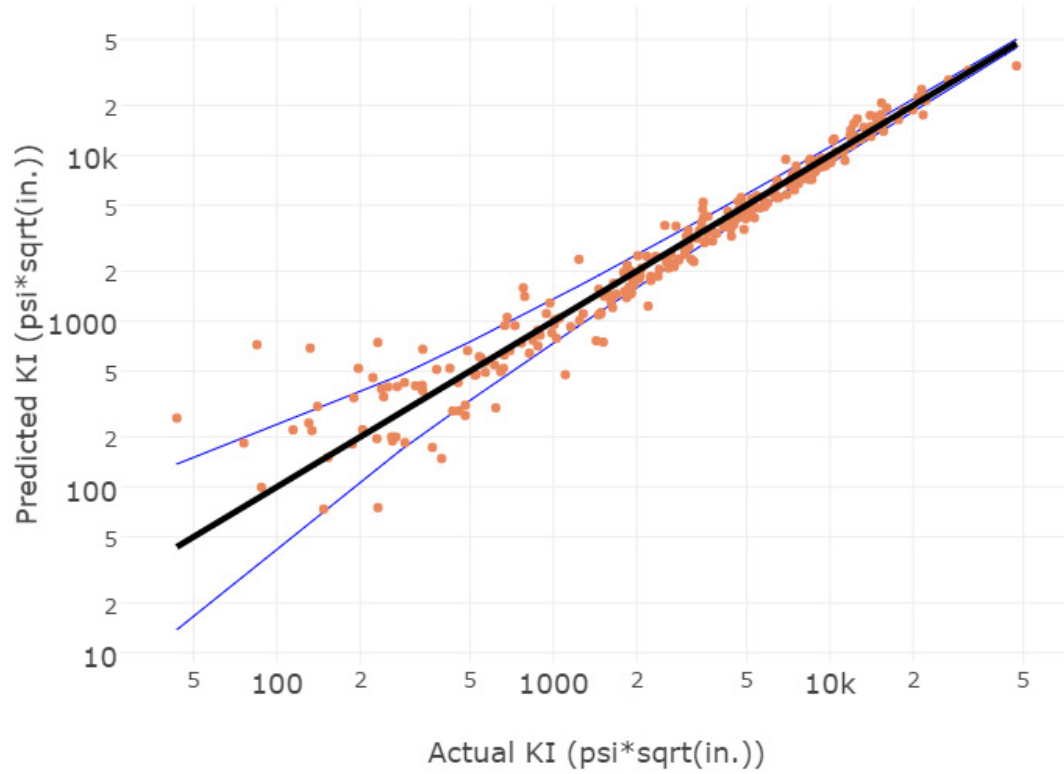


Figure D-7. GE03 SIF model predicted K_I vs. actual K_I : coarse-grid, corner crack, depth direction

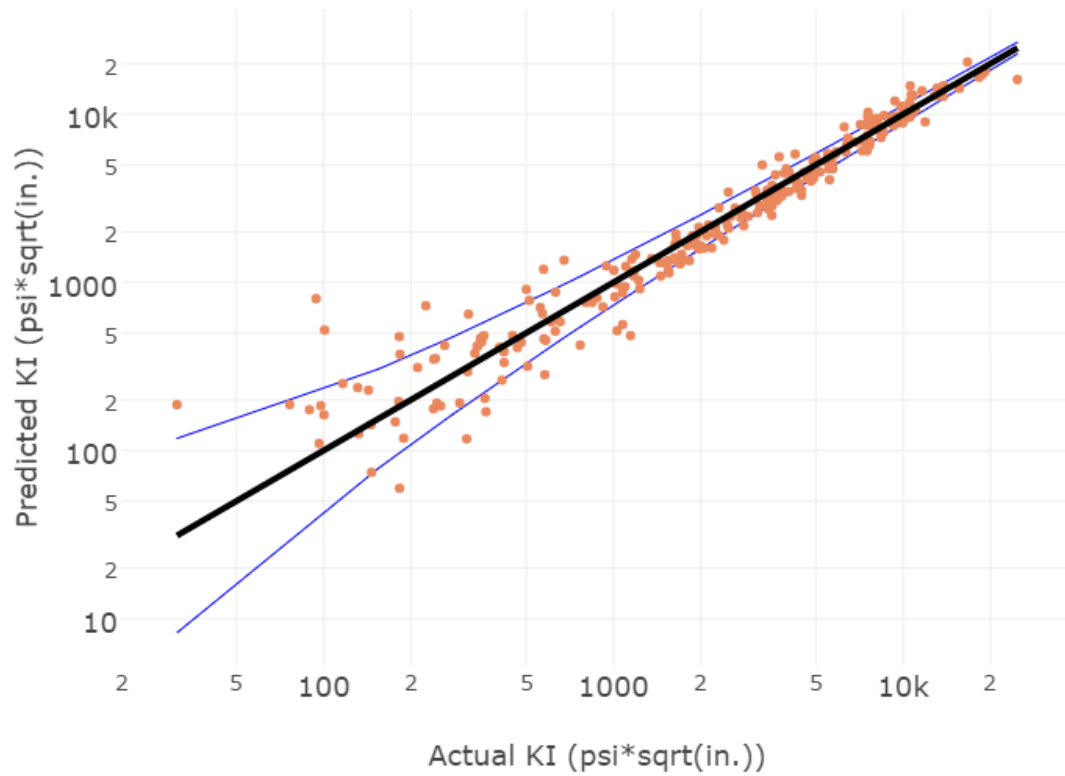


Figure D-8. GE03 SIF model predicted K_I vs. actual K_I : coarse-grid, corner crack, surface direction

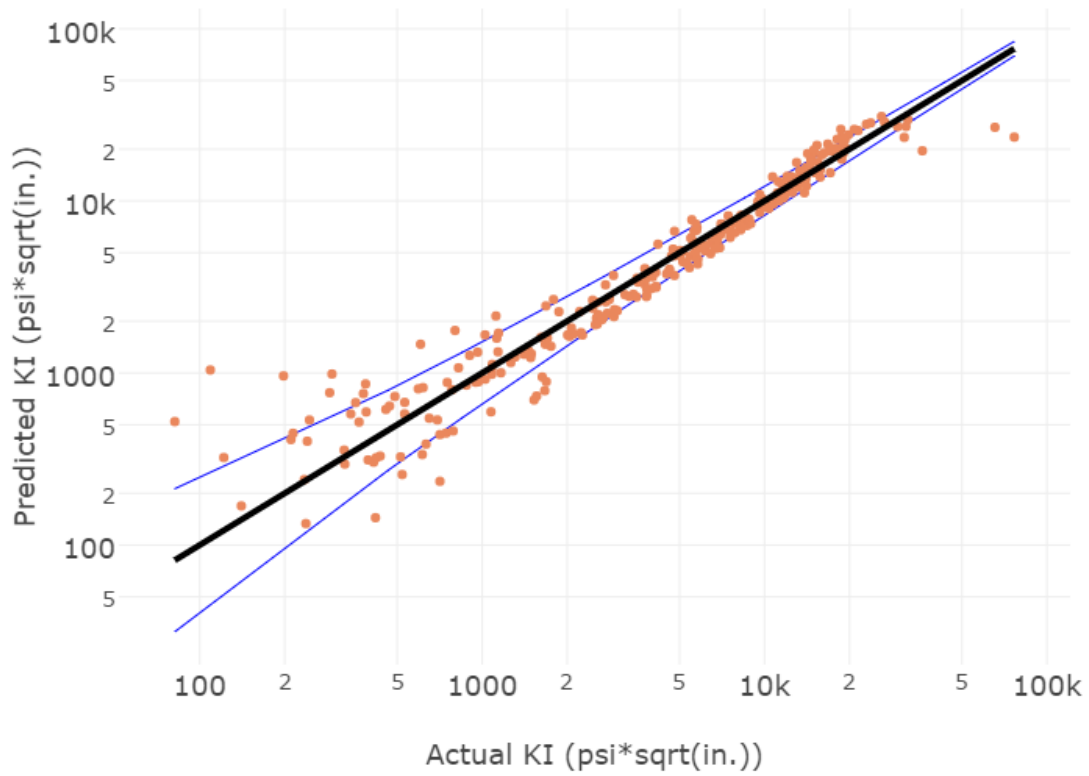


Figure D-9. GE03 SIF model predicted K_I vs. actual K_I : coarse-grid, through crack

GE04 SIF Model

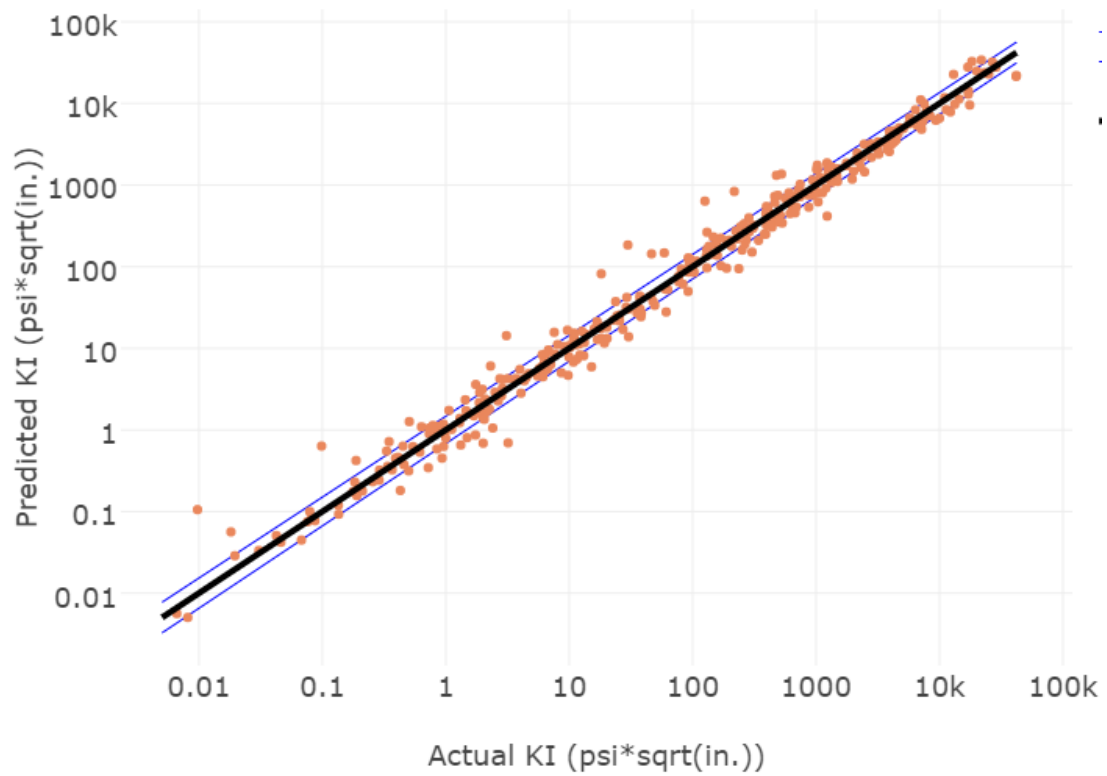


Figure D-10. GE04 SIF model predicted K_I vs. actual K_I : fine-grid, corner crack, depth direction

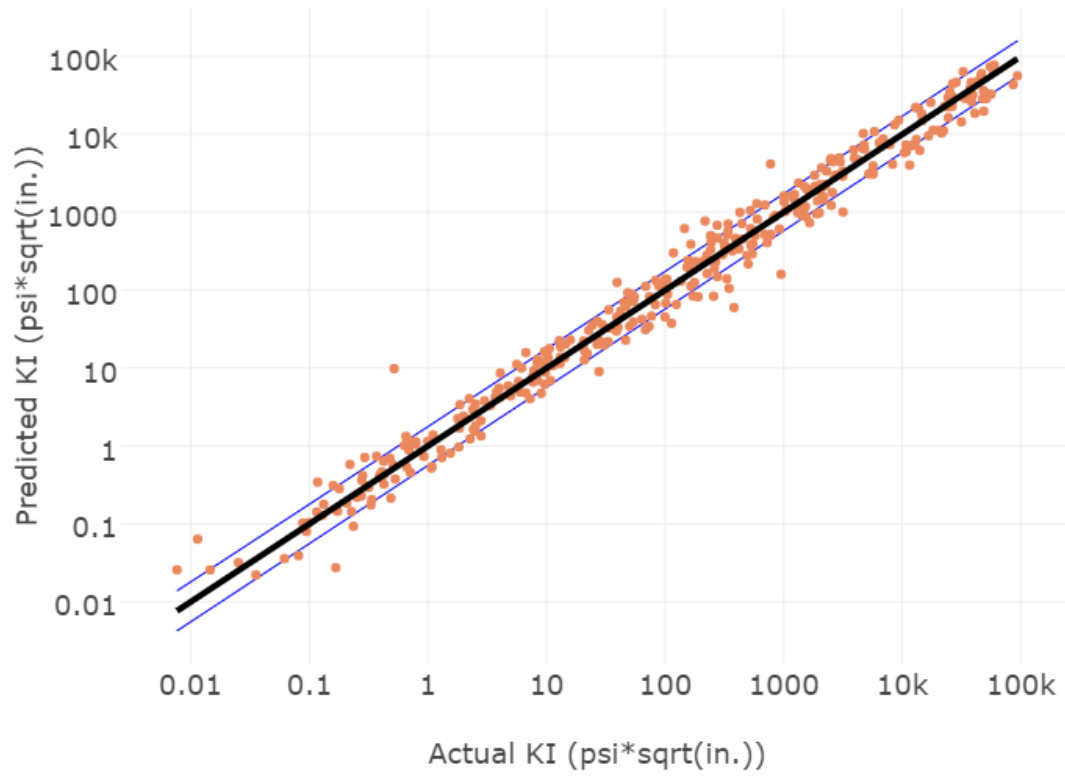


Figure D-11. GE04 SIF model predicted K_I vs. actual K_I : fine-grid, corner crack, surface direction

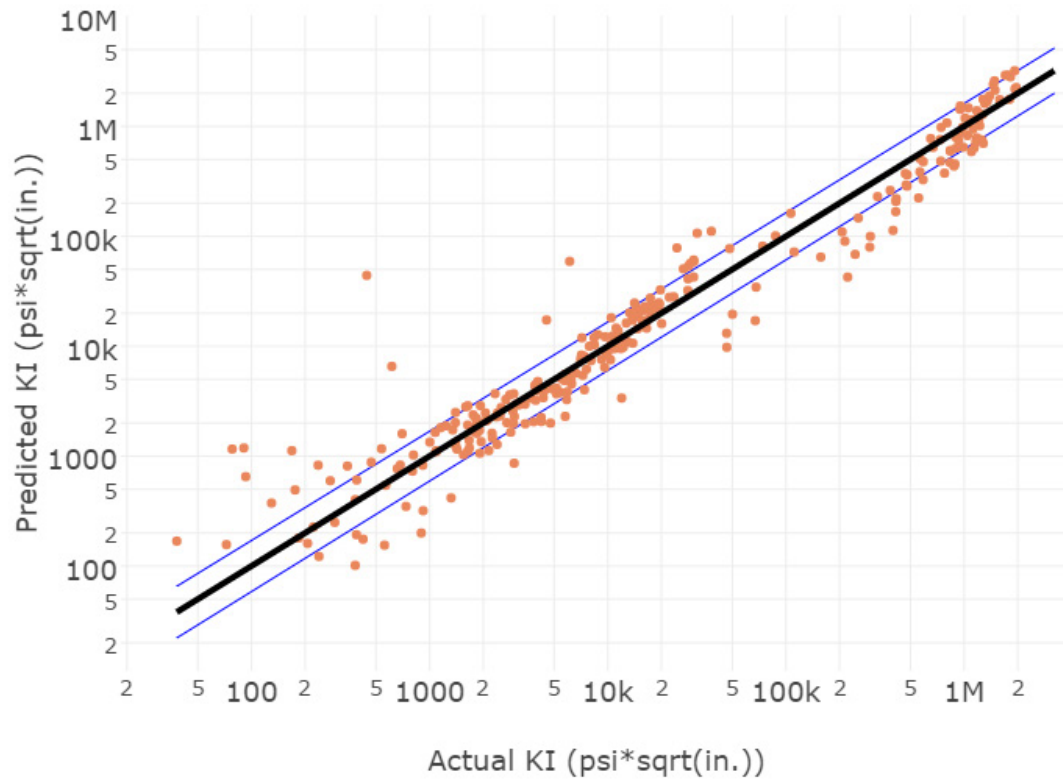


Figure D-12. GE04 SIF model predicted K_I vs. actual K_I : fine-grid, through crack

GE05 SIF Model

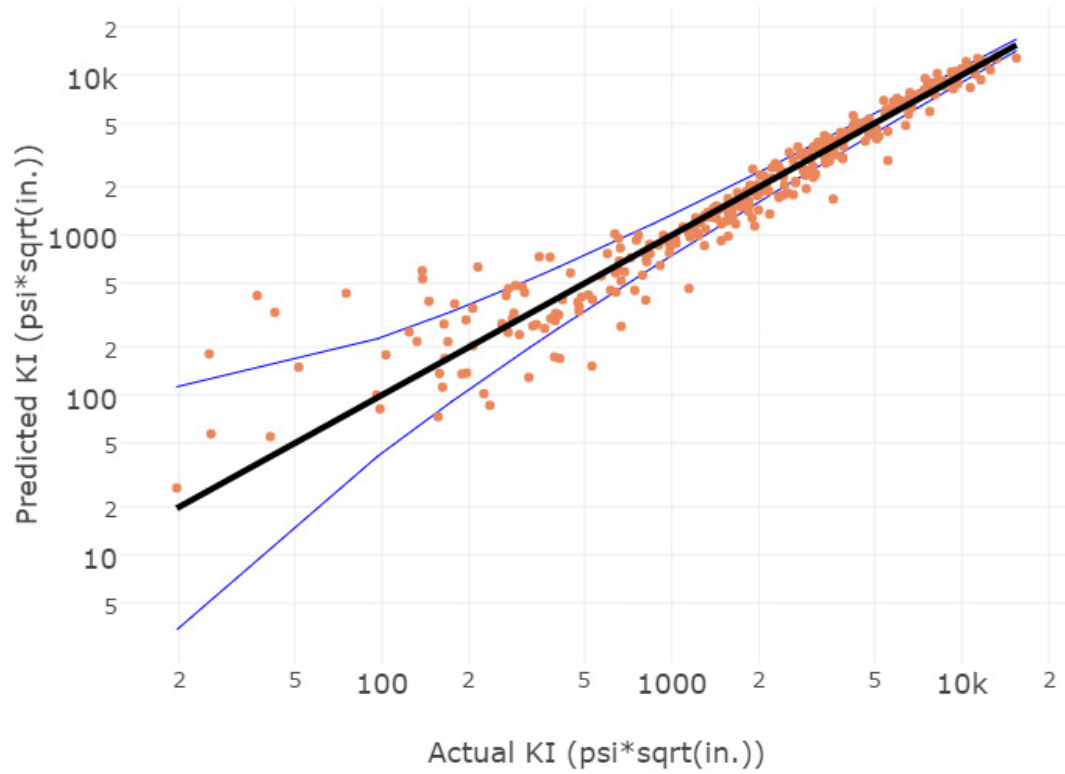


Figure D-13. GE05 SIF model predicted K_I vs. actual K_I : fine-grid, part-through crack, depth direction

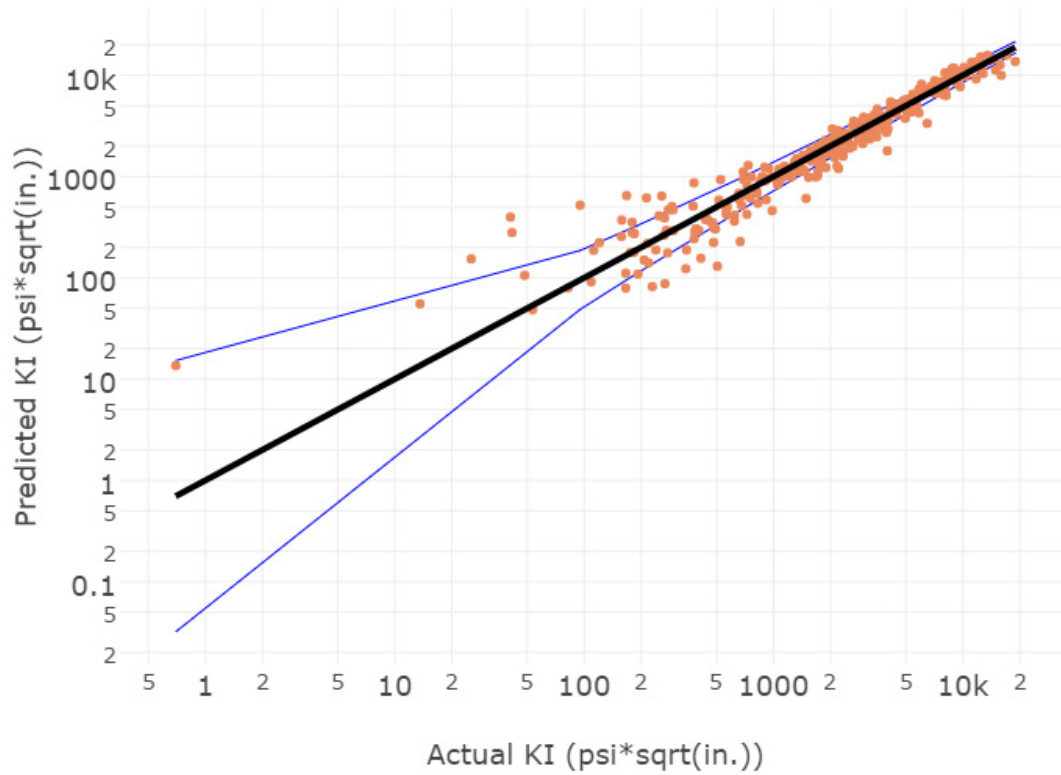


Figure D-14. GE05 SIF model predicted K_I vs. actual K_I : fine-grid, part-through crack, surface direction

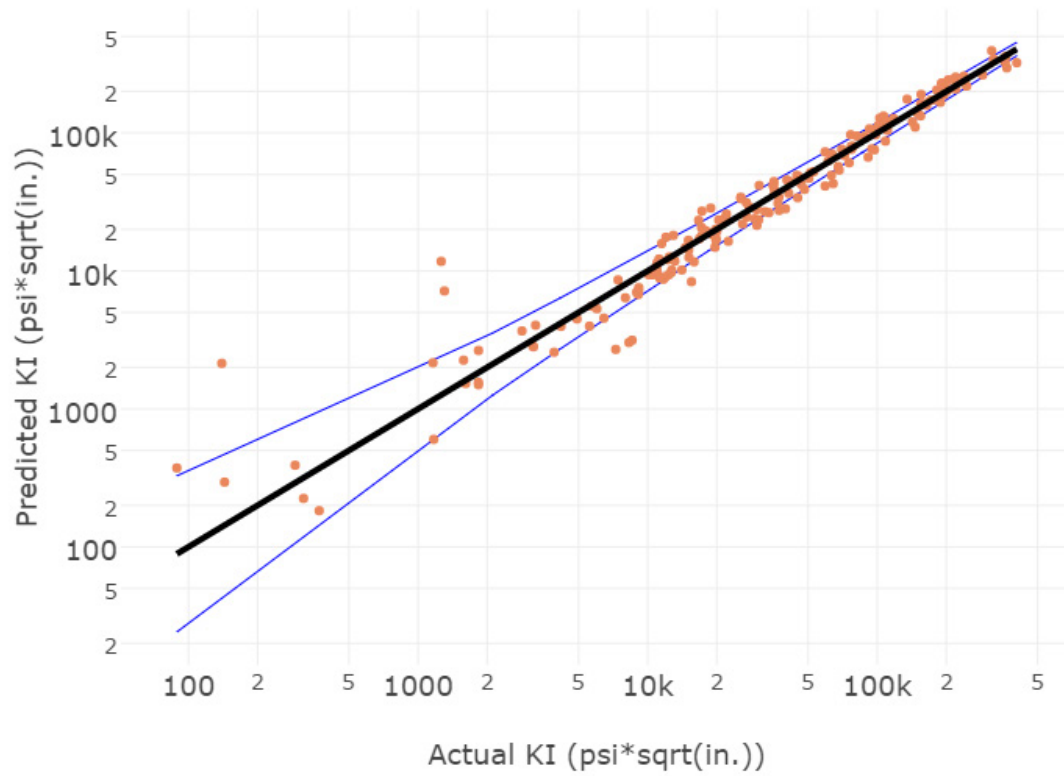


Figure D-15. GE05 SIF model predicted K_I vs. actual K_I : fine-grid, through crack

GE06 SIF Model

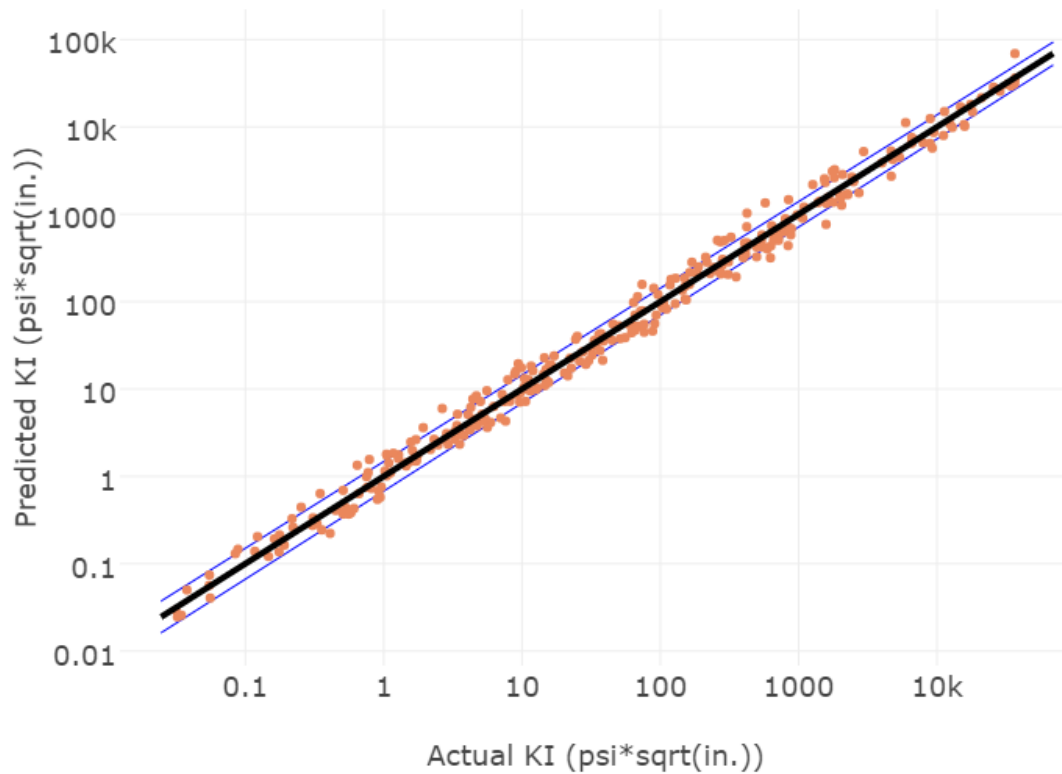


Figure D-16. GE06 SIF model predicted K_I vs. actual K_I : fine-grid, corner crack, depth direction

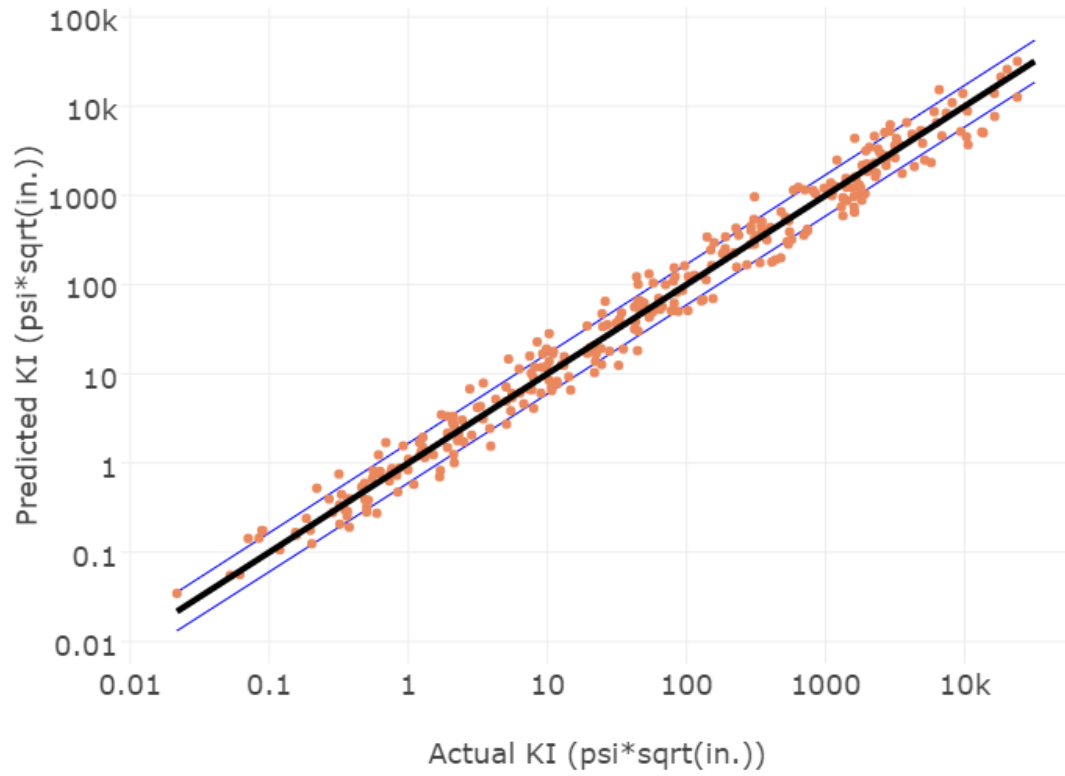


Figure D-17. GE06 SIF model predicted K_I vs. actual K_I : fine-grid, corner crack, surface direction

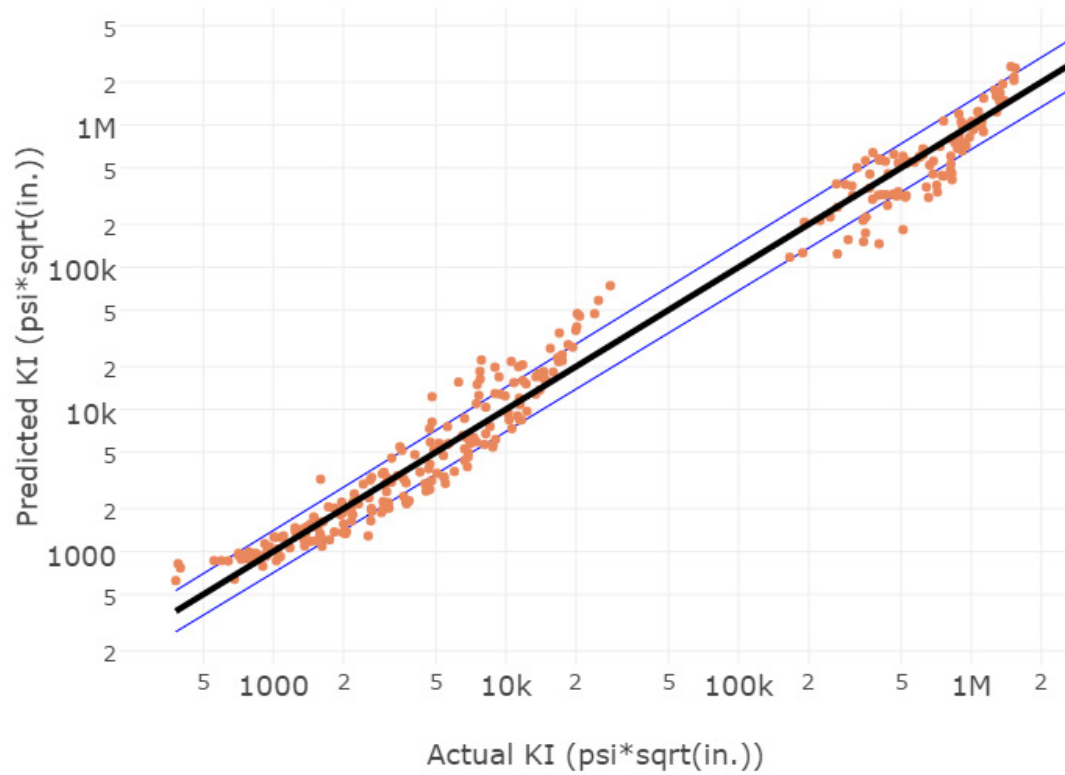


Figure D-18. GE06 SIF model predicted K_I vs. actual K_I : fine-grid, through crack

GE07 SIF Model

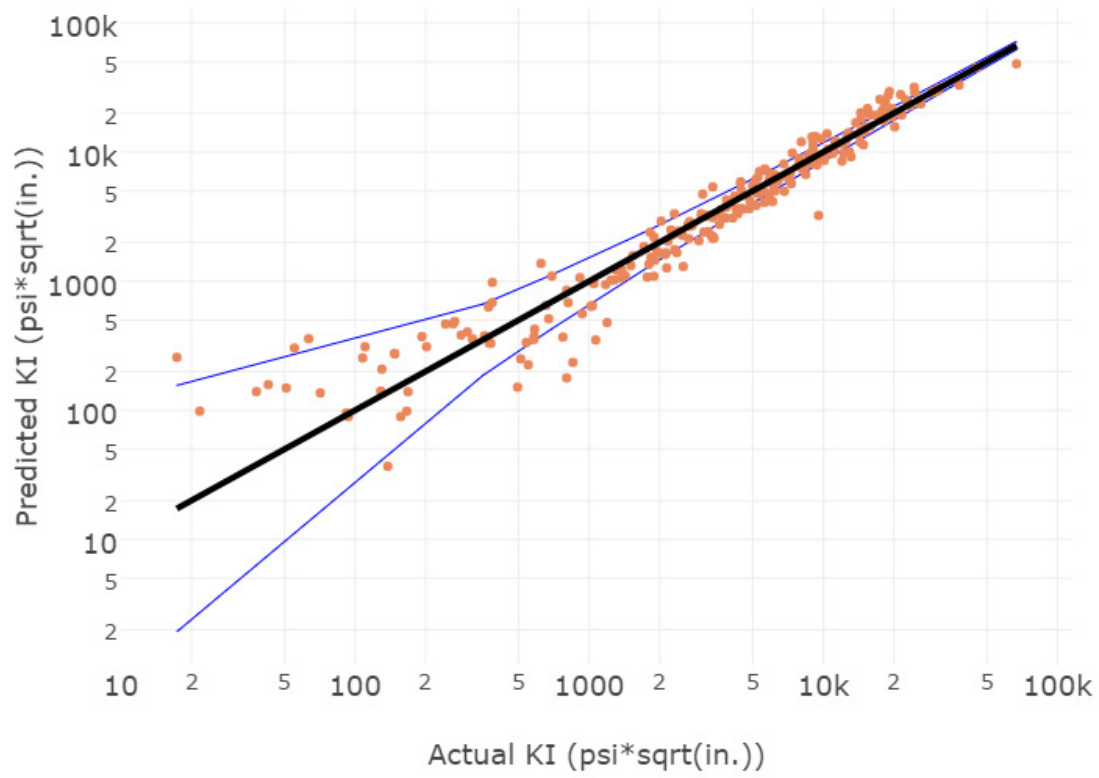


Figure D-19. GE07 SIF model predicted K_I vs. actual K_I : coarse-grid, corner crack, depth direction

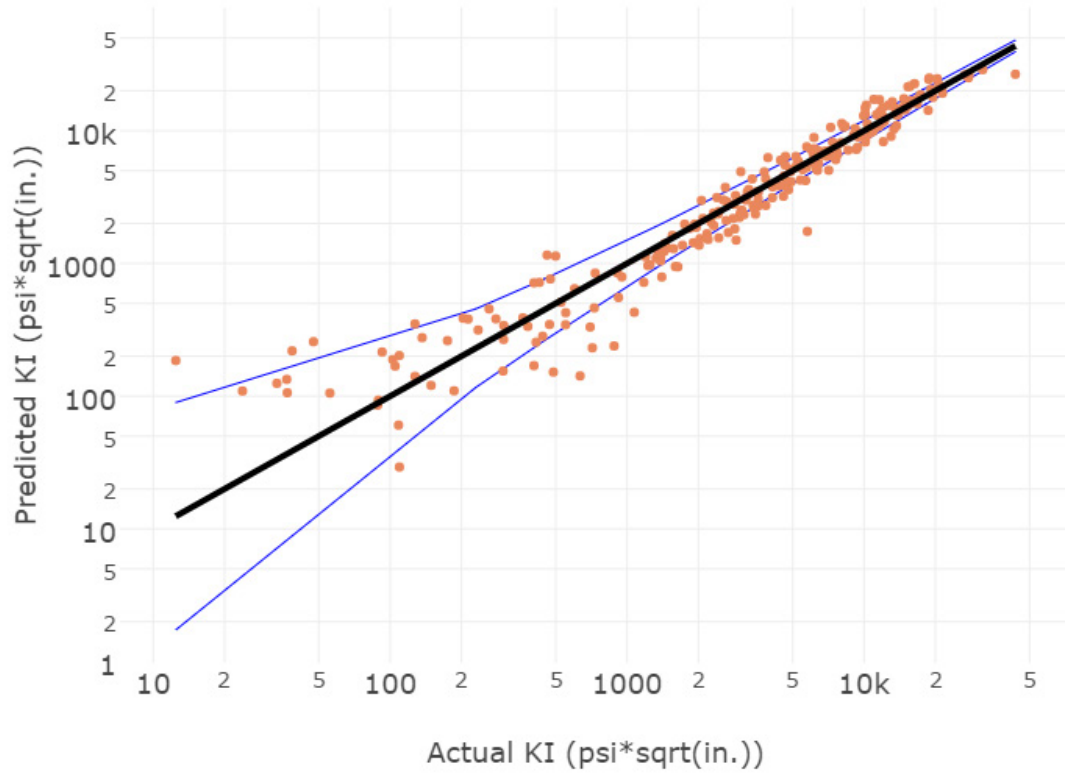


Figure D-20. GE07 SIF model predicted K_I vs. actual K_I : coarse-grid, corner crack, surface direction

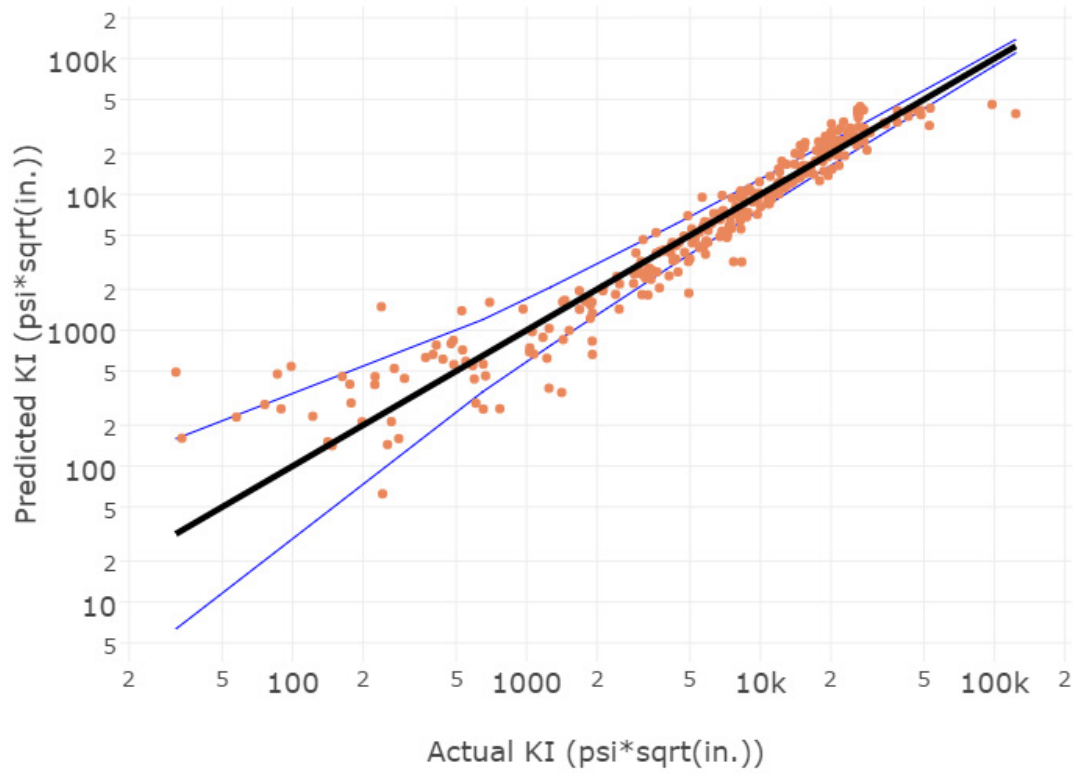


Figure D-21. GE07 SIF model predicted K_I vs. actual K_I : coarse-grid, through crack

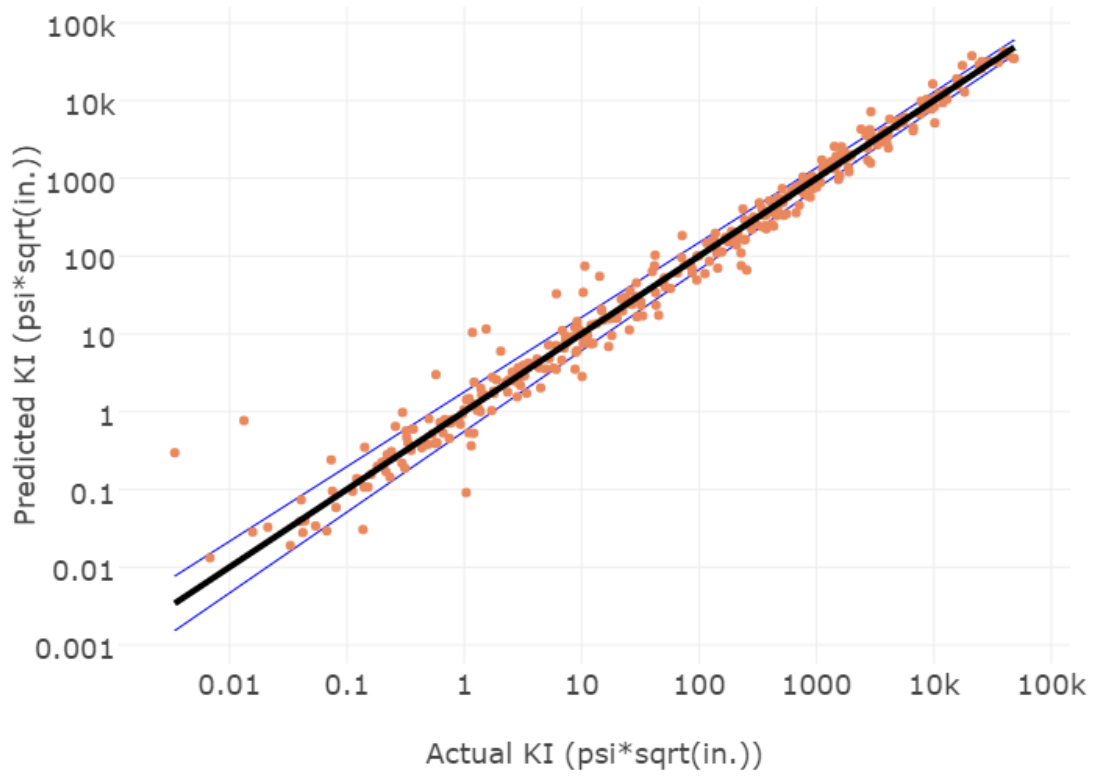


Figure D-22. GE07 SIF model predicted K_I vs. actual K_I : fine-grid, corner crack, depth direction

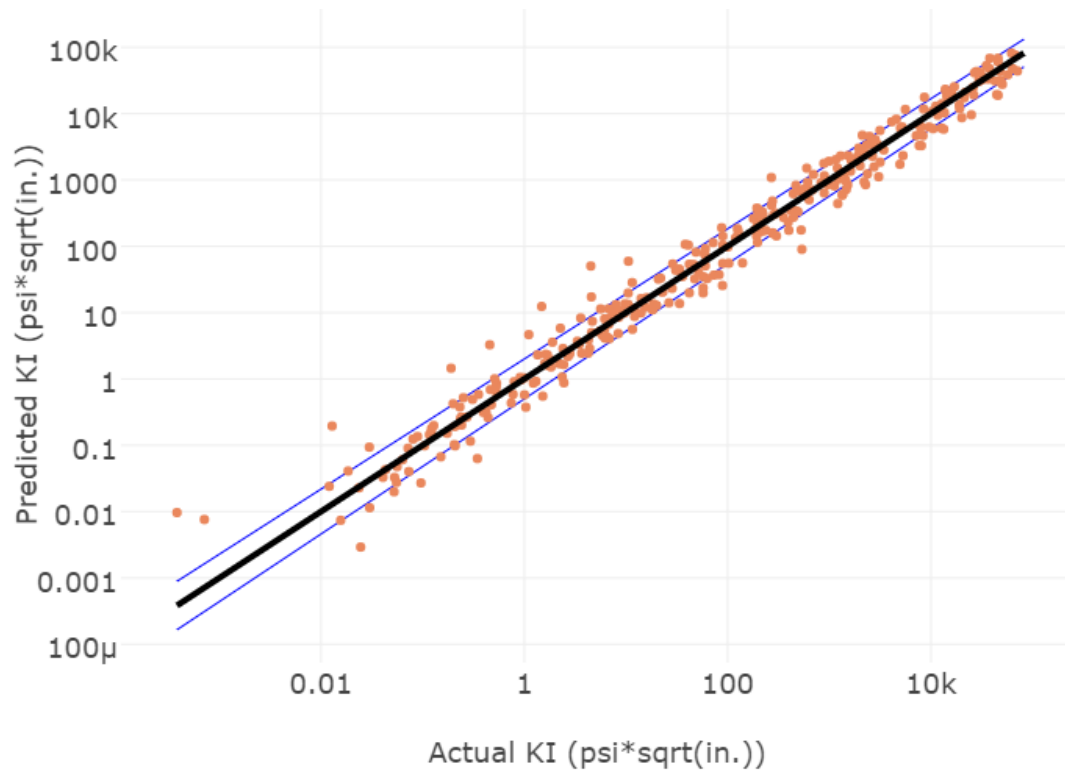


Figure D-23. GE07 SIF model predicted K_I vs. actual K_I : fine-grid, corner crack, surface direction

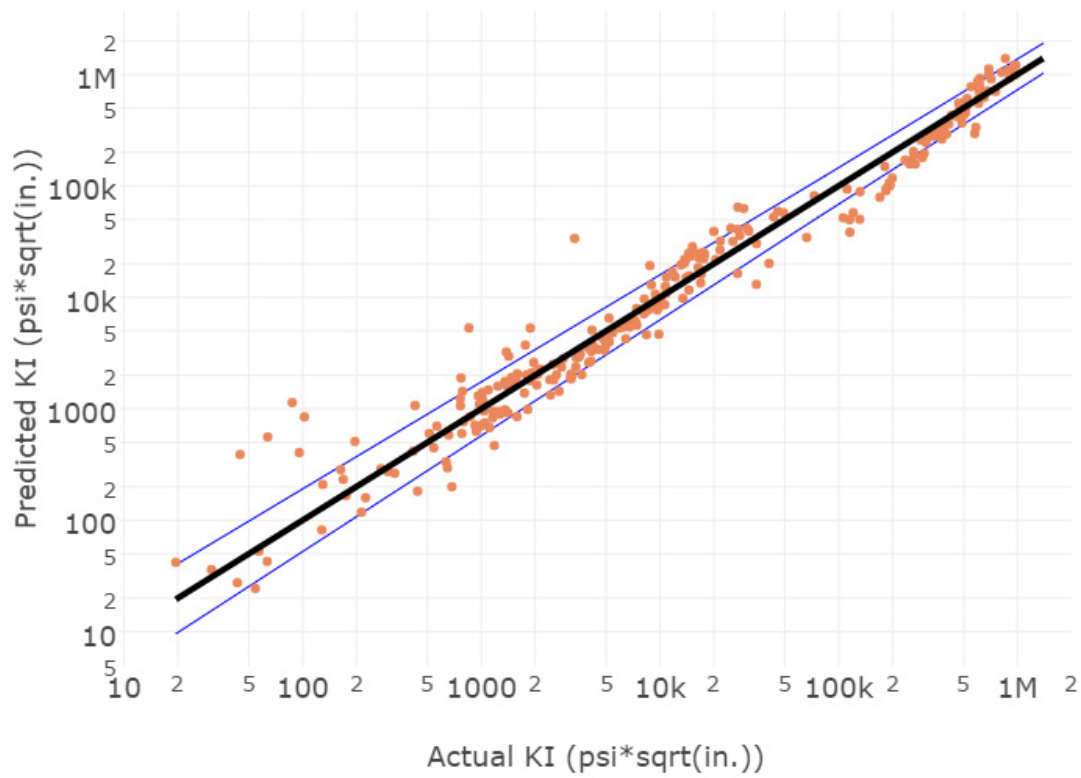


Figure D-24. GE07 SIF model predicted K_I vs. actual K_I : fine-grid, through crack

GE08 SIF Model

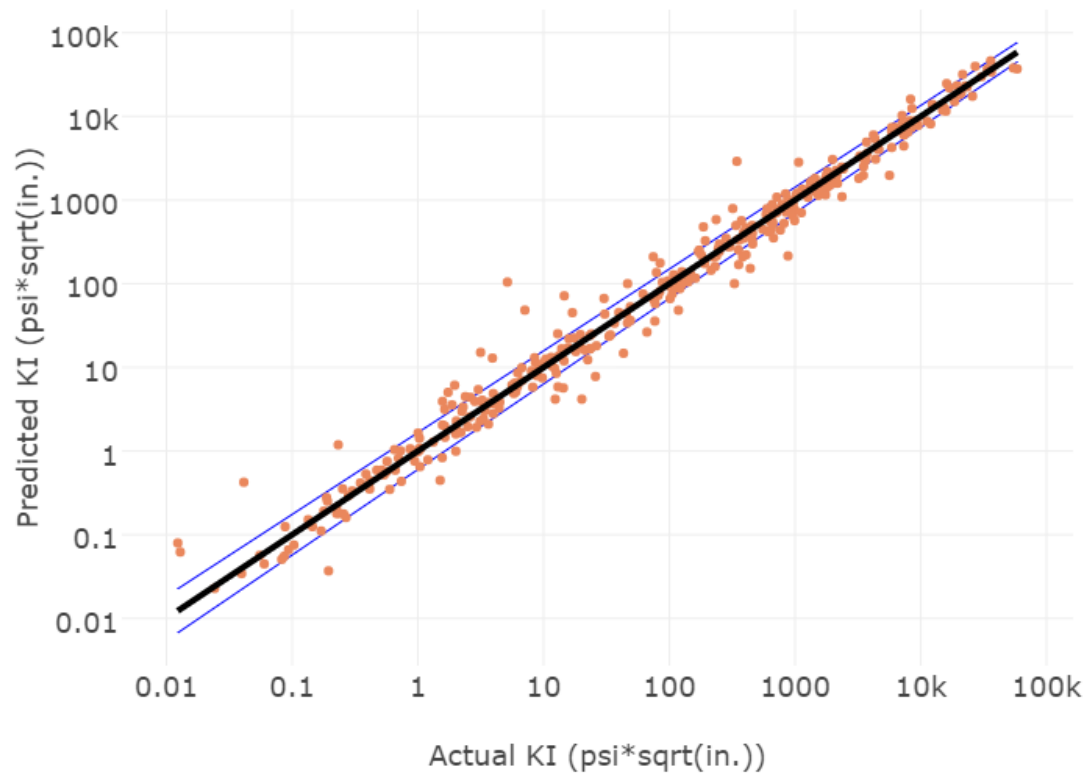


Figure D-25. GE08 SIF model predicted K_I vs. actual K_I : fine-grid, corner crack, depth direction

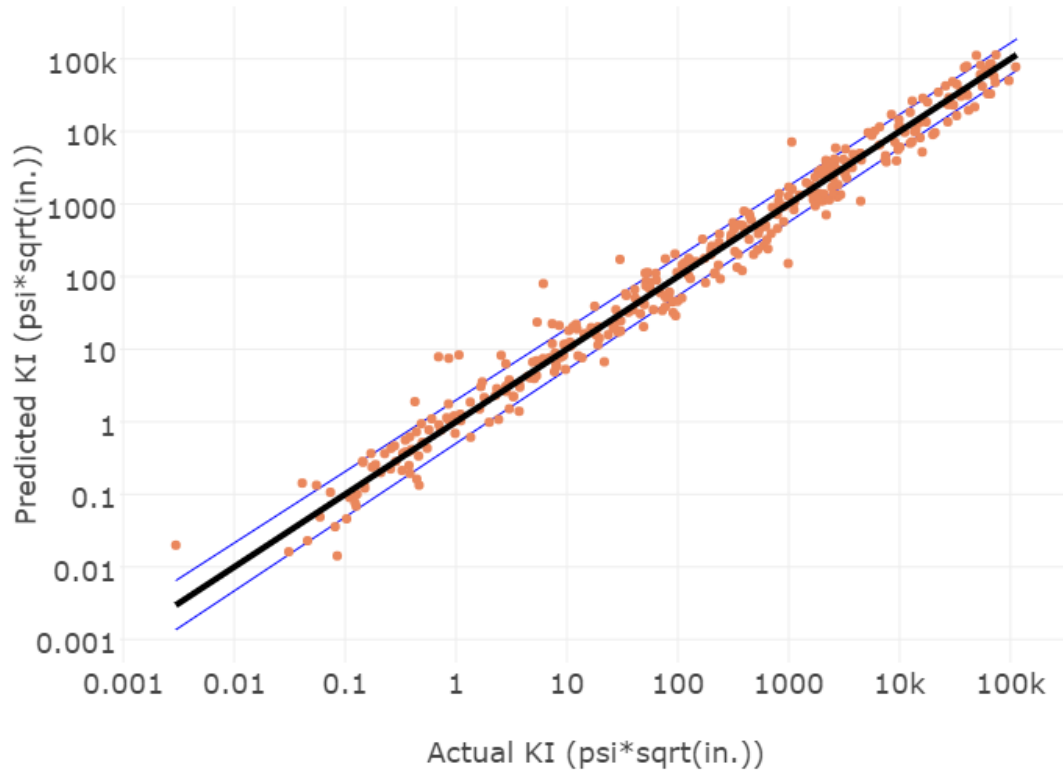


Figure D-26. GE08 SIF model predicted K_I vs. actual K_I : fine-grid, corner crack, surface direction

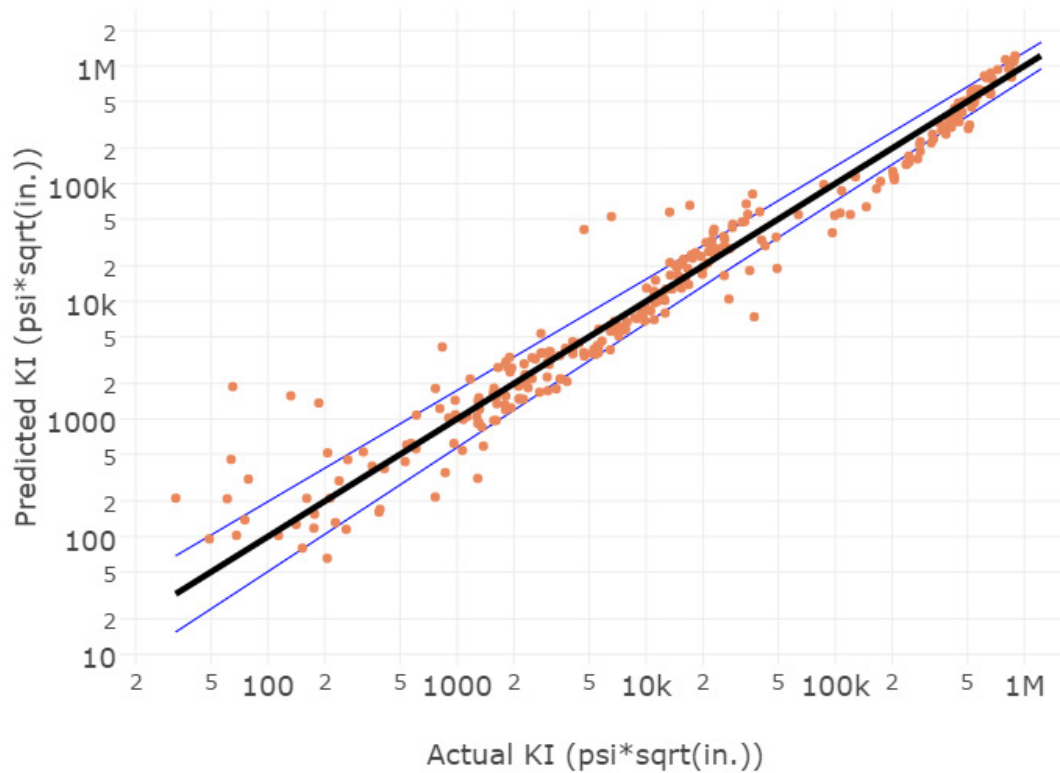


Figure D-27. GE08 SIF model predicted K_I vs. actual K_I : fine-grid, through crack

GE09 SIF Model

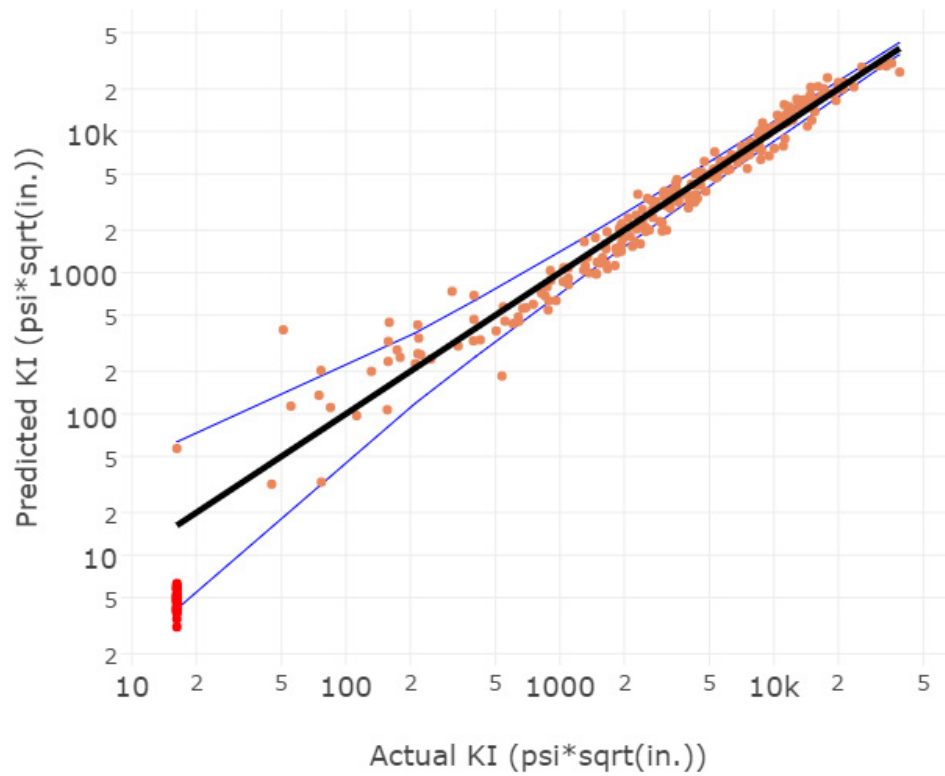


Figure D-28. GE09 SIF model predicted K_I vs. actual K_I : coarse-grid, corner crack, depth direction

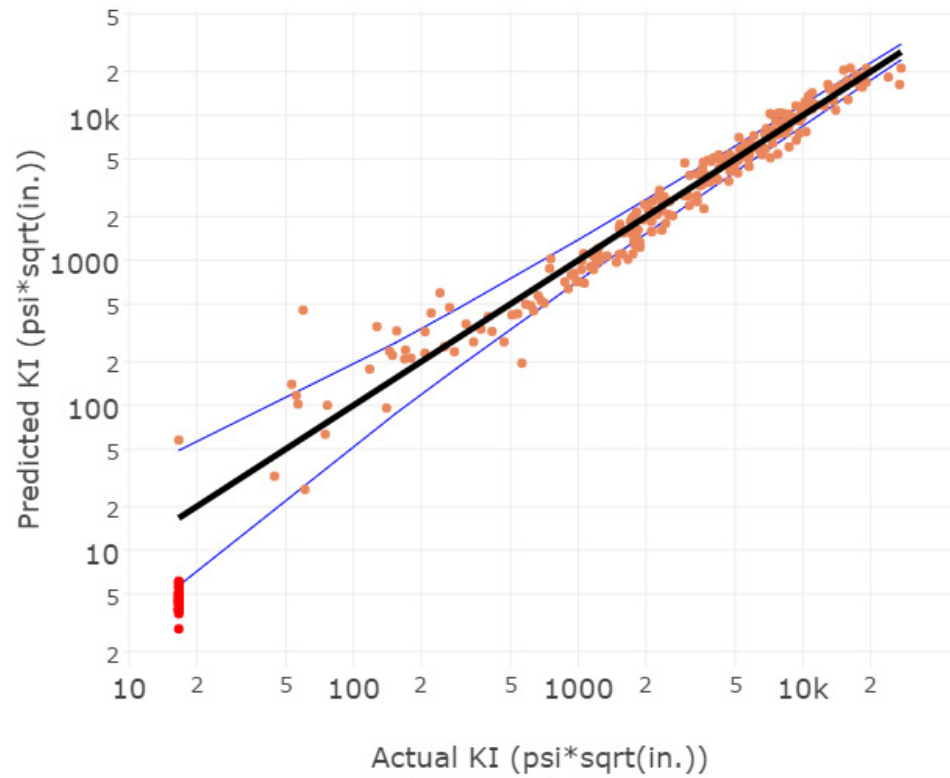


Figure D-29. GE09 SIF model predicted K_I vs. actual K_I : coarse-grid, corner crack, surface direction

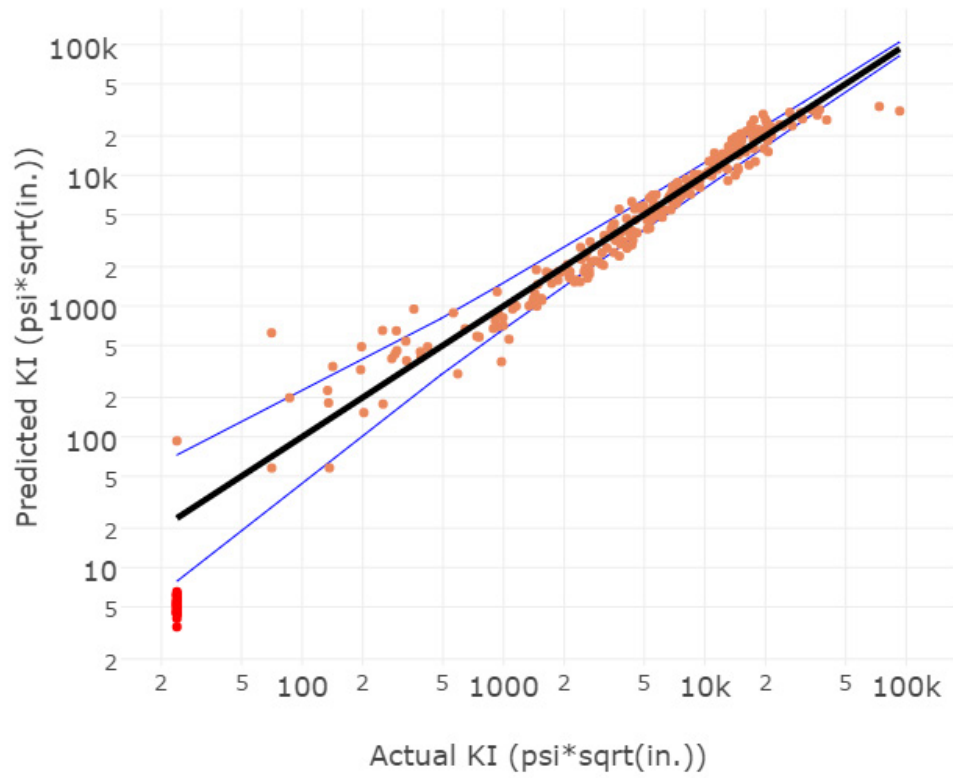


Figure D-30. GE09 SIF model predicted K_I vs. actual K_I : coarse-grid, through crack

GE10 SIF Model

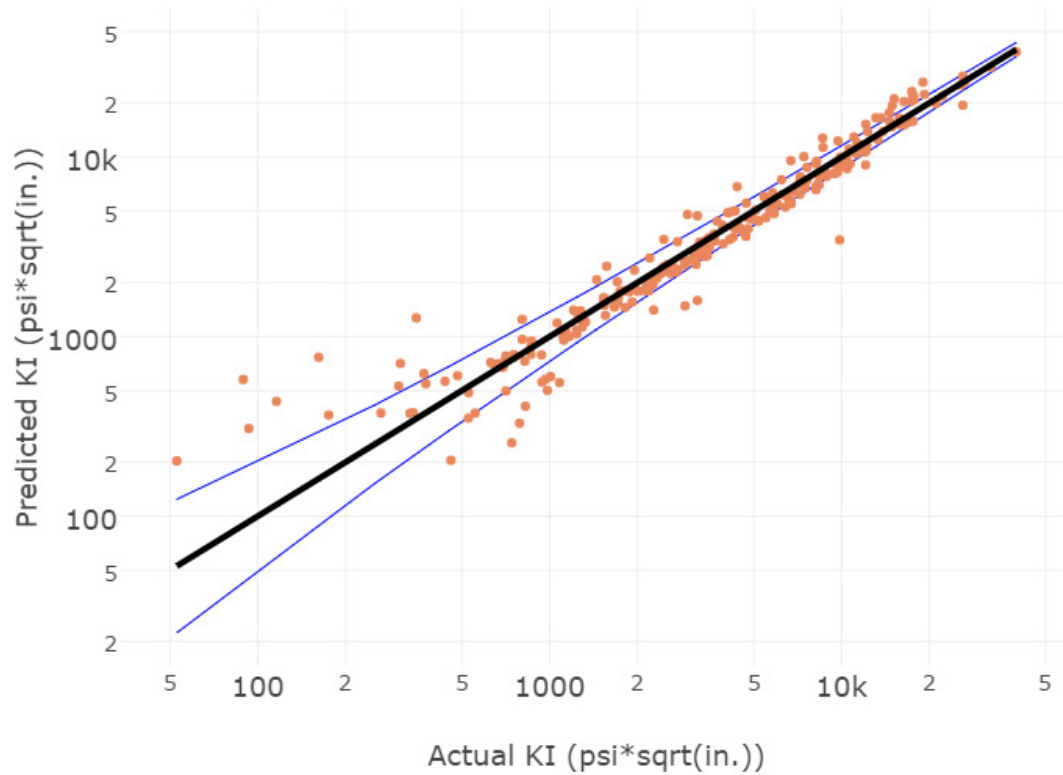


Figure D-31. GE10 SIF model predicted K_I vs. actual K_I : coarse-grid, corner crack, depth direction

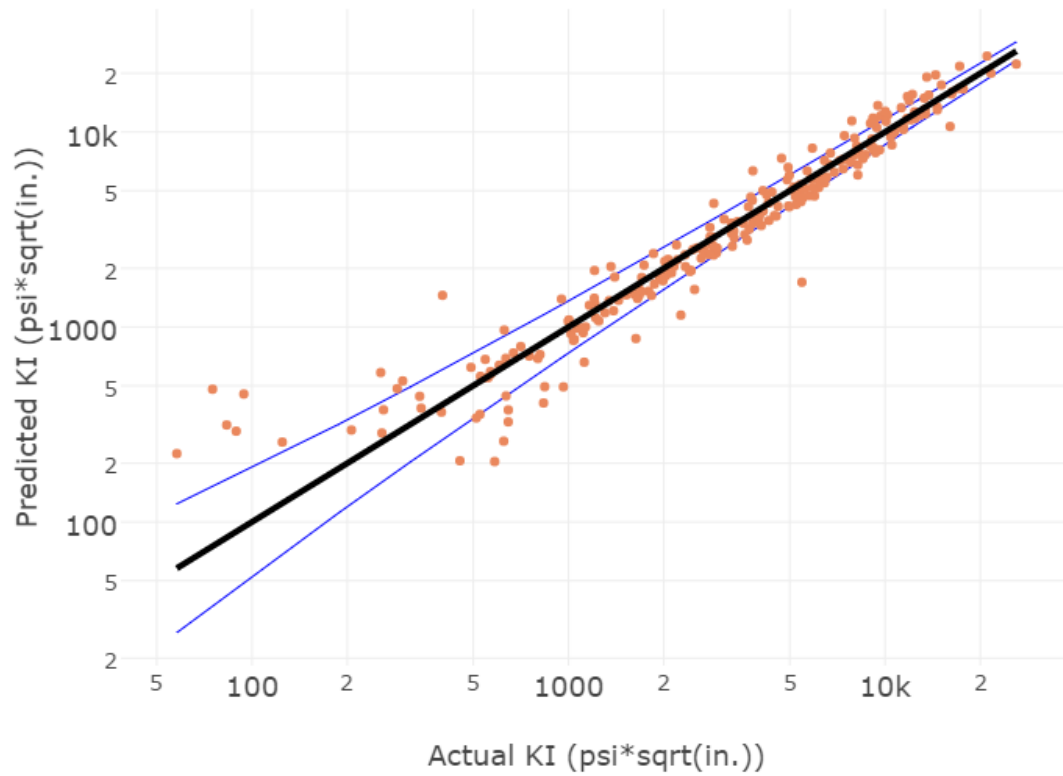


Figure D-32. GE10 SIF model predicted K_I vs. actual K_I : coarse-grid, corner crack, surface direction

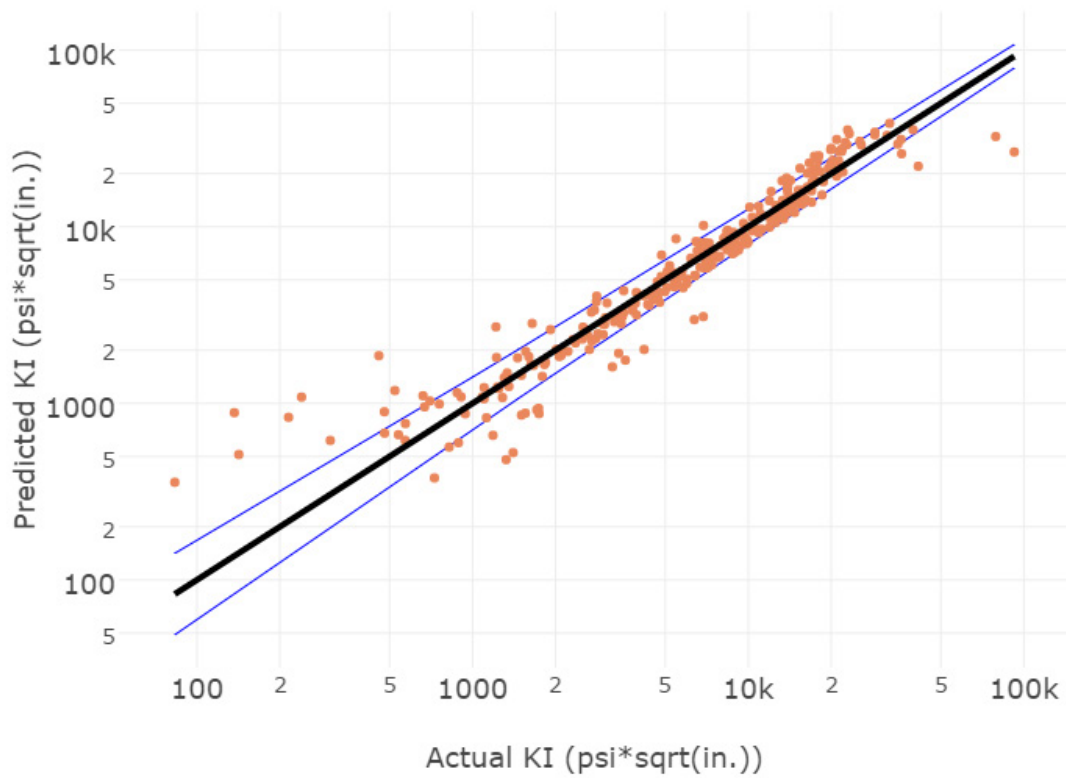


Figure D-33. GE10 SIF model predicted K_I vs. actual K_I : coarse-grid, through crack

SIF Model equations

In the SIF model equations, the variable definitions are defined by the following:

Input variables:

WB	Wing station 3 bending moment (inch-lb)
WT	Wing station 3 torsion (inch-lb)
a	Crack length (inch)
c	Crack depth (inch)
rb	Distance from surface crack origin to nearest edge of plate (inch)

Output variables:

log_KI_depth	Natural log of KI in the depth direction for a corner crack. KI is in (psi sqrt(inch))
log_KI_surf	Natural log of KI in the surface direction for a corner crack. KI is in (psi sqrt(inch))
log_KI_through	Natural log of KI in the surface direction for a through crack. KI is in (psi sqrt(inch))
sigma_depth	Standard deviation of corner crack, depth direction KI predictions.
sigma_surf	Standard deviation of the corner crack, surface direction KI predictions.
sigma_through	Standard deviation of the through crack KI predictions.

Coarse-grid corner crack

GE01 SIF Coarse-grid Model Equation

$$x1 = (WB - -2.98e+05)/1.50e+06$$

$$x2 = (WT - -3.41e+05)/6.89e+05$$

$$x3 = (\log_{10}(a) - -3.25e+00)/2.32e+00$$

$$x4 = (\log_{10}(c) - -3.03e+00)/2.36e+00$$

$$\log_KI_depth = 5.93 + 3.47*x1 + -4.79*x2 + 1.23*x3 + 1.30*x4 + -1.93*x1^2 + 1.49*x1x2 + 1.77*x1x3 + -1.36*x1x4 + 3.72*x2^2 + 0.18*x2x3 + -0.46*x2x4 + -6.70*x3^2 + 12.85*x3x4 + -6.44*x4^2$$

$$\log KI_surf = 5.67 + 3.46*x1 + -4.80*x2 + 3.73*x3 + -1.37*x4 + -1.93*x1^2 + 1.48*x1x2 + 1.85*x1x3 + -1.44*x1x4 + 3.73*x2^2 + 0.22*x2x3 + -0.50*x2x4 + -6.69*x3^2 + 13.15*x3x4 + -7.09*x4^2$$

$$\sigma_depth = \sqrt{\exp(-1.34 + 0.75*\log_KI_depth + -1.22*\log_KI_surf)}$$

$$\sigma_surf = \sqrt{\exp(-1.38 + 0.52*\log_KI_depth + -0.96*\log_KI_surf)}$$

GE02 SIF Coarse-grid Model Equation

$$x1 = (WB - -2.95e+05)/1.49e+06$$

$$x2 = (WT - -3.41e+05)/6.89e+05$$

$$x3 = (\log_{10}(a) - -3.25e+00)/1.90e+00$$

$$x4 = (\log_{10}(c) - -3.03e+00)/1.90e+00$$

$$\log_KI_depth = 4.41 + 6.76*x1 + -3.01*x2 + 0.57*x3 + 1.56*x4 + -3.94*x1^2 + 0.89*x1x2 + 0.60*x1x3 + -0.01*x1x4 + 2.44*x2^2 + 0.16*x2x3 + -0.26*x2x4 + -2.13*x3^2 + 2.65*x3x4 + -0.51*x4^2$$

$$\log KI_surf = 4.29 + 6.75*x1 + -3.01*x2 + 2.64*x3 + -0.81*x4 + -3.96*x1^2 + 0.89*x1x2 + 0.75*x1x3 + -0.15*x1x4 + 2.44*x2^2 + 0.19*x2x3 + -0.29*x2x4 + -2.43*x3^2 + 3.70*x3x4 + -0.82*x4^2$$

$$\sigma_depth = \sqrt{\exp(-0.17 + 0.34*\log_KI_depth + -0.97*\log_KI_surf)}$$

$$\sigma_surf = \sqrt{\exp(-0.38 + 0.68*\log_KI_depth + -1.27*\log_KI_surf)}$$

GE03 SIF Coarse-grid Model Equation

$$x1 = (WB - -2.98e+05)/1.50e+06$$

$$x2 = (WT - -3.41e+05)/6.89e+05$$

$$x3 = (\log_{10}(a) - -3.25e+00)/2.45e+00$$

$$x4 = (\log_{10}(c) - -3.03e+00)/2.44e+00$$

$$\log_KI_depth = 4.63 + 7.00*x1 + -2.39*x2 + 1.86*x3 + 0.68*x4 + -3.56*x1^2 + 0.75*x1x2 + 1.86*x1x3 + -1.92*x1x4 + 1.77*x2^2 + 1.05*x2x3 + -0.93*x2x4 + -7.75*x3^2 + 12.72*x3x4 + -4.85*x4^2$$

$$\log KI_surf = 4.39 + 6.99*x1 + -2.39*x2 + 4.66*x3 + -2.34*x4 + -3.57*x1^2 + 0.73*x1x2 + 1.99*x1x3 + -2.03*x1x4 + 1.76*x2^2 + 0.98*x2x3 + -0.80*x2x4 + -8.27*x3^2 + 13.96*x3x4 + -5.89*x4^2$$

$$\sigma_depth = \sqrt{\exp(2.14 + 0.73*\log_KI_depth + -1.58*\log_KI_surf)}$$

$$\sigma_surf = \sqrt{\exp(2.12 + 0.84*\log_KI_depth + -1.68*\log_KI_surf)}$$

GE04 SIF Coarse-grid Model Equation

$$x1 = (WB - -2.95e+05)/1.49e+06$$

$$x2 = (WT - -3.41e+05)/6.89e+05$$

$$x3 = (\log_{10}(a) - -3.25e+00)/2.12e+00$$

$$x4 = (\log_{10}(c) - -3.03e+00)/2.13e+00$$

$$\log_KI_depth = 3.70 + 8.96*x1 + -0.04*x2 + 2.11*x3 + 0.04*x4 + -4.50*x1^2 + -1.95*x1x2 + 0.99*x1x3 + -0.19*x1x4 + 2.07*x2^2 + -0.41*x2x3 + -0.05*x2x4 + -5.15*x3^2 + 8.67*x3x4 + -3.51*x4^2$$

$$\log KI_surf = 3.44 + 8.94*x1 + -0.04*x2 + 4.46*x3 + -2.40*x4 + -4.49*x1^2 + -1.93*x1x2 + 0.99*x1x3 + -0.20*x1x4 + 2.07*x2^2 + -0.47*x2x3 + 0.01*x2x4 + -5.15*x3^2 + 9.08*x3x4 + -4.06*x4^2$$

$$\sigma_depth = \sqrt{\exp(1.66 + 1.38*\log_KI_depth + -2.13*\log_KI_surf)}$$

$$\sigma_surf = \sqrt{\exp(1.37 + 1.56*\log_KI_depth + -2.28*\log_KI_surf)}$$

GE06 SIF Coarse-grid Model Equation

$$x1 = (WB - -2.98e+05)/1.50e+06$$

$$x2 = (WT - -3.41e+05)/6.89e+05$$

$$x3 = (\log_{10}(a) - -3.25e+00)/2.32e+00$$

$$x4 = (\log_{10}(c) - -3.03e+00)/2.36e+00$$

$$\log_KI_depth = 6.23 + 1.83*x1 + -4.39*x2 + 1.47*x3 + 1.12*x4 + -0.53*x1^2 + 1.09*x1x2 + 1.49*x1x3 + -1.22*x1x4 + 3.58*x2^2 + 0.19*x2x3 + -0.46*x2x4 + -7.07*x3^2 + 13.68*x3x4 + -6.86*x4^2$$

$$\log KI_surf = 5.96 + 1.83*x1 + -4.40*x2 + 3.96*x3 + -1.44*x4 + -0.54*x1^2 + 1.09*x1x2 + 1.55*x1x3 + -1.26*x1x4 + 3.59*x2^2 + 0.23*x2x3 + -0.50*x2x4 + -6.82*x3^2 + 13.45*x3x4 + -7.11*x4^2$$

$$\sigma_depth = \sqrt{\exp(-0.51 + 0.49*\log_KI_depth + -1.06*\log_KI_surf)}$$

$$\sigma_surf = \sqrt{\exp(-1.04 + 0.87*\log_KI_depth + -1.37*\log_KI_surf)}$$

GE07 SIF Coarse-grid Model Equation

$$x1 = (WB - -2.98e+05)/1.50e+06$$

$$x2 = (WT - -3.41e+05)/6.89e+05$$

$$x3 = (\log_{10}(a) - -3.25e+00)/2.43e+00$$

$$x4 = (\log_{10}(c) - -3.03e+00)/2.44e+00$$

$$\log_KI_depth = 3.16 + 10.30*x1 + 0.37*x2 + 2.21*x3 + -0.09*x4 + -4.86*x1^2 + -2.66*x1x2 + 0.41*x1x3 + -0.37*x1x4 + 2.09*x2^2 + -0.30*x2x3 + 0.12*x2x4 + -5.36*x3^2 + 9.30*x3x4 + -3.33*x4^2$$

$$\log KI_surf = 2.90 + 10.30*x1 + 0.38*x2 + 5.05*x3 + -3.11*x4 + -4.86*x1^2 + -2.68*x1x2 + 0.55*x1x3 + -0.49*x1x4 + 2.08*x2^2 + -0.43*x2x3 + 0.32*x2x4 + -5.75*x3^2 + 10.17*x3x4 + -3.98*x4^2$$

$$\sigma_depth = \sqrt{\exp(2.58 + 0.45*\log_KI_depth + -1.27*\log_KI_surf)}$$

$$\sigma_surf = \sqrt{\exp(1.85 + 1.18*\log_KI_depth + -1.91*\log_KI_surf)}$$

GE08 SIF Coarse-grid Model Equation

$$x1 = (WB - -2.98e+05)/1.50e+06$$

$$x2 = (WT - -3.41e+05)/6.89e+05$$

$$x3 = (\log_{10}(a) - -3.25e+00)/2.28e+00$$

$$x4 = (\log_{10}(c) - -3.03e+00)/2.26e+00$$

$$\log_KI_depth = 4.73 + 7.00*x1 + -2.15*x2 + 1.96*x3 + 0.56*x4 + -3.63*x1^2 + 0.52*x1x2 + 1.68*x1x3 + -1.46*x1x4 + 1.93*x2^2 + 0.69*x2x3 + -0.89*x2x4 + -7.86*x3^2 + 13.47*x3x4 + -5.67*x4^2$$

$$\log KI_surf = 4.47 + 6.99*x1 + -2.16*x2 + 4.47*x3 + -1.96*x4 + -3.63*x1^2 + 0.52*x1x2 + 1.70*x1x3 + -1.49*x1x4 + 1.94*x2^2 + 0.68*x2x3 + -0.86*x2x4 + -7.81*x3^2 + 13.68*x3x4 + -6.17*x4^2$$

$$\sigma_depth = \sqrt{\exp(2.48 + -0.10*\log_KI_depth + -0.76*\log_KI_surf)}$$

$$\sigma_surf = \sqrt{\exp(2.33 + -0.11*\log_KI_depth + -0.72*\log_KI_surf)}$$

GE09 SIF Coarse-grid Model Equation

$$x1 = (WB - -2.95e+05)/1.49e+06$$

$$x2 = (WT - -3.41e+05)/6.89e+05$$

$$x3 = (\log_{10}(a) - -3.25e+00)/2.58e+00$$

$$x4 = (\log_{10}(c) - -3.03e+00)/2.46e+00$$

$$\log_KI_depth = 2.72 + 12.09*x1 + -0.39*x2 + 0.63*x3 + 1.68*x4 + -6.97*x1^2 + -0.74*x1x2 + 1.97*x1x3 + -1.65*x1x4 + 1.11*x2^2 + -0.13*x2x3 + 0.12*x2x4 + -3.23*x3^2 + 4.34*x3x4 + -1.13*x4^2$$

$$\log KI_surf = 2.46 + 12.06*x1 + -0.33*x2 + 3.81*x3 + -1.52*x4 + -6.96*x1^2 + -0.75*x1x2 + 2.06*x1x3 + -1.70*x1x4 + 1.06*x2^2 + -0.25*x2x3 + 0.26*x2x4 + -4.44*x3^2 + 6.64*x3x4 + -2.46*x4^2$$

$$\sigma_depth = \sqrt{\exp(1.15 + 0.16*\log_KI_depth + -0.84*\log_KI_surf)}$$

$$\sigma_surf = \sqrt{\exp(0.43 + 0.35*\log_KI_depth + -0.93*\log_KI_surf)}$$

GE010 SIF Coarse-grid Model Equation

$$x1 = (WB - -2.98e+05)/1.50e+06$$

$$x2 = (WT - -3.41e+05)/6.89e+05$$

$$x3 = (\log_{10}(a) - -3.25e+00)/2.39e+00$$

$$x4 = (\log_{10}(c) - -3.03e+00)/2.43e+00$$

$$\log_KI_depth = 5.49 + 5.54*x1 + -3.04*x2 + 1.66*x3 + 0.61*x4 + -2.70*x1^2 + 0.12*x1x2 + 1.76*x1x3 + -1.68*x1x4 + 3.25*x2^2 + -0.40*x2x3 + 0.36*x2x4 + -5.92*x3^2 + 10.78*x3x4 + -4.59*x4^2$$

$$\log KI_surf = 5.23 + 5.54*x1 + -3.02*x2 + 4.37*x3 + -2.32*x4 + -2.71*x1^2 + 0.10*x1x2 + 1.93*x1x3 + -1.85*x1x4 + 3.24*x2^2 + -0.49*x2x3 + 0.49*x2x4 + -6.25*x3^2 + 11.63*x3x4 + -5.36*x4^2$$

$$\sigma_depth = \sqrt{\exp(1.05 + 0.17*\log_KI_depth + -0.86*\log_KI_surf)}$$

$$\sigma_surf = \sqrt{\exp(0.69 + 0.44*\log_KI_depth + -1.07*\log_KI_surf)}$$

Coarse-grid through crack

GE01 SIF Coarse-grid Model Equation

$$x1 = (WB - -2.98e+05)/1.50e+06$$

$$x2 = (WT - -3.41e+05)/6.89e+05$$

$$x3 = (\log_{10}(c) - -3.03e+00)/2.51e+00$$

$$\log_KI_through = 6.43 + 3.62*x1 + -4.22*x2 + 2.11*x3 + -1.59*x1^2 + 1.02*x1x2 + 0.04*x1x3 + 3.36*x2^2 + -0.13*x2x3 + -0.33*x3^2$$

$$\sigma_through = \sqrt{\exp(-1.00 + -0.41*\log_KI_through)}$$

GE02 SIF Coarse-grid Model Equation

$$x1 = (WB - -2.95e+05)/1.49e+06$$

$$x2 = (WT - -3.41e+05)/6.89e+05$$

$$x3 = (\log_{10}(c) - -3.03e+00)/2.72e+00$$

$$\log_KI_through = 4.88 + 6.57*x1 + -3.15*x2 + 2.98*x3 + -3.44*x1^2 + 0.84*x1x2 + 0.07*x1x3 + 2.65*x2^2 + -0.13*x2x3 + 0.15*x3^2$$

$$\sigma_through = \sqrt{\exp(-0.53 + -0.48*\log_KI_through)}$$

GE03 SIF Coarse-grid Model Equation

$$x1 = (WB - -2.98e+05)/1.50e+06$$

$$x2 = (WT - -3.41e+05)/6.89e+05$$

$$x3 = (\log_{10}(c) - -3.03e+00)/2.51e+00$$

$$\log_KI_through = 5.18 + 7.18*x1 + -1.91*x2 + 2.19*x3 + -3.49*x1^2 + 0.56*x1x2 + -0.06*x1x3 + 1.56*x2^2 + -0.12*x2x3 + -0.38*x3^2$$

$$\sigma_through = \sqrt{\exp(1.51 + -0.67*\log_KI_through)}$$

GE04 SIF Coarse-grid Model Equation

$$x1 = (WB - -2.98e+05)/1.50e+06$$

$$x2 = (WT - -3.41e+05)/6.89e+05$$

$$x3 = (\log_{10}(c) - -3.03e+00)/2.51e+00$$

$$\log_KI_through = 4.24 + 9.04*x1 + 0.31*x2 + 2.15*x3 + -4.05*x1^2 + -2.54*x1x2 + 0.41*x1x3 + 1.92*x2^2 + -0.20*x2x3 + -0.31*x3^2$$

$$\sigma_through = \sqrt{\exp(0.87 + -0.59*\log_KI_through)}$$

GE06 SIF Coarse-grid Model Equation

$$x1 = (WB - -2.98e+05)/1.50e+06$$

$$x2 = (WT - -3.41e+05)/6.89e+05$$

$$x3 = (\log_{10}(c) - -3.03e+00)/2.51e+00$$

$$\log_KI_through = 6.69 + 2.02*x1 + -3.88*x2 + 2.42*x3 + -0.33*x1^2 + 0.69*x1x2 + 0.07*x1x3 + 3.28*x2^2 + -0.19*x2x3 + -0.31*x3^2$$

$$\sigma_through = \sqrt{\exp(-2.22 + -0.26*\log_KI_through)}$$

GE07 SIF Coarse-grid Model Equation

$$x1 = (WB - -2.98e+05)/1.50e+06$$

$$x2 = (WT - -3.41e+05)/6.89e+05$$

$$x3 = (\log_{10}(c) - -3.03e+00)/2.51e+00$$

$$\log_KI_through = 3.73 + 10.23*x1 + 0.60*x2 + 2.21*x3 + -4.58*x1^2 + -2.99*x1x2 + 0.00*x1x3 + 2.02*x2^2 + -0.23*x2x3 + -0.13*x3^2$$

$$\sigma_through = \sqrt{\exp(1.83 + -0.64*\log_KI_through)}$$

GE08 SIF Coarse-grid Model Equation

$$x1 = (WB - -2.98e+05)/1.50e+06$$

$$x2 = (WT - -3.41e+05)/6.89e+05$$

$$x3 = (\log_{10}(c) - -3.03e+00)/2.51e+00$$

$$\log_KI_through = 5.23 + 7.18*x1 + -1.64*x2 + 2.36*x3 + -3.36*x1^2 + 0.06*x1x2 + -0.03*x1x3 + 1.71*x2^2 + -0.15*x2x3 + -0.29*x3^2$$

$$\sigma_through = \sqrt{\exp(0.54 + -0.53*\log_KI_through)}$$

GE09 SIF Coarse-grid Model Equation

$$x1 = (WB - -2.95e+05)/1.49e+06$$

$$x2 = (WT - -3.41e+05)/6.89e+05$$

$$x3 = (\log_{10}(c) - -3.03e+00)/2.51e+00$$

$$\log_KI_through = 3.20 + 12.26*x1 + -0.06*x2 + 1.96*x3 + -6.79*x1^2 + -1.03*x1x2 + 0.11*x1x3 + 0.95*x2^2 + -0.05*x2x3 + -0.13*x3^2$$

$$\sigma_through = \sqrt{\exp(0.57 + -0.54*\log_KI_through)}$$

GE010 SIF Coarse-grid Model Equation

$$x1 = (WB - -2.98e+05)/1.50e+06$$

$$x2 = (WT - -3.41e+05)/6.89e+05$$

$$x3 = (\log_{10}(c) - -3.03e+00)/2.51e+00$$

$$\log_KI_through = 6.01 + 5.60*x1 + -2.56*x2 + 2.19*x3 + -2.43*x1^2 + -0.20*x1x2 + 0.02*x1x3 + 2.94*x2^2 + -0.17*x2x3 + -0.30*x3^2$$

$$\sigma_through = \sqrt{\exp(-1.04 + -0.35*\log_KI_through)}$$

Fine-grid corner crack

GE04 SIF Fine-grid Model Equation

$$x1 = (WB - -3.00e+05)/1.50e+06$$

$$x2 = (WT - -3.50e+05)/6.97e+05$$

$$x3 = (\log_{10}(a) - -3.29e+00)/2.46e+00$$

$$x4 = (\log_{10}(c) - -3.29e+00)/2.59e+00$$

$$\log_KI_depth = -4.55 + 7.71*x1 + -1.64*x2 + -14.27*x3 + 27.79*x4 + -4.06*x1^2 + -0.16*x1x2 + 0.68*x1x3 + -0.29*x1x4 + 1.77*x2^2 + -0.21*x2x3 + 0.85*x2x4 + -24.87*x3^2 + 53.58*x3x4 + -31.49*x4^2$$

$$\log KI_surf = -3.98 + 7.72*x1 + -1.74*x2 + 24.73*x3 + -12.63*x4 + -3.97*x1^2 + 0.13*x1x2 + 0.88*x1x3 + -0.83*x1x4 + 1.96*x2^2 + -0.68*x2x3 + 1.00*x2x4 + -41.48*x3^2 + 85.96*x3x4 + -46.90*x4^2$$

$$\sigma_depth = \sqrt{\exp(-3.28 + 0.04*\log_KI_depth + -0.09*\log_KI_surf)}$$

$$\sigma_surf = \sqrt{\exp(-2.46 + -0.06*\log_KI_depth + 0.05*\log_KI_surf)}$$

GE05 SIF Fine-grid Model Equation

GE05 SIF Fine-grid Model Equation

$$x1 = (Radius - 1.64e-01)/7.94e-02$$

$$x2 = (WB - -2.90e+05)/1.49e+06$$

$$x3 = (WT - -3.49e+05)/6.99e+05$$

$$x4 = (\log_{10}(a) - -3.29e+00)/2.24e+00$$

$$x5 = (\log_{10}(c) - -3.30e+00)/2.41e+00$$

$$\log_KI_depth = 2.13 + -0.67*x1 + 9.98*x2 + 2.35*x3 + 2.45*x4 + 0.11*x5 + 0.12*x1^2 + 0.57*x1x2 + 0.04*x1x3 + 0.74*x1x4 + -0.82*x1x5 + -4.55*x2^2 + -3.05*x2x3 + -2.56*x2x4 + 3.29*x2x5 + 0.13*x3^2 + -1.11*x3x4 + 1.59*x3x5 + -2.42*x4^2 + 5.29*x4x5 + -3.91*x5^2$$

$$\log KI_surf = 1.94 + -0.94*x1 + 10.83*x2 + 2.69*x3 + 4.29*x4 + -2.15*x5 + 0.04*x1^2 + 0.89*x1x2 + 0.18*x1x3 + 1.44*x1x4 + -1.49*x1x5 + -5.07*x2^2 + -3.53*x2x3 + -3.90*x2x4 + 4.55*x2x5 + 0.12*x3^2 + -2.02*x3x4 + 2.44*x3x5 + -6.11*x4^2 + 13.94*x4x5 + -8.25*x5^2$$

$$\sigma_depth = \sqrt{\exp(2.48 + -1.82*\log_KI_depth + 0.91*\log_KI_surf)}$$

$$\sigma_surf = \sqrt{\exp(0.68 + 0.13*\log_KI_depth + -0.75*\log_KI_surf)}$$

GE06 SIF Fine-grid Model Equation

$$x1 = (WB - -3.00e+05)/1.48e+06$$

$$x2 = (WT - -3.47e+05)/6.95e+05$$

$$x3 = (\log_{10}(a) - -3.29e+00)/2.47e+00$$

$$x4 = (\log_{10}(c) - -3.29e+00)/2.63e+00$$

$$\begin{aligned} \log_KI_depth = & -2.20 + -0.88*x1 + -0.37*x2 + -13.34*x3 + 27.10*x4 + 2.37*x1^2 + 0.53*x1x2 \\ & + -0.74*x1x3 + 0.88*x1x4 + -0.19*x2^2 + 0.14*x2x3 + 0.38*x2x4 + -26.80*x3^2 + 56.96*x3x4 \\ & + -32.20*x4^2 \end{aligned}$$

$$\begin{aligned} \log KI_surf = & -2.00 + -0.44*x1 + 0.14*x2 + 24.78*x3 + -12.57*x4 + 2.27*x1^2 + 0.57*x1x2 + - \\ & 0.92*x1x3 + 0.16*x1x4 + -0.39*x2^2 + 1.17*x2x3 + -1.18*x2x4 + -24.14*x3^2 + 50.24*x3x4 + \\ & -27.80*x4^2 \end{aligned}$$

$$\sigma_depth = \sqrt{\exp(-3.25 + 0.03*\log_KI_depth + -0.07*\log_KI_surf)}$$

$$\sigma_surf = \sqrt{\exp(-2.69 + -0.13*\log_KI_depth + 0.14*\log_KI_surf)}$$

GE07 SIF Fine-grid Model Equation

$$x1 = (WB - -3.00e+05)/1.50e+06$$

$$x2 = (WT - -3.50e+05)/6.97e+05$$

$$x3 = (\log_{10}(a) - -3.29e+00)/2.46e+00$$

$$x4 = (\log_{10}(c) - -3.29e+00)/2.59e+00$$

$$\begin{aligned} \log_KI_depth = & -6.64 + 10.50*x1 + 1.18*x2 + -13.36*x3 + 26.05*x4 + -4.46*x1^2 + - \\ & 2.29*x1x2 + -0.31*x1x3 + -0.30*x1x4 + 0.74*x2^2 + -1.60*x2x3 + 1.90*x2x4 + -18.76*x3^2 + \\ & 41.30*x3x4 + -23.26*x4^2 \end{aligned}$$

$$\begin{aligned} \log KI_surf = & -6.46 + 11.26*x1 + 1.46*x2 + 23.63*x3 + -12.46*x4 + -4.68*x1^2 + -2.44*x1x2 + \\ & -1.31*x1x3 + -0.03*x1x4 + 0.73*x2^2 + 0.83*x2x3 + -0.95*x2x4 + -27.33*x3^2 + 59.81*x3x4 \\ & + -32.51*x4^2 \end{aligned}$$

$$\sigma_depth = \sqrt{\exp(-2.67 + 0.04*\log_KI_depth + -0.19*\log_KI_surf)}$$

$$\sigma_surf = \sqrt{\exp(-2.15 + -0.10*\log_KI_depth + 0.04*\log_KI_surf)}$$

GE08 SIF Fine-grid Model Equation

$$x1 = (WB - -3.00e+05)/1.50e+06$$

$$x2 = (WT - -3.50e+05)/6.97e+05$$

$$x3 = (\log_{10}(a) - -3.29e+00)/2.46e+00$$

$$x4 = (\log_{10}(c) - -3.29e+00)/2.59e+00$$

$$\begin{aligned} \log_KI_depth = & -5.44 + 9.61*x1 + 0.06*x2 + -15.53*x3 + 28.51*x4 + -4.36*x1^2 + -1.37*x1x2 \\ & + 1.52*x1x3 + -1.97*x1x4 + 0.36*x2^2 + -0.52*x2x3 + 0.97*x2x4 + -18.13*x3^2 + 40.76*x3x4 \\ & + -23.96*x4^2 \end{aligned}$$

$$\begin{aligned} \log KI_surf = & -4.58 + 9.41*x1 + -0.93*x2 + 24.03*x3 + -12.62*x4 + -4.30*x1^2 + -0.42*x1x2 + \\ & 0.07*x1x3 + -1.03*x1x4 + 0.96*x2^2 + -0.71*x2x3 + 0.88*x2x4 + -31.41*x3^2 + 67.31*x3x4 + \\ & -36.73*x4^2 \end{aligned}$$

$$\sigma_depth = \sqrt{\exp(-2.82 + -0.00*\log_KI_depth + -0.10*\log_KI_surf)}$$

$$\sigma_surf = \sqrt{\exp(-2.14 + -0.10*\log_KI_depth + 0.05*\log_KI_surf)}$$

Fine-grid through crack

GE04 SIF Fine-grid Model Equation

$$x1 = (WB - -2.95e+05)/1.49e+06$$

$$x2 = (WT - -3.47e+05)/6.90e+05$$

$$x3 = (\log_{10}(c) - -3.29e+00)/4.29e+00$$

$$x4 = (rb - 2.03e+00)/4.57e+01$$

$$\log_KI_through = 4.59 + 7.94*x1 + -0.46*x2 + -0.11*x3 + 6.76*x4 + -5.59*x1^2 + 1.28*x1x2 + 3.05*x1x3 + -0.56*x1x4 + 0.19*x2^2 + -0.84*x2x3 + 0.01*x2x4 + 3.69*x3^2 + 0.05*x3x4 + -5.86*x4^2$$

$$\sigma_through = \sqrt{\exp(-2.49 + -0.02*\log_KI_through)}$$

GE05 SIF Fine-grid Model Equation

$$x1 = (WB - 1.64e-01)/7.91e-02$$

$$x2 = (WT - -2.95e+05)/1.49e+06$$

$$x3 = (\log_{10}(c) - -3.47e+05)/6.93e+05$$

$$x4 = (rb - -3.29e+00)/2.94e+00$$

$$\log_KI_through = 3.77 + -0.17*x1 + 11.31*x2 + 2.39*x3 + 3.44*x4 + 0.13*x1^2 + -0.40*x1x2 + 0.26*x1x3 + 0.27*x1x4 + -5.01*x2^2 + -3.64*x2x3 + 0.51*x2x4 + 0.74*x3^2 + -0.12*x3x4 + -0.56*x4^2$$

$$\sigma_through = \sqrt{\exp(1.80 + -0.58*\log_KI_through)}$$

GE06 SIF Fine-grid Model Equation

$$x1 = (WB - -2.95e+05)/1.49e+06$$

$$x2 = (WT - -3.47e+05)/6.93e+05$$

$$x3 = (\log_{10}(c) - -3.29e+00)/4.29e+00$$

$$x4 = (rb - 2.01e+00)/2.98e+00$$

$$\log_KI_through = 6.27 + -0.25*x1 + 0.54*x2 + 0.58*x3 + 0.43*x4 + 2.27*x1^2 + -0.99*x1x2 + 0.23*x1x3 + -0.08*x1x4 + 0.21*x2^2 + -0.15*x2x3 + -0.68*x2x4 + 6.29*x3^2 + 0.00*x3x4 + 0.11*x4^2$$

$$\sigma_through = \sqrt{\exp(-3.79 + 0.04*\log_KI_through)}$$

GE07 SIF Fine-grid Model Equation

$$x1 = (WB - -2.95e+05)/1.49e+06$$

$$x2 = (WT - -3.47e+05)/6.93e+05$$

$$x3 = (\log_{10}(c) - -3.29e+00)/4.29e+00$$

$$x4 = (rb - 2.01e+00)/2.98e+00$$

$$\begin{aligned} \log_KI_through = & 1.72 + 11.17*x1 + 3.01*x2 + 1.09*x3 + 0.69*x4 + -5.34*x1^2 + -3.29*x1x2 \\ & + 1.37*x1x3 + -0.41*x1x4 + -0.31*x2^2 + -0.07*x2x3 + 0.27*x2x4 + 4.45*x3^2 + 0.17*x3x4 + \\ & -0.53*x4^2 \end{aligned}$$

$$\sigma_through = \sqrt{\exp(-1.58 + -0.15*\log_KI_through)}$$

GE08 SIF Fine-grid Model Equation

$$x1 = (WB - -2.95e+05)/1.49e+06$$

$$x2 = (WT - -3.47e+05)/6.93e+05$$

$$x3 = (\log_{10}(c) - -3.29e+00)/4.29e+00$$

$$x4 = (rb - 2.01e+00)/2.98e+00$$

$$\begin{aligned} \log_KI_through = & 3.61 + 9.41*x1 + 0.24*x2 + 0.82*x3 + 0.81*x4 + -4.56*x1^2 + -0.86*x1x2 + \\ & 0.81*x1x3 + -0.78*x1x4 + 0.16*x2^2 + 0.01*x2x3 + 0.03*x2x4 + 4.48*x3^2 + -0.16*x3x4 + - \\ & 0.20*x4^2 \end{aligned}$$

$$\sigma_through = \sqrt{\exp(-1.24 + -0.20*\log_KI_through)}$$

Appendix E – Baseline Prediction Initial Conditions

Load spectrum forecast

The forecasted loads are generated as follows. The baseline spectrum consists of 1000 flights categorized into 5 mission types. The most updated mission mix is considered for a forecast. For the results shown here, the baseline mission mix is used. The baseline mission mix, which is the same mission mix represented by the baseline spectrum, is as follows:

Table E-1: Baseline mission mix

MISSION ID	PERCENTAGE
1	20%
2	30%
3	20%
4	20%
5	10%

Each particle draws mission ID (1 to 5) based on the mission mix probabilities. Then, given that mission, the particle draws a random flight from the baseline spectrum, chosen uniformly from all possible flights with the same mission ID. This is done for every future flight (e.g. 1000 flights of forecasting) and every particle (e.g. 1000 particles). Since each flight contains around 200 bending and torque values, this results in a data set of four billion values for a single control point P²IAT run. Since storing these values can be expensive, the code can discard the data once a flight or batch has been processed.

EIFS distribution

The equivalent initial flaw size distribution used for all control points is the same distribution coming from expert knowledge. The distribution is $a_0, c_0 \sim \text{Lognormal}(-5.5, 0.7)$. All cracks are initially set to have an aspect ratio of $a/c = 1$. Depending on the separate stress intensity factor models for depth and surface of a corner crack, the aspect ratio may evolve as a crack grows.

The definition of repair was to set the flaw size distribution back to the as-built distribution. This was set as the calibrated initial flaw size from laboratory data, approximately $a_{0, \text{repair}}, c_{0, \text{repair}} \sim \text{Lognormal}(-8.4, 0.4)$. Note that when an inspection is scheduled, repair may or may not occur depending on the chance of finding a crack. The estimated repaired crack size distribution after an inspection is a combination of the as-built distribution and the current distribution, combined using the estimated probability of detecting a crack. Initially the plastic zone sizes are set equal to the crack lengths (surface and depth), and at repair they are also reset to the as-repaired crack lengths.

Crack growth model and parameters

The material at 9 of the control points (those in the wing skin) is Al 2124-T851 plate. A Walker model was fit to crack growth rate data from the Damage Tolerant Design Handbook [6]. The Walker model fits a crack growth curve that includes the stress ratio effects:

$$\frac{da}{dN} = \frac{C_0}{(1-R)^{m(1-\gamma)}} \Delta K^m \cdot \epsilon_{MAT}$$

The coefficients of the model were fit using linear regression in the log space. The result is a correlated multivariate normal distribution for the three coefficients, along with an independent normal variable representing the residual or model error term. Here the error term ϵ_{MAT} is additive in the log-space, where the linear model is fit. The result is a multiplicative model error in the da/dN space. Values for the model parameters are shown below:

$$\log C_0 \sim \text{Normal}(-8.63, 0.0817) \quad m \sim \text{Normal}(3.211, 0.078)$$

$$m(1 - \gamma) \sim \text{Normal}(0.720, 0.129)$$

$$\text{Corr}(\log C_0, m) = 0.406 \quad \text{Corr}(\log C_0, m(1 - \gamma)) = 0.973$$

$$\text{Corr}(m, m(1 - \gamma)) = 0.247$$

$$\epsilon_{MAT} \sim \text{Normal}(0, 0.035)$$

The material at CP GE09 is Al 7075-T7352 die forging (it is in the main spar). The calculations presented in this report, however, use the crack growth curve for Al 2124-T851 (described above) for all control points, including GE09. A future refinement will use a different crack growth curve for GE09.

Load interaction effects were modelled with a Wheeler retardation model. This model has two additional inputs, the yield stress (set to $\sigma_{yield} = 68.0$ ksi) and retardation exponent ($r_e = 1.3$), which were kept fixed for this demonstration.

Fracture toughness distribution

Fracture toughness is an important material property to accurately characterize since it plays a key role in computing the probability of failure. 16 data points from [7] were considered which corresponded to the manufacturers Alcoa and Reynolds. Only data for the L-T orientation is used, since no data for L-S was available. The crack growth in the surface direction corresponds to the L-T orientation, whereas the depth direction growth would correspond to the L-S orientation. Typically, in the absence of L-S data, L-T data is assumed to be sufficient for both. The resulting fracture toughness distribution is normal with a mean of $29 \text{ ksi}\sqrt{\text{inch}}$ and a standard deviation of about $1.9 \text{ ksi}\sqrt{\text{inch}}$. The fracture toughness distribution is the same for all control points. The fracture toughness is denoted as $K_{Ic} \sim \text{Normal}(29, 1.9)$.

POD model

The probability of detection (POD) model used in this report is the same for all control points. At the time of writing, sufficient data to generate separate POD models for each control point and inspection method were not available. The single POD model was fit based on preliminary data that were available. The POD curve takes as input the crack length in the surface direction and is defined as

$$POD(c) = \Phi \left(\frac{\log(c \cdot 10^3) - m_{POD}}{s_{POD}} \right)$$

Here, $\Phi(x)$ is the normal cumulative distribution function. Note that this choice of function is simply a convenient S-shaped function, and has no inherent probabilistic meaning. The parameters of the POD curve, m_{POD} and s_{POD} , are themselves uncertain and take on a correlated bivariate normal distribution as follows

$$m_{POD} \sim \text{Normal}(4.6, 0.049), \quad s_{POD} \sim \text{Normal}(0.285, 0.027)$$

$$\text{Corr}(m_{POD}, s_{POD}) = -0.142$$

To stabilize the calculations, the value of POD is prevented from reaching the values 0.0 and 1.0 exactly. Rather, the minimum value is 10^{-14} and the maximum is $(1 - 10^{-14})$.

Probability of failure calculation

For each particle in the particle filter, a value of probability of failure (POF) is assigned. Due to machine precision issues, the log of POF is the actual value assigned internally. The probability of failure is determined by comparing an applied stress intensity factor to the fracture toughness distribution. In general, if both the applied SIF and the fracture toughness are uncertain, we have the definition of POF as follows

$$POF = \text{Prob}(K_I > K_{Ic})$$

Several details must be defined to compute a relevant value of POF. First, the value of the applied K_I must reference a crack size and a loading condition. The crack size is of course the current crack size. The loading condition of interest is typically a maximal loading. The max load could be taken from the current estimated loads. In this case, one desires to assess the safety of the average attained loading. An alternative is to take a constant maximum loading that represents a limit-load. With a limit-load, safety is being assessed relative to a potential high load condition, even if achieving such a high load is unlikely. The results in this report use a limit-load condition with the bending and torque values

$$WBR3_{limit} = 1.2 \times 10^6 \text{ inch} \cdot \text{lb}, \quad WTR3_{limit} = -3.5 \times 10^5 \text{ inch} \cdot \text{lb}$$

This condition was chosen as the maximal load condition among all load conditions encountered in the runs of Stick-to-Stress V1. Also, note that the K_I models built for the control points make predictions in $\text{psi}\sqrt{\text{inch}}$, whereas the fracture toughness defined above is in units of $\text{ksi}\sqrt{\text{inch}}$.

In P²IAT, a single particle has a single value of K_I (for a given load condition, defined above). While one could consider also drawing a single value of K_{Ic} for each particle, such an algorithm would require many particles to resolve an POF on the order of 10^{-7} . Instead, P²IAT takes advantage of the known normal distribution of K_{Ic} to compute a probability of failure for each particle as

$$POF = Prob(K_I > K_{Ic}) = \Phi\left(\frac{K_I - 29.0}{1.9}\right)$$

where $\Phi(x)$ is the normal cumulative distribution function and the parameters of the fracture toughness distribution have been plugged in.

The second detail is how to define POF in the presence of the potential for both corner cracks and through cracks. The basic idea is that if a corner crack will quickly transition to a through crack, then the through crack $K_{I,through}$ should be used instead of the corner crack value $K_{I,surf}$. In the following, the stress intensity factors for a corner crack in the surface and depth directions and a through crack are $K_{I,surf}$, $K_{I,depth}$, $K_{I,through}$ respectively. The logic is as follows

- If the particle is a through crack ($a > thickness$), use $K_{I,through}$
- Otherwise,
 - If the surface POF is large ($POF > 10^{-7}$), use $K_{I,surf}$
 - If the depth POF is large ($POF > 10^{-7}$), assume that the crack will transition to a through crack and use $K_{I,through}$
 - Otherwise, the default is to use the surface value $K_{I,surf}$

A third detail is how to compute $\log(POF)$ directly to retain accuracy at very small values of POF . The normal cumulative distribution function is defined as

$$\Phi(x) = \frac{1}{2} \left[1 + \operatorname{erf}\left(\frac{x}{\sqrt{2}}\right) \right]$$

The Faddeeva function is related and can be computed more accurately. It is defined as

$$W(x) = e^{-x^2} (1 - \operatorname{erf}(-ix))$$

where i is the imaginary unit. After some simple algebra, one can compute $\log(\Phi(x))$ directly using W as

$$\log(\Phi(x)) = \log\left(\frac{1}{2}\right) - \frac{1}{2}x^2 + \log\left(W\left(-\frac{ix}{\sqrt{2}}\right)\right)$$

P2IAT Solution Algorithm: The Particle Filter

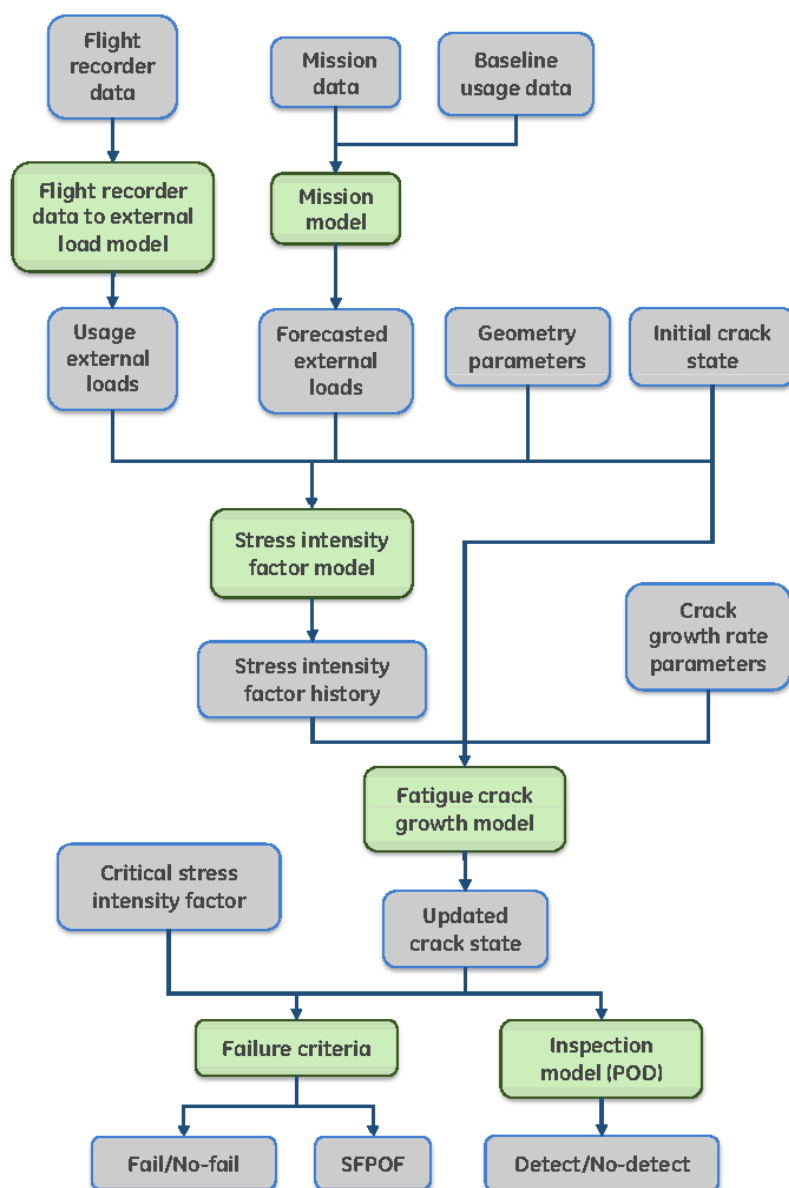


Figure E-1. SAFER-P²IAT Analysis Flow Chart

In P²IAT, uncertainty propagation is performed using a Particle Filter method. The modules and data which are the constituent parts of P²IAT are combined into a network as shown in Figure E-1. Since a probabilistic analysis is used to propagate and update uncertainty through the network, it is referred to as a Dynamic Bayesian Network (DBN) [8]. A DBN can be considered as a series of BNs (Bayesian Networks), one for each step in the data rhythm (either on a per-download basis or a per-flight basis). Based on the Markov assumption, the states of the current BN depend only on the BN at the previous time step and this dependence is generally independent of time [9]. In summary, the abilities to integrate various uncertainties and track

system evolution over time make the DBN a suitable method for building the aircraft digital model.

A more concise and general representation of a Dynamic Bayesian Network is shown in Figure E-2. The network consists of “hidden” or un-measurable states X , which evolve over time according to some relationship. The network can also predict measurable quantities Z at each time step. In analyzing the network, the uncertainty in X is initially described by a prior distribution, propagated through time using the network logic, and updated periodically using measurements of Z .

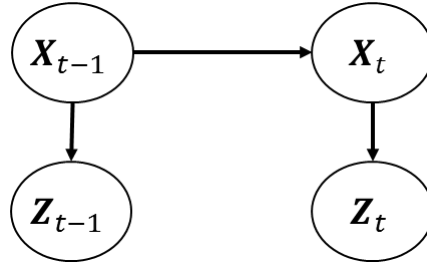


Figure E-2. A Simple Dynamic Bayesian Network

The DBN implemented in P²IAT is essentially the network shown in Figure E-1. Each blue box represents a random variable (or set of variables) in the network. Green boxes represent deterministic transformations which are developed through engineering analysis. These are generally complex and nonlinear. Arriving at this particular network structure, which represents the linking of a suite of engineering analyses, was a major accomplishment of this work. While the structure is valid for many engineering assets, it may also be easily modified or extended within the SAFER-P²IAT framework. The structure itself, along with the definitions of every element within it, are part of the input specifications.

The Kalman filter gives an exact analytical solution for a linear-Gaussian DBN where all inputs are assumed to have Gaussian distributions and all models assumed linear. Extended Kalman filter and unscented Kalman filter (UKF) provide solution for a non-linear DBN by linearizing the state function to the first or second order, but they still assume that all the state variables are Gaussian. A generic DBN framework is needed for SAFER- P²IAT, which requires: 1) handling both discrete and continuous variables; 2) handling various types of continuous variables; 3) handling linear/non-linear functional relationships; and 4) no restrictive assumption of Gaussian distribution for noise term. As a sampling-based generic algorithm, the particle filter (PF), fulfills the requirements above and is chosen to update the DBN in our digital twin model.

A brief introduction to the PF method is given here [10]. In a simplest DBN, assuming that the state variables $\mathbf{X}_k \in \mathcal{R}^m$ at time k evolves from the state variable $\mathbf{X}_{k-1} \in \mathcal{R}^m$ according to:

$$\mathbf{X}_k = f(\mathbf{X}_{k-1}, \mathbf{v}_{k-1})$$

and the measurement $\mathbf{Z}_k \in \mathcal{R}^n$ is obtained according to:

$$\mathbf{Z}_k = h(\mathbf{X}_k, \mathbf{n}_k)$$

where $\mathbf{v}_{k-1} \in \mathbb{R}^m$ and $\mathbf{n}_t \in \mathbb{R}^n$ are vectors of noise terms in the evolution and measurement, correspondingly. The most basic particle filter algorithm is the sequential importance sampling (SIS) [11]. The SIS considers the full joint posterior distribution at time k , $p(\mathbf{X}_{0:k}|\mathbf{Z}_{1:k})$. This distribution is approximated with a weighted set of particles $\{\mathbf{X}_{0:k}^i, \omega_k^i\}_{i=1}^N$. These particles approximate the joint posterior distribution $p(\mathbf{X}_{0:k}|\mathbf{Z}_{1:k})$ by:

$$p(\mathbf{X}_{0:k}|\mathbf{Z}_{1:k}) \approx \sum_{i=1}^N \omega_k^i \delta_{\mathbf{X}_{0:k}^i}$$

where $\delta_{\mathbf{X}_{0:k}^i}$ is a delta function at $\mathbf{X}_{0:k}^i$.

At time step k , the new state \mathbf{X}_k^i for the i -th particle is sampled from the current state $\mathbf{X}_{0:k-1}^i$ and all the observation $\mathbf{Z}_{1:k}$ according to a proposal density:

$$\mathbf{X}_k^i \sim q(\mathbf{X}_k | \mathbf{X}_{0:k-1}^i, \mathbf{Z}_{1:k}) \quad (21)$$

In other words, the new state \mathbf{X}_k^i of the i -th particle at time step k is sampled from a distribution which takes the current state $\mathbf{X}_{0:k-1}^i$ and the observation $\mathbf{Z}_{1:k}$ as parameters.

At time step k , the weight ω_k^i is updated from ω_{k-1}^i by:

$$\omega_k^i \propto \omega_{k-1}^i \frac{p(\mathbf{Z}_k | \mathbf{X}_k^i) p(\mathbf{X}_k^i | \mathbf{X}_{k-1}^i)}{q(\mathbf{X}_k^i | \mathbf{X}_{k-1}^i, \mathbf{Z}_k)} \quad (22)$$

In addition, the initial state \mathbf{X}_0^i from the joint prior distribution of the state variables, and the initial weight ω_0^i for each particle is $1/N$. The key component of the above equation is $p(\mathbf{Z}_k | \mathbf{X}_k^i)$ which is the likelihood of the measurements given the current state. This term updates the particle weights to match the observed data \mathbf{Z}_k .

In practice, iterations of the \mathbf{X}_k^i and ω_k^i equations may lead to particle degeneracy problem, i.e., only a few particles have significant weights. This problem can be solved by resampling: a new set of N particles is generated from the discrete approximation and the weight of each new particle is set as $1/N$ again.

Some variants of the SIS algorithm have been developed in the literature to simplify its implementation, and a most widely used one is the sequential importance resampling (SIR) algorithm [11]. The SIR algorithm takes the state transition distribution $p(\mathbf{X}_k | \mathbf{X}_{k-1}^i)$ as the proposal density distribution $q(\mathbf{X}_k | \mathbf{X}_{0:k-1}^i, \mathbf{Z}_{1:k})$, and conducts resampling at each iteration. \mathbf{X}_k^i and ω_k^i equations reduce to:

$$\mathbf{X}_k^i \sim p(\mathbf{X}_k | \mathbf{X}_{k-1}^i) \quad (23)$$

$$\omega_k^i \propto p(\mathbf{Z}_k | \mathbf{X}_k^i) \quad (24)$$

It is straightforward to implement the SIR algorithm, since it only requires sampling from the distribution $p(\mathbf{X}_k|\mathbf{X}_{k-1}^i)$ and evaluating the likelihood $p(\mathbf{Z}_k|\mathbf{X}_k^i)$. Thus, this algorithm is used to monitor the asset of interest in SAFER- P²IAT.

In the PF method, each particle is passed through the Bayesian Network separately to compute the outputs and likelihoods of that particle. Thus, the method is very scalable and easily run in parallel. The P²IAT framework is designed to take advantage of parallel processing to speed up calculations.

Updating

Bayesian updating in the PF method is performed by likelihood-based resampling. In this method, each sample (set of values for each uncertain parameter) is tagged with its likelihood. The likelihood is the probability that this set of parameter values would produce the data that was actually collected. In the case of inspection data, the data is only detected or not-detected. The likelihood of detecting the crack is calculated directly from the POD curve and the current estimate of the crack state. Thus, particles with cracks that are consistent with the expected inspection results are retained in the update, whereas particles that are inconsistent are discarded. In the case of not-failed data, any particle that suggests certain failure would be discarded.

After updating the parameter distributions, the PF method will often perform a resampling step to ensure that the particles all remain unique. The resampling step can be done with a Gaussian or Epanechnikov kernel [12]. Both of these options preserve the correlation structure and add a small amount of jitter to the particles. Adding “jitter” to a set of particles means that the value of each particle is shifted by a small random number. The shift must be small enough to preserve the distribution represented by the samples, but large enough to inject some diversity into the set of samples which potentially contains multiple identical values.

Resampling is should be performed whenever the number of unique particles becomes too large. A simple metric for this is the effective number of samples

$$N_{eff} = \frac{1}{\sum_{i=1}^N (\omega_k^i)^2}$$

The user can specify a threshold for N_{eff}/N at which resampling occurs, typically around 0.6 to 0.8. A second condition for resampling is that all the weights are approximately equal. If the range of the weights is small, all the particles are essentially equally likely and no resampling needs to occur. This condition is implemented as $|\max(\log(\omega^i)) - \min(\log(\omega^i))| < 10^{-5}$.

The P²IAT framework is quite general and could be set up to incorporate any type of measurement as long as the value can be predicted by some kind of model. For example, if some geometric parameter is initially unknown in a wide range, and some measurement of it is later obtained, the measurement can be used to update the parameter’s distribution. By this time, it may be that the output of interest is correlated with the geometric parameter. In that case, the updating will correctly preserve the correlation.

Overall Single Flight Probability of Failure Calculation

One desired output of the digital twin model is the overall single flight probability of failure (SFPOF). SFPOF at time t_k is defined as the probability of failure at t_k given that failure has not occurred before t_k . Denoting the probability of failure at time k as $P(fail_k)$, we have

$$SFPOF = P(fail_k | \sim fail_{0:k-1})$$

Two tasks are needed to compute SFPOF. First, the Bayesian Network calculates a probability of failure for each particle. These must be aggregated to form an overall probability of failure for the entire network. The mathematically correct way to do this is to take the mean across the particles. Second, the condition of not failing before t_k must be imposed. One way to do this is to supply “not-failed” data to P²IAT to use in updating. While this does give the correct value of SFPOF, it is subject to significant noise when SFPOF is very small. It is important to compute SFPOF accurately for very small values, around 10^{-7} . The method is also noisy when only a few particles have large $P(fail)$.

Another method for computing SFPOF is to perform the aggregation and conditioning at the same time in a post processing step. The post processing can also deal with the case where relatively few particles have large $P(fail)$ by spreading out their influence over time. First, the cumulative distribution function (CDF) of the probability of failure distribution is calculated for every time step. The CDF is discretized in a grid of $P(fail)$, so essentially one computes the fraction of particles above a given level of $P(fail)$ at each time step. For example, if one has $N = 1000$ particles, the computed values would be the number of particles with $P(fail) > 10^{-9}$ which may look like Figure E-3.

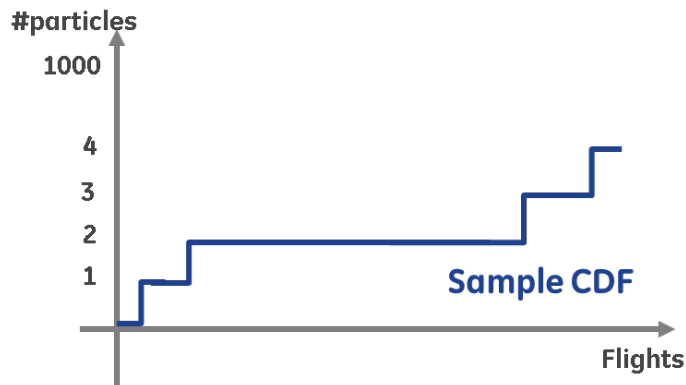


Figure E-3. Cumulative distribution function values at a particular $P(fail)$ level over time

Denoting the n_g grid points of $P(fail)$ as p_f^m , $0 < m < n_g$, the values can be expressed as:

$$F_{p_f}(p_f^m, t_k), \quad 0 < m < n_g$$

Next, the CDF values over time are smoothed. This step fixes the issue of relatively few particles failing over the course of a run. The result may look like Figure E-4. The benefit of smoothing is that at time steps between individual particle failures, there is now a fractional particle which has failed, leading to smoother SFPOF curves. Investigating linear and cubic smoothing showed little difference, so linear smoothing is used. The result is expressed

$$\widetilde{F}_{p_f}(p_f^m, t_k), \quad 0 < m < n_g$$

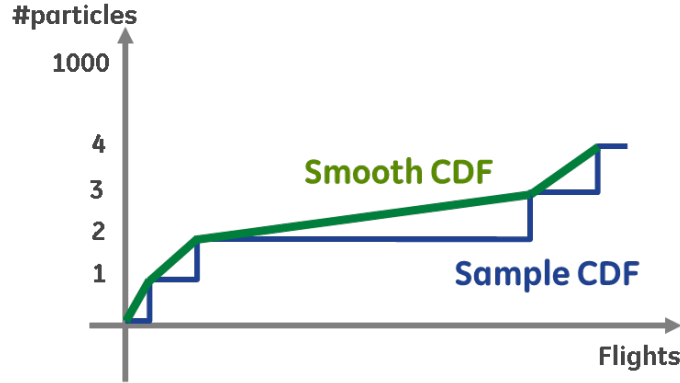


Figure E-4. Smoothed CDF values over time

By aggregating the CDF value curves for each value in the grid of $P(fail)$, one can reconstruct the CDF of $P(fail)$ at a single flight. Note that the standard empirical CDF (constructed from the particles) at a given flight would have values defined only at the points $\frac{1}{N}, \frac{2}{N}, \frac{3}{N}, \dots$. The smoothed CDF, by contrast, may have fractions of particles and thus may have points at, for example, $\frac{0.8}{N}, \frac{1.3}{N}, \dots$

The CDF can then be modified to account for the conditioning on not-failure before time t_k . This is done by weighting the CDF by $(1 - P(fail))$, assuming that previously failed particles remain failed. Since the weight is only small for $P(fail)$ close to 1 (and in this application most particles will have $P(fail) \ll 1$), one can essentially just remove particles with large $P(fail)$. Reflecting the fact that a pool of size N should not retain particles with $P(fail) > 1/N$, the threshold for removing particles is set to $1/N$.

Finally, after the CDF has been smoothed in time and truncated, the mean of the $P(fail)$ distribution can be computed using the CDF:

$$SFPOF_k = E[p_f] = \int_{-\infty}^{1/N} [1 - \widetilde{F}_{p_f}(q, t_k)] dq$$

The integration is done using Simpson's rule for the pointwise values computed for the CDF. The steps to compute the overall SFPOF can be summarized as follows.

1. Compute values of the CDF of the $P(fail)$ distribution for a grid p_f^m for each time step.
2. Smooth the CDF values over time.
3. At a single time step, get the smoothed CDF values and truncate them to apply the no-fail conditioning.
4. Compute the mean of the resulting CDF, which is SFPOF at that time step.

This approach has the benefit that one can compute time-smoothed, conditioned means (or other statistics) at any time via post-processing while preserving the un-conditional samples in the P²IAT solution.

Appendix F – Control Point Baseline Predictions

GE01 Baseline Predictions

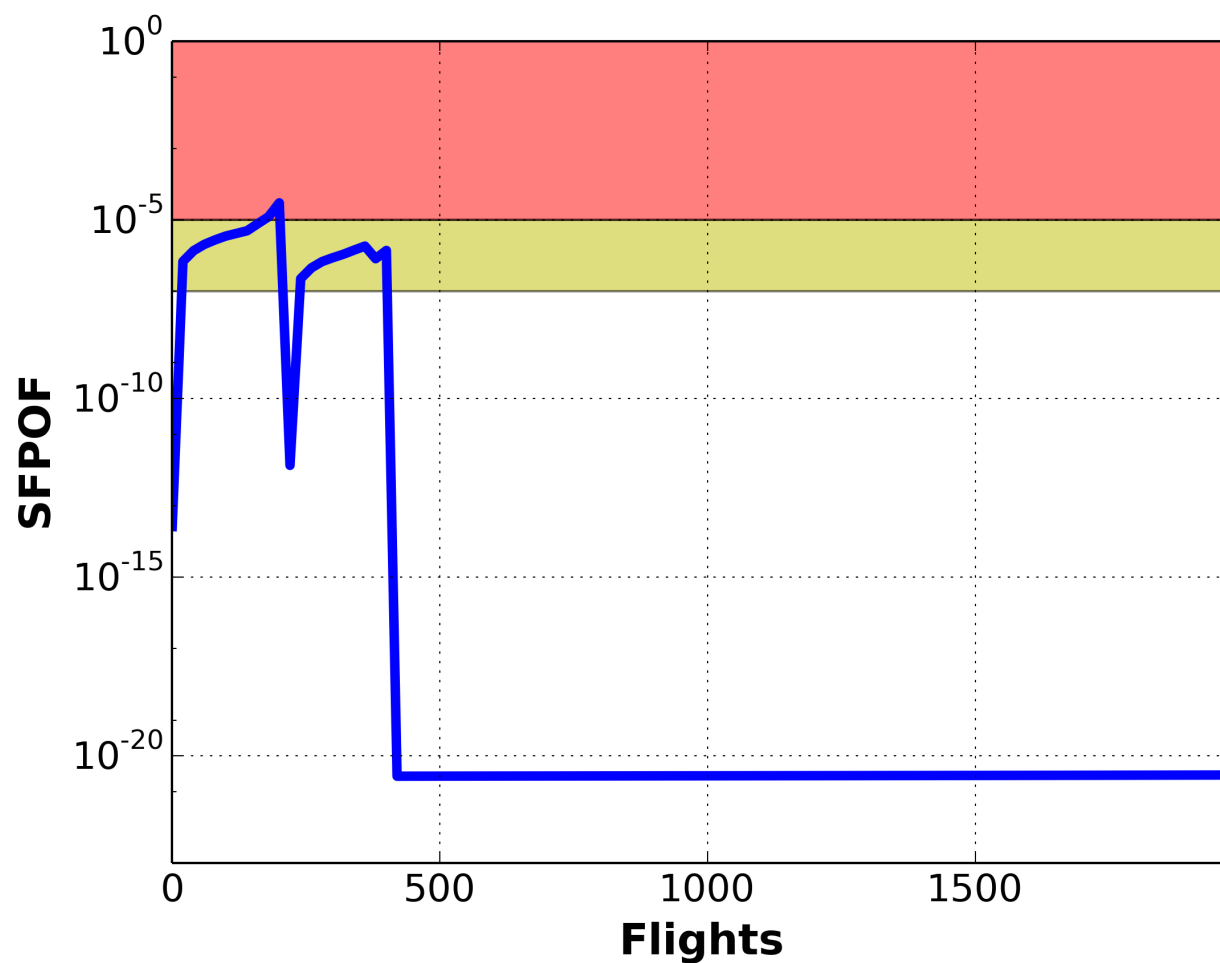


Figure F-1. GE01 SFPOF baseline forecast prediction

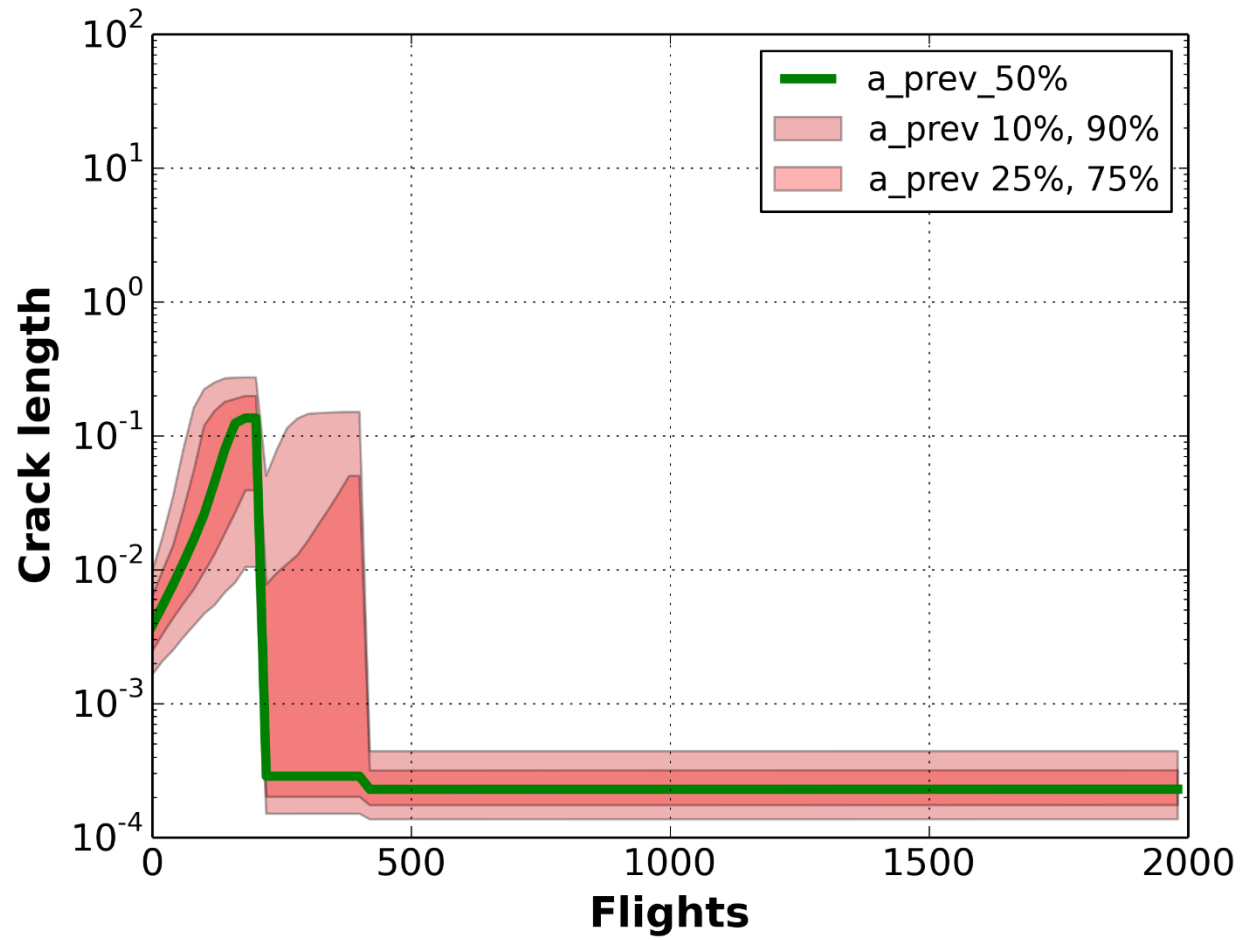


Figure F-2. GE01 baseline crack length predictions - depth direction

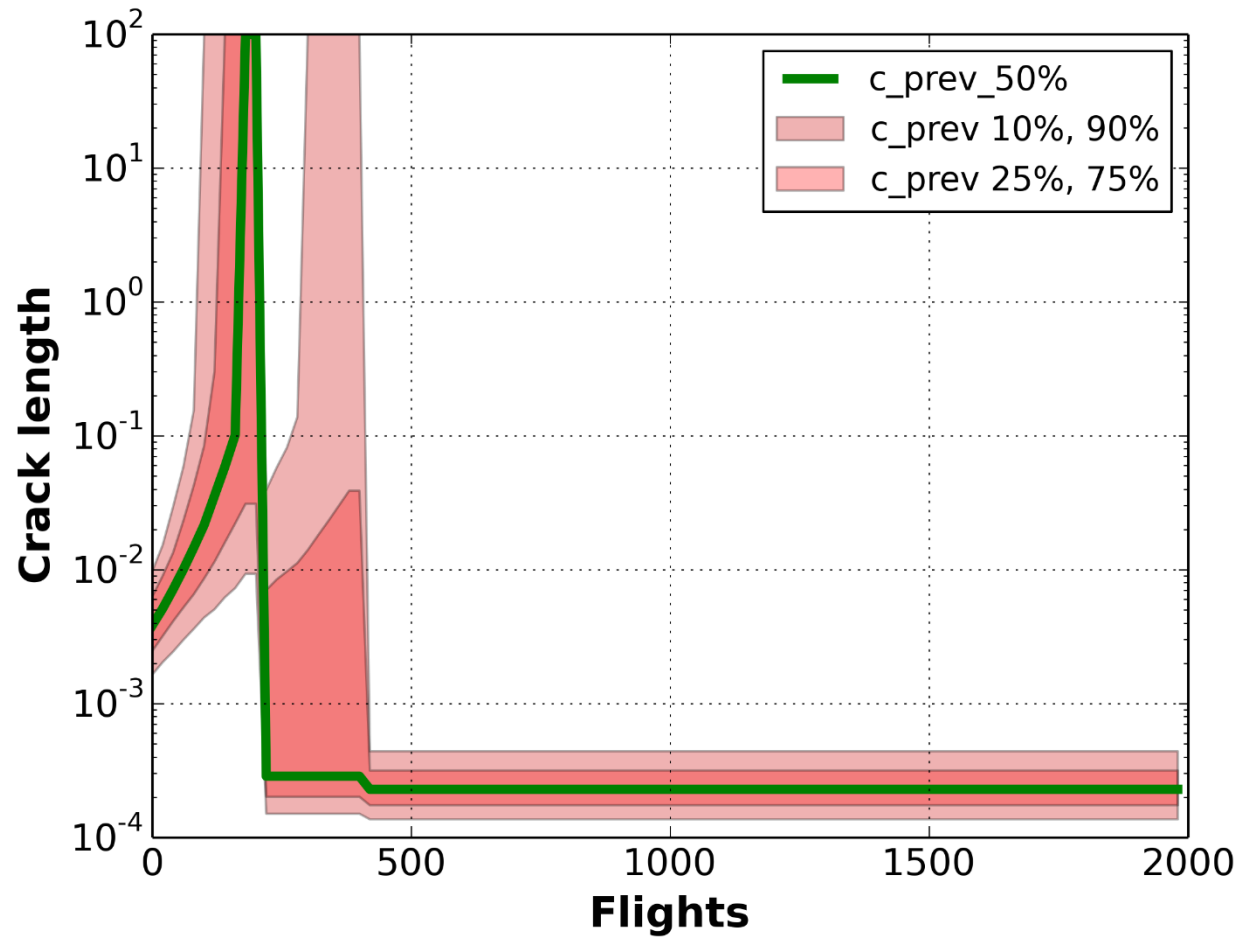


Figure F-3. GE01 baseline crack length predictions - surface direction

GE02 Baseline Predictions

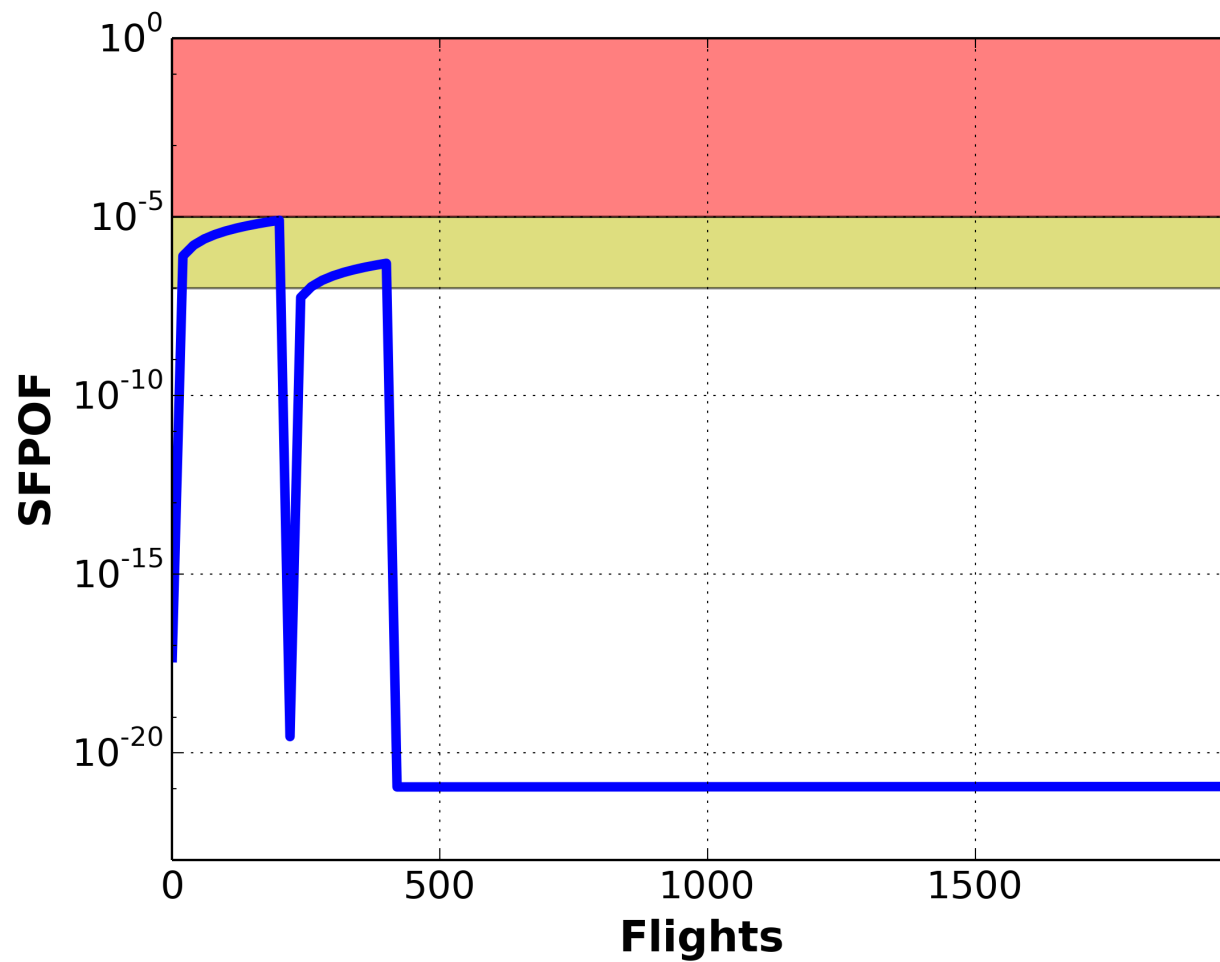


Figure F-4. GE02 SFPOF baseline forecast prediction

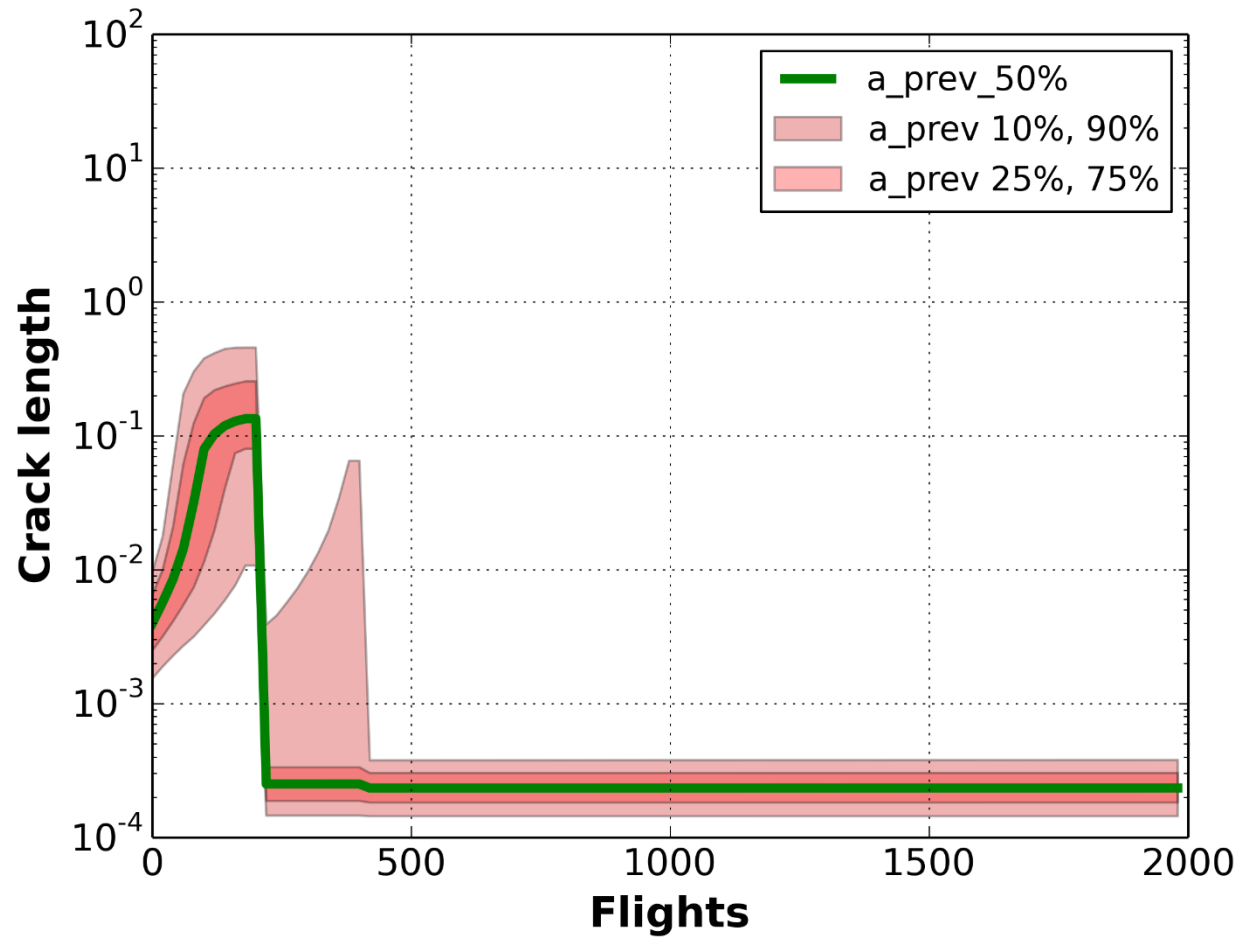


Figure F-5. GE02 baseline crack length predictions - depth direction

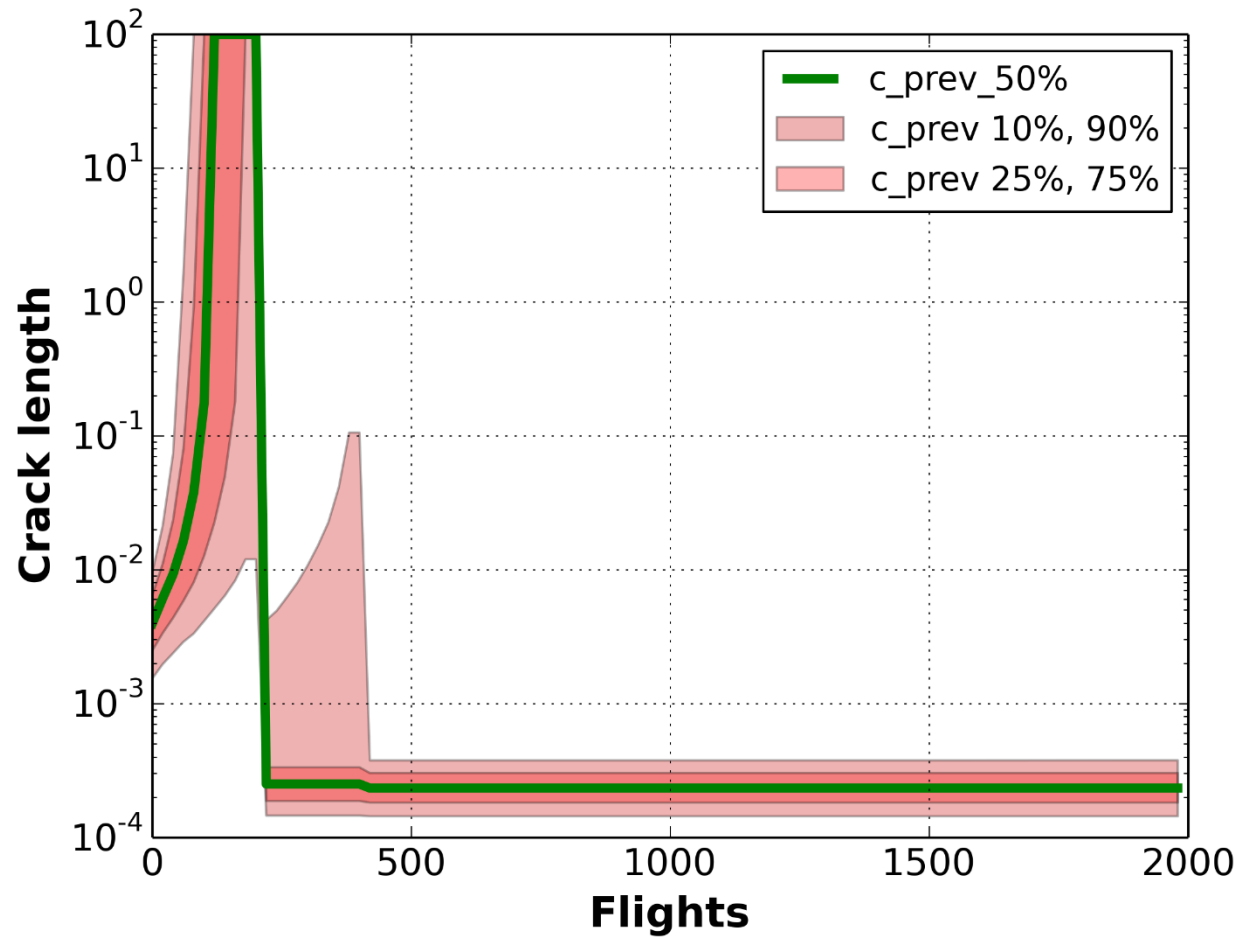


Figure F-6. GE02 baseline crack length predictions - surface direction

GE03 Baseline Predictions

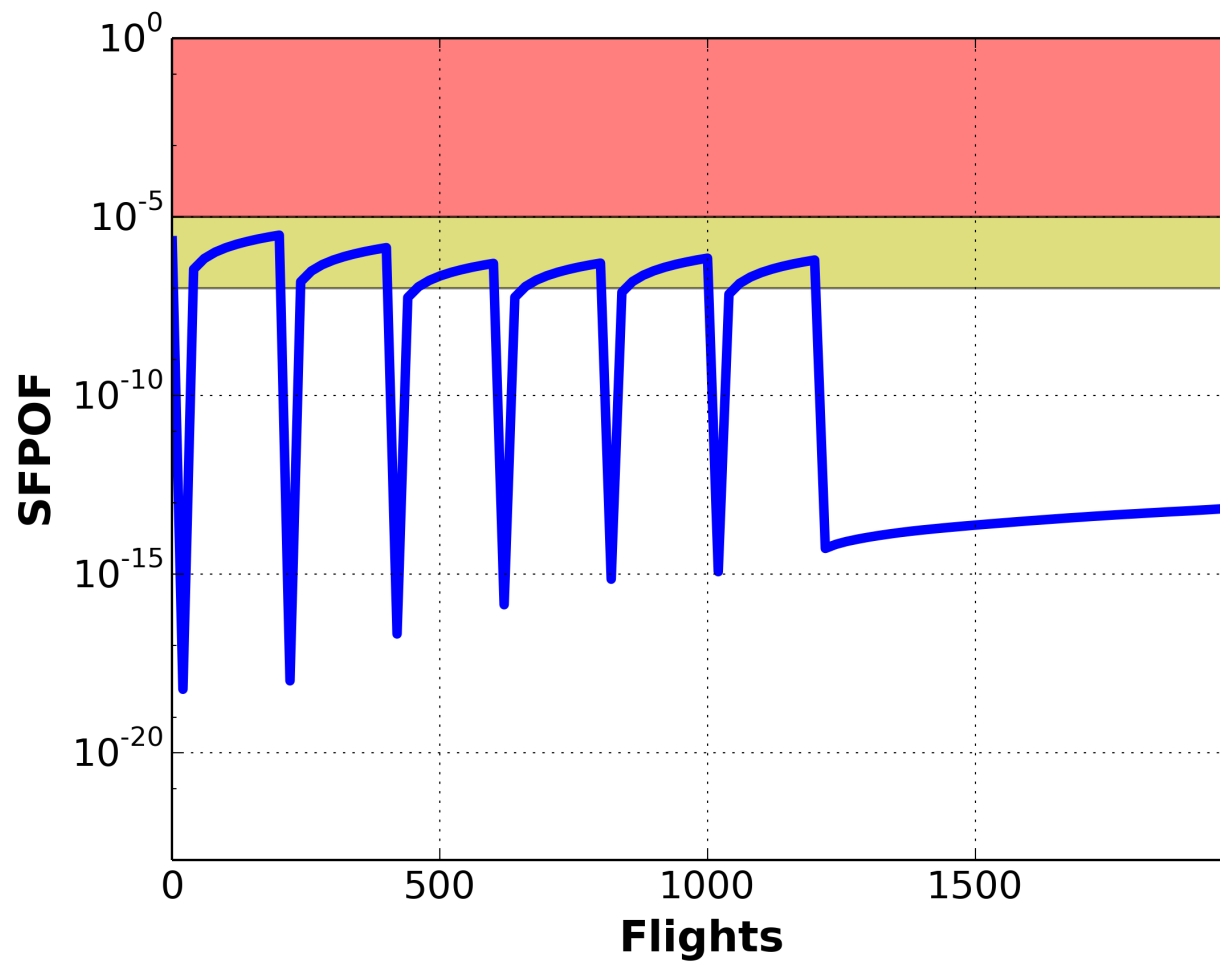


Figure F-7. GE03 SFPOF baseline forecast prediction

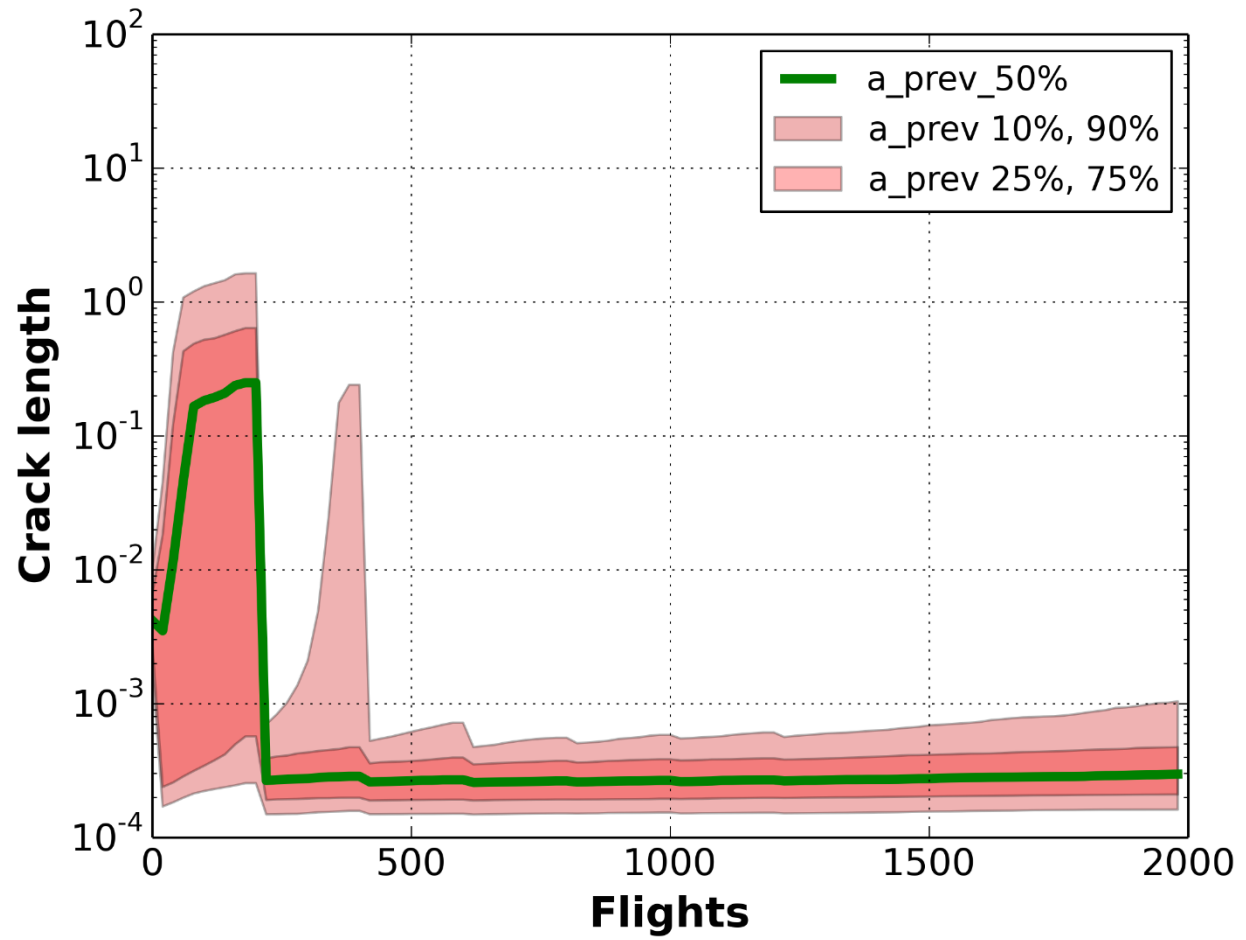


Figure F-8. GE03 baseline crack length predictions - depth direction

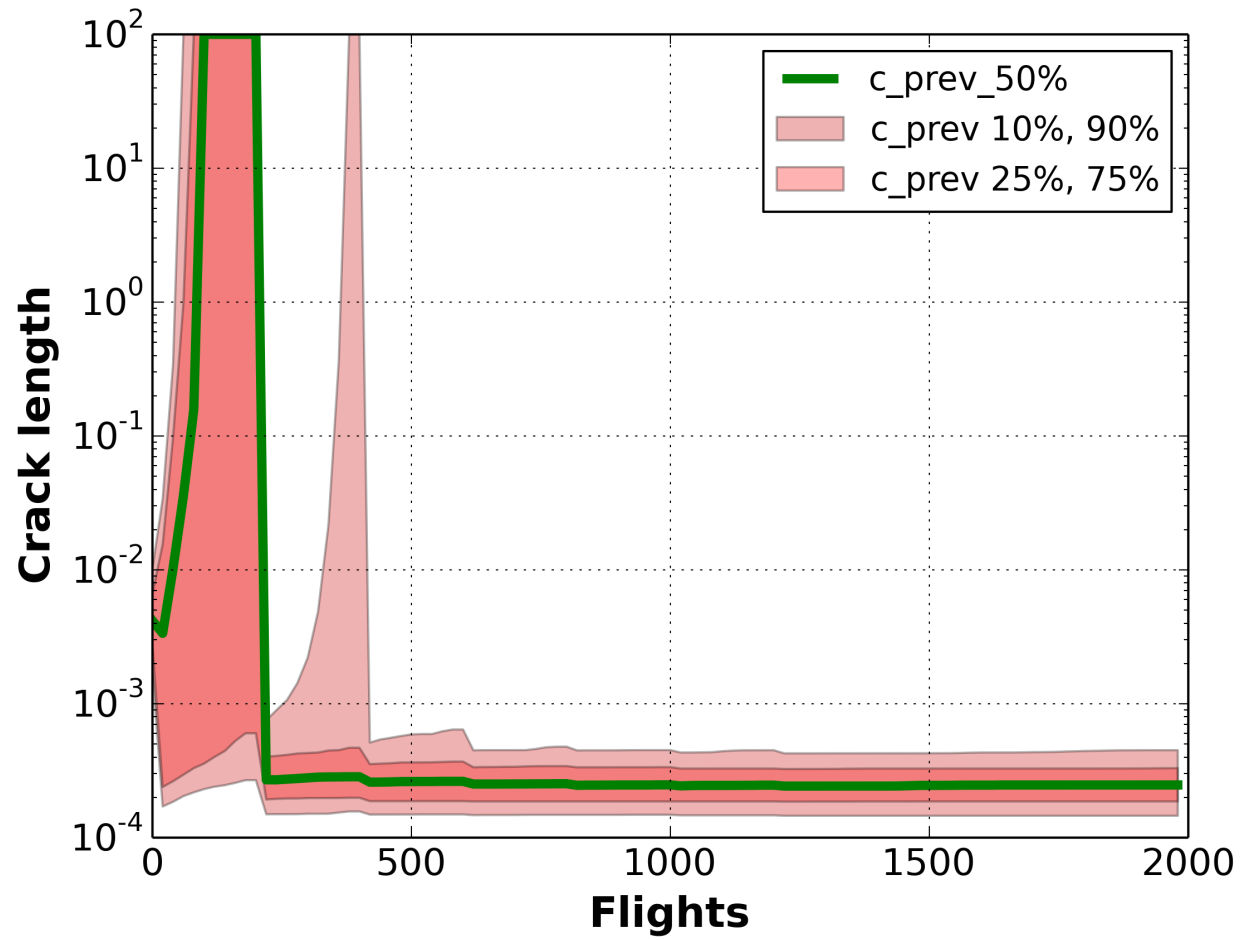


Figure F-9. GE03 baseline crack length predictions - surface direction

GE04 Baseline Predictions

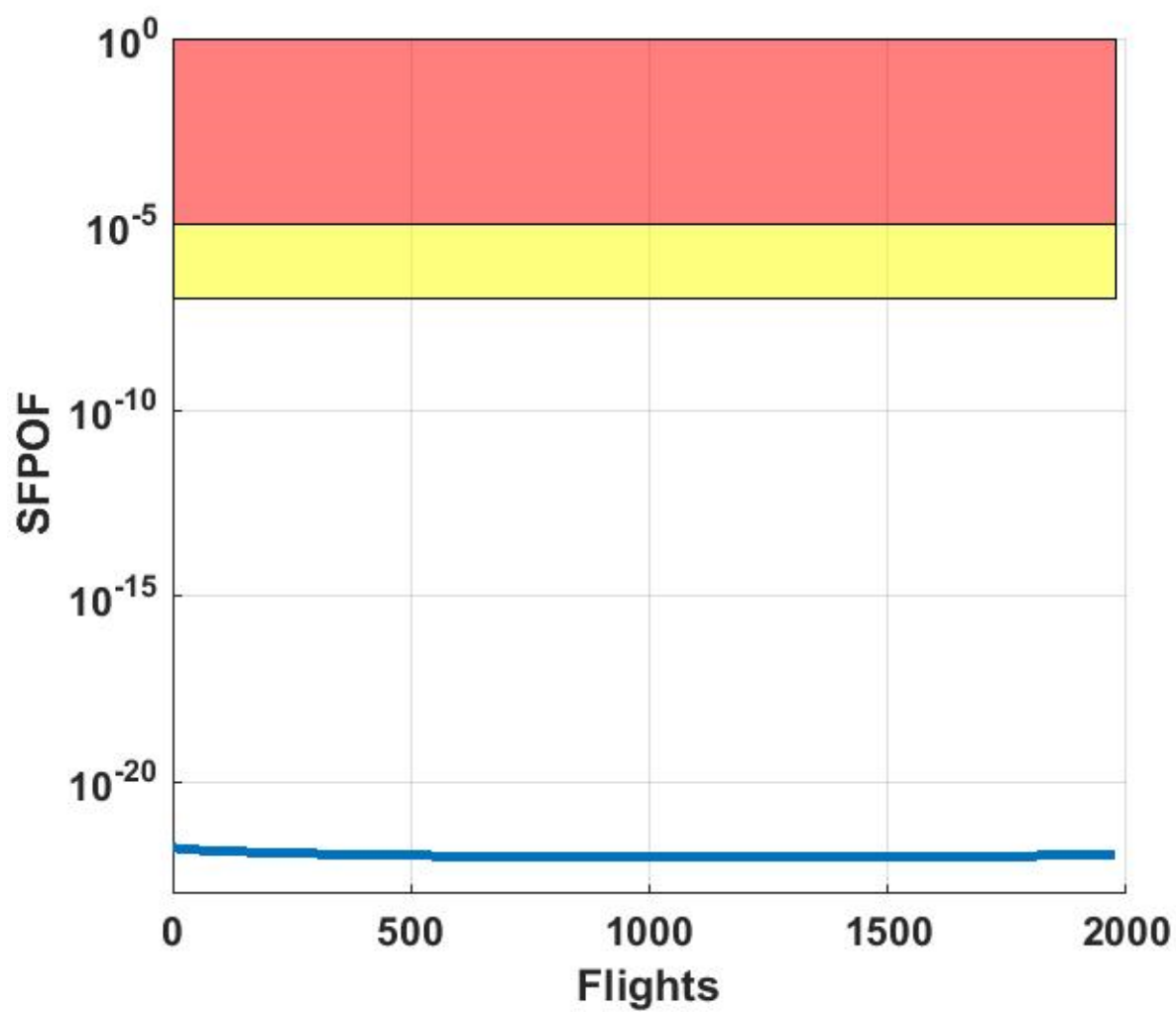


Figure F-10. GE04 SFPOF baseline forecast prediction

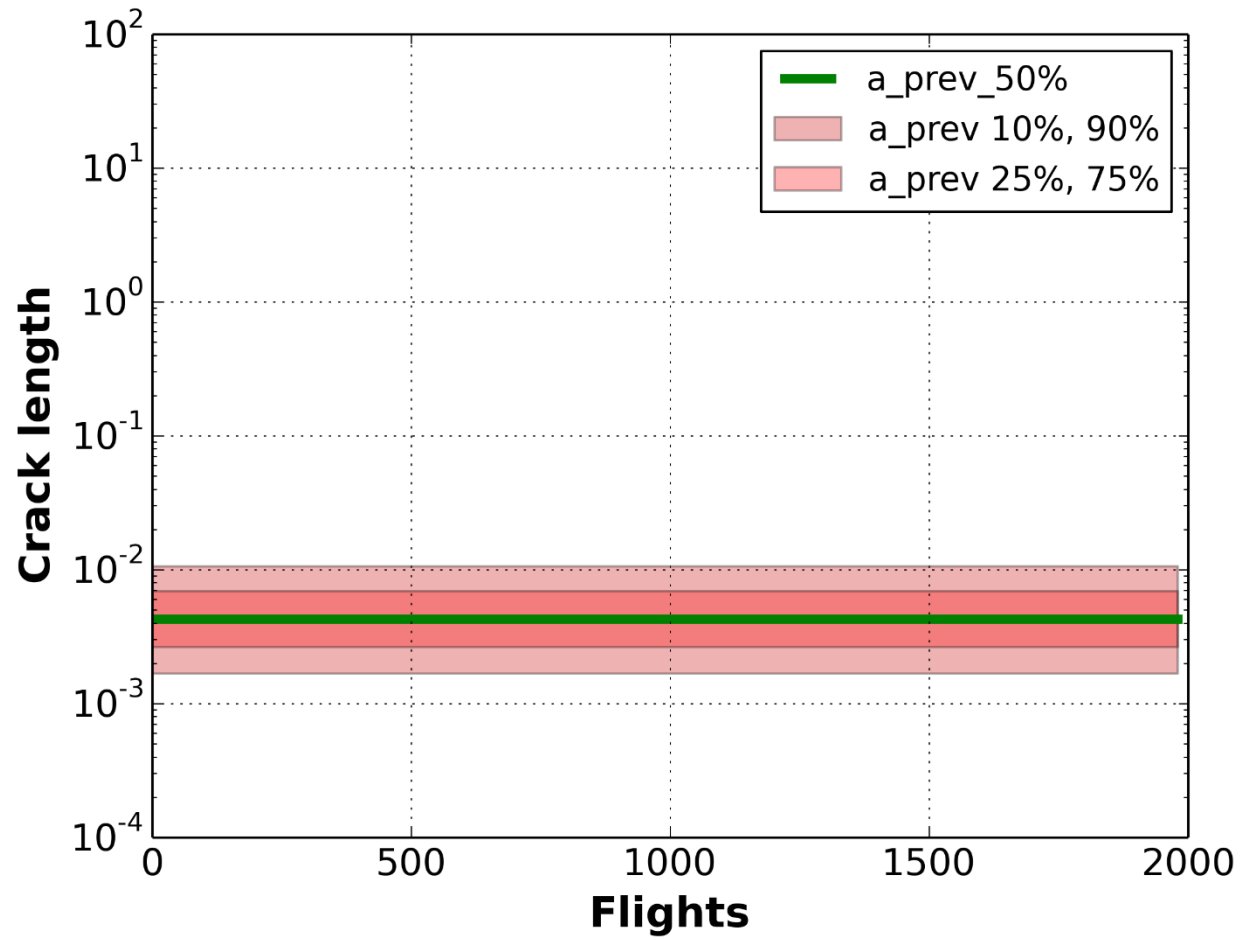


Figure F-11. GE04 baseline crack length predictions - depth direction

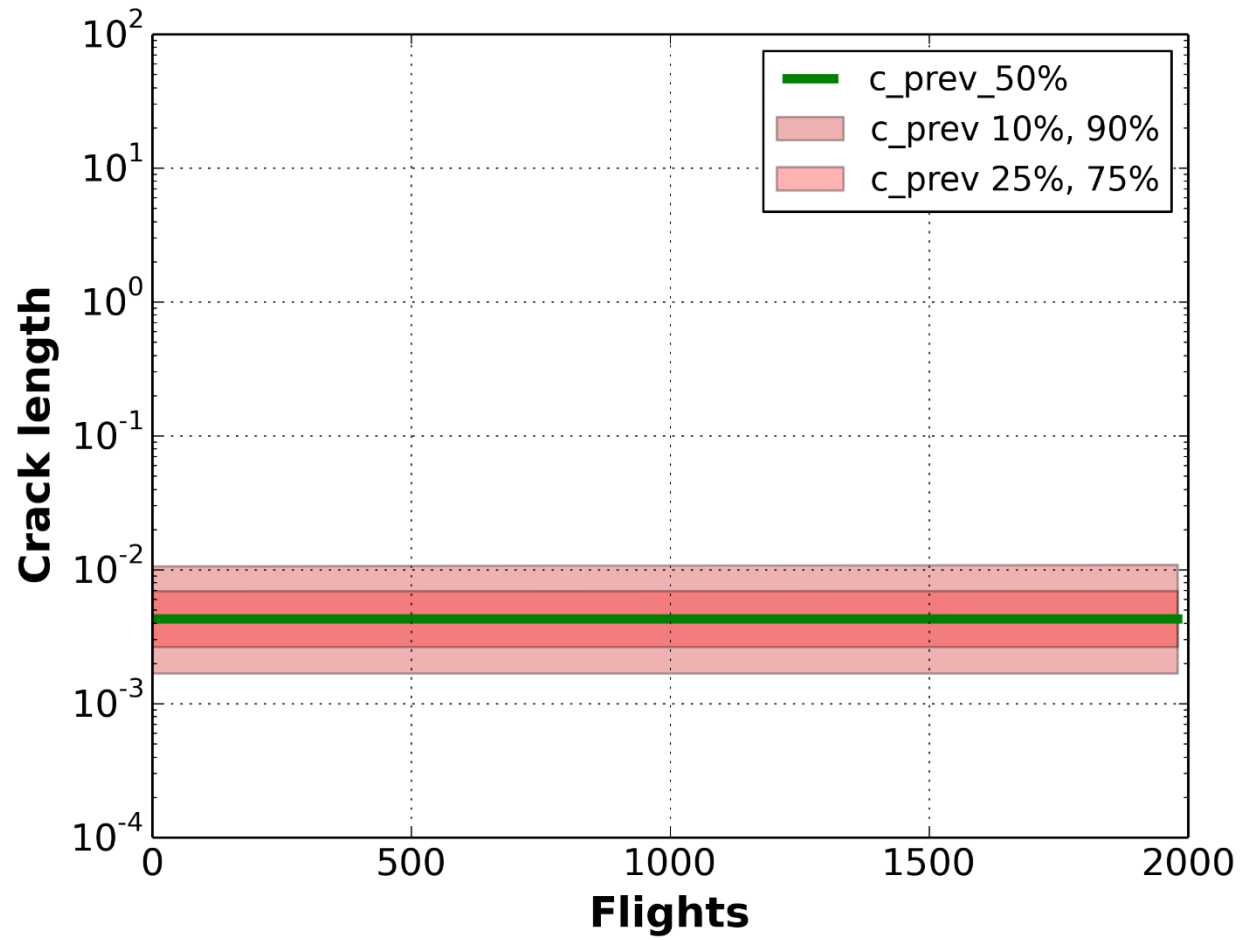


Figure F-12. GE04 baseline crack length predictions - surface direction

GE05 Baseline Predictions

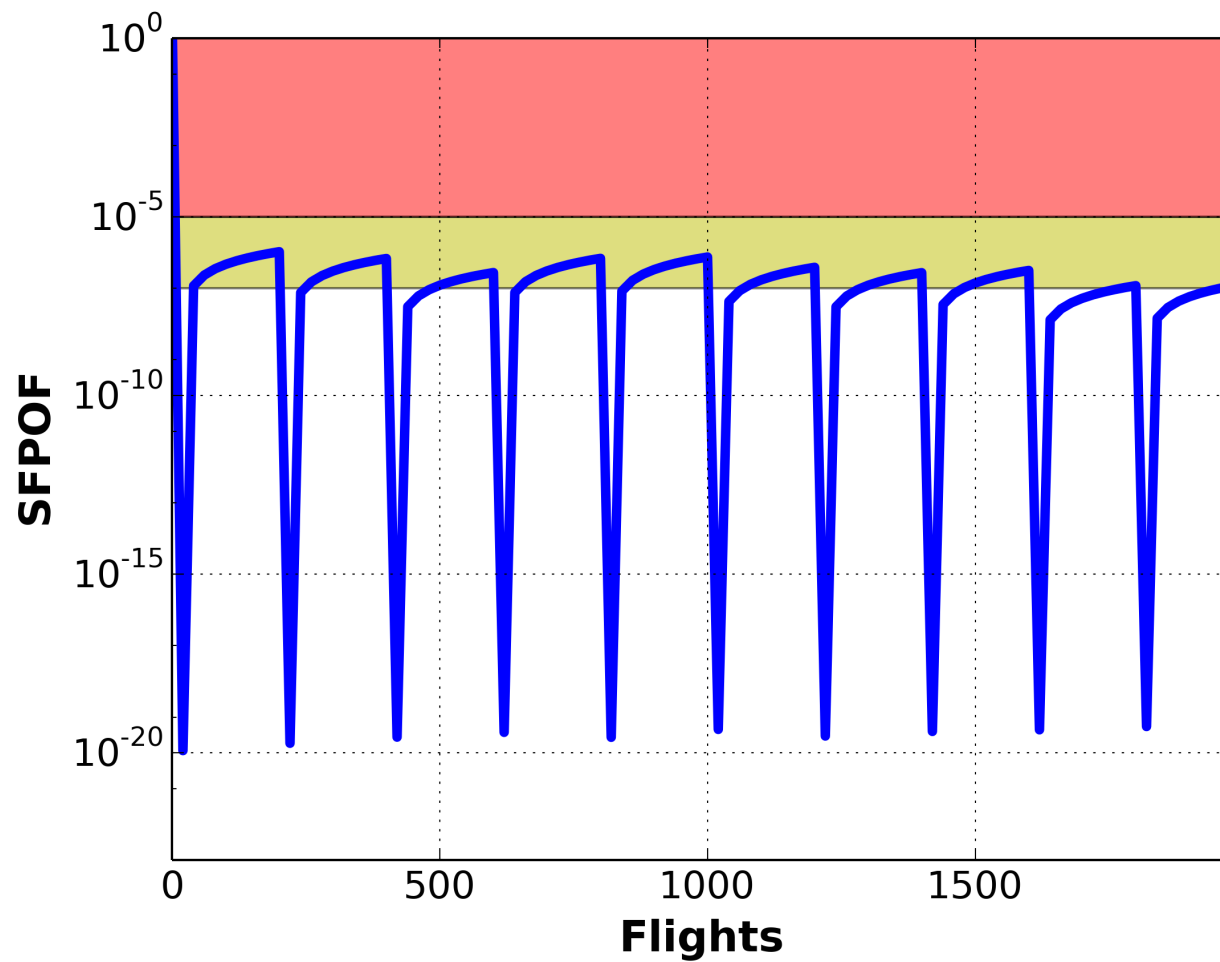


Figure F-13. GE05 SFPOF baseline forecast prediction

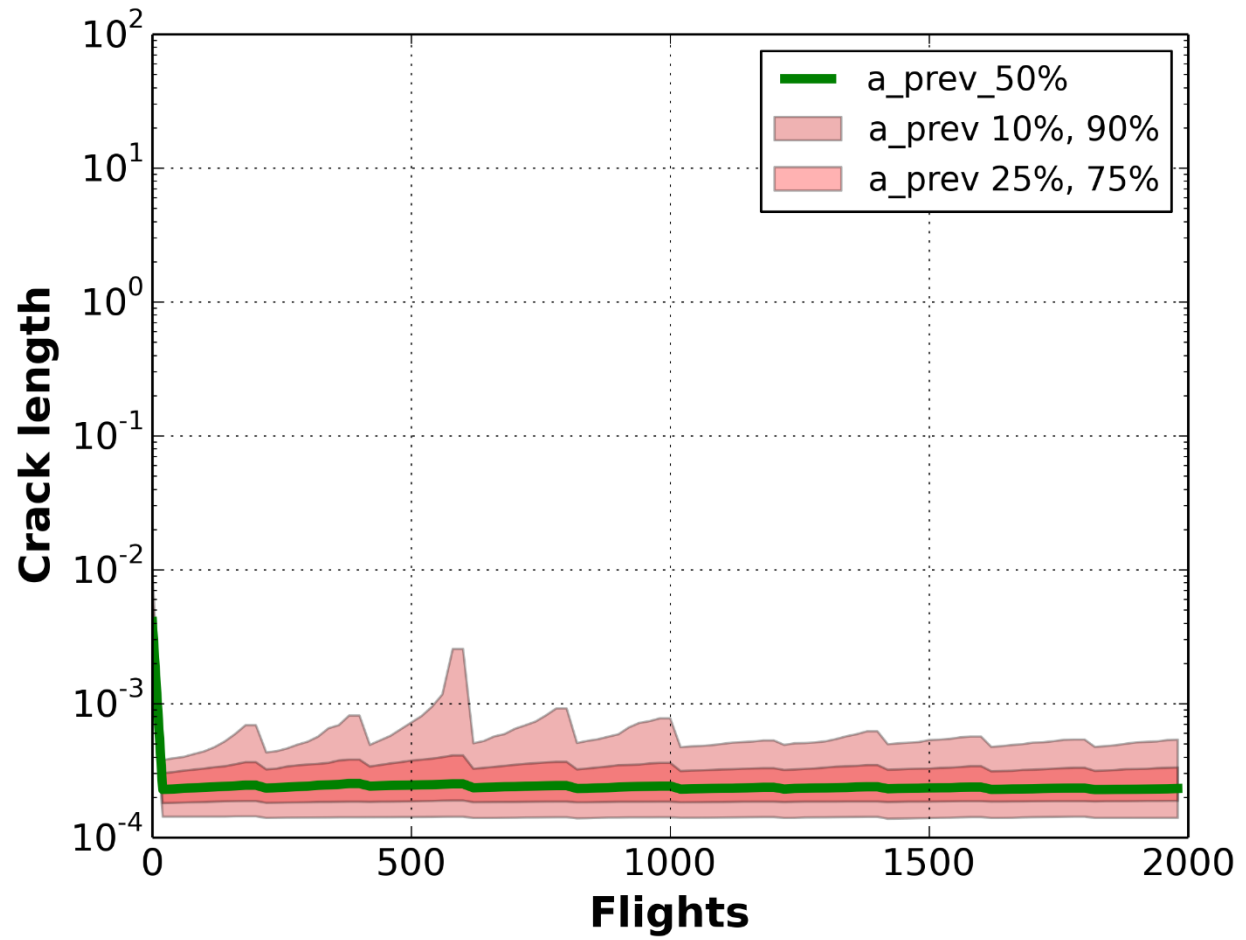


Figure F-14. GE05 baseline crack length predictions - depth direction

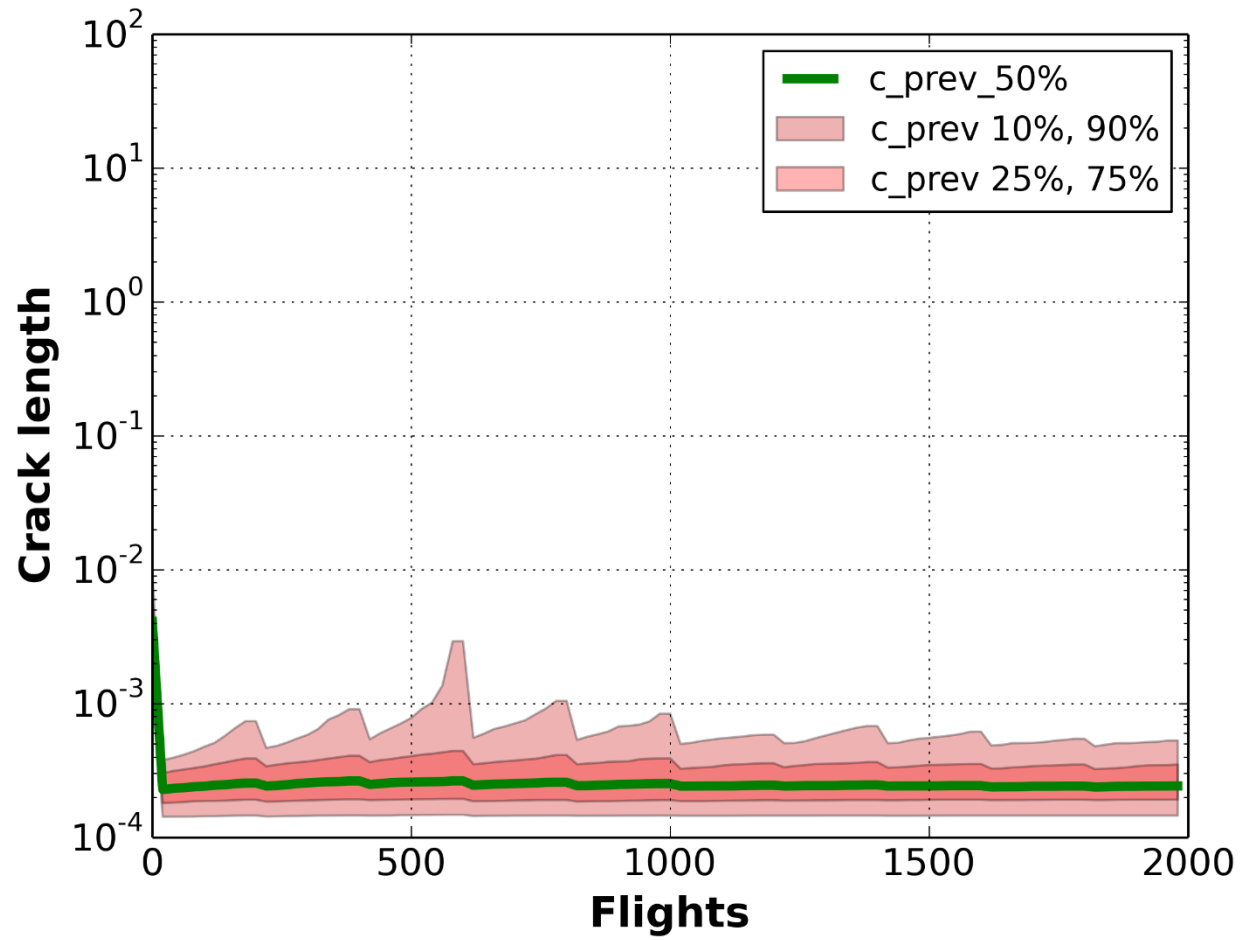


Figure F-15. GE05 baseline crack length predictions - surface direction

GE06 Baseline Predictions

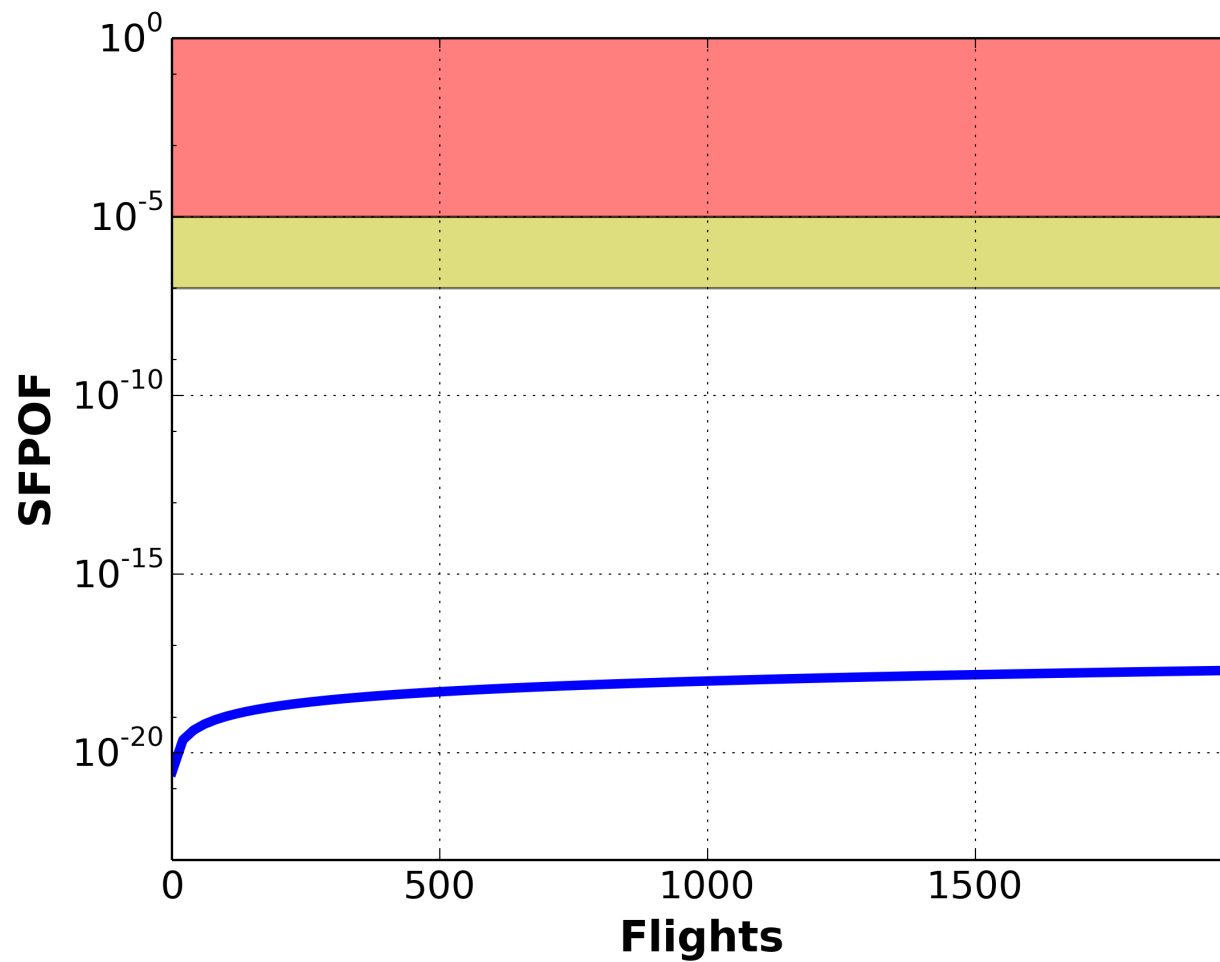


Figure F-16. GE06 SFPOF baseline forecast prediction

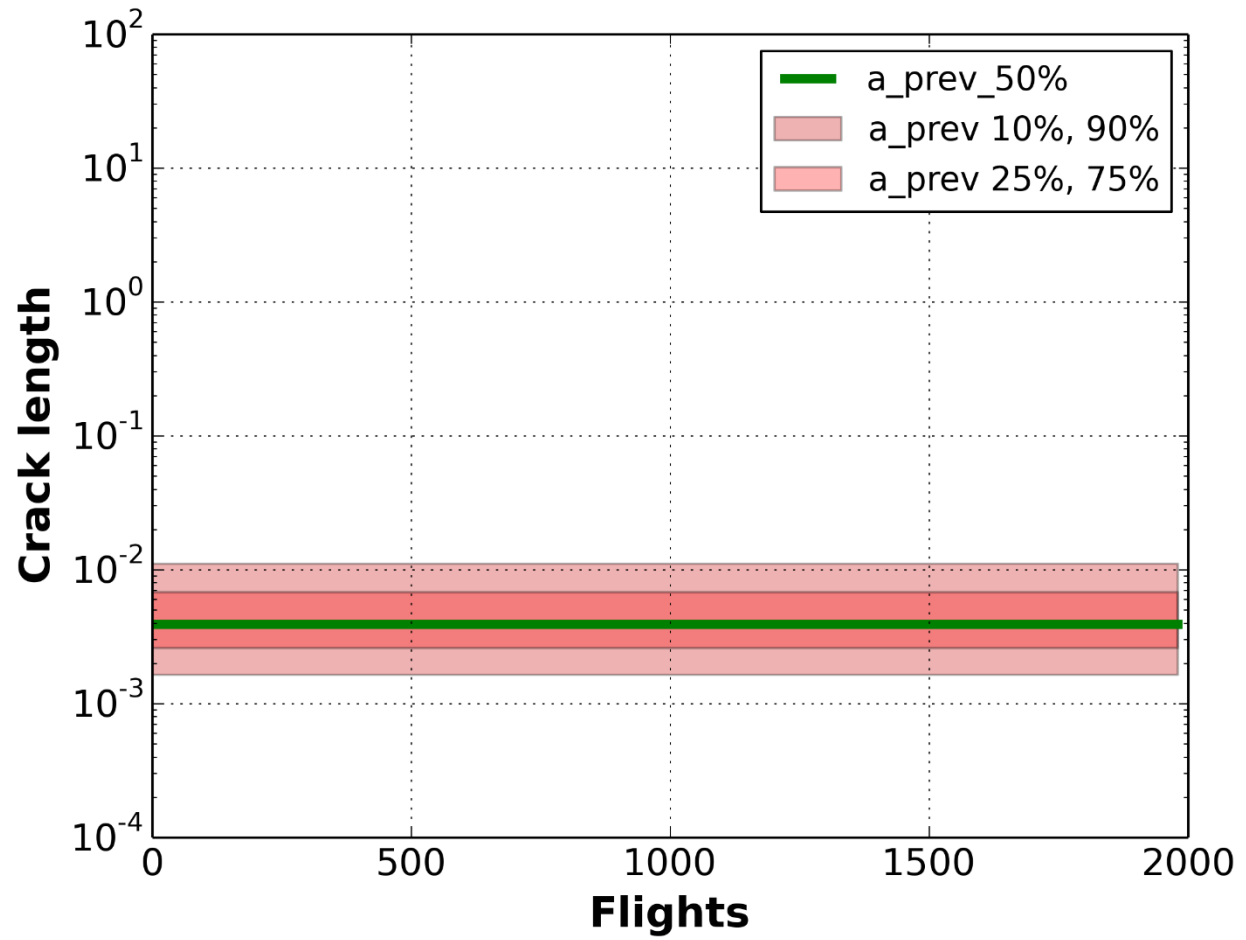


Figure F-17. GE06 baseline crack length predictions - depth direction

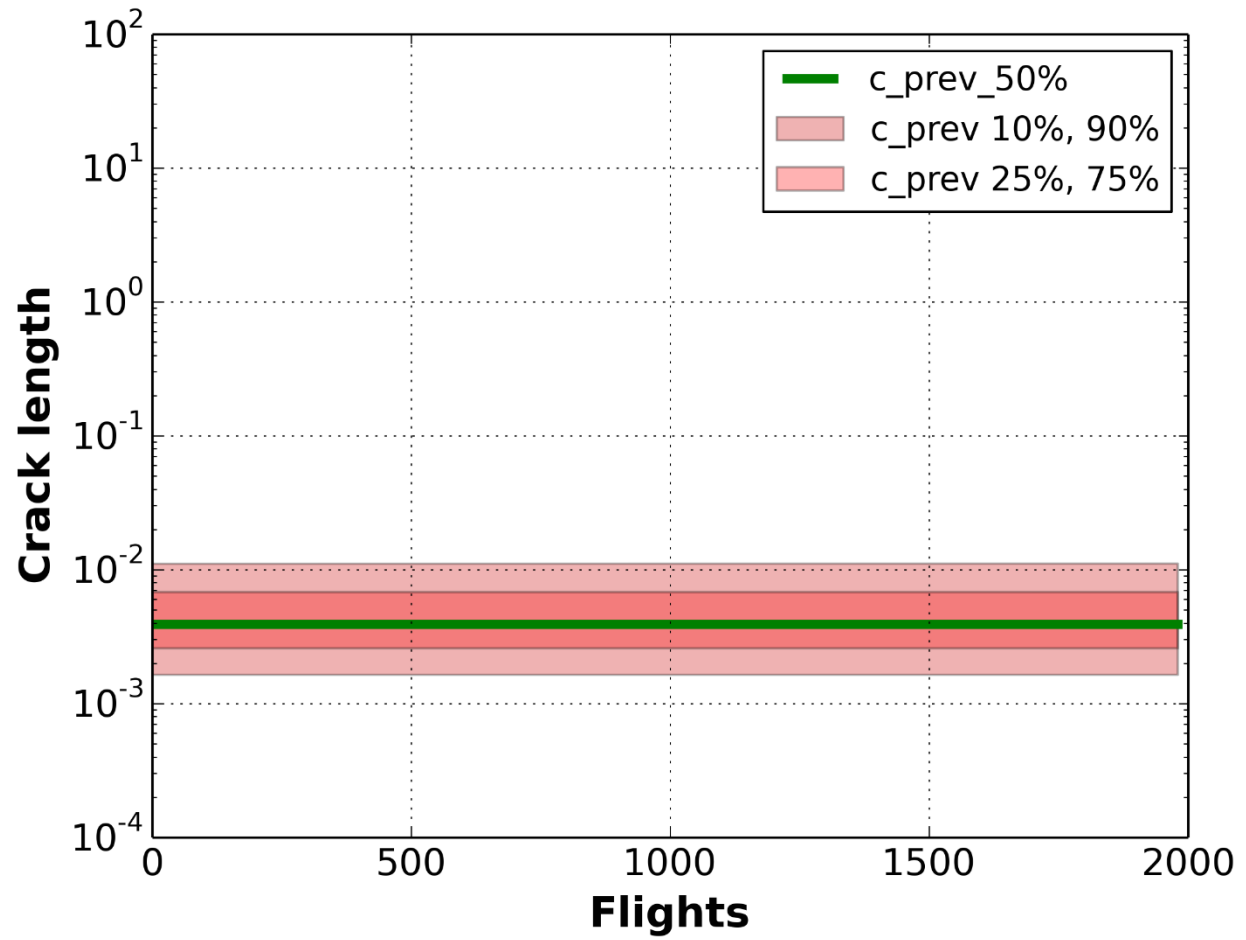


Figure F-18. GE06 baseline crack length predictions - surface direction

GE07 Baseline Predictions

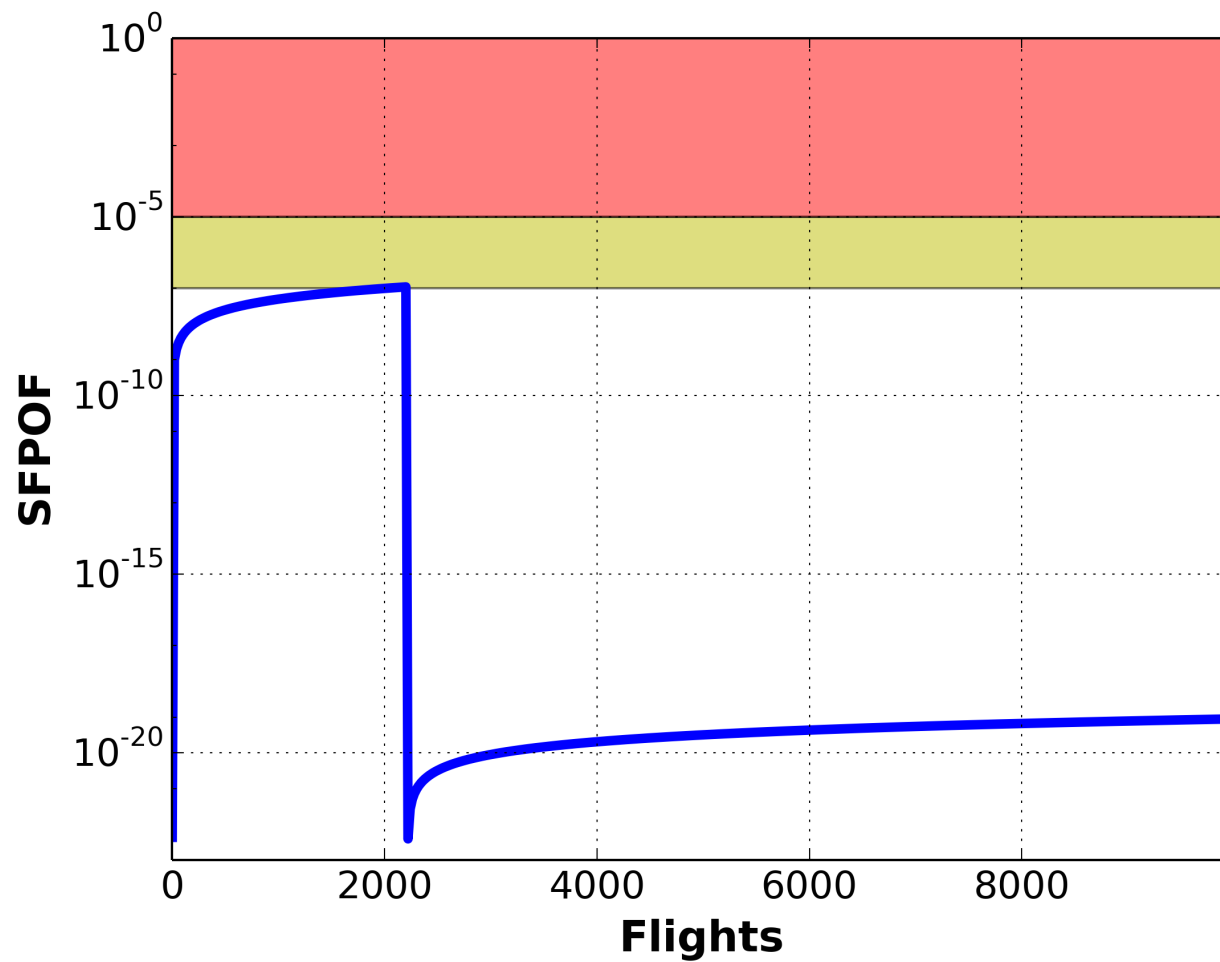


Figure F-19. GE07 SFPOF baseline forecast prediction

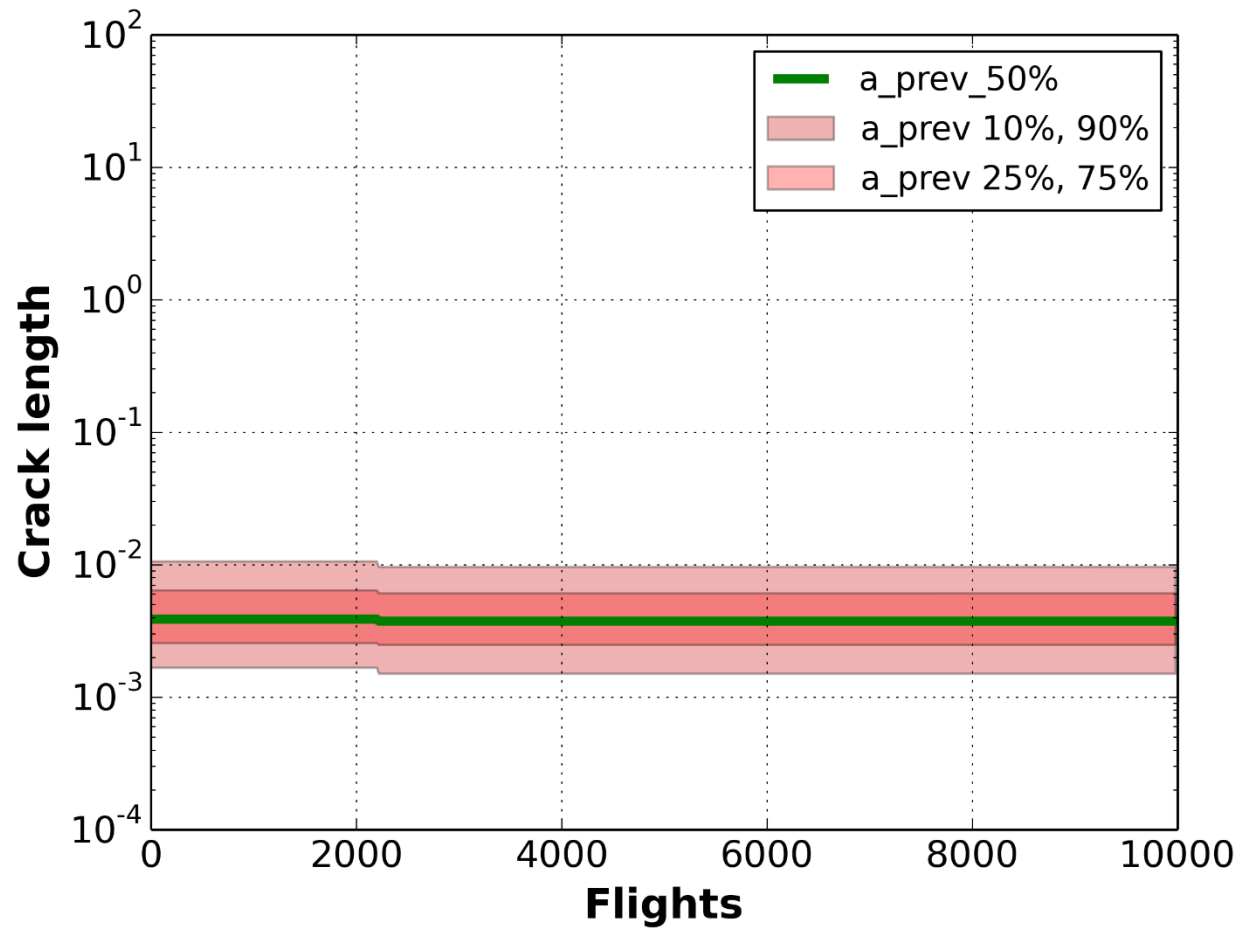


Figure F-20. GE07 baseline crack length predictions - depth direction

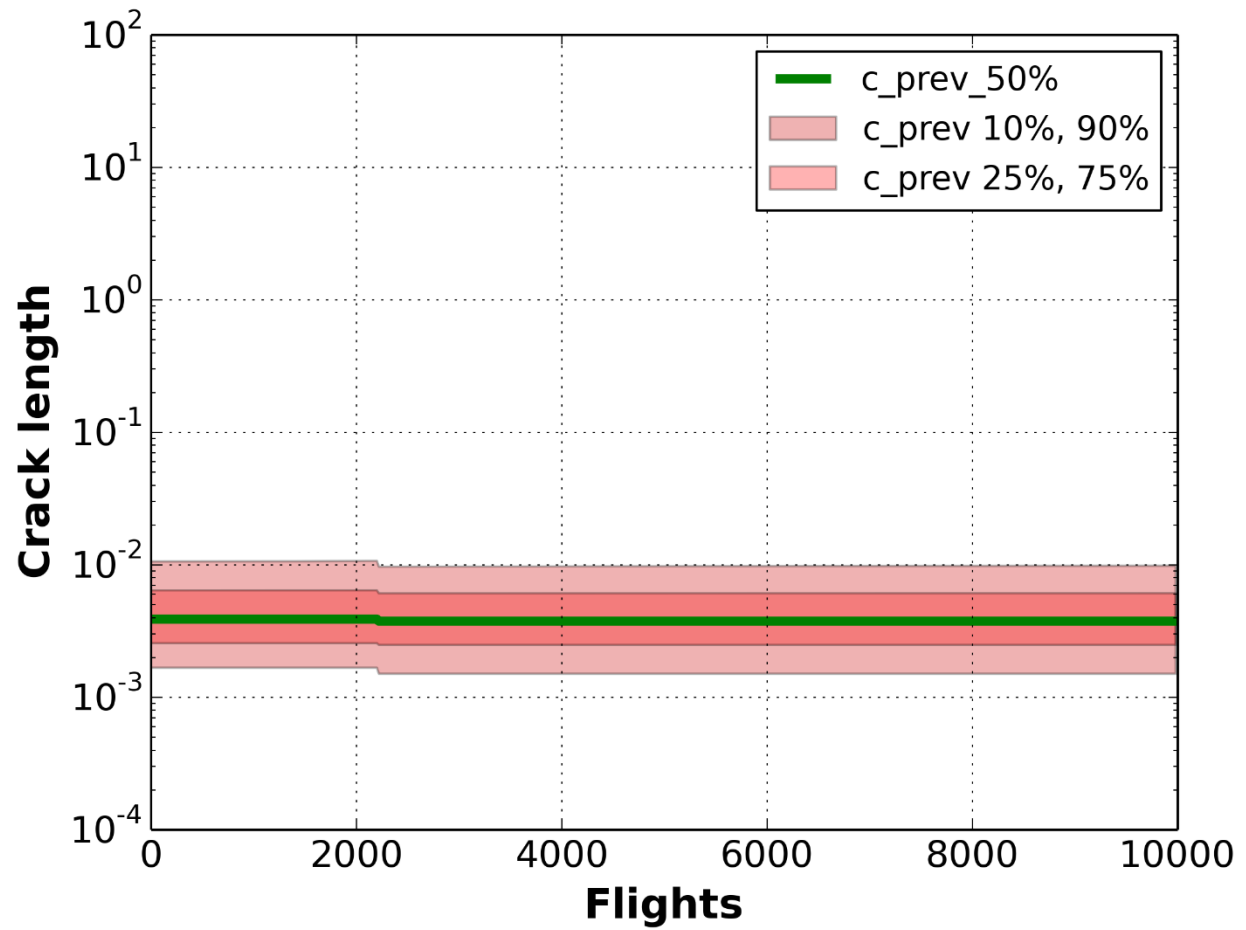


Figure F-21. GE07 baseline crack length predictions - surface direction

GE08 Baseline Predictions

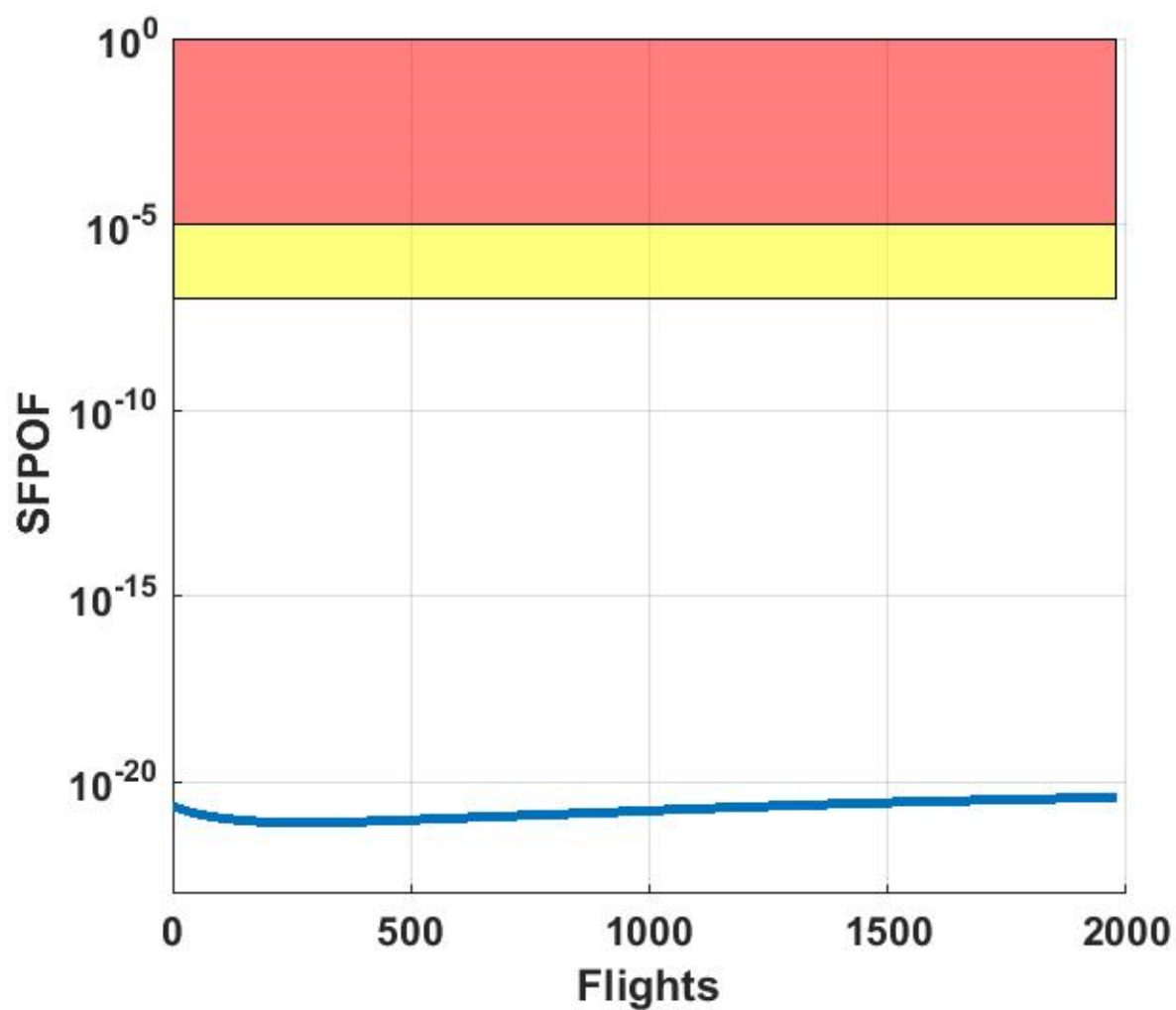


Figure F-22. GE08 SFPOF baseline forecast prediction

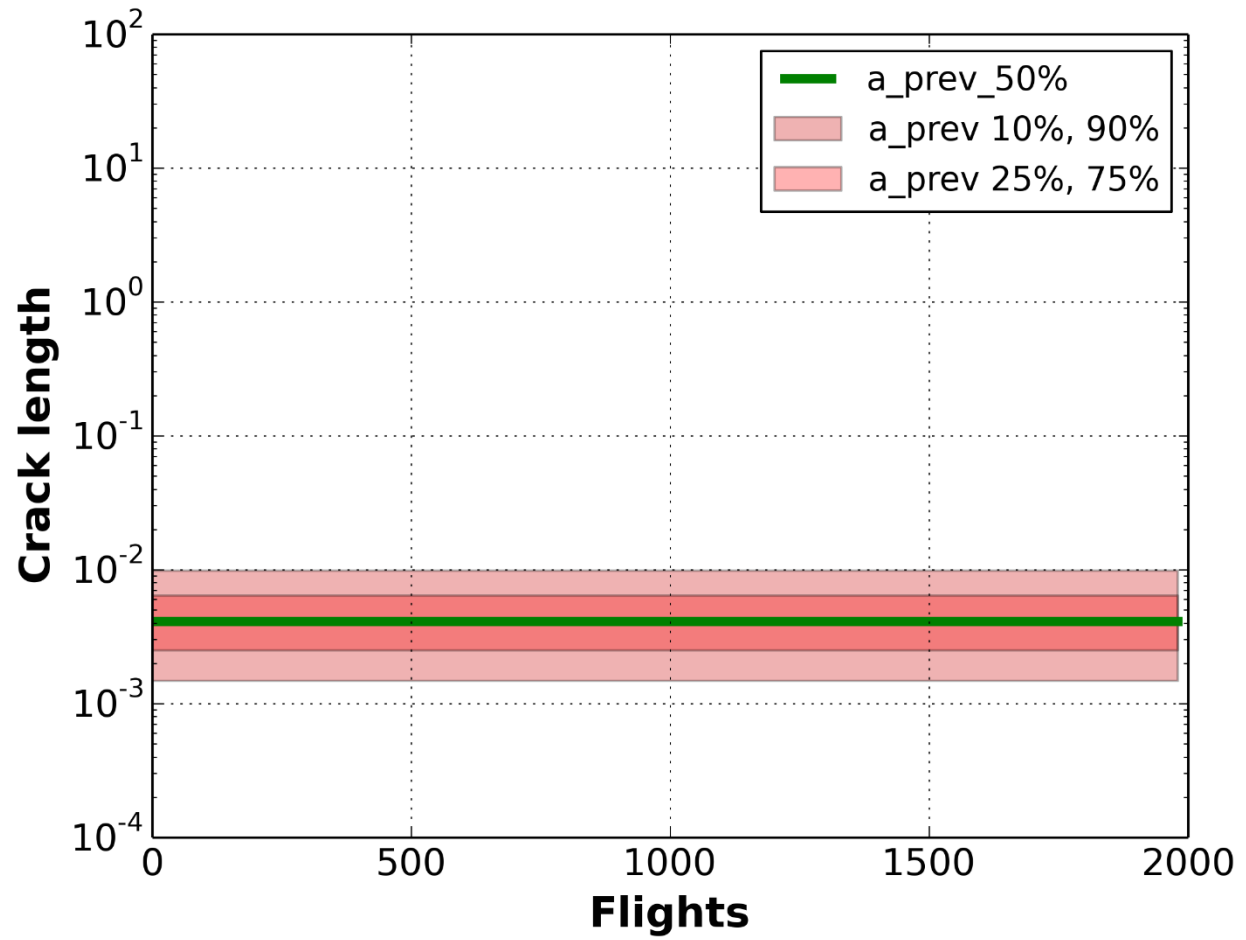


Figure F-23. GE08 baseline crack length predictions - depth direction

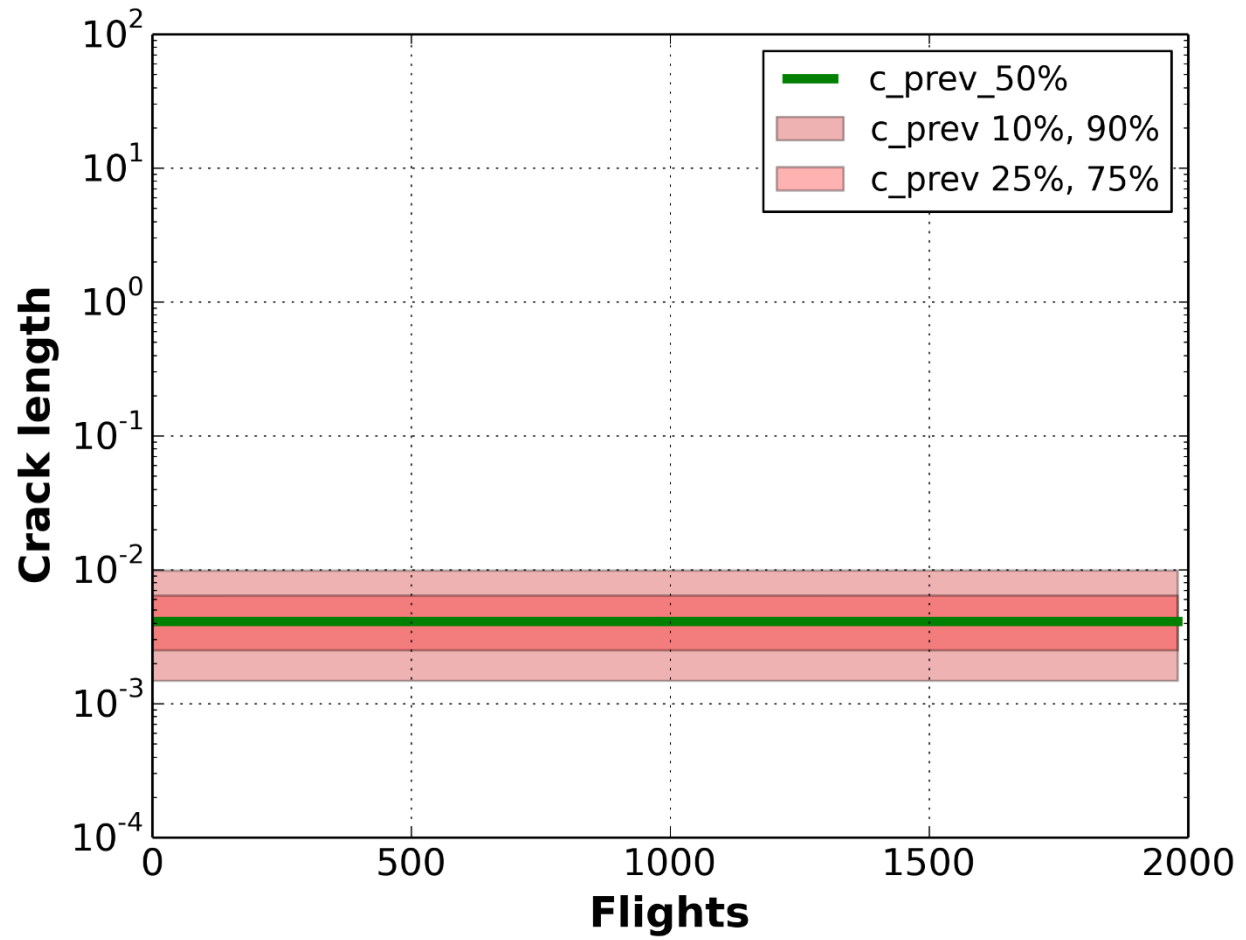


Figure F-24. GE08 baseline crack length predictions - surface direction

GE09 Baseline Predictions

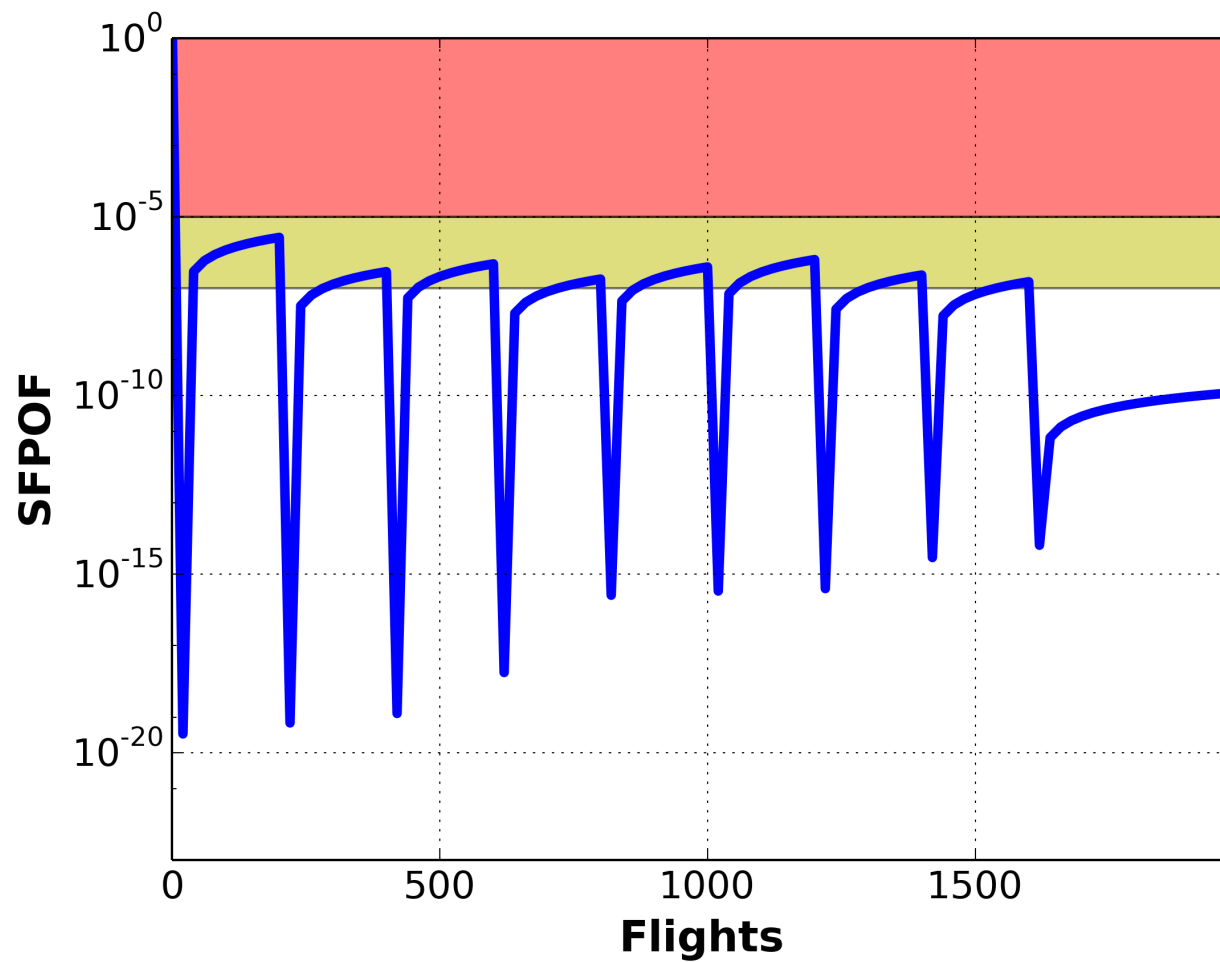


Figure F-25. GE09 SFPOF baseline forecast prediction

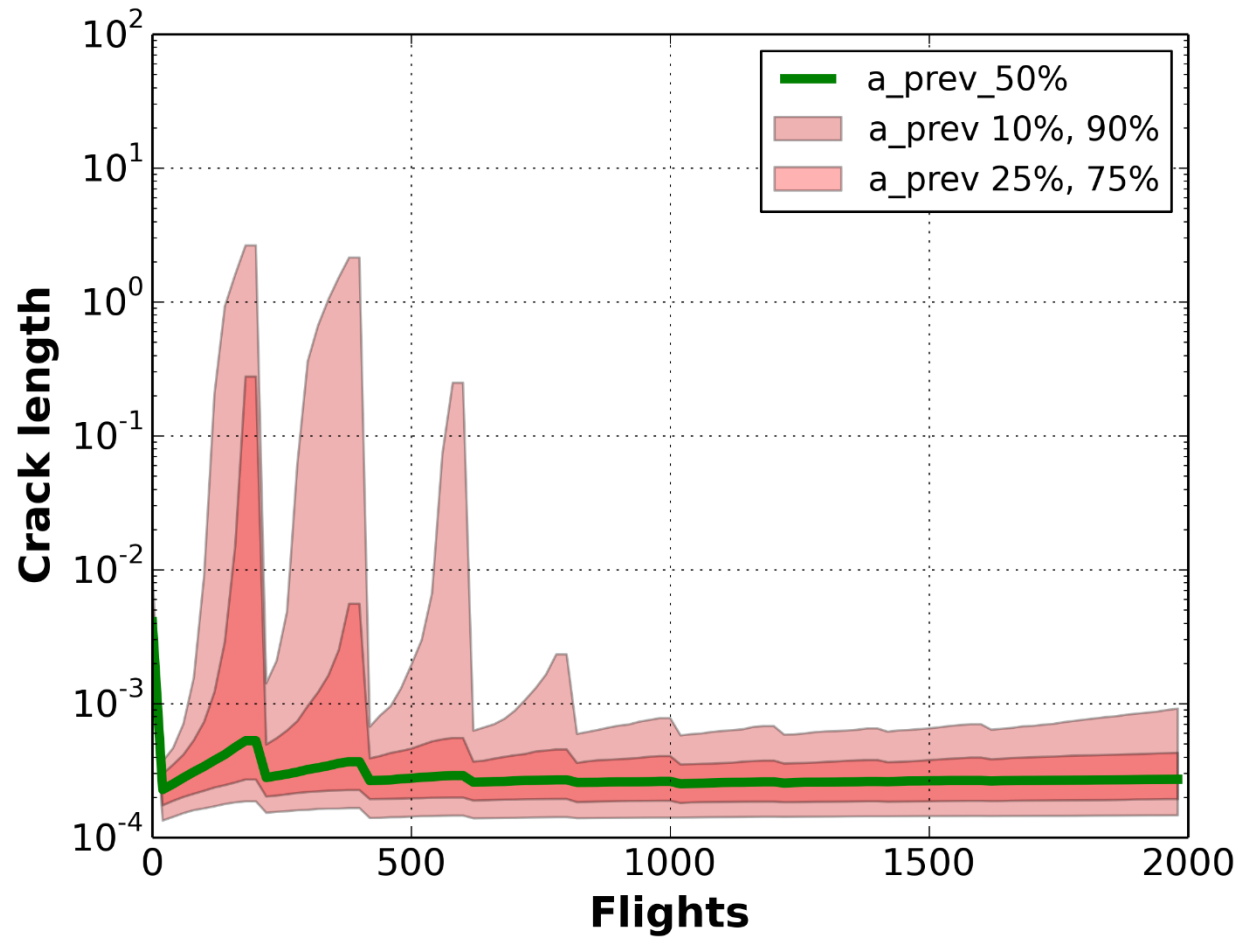


Figure F-26. GE09 baseline crack length predictions - depth direction

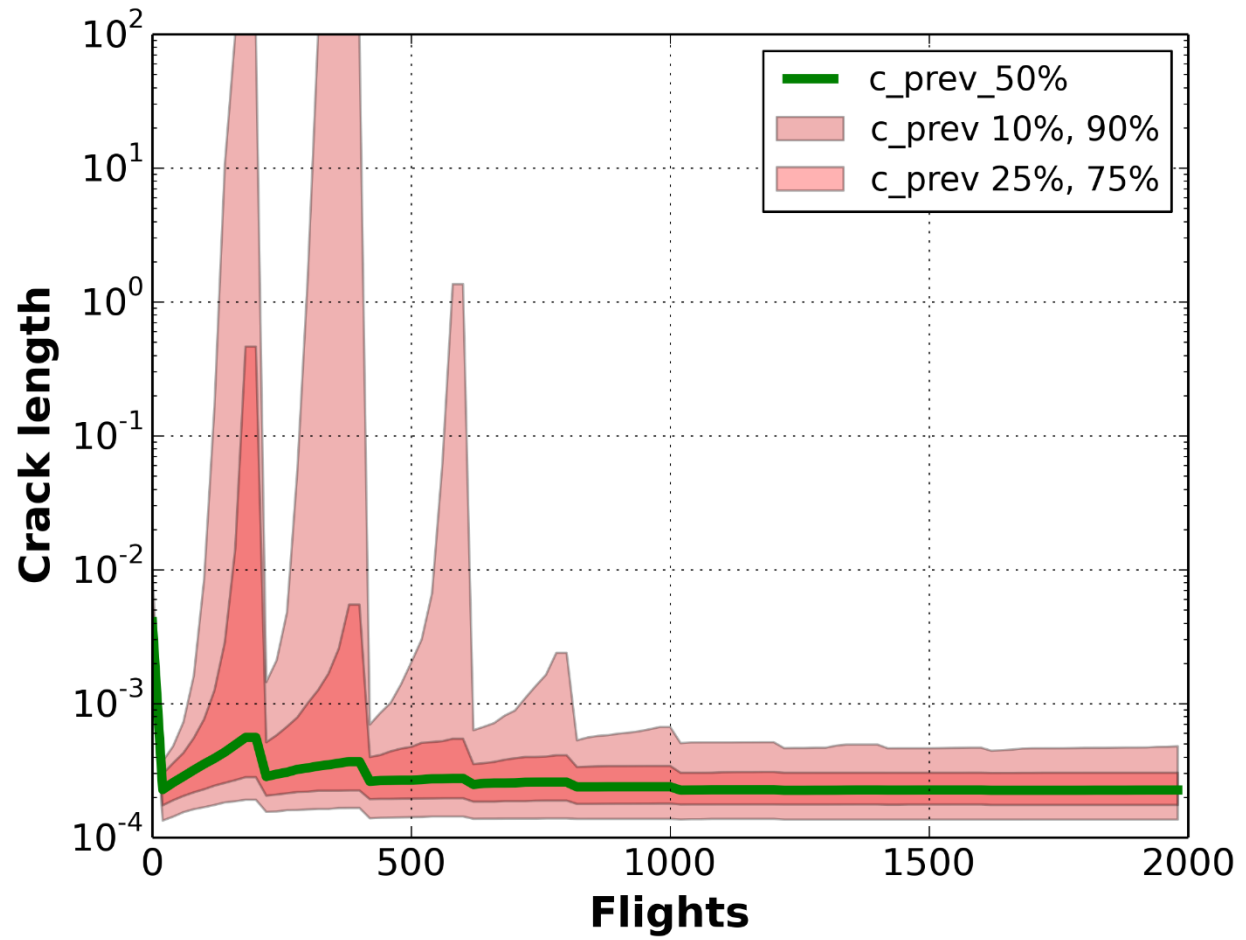


Figure F-27. GE09 baseline crack length predictions - surface direction

GE10 Baseline Predictions

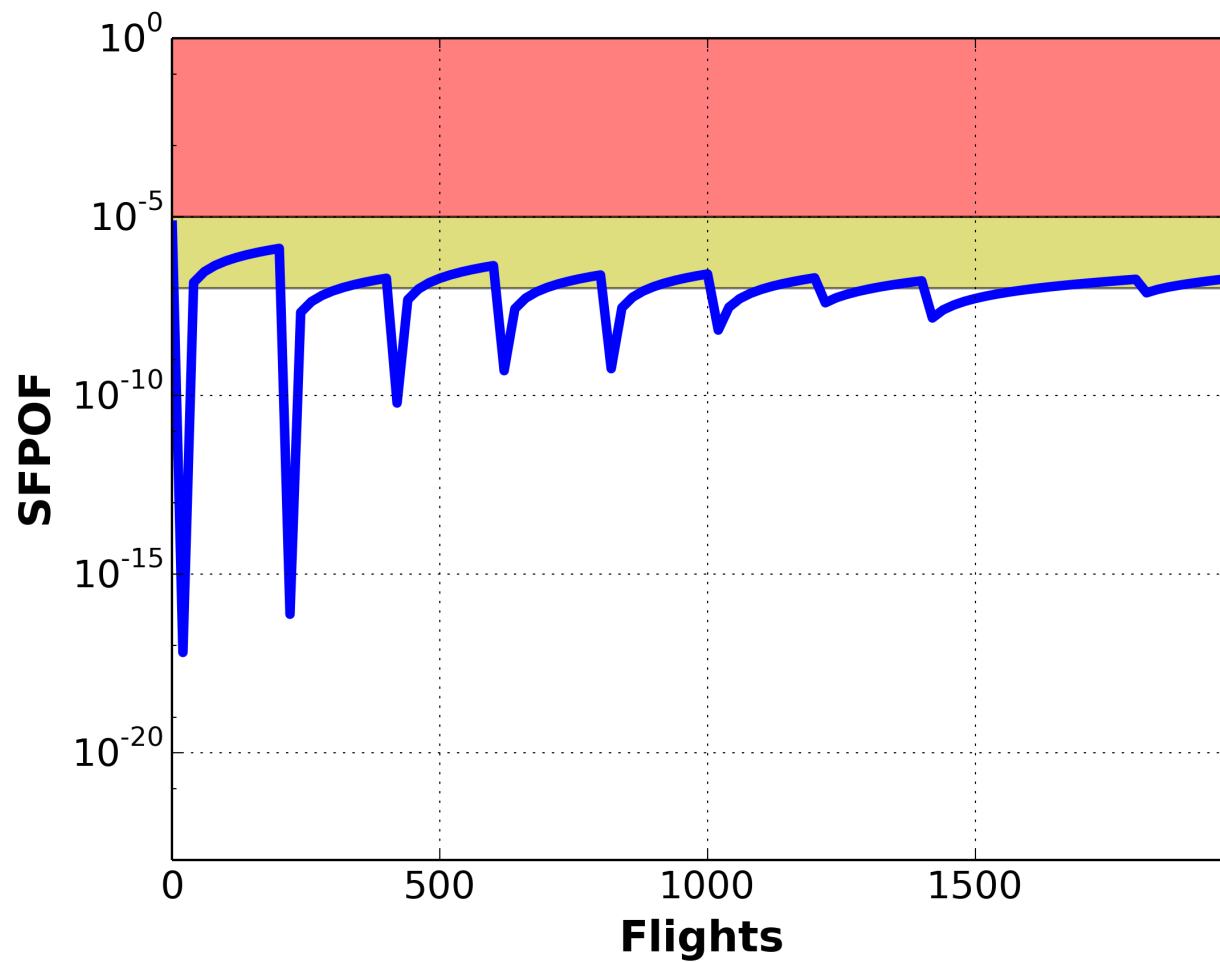


Figure F-28. GE10 SFPOF baseline forecast prediction

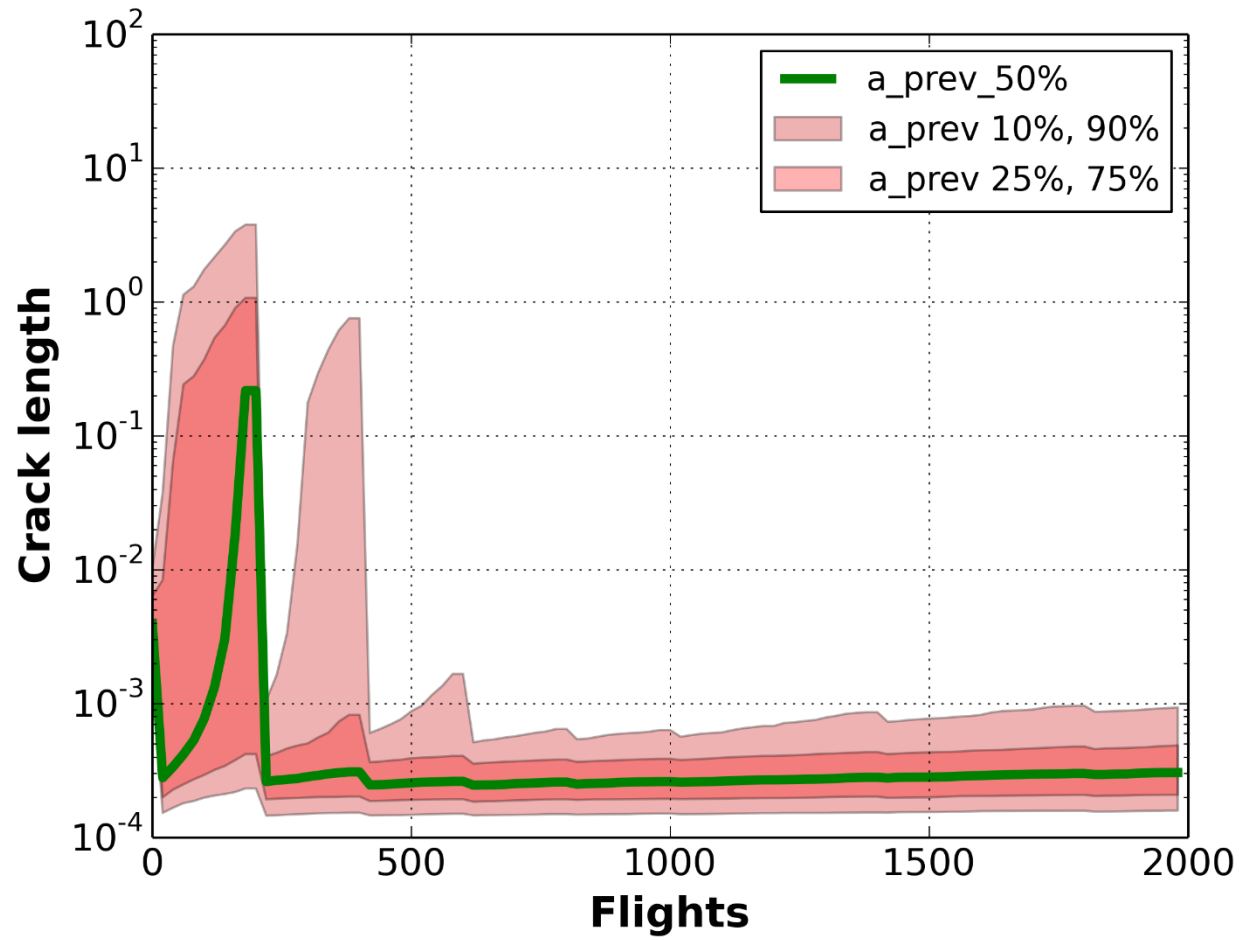


Figure F-29. GE10 baseline crack length predictions - depth direction

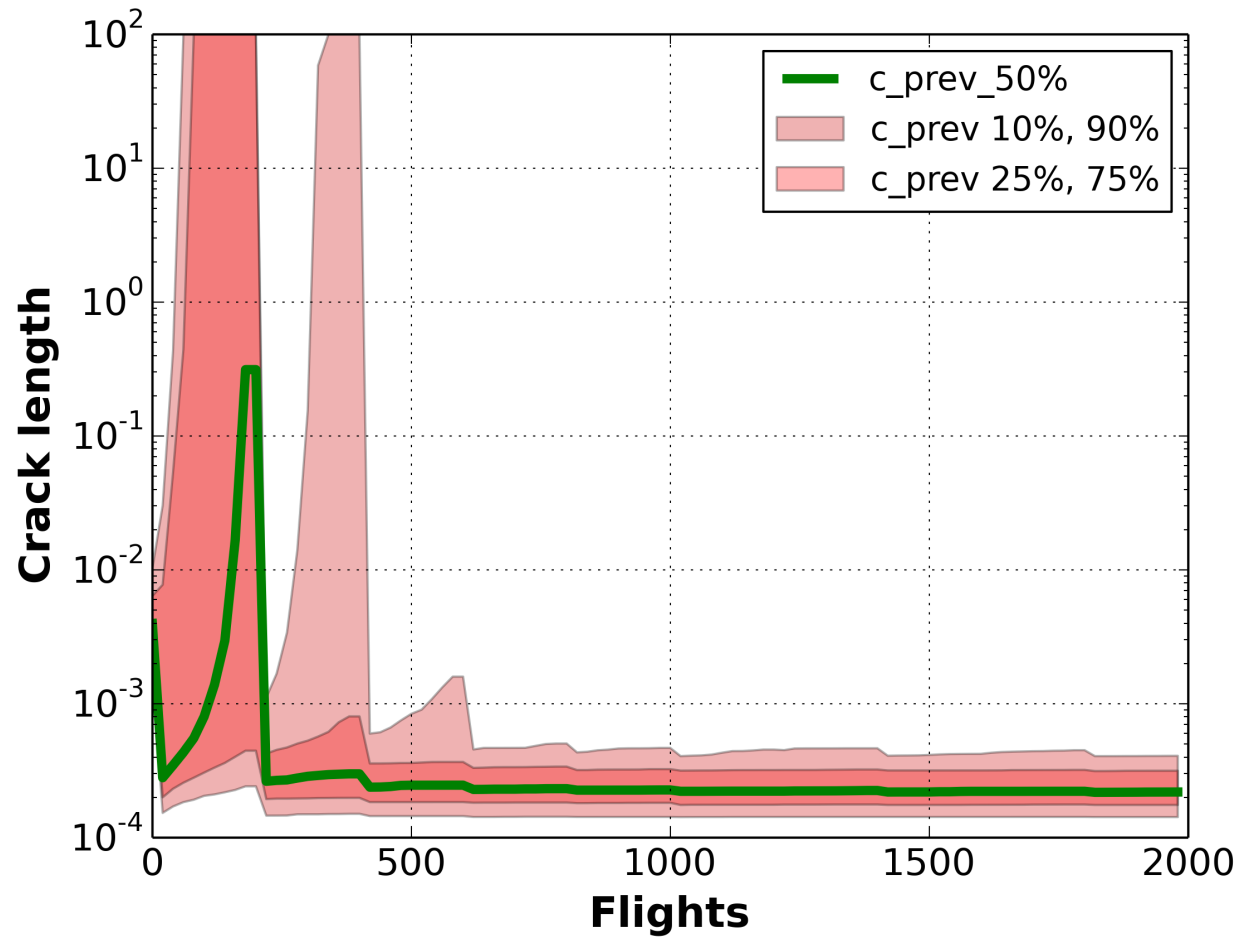


Figure F-30. GE10 baseline crack length predictions - surface direction

Appendix G – Master Event Sequence

The Master Event Sequence is available upon request to the Controlling DoD Office by readers who are authorized to receive export controlled material.

Appendix H – Load Application TRD

Test Article Description

The test article will be subjected to fatigue cycling in this program. Each is a reclaimed fighter aircraft wing consisting of both the inboard and outboard wing sections.

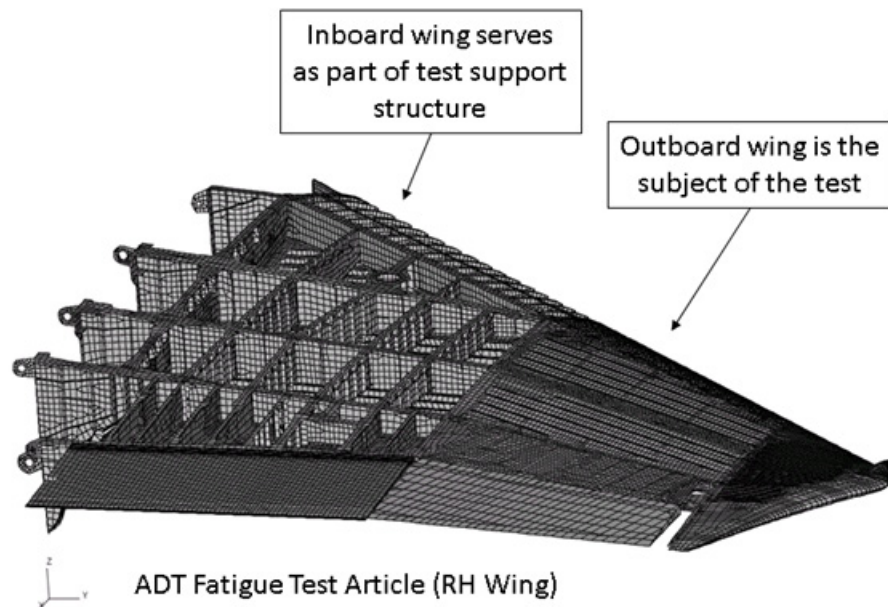


Figure H-1. ADT Fatigue Test Article

Test Purpose and Objectives

The objective of the ADT full scale test is to demonstrate the Prognostic and Probabilistic Individual Aircraft Tracking (SAFER-P2IAT) system under realistic operating conditions. The test will be based on flight spectrum loading in which flight severity and flight sequence will be program variables. During the test, the flight parameter based approach will be used to determine stresses. The IAT system will be expected to produce control point stress histories based on program provided, simulated flight recorder data. The system will be expected to handle missing data and to have suitable rules for gap filling.

Test Conditions

Test Article

The test article consists of a right hand fighter aircraft wing. The test article is a structurally complete production wing with limited modifications or hardware substitutions. A diagram of the wing is shown in Figure H-2 with upper skins removed.

All internal instrumentation required for operation of the IAT system was installed prior to delivery to AFRL/RQVS.

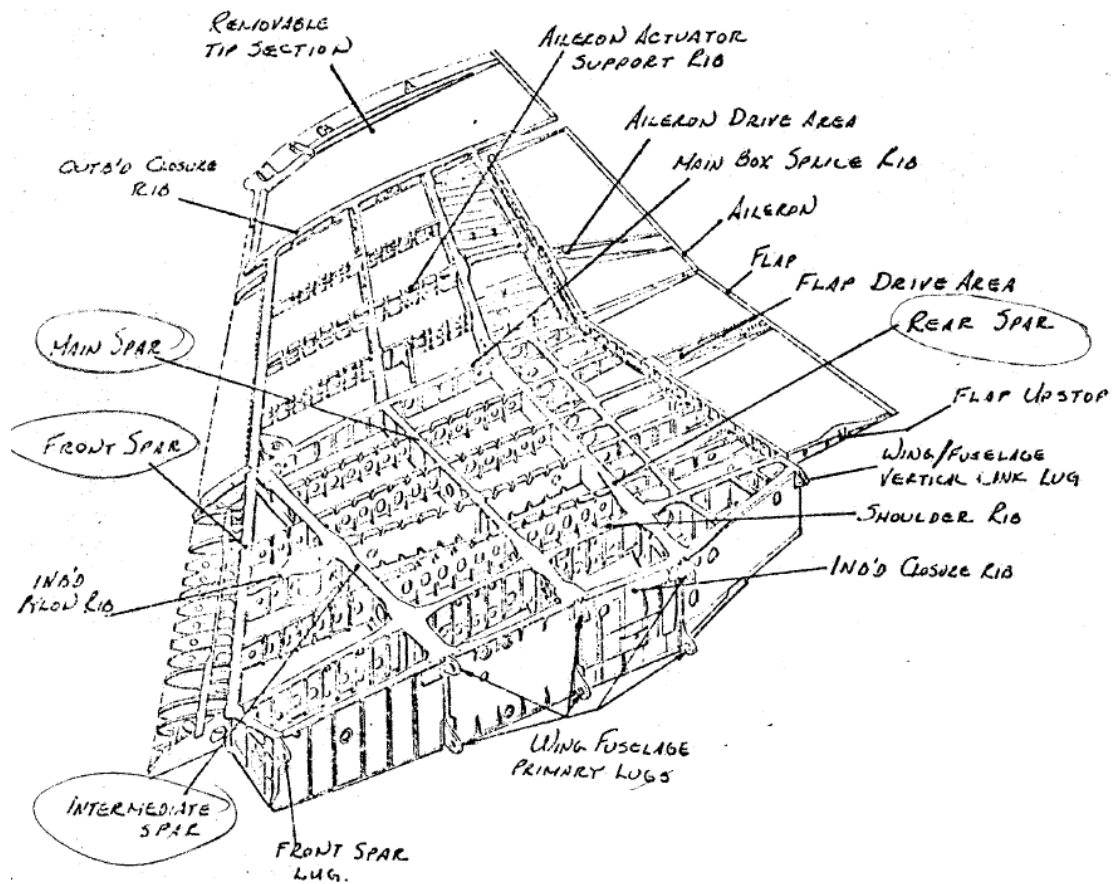


Figure H-2. ADT Fatigue Test Article

Test Load Cases

Each load case in the ADT test spectrum is defined as a linear combination of a pure moment and pure torque limit load case. The eight (five unique) limit load cases were defined based on the moment vs. torque content of the version 5 MES. The maximum and minimum moments and maximum and minimum torque values are shown in Figure H-3. (Note that Sta.3 torque values $<-3.5E5$ and $>+3.5E5$ inch-lb were deemed to be unrealistic and were excluded).

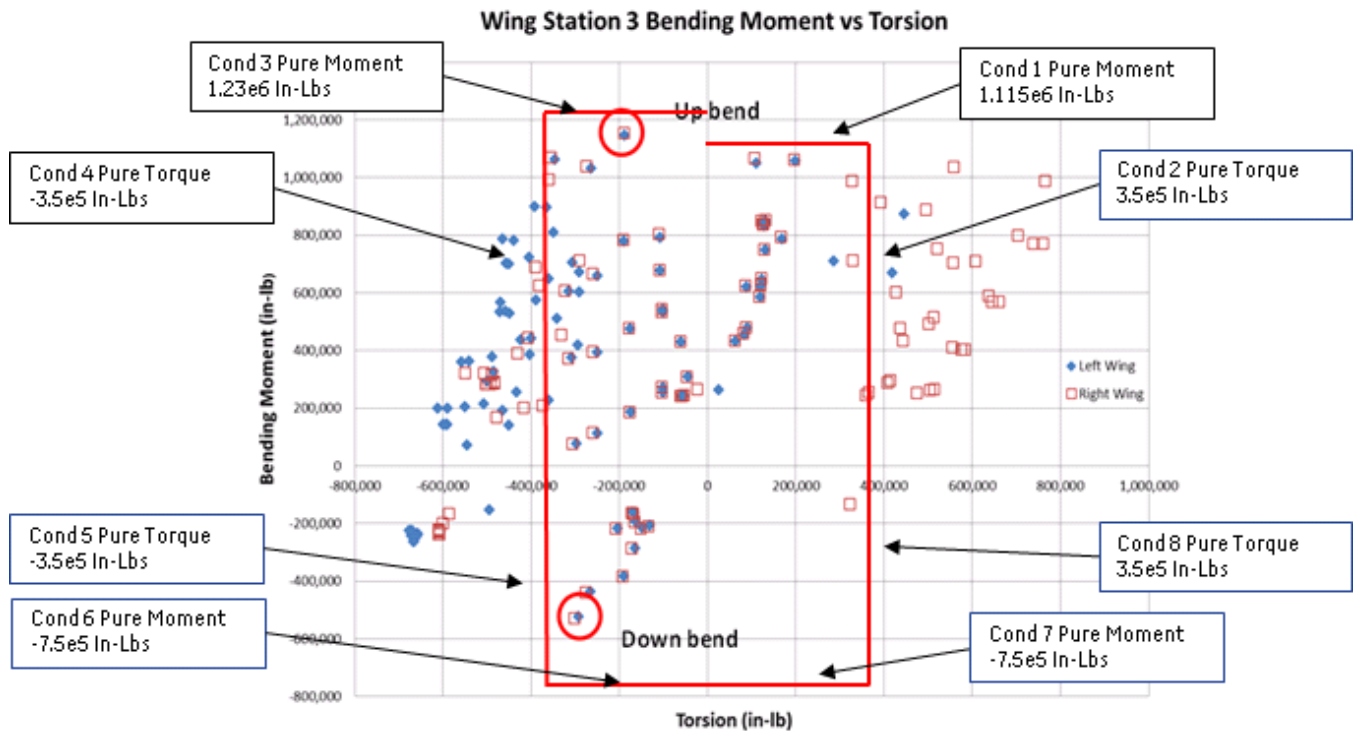


Figure H-3. Wing Sta.3 Moment vs. Torque Diagram for StS Generated Maneuver Load Cases

The span-wise distributions of moment, shear and torque for each of the five unique limit load cases are shown in Figure H-4 through Figure H-18.

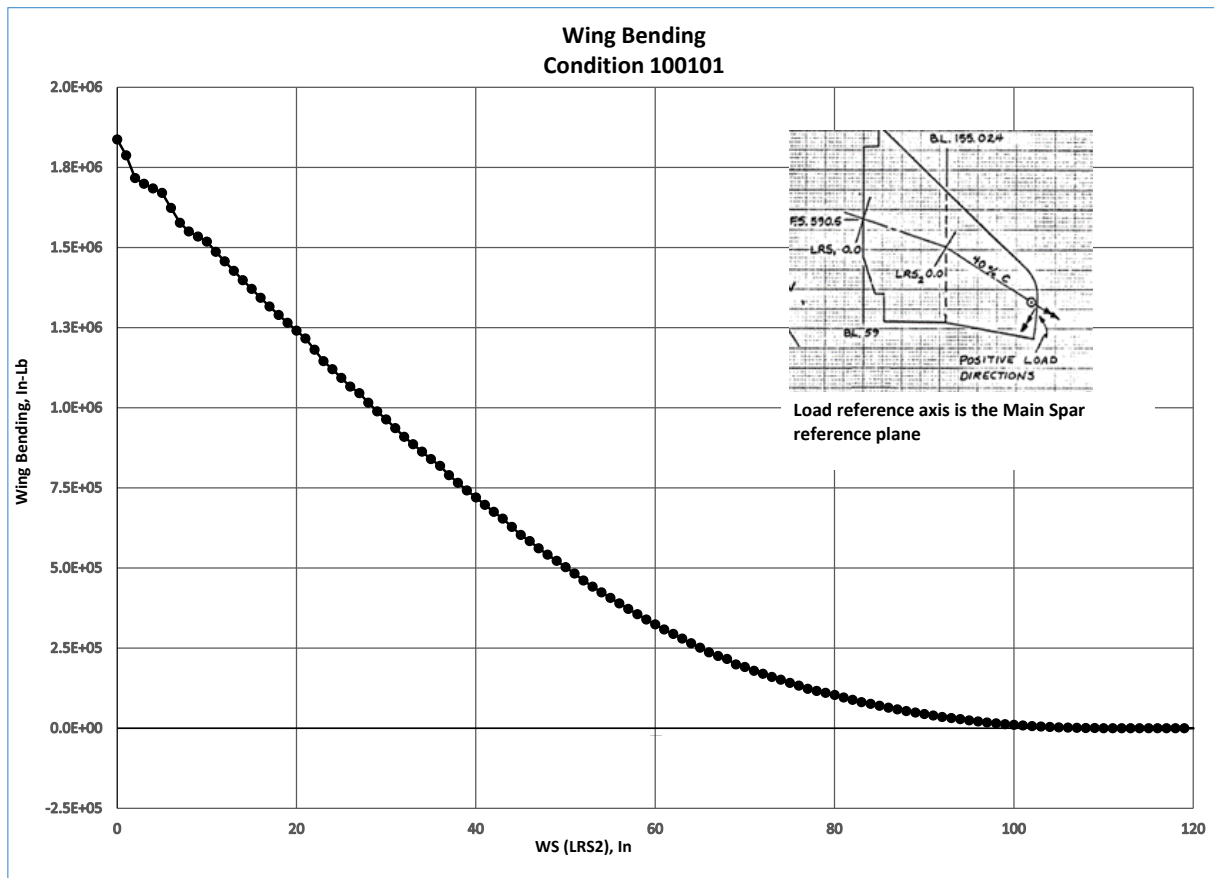


Figure H-4. Moment vs. Wing Station for Limit Load Case 100101 (Cond. 1)

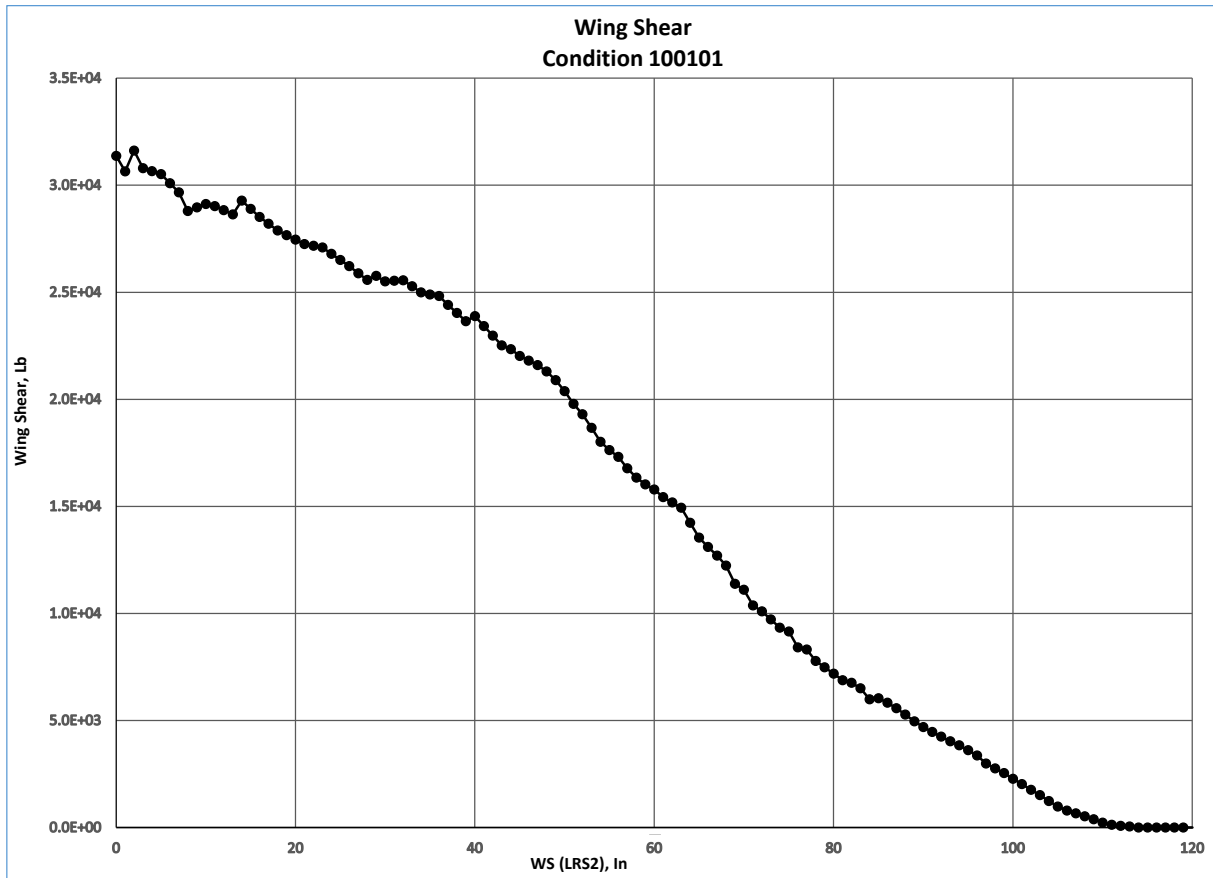


Figure H-5. Shear vs. Wing Station for Limit Load Case 100101 (Cond. 1)

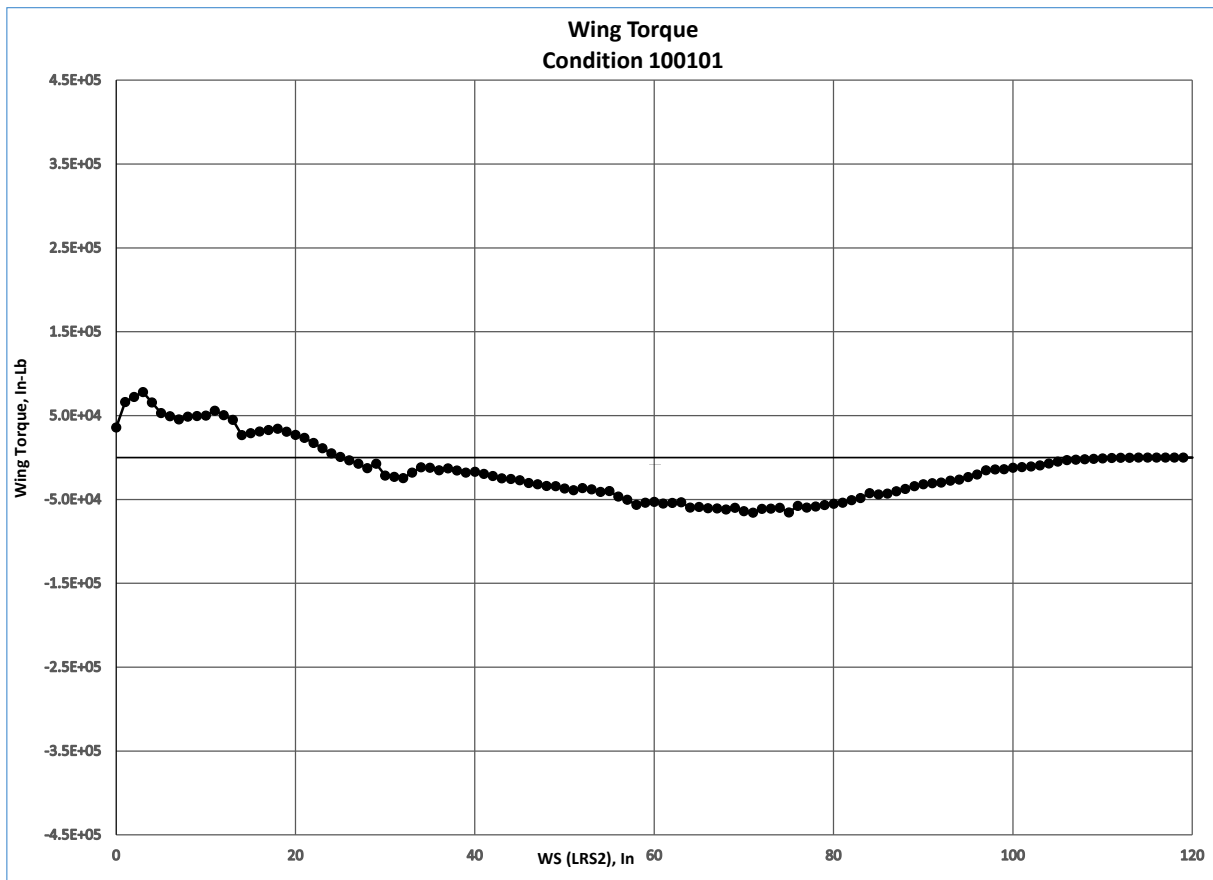


Figure H-6. Torque vs. Wing Station for Limit Load Case 100101 (Cond. 1)

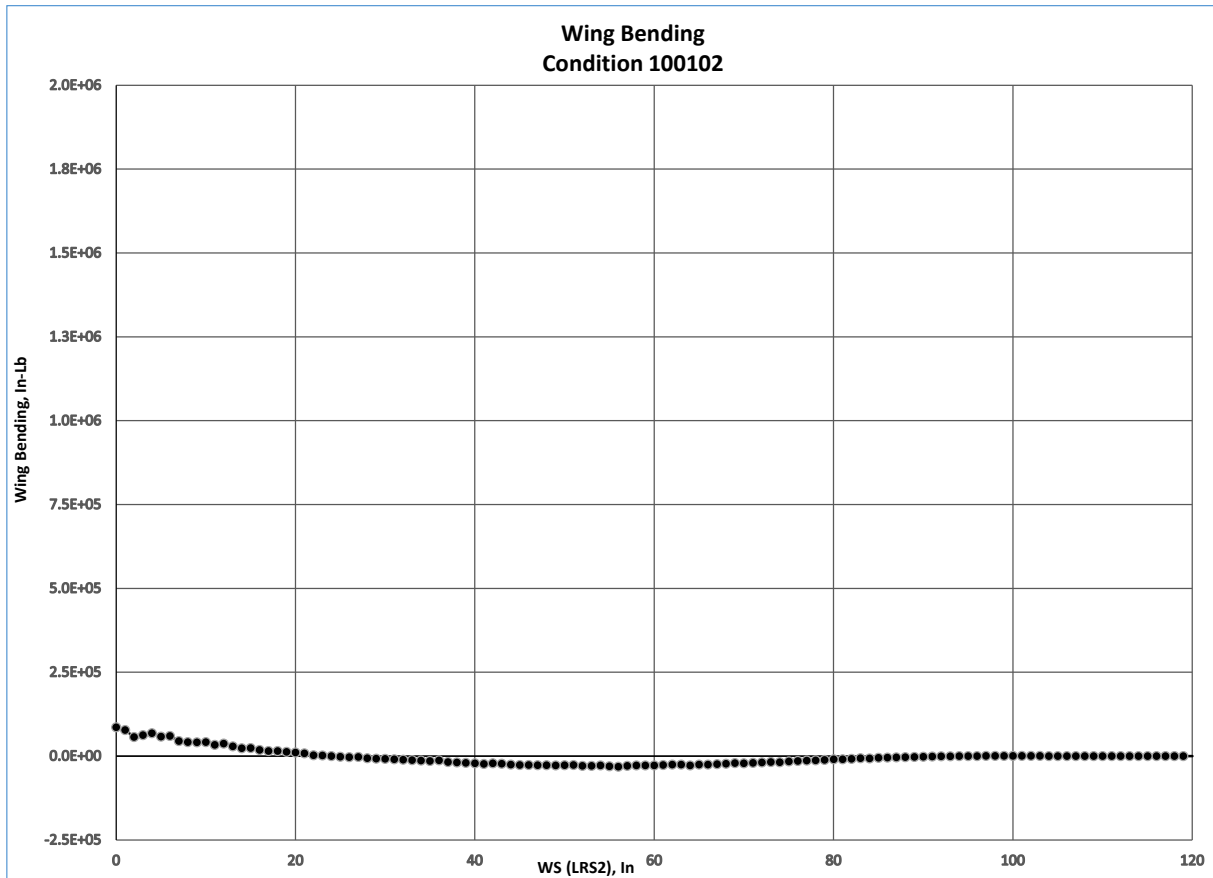


Figure H-7. Moment vs. Wing Station for Limit Load Case 100102 (Cond. 2)

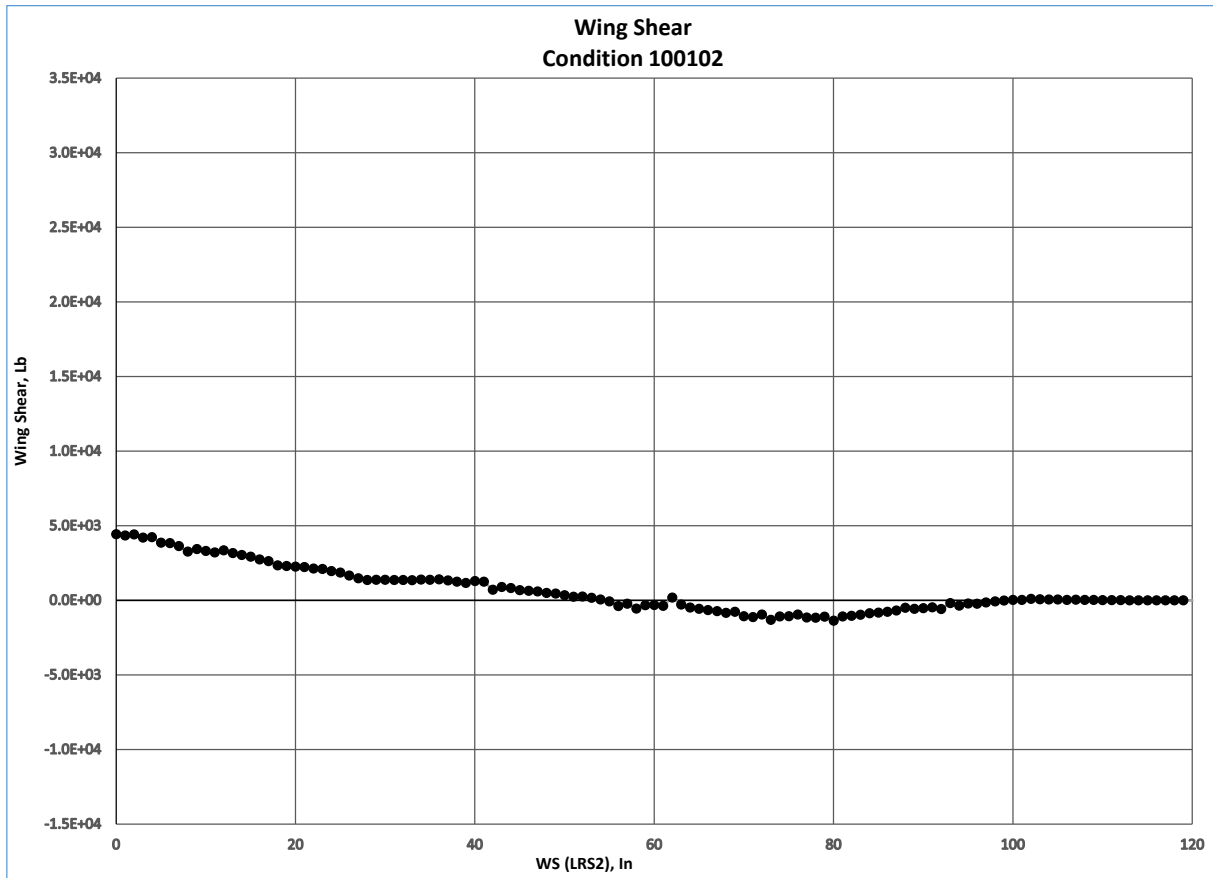


Figure H-8. Shear vs. Wing Station for Limit Load Case 100102 (Cond. 2)

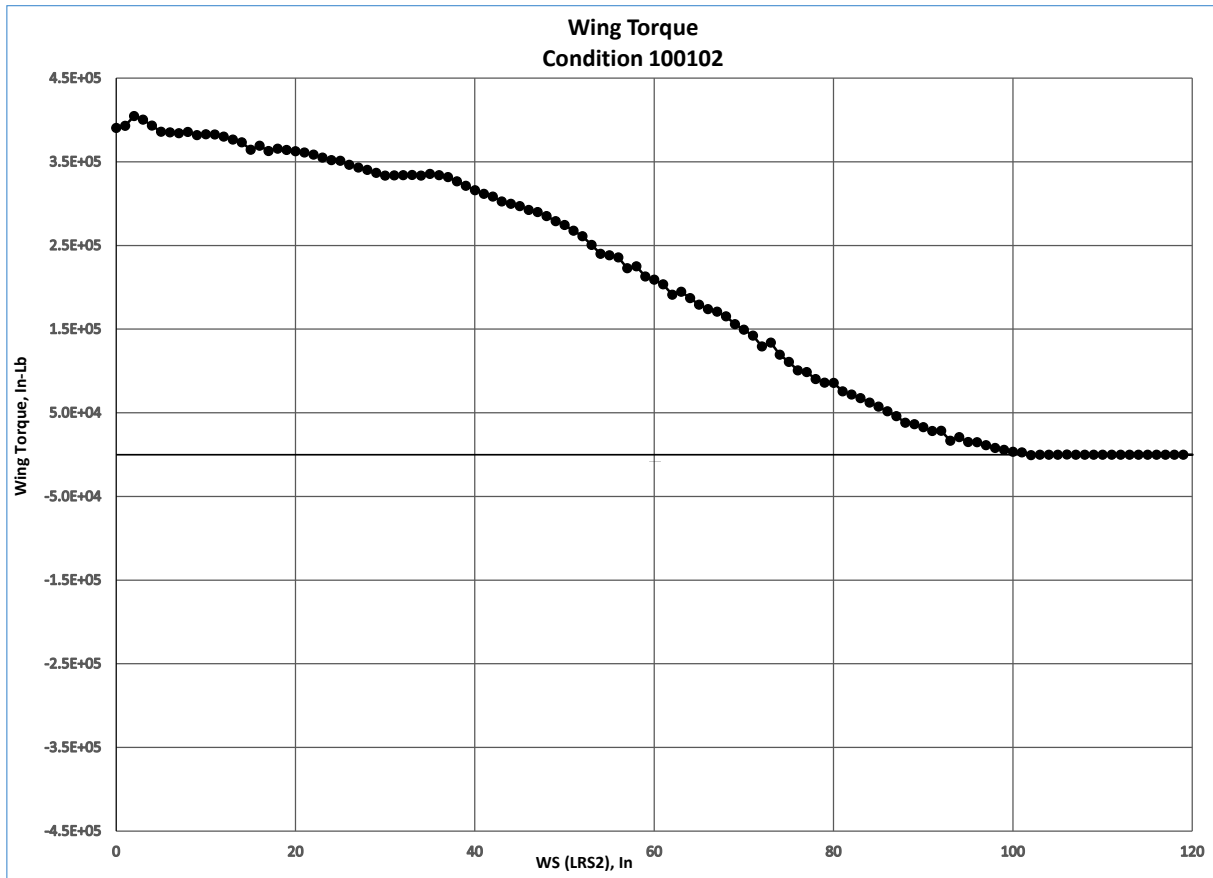


Figure H-9. Torque vs. Wing Station for Limit Load Case 100102 (Cond. 2)

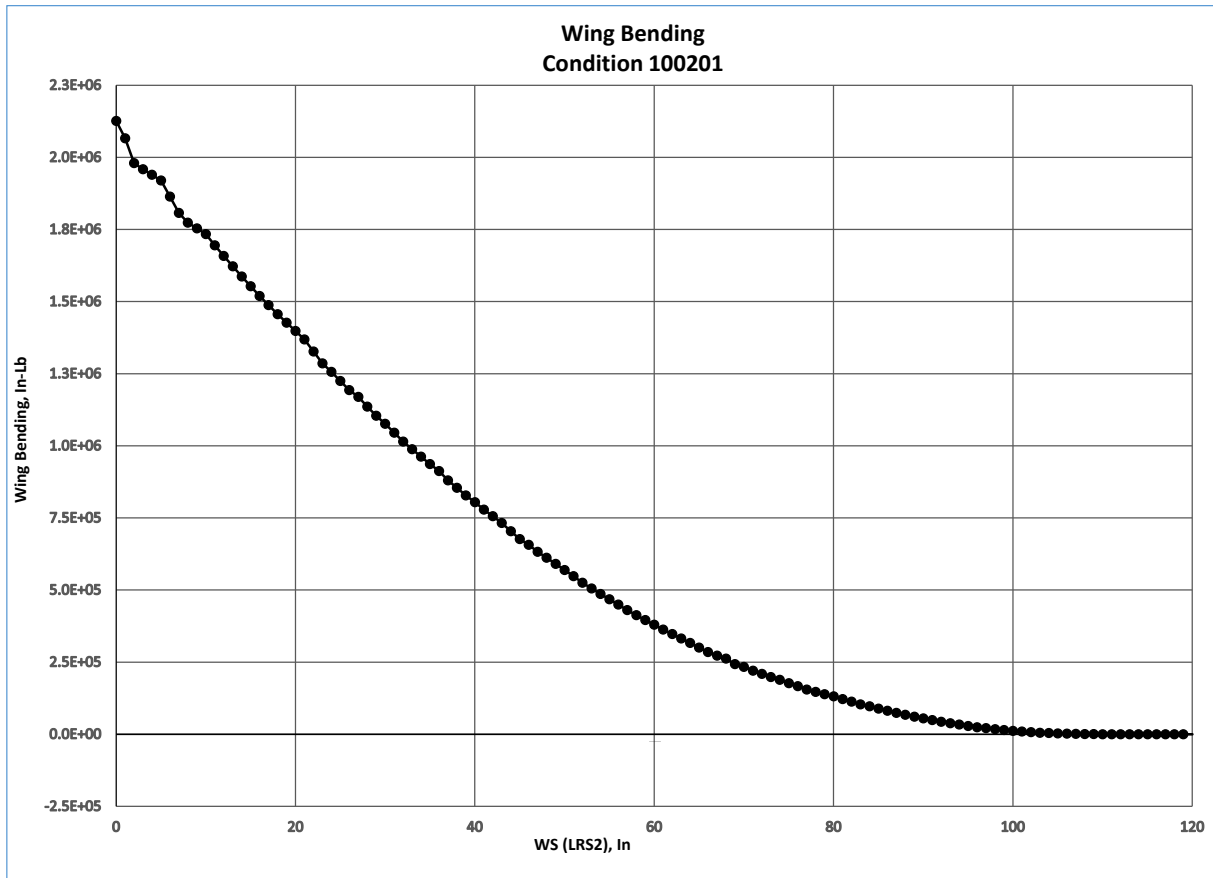


Figure H-10. Moment vs. Wing Station for Limit Load Case 100201 (Cond. 3)

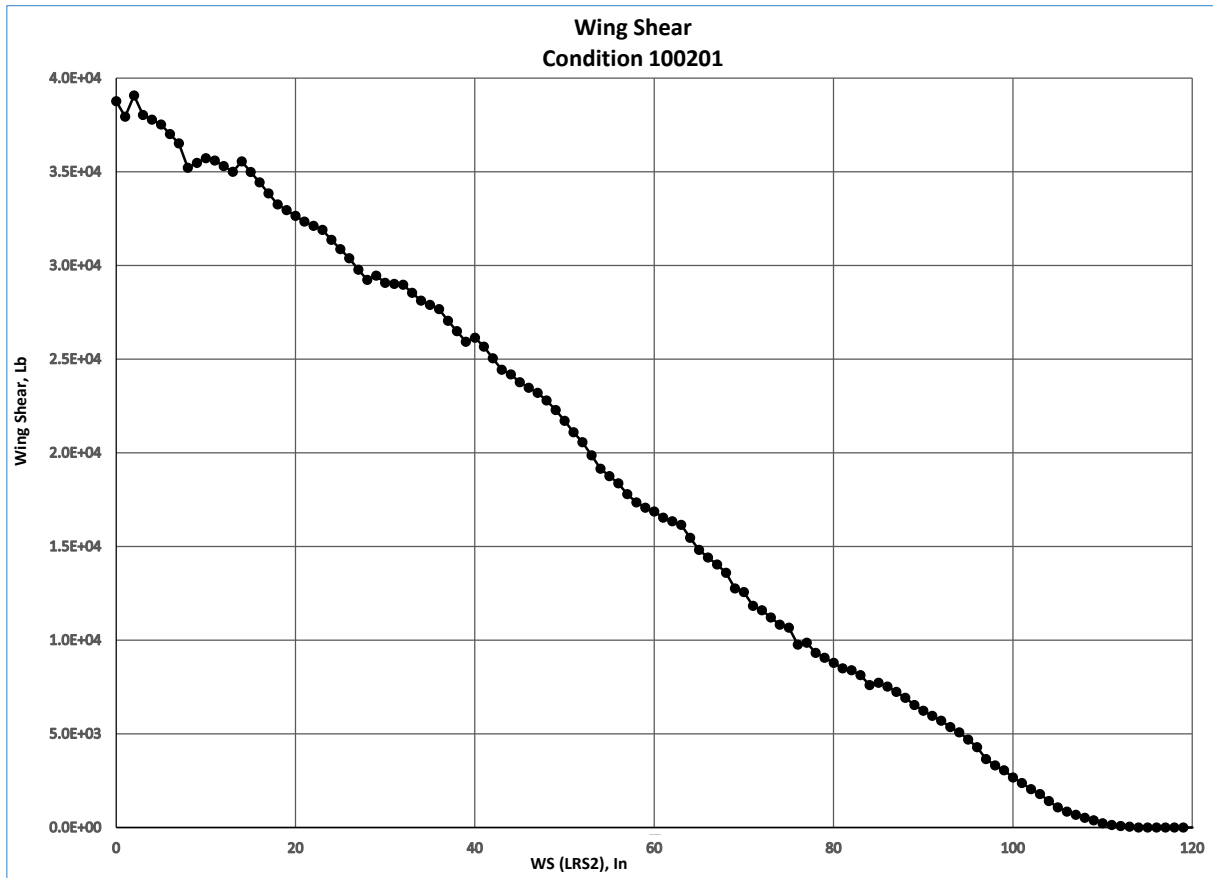


Figure H-11. Shear vs. Wing Station for Limit Load Case 100201 (Cond. 3)

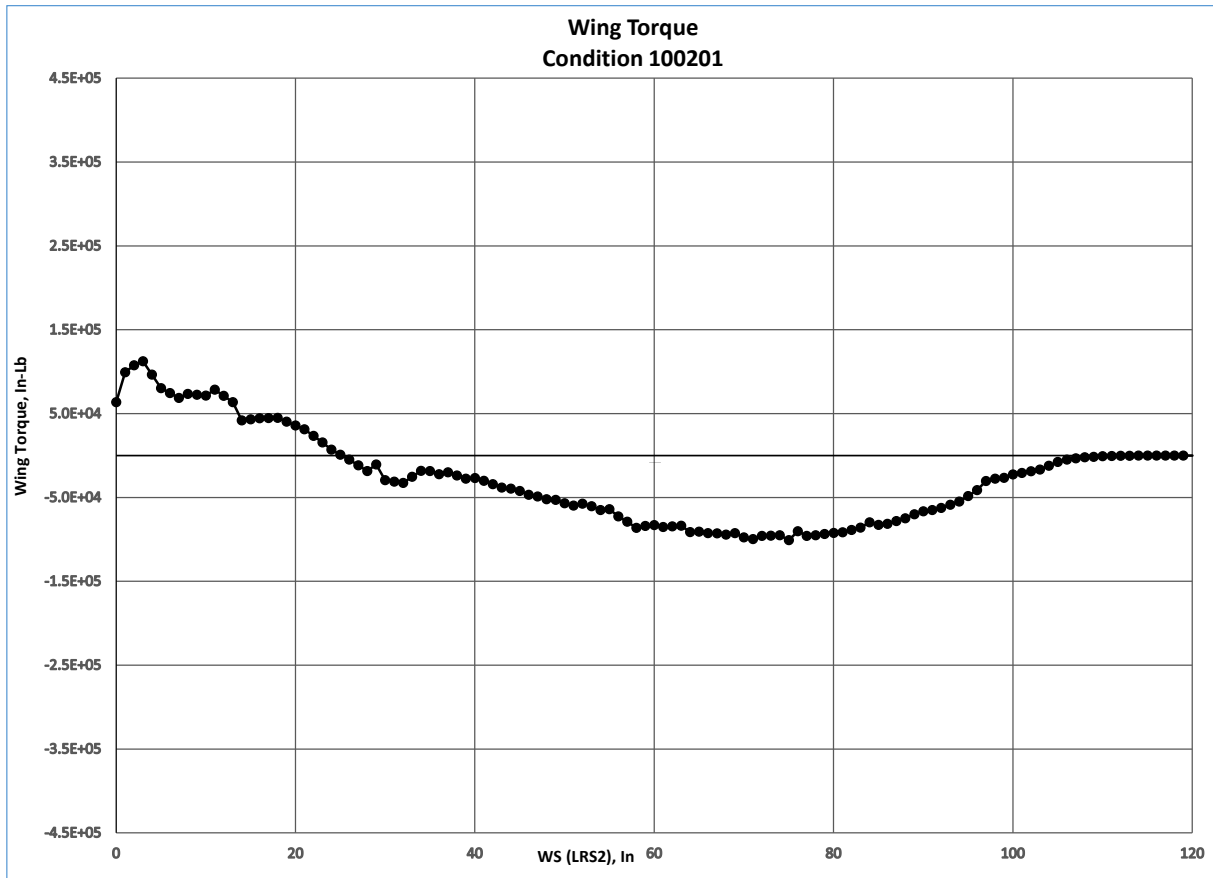


Figure H-12. Torque vs. Wing Station for Limit Load Case 100201 (Cond. 3)

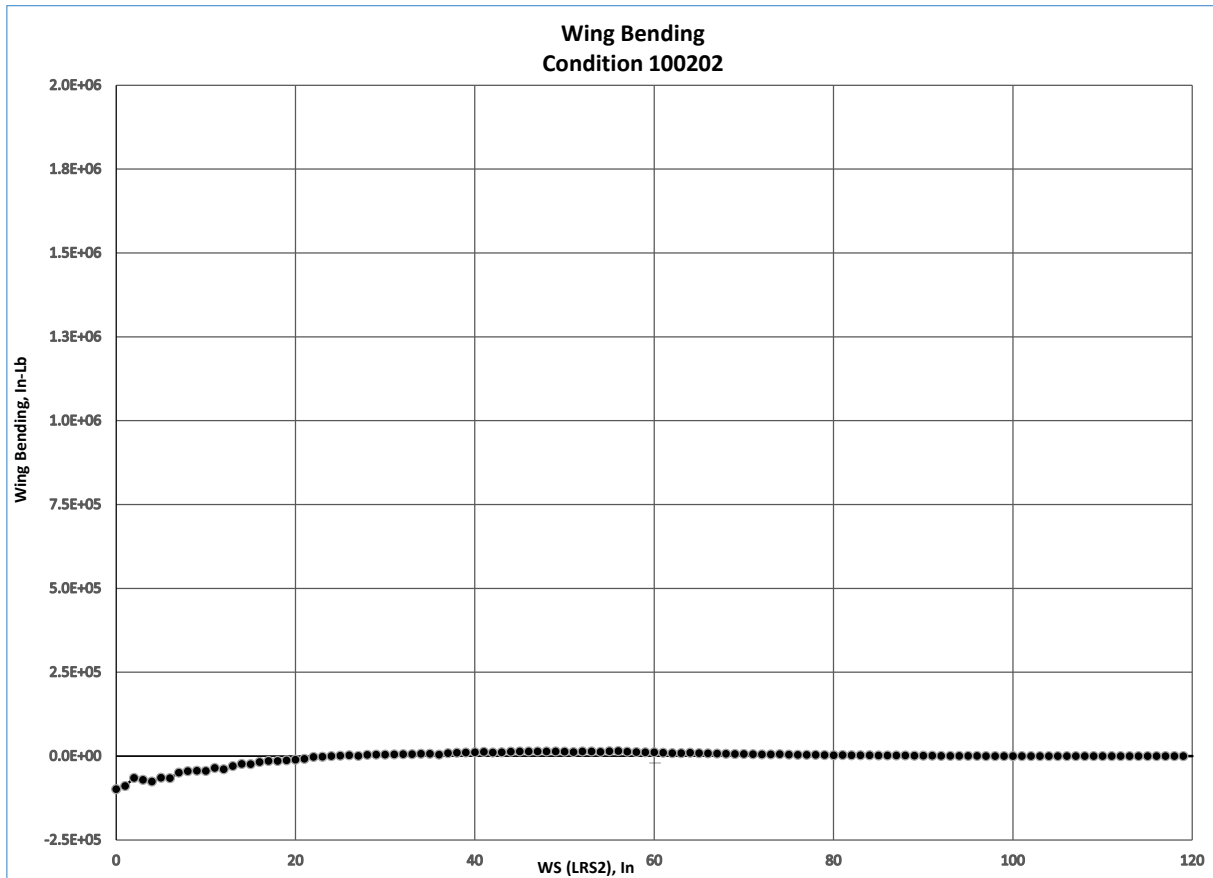


Figure H-13. Moment vs. Wing Station for Limit Load Case 100202 (Cond. 4)

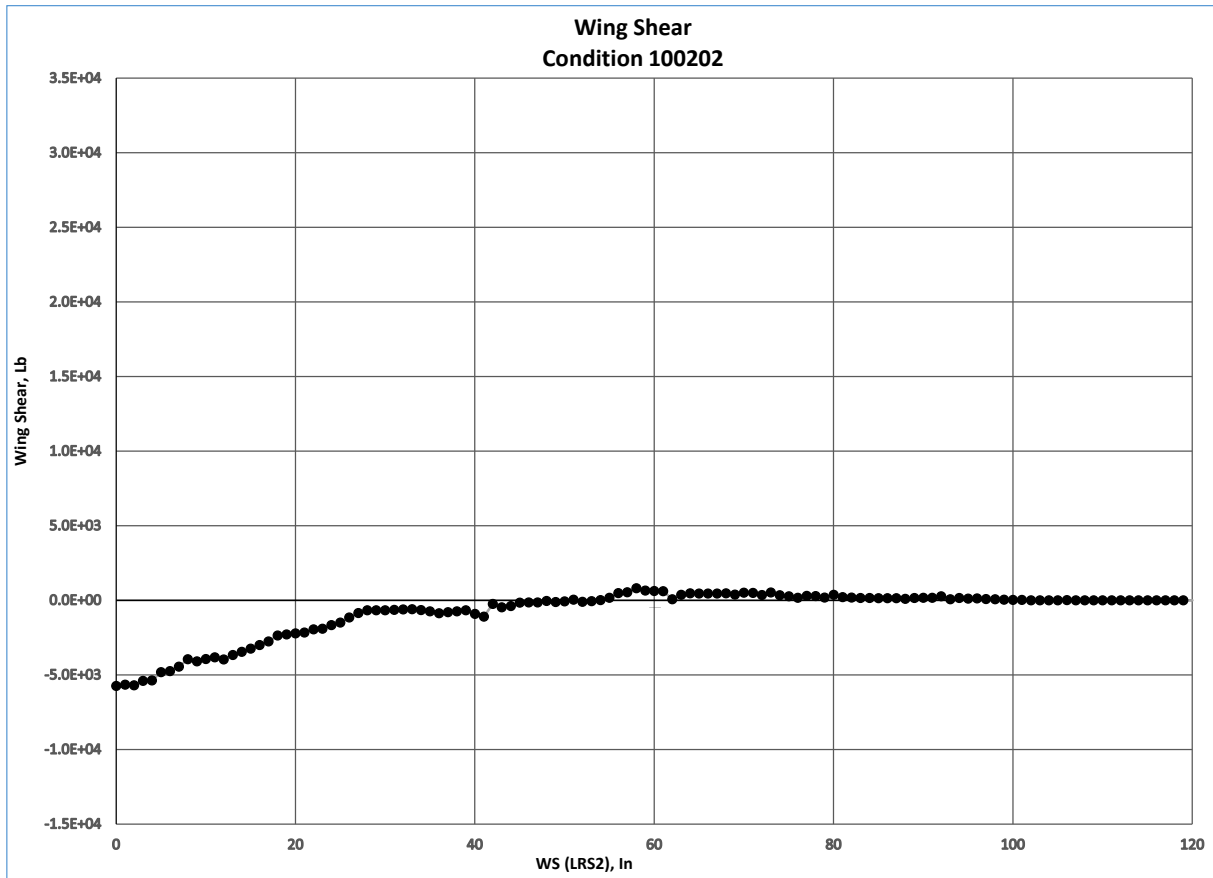


Figure H-14. Shear vs. Wing Station for Limit Load Case 100202 (Cond. 4)

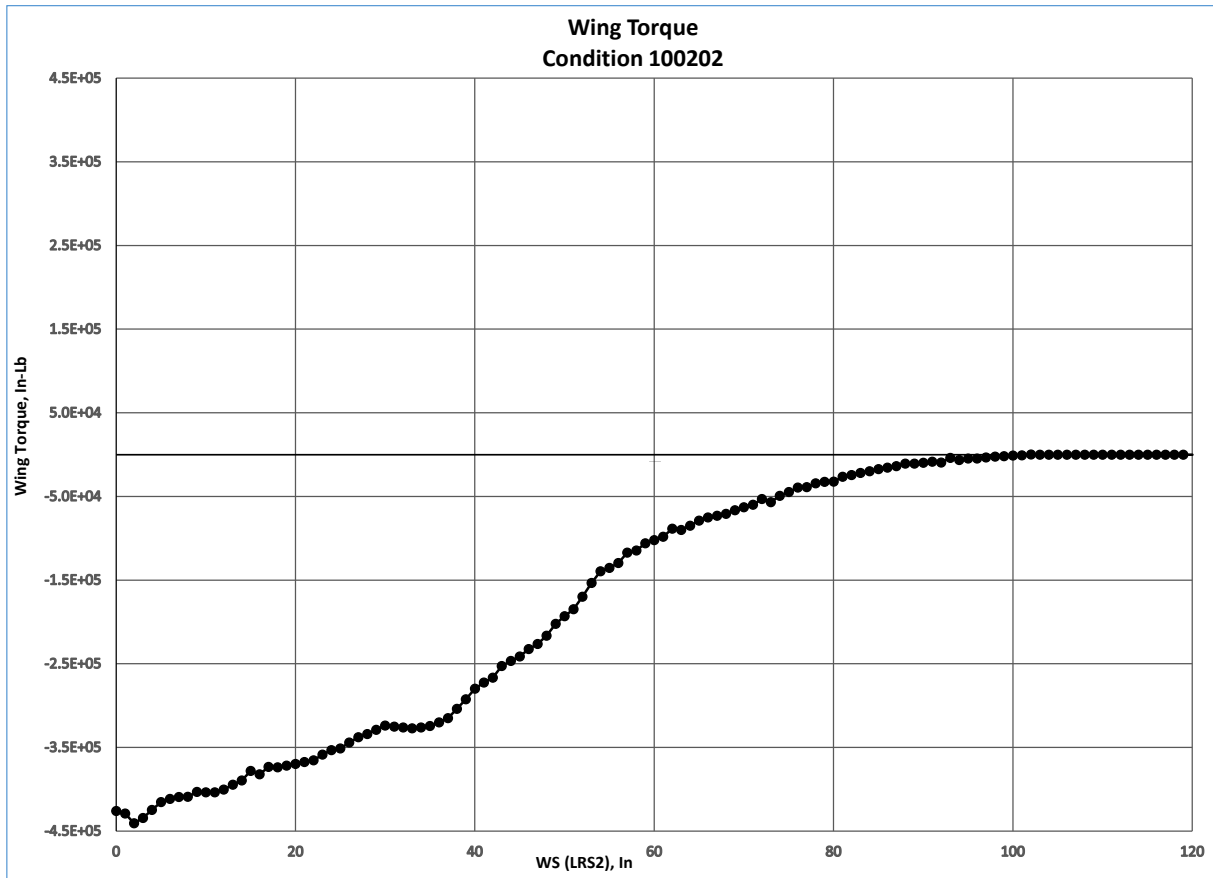


Figure H-15. Torque vs. Wing Station for Limit Load Case 100202 (Cond. 4)

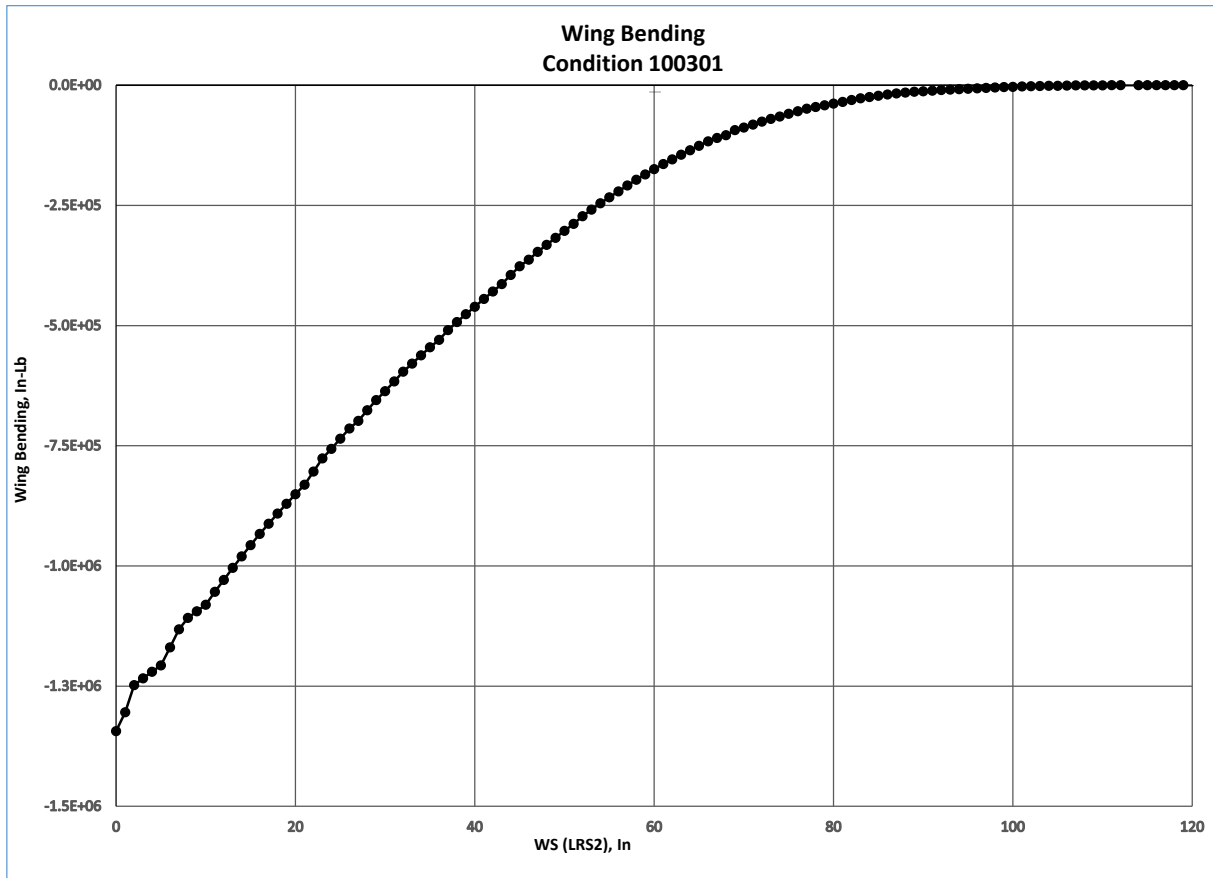


Figure H-16. Moment vs. Wing Station for Limit Load Case 100301 (Cond. 5)

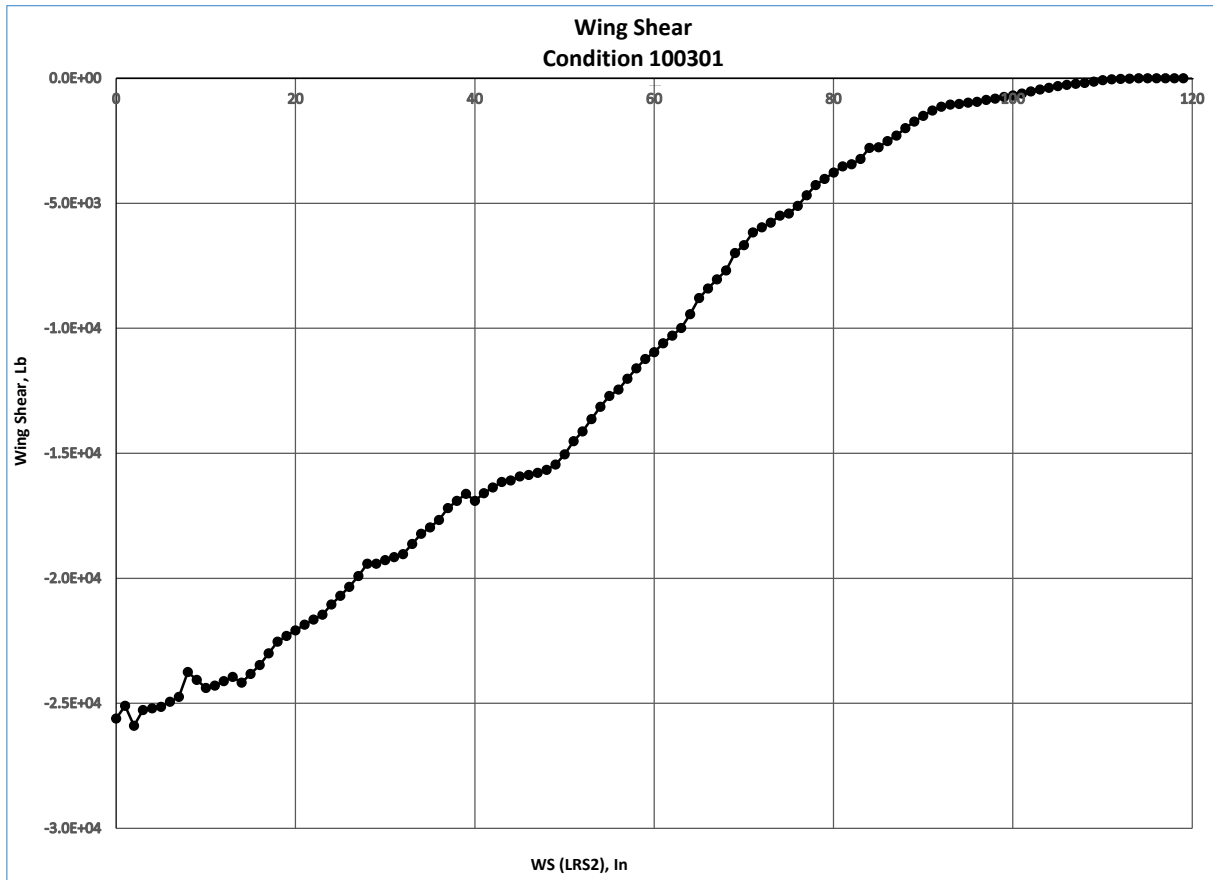


Figure H-17. Shear vs. Wing Station for Limit Load Case 100301 (Cond. 5)

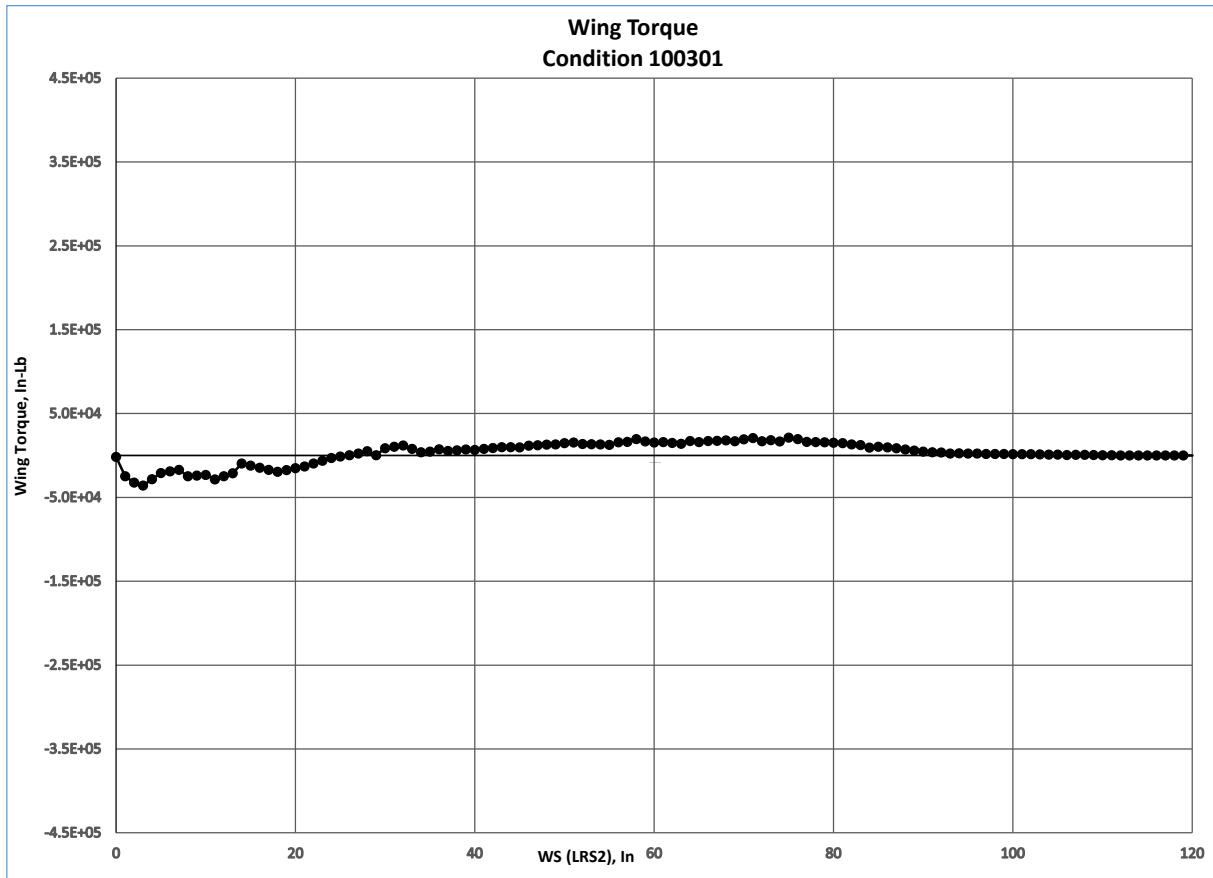


Figure H-18. Torque vs. Wing Station for Limit Load Case 100301 (Cond. 5)

The deflected wing shapes, along with maximum wing displacement at the wing tip, for each of the five unique limit load cases are shown in Figure H-19 through Figure H-23.

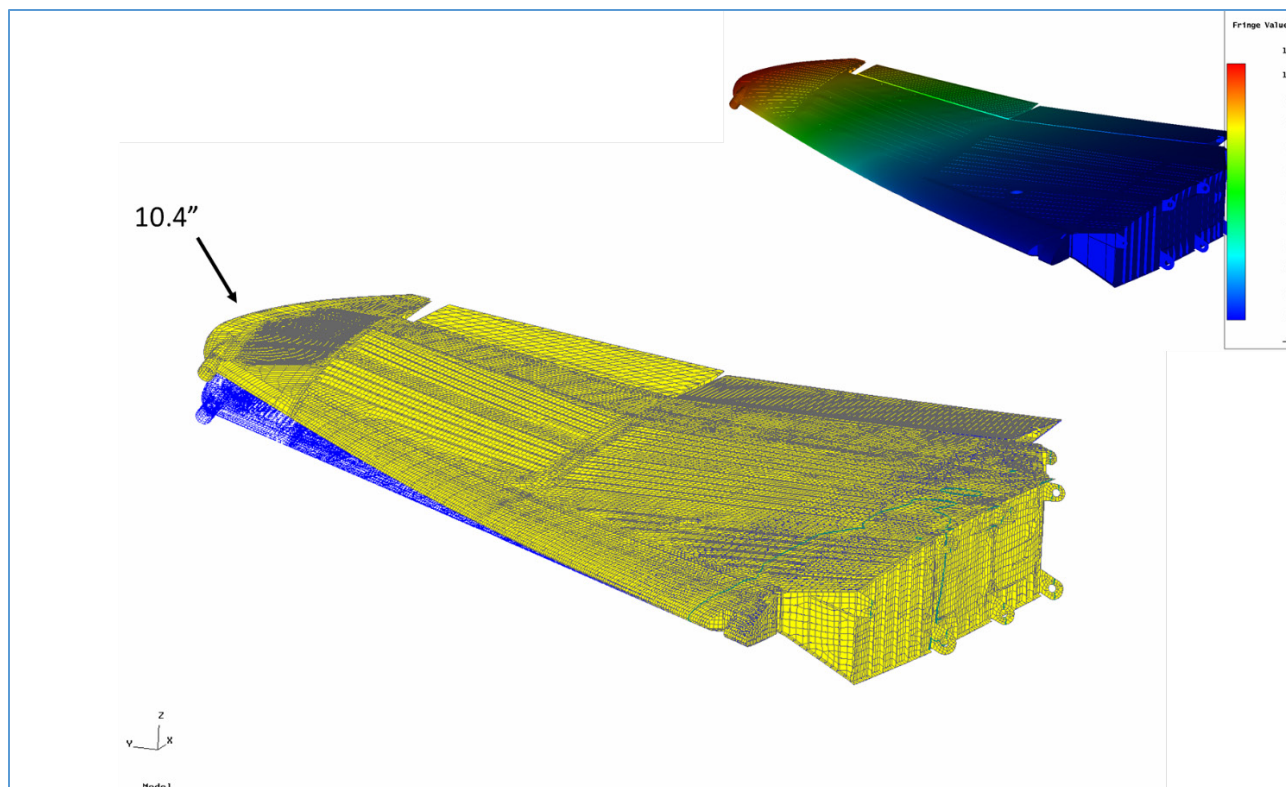


Figure H-19. Wing Displacement for Limit Load Case 100101 (Cond. 1)

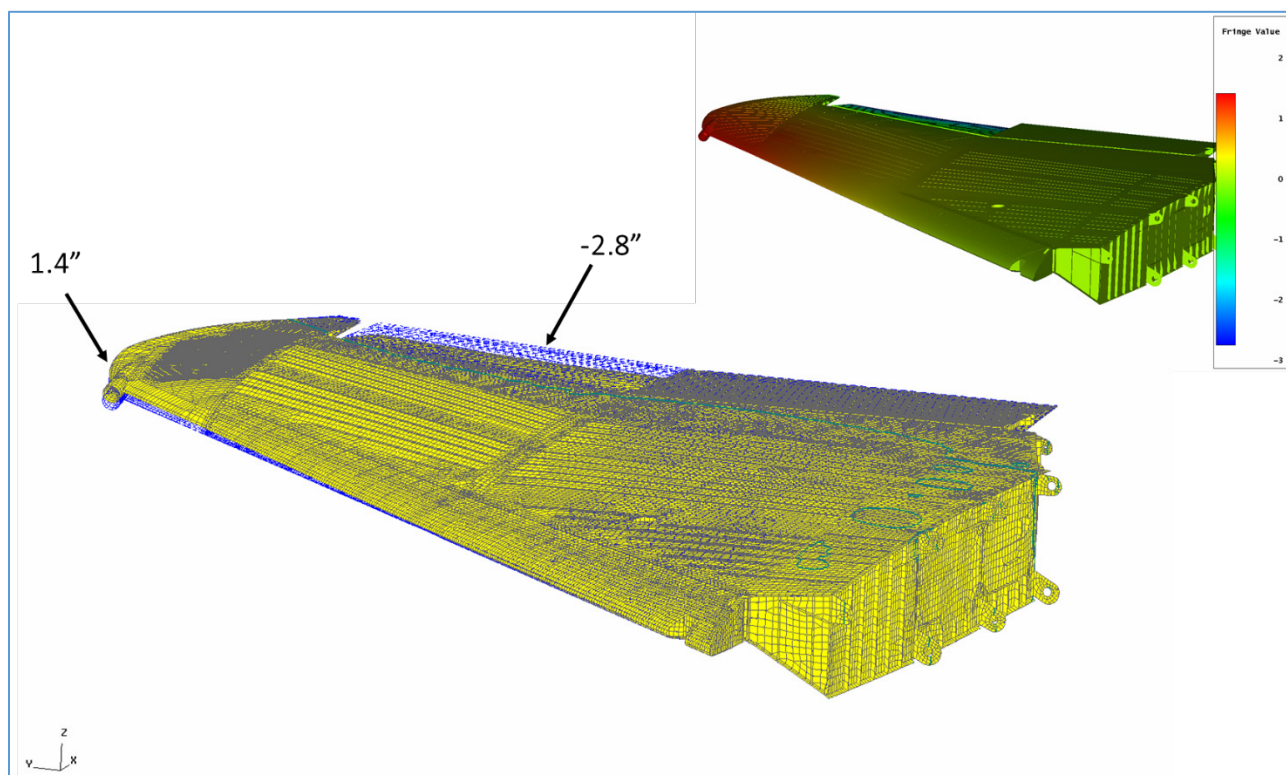


Figure H-20. Wing Displacement for Limit Load Case 100102 (Cond. 2)

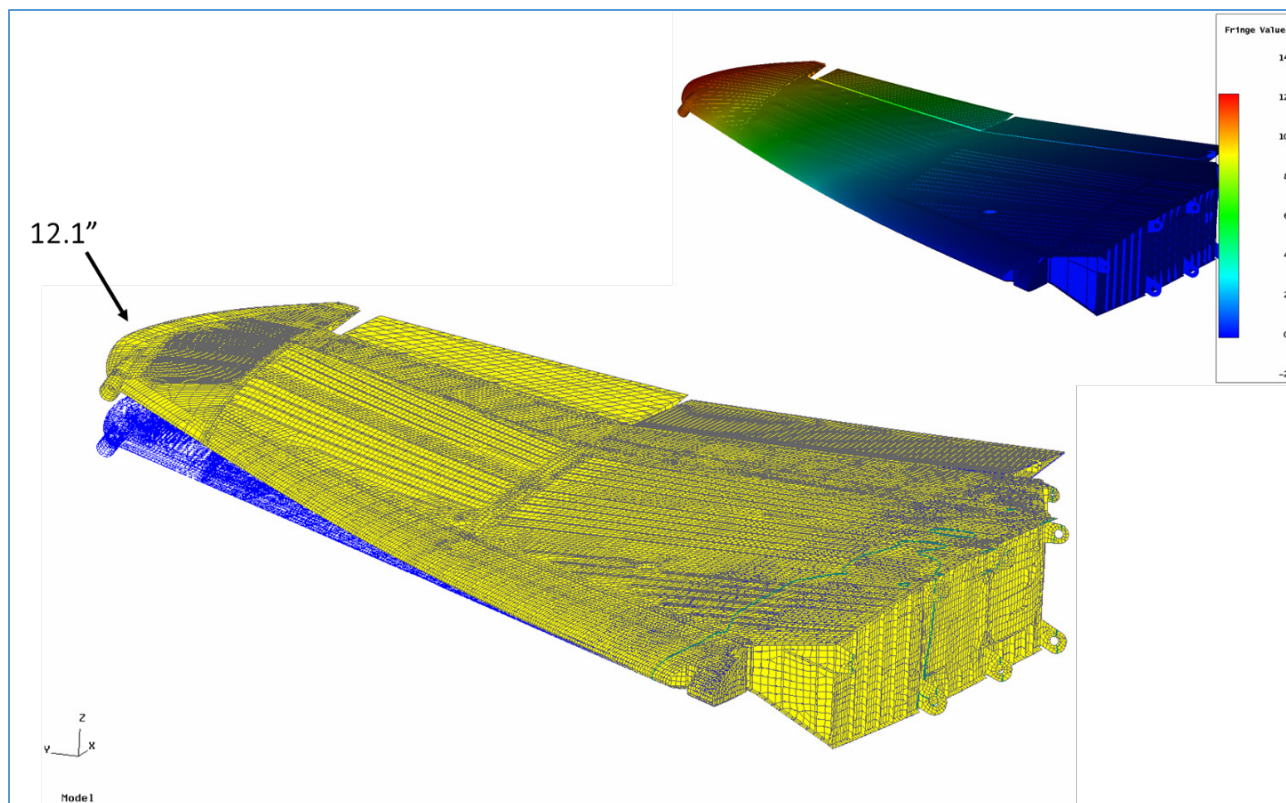


Figure H-21. Wing Displacement for Limit Load Case 100201 (Cond. 3)

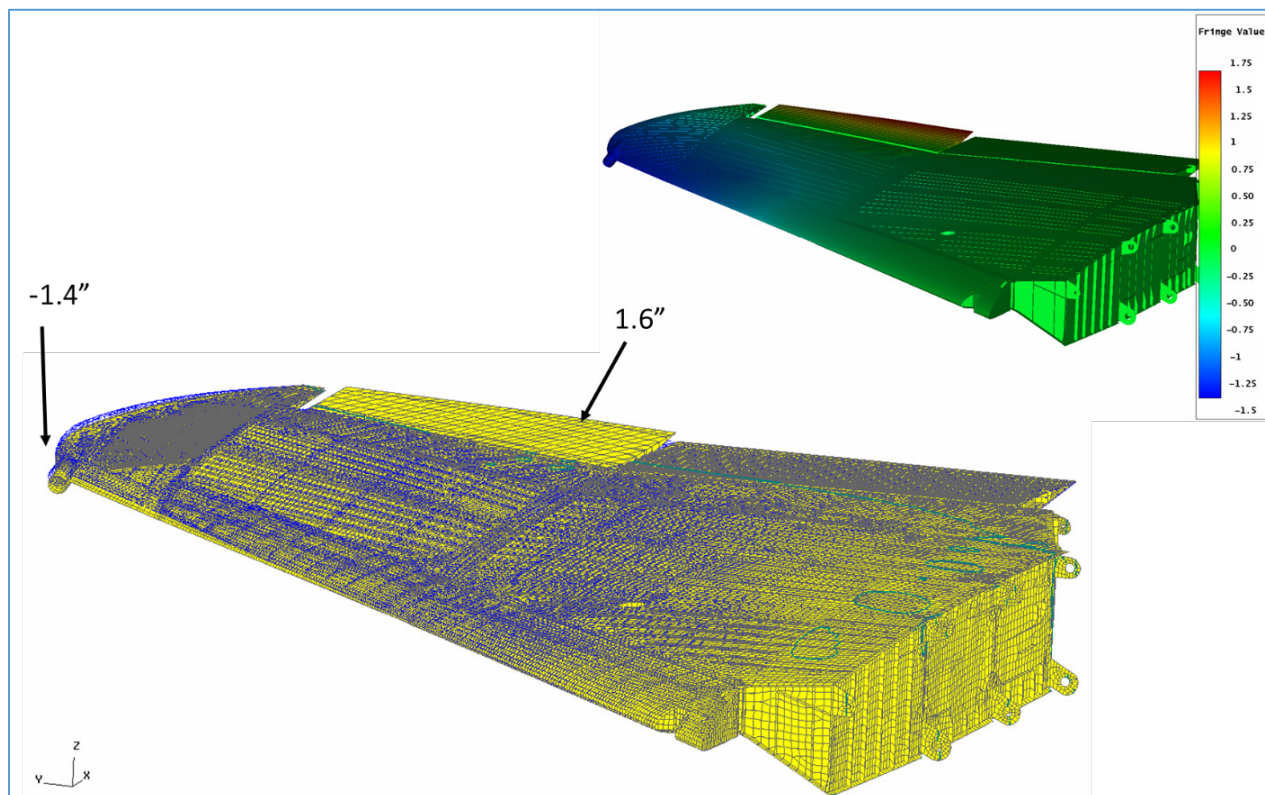


Figure H-22. Wing Displacement for Limit Load Case 100202 (Cond. 4)

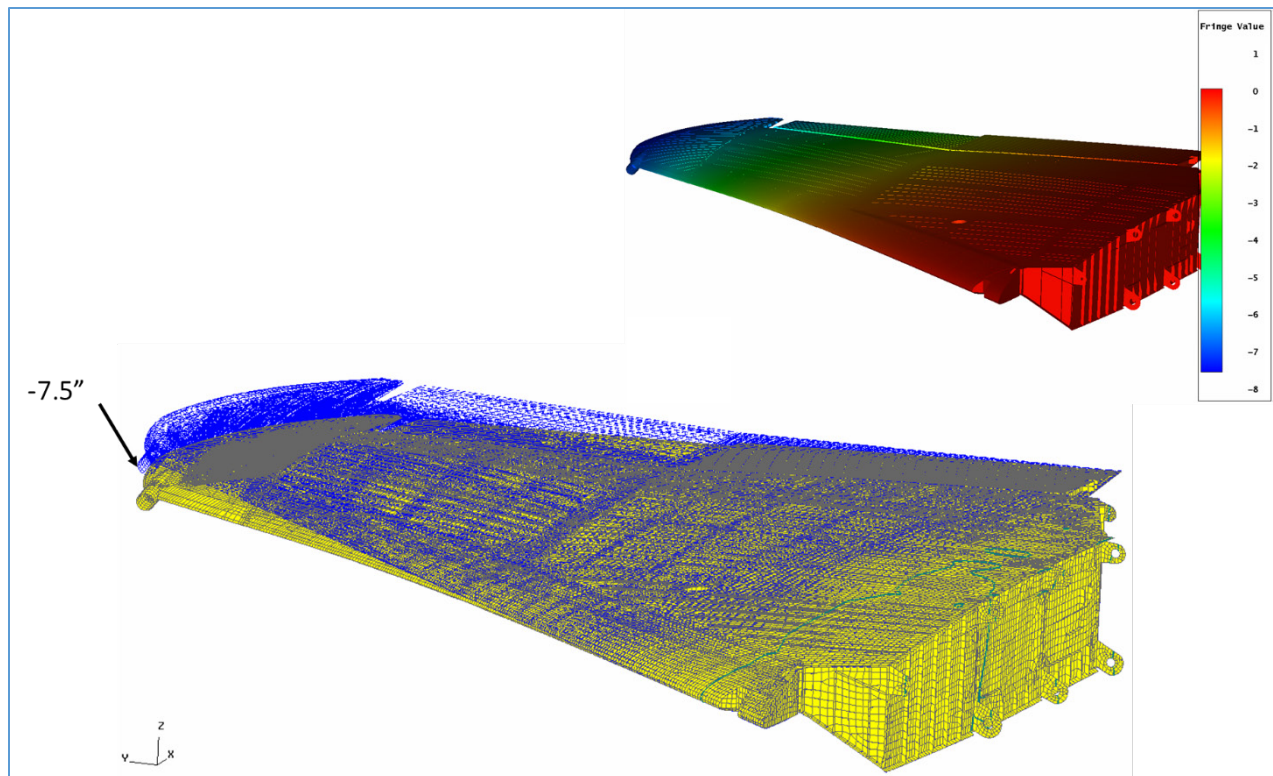


Figure H-23. Wing Displacement for Limit Load Case 100301 (Cond. 5)

Actuator Loads

As shown in Figure H-24, the loading apparatus will consist of thirteen discrete load actuators. Each actuator will be attached to a set of anywhere from three to six load pads, through a whiffle tree (not shown). The load pads will be bonded to the upper skin of the test article. AFRL/RQVS will be responsible for the design and installation of the load pads and the whiffle trees. (Note that jacks 11, 12 and 13 are exceptions in that they are connected directly to the aileron). As required by AFRL, this wing loading methodology is based on the tension/tension test approach.

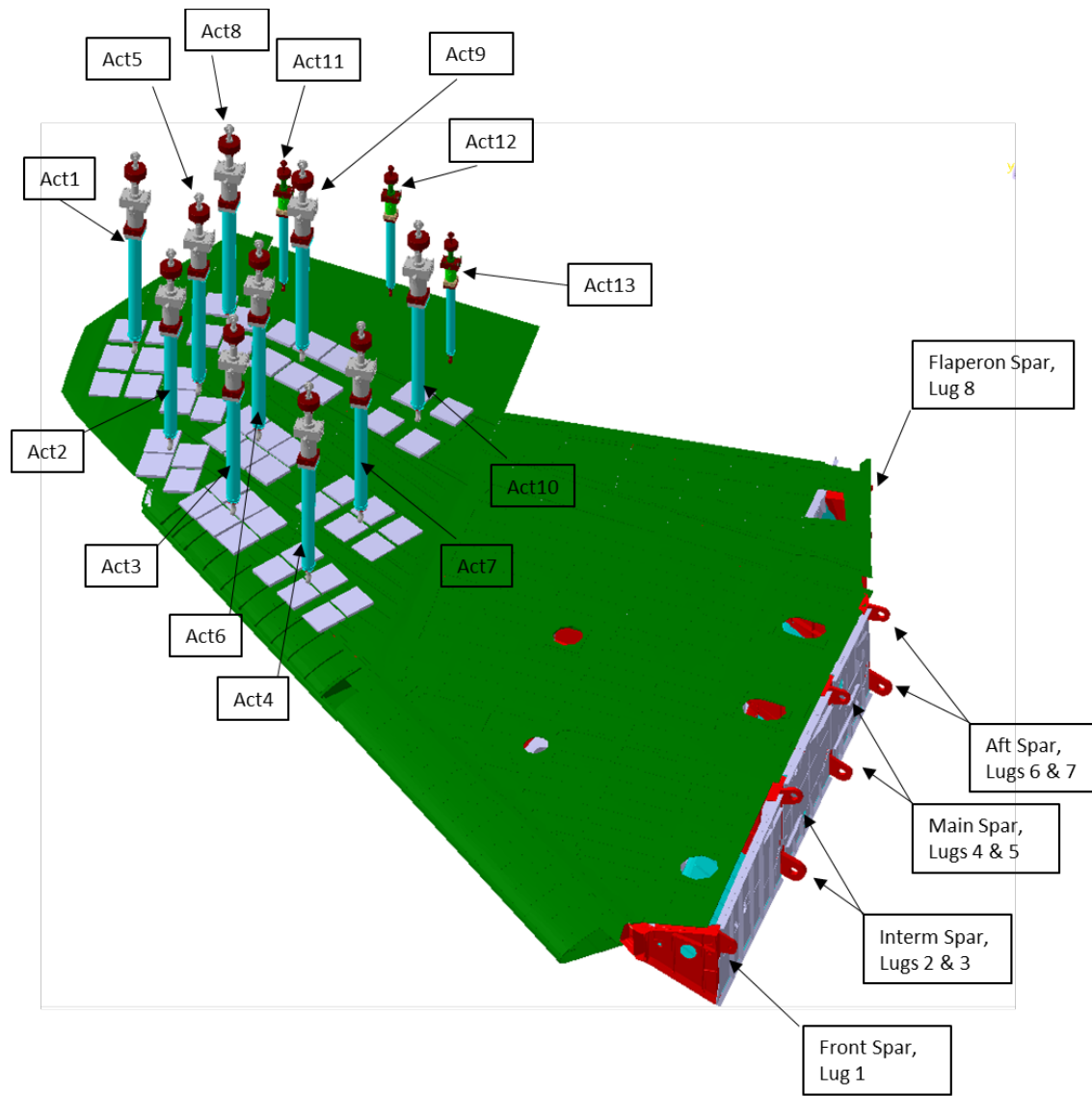


Figure H-24. ADT Test Article with Load Jacks in Place

A plan view of the general arrangement of the actuators and load pads, together with the actuator center of pressure locations (FS, BL, WL), and load vectors (direction cosines) are given in Figure H-25.

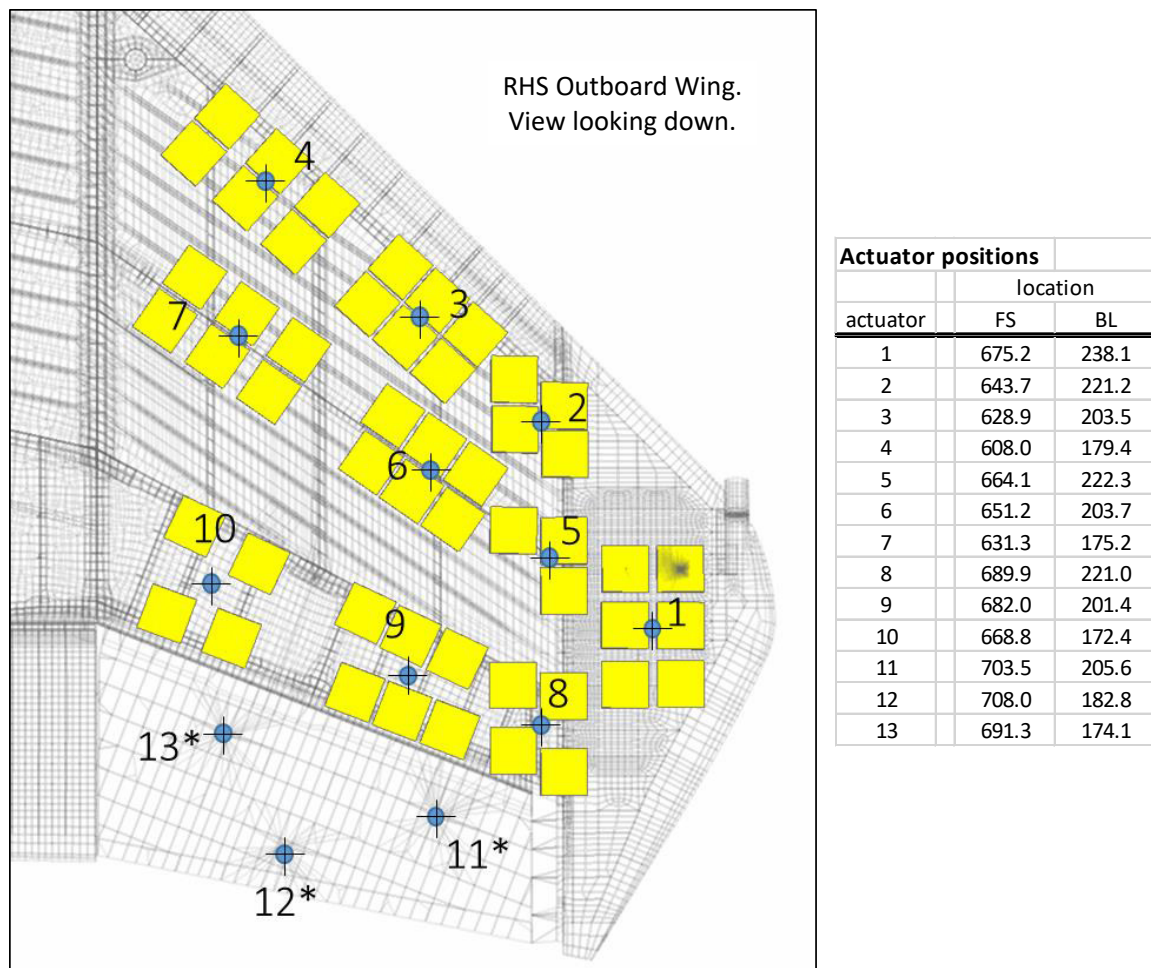


Figure H-25. Load Pad Configuration and FS-BL Coordinates (in.) For Load Actuators

The jack loads for each of the limit load cases are given in Table H-1. The minimum and maximum load and displacement (+and -) per actuator zone are given in Table H-2. The individual pad locations (FS, BL, WL) and loads are given in Table H-3.

Table H-1. Jack Loads for Limit Cases

actuator	location			limit load cases (jack loads are for load set Y003)								spectrum cases	
ID	FS	BL	WL ^[1]	100101	100102	100201	100202	100301	100302	100401	100402	min	max
1	675.2	238.1	127.8	3113	169	3075	0	-1088	-2644	-1088	863	-2198	2410
2	643.7	221.2	127.2	3087	1813	3185	-245	-1617	-3283	-1617	2058	-2755	3461
3	628.9	203.5	128.1	4557	2793	6248	-4631	-1838	-4337	-1838	3087	-3610	5198
4	608.0	179.4	129.2	4263	3087	6248	-5145	-1838	-4190	-1838	3087	-3968	5222
5	664.1	222.3	128.6	2756	919	2499	-698	-3510	-147	-3510	882	-1116	2560
6	651.2	203.7	129.4	5807	1544	4998	-1066	-7056	-294	-7056	1838	-2244	5095
7	631.3	175.2	130.5	2205	0	4998	0	-6615	-294	-6615	1838	-2111	3674
8	689.9	221.0	128.4	1519	0	3430	0	0	4802	0	-1421	-9	3798
9	682.0	201.4	128.8	2279	-735	2205	368	-882	0	-882	-2352	-266	1753
10	668.8	172.4	129.6	1372	-1201	1666	3234	-588	0	-588	-2205	-707	3464
11	703.5	205.6	127.6	73	-1464	0	439	-146	1464	-146	-615	-1137	1144
12	708.0	182.8	127.2	62	-1241	0	745	-124	323	-124	-521	-964	594
13	691.3	174.1	128.3	67	-1330	0	1330	-200	346	-200	-559	-1033	1061
[1] Water line values are on OML from the FE model													

Table H-2a. Up-bend Max Actuator Displacements Each Actuator Zone

Actuator ID	100101			100102			100201			100202			Spectrum Case Max Displacement		
	X	Y	Z	X	Y	Z	X	Y	Z	X	Y	Z	X	Y	Z
1	-0.06	0.02	8.86	0.02	-0.01	0.79	-0.07	0.02	10.35	-0.02	0.01	-0.88	-0.06	0.02	7.29
2	-0.03	0.09	6.54	-0.01	0.02	1.04	-0.03	0.11	7.65	0.00	-0.02	-1.05	-0.02	0.07	5.24
3	-0.04	0.05	4.72	-0.01	0.01	0.84	-0.04	0.06	5.60	0.01	-0.02	-0.95	-0.03	0.04	3.83
4	-0.03	0.00	2.66	-0.01	0.00	0.53	-0.03	0.00	3.21	0.01	-0.01	-0.63	-0.02	0.00	2.20
5	-0.07	-0.03	7.23	0.02	-0.01	0.73	-0.08	-0.04	8.46	-0.02	0.01	-0.81	-0.07	-0.02	5.92
6	-0.07	-0.05	5.38	0.02	-0.01	0.62	-0.07	-0.05	6.32	-0.01	0.01	-0.70	-0.06	-0.03	4.39
7	-0.05	-0.07	2.96	0.01	-0.01	0.39	-0.06	-0.08	3.55	0.00	0.01	-0.47	-0.04	-0.06	2.44
8	-0.06	0.00	7.87	0.02	-0.02	0.21	-0.07	0.00	9.28	-0.02	0.02	-0.41	-0.05	0.00	6.68
9	-0.05	-0.04	6.04	0.02	-0.02	0.08	-0.06	-0.05	7.10	-0.02	0.02	-0.25	-0.05	-0.03	5.13
10	-0.03	-0.06	3.57	0.01	-0.01	0.05	-0.04	-0.07	4.23	-0.01	0.01	-0.10	-0.03	-0.04	3.07
11	-0.02	0.08	6.99	0.06	-0.03	-1.07	-0.02	0.09	8.19	-0.03	0.01	0.42	-0.02	0.07	6.17
12	0.00	0.10	5.33	0.01	-0.01	-2.08	0.00	0.11	6.18	0.00	0.01	1.22	0.00	0.08	4.98
13	-0.02	0.01	4.22	0.08	-0.02	-0.84	-0.02	0.01	4.95	-0.05	0.02	0.50	-0.03	0.01	3.81

Table H-2b. Down-bend Min Actuator Displacements Each Actuator Zone

Actuator ID	100301			100302			100401			100402			Spectrum Case Min Displacement		
	X	Y	Z	X	Y	Z	X	Y	Z	X	Y	Z	X	Y	Z
1	0.03	-0.02	-6.42	-0.03	0.01	-1.19	0.03	-0.02	-6.42	0.02	-0.01	0.97	-0.01	0.00	-2.50
2	0.02	-0.06	-4.85	0.01	-0.04	-1.56	0.02	-0.06	-4.85	-0.01	0.03	1.23	0.01	-0.04	-2.33
3	0.02	-0.03	-3.56	0.01	-0.02	-1.24	0.02	-0.03	-3.56	-0.01	0.02	0.99	0.01	-0.02	-1.78
4	0.02	0.00	-2.05	0.01	0.00	-0.79	0.02	0.00	-2.05	-0.01	0.00	0.63	0.01	0.00	-1.07
5	0.04	0.02	-5.36	-0.03	0.02	-1.08	0.04	0.02	-5.36	0.03	-0.01	0.89	-0.01	0.02	-2.15
6	0.04	0.03	-4.07	-0.02	0.01	-0.94	0.04	0.03	-4.07	0.02	-0.01	0.76	0.00	0.02	-1.71
7	0.04	0.05	-2.30	-0.01	0.02	-0.63	0.04	0.05	-2.30	0.00	-0.01	0.50	0.01	0.02	-1.03
8	0.03	0.00	-5.69	-0.03	0.02	-0.30	0.03	0.00	-5.69	0.02	-0.02	0.32	0.00	0.01	-1.84
9	0.03	0.03	-4.44	-0.03	0.01	-0.31	0.03	0.03	-4.44	0.02	-0.02	0.19	0.00	0.01	-1.46
10	0.02	0.04	-2.70	-0.01	0.01	-0.31	0.02	0.04	-2.70	0.01	-0.01	0.14	0.00	0.02	-0.93
11	0.02	-0.06	-5.13	-0.03	0.01	0.61	0.02	-0.06	-5.13	0.02	-0.01	-0.45	0.00	-0.02	-1.31
12	0.00	-0.07	-4.03	0.00	0.00	1.01	0.00	-0.07	-4.03	0.00	0.00	-1.00	0.00	-0.02	-0.83
13	0.02	-0.01	-3.20	-0.04	0.00	0.27	0.02	-0.01	-3.20	0.04	-0.01	-0.37	-0.01	0.00	-0.86

Table H-3. Pad Locations and Loads for Minimum and Maximum Actuator Loads

actuator	Load Pad	location			limit load cases (jack loads are for load set Y003) ^[1]								spectrum cases	
		FS	BL	WL ^[2]	100101	100102	100201	100202	100301	100302	100401	100402	min	max
1	1	666.4	242.2	126.7	519	28	513	0	-181	-441	-181	144	-366.3	401.7
	2	666.4	234.0	127.7	519	28	513	0	-181	-441	-181	144	-366.3	401.7
	3	674.9	242.3	127.4	519	28	513	0	-181	-441	-181	144	-366.3	401.7
	4	674.8	233.9	128.1	519	28	513	0	-181	-441	-181	144	-366.3	401.7
	5	683.6	242.3	127.7	519	28	513	0	-181	-441	-181	144	-366.3	401.7
	6	683.7	233.9	128.2	519	28	513	0	-181	-441	-181	144	-366.3	401.7
2	1	641.9	224.8	126.4	772	453	796	-61	-404	-821	-404	515	-688.8	865.3
	2	637.9	217.4	127.1	772	453	796	-61	-404	-821	-404	515	-688.8	865.3
	3	649.1	224.9	127.4	772	453	796	-61	-404	-821	-404	515	-688.8	865.3
	4	645.4	217.5	127.9	772	453	796	-61	-404	-821	-404	515	-688.8	865.3
3	1	631.2	211.5	127.2	760	466	1041	-772	-306	-723	-306	515	-601.7	866.3
	2	626.1	205.9	127.5	760	466	1041	-772	-306	-723	-306	515	-601.7	866.3
	3	621.1	200.4	127.7	760	466	1041	-772	-306	-723	-306	515	-601.7	866.3
	4	636.7	206.7	128.4	760	466	1041	-772	-306	-723	-306	515	-601.7	866.3
	5	631.7	201.1	128.7	760	466	1041	-772	-306	-723	-306	515	-601.7	866.3
	6	626.7	195.4	128.9	760	466	1041	-772	-306	-723	-306	515	-601.7	866.3
4	1	611.9	189.3	128.3	711	515	1041	-858	-306	-698	-306	515	-661.3	870.3
	2	605.3	182.1	128.6	711	515	1041	-858	-306	-698	-306	515	-661.3	870.3
	3	598.5	174.5	128.9	711	515	1041	-858	-306	-698	-306	515	-661.3	870.3
	4	617.4	184.4	129.4	711	515	1041	-858	-306	-698	-306	515	-661.3	870.3
	5	610.8	177.1	129.7	711	515	1041	-858	-306	-698	-306	515	-661.3	870.3
	6	604.0	169.4	129.9	711	515	1041	-858	-306	-698	-306	515	-661.3	870.3
5	1	662.1	224.8	128.4	919	306	833	-233	-1170	-49	-1170	294	-372	853
	2	660.6	217.3	128.8	919	306	833	-233	-1170	-49	-1170	294	-372	853
	3	669.6	224.8	128.7	919	306	833	-233	-1170	-49	-1170	294	-372	853
6	1	652.1	211.6	128.9	967.8	257.3	833.0	-177.6	-1176.0	-49.0	-1176.0	306.3	-374.0	849.2
	2	647.8	205.5	129.2	967.8	257.3	833.0	-177.6	-1176.0	-49.0	-1176.0	306.3	-374.0	849.2
	3	643.4	199.2	129.5	967.8	257.3	833.0	-177.6	-1176.0	-49.0	-1176.0	306.3	-374.0	849.2
	4	658.9	208.2	129.3	967.8	257.3	833.0	-177.6	-1176.0	-49.0	-1176.0	306.3	-374.0	849.2
	5	654.7	202.1	129.5	967.8	257.3	833.0	-177.6	-1176.0	-49.0	-1176.0	306.3	-374.0	849.2
	6	650.4	195.9	129.8	967.8	257.3	833.0	-177.6	-1176.0	-49.0	-1176.0	306.3	-374.0	849.2
7	1	633.5	185.2	130.1	367.5	0.0	833.0	0.0	-1102.5	-49.0	-1102.5	306.3	-351.8	612.3
	2	628.1	177.4	130.4	367.5	0.0	833.0	0.0	-1102.5	-49.0	-1102.5	306.3	-351.8	612.3
	3	622.6	169.6	130.6	367.5	0.0	833.0	0.0	-1102.5	-49.0	-1102.5	306.3	-351.8	612.3
	4	639.8	180.7	130.3	367.5	0.0	833.0	0.0	-1102.5	-49.0	-1102.5	306.3	-351.8	612.3
	5	634.5	173.0	130.6	367.5	0.0	833.0	0.0	-1102.5	-49.0	-1102.5	306.3	-351.8	612.3
	6	629.1	165.2	130.8	367.5	0.0	833.0	0.0	-1102.5	-49.0	-1102.5	306.3	-351.8	612.3
8	1	685.4	224.8	128.5	253.2	0.0	571.7	0.0	0.0	800.3	0.0	-236.8	-1.5	633.0
	2	683.8	217.2	128.6	253.2	0.0	571.7	0.0	0.0	800.3	0.0	-236.8	-1.5	633.0
	3	696.8	224.9	128.0	253.2	0.0	571.7	0.0	0.0	800.3	0.0	-236.8	-1.5	633.0
	4	693.7	217.3	128.2	253.2	0.0	571.7	0.0	0.0	800.3	0.0	-236.8	-1.5	633.0
9	1	679.8	208.9	128.9	570	-184	551	92	-221	0	-221	-588	-66.5	438.3
	2	676.4	201.9	129.1	570	-184	551	92	-221	0	-221	-588	-66.5	438.3
	3	673.0	195.1	129.2	570	-184	551	92	-221	0	-221	-588	-66.5	438.3
	4	690.4	207.8	128.4	570	-184	551	92	-221	0	-221	-588	-66.5	438.3
	5	687.7	200.7	128.5	570	-184	551	92	-221	0	-221	-588	-66.5	438.3
	6	684.8	193.6	128.7	570	-184	551	92	-221	0	-221	-588	-66.5	438.3
10	1	665.6	179.3	129.7	228.7	-200.1	277.7	539.0	-98.0	0.0	-98.0	-367.5	-117.8	577.3
	2	660.0	169.6	130.0	228.7	-200.1	277.7	539.0	-98.0	0.0	-98.0	-367.5	-117.8	577.3
	3	676.7	175.1	129.2	228.7	-200.1	277.7	539.0	-98.0	0.0	-98.0	-367.5	-117.8	577.3
	4	673.0	165.4	129.4	228.7	-200.1	277.7	539.0	-98.0	0.0	-98.0	-367.5	-117.8	577.3
11	Same As FTA/6 Actuator 29													
12	Same As FTA/6 Actuator 27													
13	Same As FTA/6 Actuator 25													

[1] Actuator Loads are evenly distributed between the load Pads

[2] Water line values are on OML from the FE model

Reaction Loads

The ID and location (FS, BL, WL) for each of the eight wing to test frame attach lugs, as well as the reaction loads for each of the limit load cases are given in Table H-4.

Table H-4. Wing to Test Frame Attach Locations and Reaction Loads for Limit Load Cases

reaction	Spar	location			limit load cases (reaction loads are for load set Y003)								spectrum cases	
		FS	BL	WL	100101	100102	100201	100202	100301	100302	100401	100402	min	max
lug1-Fy	Front	509.5	58.5	131.4	-3012	1124	-3372	-1237	2235	-1093	2235	1084	-2924	366
lug1-Fz		509.5	58.5	131.4	10062	1065	12061	-1325	-7800	-1933	-7800	1425	-3366	8388
lug2-Fy	Interm	558.5	57.3	135.5	54590	15156	67258	-17905	-43319	-21593	-43319	17663	-25990	48391
lug2-Fz		558.5	57.3	135.5	5019	41	5883	-89	-3786	-354	-3786	176	-1279	4292
lug3-Fy		558.5	57.3	114.3	-56942	-17584	-70400	20660	45240	24517	45240	-20249	-51821	28464
lug3-Fz		558.5	57.3	114.3	-9335	-4547	-11877	5290	7614	5995	7614	-5085	-9757	6046
lug4-Fy	Main	595.9	56.3	133.9	87593	12997	105861	-15798	-68511	-21332	-68511	16395	-32491	72121
lug4-Fz		595.9	56.3	133.9	12093	1616	14502	-1956	-9334	-2671	-9334	2044	-4268	9955
lug5-Fy		595.9	56.3	112.9	-70995	-11897	-86159	14406	55805	19021	55805	-14797	-58141	27570
lug5-Fz		595.9	56.3	112.9	-21315	-3859	-25976	4664	16861	6089	16861	-4767	-17413	8560
lug6-Fy	Aft	626.9	55.7	132.5	81523	6622	98089	-8747	-63860	-14121	-63860	9769	-26412	68946
lug6-Fz		626.9	55.7	132.5	11248	1580	13502	-1913	-8681	-2576	-8681	1983	-4032	9235
lug7-Fy		626.9	55.7	112.0	-92757	-6419	-111278	8621	72408	14602	72409	-9866	-78686	29001
lug7-Fz		626.9	55.7	112.0	-37190	-2012	-44633	2855	29135	5313	29135	-3415	-31777	11291
lug8-Fz*	Flaperon	671.8	71.4	129.0	-1740	1761	-2014	-1855	1491	-1609	1491	1660	-2548	1083
* NOTE: reaction loads for flaperon spar lug pending fixture design. For a/c installation, lug carries z-direction load only.														

Tare Loads

The 15 reaction and 13 jack loads for support of the empty wing are given in Table H-5.

Table H-5. Tare Loads

Reaction	Spar	Load ^[1]		Actuator	Reaction
				ID	Load ^[1]
lug1-Fy	Front	-55		1	27
lug1-Fz		-5		2	14
lug2-Fy	Interm	-992		3	20
lug2-Fz		76		4	56
lug3-Fy		1088		5	15
lug3-Fz		357		6	22
lug4-Fy	Main	-1059		7	62
lug4-Fz		-44		8	19
lug5-Fy		936		9	9
lug5-Fz		370		10	78
lug6-Fy	Aft	-999		11	7
lug6-Fz		-41		12	14
lug7-Fy		1163		13	15
lug7-Fz		559			
lug8-Fz ^[2]	Flaperon	130			

[1]Reactions correspond to a T/A (including control surfaces) empty weight of 1755 Lbs.

[2] Reaction loads for flaperon spar lug pending fixture design. For a/c installation, lug carries z-direction load only.

Test Spectrum

The baseline test spectrum (BTS) was generated based on the probabilistic fatigue spectrum developed during Task Order 0001 of the ADT program [1]. It includes estimated ground and StS v1 [2] derived flight events arranged in physically meaningful flight segments, which in turn have been grouped into flights. The original TO1 spectrum was scaled to produce the estimated damage rates necessary to demonstrate an IAT system, and truncated in order to keep the test duration within a twelve month window. The resulting baseline test spectrum has 1001 flights (including one marker band flight), representing 1000 flight hours. The spectrum is written in the form of an event sequence in which the events are listed in sequential order, with all pertinent flight and sequence numbers, time values, integrated load values (M and T at both the wing root and at station 3), jack loads and control point stresses provided on a single line. The baseline

ADT fatigue test spectrum was delivered in the form of a single .csv file. A summary of the file and its contents is as follows:

ADT-TO2-JLSR6-MES

- 1000 flight hours
- 1001 flights (including marker band flight)
- 146779 end points (including 2480 marker band end points)
- Load set: ADT-TO2-R5-MES-20160603-S006
- Delivered in MSEXcel format, 50 columns of data
- Flight ID
- Flight load point (counter)
- Overall load point (counter)
- Jack load case description
- 13 jack loads
- 10 control point stresses
- Flight condition description
- Mission ID
- Cumulative flight time (minutes)
- 10 internal a/c loads
- 10 flight parameters

Sufficient information is given in this file (specifically mission type IDs, flight IDs, and flight segment descriptions) to allow construction of a modified test spectrum (MTS) as required by AFRL. It is understood that in order to simulate realistic IAT system operation with realistic aircraft usage variation, AFRL will re-sequence maneuvers within flights, re-sequence flights within the block, and will intermittently withhold FDR data during the execution of the test (in order to simulate missing flight data).

A moment vs. torque diagram for moment and torque at wing station 3 is shown in Figure H-26.

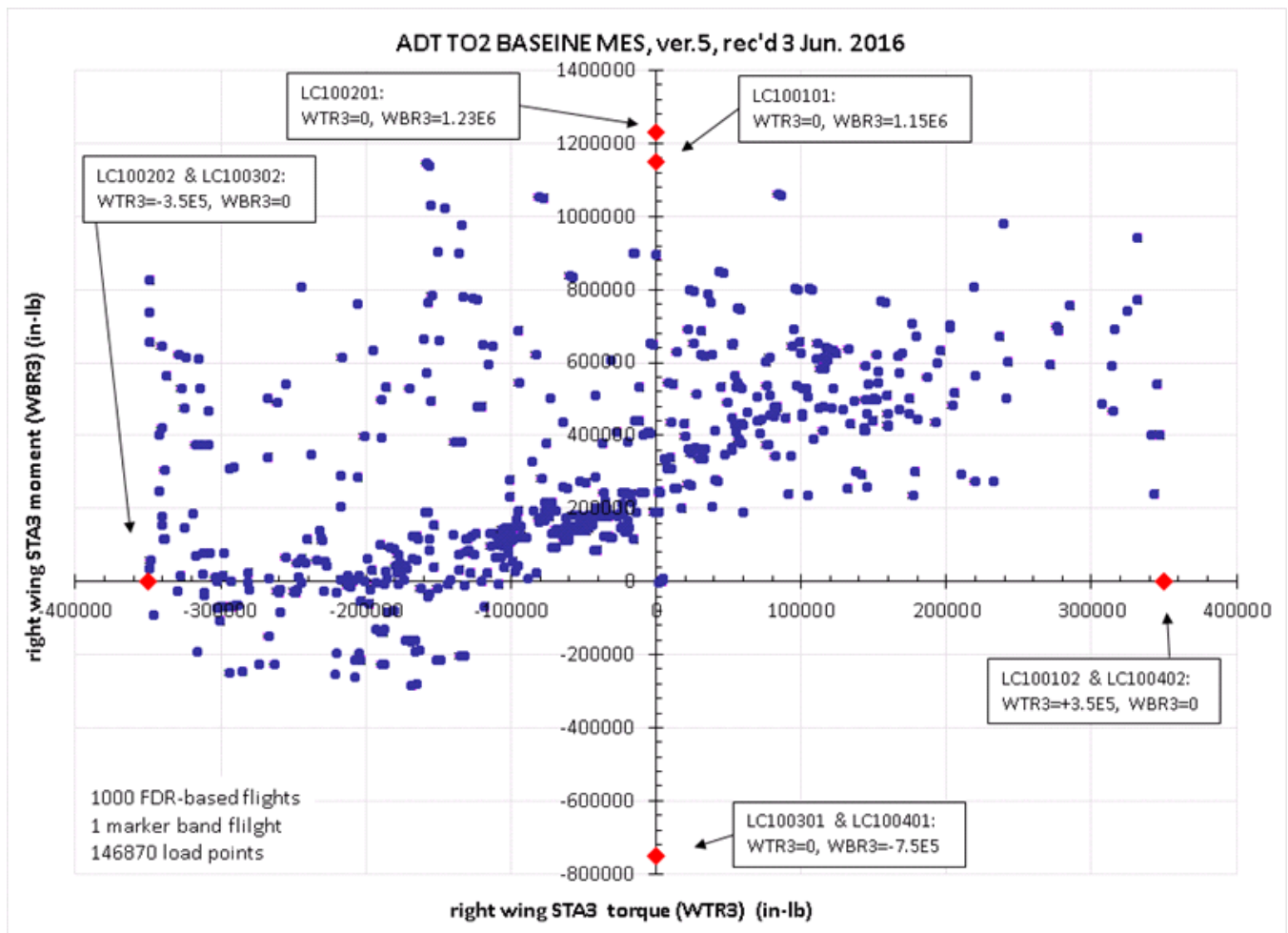


Figure H-26. Wing Sta.3 Moment vs. Torque Diagram for ver.5 baseline MES

Test Fixture

The test article will be mounted to a semi rigid test frame using the seven wing attachment lugs and one trailing edge shear link, as shown in Figure H-2. AFRL/RQVV will design and fabricate (or acquire) the test frame, the load actuators, the whiffletrees and the load pads. No attempt will be made in the design of the test fixture to simulate the aircraft fuselage stiffness.

The GE/LM team will define all actuator center of pressure locations and load vectors (direction cosines), as well as all pad locations. Pad locations will be defined either with mylar templates, or with suitable digital reference / indexing (subject to acceptance by AFRL/RQVS).

LIST OF SYMBOLS, ABBREVIATIONS, AND ACRONYMS

Acronym	Definition
ANN	Artificial Neural Network
ASTM	American Society for Testing and Materials
DOE	Design of Experiments
DTDH	Damage Tolerant Design Handbook
FE	Finite Element
FEM	Finite Element Method
FRD	Flight Recorder Data
GE	General Electric
GEBHM	GE's Bayesian Hybrid Modeling
IDACE	Intelligent Design and Analysis of Computer Experience
MCMC	Markov Chain Monte Carlo
MES	Master Event Sequence
NDI	Non-Destructive Inspection
P ² IAT	Prognostic and Probabilistic Individual Aircraft Tracking
PF	Particle Filter
POD	Probability of Detection
SFPOF	Single Flight Probability of Failure
UKF	Unscented Kalman Filter
WBR3	Wing Bending Right Side at Station 3
WTR3	Wing Torque Right Side at Station 3